Adama Science and Technology University

Research Affairs Office

Proceeding of the Third International Research Symposium

"*Emerging Technologies and Energy for Sustainable Development*"

Volume III, No. 1

May 9 – 11, 2019, Adama, Ethiopia

Disclaimer

Adama Science and Technology University is not responsible for the contents reflected in the articles published in the proceedings of this International Research Symposium. The contents of this document are solely the responsibility of the authors.

Inquiries should address to:

Office of Research Affairs
Adama Science and Technology University
P.O.Box 1888, Adama, Ethiopia
Tel: +251-22-110-0017

Members of Organizing Committee

Dr Shiferaw Feyissa (Chairperson)	**Dr Kassaye Gutema (Member)**
Dr Alemu Disassa (Secretary)	**Dr Belay Birehanu (Member)**
Dr Yadeta Chimdessa (Member)	**Mr Girma Debele (Member)**
Dr Legesse Lemecha (Member)	**Mr Kokeb Yifru (Member)**
Dr Enyew Amare (Member)	**Mr Gemechis Asfaw (Member)**
Dr Hunduma Dinka (Member)	**Mr Bejiga Yadesa (Member)**
Dr Mulugeta Kebede (Member)	

Table of Contents

Preface

The transformation of a nation can basically be achieved through the advancement of science and technology. Ethiopia has long recognized the role of science and technology in bringing about sustainable development. The country has envisioned transforming itself into a middle-income country in 2025. To this end the country has exerted relentless efforts to materialize science and technology in the country. Thus, it has made science and technology the pillar of its top priorities for transformation of the economy.

As one of the universities mandate to spearhead the transformation process, Adama Science and Technology University (ASTU) is looking forward to excel in science and technology. Its goal is to develop highly qualified, capable, competent, and innovative human resource in the field of science and technology so as to transfer relevant scientific knowledge and skills required for nation building. The university also committed to conduct need based problem solving researches for alleviating the problems of the region and the country at large. To this end the university is working in collaboration with industries in its vicinity whereby its staff members are contributing a great deal in alleviating problems. Moreover, ASTU has set centers of excellence as a platform where academia can meet stakeholders.

ASTU's development into a full-fledged science and technology university has helped it to forge strong linkage, cooperation, and partnership with various national and international universities, development sectors, stake-holders, and relevant personalities. To showcase its all-round efforts, ASTU has organized its third international research symposium titled "Emerging Technologies and Energy for Sustainable Development". This is a broad agenda that is seen as a part of the national plan of transformation of the country. Thus, this research symposium aims to further strengthen the contribution of ASTU in development endeavours of the country at large.

Message from Organizing Committee

Shiferaw Feyisa (PhD)
Vice President, RTT, ASTU
Chair of the Organizing Committee

Honorable Guests, Dear Participants, on behalf of the organizing committee, I would like to welcome you all to the 3rd International Research Symposium of Adama Science and Technology University organized on the theme **"Emerging Technologies and Energy for Sustainable Development"**.

Since its establishment as full-fledged Science and Technology University, ASTU has been exerting tremendous effort to foster research culture among its staff. Over the last five years, it has conducted various national and regional researches, community service and consultancy service projects that led to new policy initiatives and generation of new development insights. The establishment of eight centers of excellence and the construction state-of-the-art research park in ASTU also witnesses the commitment of the university towards nurturing research culture.

In the effort to disseminate its research outputs and create a platform which allows the academia in ASTU share scientific knowledge and thought with national and international scholars, ASTU had successfully held two international research symposiums so far. The 1st International Research Symposium was held in September 2012 on the theme "*Sustainable Development through Science and Technology: Lessons from Emerging Economies*" while the 2nd one was held in June 2017 under the theme "*Ensuring Sustainable Development through Research in Science and Technology*". These two symposiums have helped a lot in increasing our national and international collaborations besides nurturing better research culture in our university.

The 3rd International research symposium is also aimed at consolidating our national and international research collaboration and eventually helping ASTU achieve its vision of becoming a national hub for science and technology researches. The overwhelming response that we have received from several senior and young researchers and scientists to our "Call-for-paper" witnesses the relevance and timely nature of the theme of this symposium. The theme of ASTU's 3rd International Research Symposium was designed to offer comprehensive range of sessions that include: Manufacturing, Environment and Natural Resources, Smart Materials and Technology, Energy, Industrial Park, Infrastructure and Construction and Computational Science. A total of 42 researchers, including 14 international speakers, are expected to present their works at plenary and syndicate sessions. Nearly 400 participants from higher learning institutions, industries, research institutions, federal and regional sector offices are expected to take part in this symposium. Thus, I am very much confident that the participants can learn a lot from the symposium.

Finally, I would like to thank you all for accepting our invitation to share us your scientific knowledge and expertise. I wish you all a fruitful scientific sessions and very pleasant stay in Adama City.

Welcoming Address

Lemi Guta (PhD)
Presiden, ASTU

H.E Professor Afework Kassu, State Minister of the Ministry of Science and Higher Education,

H.E Dr. Frehiwot Woldehanna, State Minister of the Ministry of Water, Irrigation and Energy,

Dear Dr. Nurilign Tefera, President of the Addis Ababa Science and Technology University,

Dear Distinguished guests,

Dear paper presenters,

Dear participants of ASTU's International Research Symposium:

Our University is one of the two Universities that have been designated on working towards excellence in the fields of Engineering and Applied Sciences. By and large, we are working towards becoming research oriented science and technology University and diversifying postgraduate fields both at masters and PhD levels. The University is proving its excellence especially in the Centers of Excellence most of which have gone into practical activities. With all the existing bottlenecks, ASTU will keep striving to support the overall growth and development of the country by carrying out problem oriented research focusing on the need of the industries.

Dear participants:

Regardless of challenges both at the national level and at institutional level, ASTU has shown progress in the research endeavors. Our academic staff and research staff have shown significant progress on the involvement into research works which contributes for the promotion of the staff and for the University's profile too. Besides, the mindset of the staff has changed towards identification of potential areas of research and towards finding solution for problems in the industries and much beyond.

With all the existing challenges related especially with foreign exchange, we are doing our best to equip our workshops and laboratories which are used both for research and for training our students. To this end, we have created linkages and collaborations both with domestic institutions and international ones, and we hope this will significantly change our situation in relation with research infrastructure issues.

Dear Excellencies,

Dear participants of the Symposium,

Dear paper presenters:

This symposium which we are hosting with the motto ""Emerging Technologies and Energy for Sustainable Development", I believe, will be a good platform that will pave a way for our University to create more linkages and collaborations with more institutions both within and international levels. To this effect, we will organize brief sessions to discuss with guests that we have invited to this symposium. I am optimistic enough that more potential is there for ASTU to prove its excellence in its missions to support the country's development.

ASTU will prove its excellence much further when the ongoing construction of the research park complex is completed the performance of which is 97% at this time. For that matter, in collaboration with the University's Construction Project Office and other concerned bodies, we are critically following up the construction process so that we may soon utilize the buildings to mobilize activities of our centers of excellence. So far, we have tried to make arrangements for our centers of excellence by carrying out renovation works to two of the existing blocks, and we are accommodating our guest researchers in the already existing guest houses in the University and sometimes in the hotels.

When our Research Park Complex is completed, it will have enormous help. All the activities of the eight centers of excellence will then be mobilized in research park, and we will accommodate our researchers as there are excess blocks designated for guest researchers. Starting from the design, our Research Park Complex are extremely classic level one, and it will be well equipped with all facilities required for our objective of becoming excellent in research and in supporting our postgraduate activities.

Your active participation will have indispensable role to play for the quality of the symposium.

Let me take this opportunity to express my gratitude to all bodies who have contributed their level best effort to organize this symposium. For this special appreciation goes to the Research Affairs Office and the Research and Technology Transfer Wing.

There were different individuals who have operated in different committees which were established to make arrangements for the symposium. On behalf of the University management, I express my gratitude to all.

I thank you!!

Key Note Address

Prof. Jemal H. Abawajy

Director, the Parallel and Distributing Computing Laboratory, Deakin University, Australia

Topic: Fourth Industrial Revolution: Its Implication for Ethiopia

Plenary Session

Prof. Yongil Kim

Seoul National University, Dept. of Civil & Environmental Engineering, South Korea

Topic: Current and Future Korean Satellite Programs and their Applications for Environment and Disaster Management

Prof. Radovan Kopecek

Board of Director at EUREC- European Association for Research Centers involved in Renewable R&D, Germany

Topic: Status of Photovoltaic 2019 and How Ethiopia Can Benefit from This Great Technology

Mr. Tilahun Gemechu

Director, Industrial Park Development Corporation, Addis Ababa, Ethiopia.

Topic: Industrial Parks: Development, Challenges and Prospects in Ethiopia

Prof. FB Dejene

Department of Physics, University of Free State, South Africa

Topic: Light Energy (solar and luminescent materials) in Service of Man Kind - from Nanoscale to Microscale

Prof. Satish Vasu Kailas ert

Department of Mechanical Engineering, Indian Institute of Science, India

Topic: 'Climbing' up the 'Sustainable Science/Engineering' Ladder

Prof. Chul-Ho Kim

Head, Department of Mechanical & Automotive Engineering, Seoul National University of Science & Technology, South Korea

Topic: Importance of Aerodynamic Design of a Moving Vehicle for Energy Savings with Emission Reduction and Driving Stability

Session 1

Environment, Natural Resource & Social Development

Invited Speakers

Prof. Geert Haesaert

Faculty of Bioscience engineering, Ghent University, Belgium

Topic: Fungal Endophytes: a New Magic Toolbox for Sustainable Crop Production

Dr. Dimitri Deneele

Research Director DR2, IFSTTAR and IMN-CNRS, Nantes, France

Topic: Insights in Soil Stabilization Investigations in the Context of Sustainable Development

Maternal Mortality Rate in Ethiopia a Worrying and Precarious Trend. Excerpts from a Meta-analysis

Riyaz Ahmad Rather

Department of Biotechnology, School of Natural and Computational Science, Wachemo University, Hossana, Ethiopia.E-mail: astuasnegude@gmail.com

ABSTRACT

Maternal mortality and neonatal deaths are evidently higher in African countries including Ethiopia. Colloidal parameters like poverty, bad healthcare system, lack of access to quality health education are a few contributing factors leading to higher mortality rate (MR) in Ethiopia. Continuous nationwide systematic evaluation and assessment of the problem helps to design appropriate policy and strategy in Ethiopia. Hence, this study aimed to investigate the leading contributing factors of prenatal and postnatal deaths using available literature from various studies. A literature search in the databases of PubMed, MEDLINE, USAID and Google Scholar was carried out. Manual search for local data that were not available electronically, was also conducted at one local hospital. Estimates of maternal mortality with 95% Uncertainty Intervals (UI) were generated by using spatial-temporal Gaussian Process Regression (ST-GPR). Cause of Death Ensemble modelling (CODEm) was employed to find the causes of mortality rate.The meta-analysis revealed that peripartum cardiomyopathy, unwanted abortions, maternal haemorrhage, high blood pressure, postoperative sepsis, embolism, alloimmunization, and complications of anaesthesia are the top contributing factors to maternal mortality in Ethiopia. Although meta-analysis revealed sepsis (9.6%) as the least contributing factor, however, peripartum cardiomyopathy, alloimmunization, and abortions with 25.7%, 19.6%, and 19.3% respectively, were the leading cause of prenatal and postnatal deaths. Most of the postpartum deaths were either due to alloimmunization or abnormal heart function, whereas abortions and unnoticed pregnancies were the principal cause of deaths in the prenatal period. Although the study finds a certain decline in MR in the past three decades, the change was insignificant. The conclusion of the meta-analysis highlights the need for a comprehensive and collaborative approach using multi-sectoral teamwork from stakeholders for reducing maternal mortality rate in Ethiopia. As the study insights, it is advisable for policies to contemplate on postpartum period.

Keywords: *mortality, prenatal, postnatal, alloimmunization, sepsis*

1. INTRODUCTION

Maternal mortality (MR) remains the world challenge with 275,288 deaths occurring because of physiological state and impediment in 2015 (Mahler, 1987). The World Health Organization (WHO) member countries set the Millennium Development Goal for reducing the MR worldwide. Whereas some progress has been created, in keeping with WHO estimates in 2015, the Maternal Mortality magnitude relation (MMR) dropping by 44% worldwide (Kassebaum, 2016). It remains intolerably high in developing countries significantly in sub-Sahara African countries. In one in every one of these countries, Ethiopia, the MMR remains high, starting from 266–1667 per one hundred thousand Live Births (Say et al, 2014). Maternal mortality is that the most receptive indicator of the health disproportion between poorer and richer nations, and for overall development. The results of maternal mortality even have impacts on youngsters and remaining families (Yaya et al., 2014).

The MR is conceived by numerous factors. MR is having a multifactorial cause that ranges from demographic, behavioural, nutritional, or related factors. The poor healthcare system is one of the most contributing factors towards the child and maternal deaths. Inaccessible to the good healthcare system, the poor competence of providers, lack of emergency obstetric services at facilities, inefficient referral systems are the basic causes of mortality rates in Ethiopia (Gaym, 2009).

Some of the limiting factors include, where the subjects were reluctant to quote a complication to the health service provider. These mauled the complications further which tend to hover the overall mortality rate among the subjects. Ethiopia is among the nations with large equality gaps in income and education and high healthcare

disparities. Women living in these disparity regions and rural areas experience higher maternal mortality than women living in urban and sub-urban centres because those living in wealthier households, having higher education, or living in urban areas, have higher use of healthcare services than their poorer, less-educated, or rural counterparts (Lu & Halfon, 2003). There are also racial and ethnic disparities in maternal health outcomes which increases maternal mortality in marginalized groups. Sociodemographic factors such as age, access to resources and income level are significant indicators of maternal outcomes. Young mothers face higher risks of complications and death during pregnancy than older mothers, especially adolescents aged 15 years or younger. Adolescents have higher risks for postpartum haemorrhage, puerperal endometritis, operative vaginal delivery, episiotomy, low birth weight, preterm delivery, and small-for-gestational-age infants, all of which can lead to maternal death. Structural support and family support influences maternal outcomes Furthermore, social disadvantage and social isolation adversely affect maternal health which can lead to increases in maternal death (Morgan & Eastwood, 2014).

Measuring maternal mortality is difficult in low-income countries because of limited registration of births and deaths. It becomes difficult as maternal mortality is relatively a rare event besides the challenge in avoiding the technical problems related to bias and the high demand of cost to carrying out sufficiently large surveys to measure the rate per unit time or per birth with reasonable precision. Most of the previous studies in Ethiopia were based on a single data sources, or sub-national study, or without identifying the causes of maternal mortality. Unlike these studies, this study provides a unique opportunity for its use of standardised methodology using several sources of data. This study used various metadata to investigate the trends and causes of maternal mortality in the last three decades in Ethiopia.

2. MATERIALS AND METHODS

2.1. Setting the Terminology

Maternal death was defined as "the death of a woman while pregnant or within 42 days of termination of pregnancy, irrespective of duration and site of pregnancy from any cause related to or aggravated by the pregnancy and its management, but not from incidental or accidental causes (WHO, 2004).

2.2. Study Design

Owing to the rich diversity of the people in the sub-Sahara, Ethiopia is the second most populous country in the region. The demographic survey which was conducted in 2016 stated that 28% women delivered with skilled attendance at birth, 35% women practised contraception with variations across regions, 17% received postnatal care, and 62% of the pregnant women used antenatal care. The subjects who were previously reviewed in any of these categories were included in this study. Any coherence between the two studies was avoided by selecting the latest and the updated one.

2.3. Database Setting

The following database like PubMed, MEDLINE, USAID, Hinnari and Google Scholar along with the print and electronic media, were searched with specific and appropriate keywords to get the consensual hints. The studies which were carried from since 1990 were searched in the said databases. Manual search for local data that were not available electronically, was also conducted at one local hospital.

2.4. Statistics

Graph Pad Prism version 5.0 (La Jolla, CA, USA) was used for statistical analysis. For each parameter, the mean, standard error of the mean, and range were calculated. Differences were evaluated by t-tests and nonparametric Mann–Whitney test and values of p 0.05 were considered statistically significant. Estimates of maternal mortality with 95% Uncertainty Intervals (UI) were generated by using spatial-temporal Gaussian Process Regression (ST-GPR). Cause of Death Ensemble modelling (CODEm) was employed to find the causes of mortality rate.

3. RESULTS

During the search in the database, a total of twenty-five papers were selected for the data analysis. The research paper with good impact factor (IF) and indexed with major portals were preferred over non-indexed and non-IF journals. The cross analysis among the manuscripts revealed that a total of 186,614 maternal deaths was reported from 1990–2000. The highest deaths, accounting 17278 (95% UI: 14,159–20,413) were reported during 1993, whereas the lowest one was reported for the year 1997 accounting just 14,020 (95% UI: 10,159–16,413). However, there was a certain increase in the MR from 2001–2010. A total of 192,113 deaths were reported during this period. However, the increase of 2.86% was considered as non-significant ($p \geq 0.05$). From 2011 to 2013 the individual yearly death rate has dropped to just 15234/year in 2013 (Figure 1). This is a significant ($p \leq 0.05$) decrease if compared to the year 2005, which has the highest deaths of 19,853. Overall trend showed that there was a decline from 708 per 100,000 in 1990 to 497 per 100,000 in 2013.

The foremost reason of maternal death that contributed more deaths in Ethiopia till 2013 was complications of anaesthesia, embolism (air, amniotic fluid, and blood clot), and the condition of peripartum cardiomyopathy (25.7%) followed by complications of abortions (19.6%), maternal haemorrhage (12.2%), hypertensive disorders (10.3%), and maternal sepsis and other maternal infections such as influenza, malaria, tuberculosis, and hepatitis (9.6%). However, maternal deaths related to HIV/AIDS attributed for 0.5% maternal deaths (Figure 2). This pattern was also seen in preceding years. In terms of the timing of maternal death, the postpartum period accounted for the highest number of deaths over the last 23 years, whereas the late postpartum period (42 days to one year) accounted the least number of maternal deaths. In 2013, there were 237 maternal deaths per 100,000 during postpartum period while the MMR during antepartum, intrapartum and late periods were 126, 88, and 46 per 100,000, respectively.

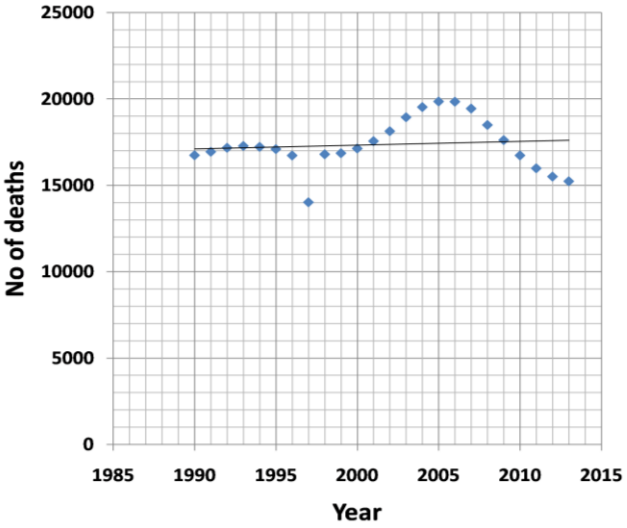

Figure 1: Number of child death

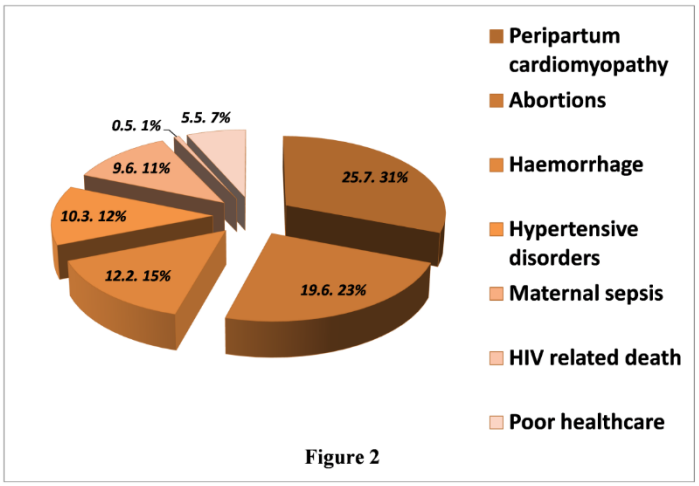

Figure 2: Causes of maternal death

The ratios of maternal mortality also varied across maternal age groups. Over the different time periods, the highest rate of maternal mortality as measured through MMR occurred in the age group 20 and 39 years. In the year 2005, the MMR was highest in the age group 20–24 years whereas it became highest among the 25–29 age group from 2010 onwards. Unlike in 1990, the MMR was reduced among 30–35 years 35–39 age groups in 2013. Over the last 23 years, maternal mortality occurred among the young adolescent girls 10–14 age group.

4. DISCUSSION

This meta-analysis variedly found that the MMR remained above the goal which was set in 2000 as the Millennium Development target. The considerable increase during the analysis period was a worrisome trend, however, the statistics found the increase as non-significant. Though the MMR estimate of 497 per 100,000 in 2013 was found to be little encouraging when compared with the data of the previous two decades as the decrease was found nonsignificant. The findings were higher than that estimated by WHO Effman (2016) (353 per 100,000), and reports in Northern Ethiopia (Godefay et al.,, 2015) (266 per 100 000), Southwest Ethiopia (425 per 100,000) (Yaya et al, 2014); however, it was lower than that reported by the EDHS (2016) report (412 per 100,000) (CSA & ICF international, 2016), and a study from Southern Ethiopia (Yaya & Lindtjohn, 2012) (1667 per 100,000). These scattered data files from southern and western regions implicate that each study is concomitant on various data parameters like sample size, estimation methodology, the source of data, etc. Hence the vast differences between the data sets are promiscuous and evident.

This study found that the major causes of maternal mortality were other direct maternal causes such as anaesthesia, embolism (air, amniotic fluid, and blood clot), and the condition of peripartum cardiomyopathy followed by complications of abortion. This is inconsistent with two reviews which reported that abortion-related complications and obstructed labor/ uterine rupture accounted for the top leading causes of maternal mortality in Ethiopia [Gayam, 2009; Birhan, 2014]. The differences in the present finding and the previous reviews are likely to be due to the inclusion of hospital-based studies. As a result, this may have led to an overestimation in some of the causes of deaths, with obstructed deaths and complications of abortions were more likely to be reported for health facilities. During the course of analysis, it was found that MMR induced due to HIV related causes or infection was relatively unwavering with a diminutive fall, over time. This decline may have resulted from the introduction various awareness programs like Prevention of Mother-To-Child Transmission (PMTCT) of HIV/AIDS services (Fedral HAFCO, 2001). A widespread counselling and workshops which are in the lead now for all regions of Ethiopia might have paved a sound impact on the decline of mortality rate caused due to HIV infections. A strong and resonating effect is visible on the ground where various NGO in support of Govt has taken a lot of initiatives to stop this menace. A study from Ethiopia conducted in 2011 also recommended that there was a remarkable progress in terms of impending treatment of PMTCT services between 2006 and 2010 (Nigatu & Woldegebriel, 2001). Furthermore, the national HIV prevalence has shown a decline in the general population, including pregnant women. As reported by other previous studies (Yaya, Data & Lindtjorn, 2015), a higher number of deaths occurred during the postpartum period over the study period. One could interpret the occurrence of a higher number of deaths during this period by assuming that, either the subject was not aware of the health snag or light knowledge of complication which lead an un-emmergetic situation, or the lack or inadequate quality obstetric services at health facilities at the visiting health centre. One of the literature cited that health providers in Ethiopia may have an inadequate aptitude in terms of managing postpartum haemorrhage and utilization of partograph for monitoring labor progress (Getachew et al, 2011). Another study from the Northwestern Ethiopia depicted that the lack of critical care and un-attending communications during the patient arrival at health centre also augment the complications to higher hierarchy (Mirkuzie et al., 2014). These reports and data suggest that a proper handling and management of the patient right from the antenatal to postnatal period will reduce the mortality rate among the high risk as well as low-risk subjects. Moreover, deliveries attended by the un-professional individuals without consulting the healthcare provider or professional, have also taken a tool on neonatal deaths. It has been also observed that children born under non-medical attention are more prone to infections and contract sepsis more easily when compared to children born under medical attention.

A remarkable finding depicted in this study shows that the age group of 20-30 are the most vulnerable cohort groups which contribute a lot to child MMR, though the latter varies a lot among various age groups. Although it is assumed in one study that the contribution towards this rate may be due to the high fertility rate in these age

groups of women and thus the potential of augmented maternal mortality (Tsegaye, 2016). Over the analysis period, it was observed that young girls of age group 10–14 years have higher death rates. This trend could be attributed due to the high prevalence of early marriage and or unmet need for family planning services or complications due to gynaecological immaturity and incomplete pelvic growth. This proposes that a consensus agenda is required to be framed out that needs to be put in the public domain with full awareness. The responsiveness campaign could save the young adolescents from getting married at an early age. This could obviously reduce the pregnancy risks and related complications that lead to a maternal death.

5. CONCLUSION

The large proportion of deaths attributed to indirect causes cannot be ignored. As direct maternal deaths decrease because of targeted interventions, efforts to reduce maternal mortality will have to be refocused on the reduction of indirect causes. The use of robust methodology and multiple sources of data that enabled us to see the overtime trends of maternal mortality in Ethiopia (Deribew et al, 2013). Though the present study was an effort to cover the different data sets, a larger and the uncommitted study analysis is warranted. Various analytical parameters of datasets from all regions of Ethiopia should be collated and final inference with a potential feedback generated. That is one of the limitations procured in this study.

ACKNOWLEDGEMENTS

I thank the Research Directorate and the management of WCU for supporting this work

REFERENCES

Yifru Berhan and Asree Berhan (2014): Causes of maternal mortality in Ethiopia: a significant decline in abortion related death. *Ethiop J Health Sci*, 24: 15–28.

CSA [Ethiopia] and ICF International. Ethiopia Demographic and Health Survey 2016: Key Indicators Report. Addis Ababa and Rockville; CSA [Ethiopia] and ICF International.

Deribew, G.A. Tessema, K. Deribe (2016): "Trends, causes, and risk factors of mortality among children under 5 in ethiopia, 1990-2013: findings from the global burden of disease study 2013," *Population Health Metrics*, *14*(1): 24-28.

Federal HIV/AIDS Prevention and Control Office. Prevention of Mother to Child Transmission of HIV. Addis Ababa; Federal HAPCO; 2001.

Gaym A (2009). Maternal mortality studies in Ethiopia–magnitude, causes and trends. *Ethiop Med J*, 47(2): 95–108.

Getachew Ashebir, Ricca J, Cantor D (2011). Quality of care for prevention and management of common maternal and newborn complications: a study of Ethiopia's hospitals. Baltimore: Jhpiego

Godefay H, Byass P, Kinsman J, Mulugeta A. (2015). Understanding maternal mortality from top-down and bottom-up perspectives: Case of Tigray Region. *Ethiopia J Glob Health. 5(1)*:010404.

Kassebaum, N.J., Steiner, C., Murray, CJL (2016). Global, regional, and national levels of maternal mortality, 1990-2015: a systematic analysis for the Global Burden of Disease Study. *Lancet*, 388(10053):1775–812.

Lu MC, Halfon, N. (2003). "Racial and ethnic disparities in birth outcomes: a life-course perspective". *Maternal and child health journal*, 7(1):13–30.

Mahler H. (1987). The safe motherhood initiative: a call to action. *Lancet*, 1(8534):668–70.

Mirkuzie AH, Sisay MM, Reta AT, Bedane MM. (2014). Current evidence on basic emergency obstetric and newborn care services in Addis Ababa, Ethiopia; a cross sectional study. *BMC Pregnancy Childbirth*. 14(1):1

Morgan KJ, Eastwood JG. (2014). "Social determinants of maternal self-rated health in South Western Sydney, Australia". *BMC Research Notes*, 7(1):1–12

Nigatu T, Woldegebriel Y. (2011). Analysis of the prevention of mother-to-child transmission (PMTCT) service utilization in Ethiopia: 2006-2010. *Reprod Health*, 8:6.

Say L, Chou D, Gemmill A (2014). Global causes of maternal death: a WHO systematic analysis. *Lancet Glob Health*, 2(6):323–33.

Trends in Maternal Mortality: 1990 – 2013. Estimates by WHO, UNICEF, UNFPA, The World Bank and the United Nations Population Division.

http://www.mamaye.org/evidence/trends-maternal-mortality-1990-%E2%80%93-2013-estimates-who-unicef-unfpa-world-bank-and-united Accessed 10 July 2016

Tsegaye, E Somigliana, T Alemayehu (2016). Ambulance referral for emergency obstetric care in remote settings. *Int J Gynaecol Obstet*. 133(3):316–9.

WHO. International statistical classifi cation of diseases and related health problems: tenth revision, volume 2. http://www.who.int/classifications/icd/ICD-10_2nd_ed_volume2.pdf In.; 2014. Accessed 10 April 2016.

Yaya Y, Data T, Lindtjorn B. (2015). Maternal mortality in rural south Ethiopia: outcomes of community-based birth registration by health extension workers. *PLoS One*, 10(3):0119321.

Yaya Y, Lindtjorn B. (2012). High maternal mortality in rural south-west Ethiopia: estimate by using the sisterhood method. *BMC Pregnancy Childbirth*, 12:136.

Yaya Y, Eide KT, Norheim OF, Lindtjorn B. (2014). Maternal and neonatal mortality in south-west Ethiopia: estimates and socio-economic inequality. *PLoS One*, 9(4):96294.

Integrated Treatment Technology for Blended Wastewater of the Sugar Industry and Ethanol Distillery

Jemal Fito[1], *, Nurelegne Tefera[1], Stijn W.H. Van Hulle[2]

[1]*Department of Environmental Engineering, Addis Ababa Science and Technology University, P.O.Box 16417 Addis Ababa, Ethiopia*
[2]*Department of Green Chemistry and Technology, Ghent University Campus Kortrijk, Graaf Karel de Goedelaan5,8500 Kortrijk, Belgium*
**Corresponding author, e-mail: fitojemal120@gmail.com*

ABSTRACT

The sugar industry is being expanded at an alarming rate and the sugarcane-based ethanol distillery has recently emerged as an alternative renewable biofuel that is replacing fossil fuels. However, the sugar industry and ethanol distilleries are discharging large volumes of high-strength wastewater into the environment without adequate treatment. This pattern causes the adverse effect on aquatic and terrestrial ecosystems. Hence, this study was designed to evaluate physicochemical properties of the sugar industry and ethanol distillery wastewater, and treat the blended wastewater of the two industries using anaerobic digestion followed by adsorption of bagasse fly ash (BFA). The wastewater samples of the two industries were collected using composite and grab- sampling techniques. The application of the integrated treatment method was performed using an initial COD concentration of 10,000 mg/L, at the hydraulic retention time of 10 days, pH 7 and a constant temperature (37°C) of the bioreactor, whereas the adsorption treatment was operated at the optimum point of BFA dose (4 g in 100 mL) and contact time (4 h) obtained in previous studies. Most of the physicochemical parameters of the two wastewaters were above the effluent discharging limits, which have the potential to cause adverse effects on the environment by interfering with physicochemical and biological processing. Under anaerobic treatment, maximum COD reduction of 65 % and color removal of 79% were recorded, whereas after adsorption treatment, COD reduction of 62% and color removal of 58% were observed. However, the integration of the two aforementioned treatment technologies resulted in an average COD reduction of 76% and color removal of 83%, which indicates a promising option to mitigate pollution of untreated wastewater and enhance the practices of reusing the treated wastewater at the industrial scales. Finally, it can be concluded that the treated effluent can also be reused for irrigation of sugarcane which will contribute to sustainable water utilization in the sector.

Keywords: *Wastewater management, environmental pollution, pollutants, anaerobic digestion, adsorption*

1. INTRODUCTION

Industrialization is the backbone of the development of many nations which contributes significantly to sustainable economic growth and the well-being of humankind (Poddar and Sahu, 2017). However, the increasing number of industries, including sugar industries and ethanol distilleries, is aggravating the pollution impacts in the environments, especially in developing countries (Sahu, 2016). The sugar industry was originally intended to produce only sugar but has evolved into a sugarcane industry which is producing sugar, ethanol, electricity and bioplastic. Sugarcane contributes about 75% - 80% of the total sugar produced in the world which is practiced mainly in more than 130 countries (Sentíes-Herrera et al. 2014; Sentíes-Herrera et al. 2017). Currently, 85% of sugar production globally is obtained from the following 15 countries: Brazil (25%), India (19%), China (8%), Thailand (7%), United States (5.3%), Mexico (4.4%), Pakistan (3.6%), Australia (3.2%), Guatemala (2.0%), Colombia (1.6%), Philippines (1.5%), Indonesia (1.5%), Argentina (1.4%), South Africa (1.4%) and Cuba (1.2%) (Sentíes-Herrera et al., 2017). Furthermore, sugarcane is a water intensive crop as reflected by its water footprint which ranges from 120 to 410 m^3/t (Chooyok et al., 2013; Gerbens-Leenes, 2018). Sugar industries have many operational processes, including milling (extraction), clarification, evaporation, crystallization and centrifugation. In these sugar production processes, many chemicals are used, such as

$Ca(OH)_2$ and H3PO4 to clarify the sugarcane juice, polyelectrolytes for coagulation of impurities, SO_2 to defecate raw sugar for color removal, and NaOH, Na_2CO_3 and HCl for periodic descaling of heater and neutralization process (Poddar and Sahu, 2017).

Globally, the substitution of fossil fuels with bioethanol has resulted in the reduction of 40 to 62% of greenhouse gas emissions into the atmosphere (Lopes et al., 2016). Currently, molasses is used as the chief source of feedstock for ethanol distilleries in many countries. Ethanol production in distillery has two key processes, which are the fermentation of the carbon sources using chemicals such as diammonium phosphate, urea, phosphate, sulfuric acid, yeast and molasses, and the extraction of ethanol by distillation. In ethanol distillery, the effluent generated from the primary column of the distillation is called distillery wastewater, spent wash or vinasse. However, the strength of spent wash mainly depends on the types of feedstock (sugarcane and beet molasses versus sugarcane and beet juices), chemical types used in the processes and the distillation efficiency of each distillery column. For every liter of ethanol production, about 14 – 22 L of water is consumed and on an average 15 L of distillery spent wash is generated (Padoley et al., 2012). Furthermore, distillery spent wash is the most complex and troublesome effluent, having high concentrations of organic matter (BOD_5 30,000 –50,000 mg/L and COD 60,000 –190,000 mg/L), high acidity (pH 3.0 – 4.5) and deep dark brown color (Kazemi et al., 2015; Mohana et al., 2009). Generally, distillery spent wash is highly charged in organic matters, nutrients and acidic compounds with very low biodegradability properties which have forced the industry to be classified as environmentally 'red category,' indicating that it has great potential to deteriorate the quality of water bodies and alter the physicochemical and microbial properties of soil in many places across the globe (Mohana et al., 2009; Nure et al., 2017). Another big challenge of distillery spent wash is the need for large wastewater treatment reactors, which cause the whole treatment process costly and unaffordable for developing countries (Basu et al., 2015a). Similarly, sugar industry effluent has also a high pollution potential to alter the physicochemical characteristics of water and impact adversely the flora and fauna communities of the effluent receiving water bodies.

Researchers are looking into various mechanisms for the removal of pollutants, particularly from the distillery spent wash, and governments have started to focus on promoting feasible waste water treatment technologies (Carolin et al., 2017). Even though the stability of operational processes, reliability to produce an acceptable wastewater quality and financial issues are very crucial components for selection of the appropriate wastewater treatment technology, the characteristics and types of pollutants and intended use of treated water are also equally important (Ding, 2017). The implementation of conventional physicochemical methods for sugarcane industrial wastewater treatment was not effective due to eventual drawbacks in terms of hazardous by-product formation, low efficiency, the large amount of sludge generation, excessive chemical utility and high energy requirements (Sahu and Chaudhari, 2015; Thanapimmetha et al., 2017). Hence, many researchers indicated that these physicochemical treatment methods can be implemented after primary biomethanation of the sugarcane industries effluents (Mohana et al., 2009). Furthermore, the drawbacks of physicochemical methods of distillery wastewater treatments have forced the researchers and scientists to shift to the investigation to high rate anaerobic reactor as primary treatment which was found to be cost effective, efficient in removing organic matter (COD reduction by 62- 76%) and environmentally friendly (Bezuneh, 2016). Hence, biological treatments have been recognized as effective treatment methods for organically saturated industrial wastewaters of the sugar industry and ethanol distillery.

Indeed, special attention is given to the implementation of anaerobic high rate reactors for the treatment of high strength agro industrial wastewater as a primary preferable option due to its high treatment efficiency, economic feasibility, environmental friendliness, operational simplicity, and offering the possibility of energy recovery option (Fito et al., 2018b). Furthermore, the high rate anaerobic reactor has the ability to differentiate hydraulic retention time from solid retention time (Rajeshwari et al., 2000). Generally, the high-rate anaerobic

reactor is considered as the state-of-the-art in the sugarcane industrial wastewater management, contributing to environmental pollution protection and providing the opportunity of wastewater reuse for environmental sustainability. Basically, the critical problem of single stage anaerobic high rate reactor in high strength wastewater treatment is the reactor failure due to the sudden decrease of pH value resulting from the rapid increase in volatile fatty acid production (Acharya et al., 2011). Hence, a two-staged anaerobic filter is proposed to provide hydrolysis and methanogenesis steps separately to minimize the limitations of single stage anaerobic digestion. Furthermore, using the two-stage anaerobic bioreactor with a special type of supporting material (bio ball) to increase the surface area for microbial communities is another unique approach used in this research.

Anaerobic digestion alone cannot remove all the pollutants from the sugarcane industrial effluent. Hence, additional treatment methods such as adsorption are required for post-anaerobic treatment. Adsorption is considered to be a viable approach for industrial wastewater treatment due to its simplicity and cost- effectiveness (Lavecchia et al., 2012). As a consequence of this, many studies focus on the development of adsorbents to be used for the removal of pollutants from drinking water and wastewater (Nigussie et al., 2007). Particularly, the application of adsorption for the removal of organic matter and color from industrial wastewater have been proven as an effective and efficient treatment technology (Kushwaha et al. 2010). However, commercial activated carbon is expensive and its application is limited in the wastewater treatment industry, especially in developing countries. Hence, researchers are still investigating to develop adsorbents which could be cheap in terms of cost, efficiency in terms of the treatment, largely available in terms of quantity and easily converted into useful forms of adsorbent. Basically, such adsorbent development is mainly focused on plant remains and industrial waste or byproducts to be used at industrial scales (Iakovleva et al., 2017). In line with this, bagasse fly ash (BFA), the sugarcane industry byproduct, is one potential area of research. BFA is a carbon-rich solid waste material collected from the stacks of the bagasse-fire boilers of sugar mills, which possesses many unique characteristics of potential adsorbent (Kumar et al., 2014a). Practically, BFA is an industrial byproduct, which is dumped into the environment without any effort to convert into useful products, especially in developing countries including Ethiopia, (Nure et al., 2017). The adsorption potential of the BFA has been proved, including 78% COD removal of acrylonitrile from aqueous solution reported by Kumar et al. (2014b) and 68% color removal from printing ink industrial wastewater reported by Noonpui et al. (2010). Adsorbent development from BFA has been carried out under different mechanisms (Wahyu et al., 2012). For instance, the surface modification of BFA using hydrogen peroxide as an activating agent improved the adsorption capacity about threefold by enhancing the positive valence on the surface (Chapman, 2003; Nagda and Ghole, 2009). This positively charged adsorbent surface in turn can improve the treatment of negatively charged color causing pigments of distillery spent wash. Generally, the novelty of the proposed approach presented here is that a waste material of the sugar industry is re-used as source to produce a useful adsorbent for the treatment of the blended wastewater of the same sector, namely the sugar and ethanol distillery.

Blending of sugar industry and ethanol distillery wastewater has many benefits, such as reducing chemical consumption for neutralization, dilution, installation of a single wastewater treatment plant, saving resources and improving treatment efficiency. However, the implementation of such approach in sugarcane industrial wastewater management is rare. Hence, the aim of this study was to investigate the physicochemical properties of the sugar industry and ethanol distillery wastewater and the removal of the COD and color from blended wastewater using mesophilic conditions of two stages of an anaerobic filter followed by adsorption of activated BFA. The overall performance of the integrated treatment system was evaluated and compliance with the environmental regulation was checked.

2. MATERIALS AND METHODS

2.1. Description of the Study Area

The Metahara sugarcane industry was established in 1965 in the Awash basin located in the east African rift valley of Ethiopia (Figure 1), about 200 km east of Addis Ababa in Oromia Regional State. Metahara is a low land area found at an altitude of 950 m above sea level with very low average annual rainfall of 600 mm. Metahara sugarcane state farm is located at 8° 54' 0" North and 39° 55' 0" East. It is characterized by an average maximum temperature of 32.8°C and a minimum of 17.5°C, which indicates semi-arid climate. Average relative humidity of the area is 77.5%, sunshine hour 8:5 h/day, wind speed of 4.1 m/s, with the rainiest period of the year from June to September. Moreover, the long term data of this area indicate average pan evaporation and reference evaporation of 6.9 and 4.8 mm/day, respectively (Degefa et al., 2016).

The Metahara estate farm is the second largest irrigation scheme in the country. This industry was established with the intent to satisfy the increasing demand of sugar in the country. Practically, the factory was a share company of the Ethiopian government and the Dutch Company called Hangler Vonder Amsterdam (HVA) (Olumana et al., 2009). The sugar factory started its first cane crushing operation with a capacity of 1,700 t/day in 1969. However, the molasses - based Metahara ethanol distillery was established lately in 2011.

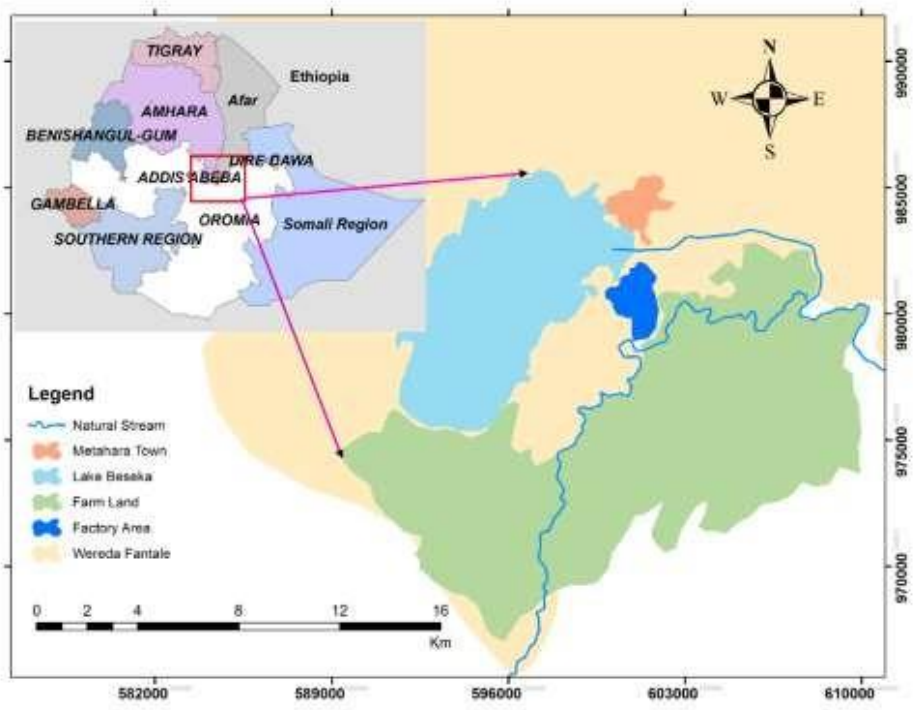

Figure 1: Location of Metahara sugarcane farm and sugar factory (J Fito et al., 2017)

Large area of land in Metahara is delineated for the sugarcane estate farm among which about 10,230 hectares of land is covered by sugarcane. Currently, the Metahara sugar factory is producing about 82,500 t of sugar annually but the sugar production capacity is 136,692 t/year. Before the establishment of the ethanol distillery in 2011, molasses which is the sugar factory byproduct was discharged daily into the environment. However, the sugarcane molasses based Metahara ethanol distillery was established recently with a production capacity of 12,500 m^3/year which is integrated with the sugar factory. The integrated sugar factory and ethanol distillery is processing every ton of sugarcane, producing about 34 kg of molasses, 298 kg of bagasse, 30 kg of the filter cake, and 100 kg of sugar on average. Similarly, in the ethanol distillery, 1 ton of molasses consumes about 4.2 m^3 process water in order to generate 258 L of ethanol and 3, 376 L of spent wash (Fito et al., 2017).

2.2. Experimental Layout

The experiment of this study was divided into three phases and its general framework is shown in Fig. 2. In the first phase, sugar factory and ethanol distillery wastewater samples were collected and laboratory analyses were performed as per standard methods. In the second phase, the pre-determined values of the pH and COD concentrations were achieved through the blending of two industrial wastewater before injecting into the anaerobic reactor. After anaerobic digestion the waste water is treated with adsorption on BFA.

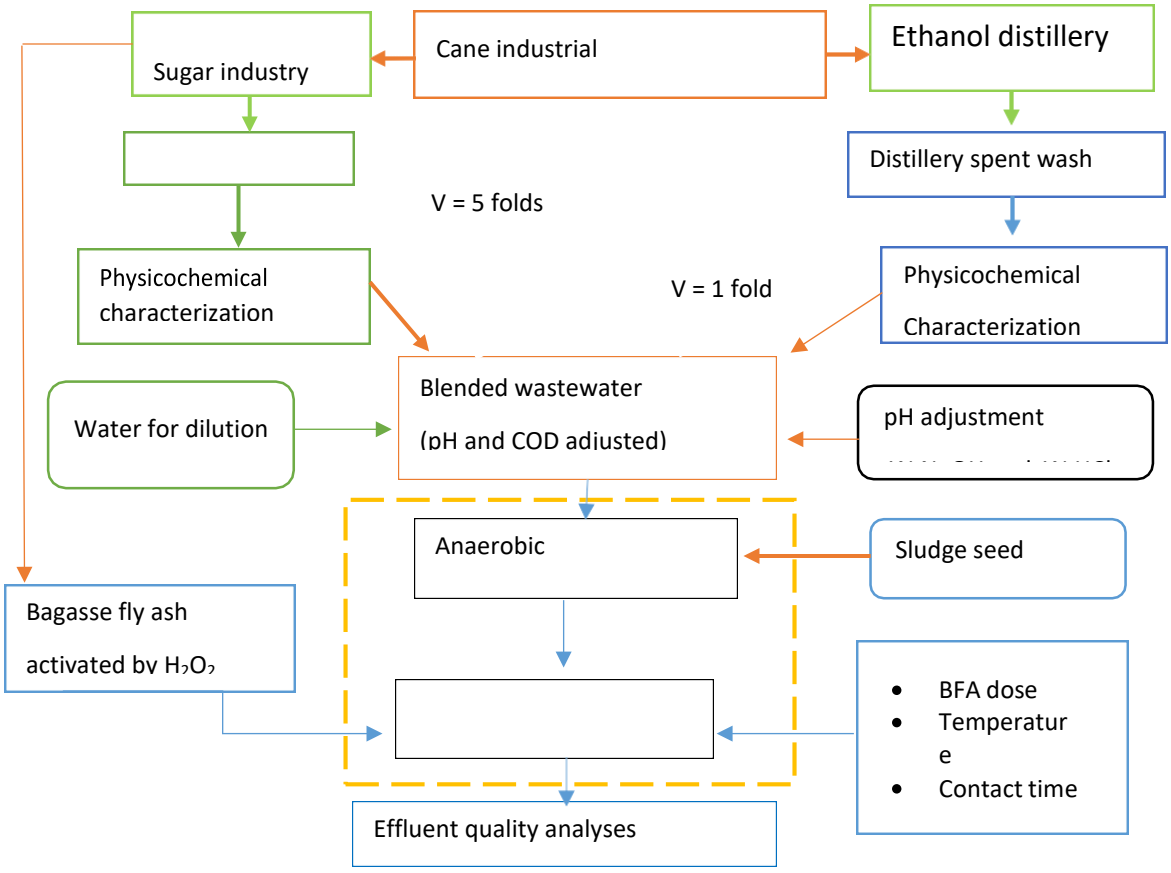

Figure 2: Schematic representation for each experimental activity of the study.

2.3. Wastewater Sampling and Characterization

Wastewater characterization was performed on the wastewater samples collected from the exit points of the Metahara sugar factory and ethanol distillery effluents. The sampling was collected at monthly time intervals for a period of the two months. Similarly, additional wastewater samples were collected from the same factories and were used for anaerobic and adsorption treatments as screening stages. Moreover, same sampling techniques were followed for the integrated wastewater treatment experiments. In all cases, grab and composite sampling techniques were applied through the study period. Well cleaned plastic bottles were used for wastewater sampling which were transported to the laboratory and placed in the refrigerator at 4°C until performing the laboratory analyses per standards methods for examination of water and wastewater (APHA, 1998). All laboratory analyses were performed on duplicate samples and the study results were disseminated in the form of average values. Additionally, experimental controls were also used in all experiments. The specific analysis of each parameter and the corresponding method are shown in Table 1.

2.4. Experimental Set-up and Inoculum Development

The experiment of the blended wastewater treatment was performed using an anaerobic filter. This bioreactor

was designed in biphasic stages, surrounded by glass wall which served for water circulation to maintain temperature. Bio balls were used for packing materials inside the reactor (anaerobic digestor PDAN 2013, Edibon, Madrid, Spain, Edibon- designs and manufactures engineering and technical teaching equipment), shown in Figure 3. Each bioreactor has a volume of 5 L and the internal part of each reactor was packed with uniform-sized bio balls. The thermostatic water bath that circulated through the water jacketed system was used as temperature control mechanism by means of regulating valves. Two calibrated peristaltic pumps were used and working sequentially. The first pump was used to inject the influent from the feeding tank into the first bioreactor whereas the second pumps was used to pump the primary treated effluent from the buffer vessel into the second bioreactor. The flow rate of the influent (wastewater) was adjusted at a specific flow meter in order to feed the bioreactor. The buffer vessel which was situated between the two bioreactors was used for pH adjustment and also served as an emergency container during overflow from the first bioreactor (PDAN and Manual, 2013).

Table 1: Physicochemical parameters of Metahara sugarcane estate wastewater and the test methods used

S.No	Parameters	Test methods/ Apparatus
1	pH	Hach HQD field case Model 58258-00
2	EC	Hach photometer HQD field case, Model 58258-00
3	Temperatur	Hach photometer HQD field case, Model 58258-00
4	TS	APHA 2540 B, Total solid dried at 103 –105°C
5	BOD_5	APHA 5210 B, 5-days BOD5 test
6	COD	APHA 5220 B, Open reflux method
7	NO_3^--N	APHA 4500 B, Ultraviolet spectrophotometric screening method
8	NH_4^+-N	APHA 4500 B,C Distillation followed titration method
9	TKN	APHA 4500b, Macro-Kjeldahl method
10	TP	Persulfate digestion method &APHA 4500-P,C
11	PO_4^{3-}	APHA 4500-P C, Vanadomolybdophosphoric acid
12	Cl^-	APHA 4500-Cl- B, Argentometric
13	SO_4^{2-}	APHA 3030E, Turbidmetric method

Figure 3: Two-stage water jacketed anaerobic filter (a), anaerobic bioball (b), and sludge seed (c) used in the bioreactor

In anaerobic treatment, the supporting materials for biofilm development usually depends on the local specific conditions, economic considerations and operational factors. However, the most common supporting

materials are quartz, activated carbon, polyvinyl chloride, hard rock particles and limestone. Usually, the main limitations of the anaerobic filter are clogging and occupation of a large volume of the reactor by inert packing materials. These problems can be overcome using the bio balls as supporting material in the anaerobic filter. Bio balls have ball-shaped spherical design (diameter 25.0 mm) made up of polypropylene plastic material having channels and holes with expanded surface area for the formation of biofilm in the anaerobic reactor (Fig. 3). Each bio ball has density of 0.92 g/cm^3 and mass of 1.7 g with an estimated specific surface area of each piece of 27.8 cm^2. The bio balls are a good alternative to traditional mineral-based media and are ideal for performance improvement of anaerobic high rate filters in wastewater treatment practice.

Acclimatization of microbial communities for anaerobic wastewater treatment was done using inoculum seed culture indicated in Fig. 3.The sludge seed was taken from well-established full scale high rate anaerobic reactor of up-flow anaerobic sludge blanket (UASB) of brewery industry from BGI, Addis Ababa, Ethiopia. The inoculum seed culture occupied 20% by volume of each reactor and was kept at a constant temperature of 37°C (Blonskaja et al., 2003; Emadian et al., 2015; Majone et al., 2010). At each experiment, blended wastewater was obtained by mixing the sugar industry effluent to ethanol distillery spent wash at the ratio of 5 to 1. But further adjustments of blended wastewaters were made using 0.1 M NaOH and HCl to pH 7 and tap water was used to correct the initial COD concentration to 10, 000 mg/L through dilution process. In acclimatization experiment, a hydraulic retention time of 12 days was used and the total experimental period lasted three months. The production of biogas, pH and color changes of the effluent were used to check the proper function of the bioreactor.

2.5. Bagasse Fly Ash (BFA) Preparation

In the adsorption experiment, BFA adsorbent was used as a post-treatment for the anaerobically treated blended wastewater. BFA surface modification was made using hydrogen peroxide as an activating agent as indicated by different adsorbent development stages shown on Fig. 4. The adsorbent samples were taken from Metahara sugarcane industry, particularly from the dumping sites nearby the sugar factory. The BFA sample was completely dried in the laboratory before chemical activation. The dried BFA sample was soaked in 30% concentrated hydrogen peroxide and kept at temperature of 60°C in an oven for the period of the 24 h. Then, the modified adsorbent was purified through washing with distilled water several times. Finally, the BFA was dried at 100°C, ground, sieved at a mesh size less 1 mm, placed in plastic bags, and stored in a desiccator to avoid moisture contact (Gupta et al., 2003).

Figure 4: Adsorbent preparation stages of the BFA

2.6. Performance of Integrated Treatment System

Once acclimatization and screening were properly performed, the actual integrated wastewater treatment

experiments were performed using the same wastewater fixed ratio of 5:1. The average COD concentration in sugar industrial wastewater was about 2,000 mg/L whereas the rough average concentration of distillery spent wash was 140,000 mg/L. Hence, to adjust the organic matter concentration of the blended wastewater, particularly the concentration of COD in the range of bio-treatability, the sugar industry to ethanol distillery wastewater ratio was fixed at 5:1. In this experimental section, the average ratio of the two industrial effluents (sugar and distillery) and tap water was calculated and found that 5:1:0.8, respectively. However, it was difficult to achieve exactly pH 7 of the blended wastewater only by mixing the two wastewaters, since the distillery spent wash contains many components that can act as typical buffering solutions. The same HRT was deliberately assigned to the two bioreactors. The last experiment was carried out at the optimum condition of the anaerobic treatment of the blended wastewater (initial COD concentration of 10,000 g/L, HRT of 10 days, pH 7 of the blended wastewater and at a constant temperature of 37°C in the bioreactor) and followed by adsorption of activated BFA at the optimum condition (4 g BFA in 100 mL, and contact time of 4 h).

3. RESULTS AND DISCUSSION

3.1. Physicochemical Analysis of the Wastewater

Characterization of the industrial effluent is a basic preliminary action before any wastewater treatment selection and plant design. It also indicates the pollution potential of the effluent and its environmental burden on the effluent receiving ecosystem. Based on this, the sugar industry and ethanol distillery effluent characteristics were investigated using certain parameters such as total solids (TS), temperature, pH, BOD_5, COD, ammonium, nitrate, total Kjeldahl nitrogen, phosphate, total phosphorus, electrical conductivity (EC), chloride and sulfate. The results are presented in Table 2 as mean and standard deviation, and are compared with other study findings and the Ethiopian industrial effluent discharge standards. Basically, the major physicochemical properties of the sugar and ethanol distillery can be classified into three groups, which are organic matter (BOD_5 and COD), pH and inorganic compounds (nitrate, phosphate, sulfates, etc.). Generally, the sugar industry and ethanol distillery wastewater characterization indicates that both wastewaters are enriched with high loadings of organic matter, total solids, nutrients and acidic compounds but the main contributor is the distillery spent wash.

In sugar industry and ethanol distillery wastewater, total solids were 2,481.5±20.5 and 162,550.0±9.7 mg/L, temperature 31.7±0.4 and 48.4±1.7°C, and EC 0.5±2.8 and 45.6±6.9 mS/cm, respectively. Regarding the aforementioned three parameters, the recorded values of the distillery spent wash parameters were much higher than those of the sugar industry wastewater. Temperature is an important factor which can accelerate the chemical reactions in the soil system and interfere with the normal function of the aquatic ecosystem. Organic and inorganic ions such as the carbonates, chlorides, sulfates, nitrates, metal ions are contributors to EC and total solids, and additionally, other impurities induced during the production process such as the fine particulate matters and silts also contribute to the total solids present in the effluents. Temperature and total solids of the ethanol distillery spent wash exceeded the permissible discharging limits of 40°C and 50 mg/L, set by Ethiopian EPA for industrial effluent regulation, respectively.

In similar studies, total solids in sugar industry wastewater were reported at 2,452.0+0.0 mg/L (Chaurasia and Tiwari, 2012), and in ethanol distillery spent wash at 10,000 –190,000 mg/L (Acharya et al., 2008). In this analysis, the total solids of both the filterable and unfilterable samples were considered. They remained as residue upon drying at a defined temperature. Practically, the presence of the particulate matters in water bodies can disrupt the ecosystem by diminishing the transparency of water bodies. This can cause high water turbidity and interferes with the natural aquatic ecosystem by rapidly depleting the available of dissolved oxygen which disturb the normal interactions of abiotic and biotic and endangering aquatic life. Generally, these analyses indicated that high concentrations of pollutants present in the effluent can affect untreated effluent receiving environments. In such situations, the pollutants can pose serious pollution impacts on the survival of living organisms in the soil

and water bodies (Jemal Fito et al., 2017). Generally, the discharge of the untreated effluents has the potential to cause adverse effects on the environment. Hence, intervention in the form of treatment is critical for environmental and public health protection.

Table 2: Physicochemical parameters of the sugarcane industrial wastewater

Parameters	Sugar industry effluent	Distillery spent wash	Discharging standards
pH	8.4±0.1	4.1±0.2	6-9
EC (mS/cm)	0.5-2.8	45.6±6.9	-
Temperatur (°C)	31.7±0.4	48.4±1.7	40
TS	2,481.5±20	162,550±9.7	50
BOD_5	1,955.9	31,706.0±2720.	60
COD	2,078.4	146,897.5	250
NO_3^--N	0.5- 0.3	4.9±1.1	-
NH_4^+-N	2.6±0.3	14.6±4.3	20
TKN	24.8±2.5	1,118.0±38.2	40
TP	19.5± 2.1	53.7±8.3	5
PO_4^{3-}	4.0±0.4	20.8±3.2	-
Cl^-	57.7±1.6	7,538.0± 20.6	-
SO_4^{2-}	44.3±1.3	5,464.5±16.2	-

The pH of the industrial wastewater is a decisive factor for wastewater treatment, particularly for biological treatment such as anaerobic digestion and engineered wetlands. In the present study, the weak alkaline nature pH 8.4±0.1 of the sugar industry effluent was within the permissible range, whereas the pH of ethanol distillery spent wash was very acidic (4.1±0.2), below the lower permissible limits of pH 6-9 set by the Ethiopian EPA regulation for industrial effluent. In similar studies, sugar industry effluent pH of 5.2-8.6 and distillery spent wash pH of 3.7- 4.5 has been reported (Jadhav et al., 2013; Saranraj and Stella, 2012). Likewise, in another study of distillery wastewater characterization, a comparable value of pH of 3.8±0.5 has been recorded (Petta et al., 2017). The weak alkalinity nature of the of the sugar industry effluent observed in the study might be attributed to the use of $Ca(OH)_2$ for juice clarification and NaOH, Na_2CO_3 for washing of the heater to avoid scaling formation. However, the high acidity of the spent ash is most likely due to the intensive use of the H_2SO_4 in the fermentation process, and sometimes, the use of H_3PO_4 to create a conducive environment for yeast at pH less than 5. The discharge of untreated industrial effluent of such lower pH (acidic) contents can alter the physiochemical and biological properties of the microbial and other living organisms in the soil and aquatic ecosystems. However, the alkaline nature of sugar industry effluent serves as neutralizing agent to acidic spent wash of an ethanol distillery when blending the two wastewaters. This creates an opportunity to reduce the consumption chemicals used for neutralization.

In agro-industrial wastewater, particularly in the sugar industry and ethanol distillery wastewater, the organic pollutants are the major components of the effluent mainly described as COD and BOD_5. BOD_5 of 1,955.9±17.1 mg/L and 31,706.0±2720.5 mg/L, and COD of 2,078.4±33.4 mg/L and 146,897.5±9,106.6 mg/L of the sugar industry and ethanol distillery spent wash were recorded, respectively. Both the BOD5 and COD of the two industries effluent extremely exceeded the permissible discharging limits of the industrial effluent, for which recommended values are for COD 250 mg/L and for BOD_5 60 mg/L. The disposal of such high organic strength effluent with high BOD5 and COD into the aquatic and soil ecosystems can cause the immediate depletion of

dissolved oxygen resulting in adverse physicochemical and biochemical reactions (Jemal Fito et al., 2017). This shows that organic pollutants removal treatment technologies are needed before the effluent released into the nearby environment. This was the main reason why organic matter perceived special attention in this study and anaerobic bioreactor and adsorption treatment technologies were designed to remove degradable and non-degradable organic matters, respectively. In another study, of sugar industry wastewater, comparable values of the BOD5 (970 mg/L) and COD (3,682 mg/L) were reported (Poddar and Sahu, 2017). High amount of the organic matters in different ranges of ethanol distillery spent wash, BOD_5 (50,000 – 60,000 mg/L and 30,000 – 70,000 mg/L) and COD (65,000 –130, 000 mg/L, 110,000 –190,000 mg/L) have been recorded in previous studies (Fito et al., 2018a; Kazemi et al., 2015; Mohana et al., 2009). Additionally, lower values of COD ranging from 60,000 to 80,000 mg/L and comparable values of BOD5 ranging from 30,000 to 40,000 in ethanol distillery spent wash have also been published (Kazemi et al., 2015).

The BOD_5/COD ratio or biodegradability index BI can provide useful information in selecting suitable type of anaerobic high rate reactor with appropriate consideration of wastewater designing parameters (Padoley et al., 2012). In line with this, BI values of the Metahara sugar industry wastewater and ethanol distillery spent wash of 0.94 and 0.22 were observed, respectively. BI value of $\geq$ 0.6, BI between 0.3 and 0.6 and BI value of $\leq$ 0.3 are considered as fairly biodegradable, through the use of the acclimatizing of microorganisms and in the difficult range for biological wastewater a treatment option, respectively (Zaher and Hammam, 2014). Hence, the observed value of BI of the sugar industry wastewater indicated the effluent was in fairly biodegradable range but the BI value of the ethanol distillery spent wash was in a highly challenging range for bioremediation. Therefore, the intention of the blending of the two industrial wastewaters was to overcome such high discrepancy of the wastewaters biodegradability.

In sugar industry and ethanol distillery wastewater the following concentrations were recorded, respectively: TKN of 24.8±2.5 and 1,118.0±38.2 mg/L, nitrate of 0.5±0.3 and 4.9±1.1 mg/L, ammonia of 2.6±0.3 and 14.6±4.3 mg/L, total phosphorus of 19.5±2.1 and 53.7±8.3 mg/L, phosphate of 4.0±0.4, 20.8±3.2 mg/L, and sulfate of 44.3±1.3 and 5,464. ±16.2 mg/L. Mohana et al. (2009) reported high concentrations of Cl^- (8,000 – 8,500 mg/L), sulfate (7,500 – 9000 mg/L) and phosphate (2,500 – 2,700 mg/L) in distillery spent wash. In Metahara sugar estate, the nutrient contents of ethanol distillery spent wash exceeded the nutrients in the sugar industry wastewater. Additionally, according to Ethiopian EPA standards, total nitrogen and phosphorus concentrations of the sugar industry and ethanol distillery wastewaters were significantly beyond the permissible limits of 40 and 5 mg/L, respectively. Hence, the effluent from these two industries can pose severe environmental pollution, particularly eutrophication of lakes and stagnant water bodies (Khairnar et al., 2013). Probably, high concentrations of the nutrients might be associated with the feedstock of the industry, especially in the ethanol production process. For instance, in Metahara ethanol distillery process, the rate application of urea ($CO(NH_2)_2$) was 1.81 kg per m^3 of ethanol and diammonium phosphate (DAP) was 0.63 kg per m^3 of ethanol production (Fito et al., 2018b). Furthermore, fertilizers like DAP ($(NH_4)_2HPO_4$) is the major sources of phosphorus and nitrogen nutrients whereas urea is the source of the nitrogen group. Both nutrients are intensively used in the fermentation process of ethanol distillery. This contributed to the high nutrient values recorded in this study. Furthermore, the high nutrient contents in sugar industrial wastewater might also be associated with the soil content on which sugarcane is cultivated. Hence, in both industrial wastewaters, the values of the nutrient observed indicted that either appropriate wastewater treatment for nutrient removal or nutrient source reduction at industrial process should be implemented to protect the environment and the public health.

3.2. Screening of the Anaerobic Treatment of Blended Wastewater

Before the application of the integrated treatment, screening to identify the optimum point for anaerobic treatment was done. For this screening, an initial COD concentration of 5,000, 10,000, 15,000 and 20,000 mg/L

of the blended wastewater was used at three different values of HRT (i.e., 2, 6, and 10 days), which resulted in 12 different experiments. Anaerobic treatment performance was evaluated in terms of COD reduction and color removal of the blended wastewater. Based on this screening, the optimum point was found at initial COD concentration of 10,000 mg/L at HRT of 10 days which resulted in maximum COD reduction of 65 % whereas the minimum COD removal was 24 % at initial COD concentration of 5,000 mg/L and HRT of 2 days. Under the same optimum point, maximum color removal was 79%; minimum color removal of 41% was obtained at COD concentration of 5,000 mg/L at HRT of 2 days. In another study of up-flow anaerobic fixed film bed reactor for removal of diethyl phthalate from wastewater, maximum removal of COD of 87% was obtained at an initial COD concentration of 300 mg/L which was actually a very low COD concentration (Yousefzadeh et al., 2017). Similarly, using anaerobic filter treatment technology for wastewater management, the average COD removal of 66% was achieved (Bodik et al., 2000). The application of photodegradation of distillery wastewater achieved 79% of color removal at an initial COD concentration of 500 mg/L (Vineetha et al., 2013).

3.3. Screening of the Adsorption Treatment for Blended Wastewater

During the screening of adsorption, the BFA adsorbent used was characterized. High carbon content of 60% by mass and fixed carbon content of 42% was observed under elemental and proximate analyses, respectively. The specific surface area and the average particle size of BFA were 160.9±2.8 m^2/g and 61 µm, respectively. Scanning electron microscope techniques were used to understand the surface morphology of BFA which indicated many cracks with non-uniform and heterogeneous shape of pore sizes. This can create the opportunity to interact with the different sizes of the adsorbent in the effluent. Finally, the FTIR analysis of BFA showed two peaks which were associated with the alcohol and carboxyl functional groups at 3, 255 cm^{-1} and 1,700 cm^{-1}, respectively. In the screening adsorption experiment, two values for each adsorption factor were selected, which were initial COD concentrations of 1,000 and 6,000 mg/L, adsorbent doses of 1 and 4 g in 100 mL, contact times 1 and 4 h and pH 3 and 8. Four factors with two levels were assigned based on full factorial experimental design with 2^4 runs conducted at room temperature. Based on the optimum point identified, maximum COD removal of 62% and color removal of 58% were found at optimum condition of BFA dose 4 g, pH 8, initial COD concentration of 6,000 mg/L and contact time of 4 h. This optimum condition was used in the next experiment which was the integrated wastewater treatment system for blended wastewater. In another study, activated bagasse fly ash was applied for the removal of acrylonitrile pollutants from aqueous solution which resulted in 78% COD reduction at C_O=100 mg/L (Kumar et al., 2014a). In another report, decolorization of distillery spent wash of 54% was achieved using UV photodegradation, which was less efficient than the adsorption efficiency of the bagasse fly ash (Apollo et al., 2013). Generally, the results of these experiments are promising for reducing organic matter, particularly COD and color from the sugarcane industrial wastewater under these specified experimental conditions.

3.4. Performance of the Integrated Treatment System

The application of the integrated treatment system of anaerobic digestion followed by adsorption of the BFA was performed at optimum conditions as described above. Thus, for the integrated system, the biological treatment was performed at an initial COD concentration of 10,000 mg/L, HRT of 10 days and pH 6.5, and followed by adsorption treatment at an adsorbent dose of 4 g in 100 mL and contact time of 4 h. Although the primary focus of the treatment was COD and color removal, the concentration of other parameters, such as nitrate, phosphate etc. was also determined. However, after blending, diluting and treatment of the industrial wastewater, the concentrations of these parameters were rather low and are not reported.

The pH of the wastewater treated by the integrated system increased from 6.5 to 7.4, which indicates that the effluent was safe regarding this parameter, complying with the Ethiopian effluent permissible limit (6-9). The rising of the pH might be attributed to the adsorption treatment. This might have happened due to the fact that,

during anaerobic treatment, the pH of the effluent is expected to decrease due to the biochemical reactions and the generation of organic acids such as acetic and propionic acids. Finally, the application of the integrated treatment system reduced the COD concentration from to 10,000 mg/L to 2,400 mg/L which resulted in 76% COD reduction and 83% of color removal. This result is promising because it is achieved at high initial COD concentration. In comparison, application of an integrated treatment technology of anaerobic digestion with UV photodegradation for distillery wastewater resulted in 85% COD and 88% color reduction at a lower total COD concentration of 5761 ± 105 mg/L (Apollo et al., 2013). In non - integrated treatment technology of distillery spent wash, the electro-Fenton process was reported to reduce COD by 41% and color by 90% (Thanapimmetha et al., 2017). The removal of COD and color by anaerobic and adsorption treatment exceeded 60% during separate treatments. Based on the removal value of the individual treatments, the overall treatment value was expected to be higher than what was actually recorded. However, this did not happen, and might be attributed to the fact that preliminary adsorption testing was done using synthetic wastewater which has fewer interferences than real wastewater. This could be a reason for diminishing the overall performance of the treatment system. Additionally, similar types of pollutants might be involved in both treatment aspects. In general, the performance of such integrated treatment technology for simultaneous COD and color removal was found efficient. However, after the application of the integrated treatment system for blended wastewater, the concentration of effluent in terms of organic matter was still above the industrial effluent discharge limits. As such, additional treatment should be foreseen.

4. CONCLUSIONS

An integrated treatment system of anaerobic digestion with adsorption was tested for blended wastewater of sugar and ethanol distillery wastewater. In all cases, the values of the physicochemical parameters of the distillery spent wash were extremely higher than those of the sugar industry wastewater. The majority of the physicochemical parameters of the two wastewaters are beyond the permissible limits of effluents set by Ethiopian EPA. The average BOD5/COD ratio of blended wastewater has clearly indicated the possibility of the anaerobic treatability of combined wastewater with acclimatized microorganisms. The application of high rate anaerobic filter is an efficient and effective treatment technology for the high strength wastewater of the blended sugar and ethanol distillery. The application of this technology resulted in a maximum COD reduction of 65% and color removal of 79%. But the effluent did not comply with environmental regulation, and the technology was coupled with adsorption which achieved COD reduction of 62% and color removal of 58%. In adsorption, bagasse fly ash was used which is another promising treatment technology for such agro-industrial wastewater. Finally, the application of the integrated treatment system of anaerobic digestion followed by adsorption resulted in COD and color removals of 76% and 83%, respectively. Generally, the experimental results of the integrated system is considered as a potential technology for agro-industry wastewater management.

ACKNOWLEDGMENTS

We would like to thank the United States Agency for International Development (USAID) for the research fund under the USAID/HED grant in the Africa-US Higher Education Initiative – grant numbers, HED 052-9740-ETH-11-01. My great appreciation and thanks also goes to Dr. Helmut Kloos for editing and language scanning of this article.

REFERENCES

Acharya, B.K., Mohana, S., Madamwar, D., (2008). Anaerobic treatment of distillery spent wash – A study on upflow anaerobic fixed film bioreactor. *Bioresource Technology*, 99: 4621–4626. doi:10.1016/j.biortech.2007.06.060

Acharya, B.K., Pathak, H., Mohana, S., Shouche, Y., Singh, V., Madamwar, D., (2011). Kinetic modelling and microbial community assessment of anaerobic biphasic fixed film bioreactor treating distillery spent wash. *Water Research*, 45: 4248–4259. doi:10.1016/j.watres.2011.05.048

APHA, (1998). *Standard Methods for the Examination of Water and Wastewater*, American Public Health Association; American Water Works Association; Water Environment Federation. American Public Health Association;

American Water Works Association; Water Environment Federation, Washington, DC.
Apollo, S., Onyango, M.S., Ochieng, A., (2013). An integrated anaerobic digestion and UV photocatalytic treatment of distillery wastewater. *Journal of Hazardous Materials*, 261: 435–442. doi:10.1016/j.jhazmat.2013.06.058
Basu, S., Mukherjee, S., Kaushik, A., Batra, V.S., (2015). Integrated treatment of molasses distillery wastewater using micro filtration (MF). *Journal of Environmental Management*, 158: 55–60. doi:10.1016/j.jenvman.2015.04.037
Bezuneh, T.T., (2016). The role of microorganisms in distillery wastewater treatment : A review. *Journal of Bioremediation & Biodegradation*, 7: 1–6. doi:10.4172/2155-6199.1000375
Blonskaja, V., Menert, A., Vilu, R., (2003). Use of two-stage anaerobic treatment for distillery waste. *Advances in Environmental Research*, 7: 671–678. doi:10.1016/S1093-0191(02)00038-2
Bodik, I., Herdova, B., Kratochvil, K., (2000). The application of anaerobic filter for municipal wastewater treatment. *Chemical Papers*, 54: 159–164.
Carolin, C.F., Kumar, P.S., Saravanan, A., Joshiba, G.J., Naushad, M., (2017). Efficient techniques for the removal of toxic heavy metals from aquatic environment: *A review. Journal of Environmental Chemical Engineering*, 5: 2782–2799. doi:10.1016/j.jece.2017.05.029
Chapman, J.S., (2003). Biocide resistance mechanisms. *International Biodeterioration & Biodegradation*, 51: 133–138.
Chaurasia, N.K., Tiwari, R.K., (2012). Physico-chemical characteristics of sugar factory and distillery effluents. *Annals of Biological Research*, 3: 4406–4408.
Chooyok, P., Pumijumnog, N., Ussawarujikulchai, A., (2013). The water footprint assessment of ethanol production from molasses in Kanchanaburi and Supanburi Province of Thailand. *APCBEE Procedia*, 5: 283–287. doi:10.1016/j.apcbee.2013.05.049
Degefa, A., Bosie, M., Mequanint, Y., Yesuf, E., Teshome, Z., (2016). Determination of crop water requirements of sugarcane and soybean intercropping at Metahara Sugar Estate. *Advances in Crop Science and Technology*, 4: 10–13. doi:10.4172/2329-8863.1000241
Ding, G.K.C., (2017). Wastewater treatment and reused the future source of water supply. *Encyclopedia of Sustainable Technologies*. doi:10.1016/B978-0-12-409548-9.10170-8
Emadian, S.M., Rahimnejad, M., Hosseini, M., Khoshandam, B., (2015). Investigation on up-flow anaerobic sludge fixed film (UASFF) reactor for treating low-strength bilge water of Caspian Sea ships. *Journal of Environmental Health Science and Engineering*, 13: 1–9. doi:10.1186/s40201-015-0181-3
Feng, Q., Song, Y., Yoo, K., Kuppanan, N., Subudhi, S., (2017). Bioresource Technology Bioelectrochemical enhancement of direct interspecies electron transfer in upflow anaerobic reactor with effluent recirculation for acidic distillery wastewater. *Bioresource Technology*, 241: 171–180. doi:10.1016/j.biortech.2017.05.073
Fito, J., Tefera, N., Demeku, S., Kloos, H., (2017). Water footprint as an emerging environmental tool for assessing Sustainable water use of the bioethanol distillery at Metahara sugarcane farm, Oromiya Region, Ethiopia. *Water Conservation Science and Engineering*, 2: 165–176. doi:/doi.org/10.1007/s41101-017-0038-y
Fito, J., Tefera, N., Hulle, S.W.H. Van, (2018a). Physicochemical Properties of the Sugar Industry and Ethanol Distillery Wastewater and Their Impact on the Environment. *Sugar Tech*. doi:10.1007/s12355-018-0633-z
Fito, J., Tefera, N., Kloos, H., Hulle, S.W.H. Van, (2018b). Anaerobic treatment of blended sugar industry and ethanol distillery wastewater through biphasic high rate reactor. *Journal of Environmental Science and Health, Part A*, 53: 676–685. doi:10.1080/10934529.2018.1438826
Fito, J., Tefera, N., Van Hulle, S.W.H., (2017). Adsorption of distillery spent wash on activated bagasse fly ash: Kinetics and thermodynamics. *Journal of Environmental Chemical Engineering*, 5: 5381–5388. doi:10.1016/j.jece.2017.10.009
Gerbens-Leenes, P.W., (2018). Green, Blue and Grey Bioenergy Water Footprints, a Comparison of Feedstocks for Bioenergy Supply in 2040. *Environmental Processes*, 1–14. doi:10.1007/s40710-018-0311-x
Gupta, V.K., Jain, C.K., Ali, I., Sharma, M., Saini, V.K., (2003). Removal of cadmium and nickel from wastewater using bagasse fly ash - A sugar industry waste. *Water Research*, 37: 4038–4044. doi:10.1016/S0043- 1354(03)00292-6
Iakovleva, E., Sillanp, M., Allen, S., Albadarin, A.B., Mangwandi, C., (2017). Manufacturing of novel low-cost adsorbent : Co-granulation of limestone and coffee waste. *Journal of Environmental Management*, 203: 853– 860. doi:10.1016/j.jenvman.2017.05.039
Jadhav, P.G., Vaidya, N.G., Dethe, S.B., 2013. Characterization and comparative study of cane sugar industry waste water. *International Journal of Chemical and Physical Sciences*, 2: 19–25.
Kazemi, N., Tavakoli, O., Seif, S., Nahangi, M., (2015). High-strength distillery wastewater treatment using catalytic sub- and supercritical water. *Journal of Supercritical Fluids*, 97:74–80. doi:dxdoi.org/10.1016/j.supflu.2014.10.02
Khairnar, P., Chavan, F., Diware, V.R., (2013). Generation of energy from distillery Wastewater. *International Journal of Science, Spirituality, Business and Technology (Ijssbt)*, 2: 29–35.
Kumar, A., Prasad, B., Mishra, I.M., 2014a. Adsorption of acrylonitrile from aqueous solution using bagasse fly ash. *Journal of Water Process Engineering*, 2: 129–133. doi:10.1016/j.jwpe.2014.05.003
Kumar, A., Prasad, B., Mishra, I.M., Ash, B., 2014b. Adsorption of acrylonitrile from aqueous solution using bagasse Lavecchia, R., Medici, F., Piga, L., Rinaldi, G., 2012. Fluoride Removal from Water by Adsorption on a High

Alumina Content Bauxite. *Chemical engineering transactions*, 26: 225–230.
Lopes, M.L., Cristina, S., Paulillo, D.L., Godoy, A., Cherubin, R.A., Lorenzi, M.S., Henrique, F., Giometti, C., Bernardino, C.D., Berbert, H., Neto, D.A., Amorim, H.V. De, 2016. Ethanol production in Brazil : A bridge between science and industry. *Brazilian Journal of Microbiology*, 47: 64–76.
Majone, M., Aulenta, F., Dionisi, D., D'Addario, E.N., Sbardellati, R., Bolzonella, D., Beccari, M., (2010). High-rate anaerobic treatment of Fischer-Tropsch wastewater in a packed-bed biofilm reactor. *Water Research*, 44: 2745–2752. doi:10.1016/j.watres.2010.02.008
Mohana, S., Acharya, B.K., Madamwar, D., 2009. Distillery spent wash : Treatment technologies and potential applications. *Journal of Hazardous Materials*, 163: 12–25. doi:10.1016/j.jhazmat.2008.06.079
Nagda, G.K., Ghole, V.S., (2009). Biosorption of congo red by hydrogen peroxide treated Tendu waste. *Iranian Journal of Environmental Health Science & Engineering*, 6: 195–200.
Nigussie, W., Zewge, F., Chandravanshi, B.S., (2007). Removal of excess fluoride from water using residue from alum Removal of excess fluoride from water using waste residue from alum manufacturing process. *Journal of Hazardous Materials*, 147: 954–963. doi:10.1016/j.jhazmat.2007.01.126
Noonpui, S., Thiravetyan, P., Nakbanpote, W., Netpradit, S., (2010). Color removal from water-based ink wastewater by bagasse fly ash, sawdust fly ash and activated carbon. *Chemical Engineering Journal*, 162: 503–508.
Nure, J.F., Shibeshi, N.T., Asfaw, S.L., Audenaert, W., Hulle, S.W.H. Van, (2017). COD and colour removal from molasses spent wash using activated carbon produced from bagasse fly ash of Matahara sugar factory,Oromiya region, Ethiopia. *Water SA*, 43: 470–479. doi:dx.doi.org/10.4314/wsa.v43i3.12
Olumana, M., Loiskandl, W., Fürst, J., Shaw, R., (2009). Effect of lake Basaka expansion on the sustainability of Matahara SE in the Awash river basin, Ethiopia. *34th WEDC International Conference*, United Nations Conference Centre, Addis Ababa, Ethiopia 1–9.
Padoley, K. V., Saharan, V.K., Mudliar, S.N., Pandey, R.A., Pandit, A.B., (2012). Cavitationally induced biodegradability enhancement of a distillery wastewater. *Journal of Hazardous Materials*, 219–220: 69–74. doi:10.1016/j.jhazmat.2012.03.054
PDAN, Manual, 2013. Anaerobic digestion practical exercise manual.
Petta, L., Gisi, S. De, Casella, P., Farina, R., Notarnicola, M., 2017. Evaluation of the treatability of a winery distillery (vinasse) wastewater by UASB , anoxic-aerobic UF-MBR and chemical precipitation / adsorption. *Journal of Environmental Management*, 201: 177–189. doi:10.1016/j.jenvman.2017.06.042
Poddar, P.K., Sahu, O., (2017). Quality and management of wastewater in sugar industry. *Applied Water Science*, 7: 461–468. doi:10.1007/s13201-015-0264-4
Rajeshwari, Balakrishnan, M., Kansal, A., Lata, K., Kishore, V.V.N., (2000). State-of-the-art of anaerobic digestion technology for industrial wastewater treatment. *Renewable and Sustainable Energy Reviews*, 4: 135–156.
Sahu, O., (2016). Treatment of industry wastewater using thermo-chemical combined processes with copper salt up to recyclable limit. *International Journal of Sustainable Built Environment*, 5: 288–300. doi:10.1016/j.ijsbe.2016.05.006
Sahu, O.P., Chaudhari, P.K., (2015). Electrochemical treatment of sugar industry wastewater : COD and color removal. *Journal of Electroanalytical Chemistry*, 739: 122–129.
Saranraj, P., Stella, D., (2012). Effect of bacterial isolates on reduction of physico – chemical characteristics in sugar Mill effluent. *International Journal of Pharmaceutical & Biological Archives*, 3: 1121–1128.
Sentíes-herrera, H.E., Gómez-merino, F.C., Valdez-balero, A., Silva-rojas, H.V., Trejo-téllez, L.I., Postgraduados, C. De, Montecillo, C., México-texcoco, C., De, E., (2014). The agro-industrial sugarcane system in Mexico : Current status, challenges and opportunities. *Journal of Agricultural Science*, 6: 26–54.
Sentíes-Herrera, H.E., Trejo-Téllez, L.I., Gómez-Merino, F.C., (2017). *The Mexican sugarcane production system: History, current status and new trends, in: Murphy*, R. (Ed.), In: Sugarcane. Nova Science Publishers, Inc:. 40–71.
Shan, L., Liu, J., Ambuchi, J.J., Yu, Y., Huang, L., Feng, Y., (2017). Investigation on decolorization of biologically pretreated cellulosic ethanol wastewater by electrochemical method. *Chemical Engineering Journal*, 323: 455–464. doi:10.1016/j.cej.2017.04.121
Thanapimmetha, A., Srinophakun, P., Amat, S., Saisriyoot, M., (2017). Decolorization of molasses-based distillery wastewater by means of pulse electro-Fenton process. *Journal of Environmental Chemical Engineering*, 5: 2305–2312. doi:10.1016/j.jece.2017.04.030
Vineetha, M.N., Matheswaran, M., Sheeba, K.N., (2013). Photocatalytic colour and COD removal in the distillery effluent by solar radiation. Solar Energy 91, 368–373. doi:10.1016/j.solener.2012.09.013
Wahyu, C., Salim, C., Hinode, H., (2012). Effect of the activation method on the properties and adsorption behavior of bagasse fl y ash-based activated carbon. *Fuel Processing Technology*, 102: 132–139. doi:10.1016/j.fuproc.2012.04.037
Yousefzadeh, S., Ahmadi, E., Gholami, M., Ghaffari, H.R., Azari, A., Ansari, M., (2017). A comparative study of anaerobic

fixed film baffled reactor and up - flow anaerobic fixed film fixed bed reactor for biological removal of diethyl phthalate from wastewater : A performance, kinetic, biogas, and metabolic pathway study. *Biotechnology for Biofuels*, 10: 1–15. doi:DOI 10.1186/s13068-017-0826-9

Zaher, K., Hammam, G., (2014). Correlation between biochemical oxygen demand and chemical oxygen demand for various wastewater treatment plants in egypt to obtain the biodegradability indices. *International Journal of Sciences: Basic and Applied Research*, 3: 42–48.

An overview of two years selected natural product chemistry research at Adama Science and Technology University

Milkyas Endale*, Yadessa Melaku

Department of Applied Chemistry, Adama Science and Technology University, P.O.Box 1888, Adama, Ethiopia
**Corresponding author, e-mail: milkyas.endale@astu.edu.et*

ABSTRACT

Conventionally neglected diseases are considered as group of 13 infectious diseases that are endemic in low income population in the tropical world. They can be classified as those caused by trypanasomal parasites, helminthes, bacteria and viruses. They cause death to an estimated 0.5-1 million people annually. In an ongoing project to analyze the chemical constituents of medicinal plants from Ethiopian biodiversity, the chemical constituents and antibacterial activity of roots extracts of Embelia schimperi, Clausena anisata, Kniphofia schimperiana, and Teclea nobilis and leaves extracts of Combretum paniculatum and Plantago lanceolata were examined. The grounded roots (500 g) were extracted with dichloromethane/methanol (1:1) to give 6.5%, 8.1%, 2.4%, and 1.74% yield for E. schimperi, K. schimperiana, T. nobilis, and C.anisata, respectively, whereas methanol extracts of leaves (300 g) of C. paniculatum and P. lanceolata gave 7.2% and 8.2% yield, respectively. Crude extracts were subjected to silica gel column chromatographic separation to afford coumarins (1-3) and a carbazole alkaloid chalepin (4) from roots of C. anisata, epicatechin (5) and flavan derivative (6) from roots of E. schimperi, verbascoside (7) from leaves of P. lanceolata, benzoylbetulin (8), furoquinoline alkaloid maculine (9) and lupane (10) from roots of T. nobilis, Knipholone derivative (11) and preanthraquinone derivative (12) from roots of K. schimperiana and a stilbene derivative (13) from roots of C. paniculatum. Antibacterial activity of the crude extracts and isolated compounds were screened using agar diffusion method against strains of Staphylococcus aureus, Escherichia coli, Pseudomonas aeruginosa and Bacillus substilis. The results of antibacterial test revealed derivative of coumarins (1,3) exhibited promising antibacterial activity against S. aureus and B. substilis (14 and 13 mm zone of inhibition, respectively) compared with ciprofloxacin (15 mm zone of inhibition). Chalepin (4) revealed more antibacterial activity against B. substilis (16mm zone of inhibition) compared with ciprofloxacin (15 mm). Epicatechin (5) exhibited comparable antibacterial activity against S. aureus and E. coli (15 and 12 mm zone of inhibition, resp.) compared with gentamicin (15 and 12 mm, respectively). Verbascoside (7) displayed promising zone of inhibition (20 mm) against S. aureus compared with ciprofloxacin (23mm). The radical scavenging activity of the methanol and ethyl acetate extract of P. lanceolata, and verbascoside (7) were 64.2%, 79.2% and 83.9%, respectively suggesting that verbascoside (7) displayed powerful radical scavenging activity. In a related work, a series of chalcones derivatives (14-18) and flavonoids (19-20) were synthesized by green synthesis protocol using zinc oxide (ZnO) nanoparticles as catalyst and water as solvent. The method was found to be effective for synthesis of chalcone derivatives comprising base sensitive functional groups with high yield, short reaction time and easy work up procedure. Promising antibacterial activity was observed for chalcones (17, 18) and flavonone (19) against S. aureus (13, 11 and 10 mm zone of inhibition, respectively) compared with cefraxone (16 mm).

Keywords: *Coumarins, alkaloid, chalcones, flavonone, antibacterial activity, radical scavenging activity*

1. INTRODUCTION

Medicinal plants, since times of immemorial, have been used in virtually all cultures as a source of medicine. Plants are efficient in developing chemical control agents for various pathogens and a significant part of pharmaceutical medicine is based on compounds isolated from plants. *P. lanceolata* is locally termed as "gurteb" in Amharic and "kortobe" in Afan Oromo (Ethiopia). Those *Plantago* is a genus of about 265 species of small, inconspicuous plants commonly called plantains. Previous studies have shown that *Plantago* species have analgesic, anti-inflammatory, antimicrobial, antioxidant, hepatoprtective activities, and cytotoxic effect on the cancer cells (Fons et al., 1998). *Combretum paniculatum* belongs to the Combretacea family. The leaves of the plants are used in folk medicine for the treatment of various diseases such as stomach pain and diarrhea (Banskota et al., 2000; Abera, 2014; Asres et al., 2001). In Ethiopia, *C. paniculatum* is used for treatment of

ringworm and wounds (Abera, 2014). Despite the traditional use of this plant against wide range of diseases, there is limited scientific report on the chemical constituents and antibacterial activities of the leaves of *C. paniculatum. Embelia schemperi* Vatke is widely used in traditional medicine as antibacterial and anthelmintic agents (Ndhlala et al., 2015). A gum obtained from the plant is used as a warming remedy in the treatment of dysmenorrheal, fevers, chest, and skin diseases (Ncube et al., 2008). *Teclea nobilis* belonging to the genus *Teclea* and family *Rutaceae* is locally termed as 'atesa' in Amharic. Previous studies have shown that the genus *Teclea* used as analgesic, antiinflammatory and antipyretic activities (Ayafor and Okogun, 1982). *Clausena anisata*, known by local name 'olmaa'ii' in Ethiopia (Afan oromo language), belongs to the family Rutaceae a shrub widely used in various parts of Africa for the treatment of bacterial and fungal infections of the skin including boils, ringworm, oral thrush and eczema (Hamza et al., 2006) and malaria (Uwaifo et al., 1984). The genus *Kniphofia moench* (*Asphodelaceae*) comprises 71 species, commonly known as "red hot pokers" because of the charismatic and conspicuous inflorescences of many species. It is traditionally used to treat wide ranges of ailments including menstrual pains, infertility, abdominal cramps, wounds, malaria, chest complaint and hepatitis B. Fifteen *Kniphofia* species have been recorded in Eastern Africa, of which seven occur in Ethiopia, of which five are endemic and two of them are wide spread including *Kniphofia foliosa* Hochst, *K. isoetifolia*, *K. schimperi, K. hildebrandtii K. insignis*. *K. thomsonii Baker and K. pumila.* (Ramdhani et al., 2008).

2. MATERIALS AND METHODS

2.1. General Experimental Materials

UV-Vis spectrum was measured with GENESY's spectrometer (200-400nm) in methanol at room temperature. Infrared (KBr pellet) spectrum was recorded on Perk-Elmer BX infrared spectrometer in the range 400-4000cm^{-1}. Nuclear Magnetic Resonance (NMR) analysis was recorded on a Bruker avance 400MHz spectrometer with tetramethylsilane as internal standard. Structural assignments were done on the basis of 1D NMR (^{1}H NMR, ^{13}C NMR, DEPT-135) and 2D NMR (COSY, gHMQC, gHMBC) spectra. Thin Layer Chromatography (TLC) was done using silica gel 60 F254. Column chromatography was performed on silica gel 60 (60-100 mesh).

2.2. Plant Material

Fresh leaves of *P. lanceolata* were collected in November, 2016 from Mugher town, Adea Berga Woreda, west shoa zone, Oromia, Ethiopia. The leaves of *C. paniculatum* were collected in February, 2017 from Debeso, Sayo Nole Woreda, Western Wollega zone, Oromia region, Ethiopia, Which is 569 km from Addis Ababa found to Western part of the country. The stem barks of *E. schimperi* were collected from the Oromia region, Horo Guduru Wellaga Zone in Jarte woreda, Sombo kumi kebele, which is 381 km west of Addis Ababa on December 08, 2016. The roots of *C. anisata* were collected from the Oromia region, west Wollega zone which is 541 km west of Addis Ababa on March, 2018. The roots of *T. nobilis* were collected in February 2018 from Sidama zone around Yirgalem town in manche kebele, Godimo place 60 km away from Hawassa town. The roots of *K. schimperiana* were collected from Oromia region, Bale Zone around Goba town specifically Fasil Angaso kebele which is 412 km from Addis Ababa. All plants were authenticated by a botanist Shambel Alemu and voucher specimen was deposited for each at National Herbarium of Ethiopia, Addis Ababa University, Addis Ababa, Ethiopia.

2.3. Extraction and Isolation

2.3.1. Extraction

Air dried grounded leaves (300 g) of *P. lanceolata* were soaked in *n*-hexane (1.5 L) for 72h at room temperature, filtered and concentrated at 40°C using rotary evaporator to afford 4.65 g (1.55%) crude extract. The marc left was sequentially extracted with ethyl acetate (1.5L) and methanol (1.5 L), filtered and concentrated to furnish 6.5g (2.16%) and 24.6 g (8.2%) crude extracts respectively. The powdered leaves of *C. paniculatum* (300 g) were successively extracted with each 1.5mL of *n*-hexane, EtOAc and MeOH for 72h at room temperature, filtered and concentrated to give 4.51 g (1.5%), 8.86 g (2.9%) and 21.5 g (7.2%), respectively. The grounded roots

of *K. schimperiana* (500g) was soaked for 72hr in dichloromethane/methanol (1:1), filtered and concentrated by using rotary evaporator to yield 40.52 g (8.104%) crude extract. The mark left was further extracted by methanol, filtered and concentrated by rotary evaporator and yielded 46.87 g (9.374%).The grounded roots (500 g) of *E. schimperi*, *T. nobilis*, and *C.anisata* were extracted with dichloromethane/methanol (1:1) to give 6.5%, 2.4% and 1.74% yield, respectively.

2.3.2. Isolation

Crude extract (8.5 g) of *C.anisata* was subjected to silica gel column chromatographic separation (150 g silica gel) and eluted with increasing gradient of ethyl acetate in *n*-hexane. A total of 65 fractions were collected. Fractions 11-12 showed yellow spot under UV light having the R_f value of 0.56 in *n*-hexane/ethyl acetate (8:2) solvent system. After concentrating, the solid material left was repeatedly washed with *n*-hexane to yield carbazole alkaloid derivative, heptazoline (**1**). Fractions 19-25 were combined, concentrated and washed repeatedly with *n*-hexane to afford coumarin derivative (**2**). Fraction 29-34 (16mg) showed a single spot on TLC using *n*-hexane: EtOAc (6:4) as a mobile phase. After concentrating, the solid was washed repeatedly with *n*-hexane to afford imperatorin (**3**). Fractions 46-50 (27mg) showed one spot on TLC using *n*-hexane: EtOAc (5:5) as eluent. After concentrating, the solid was washed repeatedly with *n*-hexane to afford Chalepin (**4**).

A total of 36 fractions were collected during silica gel column separation of the roots of *E. schmperi* using increasing gradient of ethyl acetate in *n*-hexane. Fraction 16 analyzed with EtoAc/n-hexane (9:1) afforded epicatechin (**5**) and fraction 20 which showed one major spot was repurified in a silica gel column chromatography with isocratic EtoAc/*n*-hexane (7:3) mode and afforded 12 mg of flavan derivative (**6**). A total of 27 fractions were collected during silical gel column chromatography separation of the leaves *P. lanceolata*. Fractions 22-23 (2.35 g) were combined and further purified by column chromatography (Silica gel 40 g) using methanol/Ethyl acetate (5:95, isocratic mode) as eluent to give five fractions. Fraction 3 (66 mg, compound 1) afforded verbascoside (**7**). The dichloromethane/methanol (1:1) root extract (6 g) of *T. nobillis* was subjected to silica gel column chromatography and eluted with increasing gradient of ethyl acetate in *n*-hexane. A total of 51 fractions were collected. Fraction 18 (eluted with 40% EtOAc in *n*-hexane) showed single spot which was repeatedly washed with *n*-hexane to give alkaloid (**9**, 18 mg). Fraction 6 (eluted with 20 % EtOAc in *n*-hexane) afforded benzoylbetulin (**8**, 13 mg). Similarly, the methanol extract (5g) was subjected to silica gel column chromatography and eluted with increasing gradient of ethyl acetate in *n*-hexane. A total of 35 fractions were collected. Fraction 6 of methanol extract (eluted with 20% EtOAc in *n*-hexane) yielded lupeol (**10**, 8 mg).

The dichloromethane/methanol (1:1) roots extract (12 g) of *K. schmperiana* was subjected to silica gel column chromatography on oxalic acid impregnated silica gel (150 g), 250 g silica gel deactivated with 0.75 g of oxalic acid in one liter distilled water, Merck 60 H 230-400 Mesh) and eluted with increasing gradient of ethyl acetate in *n*-hexane followed by increasing gradient of methanol in dichloromethane. A total of 136 fractions (100 mL each) were collected. Fractions 99-100 (one major spot) were combined, dried and washed successively with *n*-hexane to give knipholone derivative (**11**, 15 mg). Methanol crude extract (12 g) of *K. schmperiana* was subjected to silica gel column chromatography on oxalic acid impregnated silica gel (150 g) and a total 106 fractions (100 mL each) were collected. Fractions 64-69 were combined and repurified by silica gel column chromatography. A total of 15 fractions (15 mL each) were collected of which fractions 7-9 were combined to afford preanthraquinone derivative (**12**, 18 mg).

A total of 41 fractions each 50 mL were collected in silica gel column chromatographic separation of ethyl acetate extract (8g) of leaves of *C. paniculatum*. Fraction 4, eluted with *n*-hexane:EtOAc (7:3) as eluent, which showed 4 spots on TLC was rechromatographed over silica gel column chromatography using *n*-hexane:EtOAc:MeOH as an eluent to furnish 31 fractions each 10 mL. Fractions 15-19 (360 mg) of the ethyl acetate extract, eluted with *n*-hexane:EtOAc (1:4), after silica gel column chromatography furnished silbene derivative (**13**, 36 mg).

2.4. Synthesis of Chalcone and Flavanone Derivatives using ZnO Nanoparticle as Catalyst

2.4.1. Preparation of Zno Nanoparticles

ZnO nanoparticles were prepared. Zinc acetate dihydrated [$Zn(CH_3COO)_2$].$2H_2O$, 2.4 g) and 126 mL of water was added into a round bottom flask. The solution was heated to 60°C with magnetic stirring. The stock solution of potassium hydroxide (KOH) was prepared by dissolving 1.2g of KOH in to 70mL of double distilled water. The stock solution was dropped into the flask within 10-15min. At a constant temperature of 60°C for 2 hr. The solution was condensed to about 10-15 mL and reheated while stirring for another 5 hr before stopping the heating. The upper fraction of the solution was removed after 30min and water (50 mL) was added to the solution and stirred for 5 min. The upper fraction of the solution was discarded again after 30min and dried under vacuum to obtain ZnO nanoparticle.

2.4.2. General Procedure for Preparation of Chalcones (14-18)

A mixture of equimolar quantities of vanillin and acetophenone derivative (substituted) were mixed with ZnO (0.1mmol.) $SnC1_2.H_2O$ (10 %) and 5mL H_2O and heated at 100°C for 2hr. The progress of the reaction was monitored via TLC using *n*-hexane/ethyl acetate as eluent in (7:3) combinations. The reaction mass was cooled to room temperature and stirred with ethanol (50mL) for 30min and centrifuged for 10 min at 5000rpm. The supernatant was collected and concentrated under reduced pressure. The obtained product was checked by TLC and purified using silica gel column chromatography (230-400 mesh, Merck), with increasing gradient of ethyl acetate in *n*-hexane as the mobile phase. Finally, the product yield was recorded

2.4.3. General Procedure for Preparation of Flavonones (19-20)

A mixture of equimolar quantities of Chalcone [2'-hydroxychalcone] and Chalcone [(2'-hydroxy-4-nitrochalcone] were mixed with ZnO (0.1 mmol.) $SnC1_2.H_2O$ (10 %) and 5 mL H_2O and heated at 100°C for 2 hr. The progress of the reactions was monitored via TLC using *n*-hexane/ethyl acetate eluent in (7:3) combinations. The reaction mass was cooled to room temperature and stirred with ethanol (50 mL) for 30min and centrifuged for 10 min at 5000 rpm. The supernatant was collected and concentrated under reduced pressure. The obtained product was checked by TLC and purified by silica gel column chromatography (230-400 mesh, Merck), with increasing gradient of ethyl acetate in *n*-hexane as the mobile phase. Finally, the product yield was recorded.

2.5 Antibacterial Activity

Four microorganisms were selected for the antibacterial activity of the crude extract and isolated compounds. One Gram-positive, *Staphylococcus aureus*, and *K.neumonia* three-Gram negative bacteria, *Escherichia coli* and *Pseudomonas aeruginosa* were used for *in vitro* evaluation of the anti-bacterial activity. The disk diffusion method was used to evaluate the antibacterial activity of both crude extract and isolated compounds on nutrient agar. Briefly, the bacteria stock cultures were maintained on the nutrient agar slants, which were stored at 40°C. The test solutions were prepared by dissolving 50 mg of the test samples to achieve final stock concentrations of 50 mg/mL in DMSO. Freshly grown liquid culture of the test pathogens solution of having similar turbidity with 0.5 McFarland were seeded over the Müeller-Hinton Agar medium with sterile swab. Sterile what man filter paper discs were soaked with 30µL of the above stock solution concentration of the samples and air dried to evaporate the solvent and then applied over the seeded plates at equidistance. The plates were then inverted and incubated at 37°C for 24 hr. After the incubation period, the plates were observed for a clearance zone around the disks. The clear zones formed around each disks were measured in millimeter. Each experiment was carried out in triplicates. The mean of the inhibition zone of each test sample was taken for evaluating the antibacterial activity.

2.6. Antioxidant Activity

DPPH assay: The free radical scavenging activity of the EtOAc, MeOH extract and isolated compounds were measured by 1, 1-diphenyl-2-picryl-hydrazyl (DPPH.) method (Egwaikhide and Gimba, 2007). With this method it is possible to determine the antiradical power of an antioxidant by measuring the decrease in the absorbance of DPPH at 517 nm. As a result of the color changing from purple to yellow the absorbance is decreased when the

DPPH radical is scavenged by an antioxidant through donation of hydrogen to form a stable DPPH-H molecule (Nishibe *et al.*, 1995). Lower absorbance of the reaction mixture indicated higher free radical scavenging activity (Andrzejewska-Golec *et al.*, 1986). The EtOAc extract was dissolved in four vials containing methanol to give 500, 250, 125 and 62µg/mL. To each 1 mL of the above EtOAc extracts was added each 4 mL of 0.04%DPPH which gave 100, 50, 25 and 12 µg/mL. The resulting solution was placed in an oven at 37°C for 30 minutes and subjected to UV-Vis spectrophotometer to record absorbance at 517 nm. This was repeated for the methanol extracts and isolated compounds. The absorbance of 0.04% DPPH in MeOH solution was found to be 1.06. The percentage DPPH inhibition was calculated according to the following formula (Maksyutina, 1971).

$$\% \text{ of radical scavenging activity} = \frac{Ab_{standard} - Ab_{analayte}}{Ab_{standard}} \times 100$$

3. RESULTS AND DISCUSSION

Crude extracts were subjected to silica gel column chromatographic separation to afford coumarins (**1**-**3**) and a carbazole alkaloid chalepin (**4**) from roots of *C. anisata*, epicatechin (**5**) and flavan derivative (**6**) from roots of *E. schimperi*, verbascoside (**7**) from leaves of *P. lanceolata*, benzoylbetulin (**8**), furoquinoline alkaloid maculine (**9**) and lupane (**10**) from roots of *T. nobilis*, knipholone derivative (**11**) and preanthraquinone derivative (**12**) from roots of *K. schimperiana* and a stilbene derivative (**13**) from roots of *C. paniculatum*. The structures of these compounds were identified by exhaustive spectroscopic analysis (UV-Vis, IR, ^{1}H NMR, ^{13}C NMR, DEPT-135, COSY, gHSQC and gHMBC) (Ferew et al., 2018; Dandena et al., 2019; Babe et al., 2017; Fekadu et al., 2018; Tesfaye et al., 2018).

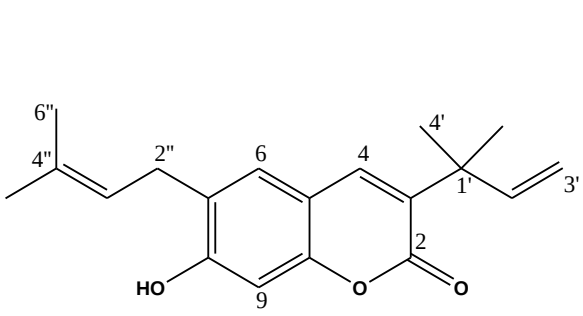

1

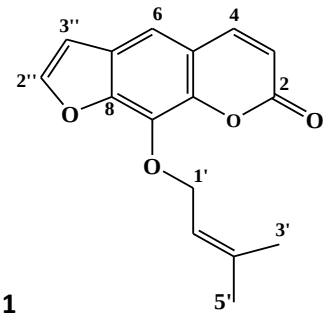

2

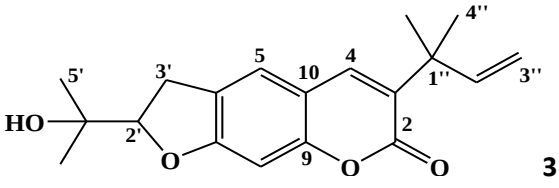

3

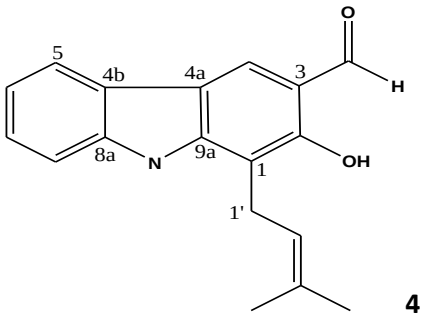

4

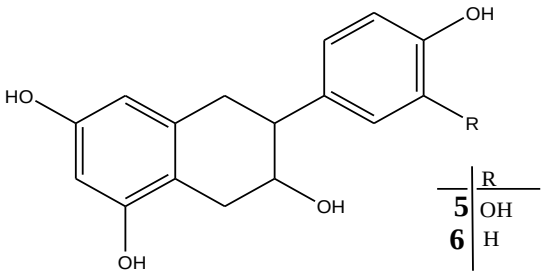

	R
5	OH
6	H

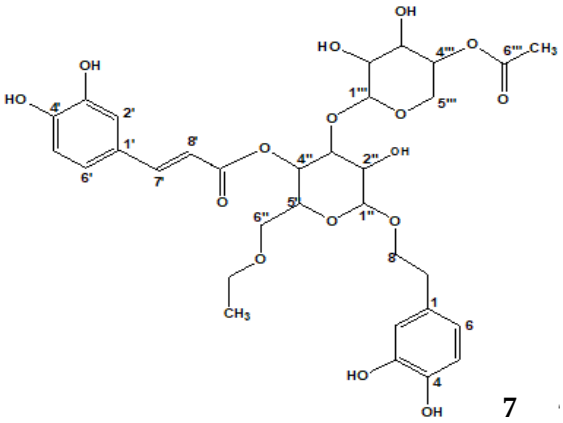

7

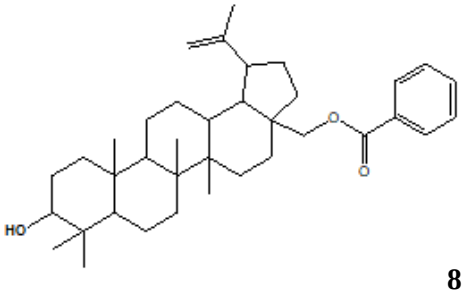

8

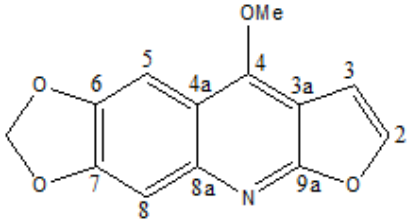

9

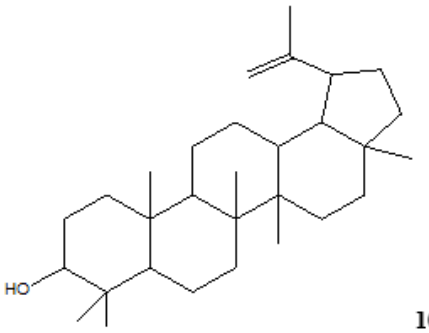

10

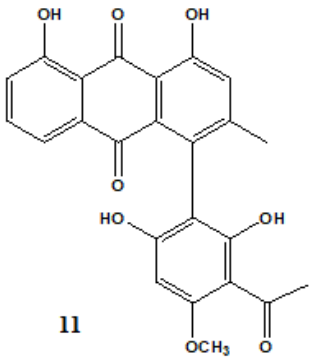

11

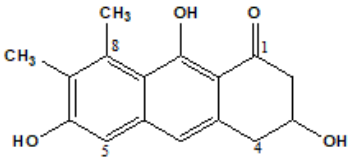

12

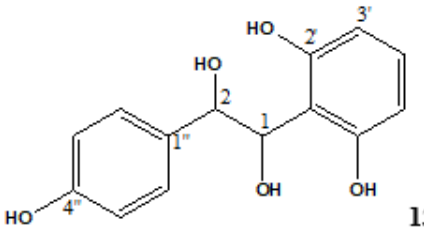

13

In a related work, a series of chalcones derivatives (**14-18**) and flavonoids (**19-20**) were synthesized by green synthesis protocol using zinc oxide (ZnO) nanoparticles as catalyst and water as solvent. The method was found to be effective for synthesis of chalcone derivatives comprising base sensitive functional groups with high yield, short reaction time and easy work up procedure (Dinka et al., 2018).

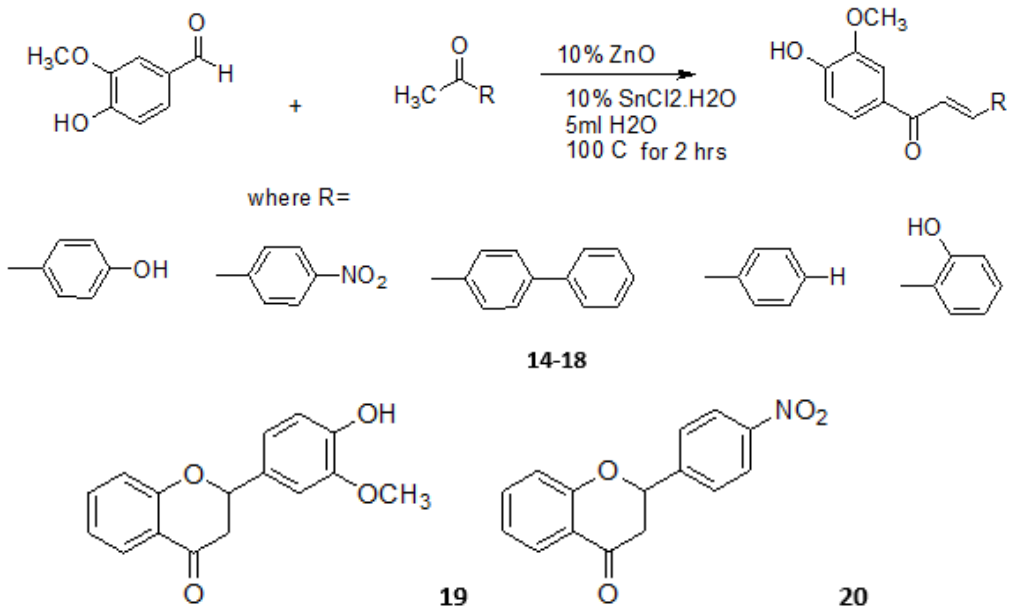

Antibacterial activity of the crude extracts and isolated compounds were screened using agar diffusion method against strains of *Staphylococcus aureus*, *Escherichia coli*, *Pseudomonas aeruginosa* and *Bacillus substilis*. The results of antibacterial test revealed derivative of coumarins (**1**,**3**) isolated from *C. anisata* (table 1) exhibited promising antibacterial activity against *S. aureus* and *B. substilis* (14 and 13 mm zone of inhibition, respectively) compared with ciprofloxacin (15 mm zone of inhibition) at a concentration of 20µg/mL. Chalepin (**4**) revealed more antibacterial activity against *B. substilis* (16mm zone of inhibition) compared with ciprofloxacin (15 mm) (Dandana et al., 2019).

Table 1: Zone of bacterial growth inhibition (mm) for crude extract and isolated compounds

Sample	*E. coli*	*S. aureus*	*B. substilis*	*P. aeruginosa*
CH_2Cl_2/MeOH extract	9 ± 0.1	11± 0.1	10± 0.1	8± 0.1
MeOH extract	n	12± 0.2	13± 0.3	9± 0.2
compound **1**	n	14± 0.1	12± 0.1	12± 0.1
imperatorine (**3**)	n	13± 0.1	14± 0.1	14± 0.1
chalepin (**4**)	n	14± 0.2	16± 0.3	12± 0.2
ciprofloxacin	14± 0.1	15± 0.3	15± 0.3	15± 0.3

$n \leq 6$ is null, and $n > 6$ is sensitive

The antibacterial tests done on crude as well as isolated compounds from leaves of *P. lanceolata* showed considerable antibacterial activity against the bacterial species used in the study. Verbascoside (**7**) showed promising activity against the tested strains except for *K. pneumoia*. The methanol extract was found to inhibit *S. aureus* and *P. miabilis* compared with EtOAc extract. On the other hand, the EtOAc extract displayed better activity than the MeOH extract against *E. coli* and *K. pneumonia*. Verbascoside (**7**) showed promising inhibition diameter (20 mm) against *S. aureus* as compared to standard drug (23mm) (Table 2, Firew et al., 2018).

Table 2: Zone of bacterial growth inhibition diameter (mm)

Sample	Types of bacteria with mean inhibition diameter (mm)			
	S. aureus	*E. coli*	*K. pneumonia*	*P. miabilis*
Ethyl acetate extract	-	8	8	-
Methanol extract	7	-	-	8
Verbascoside (**7**)	20	13	7	9
Chloroform	-	-	-	-
Ciprofloxacin	23	21	19	24

Epicatechin (**5**) isolated from *E. shemperi* (Babe et al., 2018) exhibited comparable antibacterial activity against *S. aureus* and *E. coli* (15 and 12 mm zone of inhibition, resp.) to that of gentamicin, with zone of inhibition of 15 and 12 mm, respectively, at a concentration of 20 μg/mL (table 3).

Table 3: Zone of bacterial growth inhibition (mm) for crude extract and isolated compounds from stem bark of *E.schemberi*

Extract/control	Zone of inhibition (mm)			
	S. aureus	*E. coli*	*P. mirabilis*	*K. neumonia*
Methanol extract	*n*	*n*	*n*	*n*
compound **6**	11	13	10	10
epicatechin (**5**)	15	12	6	11
Gentamicine	15	15	15	15

n≤ 6 is null and n>6 is sensitive

Stilbene derivative (**13**) demonstrated zone of inhibition of 19 mm against *S. aureus* (table 4) which was turned out to be comparable with ciprofloxacin (23 mm zone of inhibition). The results obtained from the antibacterial screening of the leaves in a good agreement with the ethnobotanical survey of the plant in the literature (Fekadu et al., 2018).

Table 4: Inhibition zone diameter of the three successive plant extract of *C. paniculatum*, compound 2, antibiotics and chloroform

Extract/control	Zone of inhibition (mm)			
	S. aureus	*E. coli*	*K. preumanin*	*P. mirabilis*
n-hexane extract	8	10	-	9
Ethyl acetate extract	15	12	-	14
Methanol extract	7	-	10	8
Stilbene derivative (**13**)	19	12	11	10
Ciprofloxacin (+ ve control)	23	21	19	24
Chloroform (- ve control)	0	0	0	0

(-) no zone of inhibition

The radical scavenging activity of the methanol and ethyl acetate extract of *P. lanceolata*, and verbascoside (**7**) were 64.2%, 79.2% and 83.9%, respectively suggesting that verbascoside (**7**) displayed powerful radical scavenging activity. The ethyl acetate, methanol extracts and verbascoside (**7**) were examined for its radical scavenging activities. The DPPH radical scavenging activity was found to be 64.2%, 79.2, 87.7 and 83.9, respectively, at 100µg/mL (table 5). The IC_{50} values of the EtOAc, MeOH, and verbascoside (**7**) were 36.6, 59.1, and 76.1, respectively. The result obtained was found to be promising as compared to ascorbic acid with percent inhibition of radical by 97% at 100µg/mL. The promising activity of verbascoside (**7**) may be attributed to the

presence of phenolic hydroxyl groups. The result suggests that the leaves of *P. lanceolata* can be used as a natural antioxidant (Firew et al. 2018).

Table 5: % scavenging activity of the extracts and isolated compounds of *P. lanceolata*

concentration	samples					
	EtOAc extract		MeOH extract		Verbascoside (**7**)	
	Absorbance	% scavenging activity	absorbance	% scavenging activity	absorbance	% scavenging activity
100	0.38	64.2	0.2	79.2	0.2	83.9
50	0.45	57.5	0.3	76.4	0.3	76.4
25	O.56	47.2	0.3	71.7	0.3	67.9
12	0.62	41.5	0.5	57.5	0.4	60.4

Synthesis yield was calculated on the basis of initial weight of the raw materials taken and the final weight of the chalcone and flavonones obtained after complete drying. It was observed that % yield of the reaction in case of ZnO NPS synthesized flavonone (**19**, 89.6%) was higher as compared to conventionally synthesized flavonone (55.7 %) (Table 6). Furthermore effect of $SnCl_2$,H_2O enhancing the cyclization of chalcone by increasing the nucleophilicity of the carbonyl and variation on the % yield of synthesized flavonone and reaction time was also evident (Dinka et al., 2018).

Table 6: Method comparison of % yield of the conventionally and ZnO NPS for synthesis of 2-(4-Nitro-phenyl)-chroman-4-one (**7**)

Method	Time taken for reaction	yield %	Temperature
Conventional	8 hr	55.7	Room
ZnO NPS	2 hr	89.6	100 ^{0}C

All the chalcones and flavonones **(14-20)** (Dinka et al., 2018) were evaluated for their antibacterial activity and all compounds exhibited some degree of inhibition zones. The chalcones **17** and **18** are active on against *S. aureus* were as Flavonone **19** active on against *E. coli* and **20** active on against *S. aureus* and *P. aeroginosa* (Figure 1).

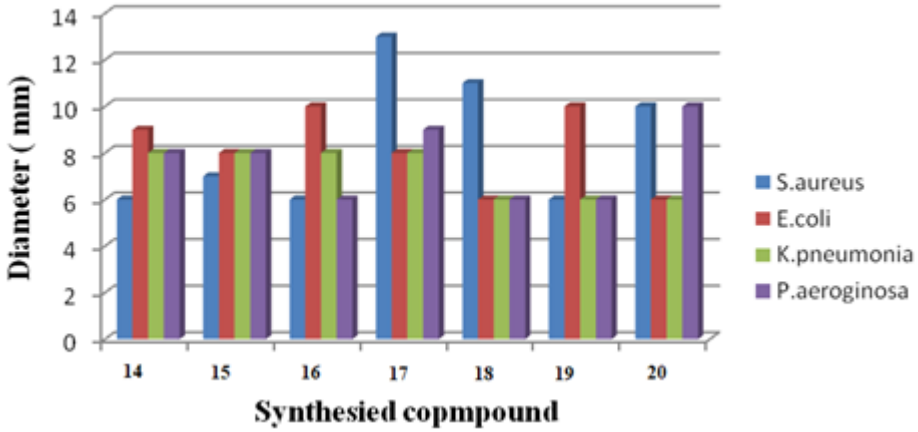

Figure 1: Zone of inhibition of chalcones (14-18) and flavanones (19-20).

4. CONCLUSION

In order to promote Ethiopian herbal drugs and traditional use of medicinal plants, there is an urgent need to evaluate the therapeutic potentials of the drugs as per the WHO guidelines. Bioactive extracts should be validated and standardized on the basis of phytochemical constituents. Despite the rich biodiversity of Ethiopian flora, there are limited information about the type of secondary metabolites present in most of these plants and their biological activity. In an ongoing project to analyze the chemical constituents of medicinal plants of Ethiopia, our group analyzed the chemical constituents and biological activity of over fifteen plants in past two years. This paper highlighted a summary of the phytochemical analysis works carried out on six plants past two years; *E. schimperi*, *C. paniculatum*, *P. lanceolata*, *K. schimperiana*, *T. nobilis*, and *C. anisata*. Comprehensive phytochemical screening tests were done on the root extracts (CH_2Cl_2/CH_3OH, 1:1) of these plants accompanied by fractionation with silica gel column chromatography and spectroscopic analysis of the pure compounds. From these six plants, thirteen secondary metabolites (**1-13**) were fully characterized. A green synthesis approach towards a series of chalcones and flavanoids (**14-20**) using nano ZnO catalysis approach were also presented. Considering the diversity of Ethiopian flora and wide traditional use of these plants, more work is recommended so as to identify drug lead secondary metabolites and validate the traditional use of Ethiopian herbal plants.

ACKNOWLEDGEMENT

We are grateful to Adama Science and Technology University for grant support. Department of Chemistry, Addis Ababa University is duly acknowledged for access to NMR, UV-Vis and IR instruments.

REFERNCES

Abebe, D., (1986): Traditional medicine in Ethiopia: the attempts being made to promote it for effective and better utilization, *SINET*, 9: 61-69.

Abebe. D., Debella. A., Urga. K., (2003): Medicinal plants and other useful plants of Ethiopia. *Ethiopian Health and Research Institute*, 262-265.

Abera, B, (2014): Medicinal plants used in traditional medicine by Oromo people, Ghimbi District, Southwest Ethiopia. *Journal of Ethnobiology*, 1: 10-40.

Asres, K., Bucar, F., Kartnig, T., Witvrouw, M., Pannecouque, C., De Clercq, E., (2001): Antiviral activity against HIV-1 and HIV-2 of ethnobotanically selected Ethiopian medicinal plants. *Journal of Phytotheraphy Research*, 15:62-69.

Ayafor, J.F., Okogun, J.I., (1982): Isolation and identification of three new phenolic furoquinoline alkaloids from *Teclea verdoorniana* Exell & Mendoca (Rutaceae). *J. Chem. Soc., Perkin Transaction*, 1: 909-915.

Babe, G., Yadessa, M., Milkyas, E., (2018): Antibacterial activity of two flavans from the stem bark of *Embelia schimperi*, *Advances in Pharmaceutical Sciences*, 9: 2-8.

Banskota, A.H., Tezuka, Y., Kim, Q.T., Tanaka, K., Saiki, L., Kadota, S., (2000): Thirteen novel cycloartane-type triterpenes from *Combretum quadrangulare*. *Journal Natural Products*, 63:57-64.

Dagne, E., Bisrat, D., Viljoen, A., Van Wyk, B.E., (2000): Chemistry of *Aloe* species. *Current Organic Chemistry*, 4(10): 1055-1078.

Dandana, T., Milkyas, E., (2018): Antibacterial activity of coumarins and carbazole Alkaloid from Roots of *Clausena anisata*, *Advances in Pharmacological Sciences*. In press.

Dinka, M., Bedasa, A., Abebe, B., Milkyas, E., (2018): Synthesis of Chalcone and Flavanone Derivatives using ZnO Nanoparticle as Catalyst for Antibacterial Activity. *Chemistry and Materials Research*, 10(6): 1-11.

Egwaikhide, P., Gimba, C., (2007): Analysis of the phytochemical content and anti- microbial activity of *Plectranthus glandulosis* whole plant. *Middle-East Journal of Scientific Research*, 2(3-4):135-138.

Fons, F., Gargadennec, A., Gueiffier, A., Roussel, J., Andary, C., (1998): Effects of cinnamic acid on polyphenol production in *Plantago lanceolata*. *Phytochemistry*, 49:697-702.

Fekadu, A., Milkyas, E., Yadessa, M., (2018): Antibacterial Stilbene Derivative from the Leaves of *Combretum paniculatum*, *Journal of Natural Science Research*, 8:8-12.

Firew, D., Milkyas, E., Yadessa, M., (2018): Antibacterial and Antioxidant Phenylpropanoid Derivative from the Leaves of *Plantago lanceolata*, *Natural Product Chemistry Research*, 6:3.

Hamza, O.J., Van den Bout-Van den, Beukel, C.J., Matee, M.I., Moshi, M.J., Mikx, F.H., Selemani, H.O., Mbwambo, Z.H., van der Ven, A.J., Verweij, P.E., (2006): Antifungal activity of some Tanzanian plants for the treatment of fungal infections, *Journal of Ethnopharmacology*, 108(1): 124- 132.

Maksyutina, N.(1971): Hydroxycinnamic acids of *Plantago major* and P. *lanceolata*. *Chemistry of Natural Compounds*, **7**(6): 795.

Murai, M., Tamayam, Y., Nishibe, S., (1995): Phenylethanoids in the herb of *Plantago lanceolata* and inhibitory effect on arachidonic acid-induced mouse ear edema. *Planta Medica*, 61(5): 479.

Ncube, N.S., Afolayan, A.J., Okoh, A.I.(2008): "Assessment techniques of antimicrobial properties of natural compounds of plant origin: current methods and future trends," *African Journal of Biotechnology*, 7(12):1797-1806.

Ndhlala, A.R., Ghebrehiwot, H. M., Ncube, B. (2015): Antimicrobial, anthelmintic activities and characterisation of functional phenolic acids of *Achyranthes aspera* Linn: a medicinal plant used for the treatment of wounds and ringworm in East Africa," *Frontiers in Pharmacology*, 6, 274.

Ramdhani, S., Barker, N.P. Baijnath, H., (2008): Exploring the Afromontane centre of endemism: *Kniphofia* Moench (Asphodelaceae) as a floristic indicator. *J. Biogeogr.* 35: 2258-2273.

Tesfaye, N., Solomon G., Yadessa, M., Milkyas, E., (2018): Benzoylbetulin from Roots of *Teclea nobilis*, *The Pharmaceutical and Chemical Journa*l, 5(4): 56-62.

Uwaifo, A.O., (1984): The mutagencities of seven coumarin derivatives and a furan derivative (nimbolide) isolated from three medicinal plants, *J. Toxicol. Environ.*, 56(3):117-121.

Water Footprint for Assessing Sustainable Water Use for Sugarcane Biorefineries

Jemal Fito[1], *, Nurelegne Tefera[2], Sisay Demeku[3] and Helmut Kloos[4]

[1]*Ethiopian Institute of Water Resources, Addis Ababa University, Ethiopia.*
[2]*Department of Chemical Engineering, Addis Ababa Science and Technology University, P.O.Box 16417 Addis Ababa, Ethiopia*
[3]*Department of Water Supply and Sanitary Engineering, Addis Ababa Science and Technology, Ethiopia.*
[4]*Department of Epidemiology and Biostatistics, University of California, San Francisco, CA, USA*
**Corresponding author, e-mail: fitojemal120@gmail.com*

ABSTRACT

In Ethiopia, sugarcane estate farms and bioethanol distilleries are being expanded at an alarming rate to provide alternative sustainable energy as renewable, affordable and low carbon footprint bioenergy for the transportation sector. The promotion of bioethanol production is definitely poised to cause high competition for water resources. Thus, the aim of this study was to investigate the water footprint (WF) of sugarcane molasses-based bioethanol production of the Metahara sugarcane farm. Ten years' of meteorological data (2007 - 2016) were collected from the Metahara weather stations and processed through the CROPWAT 8 model using the Penman-Monteith method. Sugarcane coefficient (K_c) was taken from FAO data; and sugarcane growing seasons, fertilizer application rates, sugarcane yield, and factory data were obtained from the Metahara factories. Reference evapotranspiration varied from 4.73 to 7.98 mm/day whereas effective rainfall (R_{eff}) values ranged from 256.4 to 743.6 mm/growing season of sugarcane (16 months). The estimated sugarcane water requirement (SWR) ranged from 2544.1 to 4833.3 mm/growing season. The ANOVA test ($p > 0.05$) for R_{eff} showed statistically insignificant differences in means but the test for SWR ($p < 0.05$) revealed a statistically significant differences in means. The average sugarcane WF was 217.69 m^3/t whereas the bioethanol WF was 3106.7 L/L. Hence, The WF of bioethanol production in the Metahara distillery is higher than the global average, indicating pressure on local water resources. Therefore, the results of this study may help policy makers to develop appropriate water resource management for the extensively growing sugar and bioethanol industries in Ethiopia.

Keywords: *Bioethanol, Environment, Evapotranspiration, Crop water requirements, Sustainability; Water footprint*

1. INTRODUCTION

Competition for global freshwater consumption is increasing rapidly, largely due to the growing world population and the expansion of industrialization and modern agriculture, which have resulted in unsustainable use of groundwater, pollution of water bodies, depletion of water resources, and damage to ecosystems (Perry, 2014). An increasing world population coupled with continued socioeconomic development put increasing pressure on the world's freshwater resources. Decreasing freshwater availability and quality are being observed across the globe (Mekonnen, 2011). An estimated 2.0 –2.7 billion people will face water shortage problems by 2050 and the global water resources per capita will decrease by one-third (UN-Water, 2003). Overconsumption of freshwater is significantly contributing to water scarcity in many parts of the world. Water scarcity in agriculture and industries is estimated to result in a decline in GDP of about 6% in many nations by 2050 (De Angelis et al., 2017). In addition to intensive water abstraction across the globe, water pollution is a decisive factor aggravating water scarcity since polluted water is unsuitable for human use and diminishes water productivity.

The agricultural and industrial sectors are the main contributors to freshwater overutilization and pollution. Agriculture itself accounts for 86% of global freshwater consumption (Jefferies et al., 2012). Agricultural freshwater demand is estimated to increase by 50% in developing countries and by 19% across the globe between 2000 and 2025 (Gheewala et al., 2014). With the current agricultural water utilization efficiency and use rate (approximately 7,100 km^3year^{-1}), an additional 5,700 km^3year^{-1} of water will be needed to meet the world food demand by 2050 (Ortiz-Rodriguez et al., 2015). Globally, the gap between water resources and water demand is increasing due to anthropogenic activities and population increases, exacerbating the problem of water scarcity

(Ding and Ghosh, 2017). In the 21st century, declining freshwater availability and insufficient quantities and quality are major challenges for many societies and causes of conflicts over freshwater use, creating severe tensions between countries, regions, and even among sectors (Srinivasan et al., 2017). Hence, sustainable use and conservation of freshwater is critical to ensuring sustainability of socioeconomic development. Moreover, the aim of sustainable water use application is to implement innovative water management practices to ensure sufficient water quantity and quality for present and future generations.

Freshwater availability is a key factor for development of bioenergy crops such as sugarcane for bioethanol production. However, low priority is given to environmental impacts and sustainability of the biofuel industry in many African countries, including Ethiopia, since economic profits and job creation are the primary concerns of governments (Pahlow et al., 2015). In reality, bioethanol distilleries are being developed at a fast pace because of the variability of oil prices on the world market and increasing consumption of bioethanol as an energy source and of raw plant materials by many industries (Mohana et al., 2009). Sugar factories annexed to bioethanol distilleries produce on average 95 kg of sugar, 12 L of bioethanol, 250 kg of bagasse and 155 L of spent wash per 1,000 kg of sugarcane (Siddiqui and Waseem, 2012). The bioethanol distilling process requires large volumes of fresh water. Distillery waste accounts for 88% to 95% of the total volume of the raw materials in the bioethanol production process and bioethanol constitutes only the remaining 5% to 12% (Pant and Adholeya, 2007). With respect to wastewater management, globally about 80% of all wastewater is discharged without proper treatment (UN-Water, 2017). For every liter of bioethanol produced, about 12 to 15 L of the distillery spent wash are generated (Biswas et al., 2009). At many places, most of the volume of the spent wash is not treated and is discharged into the nearby environment. This shows that bioethanol distilleries contribute significantly to water consumption and pollution along the supply chain of bioethanol production. Thus, proper water utilization and management tools such as WF are vital for sustainable water use.

The WF concept was introduced by Hoekstra (2002) as a tool for estimating freshwater consumption along the supply chain in the production of various products and to provide a useful indicator of water resources management (Lovarelli et al., 2016). WF is becoming a powerful environmental tool used by producers and consumers to assess water use along the production chain and to identify hotspots with the goal of ensuring continued availability of freshwater (Ortiz-Rodriguez et al., 2015). Thus, the ultimate goal of WF is to investigate the sustainability of freshwater use and to develop proper water management practices in different water consuming sectors. Based on the application areas of interest, different units can be used to describe the water footprint concept for different sectors. Most commonly, WF is expressed as the water volume used per unit of product (usually mass, volume, energy, and piece) or the water volume per unit of time (year) in a delineated area (e.g., nation, municipality, province, or catchment) (Lovarelli et al., 2016). The WF of a product (m^3/t) refers not only to the total volume of water used or polluted in order to produce a product, but also to direct and indirect water uses in the production process. WF comprises green, blue, and grey water use expressed as an integrated freshwater resource allocation indicator; it permits more efficient water management than traditional limited water intake measurements (Chia et al., 2015). Generally, WF is a more comprehensive and multidimensional indicator of freshwater consumption and pollution of a product within given geographical and temporal boundaries than the traditional measures of water withdrawal (Hoekstra et al., 2011).

WF can be used as an indicator of water use to monitor and predict freshwater depletion and degradation in the production of water-intensive sugarcane crops and bioethanol**.** Globally, the rapid increase in the use of biofuels in the transportation sector has increased biofuel production, and the predicted global annual WF of biofuels in 2030 will be 10 times that in 2005 (Chiu et al., 2016). The heavy use of green, blue, and grey water is a major concern in sugarcane cultivation and bioethanol production (Fachinelli and Pereira, 2015a). Expansion of sugarcane cultivation is a global trend, important to the economic development agendas of many countries for future bioethanol feedstocks (Hess et al., 2016). The global average WF of sugarcane was reported to be 209 m^3/t,

but wide variations in the WF of sugar and bioethanol production are reported from different countries (Chooyok et al., 2013). In a study in Thailand, a sugarcane WF of 226 m^3/t was reported, which consists of green (146 m^3/t), blue (31 m^3/t), and grey water (49 m^3/t (Rattikarn Kongboon and Sampattagul, 2012). Variations in WF are basically due to crop type, agricultural practices, climate conditions, and industrial water utilization efficiency(Lovarelli et al., 2016).

Ethiopia is endowed with large areas of lowlands with climate and soil types suitable for sugarcane production. The Ethiopian government has given special attention to the development of sugarcane farms and sugar and bioethanol production. The government has expanded sugarcane plantations and bioethanol production with the vision to become the leader of sugar and bioethanol production in Africa. Moreover, the tendency toward the utilization of bioethanol for transportation has recently increased in Ethiopia to meet the shortage of petroleum fuel and mitigate climate change and global warming. The promotion of bioethanol production will sharply increase water use in Ethiopia, where agriculture is the backbone of the economy and water management is poor.

Recently, Ethiopia has experienced drought mainly in the semi-arid area, resulting in declining agricultural yields. The focus of this study was to find favorable production conditions with respect to water consumption along the production chain and possibly hotspots and environmental burden on the local water system of the Metahara sugar factory and estate farm. Most sugarcane plantations and bioethanol industries in Ethiopia, including the Metahara bioethanol distillery, are located in the semi-arid climate zone, where sugarcane growing depends largely on surface water irrigation. Moreover, water is a precious resource and in very high demand in semi-arid areas, including the Awash valley, due to the fast expansion of large sugarcane estate farms and sugar industries. However, the amount of rain and irrigation water used by the Metahara farm for sugarcane production, sugarcane water requirement, and factory water demand has not been studied in an integrated way using the concept of WF. Furthermore, using WF clearly indicates an environmental pollution problem from the sugar industry and the leaching of excessive chemical fertilizer in the area. Hence, proper water management practices may generate environmental and economic benefits aimed towards ensuring sustainable sugarcane water use. Only a few studies (Chooyok et al., 2013; Flach and Javier Godar3, 2016; Gerbens-Leenes and Hoekstra, 2009; Gerbens-leenes and Hoekstra, 2012, 2011; Hobson and Renouf, 2013) exist on the WF of bioethanol production because of the complexity of data collection and the limitation of study methods. Furthermore, few WF studies have been conducted at local and regional levels in many countries, including Ethiopia. Global sugarcane and bioethanol WF studies are considered as a basis and trigger for more detailed local WF assessments (Gerbens-Leenes and Hoekstra, 2009). However, investigations of the WF of bioethanol production under Ethiopian climate conditions, agricultural practices, and water management aspects are lacking. Therefore, this study aimed to quantify the WF associated with bioethanol production in the Metahara distillery based on sugarcane cultivation, molasses processing, and bioethanol production.

2. MATERIALS AND METHODS

2.1. Description of Study Area

The Metahara sugar estate is the second largest irrigation scheme in the Awash Basin, shown in Figure 1. It was established in an agreement between the Dutch company Handelsvereenigung Amsterdam and the Ethiopian government in 1965 to meet an increasing domestic sugar demand. Metahara is located in East Shoa Zone, about 200 km east of Addis Ababa, in Oromiya Regional State, at the geographical coordinates of 8° 54' 0" North and 39° 55' 0" East. The area has a semi-arid climate, with mean maximum and minimum temperatures of 32.76°C and 17.5°C, respectively. The factory is at an altitude of 940 m above sea level and has an average annual rainfall of about 600 mm. There is no fixed rainfall trend in this semi-arid climate, but most of the rainy period is from June to September and the rest of months are dry. Currently, the Metahara sugar factory has about 10,230 hectares

of land covered with sugarcane with an average sugar production of 825,000 t/year and a bioethanol production capacity of 12,500 m^3/year (Degefa et al., 2016).

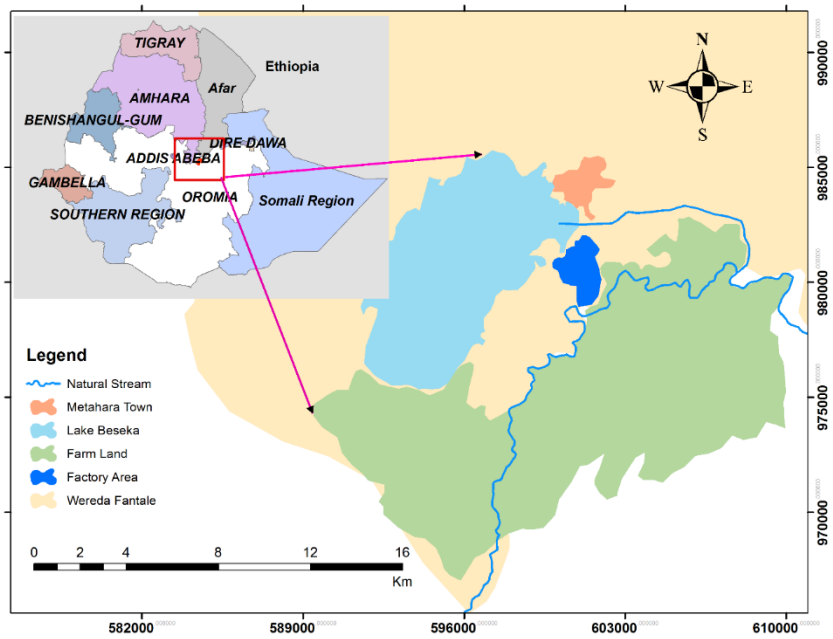

Figure 1: Locations map of Metahara sugarcane farm and sugar industry

2.2. Availability of Data and Materials

Meteorological data for the Metahara sugarcane estate farm, such as rainfall (mm), sunshine (hours), relative humidity (%), maximum and minimum temperature (°C), and wind speed (m/s), were collected and processed through the CROPWAT 8 model. The meteorological data were arranged based on monthly average data and applied in the CROPWAT 8 model to estimate reference evapotranspiration (ETo). Sugarcane growing season (calendar), nitrogen fertilizer application rates (kg/ha), and sugarcane yield (t/ha) were obtained from the Wonji Research and Development Centre. Sugarcane coefficient (K_c) values were taken from Food and Agriculture Organization of the United Nations (FAO) data, which were used for initial, mid-season, and late season sugarcane growing stages. Furthermore, factory data were collected from the Matahara sugar factory and bioethanol distillery to estimate molasses and bioethanol WF. These factory data had two sections. The first comprised the data from the sugar factory, which included the amount of filter cake, molasses, bagasse, and sugar produced from one ton of sugarcane processed in the factory. The second set of data was collected from the bioethanol distillery; these data included the amount of spent wash generated, process water consumed, and bioethanol produced from the molasses obtained from one ton of sugarcane. Finally, additional process water consumed in the bioethanol distillery for fermentation, dilution, and distillation processes was considered. In all cases, ten years' (2007-2016) data were collected and applied except for the bioethanol distillery, which was established in 2011; five years' data (2012-2016) were used for the distillery.

2.3. Determination of Reference Evapotranspiration (ET_o)

Determination of ETo refers to the estimation of evapotranspiration of an ideal (hypothetical) crop. A hypothetical reference surface assumes an extensive surface of green grass of uniform height, an actively growing crop height of 0.12 m, and a fixed surface resistance of 70 s/m (Shah et al., 2015). This ideal ETo condition can be related to actual crop water requirements (CWRs) using Kc. Although several methods exist to determine ETo, the Penman-Monteith method is recommended (Chapagain and Hoekstra, 2011). Consequently, ETo (mm day^{-1}) was computed from the Metahara weather station's data of maximum and minimum air temperature (°C), wind

speed (m/s), relative humidity (%), and sunshine duration (hours) using the CROPWAT 8 model programme by the FAO Penman-Monteith method.

A. Calculation of effective rainfall (R_{eff})

Effective rainfall refers to the portion of rainfall that can be effectively used by plants. Ten years (2007-2016) of rainfall data were used in the CROPWAT 8 model to estimate R_{eff}. The fixed-percentage method of effective rainfall calculation was used in this study; this is the recommended method for observed rainfall less than or equal to 100 mm/month. R_{eff} of actual precipitation was calculated according to Equation 1.

$$R_{eff} = \text{fixed}\% * R \quad (1)$$

Where, R_{eff} is effective rainfall (mm/day) and R is rainfall (mm/day) collected from the meteorological station. This fixed percentage method indicated that about 20% of rainfall can be lost in the form of surface runoff or infiltration into the ground without utilization for crop growth (Scholten, 2009).

B. Determination of Potential Evapotranspiration (ETc)

Determination of crop evapotranspiration is basically the same as determination of sugarcane water requirement (SWR). The amount of water required to compensate for evapotranspiration loss from the cropped field is defined as CWR. Sugarcane evapotranspiration (ETc, mm/day) was calculated for the given set of data on ET_o and Kc. Sugarcane ET_c value depends on climate ET_o, crop module, sugarcane growing season, and effective rainfall. The CROPWAT 8 model was used to determine SWR (ETc) with the help of Equation 2

$$ETc\left(\frac{mm}{day}\right) = K_c * ET_0 \quad (mm/day) \quad (2)$$

Where, ETc is sugarcane evapotranspiration, Kc is the sugarcane coefficient, and ET_o is reference crop evapotranspiration (Ortiz-Rodriguez et al., 2015).

C. Green Water Footprint (WF_{green}) Calculation

Green evapotranspiration (ET_{green}) is the amount of effective rain water (mm/time) required to evaporate from the soil surface where crops are grown, including the transpiration of water that actually passes from crops plus the water incorporated in the product. Rainfall data were used to calculate R_{eff} in the CROPWAT 8 model using the rain module. If the R_{eff} is larger than the CWR, the ET_{green} is equal to the value of the ET_c, because a crop uses as much water as possible but never more than what is required for optimal plant growth (Gheewala et al. 2014). In this analysis, the R_{eff} was smaller than the ET_c, thus the ET_{green} is equal to R_{eff} as shown in Equation 3.

$$ET_{green} = (R_{eff})\left(\frac{mm}{day}\right) \quad (3)$$

Where, ET_{green} is green evapotranspiration and R_{eff} is effective rainfall. The green component in sugarcane water use (SWU, m^3/ha) was calculated by accumulation of all daily green evapotranspiration (ET_{green}, mm/day) over the entire growing period according to Equation 4.

$$SWU_{green}\left(\frac{m^3}{\text{ha}}\right) = 10 * \sum_{d=1}^{lgp} ET_{green} \quad (4)$$

Where, SWU is sugarcane water use, lgp *is* the length of the growing period (days); ET_{green} represents green evapotranspiration, and 10 is a conversion factor (0.1 mm/day =1 m^3 /ha day). Sugarcane green water footprint (WF_{green}, m^3/t) was calculated by dividing the green component in sugarcane water use (SWU_{green}, m^3/ha) by the sugarcane yield (*Y*, t/ha) according to Equation 5.

$$WF_{green}\left(\frac{m^3}{t}\right) = \frac{SWU_{green}}{Y} \quad (5)$$

Where, WF_{green} is green water footprint, SWU_{green} (m^3/ha) is the green water used by sugarcane, and (Y) (t/ha) is sugarcane yield (Rattikarn Kongboon and Sampattagul, 2012).

D. Blue Water Footprint (WF_{blue}) Calculation

Blue evapotranspiration (ET_{blue}) is the sum amount of irrigation water (mm/time) required to evaporate from the soil surfaces, the amount of water transpired by plants, and the water incorporated in plants. The ET_{blue}, also known as the irrigation requirement (IR) (surface water), was calculated by taking the difference between the ET_c and the R_{eff}. If the R_{eff} is larger than the ETc, the ET_{blue} is zero and no irrigation is required (Aldaya et al., 2010). But in the study, the CWR is not fully met by R_{eff}. Hence, the ET_{blue} was calculated as the difference between the two values, as shown in Equation 6 (Wei et al., 2016).

$$ET_{blue} = \left(ET_c - R_{eff}\right)\left(\frac{mm}{day}\right) \quad (6)$$

Where, ET_{blue} (mm/day) is the blue evapotranspiration, ET_c (mm/day) is sugarcane evapotranspiration (mm/day), and R_{eff} is effective precipitation. The blue evapotranspiration of sugarcane is obtained by summing up the blue component of evapotranspiration over the growing period, using Equation 7 (Aldaya et al., 2010).

$$SWU_{blue}(m^3/\text{ha}) = 10 * \sum_{d=1}^{lgp} ET_{blue} \quad (7)$$

Where, SWU is sugarcane blue water use, lgp is the length of the growing period in days; and ET_{blue} represents blue water evapotranspiration. The WF_{blue} of the sugarcane was taken from the ratio of the volume of irrigation water consumed (m^3/ha) to the sugarcane yield (Y (t/ha) according to Equation 8.

$$WF_{blue}\left(\frac{m^3}{t}\right) = \frac{SWU_{blue}}{Y} \quad (8)$$

Where, WF_{blue} (m^3/t) is the blue water footprint determined from blue evapotranspiration, SWU_{blue} is sugarcane water use (m^3/ha), and Y is sugarcane yield (t/ha) (Ortiz-Rodriguez et al., 2015).

E. Grey Water Footprint (WF_{grey}) Analysis

WF_{grey} is the volume of water needed to dilute the pollutants that are emitted into a free flowing water body using an accepted water quality standard. WF_{grey} was estimated according to Hoekstra et al. (2011) by considering the effect of nitrogen fertilizer using Equation 9.

$$WF_{grey}\ \left(m^3/_t\right) = \frac{(\alpha AR)}{Yield\ \left(\frac{ton}{ha}\right)}\left(1/_{(C_{max}-C_{nat})}\right) \quad (9)$$

Where, α is the leaching-runoff fraction, AR is the chemical application rate to the farm field per hectare (kg/ha), C_{max} is the maximum acceptable concentration (kg/m^3), and C_{nat} is the natural concentration of the pollutant in water bodies (kg/m^3) (Scarpare et al., 2016). The WF of sugarcane (m^3/t) was calculated by summing the green, blue, and grey water footprint components as shown in Equation10.

$$WF_{sugarcane} = WF_{green} + WF_{blue} + WF_{grey} \quad (10)$$

2.4. Molasses Water Footprint Calculation

The stepwise accumulative approach was used; it is the generic way of calculating the WF of molasses based on sugarcane WFs that include process water of each step. Hence, the WF of molasses was calculated according to Equation 11.

$$WF_{prod}(molasses) = (WF_{proc}(molasses) + \sum_{i}^{y} \frac{WF_{sugarcane}(i)}{f_p[p,i]})\, f_v(p\ i) \quad (11)$$

Where, WF_{prod} [p] (m^3/t) is the water footprint of the product molasses; p is the product; i refers input; WF_{proc} (p) (m^3/t) is the water footprint of the process; f_p[p] is product fraction of molasses; f_v[p] is the value fraction of the product (molasses), and WF_{prod} (i) (m^3/t) is the water footprint of the product (molasses) (Scholten, 2009).

The production fraction (fp [p, i], mass/mass) is defined as the ratio of the product mass (molasses, kg) to the aggregated mass of the crop (sugarcane, kg). The product fraction of the output product molasses processed from the input sugarcane was determined using Equation 12.

$$f_p(p\ i) = \frac{w(p)}{w(i)} \quad (12)$$

Where, f_p [p, i] is a product fraction (molasses unitless), w (i) is the mass of input (sugarcane in kg), and w (p) is the mass of product (molasses in kg).

The WF of all the products with economic value is represented by their value fraction fv [p, i]. The value fraction of an output product (p) is defined as the ratio of the market value of the product to the aggregated market value of all the outputs (p = 1 to z) obtained from the inputs (sugarcane), as shown in Equation 13.

$$f_v(molasses) = \frac{Price\ (p)\ *\ w(p)}{\sum_{p\ i}^{z} Price\ \ (P)\ *\ w(p)} \quad (13)$$

Where, f_v [p, i] is the value fraction of molasses and price (p) refers to the price of product p (monetary unit/mass) and the w (p) is the mass of the products. The denominator is summed over the z output products (molasses, filter cake, bagasse, and sugar) using Equation 13 (Gerbens-leenes and Hoekstra, 2012).

2.5. Bioethanol Water Footprint Calculation

Similarly, bioethanol WF (m^3/t, L/L) was calculated from sugarcane molasses WF. The input material was molasses, the by-product was the spent wash, and the product was bioethanol. Finally, the process water in the bioethanol distillery was also taken into account in calculating WF, as shown in Equation 14.

$$WF_{prod}(p) = (WF_{proc}(p) + \sum_{i}^{y} \frac{WF_{prod}(i)}{f_p[p,i]}) f_v(p,i) \quad (14)$$

Where, WF prod [p] (m^3/t) is the water footprint of the product (bioethanol); WF_{proc} (p) m^3/t) is the water footprint of the process; f_p[p] is the product fraction of bioethanol, and f_v[p] is the value fraction of the product (bioethanol) (Chooyok et al., 2013).

2.6. Data Analysis

Using Microsoft Excel, descriptive statistical analysis and the one-way ANOVA test were used for data analyses. The ANOVA test was done for ETo mean values comparisons of monthly data of the same year and the annual means of different years but not the seasons. However, other ANOVA tests were done for R_{eff} and SWR mean values of the monthly and yearly data of different growing seasons of sugarcane for the years of 2007-2016. ANOVA was used to determine statistically significant differences between the means of the 10 independent measures of ETo, $R_{eff,}$ and SWRs. The statistical analysis was performed at a 95% confidence interval. Meteorological data were operated using CROPWAT 8 model software for estimating ETo, $R_{eff,}$ and SWR using the modules of climate/ETo, rainfall, and crop.

3. RESULTS AND DISCUSSION

3.1. Meteorological Data

Weather conditions dictate the amount of energy available for evaporation and therefore play a crucial role in determining ET_o. Monthly minimum average temperatures ranged from 10.5 to 22.5°C; maximum average temperatures ranged from 27.9 to 38.3°C. There is a direct association between temperature and CWR. Evaporation increases with increased temperature because a higher amount of energy is available to convert liquid

water to water vapor. The transpiration process is also increased because in warmer temperatures plants open up their stomata and release more water vapor. Transpiration rates increase by 20% when temperatures rise from 28 to 33°C and by 30% when they rise from 28 to 35 °C (Allen, 2008).

Monthly relative humidity values ranged from 24 to 70%. Humid air decreases evapotranspiration and therefore also decreases SWR. This is the only input parameter in this study that suppressed the CWR of sugarcane and bioethanol WF. Wind speed was another factor that was considered as an input; it ranged from 0.9 to 8.9 m/s. The role of wind speed in evapotranspiration is to transport heat and accelerate evaporation by enhancing turbulent transfer of water vapor from moist crops to the dry atmosphere. Similarly, maximum and minimum monthly average sunshine ranged from 1.14 to 12.04 hours over ten years. Solar radiation is the largest energy source, capable of changing large quantities of liquid water into water vapor. Increasing sunshine hours is positively associated with evapotranspiration and enhanced sugarcane WF.

3.2. Reference evapotranspiration calculation

The mean annual ETo value ranged from 4.73 to 7.98 mm/day, as shown in Figure 2. The average value of the ETo over the study period was 6.2 mm/day. The ETo values gradually increased from 5.51 mm/day in 2007 to a peak of 7.98 in 2011. This rise could be attributed to hot, dry weather conditions that directly influence evapotranspiration. The ETo value gradually decreased after 2011. The fluctuation in ETo value resulted from the variations in climate data, which affected crop evapotranspiration and WF. Normally, ETo value depends on climatic conditions. Hence, the variation in ETo clearly indicated the influence of the climate variability on SWR. However, this variation in ETo was not statistically significant ($p > 0.05$). A similar result was reported for sugarcane ETo, which varied from 3.66 to 6.42 mm/day and used for SWR determination (Saravanan and Saravanan, 2014). Generally, as the value of ETo increases CWR is expected to increase also.

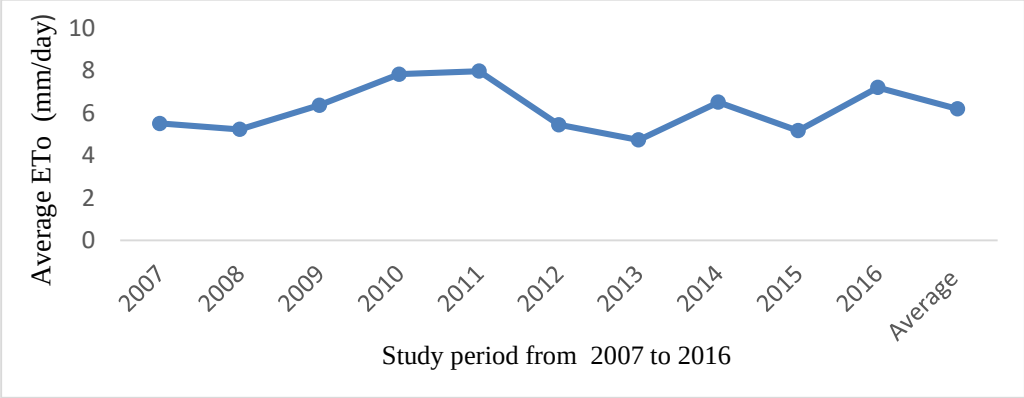

Figure 2: Variations in *ETo* over the 10 years of the study period

3.3. Effective Rainfall during Study Period

In order to calculate SWR, estimating the contribution of effective rainfall is very critical. The rainfall values ranged from 313.2 to 793.2 mm per year over the study period and the correspondence estimated effective rainfall to be in the range of 256.4-743.6 mm/season as shown in Figure 3. This amount of effective rainfall is very minimal for SWR and clearly indicated the importance of the irrigation requirement under the study conditions. Furthermore, ANOVA performed for the mean variations in annual rainfall over this period showed the means statistically insignificant at p (0.75) > 0.05.

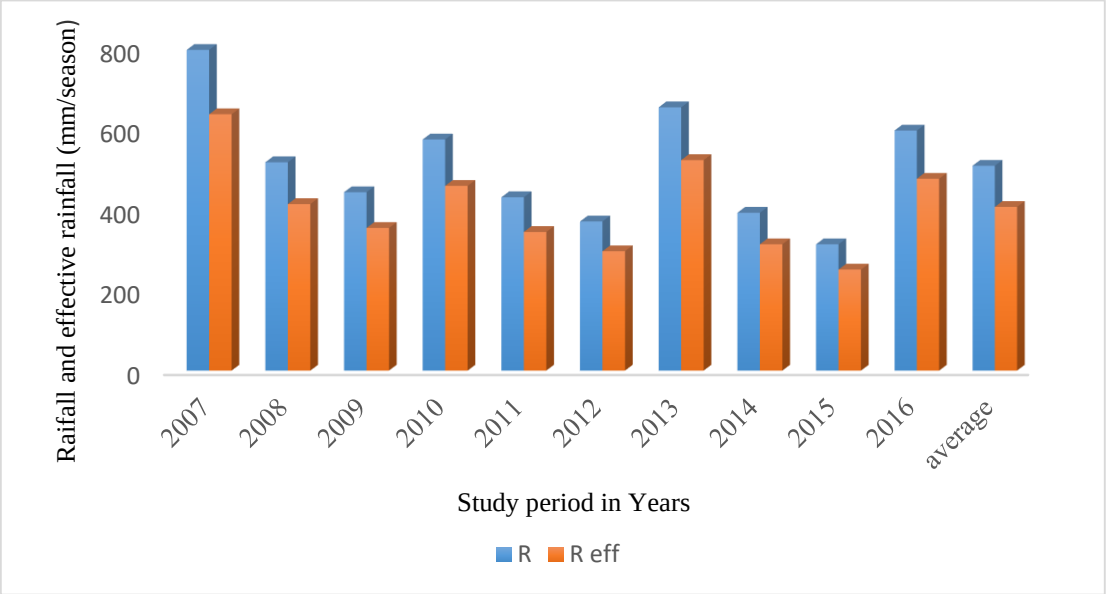

Figure 3: Annual and effective rainfall trends of Metahara sugarcane farm. Note: R = rainfall and R_{eff} = effective rainfall

3.4. Crop Evapotranspiration (ETc)

Determination of ETc was based on the calculation of ETo, effective rainfall, and the crop module. In the crop module, K_c value, critical depletion, yield response, crop development stage, rooting depth, crop height, and plantation dates are the factors that were considered. The K_c factor serves as an aggregation of the physical and physiological differences between crops and the reference definition. In this study, the growing period started in December and extended for 16 months (480 days) until harvest. The growth stages for sugarcane were divided into four; 50, 70, 200, and 140 days were classified as planting (initial), crop development, mid-season, and late-season, respectively. As the crop develops, the ground cover, crop height, and leaf area changes reflect the differences in evapotranspiration during the various growth stages. The K_c values for sugarcane were 0.4, 1.25, and 0.75 at the initial stage, mid-season, and late season, respectively. Hence, SWR was determined from the interaction of the *Kc* and *ETo* values.

The observed SWR ranged from 2544.1 to 4833.3 mm/season (Figure 4). This high variation in water requirement might be attributed to weather changes. The fluctuations in ETc throughout the seasons are due not only to crop development, but also to climate conditions. Another reason for the large SWR was the long growing season of the sugarcane. Crop evapotranspiration increases with increasing air temperature and solar radiation, which are main drivers of ETc. The high input of climate data into the CROPWAT 8 model resulted in the high CWR, but the contribution of R_{eff} to the total water requirement was insignificant. The average SWR during the growing period was 3,495.2 mm, comprised of 448.6 mm R_{eff} per growing period and 3019.2 mm IR per growing period. Considerably lower SWR values (1715.2 mm) during growing periods have been reported (Saravanan and Saravanan, 2014). In another study, a lower SWR range of 1233 - 2082 mm per growing season was reported for which the sugarcane yields varied from 31 to 119 t/ha (Gerbens-Leenes and Hoekstra, 2009). The higher SWR of sugarcane at the Metahara farm indicates the need for improved water resources management practices.

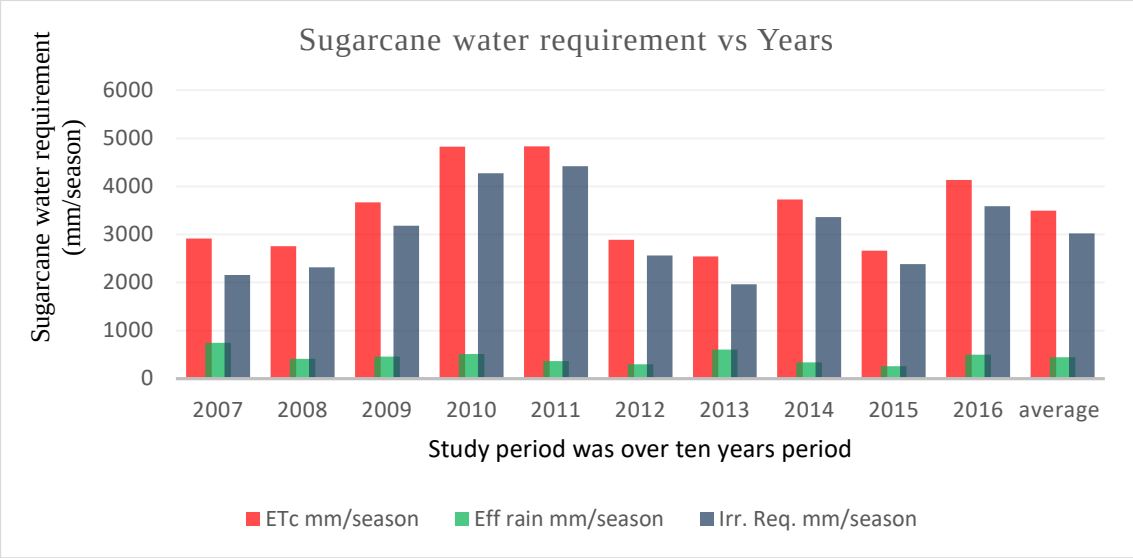

Figure 4: Contribution of R_{eff} and IR to total SWR at Metahara sugarcane farm. Note: ETc is sugarcane water requirement, Eff rain is effective rainfall, and Irr. Req. is the irrigation requirement

3.5. Analysis of Variance (ANOVA) of SWR

A one-way ANOVA was used to examine the relationship between the sugarcane growing period as the independent variable and SWR as the dependent variable (Table 1). ANOVA was used for testing the hypothesis that there were no differences between of means of SWR over the study period. The alternative hypothesis stated at least one SWR mean was different from the others. The assumption was that populations are normally distributed, population variances are equal, and sampled observations are independent.

Table 1: ANOVA test for SWR

Source of Variation	*SS*	*df*	*MS*	*F*	*p*-value	*F* crit
Between groups	143620.5	9	15957.83	45.16	0.00	1.99
Within groups	166080.5	470	353.36			
Total	309701	479				

In this analysis, the null hypothesis was rejected at $p < 0.05$ and the alternative hypothesis was accepted because there was a statistically significant difference among SWR means. But there is not sufficient evidence to determine which SWR mean was different from the others. It can be concluded that the independent variable influenced the response variable, but the analysis does not identify the specific growing season that was different from the other seasons.

3.6. Sugarcane Water Footprint Analysis

The annual sugarcane yield over the ten years ranged from 119.4 to 185.30 t/ha, with an average yield of 161.15 t/ha. However, Brazil, the largest sugarcane producer, which accounts for 34% of the world's production, obtains an average yield of 75.2 t/ha; India harvests 63.4 t/ha; Thailand 75.7 t/ha; Pakistan 56.5 t/ha; the USA 75.7 t/ha; Cuba 39.9 t/ha; and Peru 133.7 t/ha (Scarpare et al., 2016). Surprisingly, Ethiopian sugarcane yield is very high, a fact that significantly suppresses the sugarcane WF directly and the WF of bioethanol indirectly. However, the extremely high yield might be attributed to the fertile soil and climatic conditions conducive for sugarcane growing in the tropical region. The ET_{green} ranged from 256.4 to 743.6 mm/season, with an average value of 448.6 mm during the growing period. Then the SWU_{green} was 4486 m^3/ha and the green component of

sugarcane WF was 27.84 m^3/ha. In the agricultural sector, blue water consumption depends on crop variety, crop tolerance to water deficits, irrigation efficiency, and the existence of green water in the area. Inadequate R_{eff} required that most of the water for SWR came from IR. IR ranged from 1962.3 to 4416.3 mm/season, with an average value of 3019.2 mm during the growing period. Thus, the SWU_{blue} was 30,192 m^3/ha and the WF of the blue component was 187.35 m^3/t.

WF_{grey} is the volume of freshwater that dilutes the wastes, mostly fertilizers and pesticides, generated during sugarcane cultivation. WF_{grey} is therefore an indicator of freshwater pollution. For WF_{grey} calculation, the nitrogen leaching runoff fraction is assumed to be 10% (Ratchayuda Kongboon and Sampattagul, 2012). The Ethiopian Ministry of Environment, Forest and Climate Change (EFCC), and WHO recommend the concentration of nitrogen (NO_3-N) not exceed 50 mg/L (WHO, 2011). Thus, 0.05 kg/m^3 of nitrate was used as an acceptable concentration in fairly clean fresh surface water. But the zero value was considered for concentration of nitrate in natural water bodies (Fachinelli and Pereira, 2015b). The rate of urea fertilizer applied in the study area varied between the two soil fertility groups of the Metahara farm. Recently, the sugarcane farm has used urea fertilizer applied at a rate of 170 kg/ha and 230 kg/ha for soil fertility groups F1 and F2, respectively. The F1 soil fertility unit area covers 63% of the Metahara sugarcane farm (10, 230 hectares) and the rest of the sugarcane farm accounted for 37% (F2). Then the average fertilizer application rate was 207.8 kg/ha. The estimated grey component of the sugarcane WF was 2.58 m^3/t. However, only nitrogen fertilizer pollution was considered to estimate the WF_{grey}. Practically, some other nutrients and pesticides may cause more water pollution than the nitrogen, but they were not considered due to lack of specific analytic methods in the literature. Finally, the WF components of sugarcane-the green, blue, and grey- were 27.84 (12.8%), 187.35 (86.1%), and 2.58 m^3/t (1.1%), respectively. The contribution of each component is clearly indicated in Figure 5. The total estimated total WF of Metahara sugarcane is 217.69 m^3/t.

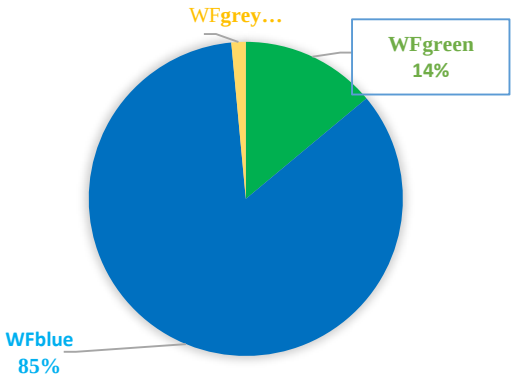

Figure 5: Contribution of each component of sugarcane WF

The proportion of the WF_{grey} has been reported to vary between 4% and 11% in sugarcane farms in different countries (Scholten, 2009). But the contribution of the WF_{grey} to the total WF of the Metahara sugarcane is only 1.1%, which is very insignificant. Ignoring the concept of WF, the water consumption of this study area is high, but the WF concept relates the water consumption with the amount of product it generates. The great limitation of the WF_{grey} calculation is the fact that it was based on the leaching rate of nitrogen fertilizer only. Generally, the Metahara sugarcane WF (217.69 m^3/t) falls in the upper two-thirds of the global range of values (120-410 m^3/t) (Chooyok et al., 2013). A WF study conducted in Thailand reported 226 m^3/t sugarcane WF, consisting of green (146 m^3/t), blue (31 m^3/t), and grey WF (49 m^3/t) (Ratchayuda Kongboon and Sampattagul, 2012). Other relatively low values of sugarcane WF were recorded under different management practices in Brazil (WF_{green} 145, WF_{blue} 38, and WF_{grey} 18 m^3/t) (Scarpare et al., 2016) and from the Paranaiba Basin in Brazil for rain cultivated (151 m^3/t)

and irrigation cultivated (142 m^3/t) sugarcane WF (Fachinelli and Pereira, 2015a). These differences in WFs appear to be largely due to differences in climate, sugarcane yields, and rate of nitrogen fertilizer application.

3.7. Molasses Water Footprint Analysis

Molasses is the residual syrup obtained by centrifugation from cane juice not forming crystalline sugar. In this study, the products and byproducts of the sugar factory are bagasse, filter cake, sugar, and molasses whereas the input material was sugarcane, as shown in Table 2. Based on the distribution of these materials, the product fraction and value fraction of molasses were determined.

Table 2: Sugar factory data with the product and value fractions of the molasses

Year	Sugarcane	Sugar	Bagasse	Filter cake	Molasses	Molasses fp
2007	11704193	1264025	3400418	426757	414553	0.035419
2008	11305414	1302661	3210388	386137	410822	0.036339
2009	12130022	1301804	3460642	376335	424823	0.035022
2010	12032489	1200343	3932880	396409.7	416791	0.034639
2011	10014000	1019623	2720078	232439	323765	0.032331
2012	9829652	931399	2840053	201401	309669	0.031504
2013	9019313	797983	3242984	336579.8	288984	0.032041
2014	11555499	1149000	3544087	349731	436850	0.037805
2015	11011609	1110515	3128629	258948.3	380011.1	0.03451
2016	7870662	698661	2196887	212504.4	254170	0.032293
Average	10647285	1077601	3167705	317724.2	366043.8	0.04000
Year		S/SC ratio	B/SC	F/SC	M/SC	fv(M)
2007		0.107998	0.29053	0.036462	0.035419	
2008		0.115225	0.283969	0.034155	0.036339	
2009		0.107321	0.285296	0.031025	0.035022	
2010		0.099758	0.326855	0.032945	0.034639	
2011		0.10182	0.271628	0.023211	0.032331	
2012		0.094754	0.288927	0.020489	0.031504	
2013		0.088475	0.35956	0.037318	0.032041	
2014		0.099433	0.306701	0.030265	0.037805	
2015		0.100849	0.284121	0.023516	0.03451	
2016		0.088768	0.279124	0.027	0.032293	
Average		0.10044	0.297671	0.029639	0.03419	0.103
kg/t of sugarcane		100.4	297.7	29.6	34	

Notes: All parameters in the table are given in unit of quintal. The symbols: S, SC, F, B and M are represented the sugar, sugarcane, filter cake, bagasse and molasses, respectively.

In the Metahara sugar factory, 1 t of sugarcane generated on average 34.0 kg of molasses, 297.7 kg of bagasse, 29.6 kg of filter cake, and 100 kg of sugar. The average annual sugarcane production at Metahara through the study period was 106,728.5t and molasses production was 36,604.4t. Hence, the molasses production fraction was 0.04. The economic value of bagasse was calculated based on the amount of electricity it generated, whereas the value of filter cake was determined from the economic value of fertilizer. The rate of fertilizer application was reduced from 230 to 170 kg/ha (by 60 kg) when the farm started to use filter cake as a fertilizer at the rate of 30 t/ha during the study period. The average price of 100 kg of fertilizer in Ethiopia was 1100 Birr during the study

period and the price of filter cake was only 660 Birr/30 t (22 Birr/t). On the other hand, 1t of sugarcane bagasse generated 0.2 kWh of electricity within the old boiler of Metahara. The price of electricity in Ethiopia was 0.69 Birr/kWh. On average, the price of 100 kg of white sugar was 690 Birr and the price of sugarcane molasses was 232 Birr/100kg. Using these data, the estimated value fraction of molasses was calculated to be 0.10 (in all cases 1 USD = 23.32 Ethiopian Birr).

The process water is the water used in the sugar factory to transform sugarcane into molasses byproduct through the process of juice extraction, clarification, evaporation, and centrifugation. Usually, process water used for a sugarcane factory varies between 1 and 21 m^3/t (Gerbens-leenes and Hoekstra, 2012), a very small amount compared to the average water consumption for sugarcane growth (Gerbens-leenes and Hoekstra, 2012; Martinelli et al., 2013; Scholten, 2009). Thus water of 10.5 m^3/t of sugarcane was considered for this study. Based on these data, the average estimated molasses WF of 553.6 m^3/t was obtained, composed of 76.65 m^3/t of green, 469.43 m^3/t, of blue, and 7.3 m^3/t of grey components. This value was high compared to the average value in another study (407 m^3/t) (Ratchayuda Kongboon and Sampattagul, 2012), which indicates high water consumption and pollution in the bioethanol production process occurred in the Metahara sugar factory.

3.8. Bioethanol WF determination

Molasses is used as feedstock for bioethanol production, which involves pre-treatment, fermentation, distillation, and dehydration processes. In these processes, the amount of bioethanol and spent wash produced from 1t of molasses with process water consumed are shown in Table 3. To allocate the WF of the sugarcane-based molasses over its bioethanol distillery products, molasses WF was used.

Table 3: Products and process water consumed in the bioethanol distillery

Time (year)	Molasses (t)	Bioethanol (L)	Process water (m^3)	Spent wash (L)
2012	1	284.53	4.12	3244.46
2013	1	279.26	3.8	5528.69
2014	1	240.73	3.61	2874.02
2015	1	250.12	4.32	2831.51
2016	1	233.17	4.90	2399.44
Average	1	257.56	4.15	3375.62

In the bioethanol production process, the main product was bioethanol and the byproduct considered was spent wash. The economic value of all the byproducts influence the WF of bioethanol. Spent wash is the wastewater generated by the distillery and often used as fertilizer, reducing other fertilizer consumption by 25%. The estimated total fertilizer cost of sugarcane cultivation in Ethiopia was 2200 Birr/ha; this price accredits 550 Birr/ha for spent wash (Gerbens-leenes and Hoekstra, 2012). The amount of spent wash per ton of sugarcane was 0.12 m^3/t whereas the sugarcane yield per hectare of the study area was 161.15 t/ha. Finally, the cost of the fertilizer reduced (550 Birr/ha) related to the amount of spent wash consumed (18.5 m^3/ha) was used to estimate cost of spent wash (29.73 Birr/m^3). Moreover, the average amount of process water consumed in the bioethanol distillery was 4.15 m^3/t. The estimated product fraction of bioethanol was 0.22. On average, 9.46 L of bioethanol was produced from molasses originating from 1t of sugarcane. The average local price of 1 L bioethanol was 11.95 Birr. Hence, the estimated value fraction of bioethanol was 0.997. For unit conversion of bioethanol WF from m^3/t into L/L, ethanol density (0.789 kg/L) was used. Finally, the average amount of bioethanol WF at the Metahara distillery was 3106.7 L/L; this figure comprises the green (433.43 L/L), blue (2627.38 L/L), and grey (45.89 L/L) WFs. The contribution of WF_{grey} to total WF in bioethanol production was really insignificant, as indicated in Figure 6.

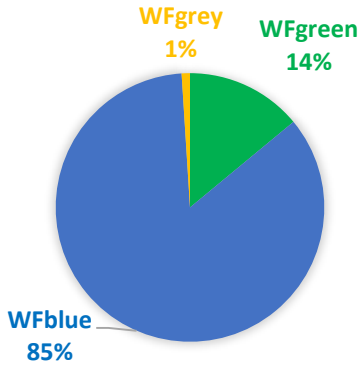

Figure 6: Contribution of each component of bioethanol WF

In this study, the estimated bioethanol WF is higher than the global average (2855 L/L). This indicates that the production of bioethanol is exerting pressure on the local water resources. In another study, a lower value of bioethanol WF of 2415.7 L/L was reported (Kongboon & Sampattagul 2012). Largely, the WF of cane-based bioethanol varied from Peru (1670 L/L), Brazil (2450 L/L), USA (2775 L/L), India (2995 L/L), and Cuba (6355 L/L), and the weighted global average was 2855 L/L (Gerbens-Leenes and Hoekstra, 2009).

4. CONCLUSION

High SWR (3,495.2 mm/growing season) at the Metahara sugarcane farm is attributed to climatic factors and water resource management in combination with prevailing agricultural practices. This high SWR may be reduced with better agricultural and sugarcane processing practices. The average sugarcane WF at Metahara (217.69 m^3/t) was higher than the global average. Exceptionally high sugarcane yield at Metahara (161.15 t/ha) suppressed the sugarcane WF of 217.69 m^3/t to a certain extent. Nevertheless, the relatively high sugarcane WF is one of the areas in the production chain of bioethanol that needs to be addressed to ensuring the sustainability of local and regional water resources. The average bioethanol WF of 3106.7 L/L was obtained, indicating that bioethanol production significantly impacts water resources by alleviating local water stress in sugarcane cultivation. An additional 252.7 L of bioethanol WF is applied per liter of bioethanol in the Ethiopian context, particularly at Metahara, compared to the global average bioethanol WF. This showed that there is ample room for improvement, further indicating the need to reduce the WFs of sugarcane and bioethanol production. Therefore, sustainable sugarcane/bioethanol production and lesser dependence on fossil fuel for transportation require reductions in water use and pollution through more efficient production processes as well as judicious fertilizer and pesticide applications. Furthermore, the results of the study may also inform government officials or policy makers as they seek to improve water resources management of this sector.

ACKNOWLEDGMENTS

We would like to thank the Ethiopian Road Authority for funding this research and Addis Ababa Science and Technology University for hosting and supervising the programme. We also thank the National Meteorological Agency, Metehara Sugar Factory, and Wonji Research Center for the provision of data and other information.

REFERENCES

Aldaya, M.M., Munoz, G., Hoekstra, A.Y., (2010). *Water footprint of cotton, wheat and rice production in central Asia. Value of water research report series* no. 41. Research report series is published by UNESCO-IHE Institute for Water Education, Delft, the Netherlands. 31.

Allen, L., (2008). Evapotranspiration Responses of Plants and Crops to Carbon Dioxide and Temperature. *Journal of Crop*

Production, 2: 37–41. doi:10.1300/J144v02n02
Biswas, A.K., Mohanty, M., Hati, K.M., Misra, A.K., 2009. Distillery effluents effect on soil organic carbon and aggregate stability of a Vertisol in India. Soil & Tillage Research 104, 241–246. doi:10.1016/j.still.2009.02.012
Chapagain, A.K., Hoekstra, A.Y., (2011). The blue , green and grey water footprint of rice from production and consumption perspectives. *Ecological Economics*, 70: 749–758. doi:10.1016/j.ecolecon.2010.11.012
Chia, C., Shiang, W., Joe, C., Wang, C., (2015). Water footprint analysis of second-generation bioethanol in Taiwan. *Journal of Cleaner Production*, 101: 271–277.
Chiu, C.C., Shiang, W., Lin, C.J., (2016). The water footprint of bioethanol. *Journal of Clean Energy Technologies*, 4: 43–47.
Chooyok, P., Pumijumnog, N., Ussawarujikulchai, A., (2013). The water footprint assessment of ethanol production from molasses in Kanchanaburi and Supanburi Province of Thailand. *APCBEE Procedia*, 5: 283–287. doi:10.1016/j.apcbee.2013.05.049
De Angelis, E., Metulini, R., Bove, V., Riccaboni, M., (2017). Virtual water trade and bilateral conflicts. *Advances in Water Resources*, 0: 1–13.
Degefa, A., Bosie, M., Mequanint, Y., Yesuf, E., Teshome, Z., (2016). Determination of crop water requirements of sugarcane and soybean intercropping at Metahara Sugar Estate. *Advances in Crop Science and Technology*, 4: 10–13. doi:10.4172/2329-8863.1000241
Ding, G.K.C., Ghosh, S., (2017). *Sustainable Water Management—A Strategy for Maintaining Future Water Resources, Reference Module in Earth Systems and Environmental Sciences*. Elsevier. doi:10.1016/B978-0-12-409548-9.10171-X
Fachinelli, Pereira, A., (2015a). Impacts of sugarcane ethanol production in the Paranaiba basin water resources. *Biomass and Bioenergy*, 83: 8–16. doi:10.1016/j.biombioe.2015.08.015
Fachinelli, Pereira, A.O., (2015b). Impacts of sugarcane ethanol production in the Paranaiba basin water resources. *Biomass and Bioenergy*, 83: 8–16. doi:10.1016/j.biombioe.2015.08.015
Flach, R., Javier Godar3, L.K.C.S.Y. 4, 2016. Towards more spatially explicit assessments of virtual water fl ows : linking local water use and scarcity to global demand of Brazilian farming commodities. *Environ. Res. Lett.*, 11, 1–10.
Gerbens-Leenes, P., Hoekstra, A.Y., (2009). *The water footprint of sweeteners and bio-ethanol from sugar cane, sugar beet and maize. Value of water research report series no. 38*, The Value of Water Research Report Series is published by UNESCO-IHE Institute for Water Education, Delft, the Netherlands.
Gerbens-leenes, W., Hoekstra, A.Y., (2012). The water footprint of sweeteners and bio-ethanol. *Environment International*, 40: 202–211.
Gerbens-leenes, W., Hoekstra, A.Y., 2011. Environmental Science The water footprint of biofuel-based transport. *Energy & Environmental Science*, 4: 2658–2668. doi:10.1039/c1ee01187a
Gheewala, S.H., Silalertruksa, T., Nilsalab, P., Mungkung, R., Perret, S.R., Chaiyawannakarn, N., (2014). Water footprint and impact of water consumption for food, feed, fuel crops production in Thailand. *Water*, 6: 1698–1718. doi:10.3390/w6061698
Hess, T.M., Sumberg, J., Biggs, T., Georgescu, M., Haro-Monteagudo, D., Jewitt, G., Ozdogan, M., Marshall, M., Thenkabail, P., Daccache, A., Marin, F., Knox, J.W., (2016). A sweet deal? Sugarcane, water and agricultural transformation in Sub-Saharan Africa. *Global Environmental Change*, 39: 181–194.
Hobson, P.A., Renouf, M.A., (2013). Development of a tool for rapid life cycle assessment of sugar and associated energy products. *Proc Aust Soc Sugar Cane Techno*, 35: 1–9.
Hoekstra, A.Y., Chapagain, A.K., Aldaya, M.M., Mekonnen, M.M., (2011). The water footprint assessment manual setting the global standard. Earthscan Ltd, Dunstan House, 14a St Cross Street, London EC1N 8XA, UK.
Jefferies, D., Muñoz, I., Hodges, J., King, V.J., Aldaya, M., Ertug, A., Milà, L., Hoekstra, A.Y., (2012). Water footprint and life cycle assessment as approaches to assess potential impacts of products on water consumption. Key learning points from pilot studies on tea and margarine. *Journal of Cleaner Production*, 33: 155–166.
Kongboon, R., Sampattagul, S., (2012). The water footprint of sugarcane and cassava in northern. *Procedia - Social and Behavioral Sciences*, 40: 451–460. doi:10.1016/j.sbspro.2012.03.215
Kongboon, R., Sampattagul, S., (2012). Water footprint of bioethanol production from sugarcane in Thailand. *Journal of Environment and Earth Science*, 2: 61–68.
Lovarelli, D., Bacenetti, J., Marco, F., (2016). Water footprint of crop productions : A review. *Science of the Total Environme*nt, 548–549: 236–251.
Martinelli, L.A., Filoso, S., Aranha, C.D.B., Ferraz, S.F.B., Andrade, T.M.B., Ravagnani, E.D.C., Coletta, L. Della, (2013). Water use in sugar and ethanol industry in the State of São Paulo (Southeast Brazil). *Journal of Sustainable Bioenergy Systems*: 135–142.
Mekonnen, M.M., (2011). Spatially and Temporally Explicit Water Footprint Accounting. A PhD DISSERTATION to obtain the degree of doctor at the University of Twente.
Mohana, S., Acharya, B.K., Madamwar, D., (2009). Distillery spent wash : Treatment technologies and potential applications.

Journal of Hazardous Materials, 163: 12–25. doi:10.1016/j.jhazmat.2008.06.079

Ortiz-Rodriguez, O.O., Naranjo, C.A., Garcia-Caceres, R.G., Villamizar-Gallardo, R.A., (2015). Water footprint assessment of the Colombian cocoa production. *Revista Brasileira De Engenharia Agricola E Ambiental*, 19: 823–828. doi:10.1590/1807-1929/agriambi.v19n9p823-828

Pahlow, M., Snowball, J., Fraser, G., (2015). Water footprint assessment to inform water management and policy making in South Africa. *Water SA*, 41: 300–313.

Pant, D., Adholeya, A., (2007). Biological approaches for treatment of distillery wastewater : A review. *Bioresource Technology*, 98: 2321–2334. doi:10.1016/j.biortech.2006.09.027

Perry, C., (2014). Water footprints: Path to enlightenment, or false trail? *Agricultural Water Management*, 134: 119–125.

Saravanan, K., Saravanan, R., (2014). Determination of Water Requirements of Main crops in the Tank Irrigation Command area using. *International Journal of Interdisciplinary and Multidisciplinary Studies (IJIMS)*, 1: 266–272.

Scarpare, F.V., Aparecida, T., Hernandes, D., Ruiz-corr, S.T., Naz, L., (2016). Sugarcane water footprint under different management practices in Brazil: Tiete/Jacare watershed assessment. *Journal of Cleaner Production*, 112: 1–9. doi:10.1016/j.jclepro.2015.05.107

Scholten, W., (2009). The water footprint of sugar and sugar-based ethanol.

Shah, P. V, Mistry, R.N., Amin, J.B., Parmar, A.M., Shaikh, M.R.A., (2015). *Irrigation scheduling using cropwat*, 2: 1–10.

Siddiqui, W.A., Waseem, M., (2012). A comparative study of sugar mill treated and untreated effluent- A case study. *Oriental Journal of Chemistry*, 28: 1899–1904.

Srinivasan, V., Konar, M., Sivapalan, M., (2017). A dynamic framework for water security. *Water Security*, 1: 12–20. doi:10.1016/j.wasec.2017.03.001

UN-Water, (2017). Wastewater: The Untapped Resource. UN World Water Development Report.

UN-Water, (2003). Water for People Water for Life. The United Nations World Water Development Report 36. doi:10.1017/CBO9781107415324.004

Wei, Y., Tang, D., Ding, Y., Agoramoorthy, G., (2016). Incorporating water consumption into crop water footprint : A case study of China ' s South – North Water Diversion Project. *Science of the Total Environment*, 546: 601–608. doi:10.1016/j.scitotenv.2015.12.062

WHO, (2011). WHO guidelines for drinking-water quality. Switzerland Typeset by Value Chain, India Printed in Malta by Gutenberg, Fourth Edition 38, 509. doi:10.1016/S1462-0758(00)00006-6

Developing Low-cost and Ecofriendly Industrial Wastewater Treatment Technology using Locally-available Substrate for the Removal of Hazardous Pollutants

Mekonnen Birhanie Aregu*, Seyoum Leta Asfaw, Mohammed Mazharuddin Khan

Environmental Pollution and Sanitation, Centre for Environmental Sciences, Addis Ababa University, Ethiopia
**Corresponding author, e-mail: mekonnen.birhanie@aau.edu.et*

ABSTRACT

High-strength wastewater defined by elevated levels of hazardous pollutants measured in BOD, heavy metals, nutrients and other toxic substances. This kind of wastewater discharged to water body without treatment from different industrial sectors that adversely affects aquatic environment and downstream water consumers. The general objective of this study is to investigate locally available, low-cost and efficient substrate for constructed wetland to remove hazardous pollutants from high-strength wastewater in ecofriendly manner. This study was conducted at Modjo town from September 2016 to March 2018. Plug flow experimental study design was carried out. The substrate (Pumice) was collected around the study area and chemical characteristics were determined using X-ray fluorescence analysis. Chrysopogon zizanioides was planted and grown for five months before running high-strength wastewater for the treatment. The composite wastewater was introduced to the constructed wetland from Modjo leather industry, Ethiopia. The physicochemical analysis of the sample wastewater was done before and after treatment at four different hydraulic retention time. Originlab 2017 and R statistical software were run for graphing and data analysis. Characterization of the untreated tannery wastewater revealed that the mean concentration of BOD_5, COD, TSS, PO_4-P, TP, NO_3-N, TN, sulfide, sulfate and total chromium were 1641±373.6, 6953.33±339.4, 1868±863.1, 88.06 ±40.8, 144.53 ±20.8, 116.66 ±26.6, 650.33 ±93.6, 241.33 ±101.2, 1072.82 ±352.7and 18.33±6.7 mg/l respectively beyond the permissible limits. The maximum removal efficiency of the constructed wetland in pumice bed revealed that BOD_5 at HRT 7and 9 days (96.42%, 96.30%), COD at HRT 5 and 7 days (96.76%, 96.91%), NO_3-N at HRT 5 and 7 days (99.99%, 99.68%), TN (98.67%, 99.00%), PO_4-P HRT 7and 9 days (96.97%,100%), TP at HRT 5 and 7 days (94.79%, 96.17%), Sulfide at HRT 7 and 9 days (99.59%, 99.76), sulfate at HRT 5 and 7 days (94.07%, 94.72%) and total Chromium at HRT 5 and 7 days (98.36%, 98.91%) respectively. Whereas, the removal efficiency of constructed wetland bed with gravel substrate used as a control subject with similar condition to pumice showed lower performance. The result between pumice and gravel bed was tested for their significance difference using two sample t-test statistics. Based on the test statistics, the pumice substrate perform better than the gravel significantly at 95% confidence interval, p-value = 0.01. Pumice substrate and Chrysopogon zizanioides have a potential ability to remove hazardous pollutants from tannery wastewater in horizontal subsurface constructed wetlands.

Keywords: *High-strength wastewater, Pumice, Constructed wetland, Chrysopogon zizanioides*

1. INTRODUCTION

Industrial wastewater is the most common source of environmental pollution in the current situation. Industrial wastes are discharged commonly with hydrocarbons, heavy metals, surfactants, toxins and salts, which may pollute receiving waters rendering them unsuitable as a water supply or pose a threat to aquatic life. In receiving waters, excessive nutrients can lead to algal blooms, oxygen deficits and increase color and turbidity. Tannery effluent is among one of the most hazardous pollutants of industry. Major problems caused by tannery wastewater containing heavy metals, nutrients, toxic chemicals, chloride, lime with high dissolved and suspended salts, and other pollutants.

Tanning is one of the oldest industries in the world. During ancient times, tanning activities were organized to meet the local demands of leather footwear, drums and musical instruments. With the growth of population, the increasing requirement of leather and its products led to the establishment of large commercial tanneries. Two methods are adopted for tanning of raw hide/skin, vegetable tanning, and chrome tanning. Tanneries are typically

characterized as pollution intensive industrial complexes which generate widely varying, high-strength wastewaters. Nearly 30 m^3 of wastewater is generated during processing of one tone of raw skin/hide (Suthanthararajan *et al.*, 2004).

Tannery operation consists of converting of the raw hide or skin into leather which consume huge amount of water in several stages, generating an enormous amount of liquid effluents which are hazardous to the environment to which they are discharged, consequently, make it as a potentially pollution intensive industry. Tannery effluents again compromise the physical, chemical and biological properties of aquatic environment. Apart from the most toxic heavy metals like Chromium (Cr) chemical impurities of tannery effluents mostly includes the following dissolved substances such as inorganic salt cations (Fe, Zn, Cu, Ca, Na, etc.); anions such as SO_4^{2}, NO_3^{-} , PO_4^{3-} and parameters such as, BOD, COD, TSS, TDS etc (Kawser *et al.*, 2011). Therefore treating tannery wastewater using natural adsorbents is very important to protect the surrounding environment.

In Ethiopia currently, there are more than 30 tannery industries in operation. Among them the majority found in Oromia region especially Mojo town and around six established in the capital city Addis Ababa. These tanneries have 153,650 sheep and goat skin soaking capacity and 9,725 cowhides soaking capacity per day. Together they also employ 4577 persons (UNIDO, 2012).

Leather is one of the most important export item of Ethiopia earning foreign exchange. On the other hand, the leather tanning industry has been recognized as one of the main causes of water and environmental pollution. With the high adoption of chrome tanning in most of the tanning industries in the country, efficient methods of chromium, nutrients and other pollutant removal from tannery wastewater are important to attain environmental quality standards.

Adsorption has been identified as one of the most promising mechanism for removal of dissolved heavy metal fractions and nutrients from wastewater. Although commercial adsorbents are available for use in adsorption, they are very expensive, resulting in various new low-cost adsorbents being studied by researchers. Babel and Kurniawan (2003) reviewed the technical feasibility of various low-cost adsorbents for heavy metals removal from wastewater and concluded that the use of low-cost adsorbents may contribute to the sustainability of the surrounding environment and offer promising benefits for commercial purpose in the future. Therefore identifying potentially efficient low-cost and locally available filter media as an adsorbent is critical for proper practice of environmental management by tanning industries. The present work aimed to investigate locally available, low-cost and efficient substrate as well potential plant for constructed wetland to remove hazardous pollutants from high-strength tannery wastewater in ecofriendly manner.

2. MATERIALS AND METHODS

2.1. Study Area and Period

This study was conducted in Oromia region east Showa zone, Modjo town at Modjo tanning industry PLC (Figure 2.1) from September 2016 to October 2018.

2.2. Study Design

Plug flow experimental study design was carried out to determine the efficiency of pumice substrate and *Chrysopogon zizanioides* plant species in horizontal subsurface constructed wetland to remove hazardous pollutants from high-strength tannery wastewater.

2.2.1. Experimental Material, Design and Setup Establishments

Pumice was collected from volcanic cones of refit valley area of Oromia region east showa zone (8°28'36"N and 39°14'29"E), Ethiopia 20-30 km far from Modjo Tannery (8°35'13"N and 39°07'23"E) approximately 70 km East of Addis Ababa (Figure 2.1). The chemical characteristics of this substrate was determined by using XRF analysis.

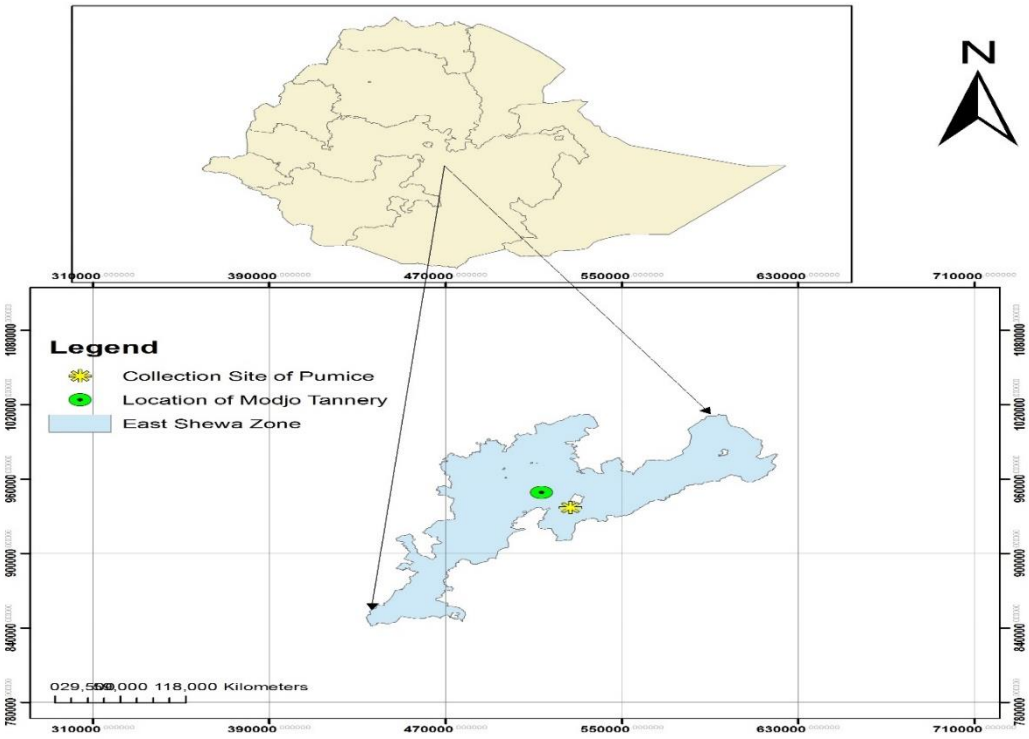

Figure 2.1: Map of study area and location of pumice

Table 2.1: Physical and chemical characteristics of pumice

Chemical Composition	Percent Weight
SiO_2	64.92
Al_2O_3	10.82
Fe_2O_3	4.62
CaO	5.74
K_2O	4.26
Na_2O	4.92
MgO	0.92
MnO	0.20
P_2O_5	0.14
TiO_2	0.15
H_2O	0.85
LOI*	3.67
pH	7.53
**Physical properties, Particle size = 0.075–0.425mm.	
Porosity (%)	73
Particle density (gcm^{-3})	2.33
Specific surface area (BET) ($m^2\ g^{-1}$)	3.50
Cation exchange capacity (CEC), mequiv. 100 g^{-1}	0.84

*LOI= Loss on ignition ** Esayas Alemayehu et al. 2011

The plant (*Chrysopogon zizanioides*) was collected from Holeta Agricultural research institute and transported to Modjo tanning industry. It was planted in the horizontal subsurface constructed wetland and grown for five months before running high-strength wastewater for the treatment.

The horizontal subsurface constructed wetland was installed at Modjo tanning industry compound for the treatment of tannery wastewater (Figure 2.2). The treatment system consists of: a primary screening and a grit removal tank; sedimentation tank for sludge settling and equalization tank connected with horizontal subsurface flow constructed wetland (HSSFCW), with an effective volume of 1.92 m^3 each which is a length of 4 m, width of 0.8 m and effective depth of 0.6 m.

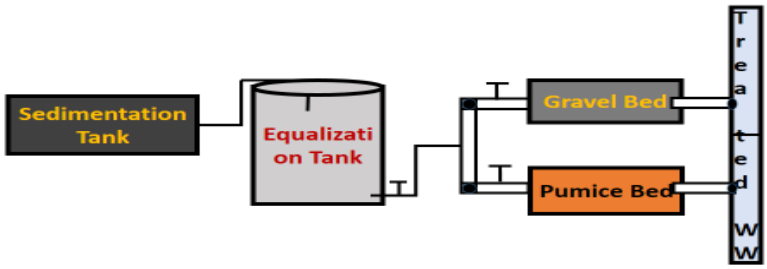

Figure 2.2: Schematic diagram of the horizontal subsurface constructed wetland

The CWs are filled with medium-sized gravel, ranging in size from 6 to 20 mm as a control and pumice 10 – 25 mm grain size substrate vegetated with *Chrysopogon zizanioides* in separate constructed wetland cell with similar size and dimensions (Fig 2.3). The pumice substrate was crushed and graded. Effective size was determined by using standard sieve. Based on the analysis the effective size (ES) (d_{10}) of the media was 1.5-4.5 and the uniformity coefficient (UC) (d_{60}/d_{10}) was 3.5 - 4.

Figure 2.3: Pumice and gravel substrate bed (Photo by Mekonnen Birhanie, 2018)

The raw wastewater is fed into a sedimentation tank from the factory after 24 hour retention time pumped to the equalization tank with volume of 5000 liter then the CWs fed from this tank through 3/4th inch pipe with control valve for each cell. Performance of this constructed wetland was recorded for two years based on four different hydraulic retention time (3, 5, 7 and 9 days).

2.2.2. Sample Collection and Laboratory Analysis

The on-site measurement of the physicochemical parameters was undertaken. The physicochemical analysis of wastewater samples was done before and after the treatment with the two different hydraulic retention time, using standard methods. The analytical parameters were pH, BOD_5, COD, Ammonium N, Nitrite N, Nitrate N, Total N, Phosphate, Total P, Sulfide, Sulfate, Chloride, TSS, TDS, Salinity, EC and Chromium. On-site measurement of the wastewater like temperature, pH and DO were carried out at the site in the tannery environmental quality control laboratory using portable pH meter (Wagtech International N374, M128/03IM, USA) and DO meter (Hach P/N HQ30d, Loveland. CO, USA) for Dissolved oxygen and temperature.

COD, Ammonium-nitrogen, Nitrite-nitrogen, Nitrate-nitrogen, Phosphate, Chloride, Sulfide and Sulfate were measured by using spectrophotometer (Hach model DR/3900 portable spectrophotometer, Germany) according

to Hach instructions. BOD_5 and total Chromium were analyzed using BOD sensor and inductive stirring system AQUA LYTIC model type ET618-4 and Flame Atomic Absorption Spectrophotometer (AAS), (model AAS NOUA-400, Germany) respectively. Total suspended solids (TSS) were determined according to the Standard Methods for the Examination of Water and Wastewater gravimetric method. Heavy metal uptake capacity of the plant and adsorption potential of the pumice were determined by Ash-Modified AOAC 923.03 and Minerals-Modified AOAAC 985.35 (APHA, 2005).

The removal efficiency of the filter media for the selected parameters were calculated as:

$$\% \text{ removal} = Ci - Cf/Ci \text{ X } 100$$

Where, C*i* is the parameter concentration in the untreated wastewater and C*f* is the parameter concentration in the treated wastewater.

2.3. Statistical Data Analysis

Mean and standard deviations were calculated to estimate the concentration of each parameter of the samples. The hypothesis has been tested by two sample t-test using R statistical software: R version 3.2.2 (2015-08-14), Platform: x86_64-w64-mingw32/x64 (64-bit) and Originlab pro 2017 to determine whether an observed difference between the means of the groups is statistically significant or not, based on the two hydraulic retention time.

2.4. Data Quality Management

To assure quality of the data by minimizing the errors the following measures had been undertaken: Apparatuses were calibrated; expiry date of reagents had been checked before starting the real analysis and standard control also prepared. Each test had been triplicated.

3. RESULTS AND DISCUSSION

3.1. Physicochemical Characteristics of Modjo Tannery Wastewater

The raw wastewater was taken from Modjo tannery for physicochemical analysis. Based on this investigation the mean concentration of selected physicochemical parameters were presented at Table 3.1.

This study revealed that the mean concentration of BOD_5, COD and TSS were 1641±375.6, 6953±339.4 and 1868±863.1 mg/l respectively (Table 3.1). This result is basically similar to different studies in Ethiopia with slight difference for different parameters for example a study done at the same tannery industry indicated that the mean concentration of COD was laid between 7950 to 15240 mg/l with the mean of 11123±563.9 mg/l (Seyoum Leta, et al. 2003). Another study also undertaken with same tannery wastewater showed that the mean concentration of BOD_5 was 1054±448 mg/l (Tadesse Alemu and Seyoum Leta, 2015) and the concentration of total suspended solid was found from 1217 to 2847 (Table 3.1) this is a bit greater than some studies for instance a study done in India indicated that 1244 mg/l (Tamal *et al*., 2010).

Nutrients like orthophosphate, ammonium, nitrite and nitrate concentration of Modjo tannery were characterized in this study, the result revealed that 88±40.8, 253.3±11.6, 1.9±0.12, 116.7±26.6 mg/l respectively. This result is comparable to a study done by Sivakumar *et al*., (2015) which indicates the concentration of nitrate in untreated tannery effluent was 116mg/l. The result of ammonium is also similar to that of the results done at Bahir Dar tannery wastewater characterization (96-420 mg/l) (Aseessefa Wosnie and Ayalew Wondie, 2014). According to Arasappan and Kalyanaraman (2015), the nitrite concentration of untreated tannery wastewater was 1.3 mg/l almost parallel to this study finding which accounts 1.9±0.12 mg/l (Table 3.1). Some variation have been seen in some parameters. This variation may be due to the utilization of chemicals for different purposes and different tanning activities among tanneries.

In terms of chromium concentration, Modjo tannery comprised 18.33±6.7 mg/l is similar to other different results presented from same tannery wastewater by Tadesse Alemu et al. (2016) the mean influent wastewater to the constructed wetland was 18.67 mg/l.

Likewise a variation exists in values of physicochemical parameters in general like BOD_5, COD, TSS, phosphate, sulfide, sulfate, etc. in every tannery wastewater characteristics, this may be because of different tanning process, methods, technology and raw material utilization by various tanning industries.

Table 3.1: Characteristics of Modjo Tannery Wastewater (Concentrations are in mg/L, except pH, Salinity and EC)

Parameters	Mean value	Range
pH	10.166±2.02	8-12
BOD_5	1641±373.6	1243-1984
COD	6953.333±339.4	6593-7267
NH_4-N	253.3333±11.6	240-261
NO_2-N	1.913333±0.12	1.77-1.99
NO_3-N	116.6667±26.6	94-146
TN	650.3333±93.6	546-727
PO_4-P	88.06667±40.8	46.5-128
TP	144.5333±20.8	128.6-168
Sulfide	241.3333±101.2	137-339
Sulfate	1072.817±352.7	668.86-1320
Chloride	1919±1271.6	657-3200
TSS	1868±863.1	1217-2847
TDS	5877.3±2294.8	3250-7489
EC (µs/cm)	8550±2089	6540-10710
Salinity (%)	0.69±0.2	0.44-0.9
TCr	18.33±6.7	14-26

3.2. Tannery Wastewater Treatment Efficiency of Horizontal Subsurface Flow Constructed Wetland HSSFCW with Pumice Substrate and Planted with *Chrysopogon zizanioides(CZ)*

The pollutant removal efficiency of horizontal subsurface constructed wetland under this investigation was high this may be due to the high adsorption capacity of pumice and the uptake potential of *Chrysopogon zizanioides* from tannery wastewater. The characteristics of tannery wastewater after treatment was alongside with the standard guideline value of the Ethiopian environmental protection authority and WHO irrigation water quality standard (Table 3.2).

3.2.1. BOD_5, COD and TSS Removal Efficiency of HSSFCW with Pumice Substrate and Planted with *Chrysopogon Zizanioides*

The three important pollutant of the tannery wastewater were analyzed before and after treatment of four hydraulic retention time, based on the finding the final effluent concentration of BOD_5, COD and TSS in mg/l were (273±91, 532.50±177.5 and 99.72±80.93) for 3 days HRT, (74±2, 225.41±11.13 and 79±13.53) for 5 days HRT, (58.67±6.5, 214.67±32.33 and 80±4.58) for 7 days HRT and (60.67±4.93, 234.67±38.79 and 74±21.65) for 9 days HRT (Table 3.2). Both BOD and COD result of 5, 7 and 9 HRT were met the standard value of WHO water quality for irrigation and EEPA (200 and 500 mg/l) but they are beyond the standard at hydraulic retention time of 3 days this is because of the time shortage to degrade organic matter. In all the allotted hydraulic retention time TSS was not achieved good result as compared to the Both WHO and EEPA guideline (50mg/l) (EEPA 2003;WHO 2011).

Table 3.2: Characteristics of Treated Wastewater by HSSFCW with Pumice Substrate and CZ at Different HRT

Parameters	Influent (mg/L, except for pH, EC and salinity)	Effluent Conc. at Different HRT(mg/L, except pH, EC & salinity)				EEPA & WHO irrigation WQS
		3 days	5 days	7 days	9 days	
pH	10.16 ±2.02	8.33±0.76	8±0.5	6.77±0.64	7.67±1.52	6-9
BOD_5	1641±373.55	273±91	74±2	58.67±6.5	60.67±4.93	200
COD	6953.33 ±339.41	532.50±177.5	225.41±11.13	214.67±32.33	234.67±38.79	500
NH_4-N	253.33±11.6	26.83±2.93	5.00±4.36	4.67±1.53	6.83±1.44	30
NO_3-N	116.66 ±26.63	10.83±2.75	0±0	0.37±0.15	0.57±0.21	10
TN	650.33 ±93.62	42±15.72	8.67±5.7	6.50±1.32	9.33±2.1	60
PO_4-P	88.06 ±40.77	6.33±2.1	3.04±1	2.67±1.26	0±0	5
TP	144.53 ±20.75	19.67±3.05	7.53±2.33	5.53±0.5	83.87±11.37	10
Sulfide	241.33 ±101.16	5.29±2.06	1.22±0.4	0.97±0.21	0.58±0.47	1
Sulfate	1072.82 ±352.74	183.27±169.78	63.63±20.88	56.67±13.31	103.38±13.72	
Chloride	1919±1271.6	796.50±88.5	480±42.72	482.67±20.03	664.67±12.85	1000
TSS	1868±863.1	99.72±80.93	79±13.53	80±4.58	74±21.65	50
TDS	5877.3±2294.77	1504.97±1286.16	1279±75	768.67±45.54	798±17.43	2100
EC (µs/cm)	8550±2089	2895.90±2610	2481.67±145.31	1488.67±71.44	1517.33±15.82	1200(µs/cm
Salinity (%)	0.69±0.22	0.27±0.11	0.23±0.01	0.14±0.02	0.14±0.021	
TCr	18.33±6.66	0.88±0.03	0.30±0.1	0.20±0.1	0.35±0.13	2

The removal efficiency of this horizontal flow subsurface constructed wetland filled with pumice substrate and planted with Chrysopogon zozanioides was high for the purification of tannery wastewater considering the three polluting agents with specific hydraulic retention time. During the first 3 and 5 days retention time BOD_5, COD and TSS were reduced by (83.36%, 92.34% and 94.66%) and (95.49%, 96.76% and 95.77%), respectively. After the second 7 and 9 days retention time also it reduced by (96.42%, 96.91% and 95.72%) and (96.30%, 96.62% and 96.02%) respectively (Table 3.3). The result achieved due to the activities of the microorganisms and the networked and spongy tuft roots of the plant to make comfortable environment for the growth of the organism in addition to absorption. The aerobic condition in the superficial wetland bed and anaerobic condition in the bottom allow for efficient removal of organic pollutants and the filtration of the wastewater is the main reason for the removal of suspended solids. A vertical subsurface wetland planted with Scirpus Alternifolios and red ferralitic soil substrate was evaluated by scholars for its wastewater purification capacity and reported as BOD, COD and TSS were reduced by (84.9%, 89.8% and 98.1%) respectively (Villara et al., 2012), the result is almost similar to this investigation especially with the first 3 and 5 hours retention time.

3.2.2. Nutrient Removal Efficiency of HSSFCW with Pumice Substrate and Planted with *Chrysopogon Zizanioides* (NH_4-N, NO_3-N, TN, PO_4-P, TP)

The plant (*Chrysopogon zizanioides*) used in this study possesses unique characteristics suitable for wastewater purification. Now a days various research findings showed its exceptional ability to absorb and to tolerate extreme levels of nutrients, to consume large quantities of water in the process of producing a massive biomass growth. These attributes indicated that this plant is highly suitable for treating high strength wastewater from different industries like tanning industries. In addition to the plant type, selection of best efficient substrate based on the selection criteria including its chemical composition is important for effective application of horizontal subsurface flow constructed wetland for the treatment of high strength industrial wastewater.

Table 3.3: Efficiency of HSSFCW with Pumice Substrate and CZ at Different HRT (Conc. in mg/L, except pH, EC & salinity)

Parameters	Influent conc.	Percentage Removal at Different HRT							
		3 days		5 days		7 days		9 days	
		Mean Conc.	% Removal	Mean Conc.	% Removal	Mean Conc.	% Removal	Mean Conc.	% Removal
pH	10.16 ±2.02	8.33±0.76	18.01	8±0.5	21.26	6.77±0.64	33.37	7.67±1.52	24.51
BOD_5	1641±373.55	273±91	83.36	74±2	95.49	58.67±6.5	96.42	60.67±4.93	96.30
COD	6953.33 ±339.4	532.50±177.5	92.34	225.41±11.1	96.76	214.67±32.33	96.91	234.67±38.79	96.62
NH_4-N	253.33±11.6	26.83±2.93	89.41	5.00±4.36	98.03	4.67±1.53	98.16	6.83±1.44	97.30
NO_3-N	116.66 ±26.63	10.83±2.75	90.72	0±0	100	0.37±0.15	99.68	0.57±0.21	99.51
TN	650.33 ±93.62	42±15.72	93.54	8.67±5.7	98.67	6.50±1.32	99.00	9.33±2.1	98.56
PO_4-P	88.06 ±40.77	6.33±2.1	92.81	3.04±1	96.55	2.67±1.26	96.97	0±0	100
TP	144.53 ±20.75	19.67±3.05	86.39	7.53±2.33	94.79	5.53±0.5	96.17	83.87±11.37	41.97
S^{2-}	241.33 ±101.16	5.29±2.06	97.81	1.22±0.4	99.49	0.97±0.21	99.59	0.58±0.47	99.76
SO_4-S	1072.82 ±352.7	183.27±169.78	82.92	63.63±20.88	94.07	56.67±13.31	94.72	103.38±13.72	90.36
Cl^-	1919±1271.6	796.50±88.5	58.49	480±42.72	74.99	482.67±20.03	74.85	664.67±12.85	65.36
TSS	1868±863.1	99.72±80.93	94.66	79±13.53	95.77	80±4.58	95.72	74±21.65	96.04
TDS	5877.3±2294.7	1504.97±1286.1	74.39	1279±75	78.24	768.67±45.54	86.92	798±17.43	86.42
EC (µs/cm)	8550±2089	2895.90±2610	66.13	2481.67±145	70.97	1488.67±71.44	82.59	1517.33±15.82	82.25
Salinity (%)	0.69±0.22	0.27±0.11	60.87	0.23±0.01	66.09	0.14±0.02	79.71	0.14±0.021	79.71
TCr	18.33±6.66	0.88±0.03	95.20	0.30±0.1	98.36	0.20±0.1	98.91	0.35±0.13	98.09

The main nutrient component concentrations like NH_4-N, NO_3-N, TN, PO_4-P and TP in Modjo tannery wastewater were determined before and after treatment using this horizontal subsurface constructed wetland to evaluate its treatment performance at four different hydraulic retention time. In the final effluent, the concentration of NH_4-N, NO_3-N, TN, PO_4-P and TP in mg/l become (26.83±2.93, 10.83±2.75, 42±15.72, 6.33±2.1 and 19.67±3.05) at 3 days HRT, (5.00±4.36, 0±0, 8.67±5.7, 3.04±1 and 7.53±2.33) at 5 days HRT, (4.67±1.53, 0.37±0.15, 6.50±1.32, 2.67±1.26 and 5.53±0.5) at 7 days HRT and (6.83±1.44, 0.57±0.21, 9.33±2.1, 0±0 and 83.87±11.37) at 9 days HRT respectively (Table 3.2).

When the result finding evaluated with the standard guideline value of WHO water quality standard and EEPA at different hydraulic retention time, NH_4-N and TN were under the maximum permitable limit at all retention time and NO_3-N and PO_4-P were met the specified limit value at 5, 7 and 9 days retention time only. But TP removal was good only at 5 and 7 days retention time. Therefore contact time of 5 days and greater are efficient retention time for the removal of major nutrients from tannery wastewater using horizontal subsurface constructed wetland filled with pumice substrate and planted with *Chrysopogon zizanioides*. Substrate composition, plant type and some microorganisms in the constructed wetland were play great role for the reduction of those nutrient components.

As various scholars reported, the removal of pollutants from wastewater are achieved by different mechanisms like sedimentation, filtration, chemical precipitation, adsorption, microbial interactions, and uptake of vegetation. The nutrient removal efficiency of this subsurface constructed wetland was generally effective. The maximum removal efficiency was seen at 5, 7 and 9 days retention time. The minimum (89.41%) and maximum (98.16%) of NH_4-N removal efficiency was achieved at 3 and 7 days retention time respectively. Almost all of NO_3-N also removed after 5 days treatment, more than 93.5% of TN was removed, PO_4-P and TP were also effectively removed in this constructed wetland, a minimum of 92.81% at 3 days HRT and maximum of 100% at 9 days HRT of PO_4-P was removed likewise TP from 41.97% at 9 days HRT up to 96.17% at 7 days HRT was removed (Table 3.3; Figure 3.1). This effective result was seen mainly because of the adsorption capacity of the substrate pumice and uptake potential ability of the plant especially pumice is effective to remove phosphate since it contains sufficient amount of aluminum and iron that favors for the removal of phosphorus (Villara et al., 2012).

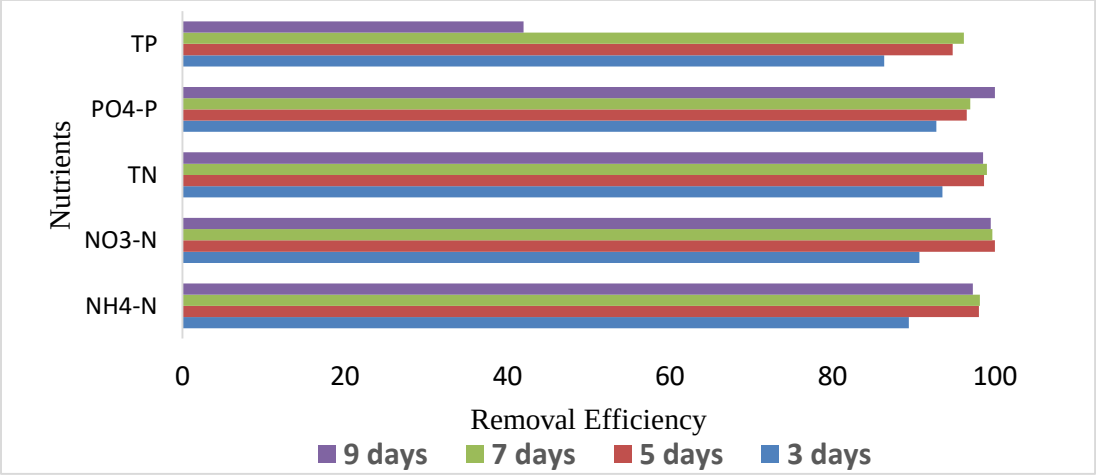

Figure 3.1: Nutrient Removal Efficiency of Pumice Substrate in HSSFCW Planted with Chrysopogon Zizanioides at Different HRT

On the other hand *Chrysopogon zizanioides* has high level of tolerance for high strength wastewater and very effective in removing pollutants from landfill leachates, particularly N and P. Nitrogen and Phosphorus absorption is also expedited because roots have direct exposure to effluents (Xia *et al.*, 2000). another study report which could support this findings also indicated that, the vetiver system is based on the use of vetiver grass (*Chrysopogon*

zizanioides), which was first recognized early in the 1990s for having "super absorbent" characteristics suitable for the treatment of wastewater and leachate generated from landfill (Truong and Stone, 1996).

3.2.3 Sulfur and Chloride Removal Efficiency of HSSFCW with Pumice Substrate and Planted with *Chrysopogon zizanioides* (Sulfide, Sulfate and Chloride)

Tanning is usually done by using tanning agents and a highly turbid, polluted wastewater is generated from the process. Sulfide sulfate and chloride are among the major components of the tannery wastewater. Thus removal of sulfide sulfate and chloride from this wastewater is very important. A number of scholars worked on the removal of sulfur and chloride from the wastewater streams, but little has been reported on the removal those pollutants from the tannery wastewater using horizontal subsurface flow constructed wetlands.

The horizontal subsurface flow constructed wetland was evaluated for the removal of sulfide, sulfate and chloride from Modjo tannery wastewater using pumice substrate and hydroponic plant type *Chrysopogon zizanioides.* The result showed that at the end of the given hydraulic retention time the effluent concentration of sulfide, sulfate and chloride were (5.29±2.06 mg/l, 183.27±169.78 mg/l and 796.50±88.5 mg/l) at 3 days HRT, (1.22±0.4 mg/l, 63.63±20.88 mg/l and 480±42.72 mg/l) at 5 days HRT, (0.97±0.21mg/l, 56.67±13.31 mg/l and 482.67±20.03 mg/l) at 7 days HRT and (0.58±0.47 mg/l, 103.38±13.72 mg/l and 664.67±12.85 mg/l) at 9 days HRT respectively. The effluent concentration of sulfide was met the standard guideline value of both EEPA and WHO at 7 and 9 days HRT only. Whereas the concentration of chloride in the treated wastewater was under the standard value at all the tested hydraulic retention time.

The overall performance evaluation of this constructed wetland to remove sulfide, sulfate and chloride indicated that 97.81%, 82.92% and 58.49%) at the first 3 days contact time, 99.49%, 94.07% and 74.99% at the second 5 days contact time, 99.59%, 94.72% and 74.85% after 7 days and 99.76%, 90.36% and 65.36% after 9 treatment days respectively (Table 3.3). The reason for this effective sulfur and chloride removal performance shown by this constructed wetland was due to the combination of physical and chemical removal mechanism, like precipitation, straining, sedimentation and adsorption, along with biological treatment by various microorganisms including both sulfur reducing and oxidizing bacteria.

High cation exchange capacity of the substrate also key factor for the efficient removal of chloride from the wastewater. This fact is evidenced by Kang & Shackelford (2010) conducted complementary research with prepared KCl solution and achieved 97.3% chloride removal efficiency. In another previous study of two-stage series of horizontal subsurface flow constructed wetland with Phragmites australis and Typha latifolia reported high removal of organics and other pollutants from tannery wastewater, up to 81% of sulfate removal was achieved operating at hydraulic retention times of 2, 5 and 7 days (Cristina *et al.*, 2009).

3.2.4. EC, TDS and Salinity Removal Efficiency of HSSFCW with Pumice Substrate and Planted with *Chrysopogon zizanioides*

Wastewater treatment using horizontal subsurface flow constructed wetland with potential substrate and plant type considered as 'all-in-one' treatment system because of its efficiency of removing various toxic pollutants including electric conductivity, total dissolved solid and salinity from high strength tannery wastewater.

There are numerous plant species and substrates suitable for wastewater treatment in a constructed wetland, the application of *Chrysopogon zizanioides and* pumice substrate in a horizontal subsurface flow constructed wetland is the main focus of this paper. For many decades *Chrysopogon zizanioides* has been applied for water and soil conservation. In the last few years, considerable research have been demonstrated in the success of this grass in the treatment of wastewater.

In this investigation, horizontal subsurface flow constructed wetland with pumice substrate and planted with *Chrysopogon zizanioides* was establish for the treatment of high strength tannery wastewater. Based on the findings, TDS, EC and salinity removal efficiency were 74.39%, 66.13% and 60.87% after 3 days and 78.24%,

70.97% and 66.09% at 5 days contact time respectively. After both 3 and 5 days hydraulic retention time, the concentration of total dissolved solid (1504.97±1286.16 mg/l and 1279±75 mg/l) in the effluent met the maximum allowable limit (2100 mg/l) but electric conductivity (2895.90±2610 µs/cm and 2481.67±145.31 µs/cm) was beyond the limit (1200 µs/cm)(Table 3.2). On 7 and 9 days retention time, TDS, EC and salinity were reduced by (86.92%, 82.59% and 79.71%) and (86.42%, 82.25% and 79.71%) respectively. The effluent concentration of TDS at both 7and 9 HRT (768.67±45.54 mg/l and 798±17.43 mg/l) were under standard limit value (2100mg/l). But electric conductivity could not reduce efficiently to reach to the maximum allowable limit set by WHO.

The reduction of those pollutants were achieved due to different mechanism under taken in the constructed wetland but the substrate ability to adsorb different ions and the plant root plays great role. An investigation done very recently on the attempt to reduce total dissolved solids by different plant parts and found that vetiver root can remove TDS in water about 55.93% by the adsorption method (Ebrahim *et al.*, 2011).

The efficiency of this constructed wetland in this pilot study to remove total dissolved solid from tannery wastewater was perform from 74% to 86%. This efficiency better than several study findings this is may be due to the cumulative effect of the plant ability and the substrate potential. The use of plants for wastewater treatment is not a new fashion. But the issue is how to improve pollutant removal efficiency. For example a project was done to examine the phytoremediation potential of water hyacinth (Eichhornia crassipes), water lettuce (Pistia stratiotes) and Vetiver (chrysopogon zizanioides) for the removal of Total dissolved solids from brine solution of textile industry by shallow pond system. The result reported after 10 days of operational period, water hyacinth showed maximum removal of 55.6% on 6th day, 48.7% using water lettuce on 7th day and 39.6 % on 3rd day under Vetiver treatment system (Abinaya *et al.*, 2018). Another study also was carried on constructed wetland to treat an aquaculture effluent using four species, *Cyperus giganteus Vahl, Typha domingensis Pers., Pontederia cordata L. e Eichhornia crassipes* in Brazil, in this study the constructed wetland perform 85.5% removal of total dissolved solid (Travaini and Sipauba, 2012).

3.2.5. Chromium Removal Efficiency of HSSFCW with Pumice Substrate and Planted with *Chrysopogon zizanioides*

Chromium is a toxic heavy metal which is found in tannery wastewater and causes serious environmental problem. Constructed wetland recently used for the removal of wastewater pollutants including heavy metals like chromium, the result of this investigation presents the chromium removal efficiency of horizontal subsurface flow constructed wetland from tannery wastewater. Based on the finding the concentration of total chromium in the tannery wastewater effluent after 3 and 5 days treatment time was (0.88±0.03 mg/l and 0.30±0.1 mg/l) respectively and this concentration further reduced to 0.20±0.1 mg/l and 0.35±0.13 mg/l after 7 and 9 days retention time respectively (Table 3.2). The effluent concentration at all retention time was under the standard guideline value of 2 mg/l set by WHO.

The total chromium removal efficiency of this constructed wetland with pumice substrate and *Chrysopogon zizanioides* was calculated and become 95.20 %, 98.36%, 98.91% and 98.09% at 3,5,7 and 9 days retention time respectively (Fig. 3.2). In this investigation the chromium adsorption capacity of pumice was analyzed, the result showed that 58.15mg of total chromium was adsorbed per one kilogram of pumice substrate. This result is similar to the previous research finding on phytoremediation of chromium by model constructed wetland which accounts 97-99.6% at all system of the constructed wetland with different plant species (Catherine *et al*., 2006).

The mechanism of heavy metals removal in horizontal subsurface constructed wetlands is a combination of different processes mainly physicochemical and biological which includes filtration, sedimentation, straining on the substrate, plant uptake, and precipitation as insoluble forms (Kadlec and Wallace, 2009). The most important reaction zone in constructed wetlands is the root zone (rhizosphere) where physicochemical and biological processes take place (Stottmeister *et al*., 2003). For this reason, this high chromium removal efficiency was achieved because of the metal adsorption potential ability of pumice substrate and the uptake capacity of the plant

Chrysopogon zizanioides. Various research works and experiments were done in both laboratory and full scale on the chromium removal efficiency of constructed wetland, for example Dotro *et al*., (2011) reported that 90-99% of chromium removed from tannery wastewater by subsurface constructed wetland with pea gravel substrate and Typha spp.

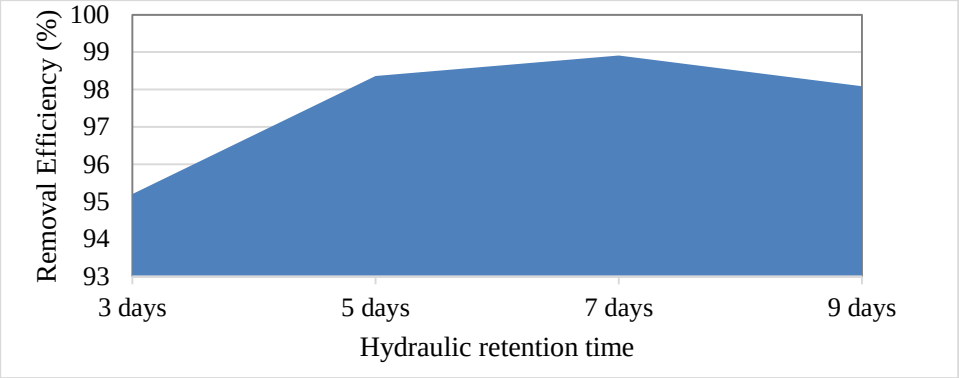

Figure 3.2: Chromium Removal Efficiency of HSSFCW with Pumice Substrate and Planted with *Chrysopogon Zizanioides*

3.2.6 Comparison between Pumice (test substrate) and Gravel (Control substrate) on the Tanner Wastewater Treatment efficiency of HSSFCW Planted with CZ

The treatment efficiency of constructed wetland varied according to the type of substrate, plant type, seasonal variation, climatic change and other factors. Even though the plant type is similar in both two beds (control and study), the result of this investigation also varied between the gravel and pumice substrate (Table 3.4). In this investigation at the first 3 days HRT only BOD_5 and COD were removed by gravel substrate (89.05% and 93.82%) better than pumice substrate (83.36% and 92.34%) but in all other retention time the pumice substrate showed better result than gravel (Table 3.4; Figure 3.3).

Table 3.4: TWW Treatment Efficiency of HSSFCW with Gravel and Pumice Substrate and Planted with CZ at Different HRT

Parameters	Influent conc.(mg/l)	3days HRT		5days HRT		7days HRT		9days HRT	
		Pumice (%)	Gravel (%)	Pumice (%)	Gravel (%)	Pumice (%)	Gravel (%)	Pumice (%)	Gravel (%)
BOD_5	1641±373.55	83.36	89.05	95.49	89.58	96.42	90.96	96.30	91.85
COD	6953.33 ±339.41	92.34	93.82	96.76	95.81	96.91	95.94	96.62	96.33
NH_4-N	253.33±11.6	89.41	19.08	98.03	34.47	98.16	52.63	97.30	61.97
NO_3-N	116.66 ±26.63	90.72	66.29	100	77.15	99.68	80.86	99.51	86.00
TN	650.33 ±93.62	93.54	68.27	98.67	86.11	99.00	90.42	98.56	88.67
PO_4-P	88.06 ±40.77	92.81	90.92	96.55	95.20	96.97	95.68	100	96.33
TP	144.53 ±20.75	86.39	88.47	94.79	88.93	96.17	91.47	41.97	92.16
Sulfide	241.33 ±101.16	97.81	96.10	99.49	98.40	99.59	98.49	99.76	97.02
Sulfate	1072.82 ±352.74	82.92	65.46	94.07	89.22	94.72	90.34	90.36	89.36
Chloride	1919±1271.6	58.49	68.96	74.99	72.38	74.85	72.21	65.36	64.22
TSS	1868±863.1	94.66	95.41	95.77	95.93	95.72	96.09	96.04	96.25
TDS	5877.3±2294.77	74.39	79.96	78.24	79.95	86.92	81.96	86.42	81.23
EC (µs/cm)	8550±2089	66.13	73.01	70.97	76.82	82.59	79.12	82.25	78.71
Salinity (%)	0.69±0.22	60.87	63.77	66.09	63.77	79.71	65.22	79.71	63.77
TCr	18.33±6.66	95.20	96.40	98.36	97.27	98.91	97.44	98.09	97.27

The result between the study and control bed was tested using Two-Sample t-Test, the result showed that significantly differ at 95% confidence interval, p-value=0.01and hence, this substrate can be useful for the treatment of high strength wastewater in horizontal subsurface constructed wetland better than the conventional gravel substrate.

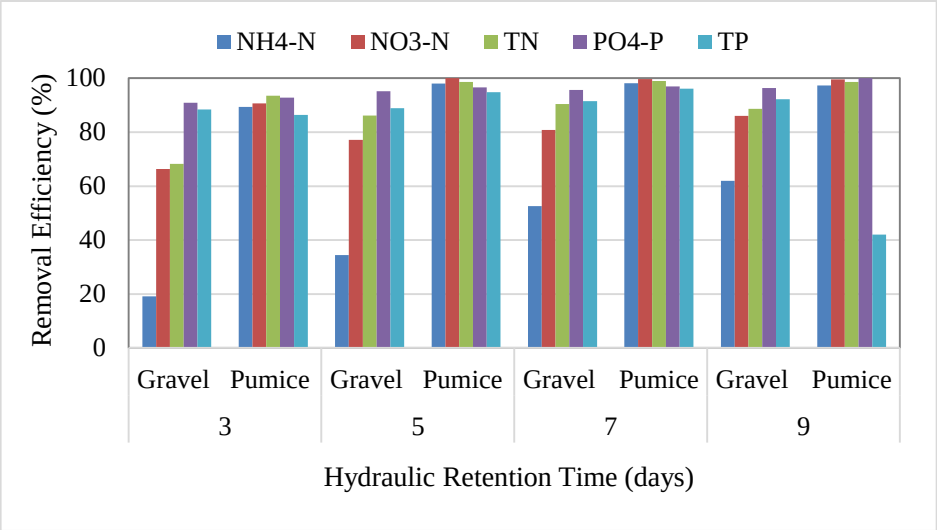

Figure 3.3: Nutrient Removal Efficiency of HSSFCW with Gravel and Pumice Substrate

Chromium removal efficiency of pumice substrate was better than gravel at all hydraulic time except the first three days that pumice achieved 95.2% while gravel achieved 96.4% (Table 3.3, Figure 3.4).

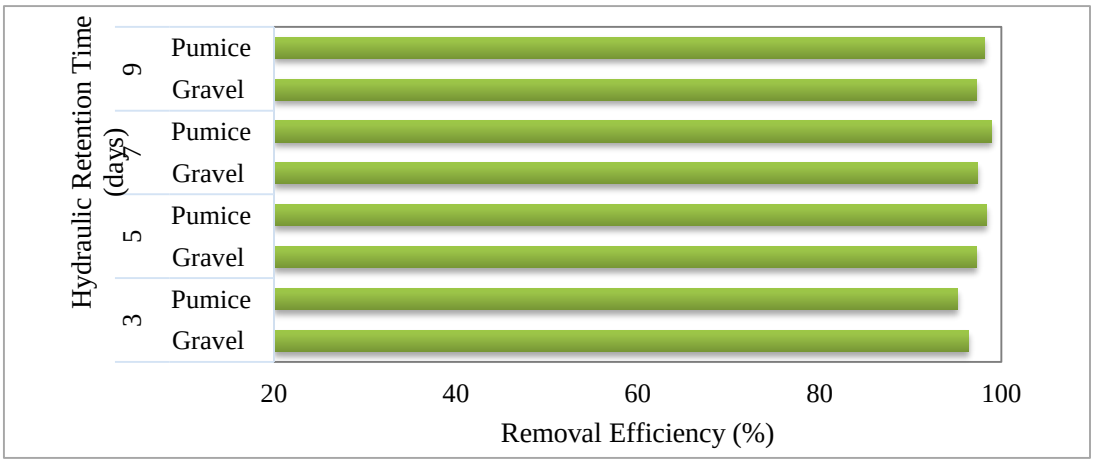

Figure 3.4: Chromium Removal Efficiency of HSSFCW with Gravel and Pumice Substrate

The biometry data of the plant *Chrysopogon zizanioides* was analyzed for both gravel and pumice substrate. The result showed that the growth of the plant at the sixth month above the ground in cm was 58.66 and 113.33 and below the ground was 43.33 and 24.33 in gravel and pumice substrate bed respectively. The plant dry weight also indicate that 77, 130.8 gm above ground and 80, 89 gm below the ground in gravel and pumice substrate respectively (Table 3.5).

The chromium uptake capacity of the plant in both substrate beds was evaluated and revealed that, the plant below the ground uptake more chromium than above the ground that was (8.8, 36.62mg/kg) and 10.24, 39.72gm/kg) in gravel and pumice substrate bed respectively (Table 3.5).

Table 3.4: Biometry Data of Chrysopogon zizanioides in Gravel and Pumice Substrate Bed

Substrate	Above Ground			Below Ground		
	Length (cm)	Dry weight (gm)	Cr Uptake (mg/kg)	Length (cm)	Dry weight (gm)	Cr Uptake (mg/kg)
Gravel	58.66	77	8.8	43.33	80	36.62
Pumice	113.33	130.8	10.24	24.33	89	39.72

Based on the result found from the biometry data, The Cr bioaccumulation factor (BAF) and Translocation factor (TF) of Chrysopogon Zizaniodes plant species was estimated, (as a method described by Baker, *et. al*., 2000 and Shanker *et al*., 2004):

$$BAF = \frac{mg\frac{Cr}{kg}\, dw\ plant}{mg\frac{Cr}{L}\ Wastewater}$$

Translocation factor of Cr was also calculated as:

$$BAF = \frac{mg\frac{Cr}{kg} dw\ above\ ground}{mg\frac{Cr}{kg}\ dw\ below\ ground}$$

Therefore BAF of this plant were above the ground (0.48, 0.56 Lkg^{-1}) and below the ground (1.99, 2.17 Lkg^{-1}) in gravel and pumice substrate beds respectively. Whereas TF were (0.24 and 0.26) in gravel and pumice substrate bed respectively.

Plants with more BAF and TF values can remove metals like chromium from the wastewater in the constructed wetland that may be due to the harvesting the areal part of the plant removes chromium from the bed. Plant species with high capacity to translocate chromium from below the ground to above the ground enhances absorption of chromium from the constructed wetland bed (Skiffington et al., 1976; Perk, 2006). Translocation can reduce again chromium concentration and hence that reduce toxicity potential of to the root.

4. CONCLUSION AND RECOMMENDATION

4.1. Conclusion

Based on this investigation the following major conclusions has been drawn:

- Modjo tannery wastewater characteristics was very high strength wastewater with different hazardous pollutants.
- The bioaccumulation and translocation factor of *Chrysopogon zizanioides* were greater in pumice substrate bed than the gravel which means that this plant can remove more chromium in pumice media than gravel one.
- The tannery wastewater treatment efficiency of pumice substrate was better than gravel substrate
- Horizontal subsurface flow constructed wetland with pumice substrate and *Chrysopogon zizanioides* plant species has a potential to treat high strength tannery wastewater by different mechanisms including adsorption, filtration, microbial activities and plant uptake. Therefore the use of such kind of constructed wetland with locally-available low-cost substrate and potential plant type may contribute to the low technology solution for sustainable industrial wastewater management in ecofriendly manner.

4.2. RECOMMENDATIONS

Further investigation on the effect of other plant type with this substrate is recommended.

ACKNOWLEDGMENTS

I would like to express my deepest gratitude to my supervisors Dr. Seyoum Leta and prof. Mohammed Mazharuddin Khan for their advice, guide and constructive comments throughout this work. I am grateful to Addis Ababa University for the financial support in making the study a reality. I would like to forward my gratitude to Modjo tannery PLC management officials for their cooperation. I would like to acknowledge Holeta Agricultural research institute for the kind cooperation during the plant identification and seedling transportation to the study site.

REFERENCES

Abinaya, S., Saraswathi, R., Rajamohan, S. and Mohammed S.A.M. (2018): Phyto-remediation of total dissolved solids (TDS) by *Eichhornia Crassipes*, *Pistia Stratiotes* and *Chrysopogon Zizanioides* from second stage, RO-Brine solution, *Res. J. Chem. Environ*., 22 (5): 36-41.

APHA (2005): *Standard Methods for the Examination of Water and Wastewater*, 21stedn. American Public health association, Washington.

Arasappan, S. and Kalyanaraman, R. (2015): Characterization of Physicochemical Parameters and heavy metal Analysis of Tannery Effluent. *Int.J.Curr.Microbiol. App.Sci*, 4(9): 349-359.

Assefa Wosnie, Ayalew Wondie (2014): Bahir Dar tannery effluent characterization and its impact on the head of Blue Nile River.Afr. *J Environ. Sci. Technol*, 8 (6):312-318.

Babel, S. and Kurniawan, T.A. (2003): Low-cost adsorbents for heavy metal uptake from contaminated water: A review, *J. Hazard. Mat.* , 97:219-243.

Baker, ATM. Mcgranth, Reeves, RD. and Smith, JAC. (2000): Metal Hyper Accumulator Plants. A review of the Ecology and Physiology of Biochemical Resource for Phytoremediation of Contaminated Soil and Water: PP.85-107.

Catherine, M., Sylvia, C., John, W., Elias, T. (2006): Phytoremediation of chromium by model constructed wetland, *Bioresource Technology*, 97: 1767-1772.

Cristina, S.C., Calheiros, O.S.S., Rangel, M.L.C. (2009): Treatment of industrial wastewater with two-stage constructed wetlands planted with Typha latifolia and Phragmites australis, *Bioresource Technology*, 100:3205-3213.

Dotro, G., Larsen, D., Paul, P. (2011): Preliminary evaluation of biological and physical chemical chromium removal mechanisms in gravel Media used in constructed wetlands. *Water Air Soil Pollut.*, 215: 507-515.

Ebrahim, A., Ali, M., Gautham, J.N., Hariram, S. (2011): A preliminary attempt to reduce total dissolved solids in ground water using different plant parts, *Int. J. Pharm. Bio. Sci.*, 2(2): B414-B422.

EEPA (Federal Environmental Protection Authority of Ethiopia) (2003): Standards for industrial pollution control in Ethiopia, Part Three: Standards for Industrial effluents. ESIS project US/ETH/99/ 068/ETHIOPIA, EPA/UNIDO, Addis Ababa.

Esayas Alemayehu, Soren, T.B., Bernd, L. (2011): Adsorption behavior of Cr(VI) onto macro and micro vesicular volcanic rocks from water. *Separation and Purification Technology*, 78: 55-61.

Kadlec, R.H., Wallace, S. (2009): *Treatment Wetlands*, 2nd. Boca Raton: CRC press, Boca Raton, Florida, USA.

Kang, J., Shackelford, C. (2010): Membrane Behavior of Compacted Clay Liners, *Journal of Geotechnical and Geoenvironmental Engineering*, 136(10):1368-1382.

Kawser, A.M.d., Monika, D., Monirul, I.M., Mosammat, S.A., Shahidul, I. and Muhammad A.A. (2011): Physicochemical Properties of Tannery and Textile Effluents and Surface Water of River Buriganga and Karnatoli, Bangladesh, *World Applied Sciences Journal* 12 (2): 152-159, ISSN 1818-4952.

Perk, M.V.D. (2006): *Soil and Water Contamination: From Molecular to Catchments Scale*. London; JK.

Seyoum Leta, Fassil Asefa, Gunnel, D. (2003): Characterization of tannery wastewater and assessment of downstream pollution profiles along ModjoRiver in Ethiopia, *Ethiopian Journal of Biological Sciences*, 2(2): 157-168.

Shanker, A.K., Djanaguiraman, M., Sudhagar, R., Chandrashekar, C.N. and Pathmanabhan, G. (2004): Plant Science. 166:1035.

Sivakumar, P., Kanagappan, M. and Sam M.D.S. (2015): Physicochemical Characteristics of Untreated Effluent from Tannery Industries in TamMil Nadu: A Comparative Study, *Int J Pharm Bio Sci.*, 6(1): (B) 446-451.

Skeffington, R., Shwery, PA., Peterson, PJ. (1976): Chromium Uptake and Transport in Barely Seedlings (*Hordeum vulgare* L.). *Plantrta (Ber*), 132:209-214.

Stottmeister, U., Wiebner, A., Kuschk, P., Kappelmeyer, U., Kastner, M., Bederski, O., Muller, R.A., Moormann, H. (2003): Effects of plants and microorganisms in constructed wetlands for wastewater treatment. *Biotechnol. Adv*. 22:93-117.

Suthantharajan, R., Ravindranath, E., Chits, K., Umamaheswari, B., Ramesh, T., Rajamam, S. (2004): Membrane application for recovery and reuse of water from treated tannery wastewater, *Desalination*, 164:151-156.

Tadesse Alemu and Seyoum Leta (2015): Evaluation of selected wetland plants for removal of chromium from tannery wastewater in constructed wetland, Ethiopia. *A J Environmental science and technology*, 9(5): 420-427.

Tadesse Alemu, Eshetu Lemma, Andualem Mekonnen, Seyoum Leta (2016): Performance of Pilot Scale Anaerobic-SBR System Integrated with Constructed Wetlands for the Treatment of Tannery Wastewater, *Environ. Process*. 3:815–827, DOI 10.1007/s40710-016-0171-1.

Tamal, M., Dalia, D., Subhasis, M., Siddhartha, D. (2010): Treatment of leather industry wastewater by aerobic biological and Fenton oxidation process, *J Hazardous Materials*, 180: 204-211.

Travaini, L.F. and Sipauba, T.L.H. (2012): Efficiency of a constructed wetland for wastewaters treatment, *Acta Limnologica Brasiliensia*, 24 (3): 255-265.

Truong, P. and Stone, R. (1996): Vetiver grass for landfill rehabilitation: Erosion and leachate control, Report to DNR and Redland Shire Council, Queensland, Australia.

UNIDO (2012): Technical assistance project for the upgrading of the Ethiopian leather and leather products industry, Independent Evaluation Report Ethiopia. https://www.unido.org/fileadmin/user/Evaluation/Ethiopia_leather_valuation FINAL_report_131302.pdf. Accessed Sep 2016.

Villara, M.M., Domíngueza, E.R., Tackb, F., Ruiza, J.M, Moralesa, R.S., Arteaga, L.E (2012): Vertical subsurface wetlands for wastewater purification, 20th International Congress of Chemical and Process Engineering CHISA, *Procedia Engineering*, 42: 1960 -1968, Available online at www.sciencedirect.com.

WHO (1996): Guidelines for drinking water quality, vol 2: Health criteria and other supporting information, Geneva.

Xia, H., Liu, S. and Ao, H. (2000): Study on purification and uptake of garbage leachate by vetiver grass., In: Proc. of the 2nd International Conference on Vetiver, Thailand.

Modeling Blue and Green Water Resources Availability at the Basin and Sub-Basin Level under Changing Climate in the Weyib River Basin in Ethiopia

Abdulkerim Bedewi Serur

Water Resources Engineering Department, School of Civil Engineering and Architecture, Adama Science and Technology University, P.O. Box: 1888, Adama, Ethiopia, e-mail: abdulkerim.bedewi@astu.edu.et

ABSTRACT

The Weyib River basin, water from which is utilized for diverse water resources schemes, is one of the important rivers of Ethiopia. However, increase in temperature and change in both magnitude and its spatiotemporal distribution of rainfall under changing climate are adversely affecting the freshwater resources availability. This study aims to model the blue and green water resources availability under changing climate within Weyib River basin in Ethiopia at both basin and sub-basin level using ArcSWAT hydrologic model. All water balance components including blue water flow (sum of the water yield and the deep aquifer recharge), green water flow (actual evapotranspiration), and green water storage (soil water) at both entire basin and sub-basin level were examined. Results reveal that mean annual blue water flow, green water flow, and green water storage exhibit a rise in the entire basin and in all the sub-basins under all coupled model inter-comparison project 5 representative concentration pathway (CMIP5 RCP) scenarios. The mean annual blue and green water flow increases by 27.97 and 29.26% under RCP8.5, 19.61 and 28.78% under RCP4.5, and 17.06 and 28.15% under RCP2.6 scenarios respectively, while the mean annual green water storage rises by 13.87, 13.62, and 13.60% under RCP 8.5, RCP4.5, and RCP2.6 scenarios respectively in the entire basin. The sub-basin level analysis reveals that variations of blue and green water resources availability in all the sub-basins are very high as compared to that of the entire basin analysis under all RCP scenarios. This study provided significant insights into freshwater availability on a sub-basin level under future changing climate and it is paramount important to develop climate change adaptation and mitigation strategies for optimum planning and management of freshwater resources availability within the Weyib river basin in upcoming period.

Keywords: *Blue and Green Water Resources Availability; ArcSWAT Hydrologic Model; CMIP5 RCP Scenarios; Entire Basin and Sub-Basin Level; Weyib River Basin in Ethiopia*

1. INTRODUCTION

Up to now, studies of freshwater availability have predominantly focused on the quantification of the ''blue water'', while ignoring the ''green water'' as part of the water resource and its great importance especially for rainfed agriculture; e.g., in sub-Saharan Africa more than 95% is rainfed (Rockstrom et al., 2007). Based on Diekkrüger et al. (2018) definition, BWF (blue water flow) is the sum of streamflow (which includes surface runoff contribution to the stream, sub-surface contribution to the stream, and shallow groundwater contribution to the stream), deep aquifer recharge, and water storage (lakes, ponds, wetlands, etc.). However, BWF in this study was restricted to the sum of streamflow and deep aquifer recharge. GW (green water) has two components, GWF (green water flow), which is actual evapotranspiration and GWS (green water storage), which is soil moisture. Soil moisture (soil water content) is being the primary source of actual evapotranspiration (i.e., green water flow). Spatially and temporally detailed assessments of the different components of freshwater availability are essential for locating critical regions, and thus, the basis for rational decision-making in water resources planning and management.

Climate change has already knocked water resources and agriculture sectors in Ethiopia. An increment of temperature was observed in Ethiopia (Asfaw et al., 2018; Abdulkerim Bedewi and Sarma, 2017c; Shawul et al., 2016; Legesse et al., 2013; ENMA, 2007), and the temperature is predicted to further rise in Ethiopia and the rest of Africa (Alexandrov and Genev, 2003; Boko et al., 2008; Dinar 2006; Loukas et al., 2015; IPCC, 2013; Kruger and Shongwe, 2004; New et al., 2006; Unganai, 1996). At the same time, precipitation is the largest factor in the water balance of catchment hydrology (Mpelasoka and Chiew, 2009). Significant spatiotemporal variations of precipitation was observed throughout Africa (Shongwe et al., 2009; Faramarzi et al., 2013). The recent flooding

and drought events in Ethiopia is sited as visible evidences for adverse impacts of recent climate change, so identifying localized impact of climate change at a catchment level in Ethiopia can reveal the degree of vulnerability of local freshwater resources availability (blue and green water resources) to climate change and plan appropriate adaptation measures, which is fundamental for water resources management in Ethiopia.

The ensembles of earth system models (ESMs) in a particular study area is of paramount important to minimize uncertainty arise (Maurer et al., 2007; Brekke et al., 2008; Reichler and Kim. 2008; Pierce et al., 2009), so in this study, outputs from three ESMs (GFDL-ESM2M, CanESM2, and GFDL-ESM2G) were used. Due to the spatial resolution of ESMs is too coarse (Mondal and Mujumdar, 2012; Goyal et al., 2011; Samadi et al., 2013; Frey-Buness et al., 1995), it is impossible to directly apply these outputs of ESMs for hydrological modelling and then reveal potential impacts of climate change on freshwater availability at catchment scale. Therefore, statistical downscaling of climate parameters at local or catchment scale will bridge the scale gap between ESM outputs supplied and hydrological models required to simulate catchment freshwater availability.

Farjad et al. (2016) investigated that mean annual variations of hydrological processes in Elbow River basin in Canada for the ensembles of CMIP3-GCMs up to the year 2070 and they found that mean annual BWF and GWF observed to increase significantly. The impact of climate change on freshwater availability in four African River basins (Niger, Upper Blue Nile, Oubangui, and Limpopo) from ensembles of CMIP5-ESMs for the RCP 8.5and RCP2.6 have been modeled (Aich et al., 2014) and found that a tendency to increase BWF in three of the four basins (not for the Oubangui). Faramarzi et al. (2013) modeled that whole African continent under ensembles of CMIP3-GCMs for various emission scenarios and found that an increment of BWF under some climate models and decreasing trend was observed under some climate models with significant spatial variability. Water resources components of blue water flow, green water flow and green water storage were estimated at the HRU (Hydrological Response Unit) scales in the Wei River basin in Chaina and they found that small spatiotemporal variations of green and blue water resources in the basin (Xu and Zuo, 2014).

The application of various hydrological models into the hydrological regime of a watershed in Ethiopia have been investigated (Conway and Hulme, 1993, 1996; Johnson and Curtis, 1994; Conway, 2000; Kebede et al., 2006). However, the SWAT application in Ethiopia is very few (Setegn et al., 2010, 2011; Shawul et al., 2013). In this study, therefore, we have motivated on the application of ArcSWAT hydrological model to simulate freshwater resources availability of agricultural land under changing climate. Against this background, the main objective of this study is to estimate BWF (water yield plus deep aquifer recharge), GWF (actual evapotranspiration), and GWS (soil water) under changing climate within Weyib River basin in Ethiopia at both basin and sub-basin level.

2. MATERIALS AND METHODS

2.1. Brief Description of Weyb River Basin

The Weyb River basin (Fig. 1a) covers an area of 4215.93 km^2 and is situated between 6.50-7.50°N latitude and 39.50-41.00°E longitude. Within the basin, the altitude variation ranges around 4389 m (a.m.s.l) at the highest point to 898 m at the confluence point. The mean annual maximum and minimum temperature (Figure 1b) in the study area are 22.30°C and 7.60°C respectively (1981-2007). The mean annual precipitation ranges from 749.34 to 1368.90 mm (with mean of 1037.40mm). The study area experiences bimodal rainfall pattern of double peaking on the month of April and August (Figure 1c).

The entire basin (4215.93 km^2) is subdivided into six sub-basins (Figure 1a). The sub-basin 3 (SB3) has larger area (1160.60 km^2) with 7 HRUs whereas sub-basin 6 (SB6) has the smaller area (284.27 km^2) with 17 HRUs. The drainage area (km^2) with HRUs (numbers) of SB1, 2, 4, and 5 are 942.35 with 10, 689.11 with 13, 742.44 with 17, and 397.12 with 13 respectively. The total number of HRUs in the entire basin the then becomes 77. The mean annual BWF in the entire Weyib River basin is 2333.39 million cubic meters (Mm^3) for the record period

of 1981-2004. The mean annual BWF of SB1, 2, 3, 4, 5, and 6 are 309 .05, 240.96, 1041.87, 364.98, 162.42, and 214.14 Mm^3 respectively for the period mentioned above (Abdulkerim Bedewi and Sarma, 2017c).

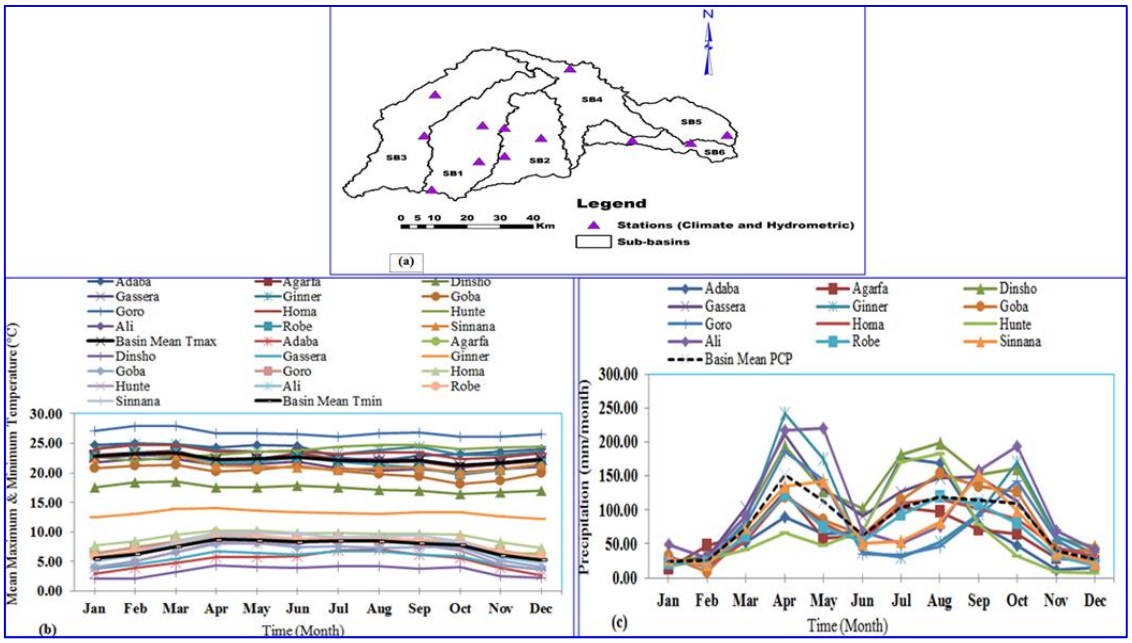

Figure 1: a) Weyib River basin ArcSWAT demonstration (climate and hydrometric stations), b) Spatial variations of mean monthly maximum and minimum temperature characteristics within the study area for the period 1981-2005, c (bottom right): same as fig 1b but for precipitation

2.2. Earth System Models (ESMs) and RCP Scenarios

Simulations by three ESMs (GFDL-ESM2M, CanESM2, and GFDL-ESM2G) under RCP8.5, RCP4.5, and RCP2.6 scenarios were used in this study. These models are adopted due to the facts that they are widely applied in various climate change impact studies and can offer huge amount of simulations and predictions which can be directly input into Statistical Downscaling Model (SDSM). Based on latitude and longitude ranges of the Weyb river basin, related historical simulations and future predictions by three ESMs were downloaded through Canadian Centre for Climate Modeling and Analysis (http://ccds-dscc.ec.gc.ca/?page=pred-canesm2) and NOAA-GFDL CMIP5 official data portal (https://pcmdi.llnl.gov/search/cmip5/). The downloaded predictor variables are then arranged as per the SDSM data file format to downscale local climate variables. Therefore, in this study, a multiple regression based statistical downscaling technique using SDSM has been employed to downscale Ensembles of daily temperatures (maximum and minimum) and rainfall data for the future RCP scenarios.

The ability of SDSM to replicate (simulate) local climate variables (maximum and minimum temperature and rainfall) for historical time period (1981-2005) is evaluated and has very good performance, For maximum temperature data, R^2, RMSE, and NSE values are 0.95, 0.44, and 0.82 respectively for calibration period (1981 to 1993) while 0.94, 0.46, and 0.79 respectively for validation period (1994 to 2005). For minimum temperature data, R^2, RMSE, and NSE values are 0.93, 0.58, and 0.88 respectively for calibration period whereas 0.92, 0.58, and 0.86 for validation period. For precipitation data, R^2, RMSE, and NSE values are 0.86, 0.79, and 0.78 respectively for calibration period whereas 0.83, 0.98, and 0.84 respectively for validation period (Abdulkerim Bedewi and Sarma, 2018).

2.3. The ArcSWAT Hydrologic Model

Among numerous hydrological models available, SWAT is currently applied worldwide and considered as a versatile model that can be used to integrate multiple environmental processes, which support more effective river

basin management and development (Gassman et al. 2005). Considering the aim we are going to achieve, ArcSWAT model was used to simulate fresh water availability within the Weyib River basin. Surface runoff is estimated by a modified Soil Conservation Service (SCS) curve number equation (USDA, 1972) using daily precipitation data based on soil hydrologic group, land use/land cover characteristics and antecedent soil moisture. The potential evapotranspiration of the study area was estimated using Penman-Monteith method (Monteith, 1965). Actual evapotranspiration (AET), the green water flow was predicted based on the methodology developed by Ritchie (1972).

Data used for ArcSWAT hydrologic model includes: **(i)** daily weather data (rainfall, temperatures (maximum and minimum), wind speed, solar radiation and relative humidity), **(ii)** spatial data (DEM, soil map, and LULC map), and **(iii)** streamflow data. The daily weather data for 12 various climate stations which are found inside the basin (spatial distribution of climate stations, temperatures and rainfall characteristics of study area during base period is presented in Fig. 1a, 1b, and c respectively) has been collected from National Meteorological Agency (NMA) of Ethiopia. A 30 m resolution DEM obtained from ASTER official website was used in this study. A soil map as well as major soil physicochemical properties, and LULC map used in this study were found from Ministry of Water, Irrigation, and Electricity (MoWIE). The daily streamflow data of the basin at the outlet point (Alemkerem gaging station) for the years 1981-2004 used in this study was found from MoWIE department of hydrology. The standard procedure of ArcGIS interface ArcSWAT hydrologic model was applied to simulate current and future blue and green water resources availability within the basin.

2.4. Analysis of Future Climate Change Impacts on Blue and Green Water Resources Availability

The three coupled model inter-comparison project 5 (CMIP5-ESMs) outputs, which were downscaled to the Weyib River catchment level for various climate stations using SDSM, were used to generate future blue and green water resources availability in the basin. The ArcSWAT model first ran for historic period (1981-2004) for entire basin then calibrated through an autocalibration tool which embedded in ArcSWAT model using ParaSol (Parameter Solutions) optimization techniqueand for the period 01 January 1984 to 31 December 1994 and then validated for the period 01 January 1995 to 31 December 2004 accordingly on daily-basis. The calibration and validation analysis of BWF (blue water flow) gave satisfactory results with R^2, NSE, RSR, and Pbias values of 0.86, 0.83, 0.25, and 1.72 respectively for calibration period and with R^2, NSE, RSR, and Pbias values of 0.84, 81, 0.31, and 2.69 respectively for validation period (Abdulkerim Bedewi and Sarma, 2017c).

After successful validation, the model has then been re-run on the basins using Ensembles of three ESMs climate data under RCP8.5, RCP4.5, and RCP2.6 scenarios without changing other parameters. The analysis for climate change scenarios have then been divided into three time slices of thirty years which are near term (2011-2040 and represented by 2020s), medium term (2041-2070 and represented by 2050s), and long term (2071-2100 and represented by 2080s). The outputs of future downscaled climate variables for three RCP scenarios have been analyzed first at the entire basin level to quantify their possible impacts on BWF, GWF, and GWS. Successively, detailed analyses have been performed on the basin to quantify the impacts at the sub-basin level. The analysis of future temperatures, rainfall, BWF, GWF, and GWS were carried out on an annual basis.

3. RESULTS AND DISCUSSION

In this section, the annual changes related to climate scenarios are first described, followed by the simulation results of blue and green water resources in response to climate change in the entire river basin as well as sub-basins level.

3.1. Mean Annual Change in Temperature and Precipitation

Based on predictions by three ESMs, the mean annual temperature and precipitation would rises under all the RCP scenarios in the near term (2020s), medium term (2050s), and long term (2080s) compared to baseline scenario (1981-2005) (Figure 2a and b).

Simulations of GFDL-ESM2M model predict greater increment in mean annual temperature ranging from 0.31°C in 2020s to 0.78°C in 2080s under RCP8.5, 0.29°C in 2020s to 0.49°C in 2080s under RCP4.5, and 0.30°C in 2020s to 0.38°C in 2050s under RCP2.6; Simulations of GFDL-ESM2G model predict less increment in mean annual temperature ranging from 0.15°C in 2020s to 0.58°C in 2080s under RCP8.5, 0.13°C in 2020s to 0.29°C in 2080s under RCP4.5, and 0.15°C in 2020s to 0.18°C in 2050s under RCP2.6; Simulations of CanESM2 model predict moderate increment in mean annual temperature ranging from 0.23°C in 2020s to 0.68°C in 2080s under RCP8.5, 0.21°C in 2020s to 0.39°C in 2080s under RCP4.5, and 0.23°C in 2020s to 0.28°C in 2050s under RCP2.6 (Figure 2a).

Simulations of GFDL-ESM2M model predict more increment in mean annual precipitation ranging from 19.70% in 2020s to 33.69% in 2080s under RCP8.5, 14.54% in 2020s to 21.94% in 2080s under RCP4.5, and 13.68% in 2020s to 17.93% in 2050s under RCP2.6; Simulations of GFDL-ESM2G model predict less increment ranging from 12.70% in 2050s to 26.96% in 2080s under RCP8.5, 7.54% in 2020s to 14.94% in 2080s under RCP4.5, and 6.68% in 2020s to 10.93% in 2050s under RCP2.6; Simulations of CanESM2 model predict moderate increment ranging from 14.70% in 2020s to 28.69% in 2080s under RCP8.5, 9.54% in 2020s to 16.69% in 2080s under RCP4.5, and 8.68% in 2020s to 12.93% in 2050s under RCP2.6 (Fig. 2b). The variability of temperature and precipitation is higher for three ESMs in the RCP8.5 than RCP4.5 and RCP2.6 scenarios and the future trend in the RCP8.5 and RCP4.5 scenarios have indicated that significant increasing trend for both mean annual temperature and precipitation until the end of the century (Figure 2c and d).

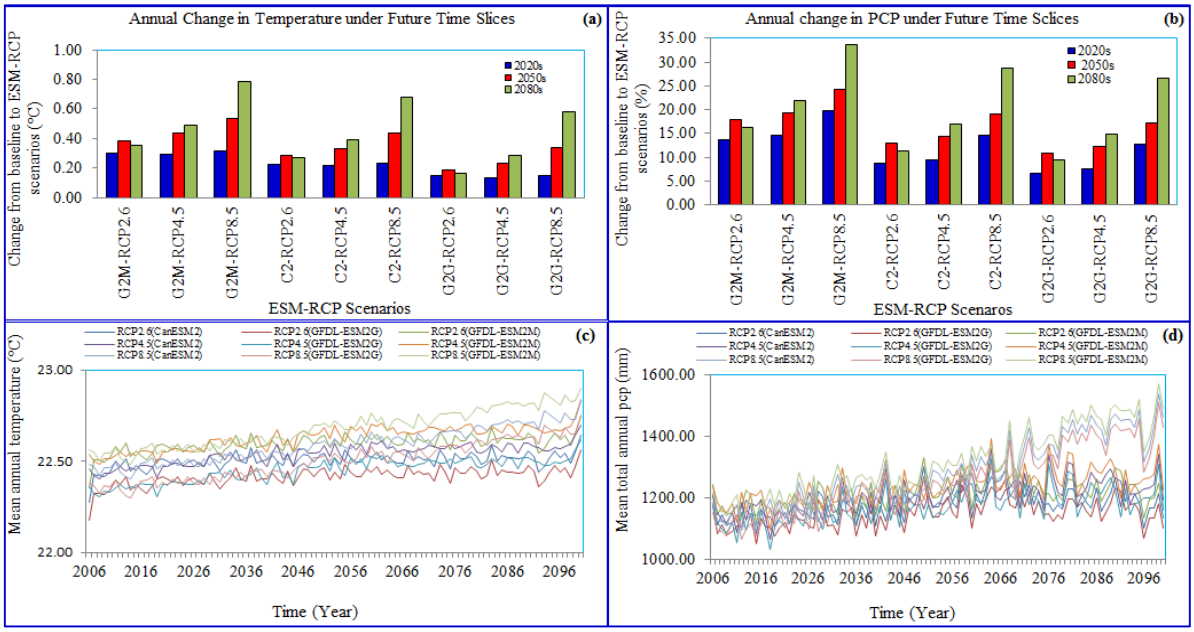

Figure 2: Mean annual changes (a and b) and future trend in temperature (c) and precipitation (d) under three RCP scenarios simulated by three ESMs

3.2. Climate Change Impacts Analysis on Blue and Green Water Resources Availability (Entire Basin and Sub-Basin Level)

In this section, current and under changing climate, blue and green water resources availability namely; blue water flow (BWF), green water flow (GWF), and green water storage (GWS) were performed for entire basin (EB) and sub-basin (SB) level.

3.2.1. Annual current blue and green water resources availability at the basin and sub-basin level

In this sub-heading, the annual BWF (water yield plus deep aquifer recharge), **GWF** (actual evapotranspiration), and GWS (soil water) were estimated for EB and each SBs for baseline period (1981-2004).

The three years (1981-1983) has left as a warming up (model stabilization) period. Results revealed in Fig. 3a-c that EB and SBs level analysis of blue and green water resources availability are found to be different in Weyib River basin. This is, probably, due to the basin characteristics that govern the hydrological regime of the EB and SBs. Therefore, we can pledge that there has been observed a significant spatiotemporal variation of blue and green water resources availability in Weyib River basin during baseline simulation.

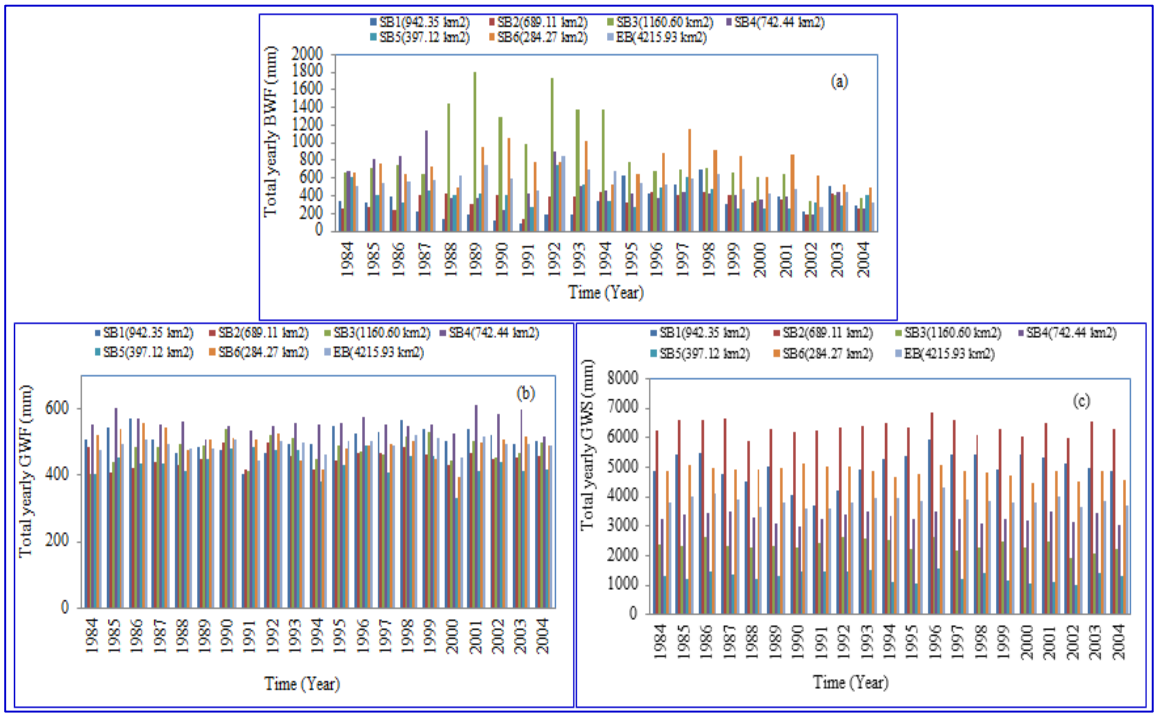

Figure 3: a) Spatial and temporal variation of total yearly blue water flow (BWF) during baseline (1984-2004) simulation, b) same as figure a) but for green water flow (GWF), c) same as figure a) but for green water storage (GWS)

The total annual BWF in Fig. 3a is found to be high in SB4 during baseline simulation (1984-1987) as relative to EB and other SBs. SB3 (1160.60 km^2) has shown relatively more BWF than others SBs Between years 1988-1995. In the remaining time series of baseline simulation (1996-2004), the SB6 (284.27 km^2) revealed more BWF than EB and other SBs. The total annual GWF was observed to be more in SB4 (having an area of 742.44km^2) than EB and other SBs throughout simulation period of 1984-2004 (Fig. 3b). As we can see Fig. 3c, the total annual GWS was found to be more in SB2 (689.11 km^2) than the EB and other SBs throughout simulation periods (1984-2004). As relative to all other components of freshwater availability magnitudes of GWS for EB as well as for each SB are very high and this might be due to soil characteristics in the particular SBs. The BWF, GWF, and GWS in the Weyib river basin were generally high in upstream sub-basins and low in downstream sub-basins.

3.2.2. Mean annual blue and green water resources availability at the basin and sub-basin level under changing climate

As described in Figure 4a-g) that mean annual change in BWF, GWF, and GWS shows an increase with greater spatial variability for all the RCP scenarios in the EB and in all the six SBs. For simplicity and avoiding repetition reasons, results for each ESM are not included, but detailed as a mean of the three ESMs with corresponding RCPs.

In the EB analysis, shown in Figure 4a), the mean annual BWF, GWF, and GWS shows an increases by 27.97, 29.26, and 13.87% respectively (RCP8.5); 19.61, 28.78, and 13.62% respectively (RCP4.5); and 17.06, 28.15,

and 13.60% respectively (RCP2.6). In the SB1 analysis**,** the mean annual BWF, GWF, and GWS reveals an increase by 48.17, 25.17, and 21.24% respectively (RCP8.5); 31.07, 22.98, and 19.70% respectively (RCP4.5); and 25.25, 22.13, and 19.59% respectively (RCP2.6) (Fig. 4b). In the SB2 analysis, the mean annual BWF, GWF, and GWS shows a rise by 29.67, 28.41, and 8.37% respectively (RCP8.5); 22.53, 28.19, and 8.31% respectively (RCP4.5); and 20.87, 26.71, and 8.20% respectively (RCP2.6) (Fig. 4c). In the SB3 analysis, the mean annual BWF, GWF, and GWS reveals a rise by 5.32, 31.13, and 14.99% respectively (RCP8.5); 4.32, 27.14, and 15.19% respectively (RCP4.5); and 3.72, 25.98, and 14.97% respectively (RCP2.6) (Figure 4d)).

In the SB4 analysis, the mean annual BWF, GWF, and GWS shows an increase by 69.81, 22.97, and 8.51% respectively (RCP8.5); 52.73, 27.49, and 9.83% respectively (RCP4.5); and 46.43, 27.88, and 10.12% respectively (RCP2.6) (Fig. 4e). In the SB5 analysis, the mean annual BWF, GWF, and GWS reveals an increase by 28.12, 54.79, and 28.12% respectively (RCP8.5); 26.73, 56.59, and 28.13% respectively (RCP4.5); and 26.19, 56.26, and 28.75% respectively (RCP2.6) (Fig. 4f). In the SB6 analysis, the mean annual BWF, GWF, and GWS observes a rise by 53.92, 25.73, and 8.21% respectively (RCP8.5); 26.73, 25.71, and 8.07% respectively (RCP4.5); and 22.79, 26.63, and 8.17% respectively (RCP2.6) (Figure 4g)).

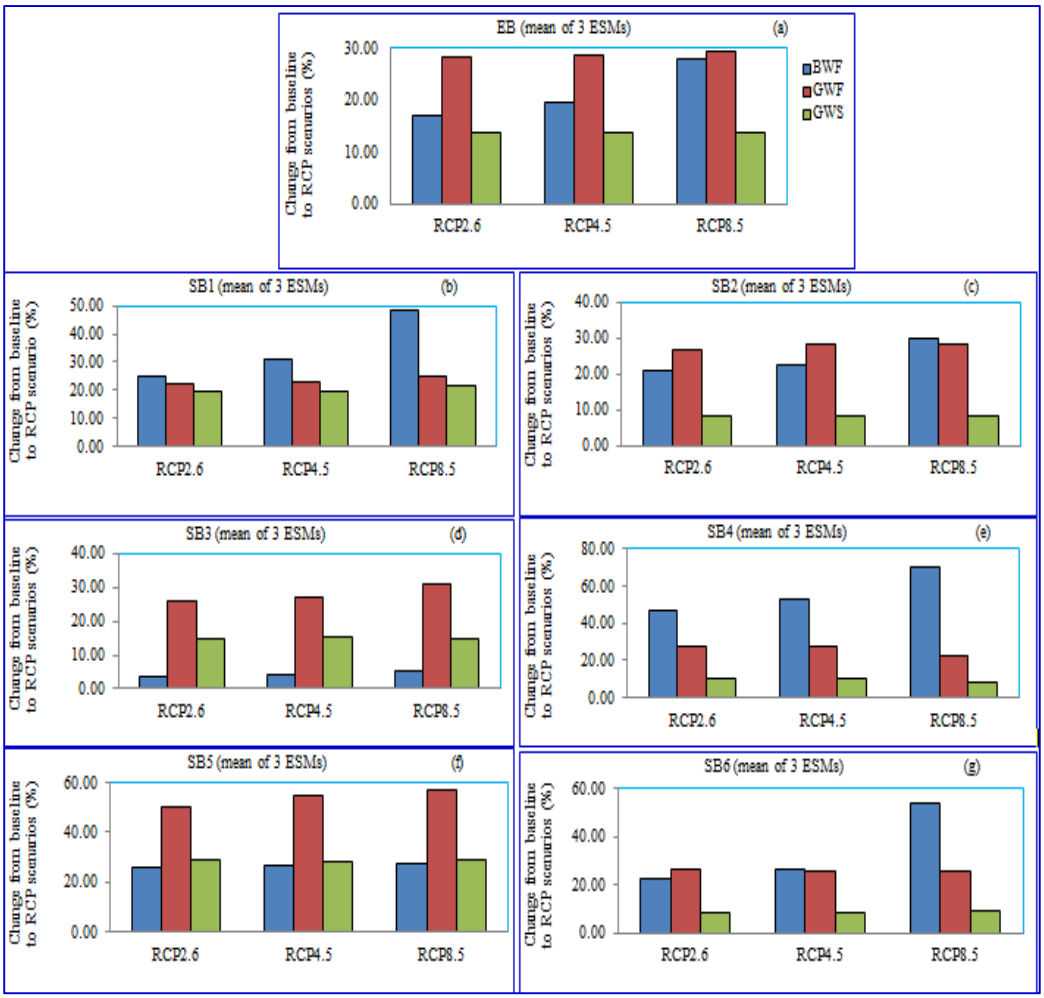

Figure 4: Mean annual percentage changes in BWF, GWF, and GWS (mean of 3 ESMs) under RCP2.6, RCP4.5, and RCP8.5 scenarios in the EB and SBs. Legend given in (a) is the same as in all figures

An increment of temperature was observed in Ethiopia (Asfaw et al., 2018; Shawul et al., 2016; Legesse et al., 2013; ENMA, 2007), and the temperature is predicted to further rise in Ethiopia and the rest of Africa (Alexandrov and Genev, 2003; Boko et al., 2008; Dinar, 2006; Loukas et al., 2015; IPCC, 2013; Kruger and

Shongwe, 2004; New et al., 2006; Unganai, 1996). Significant spatiotemporal variations of precipitation was observed throughout Africa (Shongwe et al., 2009; Faramarzi et al., 2013), which is also the case in this study. The mean annual temperature and precipitation of this study comes to an agreement with all the literature given above regarding direction (pattern), but slight variation in terms of magnitude (amount). This slight variation might arise due to types of ESMs, RCP scenarios, and method of downscaling used.

The model results compared with other studies for BWF only, as to the best of my knowledge, the GWF and GWS were not explicitly quantified most hydrological studies numerically. The mean annual BWF in the EB shows an increase (Farjad et al., 2016; Faramarzi et al., 3013; Aich et al., 2014), in agreement with this study too. The mean annual BWF, in this study, reveals a rise by 27.97% (RCP8.5), 19.61% (RCP4.5) and 17.68% (RCP2.6). These results are not consistent with the various studies regarding magnitude (amount). This dissimilarity arise might be due to different in GCMs, SRES, methods of downscaling and also hydrological modeling used in their studies. The annual variations of freshwater resources availability in general and BWF in particular for all the six SBs are similar in terms of direction but different in magnitude to the EB analysis, and is discussed in this study and taken to be an advantage over the other studies which focused only EB analysis.

4. CONCLUSIONS AND RECOMMENDATION

This study aims to model the blue and green water resources availability under changing climate within Weyib River basin in Ethiopia at both basin and sub-basin level using ArcSWAT hydrologic model. The climate change impacts on temperature and precipitation characteristics within the basin have been studied using GFDL-ESM2M, CanESM2, and GFDL-ESM2G models for RCP8.5, RCP4.5, and RCP2.6 scenarios from coupled model inter-comparison project 5 (CMIP5) which have been downscaled by SDSM. Results indicated that not only warming is predicted to occur in the whole Weyb river basin, but also the variabilities of precipitation, maximum temperature, and minimum temperature are significant and they are predicted to be higher under RCP8.5 scenario than those under RCP4.5 or RCP2.6 scenario in simulations of all three ESMs. Recent land-use pattern changes and extensive agricultural practices appear to have a bearing on the observed warming trend. Increase in average annual precipitation is also predicted in the study area and this might be possibly due to changes in local circulation and high-level moisture transport from the Indian Ocean and the Atlantic.

Various freshwater resources components have been computed and which highlighted an enormous spatiotemporal variation in the entire river basin and sub-basin level. The sub-basin level analysis of surface and groundwater interactions could explore the long term simulation of spatiotemporal variability of blue and green water resources availability in the Weyib River basin. The annual variations of the BWF, GWF, and GWS for each RCP scenarios might be resulted from changing climate and other hydrogeological characteristics in the Weyib River Basin. Since the variation of BWF among the six sub-basins in upcoming period is high, there is a scope of meeting agriculture water demand through water transfer from sub-basin having more available water in small area to the sub-basin having less available water in a larger agricultural area.

ACKNOWLEDGEMENTS

I am grateful to the National Meteorological Agency of Ethiopia for providing me meteorological data and MWIE for providing me hydrological and spatial data for this study.

REFERENCES

Abdo KS, Fiseha BM, Rientjes THM. (2009): Assessment of climate change impacts on the hydrology of Gilgel Abay catchment in Lake Tana basin, Ethiopia. *Hydrol Process* 23:3661–3669. doi: 10.1002/hyp.7363

Abdulkerim Bedewi and Sarma AK. (2018): Statistical downscaling of daily temperatures and precipitation data from coupled model inter-comparison project 5 (CMIP5)-RCPs experiment: In Weyb River Basin, Southeastern Ethiopia, V.P. Singh, S. Yadav, R.N. Yadava (Eds.), *Climate Change Impacts, in water science and technology library series*, Chapter 5, Vol. 82, 274 pp**,** DOI: 10.1007/978-981-10-5714-4_5, ISBN: 978-981-10-5713-7

Abdulkerim Bedewi and Sarma AK. (2017c): Climate change impact analysis on hydrological processes in the Weyb river basin in Ethiopia. *Theoretical and Applied Climatology*, 133(x-y): 1-9, DOI 10.1007/s00704-017-2348-6

Aich, V., Liersch, S., Vetter, T., Huang, S., Tecklenburg, J., Hoffmann, P.,Hattermann, F. F. (2014): Comparing impacts of climate change on streamflow in four large African river basins. *Hydrology and Earth System Sciences*, *18*(4), 1305–1321. https://doi.org/10.5194/hess-18-1305-2014

Alexandrov, V. and Genev, M. (2003): Climate Variability and Change Impact on Water Resources in Bulgaria. *European Water*, *12*, 25–30.

Asfaw, A., Simane, B., Hassen, A., Bantider, A. (2018): Variability and time series trend analysis of rainfall and temperature in northcentral Ethiopia: A case study in Woleka sub-basin. *Weather and Climate Extremes*, *19*(June 2017), 20–28. https://doi.org/10.1016/j.wace.2017.12.002

Boko, M., Niang, I., Nyong, A., Vogel, C., Githeko, A., Medany, M.,Yanda, P. (2008): Africa. *Climate Change 2007: Impacts, Adaptation and Vulnerability. Contribution of Working Group II to the Fourth Assessment Report of the Intergovernmental Panel on Climate Change*, 433–467. https://doi.org/10.2134/jeq2008.0015br

Brekke, L. D., Dettinger, M. D., Maurer, E. P., Anderson, M. (2008): Significance of model credibility in estimating climate projection distributions for regional hydroclimatological risk assessments. *Climatic Change*, *89*(3-4), 371–394. https://doi.org/10.1007/s10584-007-9388-3

Conway, D. (2000): The Climate and Hydrology of the Upper Blue Nile River Linked references are available on JSTOR for this article : The Climate and Hydrology of the Upper Blue Nile River, *166*(1), 49–62.

Conway, D. and Hulme, M. (1993): Recent fluctuations in precipitation and runoff over the Nile sub-basins and their impact on main Nile discharge. *Climatic Change*, *25*(2), 127–151. https://doi.org/10.1007/BF01661202

Diekkrüger, B., Kapangaziwiri, E., Badou, D. F., Mbaye, M. L., Yira, Y., Lawin, E. A., Afouda, A. (2018): Modelling blue and green water availability under climate change in the Beninese Basin of the Niger River Basin , West Africa, (April), 2526–2542. https://doi.org/10.1002/hyp.13153

Dinar, A. (2006): District Level Hydro-climatic Time Series and Scenario Analysis to Assess the Impacts of Climate Change on Regional Water Resources and Agriculture in Africa. Discussion Paper No. 13. Special Series on Climate Change and Agriculture in Africa, 60 pp. ISBN 1-920160-01-09.

Ethiopian National Meteorological Agency (2007): Climate Change National Adaptation Programme of Action (Napa) of Ethiopia. 1–73pp.

Faramarzi, M., Abbaspour, K. C., Ashraf Vaghefi, S., Farzaneh, M. R., Zehnder, A. J. B., Srinivasan, R., Yang, H. (2013): Modeling impacts of climate change on freshwater availability in Africa. *Journal of Hydrology*, *480*, 85–101. https://doi.org/10.1016/j.jhydrol.2012.12.016

Farjad, B., Gupta, A., Marceau, D. J. (2016): Annual and Seasonal Variations of Hydrological Processes Under Climate Change Scenarios in Two Sub-Catchments of a Complex Watershed. *Water Resources Management*, *30*(8), 2851–2865. https://doi.org/10.1007/s11269-016-1329-3

Frey-Buness F, Heimann D, Sausen R. (1995): A statistical-dynamical downscaling procedure for global climate simulations. *Theor Appl Climatol* 50(3–4):117–131

Gassman WP, Reyes MR, Green CH and Arnold JG. (2005): SWAT peer-reviewed literature: A review, Proceedings of the 3rd International SWAT conference, Zurich

Goyal MK, Ojha CSP, Burn DH. (2011): Nonparametric statistical downscaling of temperature, precipitation, and evaporation in a semiarid region in India. J Hydrol Eng 17(5):615–627

IPCC. (2013). Climate Change 2013: The Physical Science Basis. Contribution of Working Group I to the Fifth Assessment Report of the Intergovernmental Panel on Climate Change. *Intergovernmental Panel on Climate Change, Working Group I Contribution to the IPCC Fifth Assessment Report (AR5)(Cambridge Univ Press, New York)*, 1535. https://doi.org/10.1029/2000JD000115

Kebede, S., Travi, Y., Alemayehu, T., Marc, V. (2006): Water balance of Lake Tana and its sensitivity to fluctuations in rainfall, Blue Nile basin, Ethiopia. *Journal of Hydrology*, *316*(1-4), 233–247. https://doi.org/10.1016/j.jhydrol.2005.05.011

Kruger, A. C. and Shongwe, S. (2004): Temperature trends in South Africa: 1960-2003. *International Journal of Climatology*, *24*(15), 1929–1945. https://doi.org/10.1002/joc.1096

Legesse SA, Rao PVVP, Rao MMN. (n.d.): Statistical Downscaling of Daily Temperature and Rainfall Data From Global Circulation Models : in South Wollo Zone , North Central Ethiopia. 27–39.

Loukas, A., Sidiropoulos, P., Mylopoulos, N., Vasiliades, L., Zagoriti, K. (2015): Assessment of the effect of climate variability and change and human intervention in the lake Karla aquifer, 19–31.

Maurer, E. P., Brekke, L., Pruitt, T., Duffy, P. B. (2007): Fine-resolution climate projections enhance regional climate change impact studies. *Eos, Transactions American Geophysical Union*, *88*(47), 504–504. https://doi.org/10.1029/2007EO470006

Mondal A. and Mujumdar PP. (2012): On the basin-scale detection and attribution of human-induced climate change in monsoon precipitation and stream flow. *Water Resour Res* 48(10)

Monteith JL. (1965): Evaporation and the environment. In The State and Movement of Water in living Organisms, XIXth Symposium. Soc. For Exp. Biol., Swansea, Cam-bridge University Press. pp. 205-234

Mpelasoka, F. S., Chiew, F. H. S. (2009): Influence of Rainfall Scenario Construction Methods on Runoff Projections. *Journal of Hydrometeorology*, *10*(5), 1168–1183. https://doi.org/10.1175/2009JHM1045.1

New, M., Hewitson, B., Stephenson, D. B., Tsiga, A., Kruger, A., Manhique, A.,Lajoie, R. (2006): Evidence of trends in daily climate extremes over southern and west Africa. *Journal of Geophysical Research Atmospheres*, *111*(14), 1–11. https://doi.org/10.1029/2005JD006289

Pierce, D. W., Barnett, T. P., Santer, B. D., Gleckler, P. J. (2009): Selecting global climate models for regional climate change studies. *Proceedings of the National Academy of Sciences*, *106*(21), 8441–8446. https://doi.org/10.1073/pnas.0900094106

Reichler, T. and Kim, J. (2008): How well do coupled models simulate today's climate? *Bulletin of the American Meteorological Society*, *89*(3), 303–311. https://doi.org/10.1175/BAMS-89-3-303

Ritchie JT. (1972): A model for predicting evaporation from a row crop with incomplete cover. *Water Resources Research* **8**: 1204–1213

Samadi S, Wilson CA, Moradkhani H. (2013): Uncertainty analysis of statistical downscaling models using Hadley Centre Coupled Model. *Theor Appl Climatol* 114(3–4):673–690

Setegn, S. G., Rayner, D., Melesse, A. M., Dargahi, B., Srinivasan, R. (2011): Impact of climate change on the hydroclimatology of Lake Tana Basin, Ethiopia. *Water Resources Research*, *47*(4), 1–13. https://doi.org/10.1029/2010WR009248

Shawul AA, Alamirew, T., Melesse, A.M. and Chakma, S. (2016): Climate change impact on the hydrology of Weyb river watershed, bale mountainous area, Ethiopia. In Landscape dynamics, soils and hydrological processes in varied climates (pp. 587-613). Springer international publishing

Shawul, A. A., Alamirew, T., Dinka, M. O. (2013): Calibration and validation of SWAT model and estimation of water balance components of Shaya mountainous watershed, Southeastern Ethiopia. *Hydrology and Earth System Sciences Discussions*, *10*(11), 13955–13978. https://doi.org/10.5194/hessd-10-13955-2013

Shongwe, M. E., Van Oldenborgh, G. J., Van Den Hurk, B. J. J. M., De Boer, B., Coelho, C. A. S., Van Aalst, M. K. (2009): Projected changes in mean and extreme precipitation in Africa under global warming. Part I: Southern Africa. *Journal of Climate*, *22*(13), 3819–3837. https://doi.org/10.1175/2009JCLI2317.1

Unganai, L. S. (1996): Historic and future climatic change in Zimbabwe. *Climate Research*, *6*(2), 137–145. https://doi.org/10.3354/cr006137

USDA-SCS (United States Department of Agriculture-Soil Conservation Service) (1972): National Engineering Handbook Section 4 Hydrology, Chapters 4-10.

Xu, Z. and Zuo, D. (2014): Simulation of blue and green water resources in the Wei River basin, China. *Proceedings of the International Association of Hydrological Sciences*, *364*(June), 486–491. https://doi.org/10.5194/piahs-364-486-2014

Is Science Value Free? Democratization of Technology towards Ethiopian Culture

Eyasu Berento Assefa

Department of Philosophy, Mekelle University, Ethiopia, e-mail: shambelber@gmail.com

ABSTRACT

We are in the age of technology where every human society is forced to think through the fabrics of modern science and technology. But, is science objective and value free? Is technology in Ethiopia a logical transformation from the "pre-techne" to modern world, a kind of internal evolution within cultures, accepted by all culture groups as an inevitable process? How could "foreign technologies" go in line with indigenous peoples' stored traditional wisdom? These are some of the central questions that are addressed in this article. The objective of the study is to call for the culture conscious adoption of technology and democratization of technology towards Ethiopian Indigenous Knowledge Systems (IKSs). The article is a philosophical reflection on the contradictions of harmonizing modern technology with the different culture traits in Ethiopian context. Qualitative research method is employed from the critical social theory perspective. Critical social theory is the 20th C movement by the "Frankfurt School" scholars that tries to incorporate philosophy with other social sciences to deal with the irrationalities and contradictions that suppress human freedom. The article tries to unhide the undemocratic side of technology that shackle the development of IKSs which in turn jeopardizes genuine human development in Ethiopia. In line with Santos (2014) and Harding (1976), it is argued that the technology of the west appears to be value laden in suppressing the epistemologies of the south; and such value laden-ness of technology, Marcuse (1964) argues, results in suppressing human freedom and genuine human development. The mass transfer of technology through education, policy implementation, and mass media appear to be an imposition and suppression to the long held folk wisdoms of the indigenous people in Ethiopia, who hardly understand the language of technology. This in turn results in creating communication gaps between the generations (educated and illiterate) in such a way that highly affects the social fabric of the people. As a recommendation, technology transfer must be backed up by the culture sensitive mentality of the educated as a representation from the people; for true wisdom is actualized by the genuine hermeneutic enterprises between the modern science and IKSs.

Keywords: *Culture, Democratization of Technology, Folk Wisdom, Science and Technology, Value Laden-ness and Ethics of Technology*

1. INTRODUCTION

In their contemporary connotation and denotations, science and technology are the two sides of the same coin. Narrowly defined technology assists science as the byproduct of scientific process and science produces more advanced technology to facilitate its workings. Throughout human history science appears to be in a continuous progress while human culture, studies in humanities and philosophy are conceived by many to be in stagnation the view that Will Durant criticized (1961). But one thing is obvious that science appeared as imperial in human life by considering itself as the only owner of objective truth with its gross impacts in the progress of material aspect of life. (Glock, 2008; Hacker, 2007)

The recent development in the natural sciences backed up by the thesis of the "unity of the sciences" which argues that the study in every aspect of human life, including the humanities, behavior, culture and history, social organization and the like are reducible to the methods of the natural sciences and the laws that determine scientific studies. (Hacker, 2007) While such thesis faced different challenges and responses, it is effective at least in the establishment of 20th century movements like logical positivism and analytic philosophy. (Glock, 2008)

This appeal to the natural sciences and conception of the IKSs as "irrational and superstitious assertions" of culture, religion and ethics resulted in the calamities of the humanities studies and social fabrics that determine the traditional relationships of humans as social beings. (Albert Schweitzer, 1961) The crisis in the European culture, Schweitzer argues, is attributable to the devotion we give to the science and technology and our betrayal from culture, "a universal will to progress which recognizes the ethical as the highest value."(P. 1). The suppression of culture and adherent to the will to life and world affirmation resulted in tragedy.

> Nevertheless, the course of modern European man thought reveals a tragedy. By a slow but irresistible process, the union of the ethical and the world-affirmation and the life-affirmation has been dissolving and threatens to disappear

> completely. Consequently, European humanity is infused and impelled by a will to progress which is superficial and improperly oriented. (P. 5)

Such unlimited power of science reached into its peak in the renaissance when Bacon declared that the myth must be replaced with knowledge and human mind should better understand nature so as to employ it for human ends. Such appeals to reason and scientific rigor manifested in the absolute control of nature by man, a "happy match" between human understanding and the nature of things; where knowledge is assumed to be the most powerful thing no wealth or political power can influence. (Adorno and Horkheimer, 2002) An absolute dependent on technology by man resulted in the uniformity of thought and the way of life by all where there are no rooms for the choice of one's life forms. Such suppression of human freedom produces "one dimensional society". (Marcuse, 1964)

When it comes to the third world, the story appears in the tragic forms of colonialism and neocolonialism (mental colonization). This is due to the gross introduction of scientific precepts and technology with a two sided sword. On the one hand, the imperialist nature of science and technology ruled out traditional wisdom (IKSs) as useless and irrational which are incompatible with modern form of life. (Wiredu, I976) On the other hand, the ideologically value laden orientations of the developed countries determine the strategies and practices of human development plans by politically and financially powerful governmental and non-governmental organizations. (Hanckok, 1989)

Not surprisingly, such ideologically value laden orientations founded their footings in the schools (universities) of the third world. (Smith, 2005; Charless Verharen, 2013; Bekele Gutema, 2005). The imperialism of the epistemologies of the North commits "*epistemicide* [to the epistemologies of the South], the murder of knowledge. Unequal exchanges among cultures have always implied the death of the knowledge of the subordinated culture, hence the death of the social groups that possessed it." (Santos, 2014, p. [135]) In his book titled *The End of the Cognitive Empire: the coming of age of epistemologies of the south*, he tries to disclose the invisible hands of western epistemologies against the voices of the epistemologies of the south.

> As a collection of knowledges born of and anchored in the experiences of marginalized peoples who actively resist capitalism, colonialism, and patriarchy, epistemologies of the South represent those forms of knowledge that are generally discredited, erased, and ignored by dominant cultures of the global North. Noting the declining efficacy of established social and political solutions to combat inequality and discrimination, Santos suggests that global justice can only come about through an epistemological shift that guarantees cognitive justice. (https://b-ok.org/book/3599926/e40ea9)

Ethiopia is not exceptional. The nation has long history of intercourse with the external world and is loyal to adhere to the international charters and declarations related to peace and security, democracy, human development, environmental protection and the like. By simple logic, it is bound by the philosophies of contemporary globalization, introducing modern science and technology, adopting the laws that determine trade, investment and education. There is no problem to adopt science and technology that make life easier in solving the most pressing problems relating to health, communication, transportation, industrialization, peace and so on. The problem is in the appropriation of science and technology and its integration with the great wisdoms of our forefathers. It is the conviction of the researcher that modern science and technology with their value laden orientations are manifested in the form of *epistemicides* to the IKSs of Ethiopia.

Statement of the Problem: the statement of the problem this article raised is the miscommunication of Ethiopian culture and modern science and technology and the loophole we find ourselves in the time of modernity.

It is in the name of the scientific methods used in the study of humanities that the studies come up with the most forms of divisive fault lines between cultures; in the name of scientific and rational explanations of the past, history, the most conflicting claims, irreconcilable discourses emerged; adopting modern peacekeeping mechanisms turned out into the most susceptible and exploitative devices of the police force and the military; in

the name of scientific solutions of health problems that the most sophisticated and expensive medications traded off the cultural medicine along with the psycho of the rural society; in the name of mechanized agriculture and investment that the farmers exiled from their lands, the lands at times assumed to be the dwelling places of the ancestral spirit of the indigenous people. The Irrationalities in the name of reason have done injustice against the time tested collective wisdoms of the indigenous people elsewhere. The devices of communication put the knife on the traditional ways of social ties and subject to misuse. (Setargew Kenaw, 2012)

This all is in the name of the advancements in science, technology and adherence to the modern way of life for the sake of compatibility with the global community assisted by the policy and huge amount of budget from the government. The byproduct of such appeal to science and technology are environmental degradations, climate change, food insecurity, maladministration, social injustices and destructions in the social fabrics, religious and cultural views of the society – making us far from ourselves to be nearer to other selves. (wa Thiong'o, 1981)

It is against such contradictions along with the research questions bellow this article attempts to disclose the invisible hands of technology, its value laded nature and the injustices it have done so far to the cultural wisdoms of Ethiopia.

It is argued that the education system, the introduction of technology and implementation of scientific methods to solve our problems fall short of addressing the problems. This is due to different factors. First, due to their imperialism over the time tested IKSs of our forefathers, second due to their hidden socio-cultural, epistemological and political agendas, contradictions between theory and practice. The third reason is attributable to the parrot copying of technology without internalizing its relation with the socio-cultural, religious and political realities of Ethiopia. And finally, there is lack of communication between the generations due to the huge gap the language of technology created. Hence, an immediate response to such and related problems should come from the scholars and policy makers.

The general objective of this article is to call the attention of culture conscious educators and technology transfer that is friendly to the huge IKSs we bequeathed from our forefathers. In other words, it is a call for the democratization of technology towards the Ethiopian culture for the practical success of contemporary wisdom in addressing pressing socio-economic, cultural and political problems.

Research Questions: besides the big question in the title and questions in the abstract of the article, there are many research questions that this article attempts to address.

- Can the introduction of modern science and technology in Ethiopia replace IKSs?
- Is the appropriation of science and technology in Ethiopia friendly to the IKSs?
- How can modern technology be integrated to the long held traditional knowledge of Ethiopians?
- What are the professional duties of Ethiopian scholars and policy makers to incorporate the modern technology with the IKSs for the successful practical and theoretical success of Ethiopia education system in solving the most pressing existential problems in contemporary Ethiopia?
- What kind of philosophical method can be employed for the healthy marriage between the traditional and modern wisdoms in Ethiopia?

These and other numerous questions reveal the contradictions between modern technology and the existence of recurrent problems. This in turn leads us to dig out what is missed in the ways of life we are living and in the appropriation of technology we are using.

2. METHOD AND MATERIAL

Qualitative research method is employed to address the above problem and to meet the intended objective of this article. As a philosophical reflection I follow a critical social theory perspective. Critical social theory is 20th century multidisciplinary movement that aims to address problems related to politics and social contradictions.

> A "critical social theory" is both the process and the outcome of a transformational agenda and brings together multiple beliefs about human understanding and misunderstanding, the nature of change, and the role of critique and education in society. It is an evaluative as well as a political activity that involves assessing how things are in order to transform them into what they ought to be. (Freeman, M., & Vasconcelos, E.F.S., 2010, p. 7)

Brian Harney conceived critical theory as: "Drawing on diverse intellectual traditions, critical theory seeks to expose the domination, control and suppression that hides behind that which at first appears neutral, progressive and necessary." (2017, p. 1) Using critical social theory approach, this article tries to demystify the myth of technology and science and the injustices it is doing to the cultures of Ethiopia.

As the recommendation and the central argument of this article is towards democratization of science and technology to the culture of Ethiopia, intercultural and hermeneutics are used as a methods of reconstruction towards the relationships between science and culture in Ethiopia. The first approach is the view that there must be a communication between cultures (Eguale, 2003); and the second is the view that contextual interpretation of cultures is needed. In line with these approaches this article at the end will argue for the fair interplay and democratic communications, dialogue between the foreign and the Ethiopian culture. And at times when adoption is needed, the translation, appropriation and interpretation must be genuine hermeneutics which is witnessed in the Ethiopic translation of classical literatures of the west. (Levine, 1974; Sumner, 1985)

Therefore, the methodological framework of this article can be conceived in two distinct but related approaches. At the first level, it is a critical reflection (using critical social theory from philosophical perspective) on the injustices and contradictions of science and technology towards Ethiopian culture. At the second level it is an argument towards a healthy introduction of culture and genuine knowledge development by amalgamation Ethiopian culture with foreign science and technology; it is an attempt of indigenizing technology (using intercultural approach and hermeneutics).

The material source basically depends on the literature of the philosophical reflections of science and technology, the scholarly articles on the impact of technology in Ethiopian life in particular and culture in general, oral tradition and written wisdom of Ethiopian folk thought.

The article has three parts. The first part deals with the nature of science and technology. It tries to address the question "is science value free"? The second part deals with Ethiopian culture and exemplary IKSs. The third part is an articulation on democratization of technology towards the IKSs and culture in Ethiopia. It calls for the equal marriage of the cultures through hermeneutics and interculturalism. And conclusion and recommendation is forwarded at the end.

3. IS SCIENCE VALUE FREE?

> *"Science and technology have reached a point where our means are finally catching up with our imaginations, and the only thing preventing us from doing truly visionary works are these moral base restrictions that law makers put up in the name of public policy."*
> *"The advances of science, which is supposed to expand our knowledge of the universe will if not carefully controlled, destroy the world as we know it. I will take the logical ambitions if not only driven us to the point of catastrophe. The catastrophe has already begun."*[1]

The two quotes above can capture the debate on the advancement of science on the one hand and socio-cultural values on the other hand. After precisely defining the natures of science and technology, I will consider the values that are ascribed to it in line with their impact on folk wisdoms of indigenous people. In this case I will see the value laden oppressive power of technology to the universal human culture and human freedom in general and the appearance of science and technology to cultural wisdoms of Ethiopia in the antithesis form that seeks ta otal

[1] These two contradictory views on the advancement of science and technology in line with human culture and morality are taken from "Fringe", a series of scientific movie, Season 1, Episode 6, minutes 25:50' onwards and Season 1, Episode 14, minutes 16: 50 onwards respectively.

replacement of IKSs by modern science. I will show how it detached the contemporary Ethiopian man from the self.

As the very title asks whether science is value free or not, I must be clear of the employment of the term "value" in the paper. When we state of value it is not to mean the worth or instrumental benefit the, "valuableness" inherent to science and technology. It is used to refer to the side effects of science and technology that the owner, designer of science implicitly intends to impose and the anomalies that are natural to the very innovation and employment of science itself. For example, the Nano technology may be designed to serve as a detective instrument which has an adverse effect in the freedom of the targeted subject. This is the very intention of the user of technology that the value the designer ascribed to or installed in the technology which is no desirable by the targeted ones.

The other example, that elaborates value as the side effect of science and technology is the use of contraceptive. The very design/purpose of using the technology of contraceptive is to relieve the pregnant from unwanted burden or from health problems. But this is against cultural and religious claims of the user, and against the laws of nature that shackles the actuality of conception in the form of a human being as well as against the right of the other partner to have baby. The value in this context refers in short the ideologically engendered intentional or unintentional contradiction between the appearance and the reality of technological instrument or scientific, philosophical claims which results in the clash with the world views and rights of the user.

Since technology is not mere passive instrument to be used only in the desired way but also a process that have adverse effects in human life (Nebiyou, 2015, p. 16), some sort of value is entrenched either in its design or in its employment.

It is undeniable fact that science has made an accelerated progress and makes life easy in many ways. The fact that science's appearance as the only right way of solving human problems, attaining truth and objective reality with the methods of rationality, rigor and experimentation made it to appear in the form of scientific imperialism. (Glock, 2008)

When I use the terms "science" and "technology" partly I am using the already established usage of the concepts and at times I may use them interchangeably without overriding the possible distinctions between them. As I have tied to claim above, science is broader concept that comprises the philosophies, theory developments, hypotheses, methods and technology that may serve as the means of scientific activity itself or the final end of the scientific process to serve as means for other ends. But this does not mean that technology is merely physical. Technology too has procedural and methodological constituents in the process of its employment. In this case, some associate technology to connote the applied sciences the view that Mitcham denied. (Mitcham, 1994 cited in Nebiyou, 2015; p. 14)

For my purpose, therefore, science and technology refer to the theoretical and practical innovations that manifest in the form of matter or idea. The instruments that we use in our day to day activities, the claims about the laws of nature, the ideologies that appear in the form of politics, religion, and philosophy are the outcomes of developments in the history of human thought. The very nature of scientific claims is that they appear to be the final appeals of truth and wisdom; the only possible options to solve human problems. (Glock, 2008; Hacker, 2007)

Some argue that science and technology are value neutral. "Science and values only touch; they do not interpenetrate." (Hugh Lacey, 1999, p. 1) According to this argument, science and technology have only instrumental or use value. Others argue that science and technology are subsidized by the financial and political powers of their innovator, designer and owners. (Glock, 2008; Harding, 1997). When the colonial powers come to Africa, they appear with the instruments of missionaries, the hypocritical claims of "programs of development" emancipating Africans from their backwardness and to prepare them to the God's province. At the very heart of such development and evangelical promises is that whatever African is "irrational, barbaric, superstitious and unscientific." On the contrary, what is European is scientific, rational, from heavens, and genuine. (Messay

Kebede, 2004; Wiredu, 1976) The value imposition in the name of development at its first stage turned out into a forceful mechanism of ruling Africa and Europeanizing African life which manifested in "[…] separating the mind from the body. On a larger social scale it is like producing a society of bodiless heads and headless bodies." (Wa Thiongo, 1981, p. 28)

In the global epistemological arena, the value laden orientations of science and technology appeared in the form of epistemicide to the IKSs of the indigenous people in the south. This finally developed into grand narratives that acclaim Europe as the only owner of true wisdom, development and form of life that others should follow as a role model. Setting aside the debates on the origins of human knowledge[2], for the sake of scope, my focus will be on the implications of the Eurocentric epistemological assumptions to the IKSs of Ethiopia.

Nebiyou asks whether technology is value free or value laden. (P. 19) The answer to the question is obviously 'no'. The development of science and technology is partly the outcome of political competition. This by itself suggests something about the value laden-ness of technology. "[…] not only politics influence the development of technology. There is also politics within the technological system – politics is an element of the technological system." (Nebiyou, 2015, p. 27) hence "—no part of modern technology can be judged neutral *a priori*." (Winner, as cited in Nebiyou, ibid. p. 29)

The problem of scientism, the myths of rationality, enlightenment and scientific imperialism resulted in the suppression of human freedom and one directional thought in modern world which many critical social theorists adversely criticized. For example, Horkheimer and Adorno (2002) argue that rationality, enlightenment and scientific explanation of nature that are assumed to free man from traditional myths and irrationalities turned out themselves into modern myths. Tim Dant argues in the same line:

> Myth appears to be displaced by the instrumental reason of post enlightenment thinking that both provides a powerful critique of the factual contents of myths and offers alternative narratives of cause and effect. Now scientific thinking may be very powerful in describing the process of the natural or material world but it has proved less effective in the arena of morality: the ways in which human beings should act and the effects of those actions on the human condition. (2003, p. 19)

Such value laden and mythical imperialisms of science resulted in the suppression of culture and morality in human social fabrics. The suppressions of science manifest in the internal anarchism of human life and an attempt to understand everything using scientific method, that in turn lead to the communication gaps between the generations in the indigenous peoples like Ethiopia. Because it is an attempt to totally replace the traditional with modern. It commits epistemicide to the time tested great ideas of the folk wisdom. The herald that "what is rational is real and what is real is rational" by Hegel have such implications on the value laden judgments of the west on African wisdom. (Scheweitzer, 1961, pp. 5-6)

Before dealing with the healthy marriage between IKSs and science and technology in Ethiopia, let's discuss some of the exemplary wisdoms of Ethiopia.

4. EXEMPLARY IKSS OF ETHIOPIA[3]

[2] In the debates about the roots of philosophy, science and development, some argue that the Greek origins of philosophy is the root of European wisdom. Such Eurocentric claims on the epistemological and scientific ownerships go up to the conclusion by great philosophers that Africans and other developing world communities have not contributed to the overall progress of human history. Others on the contrary argue for the African roots of thought and science.

[3] The discussion in this section is extracted from my previous unpublished works presented at different conferences of Ethiopian universities. Basically it is taken form four articles: "Integrating Indigenous Knowledge (IK) to Environmental Protection, Multiculturalism, and Sustainable Development: A Philosophical Reflection on the Role of Higher Education in Ethiopia" (2017) paper sent to the Arba Minch University; "Can the "Stick and Bullet" Sustain Peace and Justice? (A Philosophical Reflection on the Police Professional Ethics and Culture of Peace in Ethiopia)" (2018) paper presented to the first National Conference on Law Enforcement in Ethiopia by the Ethiopian Police University College; "Humanity, Public Rationality, Social Justice and Mutual Coexistence in Multiethnic Society: Perspectives from Classical Ethiopian Philosophy"

The IKSs discussed here are by no means complete representations of the Ethiopian huge culture traits. It is for the sake of brief summary that I selected few samples for this discussion. Before the discussion of IKSs it is better to articulate what culture is. Culture is the collective wisdom of a given community accumulated for the ages through socialization processes. It is the broader aspect of life that includes different IKSs. The adaptation to socio-political, economic and natural conditions of a given environment and socialization process of a given community evolves into an accumulation of culture.

> Culture is the characteristic and knowledge of a particular group of people, defined by everything from language, religion, cuisine, social habits, music and arts. … [It is a collection of] shared patterns of behaviors and interactions, cognitive constructs and understanding that are learned by socialization. Thus, it can be seen as the growth of a group identity fostered by social patterns unique to the group." (Zimermann, 2015)

Most repeatedly quoted definition of culture is given by Edward B. Tylor (1871) that "culture or civilization taken in its wider ethnographic sense, is that complex whole which includes knowledge, belief, art, morals, law, custom, and any other capabilities and habits acquired by man as a member of society." (Quoted in Yeraswork Admasie, 2004 E.C, p. 3).

The culture of any society bears its IKSs that are relevant to understand nature, to advance the quality of life, to solve most pressing problems of that community, to nurture the behaviors and wisdoms of the youth and look after the week and the elderly. IK refers to the collective wisdom of a given society that is accumulated through the ages in response to man's relation with nature and interaction with other human beings. Knowledge production is a cooperation action (Workineh, et al, 2010, p. 3). IK is an example of knowledge created though cooperation action of the socialization process. I can use Charles Takoyoh Eyong's definition of IKS for my purpose. It goes like this:

> IKS refers to the set of interactions between the economic, ecological, political, and social, environments within a group or groups with a strong identity, drawing existence from local resources through patterned behaviours that are transmitted from generation to generations to cope with change. These patterns are sustained by micro level institutional arrangements vested with differentiated responsibilities that ensure the group's continuous survival. (2007, p. 122).

IK is tailored to the day to day practical activities of the society and by virtue of its shared nature represents the social psyche of the people in understanding nature, solving problems and assisting the healthier processing of shared values of a certain cultural community.

If culture and IK are intertwined and there is strong link between them, then what is Ethiopian culture and unifying Ethiopian IKSs *per se*? Trying to answer this question in a hurry and descriptive terms turns out to be futile and that may be misleading to a hasty conclusion. It is the conviction of the researcher that identifying single unifying Ethiopian culture and identifying a signboard of IKSs is to miss the complexities of culture traits the Ethiopians established with contextual variability that are relevant to solve the pressing problems everywhere in the country and the web like communality they form through their continuous interactions.

Some argue that distinguishing the Ethiopians in ethnic lines is a wrong conception of the nature of Ethiopian unity that resulted in racial mixing, cultural hybridity and communal identity. Part of the culture traits of some groups (e.g., the Oromo's philosophy of integrating new comers as *gudificha, and mogasa,* Afars' social tie with others called *Kataisa, Rayan peoples' intermixing, intra religious marriages*) played positive roles in assisting such intermixing that evolved into strong unity which sustains Ethiopia as a sovereign nation for the millennia.

---

presented in the conference of Justice and Sustainable Development by Hawassa University, (May 2018); and "African Philosophy as an Intellectual Weapon for Continental Peaceful Mutual Coexistence and Global Social Wellbeing" first presented as a key note speech for the international conference hosted by Mekelle University the department of Philosophy and the Jain Society (June 2017) and currently on the process of publication as a book chapter.

Two prominent foreign scholars come into front to strengthen this line of argument. The first is the known sociologist, Donald Levine, who argues that the Ethiopians of diversified community evolved into strong unified multiethnic society through mutual influences. "To see Ethiopia as a mosaic of distinct peoples is to overlook the many features they have in common and the existence of discernable culture areas, and to ignore the numerous relationships these groups have had with one another." (Levine, 1974, p. 21). Levine's argument is stretched to the conclusion that Ethiopians evolved from a proto Ethiopian culture trait.

> The fact is that the peoples of Greater Ethiopia are relatively homogeneous in a number of respects. Some of the culture traits they share may derive from a common aboriginal proto- Ethiopian culture, some may represent adaptive responses to similar situations, and others probably reflect a coalescence of traits from prolonged interaction in the distant past. Whatever their origins, there seems to be a sufficiently large number of pan-Ethiopian culture traits that one can plausibly refer to greater Ethiopia as culture area …[where there are peoples with Ethiopian culture called Ethiopians.*](Emphasis mine pp. 46-47)*

The second scholar, Claude Sumner who declared "I am Canadian by birth but Ethiopian by choice", argues that there are no racial differences between different ethnic groups in Ethiopia. After writing over a dozen of books on Ethiopian Philosophy of which three of them are on the "Oromo Wisdom Literature" analyzing the philosophical contents of the oral literature, Sumner comes into a conclusion on the real nature of the Ethiopians. Though there are linguistic and religious and to some extent cultural varieties, the current Ethiopian identity is an evolution between the mixtures of two physical types.

> As there has been so much racial intermixing, racial identifications are of limited use in Ethiopia. Periodic migrations of Caucasoid peoples from across the red sea and Negroid peoples from the west have produced a population that predominantly manifests a blend of the two physical types. (1985, p. 2)

Such racial intermixing is tantamount to the evolution of strong link between peoples that leads to the evolution of multilingual, multicultural, multi religious communities in Ethiopia witnessed with peaceful mutual coexistence. The 18th C traveler, De Abbadie's eye witness is relevant here:

> One strange thing a European traveler witnesses in Ethiopia is the reality of strange individuals, families, and at times even a village community situated in the original settlers of certain areas. Even though they are from different racial or ethnic group of the host society, this does not hinder them to live in peace with the aboriginals. While the new comers are expected to respect the laws and cultural norms of the host community for the sake of peaceful coexistence, they are not forced to denigrate, betray, forget or suppress the cultures and ways of life of their own forefathers. This is the reason why the diversified communities of Ethiopia live in peaceful and respectful neighborhood.[4] (Own Translation) (2009 E.C, p. 73)

According to the historian Tekletsadik Mekuria, the people of Ethiopian have been passed through cultural and racial intermixing with the people around the region due to different intercourse.[5]

It is from such and similar experiences of interaction that Ethiopian culture trait and IKSs evolved. The culture traits of diversified society are rich of different IKSs that are related to folk art, literature, philosophy, morality, medicine, architecture, astrology and etc. They are manifested in the highest forms of wisdom conceived as human development; the cultivation of good behavior, rationality and humanity - in the form of religious calamity or contemplative philosophic lives. These IKS can play significant roles in environmental protection, social harmony, enlightenment, social justice and sustainable development agendas and programs in contemporary Ethiopia in line with the foreign science and technology.

[4] This De Abbadie' observation is practically proven historical fact. The settlement programs of 1960s and before to Gambela, Elibabora, Assossa and different parts of Southern and western Ethiopia from the North as a response to the drought and famine were welcomed by the indigenous people. The Zai people around Ziway Islands and the Gurage People's Narrative though to be researched, are good testimonies. The nine saints, the peaceful reception of Muslims in 7th C etc. are manifestations of the culture of peace and multiculturalism in Ethiopia. It is also supported by the research findings of D. Levine (1974) and Desaalegn Rahmato (2009).

The IKSs comprise among others: Food Security, Development, Environmental Wellbeing (e.g. the *Enset* technology, indigenous farming and animal breading, bee keeping, the Borrana Oromo Ecotheology); Art (e.g. Wood works, Leather, pottery, weaver, architecture and painting); Gender Equality (e.g. the Philosophies of Zara Yacob and Wolde Hiwot); Multiculturalism (e.g. mutual peaceful coexistence, gudificha, Wolde Hiwot); Political Philosophy (Solomonic Dynasty, Gadaa System); Social Justice and peace making (e.g. Bela Libeliha, Afersata, Shimgilina, the Book of The Wise philosophers); Traditional Medicine (e.g. Animal healing, Body treatment, Wound healing, Psychedelic and therapy, Holy water); Religious (e.g. metaphysical, moral and epistemological teachings of Judaism, Islam and Christianity, Waqefenna, and Indigenous religions); Enlightenment and Philosophy (Qine, Written and Oral literature of translated and original works), formal and informal educations etc.

The traditional justice institutions of arbitration (*shimgilina*), the *bela libeliha* court system and the *afersata* investigation of criminals are social norms of many societies throughout the country with certain cultural variability.

According to my research, a good analysis of the law and IKSs, related to peace and justice institutions of different cultural groups in Ethiopia is presented by Abera Jembere. He briefly summarized the customary laws and justice administrations of ten[6] cultural groups in Ethiopia. Although his selection of the culture groups can be contested, his rationale of selecting the samples is the population size and the representative power of the given cultural groups to the remaining culture groups in the country. His argument is that we can take some customary laws that may commonly practices among societies that share similar socio-economic, cultural and geographical patterns. He categorized these uniting fundamental patterns into four groups: (1) the highland or plateau farming culture (Amhara, Tigray, Eritred, and the Oromo Culture), (2) the pastoralist nomadic culture (Afar, Somalie-Saho, Asawrts and partially Sidama's culture), (3) the *Inset* culture (Gurage and part of the Oromo society) and (4) the boarder peripheral culture (*yeEthiopia Yeteref mekenet kifl bahil)* (the Kunama, Agnuak, Anuar, Geleb and the like). (2006, Pp. 138-139)

The traditional schools (church and Mosque) teachings, informal education and oral literature, the Gada System of holistic education and the like contributed for the cultivation of highest forms of wisdom and the transfer of IKSs between generations. (Hailegebrael Dagne, 2007 E.C) It is against these and other IKSs that the introduction of new science and technology imposes its value laden ideological, political and epistemological orientations. (Santos, 2014; Harding 1997) Since the majority of the people are far from understanding the language of modern science and technology, there is communication gaps between generations. It is not far from our memory that the introduction of telecommunication was considered as the work of the devil by the majority of the people in the country side and it is only few decades when the inhabitants of the towns in Ethiopia laughed or amazed at someone who is in mobile phone communication as a mad man/woman who talks to his/herself. The next part of the paper argues for the democratization of science and technology towards the Ethiopian culture and IKSs.

5. DEMOCRATIZATION OF TECHNOLOGY TOWARDS ETHIOPIAN CULTURE

Let me open this section with reasonably long quotation from Jaroslav Pelikan's book, *The Vindication of Tradition:*

> […] the dichotomy between tradition and insight breaks down under the weight of history itself. A "leap of progress" is not a standing broad jump, which begins at the line of where we are now; it is running broad jump through where we have been to where we go next. The growth of insights – in science, in the arts, in philosophy and theology – has not come progressively sloughing off more and more of tradition, as though insight would be purest and deepest when it has finally freed itself of the dead past. It simply has not worked that way in the history of the tradition, and

[6] He has dealt with a brief analysis of the Eritrea-Tigray, Amhara, Oromo, Kunama, Gurage, Afar, Sumalie, Wolayta, Keffa and Aguwak customary laws. (2006 E.C, Pp. 53-138)

> it does not work that way now. By including the dead in the circle of discourse, we enrich the quality of the conversation. Of course we do not listen only to the dead, nor are we a tape recording of the tradition. That really would be the dead faith of the living, not the living faith of the dead. (1984, pp. 81-82)

Three important things can be noted from this quote. First, tradition is important and must be incorporated to the current state of affairs. Second, in contemporary world of science and technology, insight, rationality and objectivity are needed. Third, the balance and appropriate harmonization of tradition and insight is needed to enrich our discourse. Therefore, democratization of technology towards culture is an essential assignment of the agents of technology transfers in Ethiopia.

Modern science and technology appear to Ethiopian in the form of numbers, "objective measurements", and appeals to universality, rigor, experimentation, and compatibility with the global world. This insistence on these scientific theories and gross employment of the technological instruments with its aggressive powers penetrate the "untouchable" aspects of huge wisdom. Tradition is expected to leave room for the introduction of such scientific methods. In accordance with the understanding of the humanities, what the founders of social science research methods introduced is the calculable and describable aspects of culture groups distinctive features of certain socio-cultural and linguistic group, searching the differentia that makes it peculiar from others. It appears in the studies of history that insists on the trust of the sources presented to the historian and arrives at rational conclusions that adhere to the laws of logic.

Such fact establishing and rule making normative apparatuses in the social and natural sciences in the name of objective truth and compatibility to modern thought miss something inherent and natural ways of life and thought by the indigenous people, which are beyond the reach of the language and methods of researchers. (Wiredu, 1976) In the highest form of established norms of life, rationality or enlightenment and adherence to science, appear in the linear mainstream theorization of modernity, development and genuine existence to be followed as a role model. In its "political" aspect, it appears as the obstacle of freedom of individuals and dictator on the indigenous forms of thought that are assumed to be "irrational and superstitious". (Harding, 1997; Marcuse, 1964; Adorno and Horkheimer, 2002; Santos, 2014)

It is to rule out the imperialism of science, technology and modernity, the injustice it have done to culture and IKSs in Ethiopia that we need a balanced relationship between the two forms of thought. This proposal is not a comment from the conservative against revolutionary thoughts. There are different reasons for the quest of balanced relationships between technology and culture. Some argue that science and technology alone cannot penetrate human understanding in societies like ours. Because, the majority of the society is highly associated with tradition that cannot easily be attached with the newly introduced ways of thinking and acting. The logical implication of such mismatch between indigenous thinking and life style on the one hand and the philosophy and advancement of modern science on the other hand is the creation of generation gap. (Eguale Gebreyohannes, 2003)

> Until the right reconciler of cultures is emerged, the two cultures (Western and Ethiopian) kept as if they are enemy to one another. Time will pass without communication between them. There are generations who pass without participation in either of the cultures. The old is left as useless; the new is ignored without attention; for it demands strong effort to be internalized by the community. … At the end, the citizens of this era live a meaningless life and finally their attention will be dived into superficial material desires, they pass without any significant contribution to human development. (Own translation, first published 1956 E.C; 2003 E.C, p. 78)

According to Eguale, the existential dilemmas between adopting the new and leaving the "old fashioned" put man in psychological despair ("የመንፈስ መረበሽ") (p. 77); in the highest social level a form of cultural crisis. Such cultural crisis is manifested in the miscommunication between generations and cultural domination, political oppression and epistemicide, in Marxian expression "alienation of man from himself". (Carver, 1991, p. 441) To save man from such existential challenges, Eguale comments, hermeneutics is a necessary tool.

> In such challenging times, there are energetic intellectuals who understand the problem and attempt to solve it. They act as agents of communication and interaction between two cultures, who decide on the healthy marriage of the two relative cultures. It is this task, the contemporary Ethiopian intelligentsia faces in front of him/her. (Own translation, Eguale, 2003, p. 78)

Others argue that there are different possible ways of approaching and interpreting a given data. Allowing alternative ways of approaching it is doing fairness to truth, and doing justice for unheard voices from other cultures. An insistence to single science with a single cultural, political and social attachment is against intellectual honesty that closes the door for the possibility of learning from other cultures. It is such intellectual honesty the Westerners lack when they deny the epistemologies of the South. The erroneous conclusion is thus they leave intact (left unquestionable) the "modern science vs. ethnoscience" construct, the unbalanced valuing of modern vs. other scientific traditions, ignorance about ways in which the histories and destinies of Northern and other traditions are linked, and set of puzzling philosophical positions. (Harding, 1997)

Hermeneutic approach to foreign texts is desire to learn from them. "In approaching aforeign text or culture, we must keep in mind the possibility that we mighthave something to learn. That is one lesson of the hermeneutic tradition […]" (Glock, 2008, p. 113) that we should realize when we approach our fathers' wisdom and the foreign wisdom.

What do such arguments suggest to the discussion at hand? The answer is obvious: the need for hermeneutics and intercultural approach to technology and traditional knowledge. Such translation and appropriation approach is what Santos calls, borrowing Raymond Panikkar's phrase, "*Diatopical Hermeutics"* which "consists of interpretation work between two or more cultures to identify isomorphic concerns among them and the different responses thereby provided." (2014, p. [329])

In adopting a foreign technology, theory, philosophy or thought it is in conviction that the methods to be employed are relevant solve problems, to advance the quality of life and knowledge production. In doing so, the Ethiopian scholar is engaging in the "soul searching activity." This soul searching process has two objectives. "Apart from removing the false identity imposed on the African, and deconstruct the mythical self-image of the white man, African philosophy has the important task of being the solution to the African problems." (Bekele Gutema, 2005, p. 209) The result of this soul searching task is finding the nature of the thoughts and wisdoms of his/her forefathers, the ways by which they can harmonize with the Western thought, and attempting to establish genuine theoretical and practical mechanisms for solving political, economic, cultural, social and epistemological challenges of the society. These energetic "[…] contemporary African philosophers belong to two cultural traditions, the African and the Western. This can be an advantage, because working in more than one tradition can broaden your mind by acquainting you with a multiplicity of fundamentally different conceptual options." (Wiredu, 2004, p. 11).

When I quote these African philosophers, it is in the conviction that their comments on the role of African intelligentsia applies to contemporary Ethiopian scholars. At the fore front of the professional duties of contemporary Ethiopian scholars is the same task that Eguale cautions for the scholars of half a century ago.

6. CONCLUSION AND RECOMMENDATION

As the conclusion of our discourse, let's take the words of Parsier Rede quoted from the Albert Scheweitzer's *Pilgrimage to Humanity* "The world – majesty masking the dreadful, the absurd hidden in the rational, joy embracing suffering" (1961, p. 1) As we have seen in the above discussion and the literature we can arrive at a conclusion that there is no democratic relation and interaction between modern and traditional wisdom in Ethiopia. The modern science and technology with its Western political and epistemologically value laden orientations is doing injustice to the time tested IKSs in Ethiopia. The uncontrolled introduction of science and technology is alienating the Ethiopian man from his/her culture, the wisdom and world views of his/her forefathers. Such alienation in the form of distancing one from his/her true self creates a cultural crisis.

The imperialism in science and technology have double edged problems to the accumulation of global wisdom by oppressing the world views from the indigenous people and closing the door for alternative world views from the South. As I have argued above there must be a democratic relation between traditional wisdom and the introduction of modern science and technology. The methodological apparatus of intercultural approach and hermeneutics of the foreign and indigenous culture will result in the reach theoretical and practical weapons for solving the most pressing political, cultural, social, economic, and environmental problems we are facing in contemporary Ethiopia.

Both fanatic proponents of tradition and committed proponents of modern science and technology should come into dialogue to overcome the false dichotomy between rationality and mythology (Messay, 2004). There must be a culture conscious adoption of technology technologically supported cultural way of life. It should be noted that insistence to culture and religious life forms is as dangerous as the denial of IKSs for the sake of technology and science.

Finally recommendation is forward for policy makers, scholars and educators to consider the valuable IKSs from our forefathers and their healthy marriage with the science and technological innovations of the West.

REFERENCES

Adorno, T. W., & Horkheimer, M. (2002). *Dialectic of Enlightenment: Philosophical Fragments*. Stanford, California: Stanford University Press.

Bekele Gutema (2005). The Need for Intercultural Approach in African Philosophy in Bekele Gutema and Daniel Smith (2005) (edrs.) African Philosophy at the Threshold of the new Millinium, Addis Ababa University Printing press. Pp. 203-314.

Carver, T. (1991) (ed.). The Cambridge Companion to Marx. Cambridge: Cambridge University Press.

Dant, T. (2003) Critical Social Theory: Culture, Society and Critique. SAGE Publications.

Durant W. (1961) The Story of Philosophy: The Lives and Opinions of Great Philosophers of the Western World, Simon and Schuster Publishers.

Eyong, C. T. (2007) Indigenous Knowledge and Sustainable Development in Africa: Case Study on Central Africa. In Tribes and Tribals, Special Volume No.1. pp. 121-139

Freeman, M., & Vasconcelos, E.F.S. (2010). Critical Social Theory: Core Tenets, Inherent Issues. In M. Freeman (Ed.), Critical social theory and evaluation practice. New Directions for Evaluation, 127, 7–19.

Glock, H.-Johann (2008) What is Analytic Philosophy? Cambridge University Press

Hacker, P.M.S. (2007) "Wittgenstein and the Autonomy of Humanistic Understanding." e-Journal Philosophie der Psychologie.

Hancock, G. (1989) Lords of Poverty: The Power, Prestige and Corruption of the International Aid Business. The Atlantic Monthly Press, New York.

Harding, S. (1997) "Is Modern Science an Ethnoscience? Rethinking Epistemological Assumptions" in Emmanuel Chukwudi Eze (edr.) Postcolonial African Philosophy: A Critical Reader. Blackwell Publishers, Ltd. pp. 45-70.

Harney, B. (2017) Critical Theory. Encyclopedia of Management.

Lacey, H. (1999) Is Science Value Free? Values and Scientific Understanding. Routledge.

Levine, D. N. (1965, 1972) Wax & Gold: Tradition and Innovation in Ethiopian Culture, University of Chicago Press, Chicago and London.

Levine, D. N. (1974) Greater Ethiopia: The Evolution of a Multiethnic Society, The Univertiy of Chicago Press, Chicago & London.

Marcuse, H. (1964) One-Dimensional Man: Studies in the Ideology of Advanced Industrial Society, Beacon Press, Boston.

Messay Kebede (2004) Africa's Quest for a Philosophy of Decolonization, Editions Rodopi B.V, Amsterdam

Messay Kebede, (2004) Africa's Quest for a Philosophy of Decolonization, Editions Rodopi B.V, Amsterdam

Mriye Workineh et al (2010) Indigenous Knowledge Creation Practices: The Case of Ethiopia 18th European Conference on Information Systems.

Nebiyou Ermias Asfaw (2915) The Politics of Technology: Discourse in Philosophy of Technology. (MA Thesis, Addis Ababa University).

Pelikan, J. (1984) The Vindication of Tradition. New Heaven and London: Yale University Press.

Santos, B. De S. (2014) Epistemologies of the South: Justice against Epistemicide. Taylor & Francis New York

Santos, B. De S. (2018) The End of the Cognitive Empire: the coming of age of epistemologies of the south. Durham and London: Duke University Press

Scheweitzer, A. (1961) Pilgrimage to Humanity. Walter E. Stuermann (translator)The Wisdom Library a division of philosophical library, Inc. 1961 New York

Setaergew Kenaw (2012) Cultural translation of mobile telephones: mediation of strained communication among Ethiopian married couples. Cambridge University Press.

Short review of Santos' book accessed at https://b-ok.org/book/3599926/e40ea9

Smith, D. (2005) "Universities at the Threshold of the New Millennium", in Bekele Gutema and Daniel Smith (2005) (edrs.) African Philosophy at the Threshold of the new Millinium, Addis Ababa University Printing press. Pp. 168-204

Sumner, C. (1985) Classical Ethiopian Philosophy, Commercial Printing Press, Addis Ababa.

Sumner, C. (1998) "Ethiopia: Land of Diverse Expressions of Philosophy, Birthplace of Modern Thought" in Sumner, C. (1998) Proceedings of the Seminar on African Philosophy, December 1-3, 1976, 2nd edn. Addis Ababa University. Pp. 327-333

Verharen, C. C. (2013) "Philosophy and the Future of African Universities: Ethics and Imagination", in Bekele Gutema and Charles C. Verharen (2013) (edrs.) African Philosophy in Ethiopia. The Council for Research in Values and Philosophy. Pp 9-17

wa Thiong'o, N. (1981), Decolonising the Mind: The Politics of Language in African Literature, Zimbabwe Publishing House (Pvt.) Ltd.

Wiredu, K. (2004) Introduction: African Philosophy in Our Time, in Kwasi Wiredu (edr.) (2004) A Companion to African Philosophy, Blackwell Publishing Ltd. Pp. 1-27.

Wiredu, K. (1976). How Not to Compare African Traditional Thought with Western Thought Transition, No. 75/76, Indiana University Press. Pp. 320-327.

Zimmermann, K. A. (2015) what is Culture? Live Science. Accessed at https://www.coursehero.com/file/13259568/What-is-Culture/

ታይለ ገብርኤል ዳኜ (2007) ባህልና ትምህርት በኢትዮጵያ (Studies on Education in Ethiopian Tradition) አዲስ አበባ ዩኒቨርሲቲ ፕሬስ፣ አዲስ አበባ

ተክለ ጻዲቅ መኩሪያ (ፀፀየሃዕ) የኢትዮጵያ ታሪክ: ኑብያ-አክሱም ዛጉዬ እስከ አዬ ይኩኖ አምላክ ዘመነ መንግሥት ፭ኛ መጽሐፍ። ትንሣኤ ዘጉባኤ ማተሚያ ቤት፣ አዲስ አበባ።

እጓለ ገብረ ዮሐንስ (2003 E.C) የከፍተኛ ትምህርት ዘይቤ (2ኛ እትም)። አዲስ አበባ: አርቲስቲክ ማተሚያ ድርጅት።

የራስ ወርቅ አድማሴ (ዶር) "ባህልና ልማት፤ ምንነታቸው እና ትስስራቸው" (ገጽ 5) in ባህልና ልማት በኢትዮጵያ ሽፈራው በቀለ (አርታኢ) 2004 ዓ.ም ፎረም ፎር ሶሻል ስተዲስ፣ አዲስ አበባ ገጾች 1-25.

ገነት አየለ አንበሴ (ተርጓሚ) (2009 E.C) አርኖ-ሚሼል ዳባዲ: በኢትዮጵያ ከፍተኛ ተራሮች ቆይታዬ። Addis Ababa.

Evaluation of SWAT Performance in Modeling Nutrients of Awash Basin

Amare Shiberu Keraga[1,*], Zebene Kiflie[2], Agizew Nigussie Engida[3]

[1]*Department of Water Supply and Environmental Engineering, Technology Institute of Hawassa University, Hawassae, Ethiopia*
[2]*School of Chemical and Bio-Engineering, Addis Ababa University, Addis Ababa, Ethiopia*
[3]*School of Civil and Environmental Engineering, Addis Ababa University, Addis Ababa, Ethiopia*
**Corresponding author, e-mail: akeraga32@gmail.com*

ABSTRACT

Awash River basin has been recognized as exporting the highest amount of various pollutants in Ethiopia since the basin encompasses the main urban, industrial and agricultural centers of the nation. However, investigation of pollution level of the basin by nutrients is necessary for decision makers to safeguard Awash river and its end users, which has not been addressed yet. This study, therefore, evaluated performance of the Soil and Water Assessment Tool (SWAT) by modeling nitrate and phosphate at the basin scale. First, the model was set up using digital elevation model (DEM), climate, soil, and land use data. Thereafter, overall performance of the model was assessed by linking its outputs to the Sequential Uncertainty FItting Version 2 (SUFI2) procedure of the SWAT Calibration and Uncertainty Program (SWAT-CUP). The most sensitive parameters for the flow and nutrients were identified using t-stat and p-values from global sensitivity analysis of the SWAT-CUP. The goodness-of-fit of the monthly calibration measured by coefficient of determination (R^2), Nash-Sutcliffe Efficiency (NSE), and root mean square error-observations standard deviation ratio (RSR) were, respectively 0.79, 0.64 and 0.60 for flow; 0.73, 0.71 and 0.54 for nitrate and 0.77, 0.76 and 0.49 for phosphate. During validation, the objective functions were, respectively 0.81, 0.52 and 0.70 for flow; 0.68, 0.63 and 0.61 for nitrate and 0.82, 0.81 and 0.44 for phosphate. The results suggested that the simulated values of the variables fitted well with the observed ones and hence, SWAT is found to be promising to simulate nutrients in the basin.

Keywords: *Nitrate, Phosphate, SUFI2 algorithm, SWAT-CUP, Water quality*

1. INTRODUCTION

Nationally, Awash is the most important river with respect to its economic value and exposure to various pollutants. The exposure is due to its services as a major water supply source for the domestic, industrial and small to large scale irrigation schemes and as a sink for the basin-wide waste. On the other hand, there are no significant treatment systems corresponding to the wastewater generated. Consequently, a number of water-borne and water-related diseases were recorded from consumers of the resource (Tamiru Alemayehu, 2001; Eleni Ayalew, 2009). Notably, pollution loads of heavy metals, nitrate, helminthes, bacteria, toxicity level and salinity effects of the river were reported to be too high to use it for intended purposes (Amare Shiberu et al., 2017b).

Watershed models are fundamental to water resources management, development and assessment by analyzing, for instance, the quality of streams since monitoring of water quality continuously is expensive and impractical in mixed land uses (Chu et al., 2004). They enable us in understanding dynamic interactions between climate and land-surface hydrology and estimating the effects of management practices by considering the long-term weather, soil, land use/cover and topography variability. On a basin scale, models are used, among others, for water-quality evaluation (Santhi et al., 2001; Singh and Woolhiser, 2002). A number of watershed and receiving water quality models have been developed by different scholars since 1925 when Streeter and Phelps built the first water quality model to manage river pollution (Wang et al., 2013). These include AGNPS (Young et al., 1989), ANSWERS (Beasley et al., 1980), AQUATOX (Shoemaker et al., 2005), EFDC (Shoemaker et al., 2005), CREAMS (Knisel, 1980; Krysanova et al., 1998), QUALs (QUAL2E, QUAL2K, QUAL2Kw) (Kannel et al., 2007), HSPF (Bicknell et al., 2001), SWAT (Arnold et al., 1998; Gassman et al., 2007), GWLF (Qi et al., 2017; Shoemaker et al., 2005), and WASP (Paul et al., 2010; Sharma and Kansal, 2013).

To select for water quality simulation, models are evaluated mainly based on the types of water quality problems; potential sources and timing of their occurrence; desired spatial and temporal scales; data requirements and availability; model application, complexity and operation; model uncertainty; available resources and technicality (Bahadur et al., 2013; Sharma and Kansal, 2013; Shoemaker et al., 2005). Based on these evaluation criteria and since it can easily be linked to GIS, calibration, sensitivity and uncertainty analysis tools (Griensven et al., 2012), the water quality and hydrologic model Soil and Water Assessment Tool (SWAT) was selected and applied in this study. Since the Ethiopian water sector policy focuses mainly on river basins as fundamental planning unit of managing the resource, the research is believed to contribute to the realization of these issues as SWAT is a basin scale model.

Application of SWAT to assess hydrology and sediment in the horn of Africa is well documented (Baker and Miller, 2013; Shimelis Gebriye et al., 2008). SWAT is found to be a favorable model for continuous and long-term simulations of all major components (chemical, sediment, and hydrology) in agriculture-dominated basins (Borah and Bera, 2003). The model is applicable to semi-arid and similar environments where limited number of gauge stations are found (Gebremedhin Kiros et al., 2015). However, it is practically impossible to include all pollutant sources as it is difficult to represent all components of the system in the modeling effort. Therefore, only nitrate (NO_3^-) and phosphate (PO_4^{2-}) were considered here as pollutants of interest because they are causes for freshwater eutrophication which in turn have effects of increased growth of algae and aquatic weeds that interfere with the intended use of Awash river. The objective of this study was therefore to evaluate performance of the SWAT model in simulating the nutrients in Awash River basin.

2. MATERIALS AND METHODS

2.1. Description of the study area

The basin, located between 7°53′N - 12°0°N and 37°57′E - 43°25′E, covers a total area of about 114,000 km^2 (Figure 1). The Awash River has a length and annual flow respectively, of 1250 km and 4600 million m^3 (MCM) and originates at an elevation of about 3000 m in the central Ethiopian highlands. It flows in north-easterly direction along the Rift Valley and eventually discharges into the salty Lake Abbe at the border of Ethiopia and Djibouti, which has an altitude of about 250 m.a.s.l (Fitsum Tesfaye et al., 2013; Fasil Degefu et al., 2013; Amare Shiberu et al., 2017b). The two main physiographic units of Awash River basin are highlands (Ethiopian plateaus) and the main Ethiopia Rift widening to the north of Afar triangular depression (Halcrow, 1989). The basin is covered by agriculture, forest, various types of water bodies, grass, shrubs (dominated by the invasive plant species, Prosopis juliflora), urban, bare lands, sands, and exposed rocks (Zeraye Haile, 2015).

The seasonal distribution and pattern of rainfall that vary linearly with altitude in Awash Basin are determined by the annual migration of inter-tropical convergence zone (Belete Birhanu and Semu Ayalew, 2013). The mean yearly rainfall varies between 160 mm at Asayita and 1978 mm at Ankober but throughout the western basin it is about 850 mm (Fitsum Tesfaye et al., 2013; Halcrow, 1989). The total annual water resource of the basin, draining from the western plain of the valley, amounts to about 4527 MCM (Fitsum Tesfaye et al., 2013; Ndomba and Griensven, 2011). The mean annual temperature in the basin varies spatially from 16.7°C at Addis Ababa to about 34.5°C at Lake Abe area. The mean relative humidity of the basin varies between 60.2% and 49.7% per annum while the mean annual wind speed is 1.85 m/s (Fitsum Tesfaye et al., 2013; Halcrow, 1989; Ndomba and Griensven, 2011). The basin extends from semi-desert (arid) lowlands to cold high mountain (humid subtropical) agro-ecological zones (Amare Shiberu et al., 2017b).

2.2. Theoretical description of the SWAT model

SWAT is a very flexible, continuous, and conceptual hydrologic and water quality model that simulates on a daily time basis. It can simulate a variety and high level of spatial detail that are planned to forecast the impact of land management practices on water, sediment, and agricultural chemical yields in long periods of time since it is

computationally efficient (Gebremedhin Kiros et al., 2015; Gassman et al., 2007; Neitsch et al., 2011). A basin by SWAT is classified into many sub-basins, which are again subdivided into unique soil, slope, and land use characteristics called Hydrologic Response Units (HRUs) (Gassman et al., 2007). The water budget of every HRU is expressed by the four storage volumes: deep aquifer, shallow aquifer, soil profile, and snow. Pollutant and sediment loads as well as flow generation are added across all HRUs in a sub-basin, then the resulting flow and loads are routed via channels, reservoirs, and ponds to the basin outlet (Jha et al., 2007). Eight components: land management, pesticides, nutrients, crop growth, soil temperature, erosion and sediment transport, weather, and hydrology are simulated by SWAT for each HRU (Arnold et al., 1998; Jha et al., 2007; Neitsch et al., 2002). They are simulated on the basis of water balance equation (**1**) (Neitsch et al., 2002; Shimelis Gebriye et al., 2008; Jha et al., 2007; Kim et al., 2010):

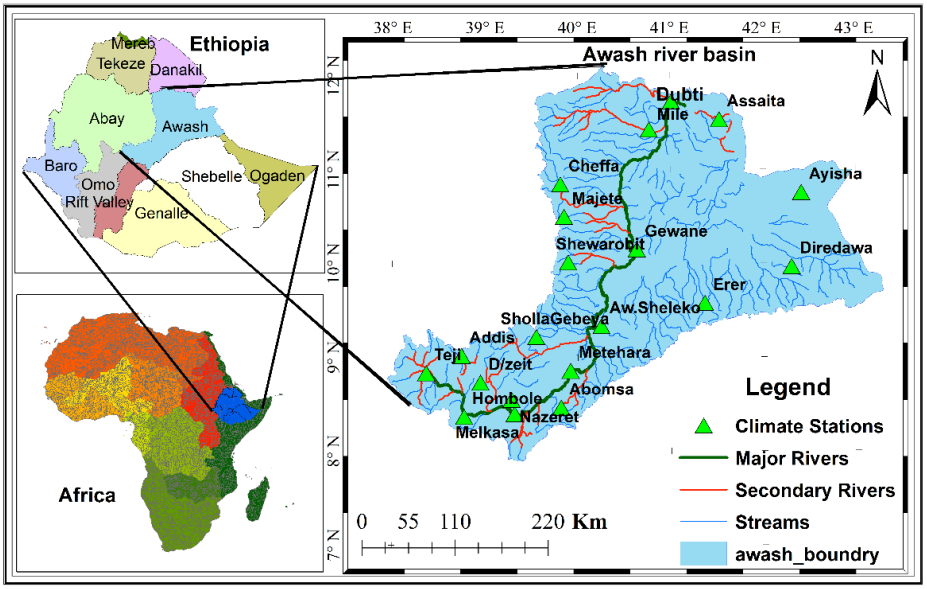

Figure 1: Location Map of Awash River Basin with its stream networks and climate stations

$$SW_t = SW_0 + \sum_{i=1}^{t} \left(R_{day} - Q_{surf} - ET - W_{seep} - Q_{gw}\right) \ldots\ldots\ldots\ldots\ldots\ldots\ldots (1)$$

Where, SW_t is the final soil water content (mm water), SW_o is the initial soil water content (humidity) in day i (mm water), t is the time (days), R_{day} is the quantity of precipitation (rainfall volume) in day i (mm water), Q_{surf} is the quantity of surface runoff in day i (mm water), ET is the amount of evapo-transpiration in day i (mm water), W_{seep} is the amount of water entering the vadose zone from the soil profile in day i (mm water), and Q_{gw} is the amount of ground water runoff (return flow) in day i (mm water) considering all the processes involved in the hydrologic cycle.

Based on a watershed physical characteristics and objective of the watershed modeling, either SCS CN procedure or Green and Ampt infiltration method has been suggested for SWAT to generate run-off (Ficklin and Zhang, 2013; Gebremedhin Kiros et al., 2015). The SCS curve number equation was used in this study to predict surface runoff from a watershed because of the unavailability of sub-daily weather data for Green and Ampt method (Gebremedhin Kiros et al., 2015). SCS CN method estimates the amount of runoff based on local land use, soil type, and antecedent moisture condition (Jha et al., 2007). In fact, the formula specifically applied for SCS CN method (USDA-SCS 1986) is depicted by equation (2).

$$Q_{surf} = \frac{(P-I_a)^2}{(P-I_a)+S} = \frac{(P-0.2S)^2}{(P+0.8S)}, if\ P > 0.2S; Q = 0\ otherwise \ldots\ldots\ldots (2)$$

Where, Q_{surf} is the accumulated runoff or rainfall excess (mm), P is the rainfall depth for the day (mm); I_a is the initial abstraction of water (mm), S is the retention parameter (mm), which is defined by equation (3).

$$\boldsymbol{S = 5I_a = 254\left(\frac{100}{CN} - 1\right)} \ldots\ldots\ldots\ldots\ldots\ldots\ldots\ldots\ldots\ldots\ldots\ldots \text{(1),}$$

Where; CN is the curve number for the day (Chow et al., 1988).

Evapo-transpiration (ET) is one way by which water is withdrawn from a basin. ET can be estimated in three ways: Penman-Monteith, Priestley-Taylor, and Hargreaves, (Jha et al., 2007; Zhao et al., 2013). In the present study, the Hargreaves method (equation **4**) is used in the edition of the ET parameter since the method is an energy-based method of estimating ET selectively in arid, semi-arid and grasslands (Zhao et al., 2013) and since it is slightly superior to the two others (Wang et al., 2006).

$$ET = 0.0135(T + 17.8)\frac{R_S}{\lambda} \ldots\ldots\ldots\ldots\ldots\ldots\ldots\ldots\ldots\ldots\ldots\ldots \text{(2),}$$

Where, ET is potential evapo-transpiration (mm/ d); T is mean air temperature (°C); R_s is short wave radiation (MJ / ($m^2 \cdot d$)); and λ is latent heat of vaporization (kJ/kg).

2.3. Nutrient dynamics and their simulation in SWAT

The transport and fate of pollutants in general and nutrients in particular, depend on the sources, sinks, reactions, decay mechanisms and transformation that the compounds undergo on and in the soil (Hemond and Fechner, 2014; Maidment, 1993; Ramaswami et al., 2005). In the soil, transformations of phosphorus and nitrogen from one form to another due to their sources and sinks are results of soil weathering and erosion processes, which are governed by nitrogen and phosphorus cycles (Neitsch et al., 2002). From their different pools in the soil monitored by SWAT, the reactive nitrogen (NO_3^-) and reactive phosphorus (PO_4^{2-}) forms were modeled by SWAT completely for the basin.

2.4. Input data acquisition and preparation

The basic dataset required to simulate the SWAT model as prerequisites including: meteorological data; topography (DEM); soil properties; and land use/land cover data were sought. Hydrological data (including river discharge gage data and water quality data) were also considered as inputs in the study (Neitsch et al., 2011). The dataset has been pre-processed to make it suitable for the model use.

2.5. Hydro-meteorological data

The climate data collected for the model simulation include daily values of: precipitation, minimum and maximum temperature, relative humidity, wind speed and sun shine hour (solar radiation) of 20 stations. These daily meteorological datasets for the required weather stations (for 1/1/1994-12/31/2014) in the study area were gathered from the National Meteorological Service Agency (NMSA). Additional data were also captured from the global weather database (http://globalweather.tamu.edu/) of Texas A&M University Climate Forecast System Reanalysis (CFSR) to fill the missing parts as recommended by Dile and Srinivasan (2014), Fuka et al. (2013). Then the data was formatted so that it could be fed to the SWAT model. The measured data on flow for the period 1972–2013 were collected from the hydrology and water quality department of Federal Ministry of Water, Irrigation and Electricity (MoWIE) of Ethiopia. Moreover, shape files and all the GIS data were gathered from the GIS department of MoWIE and the long-term water quality data was taken from Awash Basin Authority.

2.6. Topography

Topography (DEM) was used as input for the model to delineate and discretize the basin, to further divide it into sub-basins and HRUs and to determine flow direction, flow accumulation, stream length, and outlet selection. It calculated the basin's and sub-basins' parameters such as area, slope and slope length (Bingner et al., 1997; Gassman et al., 2007). The DEM data, captured from the global land cover facility, was obtained from the Shuttle

Radar Topography Mission (SRTM) of paths 44 and 45 and rows 10 and 11. It was of 90-m spatial resolution and divided the basin into five slope classes **(**Figure 2a).

2.7. Soil data

The soil input file governs movement of air and water through the profile and have a major impact on the cycling of water within the HRUs (Neitsch et al., 2002). Awash river basin contains 16 (Figure 2b) of the 28 major soil groups in the legend of world soil map (FAO/UNESCO), each of which were characterized by Driessen et al., 2000 and FAO et al., 2012. Therefore, the soil data requirement for the model was prepared from the digital world soil map of scale 1: 5,000,000. It was first cut by the study area's shape file and conversion of vector into raster and vice-versa was undertaken. In addition to soils' properties fetched from FAO soil, additional characteristics of soil required to set up the model such as soil saturated hydraulic conductivity, bulk density, soil available water content and texture class of each soil type at different soil depths were determined using the Soil Plant Air Water (SPAW) hydrology model.

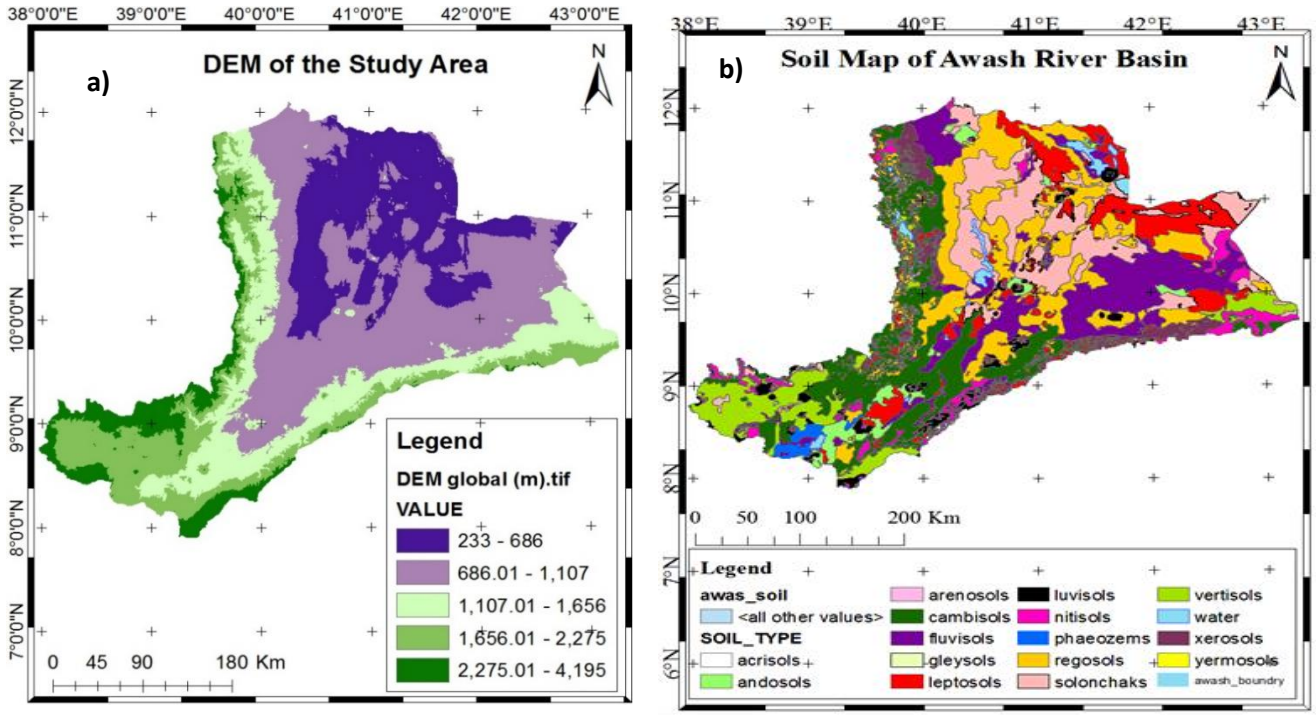

Figure 2: Maps of DEM (a) and soil (b) Awash River Basin

2.8. Land use/land Cover

The source for Land use/land cover data was Earth Resources Observation and Science (EROS) Center of USGS Global Visualization (GloVis) Viewer (http://glovis.usgs.gov/). From the site, the cloud-free Landsat 5 Thematic Mapper imageries of eight scenes were downloaded. The scenes were of paths and rows: 166-53, 167-52, 167-53, 167-54, 168-52, 168-53, 168-54, and 169-54. After layer stacking these images, mosaicking and cutting by the study area shape file, they were made ready for classification. GPS readings of sub-classes of each land use class were gathered from different locations of the catchment, in addition to Google Earth, to be used as training sites for verification. The mosaicked land use was then classified using supervised classification technique coupled with maximum likelihood classification algorithm (Figure 2c).

2.9. SWAT Model Performance Evaluation

Performance of hydrologic models need to be evaluated: to examine improvements to the modeling approach; to get a quantitative estimate of the model's capability of reproducing watershed behavior; and to compare results

of different modeling efforts (Krause et al., 2005). For the evaluation, a public domain computer program called SWAT Calibration and Uncertainty Programs (SWAT-CUP) of version 5.1.6 was used. In the SWAT-CUP, parameters and their ranges were manually adjusted iteratively (Arnold et al., 2012). The program was produced in the Swiss Federal Institute of Aquatic Science and Technology (Eawag) (Abbaspour, 2015) and it is capable of linking each of the Sequential Uncertainty FItting Version 2 (SUFI2), Particle Swarm Optimization, Generalized Likelihood Uncertainty Estimation, Parameter Solution, and Markov Chain Monte Carlo algorithms to SWAT outputs (Abbaspour, 2015). In this study, SWAT outputs were linked to the SUFI2 procedure of SWAT-CUP program to see the overall performance in the process.

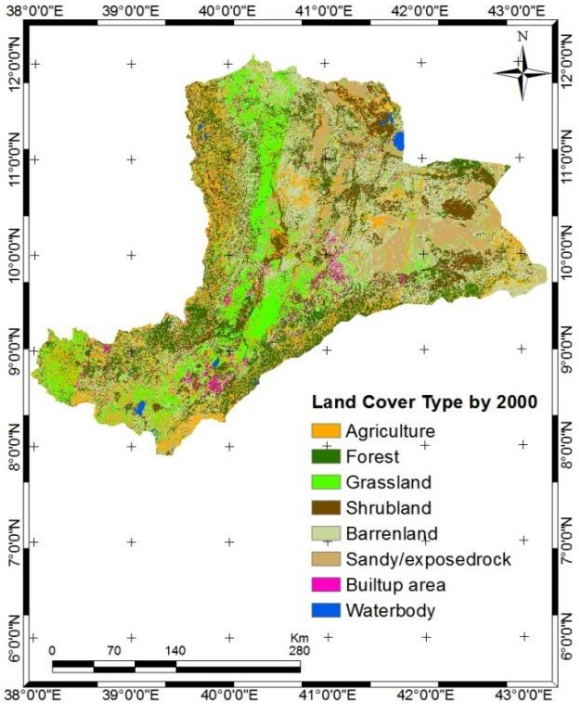

Figure 2c: Maps of land use/land cover of Awash River Basin

2.10. Sensitivity Analysis

Sensitivity Analysis (SA) is the process of determining the rate at which model outputs change with changes in model inputs (parameters) and decreases the number of parameters in the calibration procedure by eliminating the parameters identified as not sensitive (Abbaspour et al., 2017; Arnold et al., 2012; Yuan et al., 2015). There are two types of SA: *global* and *local*. In global or all-at-a-time SA, sensitivities of parameters are estimates of the average changes in the objective function resulting from changes in each parameter, while changing all the rest parameters. Relative significance of the parameters was identified by *t*-test. Here the larger, in magnitude, the t-stat and the smaller the p-value, the more sensitive would the parameter be (Abbaspour, 2007; Abbaspour et al., 2017; Arnold et al., 2012). Local or one-at-a-time SA shows the sensitivity of a variable to the changes in a parameter if all other parameters are kept fixed (Abbaspour et al., 2017).

2.11. Calibration and Validation

SWAT, being semi-physically based model, needs calibration and validation of its outputs (Arnold et al., 2012) before using the result in research and real-world applications (Guzman et al., 2015; Moriasi et al., 2012). In hydrologic and water quality models like SWAT, calibration denotes to a procedure where the difference between model simulation and observation are minimized. This reduces simulation uncertainty thereby model simulations better represent site-specific conditions (Abbaspour et al., 2017). It is done by selecting model parameters to be

optimized, adjusting their ranges carefully, simulating and comparing predicted output variables with observed data for specific conditions (Daggupati et al., 2015; Arnold et al., 2012). Validation is the process of showing that a given site-specific model is able to make sufficiently accurate simulations (Moriasi et al., 2007). It is used to be confident in the calibrated parameters. Hence, the calibrated parameter ranges were applied to an independently measured dataset by iterating only once without further changes either in the parameters or in their ranges (Abbaspour et al., 2017). These model validation and calibration are measured by p-factor, r-factor and objective functions such as: coefficient of determination (R^2), Nash-Sutcliffe Efficiency (NSE), and RMSE-observations standard deviation ratio (RSR).

R^2 indicates how strongly the observed values are related with the predicted ones (equation **5**). It explains the fraction of the variance in observed data described by the model. The Nash-Sutcliffe Efficiency (NSE) however defines the magnitude of the residual variance ("noise") relative to the measured data variance ("information"). NSE, computed by equation (**6**), shows the extent of fitness of the plot of measured versus predicted data with the 1:1 line (Moriasi et al., 2007). To explicitly qualify the low value of Root Mean Square Error (RMSE) recommended by Singh et al. (2004) for good model performance, Moriasi et al. (2007) developed RMSE-observations standard deviation ratio (RSR) standardizing RMSE using the observations standard deviation. It is computed by the ratio of the RMSE and standard deviation of observed data, as indicated by equation (**7**) (Moriasi et al., 2007):

$$R^2 = \frac{[\sum_{i=1}^{n}(O_i-\bar{O})(P_i-\bar{P})]^2}{\sum_{i=1}^{n}(O_i-\bar{O})^2\sum_{i=1}^{n}(P_i-\bar{P})^2} \quad \text{.....(3)}$$

$$NSE = 1 - \frac{\sum_{i=1}^{n}(O_i-P_i)^2}{\sum_{i-1}^{n}(O_i-\bar{O})^2} \quad \text{.....(4)}$$

$$RSR = \frac{RMSE}{STDEV_{obs}} = \frac{\sqrt{\sum_{i=1}^{n}(O_i-P_i)^2}}{\sqrt{\sum_{i=1}^{n}(O_i-\bar{P})^2}} \quad \text{.....(5)}$$

Where, O_i, $\bar{O}$, P_i, $\bar{P}$ and n are, respectively the i^{th} observation, the mean of observed data, the i^{th} predicted value, the mean of predicted data for the constituent being evaluated and the total number of observations.

Performance evaluation criteria for recommended statistical performance measures for watershed-scale models as formulated by Moriasi et al., 2007 and Moriasi et al., 2015 are indicated by Table 1.

Table 1: General performance ratings for recommended statistics in monthly time step

Objective function	Output Response	Performance Ratings			
		Very good	Good	Satisfactory	Unsatisfactory
R^2	Streamflow	$0.85 < R^2 \leq 1.0$	$0.75 < R^2 \leq 0.85$	$0.60 < R^2 \leq 0.75$	$R^2 \leq 0.60$
	N, P	$R^2 > 0.70$	$0.60 < R^2 \leq 0.70$	$0.30 < R^2 \leq 0.60$	$R^2 \leq 0.30$
RSR	Streamflow, N, P	$0 \leq RSR \leq 0.50$	$0.50 < RSR \leq 0.60$	$0.60 < RSR \leq 0.70$	$RSR > 0.70$
NSE	Streamflow	$0.80 < NSE \leq 1.0$	$0.70 < NSE \leq 0.80$	$0.50 < NSE \leq 0.70$	$NSE \leq 0.50$
	N, P	$0.65 < NSE \leq 1.0$	$0.50 < NSE \leq 0.65$	$0.35 < NSE \leq 0.50$	$NSE \leq 0.35$

Adopted from Moriasi et al. (2007) and Moriasi et al. (2015)

Calibration and validation of the SWAT model for NO_3^- and PO_4^{2-} are very important since the nitrogen and phosphorus components in the model are very complex and their input data requirements are intensive. Calibration and validation of flow and nutrients were typically performed with data collected at the assumed outlet, Dubti, of the basin to which approximately about 80% of the entire basin drains. The dataset used as observed during calibration and validation of the simulated nutrients was generated from the flow and the monthly analyzed water

quality result of eight years (2006-2013). The first 5 years' data (2006-2010) was utilized for calibration while the remaining 3 years' data was set for validation. The concentrations of NO_3^- and PO_4^{2-} were obtained, according to Smarzyńska and Miatkowski (2016), from the monthly discharge and water quality data related by equation (8).

$$L = \sum_{t=1}^{t=T} (86.4\overline{Q_t}C_t^l) \quad \ldots\ldots\ldots\ldots\ldots\ldots\ldots\ldots\ldots\ldots\ldots\ldots\ldots\ldots (8)$$

Where, L = NO_3^- and PO_4^{2-} loads, kg; C_t^l= mean monthly NO_3^-/ PO_4^{2-} concentrations, mg/l; $\overline{Q_t}$= mean monthly discharge, m^3/s; t = time, months.

2.12. Uncertainty analysis

Uncertainty arises from the fact that almost all measurements are subject to some error, models are simplifications of reality, and the inferences are usually statistical (Abbaspour et al., 2017). Specifically, in SUFI2, parameter uncertainty considers all sources of uncertainties (Abbaspour, 2015). The level of accounting all uncertainties is measured by *P-factor* – defined as the percentage of observed data bracketed by the 95% prediction uncertainty (95PPU) band. The 95PPU is computed at the 2.5% and 97.5% levels of the overall distribution of output variables got by Latin hypercube sampling (Abbaspour et al., 2007). The other measure quantifying the strength of a calibration/uncertainty analysis is the *R-factor* – described as the average thickness of the 95PPU band divided by the standard deviation of the corresponding measured data. Usually, the *value of P-factor* ranges from 0 to 100% while that of *R-factor* ranges from 0 to infinity (Abbaspour, 2015).

2.13. Watershed delineation, characterization and model setup

Awash basin consists of 8 land uses, 16 soil types and 5 major slope classes (Figure 2). The watershed delineation step, which was accomplished by overlaying DEM, Land use, and soil maps, discretized the basin into 53 sub-basins after all pre-processing tasks have been carried out. The sub-basins were further discretized using areas with identical land use, soil types and slope to create 665 HRUs. Finally, the 20 weather stations were submitted and all the necessary data were fitted to run the model. The preliminary model was set up using ArcSWAT2012 GIS interface for a drainage area of 105,191.98 km^2 as the threshold for delineation of the watershed. The model was then run successfully for the period 1997–2014, leaving the first 3 years' time (1994-1996) as a warm-up period.

3. RESULTS AND DISCUSSION

Nineteen hydrologic parameters that might have influences on stream flow of Awash River were used in the sensitivity analysis. The model parameters, their definition, initial ranges of the parameters, t-stat, p-values and their sensitivity ranks were given in Table 2. The rank was assigned with respect to absolute values of t-Stat and p-values in the grid from the global SA according to Khalid et al. (2016). Parameters of larger t-Stat in absolute values or those of p-values less than or equal to 0.05 have been taken as those to which the model variable (stream flow) was most sensitive. On the basis of the p-values, the first ten ranked (in the increasing order of sensitivity) parameters (Table 2) were therefore pointed out to be more sensitive, namely; GW_DELAY.gw, EPCO.bsn, RCHRG_DP.gw, ESCO.hru, GWQMN.gw, SOL_K (..).sol, SOL_BD(..).sol, SLSUBBSN.hru, HRU_SLP.hru, and CN2.mgt. Hence, these parameters were found to be the most crucial parameters for the studied basin as they generally govern the surface hydrological processes and stream routing. The hydrology is observed to be exceptionally sensitive to curve number (CN2).

3.1. Quantification of the SWAT model performance

Performance of flow of the model output was seen first and those of nutrients (nitrogen and phosphorus) were considered next. For both flow and nutrients, sensitive parameters were identified before calibration and validation of their outputs by the model.

3.2. Sensitivity Analysis of Flow

3.2.1. Monthly calibration, validation and uncertainty analysis of the river flow

The ten flow determining parameters identified as most sensitive were considered in the model calibration of the flow. The long term monthly observed flow data of 1997-2005 with 3 escape years (1994-1996) were used for automatic calibration of the stream flow at Dubti. The monthly simulated versus observed stream flow is also plotted in Figure 3. Model efficiency during monthly calibration of the model flow simulation evaluated by R^2, NSE and RSR of stream flow were respectively 0.79, 0.64 and 0.60 as shown in Table 3, implying that the discrepancy between observed and predicted stream flow was less. Validation was performed by running the SWAT-CUP for dataset of time period 2006-2014, using the previously calibrated input parameters. Table 3 shows the monthly graphical performance evaluation of SWAT model during calibration and validation periods. The plot in Figure 4 implies that the model simulation is best fitted with the observed flow measurement. During validation 0.81, 0.52, and 0.70 were obtained as the respective values of R^2, NSE and RSR (Table 3). For monthly and watershed-scale hydrological models, Moriasi et al. (2015) and Moriasi et al. (2007) in their evaluation criteria for recommended statistical performance measures for flow indicated in Table 1 suggested both for calibration and validation that NSE in the range of (0.5, 0.7] imply that a model is satisfactory.

Table 2: Selected input parameters to SWAT-CUP in the sensitivity analysis of stream flow

Input Parameter Name	Description of Parameter	Min/ Max	t-Stat	P-Value	Rank
V__CH_K2.rte	Effective hydraulic conductivity of channel (mm/hr)	0-0.3	-0.15	0.88	19
R__OV_N.hru	Manning's "n" value for overland flow	-1.1	0.21	0.831	18
V__GW_REVAP.gw	Groundwater "revap" coefficient	0.02-0.2	-0.29	0.775	17
V__ALPHA_BF.gw	Base flow alpha factor (days)	0-1	0.58	0.561	16
V__ALPHA_BNK.rte	Base flow alpha factor for bank storage (days)	0-1	0.62	0.535	15
V__SURLAG.bsn	Saturated hydraulic conductivity (mm/hr)	-34	0.71	0.479	14
V__REVAPMN.gw	Threshold water level in shallow aquifer for revap or percolation to deep aquifer (mm H_2O)	0-500	0.99	0.323	13
V__CH_N2.rte	Manning's "n" value for the main channel	0-15	-1.1	0.27	12
R__SOL_AWC(..).sol	Available water capacity of the soil layer (mm H_2O/mm soil)	-0.6	1.92	0.056	11
V__GW_DELAY.gw	Groundwater delay (days)	0-500	2.02	0.044	10
V__EPCO.bsn	Plant water uptake compensation factor	0.01-1	-2.09	0.037	9
V__RCHRG_DP.gw	Aquifer percolation coefficient	0-1	-2.36	0.019	8
V__ESCO.hru	Soil evaporation compensation factor	0.01-1	-2.95	0.003	7
V__GWQMN.gw	Threshold water level in shallow aquifer for base flow (mm H_2O)	0-5000	-3.12	0.002	6
R__SOL_K(..).sol	Saturated hydraulic conductivity (mm/hr)	0-2	-3.18	0.002	5
R__SOL_BD(..).sol	Bulk density of soil's first layer (Mg m^{-3})	-1.1	-5.28	0	4
V__SLSUBBSN.hru	Average slope length (m)	10-150	5.44	0	3
V__HRU_SLP.hru	Average slope steepness (fraction)	-1.5	-7.34	0	2
R__CN2.mgt	SCS runoff curve number	-30	-33	0	1

Explanations: V— existing parameter value is to be replaced by given value or absolute change; R— existing parameter value is multiplied by (1 + a given value) or relative change (Abbaspour 2015). (..) first layer of soil profile

Their suggestion of R^2 in the range (0.75, 0.85] indicate that a model performance is good. Since performances of this study measured by NSE and R^2 lie respectively in these ranges, the statistics were satisfactory and good. Similarly, RSR values of 0.60 and 0.70 generated respectively, during calibration and validation of flow were also in permissible ranges as their ratings, as recommended by Moriasi et al. (2007), were good and satisfactory. According to the arguments by Moriasi et al. (2007) and Moriasi et al. (2015), the values of the objective functions of this study both in the calibration and validation periods indicated that the model's overall performance for flow was good and is in the acceptable limit.

Uncertainties might have been born either from the observed or from the predicted flows since abnormal patterns and deviations of the observed data from the corresponding months' simulated ones were seen, for instance, in Jan 2000, Aug 2000, Aug 2001, Aug 2002, Sep 2003, Apr 2004, Aug 2004, and Aug 2005. Some values of flow, e.g. increasing in Nov 1997, Sept 1999, Jan 2000, April 2004, being dry seasons and decreasing in all years of June being wet seasons encountered both in the observed and predicted results were a bit far from expectations.

The reason for the mismatch of observed flows with the corresponding predicted ones might either be due to inaccurate measurement of discharge at the gauging station or due to the observed flow from the sudden discharge releases of the Tendaho dam just upstream of the station, which stores water during the rainy season and releases afterwards as required. However, errors from the predicted flow might be attributed to inaccuracies in the rainfall data used in setting up the model. Generally, the model simulation is seen to give higher values of flow than the observed ones.

Table 3: Summary of model performance for calibration and validation of flow at Dubti

Variable	Year	Period	Performance evaluation of the parameters				
			p-factor	r-factor	R^2	NSE	RSR
FLOW_OUT_3	1997-2005	Calibration	0.46	0.52	0.79	0.64	0.60
FLOW_OUT_3	2006-2014	Validation	0.59	0.82	0.81	0.52	0.70

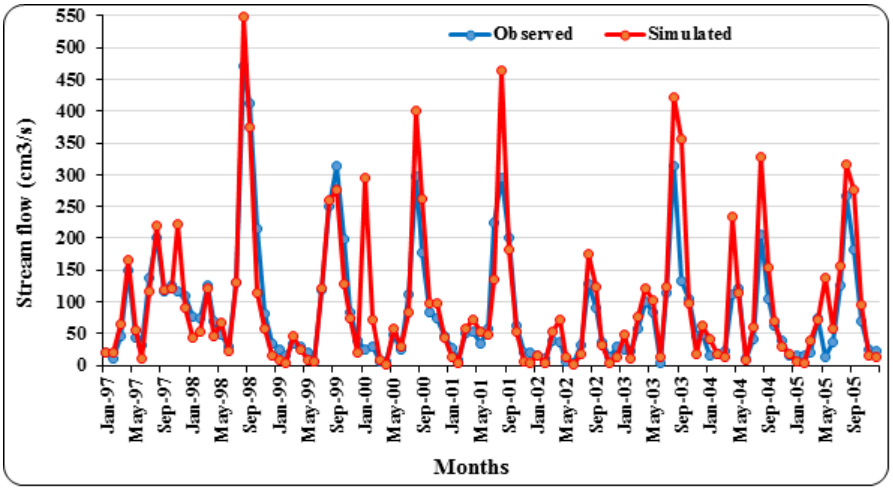

Figure 3: Observed and predicted river flow after monthly calibration of the model simulation

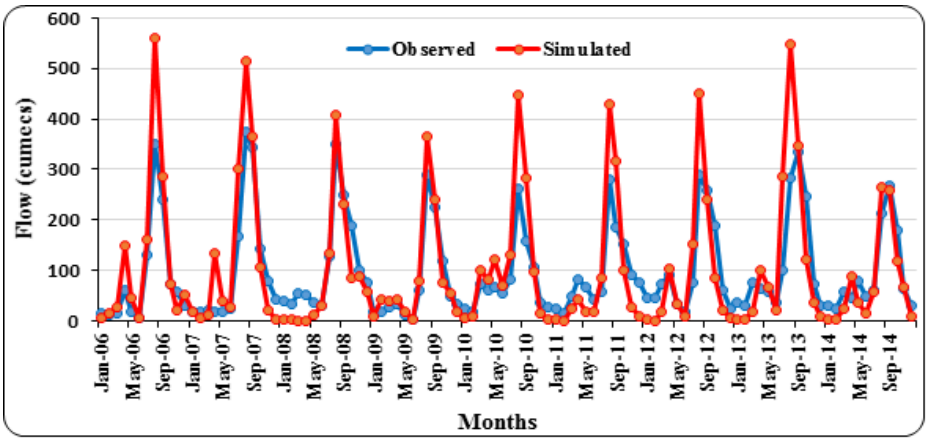

Figure 4: Observed and predicted flow after monthly validation of the model simulation

Uncertainty at Dubti gauging station depicted that the 95PPU seems to be poor for the monthly time series simulation of discharge since only about 46% of the observed stream flow was bracketed by the 95PPU band (Table 3). Though bracketing of the observed data by the 95ppu seems to be somehow far from the ideal expectation of unity, thickness of the band confirmed by the r-factor value of 0.52 (a bit close to zero) is relatively good. This implies that the model is within the acceptable range of uncertainty since it is compromised by good NSE and R^2 values. P-factor could be made as close to 1 as possible at the expense of r-factor by repeating the iteration but such actions have risks of reducing values of R^2 and NSE sometimes.

3.2.2. Sensitivity analysis, monthly calibration and validation of nitrate (NO_3^-)

To analyze the relative sensitivity of different parameters to nitrate, eighteen water quality parameters (Table 4) that might have a potential influence on mineral nitrogen load of Awash River were used. Setting the number of simulations to be 600, SWAT-CUP was run with these parameters. The table shows the model parameters, minimum and maximum values, t-stat, p-value and their sensitivities (ranked in its last row) with respect to absolute values of t-stat in the grid from the global SA according to Khalid et al. (2016). Therefore, only eight of the parameters were pointed out to be more sensitive to NO_3^-, namely (in the increasing order of sensitivity); RCN.bsn, BC1_BSN.bsn, SDNCO.bsn, NFIXMX.bsn, CMN.bsn, BC2_BSN.bsn, RSDCO.bsn, and NPERCO.bsn, as their p-values are less than or equal to 0.05 and those of little bit greater than 0.05. Hence, these parameters were found to be the most vital parameters for the studied basin as they generally control the surface nitrate loading. The table shows that NO_3- was exceptionally sensitive to nitrogen percolation coefficient (NPERCO) followed by CDN, and then by SDNCO.

Table 4: Selected input parameters to SWAT-CUP in the sensitivity analysis of NO_3^-

Input Parameter	Description of Parameter	Min/Max	t-Stat	P-Value	Rank
V__BC1_BSN.bsn	Rate constant for biological oxidation of NH_3	0.1-1	-0.73	0.46	13
V__BC2_BSN.bsn	Rate constant for biological oxidation NO_2 to NO_3^-	0.2-2	-1.04	0.3	8
V__BC3_BSN.bsn	Rate constant for hydrolysis of organic nitrogen to ammonia	0.02-0.4	0.6	0.55	15
V__NFIXMX.bsn	Maximum daily-n fixation	1-20	-0.31	0.76	17
V__CMN.bsn	Rate factor for humus mineralization of active organic nitrogen	0-0.7	-0.47	0.64	16
V__NPERCO.bsn	Nitrogen percolation coefficient	0-1.0	-22.4	0	1
V__N_UPDIS.bsn	Nitrogen uptake distribution parameter	10-60	1.26	0.21	6
V__SOL_NO3.bsn	Initial NO_3 concentration in the soil layer	0-100	0.91	0.36	9
V__SOL_ORGN.bsn	Initial organic N concentration in the soil layer	0-100	0.74	0.46	12
V__RSDCO.bsn	Residue decomposition coefficient	0-0.5	-0.9	0.37	10
V__SDNCO.bsn	Denitrification threshold water content	0-1.0	-11.37	0	3
R__ANION_EXCL.sol	Fraction of porosity from which anions are excluded	0-1.0	1.31	0.19	5
V__CDN.bsn	Denitrification exponential rate coefficient	0-3	13.41	0	2
V__CH_ONCO.rte	Channel organic nitrogen concentration in basin	0-100	0.86	0.39	11
V__ERORGN.hru	Organic N enrichment ratio	0-1	1.15	0.25	7
V__FIXCO.bsn	Nitrogen fixation coefficient	0-1	0.7	0.48	14
V__SHALLST_N.gw	Concentration of nitrate in groundwater contribution to stream flow from sub-basin	0-0.05	1.91	0.06	4
R__RCN.bsn	Concentration of nitrogen in rainfall	0-15	0	1	18

V—parameter value is replaced by given value or absolute change; R—parameter value is multiplied by (1 + a given value) or relative change.

Table 5: Summary of model performance for calibration and validation of NO3- at Dubti

Variable	Year	Period	Performance evaluation of NO_3 parameters				
			p-factor	r-factor	R^2	NSE	RSR
NO_3_OUT_3	2006-2010	Calibration	0.64	1.24	0.73	0.71	0.54
NO_3_OUT_3	2011 – 2013	Validation	0.53	0.72	0.68	0.63	0.61

After calibration and assessment of the hydrology, N-related parameters reported in the top ranks of Table 4 were adjusted during monthly calibration. The long-term observed monthly NO_3^- concentrations of 2006-2010 were used for calibration. With the identified sensitive parameters of minimum and maximum ranges remaining as that of the sensitivity analysis, SWAT-CUP was run for 500 simulations first. Then re-running the program repeatedly by replacing the initial min and max ranges of the parameters by ranges of the new pars generated in the previous iteration, optimum values of objective functions were obtained (Table 5) in the summary stat of the last iteration of the SUFI2 algorithm. Validation was performed by running the model for dataset of time period 2011 – 2013 using the calibrated input parameters. Figure 6 shows the monthly graphical performance evaluation of SWAT model in validating NO_3^-. The monthly graph implied that the model simulation is well fitted with the observed flow measurement.

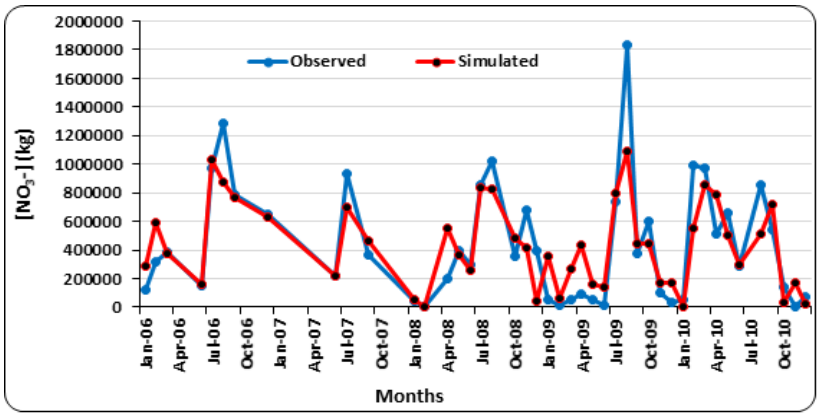

Figure 5: Observed and predicted Nitrate after monthly calibration

Assessment of performance of calibration of nitrate at the presumed outlet station was undertaken to see fitness of the simulated dataset with the observed ones. The monthly calibration result of the model simulation, shown in Table 5, produced R^2, NSE and RSR values of 0.73, 0.71 and 0.54, respectively. While R^2 and NSE lie in the 'very good' rating ranges recommended for nutrients, the RSR lies in the 'good' range of Moriasi et al. (2007) and Moriasi et al. (2015). The functional values of R^2, NSE and RSR obtained during monthly validation of NO_3^-, shown in Table 5, were respectively 0.68, 0.63 and 0.61. While both R^2 and NSE lie in the 'good' rating ranges, the value of RSR lies in the 'satisfactory' range of Table 1. Come what may, all the values were found to be in the acceptable limit, indicating that the measured data fits well with the predicted ones.

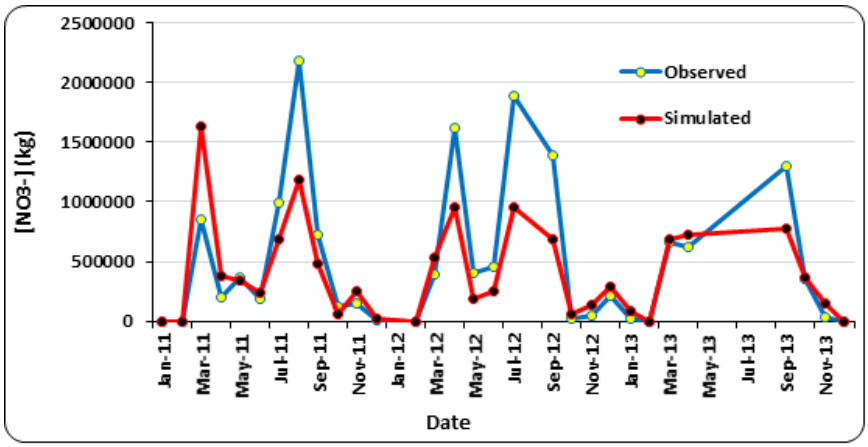

Figure 6: Observed and predicted Nitrate after monthly validation of the model simulation

There were under predictions of NO_3^- in months, for instance, of August 2006, July 2007, August 2008, August 2009, and August 2010. This may be associated to the lower values of weather data (fed to the model) of the station surrounding Dubti during calibration (Figure 5). However, this is consistent with the under prediction of the species when validating the model as could be seen in Figure 6. The p-factor in the case of nitrate has grown to 64% as opposed to that of flow at the expense of going further away from zero of r-factor (value 1.24). Similar to the case of flow, because efficiencies during calibration and validation of nitrate were in the acceptable ranges and the p-factor is good enough to approach to 1, the uncertainty may also be considered as tolerable.

3.2.3. Sensitivity analysis, monthly calibration and validation of phosphate

Sensitivity analyses of different parameters that might potentially determine mineral phosphorus (PO_4^{2-}) was undertaken by considering seventeen phosphorus-related parameters listed in the first column of Error! Reference source not found..

Input Parameter	Description of Parameter	Min/ Max	t-Stat	P-Value	Rank
PSP.bsn	Phosphorus sorption coefficient	0.01-0.7	-0.66	0.51	13
PHOSKD.bsn	Phosphorus soil partitioning coefficient	100-200	3.06	0	5
P_UPDIS.bsn	Phosphorus uptake distribution parameter	0-100	6.8	0	4
SOL_ORGP(..).chm	Initial organic P concentration in surface soil layer	0-100	-12.9	0	3
BC4.swq	Rate constant for decay of organic phosphorus to dissolved phosphorus	0.01-0.7	-17.7	0	2
ERORGP.hru	Organic P enrichment ratio	0-5	-21.4	0	1
CH_OPCO.rte	Channel organic phosphorus concentration in basin	0-100	-0.5	0.62	15
RSDCO.bsn	Residue decomposition coefficient	0.02-0.1	-0.88	0.38	10
PSETLP1.pnd	Phosphorus settling rate in pond for months IPND1 through IPND2	0-20	-1.15	0.25	8
PSETLW2.pnd	Phosphorus settling rate in wetlands for months other than IPND1-IPND2	0-20	-0.01	0.99	17
PSETLP2.pnd	Phosphorus settling rate in pond for months other than IPND1-IPND2	0-20	-0.62	0.54	14
PSETLW1.pnd	Phosphorus settling rate in wetland for months IPND1 through IPND2	0-20	0.67	0.5	12
SOL_LABP(..).chm	Initial labile (soluble) P concentration in surface soil layer	0-100	-1.84	0.07	6
SOLP_CON.hru	Soluble phosphorus concentration in runoff, after urban BMP is applied	0-3	1.14	0.26	9
GWSOLP.gw	Concentration of soluble phosphorus in groundwater contribution to stream flow from sub-basin	0-0.5	0.22	0.83	16
ORGP_CON.hru	Organic phosphorus concentration in runoff, after urban BMP is applied	0-50	1.69	0.09	7
PPERCO.bsn	Phosphorus percolation coefficient	9-16.5	0.72	0.47	11

After running 500 simulations, sensitivity of PO_4^{2-} to the parameters was identified. With respect to absolute values of t-Stat in the grid from the global SA, sensitivities of the parameters were ranked and put in Table 6 according to Khalid et al. (2016). Therefore, nine parameters were identified to be most crucial to which the surface phosphate loading is sensitive, namely (in the increasing order of sensitivity (t-Stat value)); SOLP_CON.hru, PSETLP1.pnd, ORGP_CON.hru, SOL_LABP(..).chm, PHOSKD.bsn, P_UPDIS.bsn, SOL_ORGP(..).chm, BC4.swq, and ERORGP.hru, as their p-values is less than or equal to 0.05.

After calibration and assessment of the hydrology, PO_4^{2-}-related variables reported in the top rank of Table 6 were adjusted during calibration. Observed long-term dataset of 2006-2010 were used for calibration. Similarly, calibration and validation of the model phosphate output were made on a monthly basis and evaluated for goodness-of-fit using r-factor, p-factor, R^2, NSE and RSR values as measuring objective functions. With the

identified sensitive parameters of minimum and maximum ranges remaining as that of the sensitivity analysis, SWAT-CUP was run for 500 simulations first. Then re-running the program now and then replacing the initial minimum and maximum ranges of the parameters by that of the new pars generated in the preceding iteration, optimum values of objective functions were obtained. As a result, the calibration has given values of the objective functions of R^2, NSE and RSR respectively 0.77, 0.76 and 0.49 (Table 7). The table tells us that the performance ratings of the functions, according toTable 1, were all 'very good' since R^2 and NSE values were respectively above 0.70 and 0.65 and RSR was also less than 0.5. A good fit between the simulated and the observed concentrations is shown by these results. The output is also depicted in Figure 7.

Table 7: Summary of model performance for calibration and validation of PO42- at Dubti

Variable	Year	Period	Performance evaluation of PO_4^{2-} parameters				
			p-factor	r-factor	R^2	NSE	RSR
PO_4_OUT_3	2006-2010	Calibration	0.32	1.34	0.77	0.76	0.49
PO_4_OUT_3	2011–2013	Validation	0.33	1.09	0.82	0.81	0.44

The validation was performed by running the SWAT-CUP for time period 2011 – 2013 using the calibrated input parameters. Figure 8 shows the monthly graphical performance evaluation of SWAT model in validating PO_4^2. The monthly graph implies that the model simulation is best fitted with the observed flow measurement.

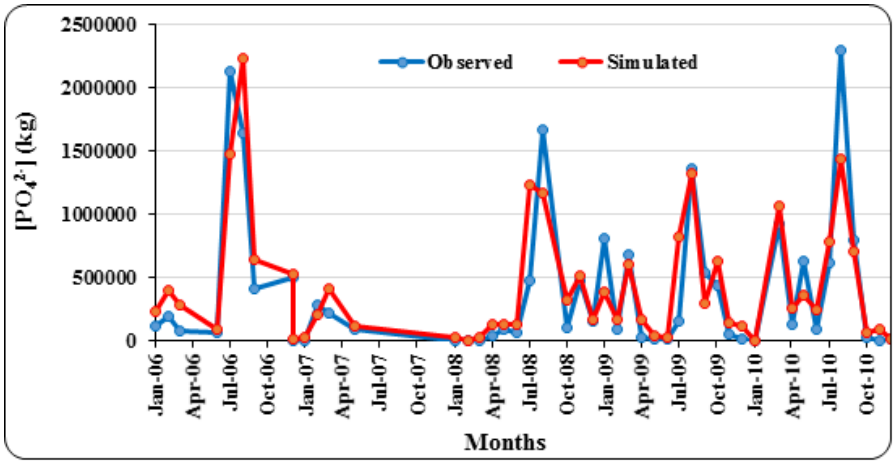

Figure 7: Observed and predicted phosphate after monthly calibration of the model simulation

On the other hand, the values for the respective objective functions during validation, shown in Table 7, were 0.82, 0.81 and 0.44, which all are in the 'very good' rating ranges for nutrients. This implies that the predicted mineral phosphorus agrees well with the observed one. Similarly, phosphate predictions were also seen to be less than the corresponding observed ones in wet seasons as in the case of August 2008 and August 2010 during calibration and in July 2012 and August 2011 during validation. The under-prediction of phosphorus loading could be due to the fact that phosphorus from atmospheric deposition and stream banks were not taken into consideration in the SWAT model. In the validation the evaluating statistics of the model, R^2 and NSE, were slightly better than those obtained in the calibration. This shows that the model has an ability to mimic discharge and phosphate loads in a wide range of hydrologic conditions.

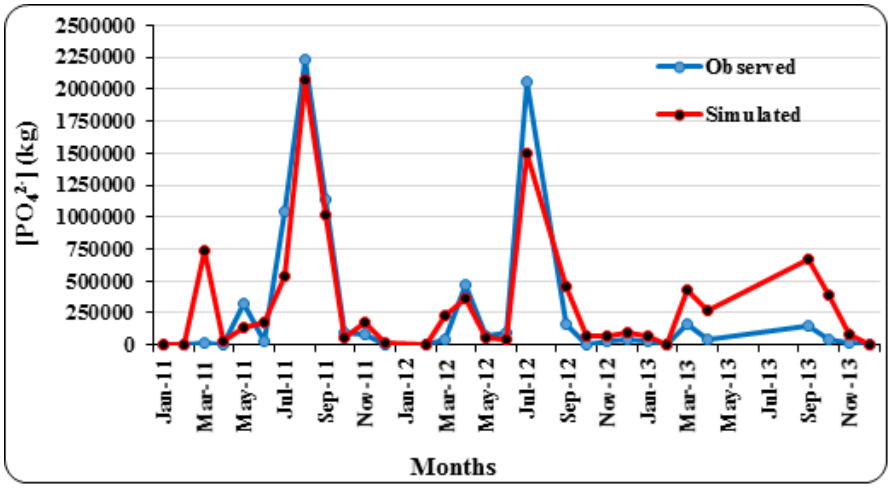

Figure 8: Observed and predicted phosphate after monthly validation of the model simulation

4. CONCLUSION

Performance of the hydrological and water quality model, SWAT, was evaluated in this study when simulating nutrients in Awash River basin although it has not yet been applied to model water quality in the basin. Setting up the model with the required data, 53 sub-basins and 665 number of HRUs were produced in the basin. Then the simulated flow was calibrated and validated using the long-term record of observed data on a monthly basis and the performances measured by R^2, NSE and RSR were found to be good. Next, the simulated nitrate and phosphate were also calibrated and validated with their historical records of observed data. The objective functional values during calibration and validation of the nutrients were found to be within the acceptable ranges of the standards put in literature. The study shows that SWAT is a promising model to predict water quality provided that there is minimum amount of measured data required for calibration and validation.

REFERENCES

Abbaspour, K., Yang, J., Maximov, I., Siber, R., Bogner, K., Mieleitner, J., Zobrist, J. and Srinivasan, R. (2007). Modelling hydrology and water quality in the pre-alpine/alpine Thur watershed using SWAT, *Journal of Hydrology*, 333(2-4): 413– 430.

Abbaspour, K.C. (2015). SWAT-CUP: SWAT calibration and uncertainty programs–a user manual. Version4, *Swiss Federal Institute of Aquatic Science and Technology, Eawag*.

Abbaspour, K.C., Rouholahnejad, E., Vaghefi, S., Srinivasan, R., Yang, H. and Kløve, B. (2015). A continental-scale hydrology and water quality model for Europe: Calibration and uncertainty of a high-resolution large-scale SWAT model. *Journal of Hydrology*, 524: 733-752.

Abbaspour, K.C., Vaghefi, S.A. and Srinivasan, R. (2017). A Guideline for Successful Calibration and Uncertainty Analysis for Soil and Water Assessment: *A Review of Papers from the 2016 International SWAT Conference*.

Amare Shiberu, Zebene Kiflie, and Agizew Nigussie (2017b). Evaluating water quality of Awash River using water quality index. *International Journal of Water Resources and Environmental Engineering*, *9*(11): 243-253.

Arnold, J.G. Srinivasan, R. Muttiah, R.S. and Williams, J.R. (1998). Large area hydrologic modeling and assessment part 1: Model development. *Journal of the American Water Resources Association*, 34(1): 73–89.

Arnold, J.G., Moriasi, D.N., Gassman, P.W., Abbaspour, K.C., White, M.J., Srinivasan, R., Santhi, C., Harmel, R.D., Van Griensven, A., Van Liew, M.W., Kannan, N. (2012). SWAT: Model use, calibration, and validation. *Transactions of the ASABE*, 55(4): 1491–1508.

Bahadur, R., Amstutz, D.E. and Samuels, W.B. (2013). Water contamination modeling—a review of the state of the science. *J Water Resource Prot*, 5(02): 142–155.

Baker, T.J. and Miller, S.N. (2013). Using the Soil and Water Assessment Tool (SWAT) to assess land use impact on water resources in an East African watershed. *Journal of Hydrology*, 486: 100-111.

Beasley, D.B., Huggins, L.F. and Monke, A. (1980). ANSWERS: A model for watershed planning. *Transactions of the ASAE*, *23*(4): 938-0944.

Belete Birhanu and Semu Ayalew (2013). Background Report: Hydro-Meteorological Trends. Awash River Basin Water Audit (ARBWA) Project, Addis Ababa, Ethiopia.

Bicknell, B.R., Imhoff, J.C., Kittle, Jr J.L., Jobes, T.H., Donigian, Jr A.S. and Johanson, R. (2001). Hydrological Simulation Program–FORTRAN: HSPF Version 12 User's Manual. Mountain View, CA: AQUA TERRA Consultants. Cooperation with the US Geological Survey and US Environmental Protection Agency 845

Bingner, R.L., Garbrecht, J., Arnold, J.G. and Srinivasan, R. (1997). Effect of watershed subdivision on simulation runoff and fine sediment yield. *Transactions of the ASAE*, 40(5): 1329–1335.

Borah, D.K. and Bera, M. (2003). Watershed-scale hydrologic and nonpoint-source pollution models: Review of mathematical bases. *Transactions of the ASAE*, 46(6): 1553.

Chow, V.T., Maidment, D.R. and Mays, L.W. (1988). Applied hydrology, 572 pp. *Editions McGraw-Hill, New York*.

Chu, T.W., Shirmohammadi, A., Montas, H. and Sadeghi, A. (2004): Evaluation of the SWAT model's sediment and nutrient components in the Piedmont physiographic region of Maryland. *Transactions of the ASAE*, 47(5): 1523.

Daggupati, P., Pai, N., Ale, S., Douglas-Mankin, K. R., Zeckoski, R. W., Jeong, J. ... and Youssef, M. A. (2015). A recommended calibration and validation strategy for hydrologic and water quality models. *Transactions of the ASABE*, 58(6): 1705–1719.

Dile, Y.T. and Srinivasan, R. (2014): Evaluation of CFSR climate data for hydrologic prediction in data-scarce watersheds: an application in the Blue Nile River Basin. *JAWRA Journal of the American Water Resources Association*, 50(5): 1226–1241.

Driessen, P., Deckers, J., Spaargaren, O. and Nachtergaele, F. (2000): *Lecture notes on the major soils of the world* (No. 94). Food and Agriculture Organization (FAO) of the United Nations, 307 pp, Rome.

Eleni Ayalew Belay (2009): Growing lake with growing problems: integrated hydrogeological investigation on Lake Beseka, ZEF, Germany.

FAO, IIASA, ISRIC, ISSCAS, JRC (2012): Harmonized world soil database (version 1.2). FAO, Rome, Italy and IIASA, Laxenburg, Austria.

Fasil Degefu, Aschalew Lakew, Yared Tigabu, and Kibru Teshome (2013): The Water Quality Degradation of Upper Awash River, Ethiopia. Ethiopian Journal of Environmental Studies and Management, 6(1): 58–66.

Ficklin, D.L. and Zhang, M. (2013): A comparison of the curve number and Green-Ampt models in an agricultural watershed. *Transactions of the ASABE*, 56(1): 61–69.

Fitsum Tesfaye Berhe, Assefa Mekonnen Melesse, Dereje Hailu, Yilma Sileshi (2013): MODSIM-based water allocation modeling of Awash River Basin, Catena 109: 118–128.

Fuka, D.R., Walter, M.T., MacAlister, C., Degaetano, A.T., Steenhuis, T.S. and Easton, Z.M. (2013): Using the Climate Forecast System Reanalysis as weather input data for watershed models. *Hydrological Processes*, 28(22): 5613–5623.

Gassman, P.W., Reyes, M.R., Green, C.H. and Arnold, J.G. (2007): The soil and water assessment tool: historical development, applications, and future research directions. *Transactions of the ASABE*, 50(4): 1211–1250.

Gebremedhin Kiros, Shetty, A. and Nandagiri, L. (2015): Performance evaluation of SWAT model for land use and land cover changes in semi-arid climatic conditions: a review. *Hydrology: Current Research.*, 6(3): 1.

Griensven, A.V., Ndomba, P., Yalew, S. and Kilonzo, F. (2012): Critical review of SWAT applications in the upper Nile basin countries. *Hydrology and Earth System Sciences*, 16(9): 3371–3381.

Guzman, J.A., Shirmohammadi, A., Sadeghi, A.M., Wang, X., Chu, M.L., Jha, M.K. ... and Hernandez, J.E. (2015): Uncertainty considerations in calibration and validation of hydrologic and water quality models. *Transactions of the ASABE*, 58(6): 1745–1762.

Halcrow (1989): Masterplan for the development of surface water resources in the Awash basin. Final Report-vol.6, Ministry of Water Resources, Addis Ababa, Ethiopia.

Hemond, H. F. and Fechner, E. J. (2015): *Chemical fate and transport in the environment*. Third edition, *Elsevier*, San Diego, USA.

Jha, M.K., Gassman, P.W. and Arnold, J.G. (2007): Water quality modeling for the Raccoon River watershed using SWAT. *Transactions of the ASABE*, 50(2): 479–493.

Kannel, P.R., Lee, S., Lee, Y.S., Kanel, S.R. and Pelletier, G.J. (2007): Application of automated QUAL2Kw for water quality modeling and management in the Bagmati River, Nepal. *ecological modelling*, 202(3): 503–517.

Khalid, K., Ali, M.F., Rahman, N.F.A., Mispan, M.R., Haron, S.H., Othman, Z. and Bachok, M.F. (2016): Sensitivity analysis in watershed model using SUFI-2 algorithm. *Procedia engineering*, 162: 441–447.

Kim, N.W.; Lee, J.W.; Lee, J. and Lee, J.E. (2010): SWAT Application to Estimate Design Runoff Curve Number for South Korean Conditions, Hydrological Processes 24(15):2156-2170.

Knisel, W.G. (1980): CREAMS: a field scale model for Chemicals, Runoff, and Erosion from Agricultural Management Systems [USA]. United States. Dept. of Agriculture. Conservation research report (USA).

Krause, P., Boyle, D.P. and Bäse, F. (2005): Comparison of different efficiency criteria for hydrological model assessment. Advances in geosciences 5:89–97.

Krysanova, V., Müller-Wohlfeil, D.I., and Becker, A. (1998): Development and test of a spatially distributed hydrological/water quality model for mesoscale watersheds. Ecological Modelling 106(2-3): 261–289.

Maidment, D.R. (1993): *Handbook of hydrology* (Vol. 1). McGraw-Hill, New York.

Moriasi, D.N., Arnold, J.G., Van Liew, M.W., Bingner, R.L., Harmel, R.D. and Veith, T.L. (2007): Model evaluation guidelines for systematic quantification of accuracy in watershed simulations. Transactions of the ASABE, 50(3): 885–900.

Moriasi, D.N., Gitau, M.W., Pai, N. and Daggupati, P. (2015): Hydrologic and water quality models: Performance measures and evaluation criteria. *Transactions of the ASABE*, 58(6): 1763–1785.

Moriasi, D.N., Wilson, B.N., Douglas-Mankin, K.R., Arnold, J.G. and Gowda, P.H. (2012): Hydrologic and water quality models: Use, calibration, and validation. *Transactions of the ASABE*, 55(4): 1241–1247.

Ndomba, P.M. and Griensven A. (2011): Suitability of SWAT Model for Sediment Yields Modelling in the Eastern Africa. *In* Advances in Data, Methods, Models and Their Applications in Geoscience. InTech.

Neitsch, S.L., Arnold, J.G., Kiniry, J.E.A., Srinivasan, R. and Williams, J.R. (2002): Soil and water assessment tool user's manual version 2000. *GSWRL report*, *202*(02-06), *Texas Water Resources Institute*. TR-192, College Station, Texas.

Neitsch, S.L., Arnold, J.G., Kiniry, J.R. and Williams, J.R. (2011): Soil and water assessment tool theoretical documentation version 2009. Texas Water Resources Institute.

Qi, Z., Kang, G., Chu, C., Qiu, Y., Xu, Z. and Wang, Y. (2017): Comparison of SWAT and GWLF Model Simulation Performance in Humid South and Semi-Arid North of China. *Water*. 9(8): 567.

Ramaswami, A., Milford, J.B. and Small, M.J. (2005): Integrated environmental modeling: pollutant transport, fate, and risk in the environment. John Wiley & Sons.

Santhi, C., Arnold, J.G., Williams, J.R., Dugas, W.A., Srinivasan, R. and Hauck, L.M. (2001): Validation of the SWAT model on a large river basin with point and nonpoint sources. *JAWRA Journal of the American Water Resources Association*, 37(5): 1169–1188

Sharma, D. and Arun, K. (2013): Assessment of river quality models: a review. Reviews in Environmental Science and Bio/Technology, 12(3): 285–311.

Shimelis Gebriye, Srinivasan, R. and Dargahi, B. (2008): Hydrological modelling in the Lake Tana Basin, Ethiopia using SWAT model. Open Hydrology Journal 2(1).

Shoemaker, L., Dai, T., Koenig, J. and Hantush, M. (2005): TMDL model evaluation and research needs. National Risk Management Research Laboratory, US Environmental Protection Agency. Tetra Tech, Inc

Singh, V.P. and Woolhiser, D.A. (2002): Mathematical modeling of watershed hydrology. *Journal of hydrologic engineering*, 7(4): 270–292.

Smarzyńska, K. and Miatkowski, Z. (2016): Calibration and validation of SWAT model for estimating water balance and nitrogen losses in a small agricultural watershed in central Poland. Journal of Water Land Development 29(1): 31–47.

Tamiru Alemayehu (2001): The impact of uncontrolled waste disposal on surface water quality in Addis Ababa, Ethiopia. SINET-Ethiopian journal of Science, 24(1): 93–104.

US Department of Agriculture-Soil Conservation Service (USDA SCS) (1986): Urban hydrology for small watersheds. Technical release 55: 2–6.

Wang, Q., Li, S., Jia, P., Qi, C. and Ding, F. (2013): A review of surface water quality models. *The Scientific World Journal*, *2013*.

Wang, X., Melesse, A.M. and Yang, W. (2006): Influences of potential evapotranspiration estimation methods on SWAT's hydrologic simulation in a northwestern Minnesota watershed. *Transactions of the ASABE*, 49(6): 1755-1771.

Young, R.A., Onstad, C.A., Bosch, D.D. & Anderson, W.P. (1989): AGNPS: A nonpoint-source pollution model for evaluating agricultural watersheds. *Journal of soil and water conservation*, 44(2): 168–173.

Yuan, Y., Khare, Y., Wang, X., Parajuli, P.B., Kisekka, I. & Finsterle, S. (2015): Hydrologic and water quality models: Sensitivity. *Transactions of the ASABE*, 58(6): 1721–1744.

Zeraye Haile (2015): The invasion of Prosopis juliflora and Afar pastoral livelihoods in the Middle Awash area of Ethiopia. *Ecological Processes*, 4(1): 13.

Zhao, L., Xia, J., Xu, C.Y., Wang, Z., Sobkowiak, L. & Long, C. (2013): Evapotranspiration estimation methods in hydrological models. *Journal of Geographical Sciences*, *23*(2): 359-369.

Effects of Total Quality Management Practices on Performance: An Empirical Study of Gafat Armament Industry, Ethiopia

Ajit Pal Singh

Engineering Department, College of Engineering Defense University, Bishoftu, Ethiopia
**Corresponding author, e-mail: singh_ajit_pal@hotmail.com*

ABSTRACT

Total quality management (TQM) is a industry-wide management philosophy of continuously improving the quality of the products, services, processes by focusing on the customers' needs and expectations to enhance customer satisfaction and firm performance. This study investigat-ed effects of TQM practices on performance measures in Gafat Armament Industry, Bishoftu (Ethiopia). A cross-sectional survey methodology was used in this study, and the unit of the sample was at the six operational department's level under industry. Primary data was collect-ed through structured questionnaire based on five - point Likert scale. Two hundred forty four usable questionnaires were obtained, with a good response rate of 97.6 percent. TQM practices viz., leadership, knowledge and continuous improvement, training, supplier management, cus-tomer focus, strategic quality planning, employee management, and information analysis are consider as independent variables and performance viz., quality performance, operational per-formance, and industry performance are consider as dependent variables. Exploratory factor analysis and multiple regression analysis were conducted. This study has shown that different TQM practices significantly affect different performance outcomes. It is recommended that in-dustry should continue implement TQM practices with all variables to improve performance.

Keywords: *Total Quality Management, Quality Performance, Operational Performance, Industry Perfor-mance*

1. INTRODUCTION

Total quality management (TQM) is a systematic quality improvement approach for firm-wide management for the continuously improving the quality of the products/services/processes by focusing on the customers' needs and expectations to enhance customer satisfaction and in-dustry performance. As per Kaynak (2003), Nair (2006), and Sadikoglu and Zehir (2010), there are mixed results about the relationship between TQM practices and performance. Ac-cording to Nair (2006), and Sadikoglu and Zehir (2010), the results of the previous TQM practices and performance studies were positive, some of the results were negative or non-significant also. The reasons of the various mixed result can be by using different methods, different TQM variables, and different performance measures in their research study, studies were performed in different countries and industries, and barriers to TQM practices in differ-ent countries and industries. Research with suitable methodologies and measuring tools can significantly contribute to investigating the relationship between TQM practices and perfor-mance.

The objective of this study was to find the effects of TQM practices on performance viz., quality performance, operational performance and industry performance, and to investigate the relationship between TQM practices and performances by using appropriate statistical analysis methods. This empirical study was conducted at Gafat Armament Industry, Bishof-tu, Ethiopia.

2. TQM PRACTICES AND PERFORMANCE

Overall TQM Practices: Most of the studies has reported that overall TQM practices have positively related to productivity and manufacturing performance (Chenhall, 1997; Mann and Kehoe 1994), quality performance (Prajogo and Hong, 2008; Fuentes et al., 2006; Lee et al., 2003; Curkovic et al, 2000), employee satisfaction/performance (Sadikoglu and Zehir, 2010; Fuentes et al., 2006), customer satisfaction/results (Fuentes et al., 2006; Das et al., 2000), and aggregate firm performance (Sadikoglu and Zehir, 2010; Sharma, 2006; Kaynak, 2003; Merino-Diaz de Cerio, 2003; Brah et al., 2002; Douglas and Judge Jr., 2001). However, some studies have shown negative or insignificant results (Prajogo and Sohal, 2006; Sadikoglu, 2004). Thus, based on the literature reviewed, the following hypothesis (H) was proposed.

H1: TQM practices are positively related to performance.

Leadership: Top management commitment and participation in TQM practices are the most important factors for the success of TQM practices. Managers should demonstrate more leadership than traditional management behaviors to increase employees' awareness of quality activities in TQM adoption and practices (Goetsch and Davis, 2010; Criado and Calvo-Mora, 2009).

Previous studies results have shown that leadership improves operational performance (Phan et al., 2011; Ahire and O'Shaughnessy, 1998), employee performance (Phan et al., 2011; Samson and Terziovski, 1999), customer results (Parast and Adams, 2012), and overall firm performance (Macinati, 2008; Zu et al., 2008). TQM theory holds that, with a full commitment to a total quality setting, leaders can organize and synergize people's activities to achieve the common goal of the organization. Thus, based on the literature reviewed, the following hypothesis was proposed.

H2: Leadership is positively related to performance.

Supplier Management: Supply chain management in TQM implies reducing and streamlining the supplier base to facilitate managing supplier relationships (Krause, 1997), developing strategic alliances with suppliers (Copacino, 1996; Mason, 1996), working with suppliers to ensure that expectations are met (Watts and Hahn, 1993), and involving suppliers early in the product development process to take advantage of their capabilities and expertise (Ragatz et al., 1997; Monczka et al., 1994).

Previous studies results have shown that supplier quality management positively affects operational performance (Phan et al., 2011; Kannan and Tan, 2005) and overall firm performance (Zehir and Sadikoglu, 2012). Thus, based on the literature reviewed, the following hypothesis was proposed.

H3: Supplier quality management is positively related to performance.

Training: Effective training in management and improvement in quality bring success for the firms. Employees' effective knowledge and learning capability will provide sustainability of quality management in the firm. Training should be given to all employees based on the results of the training needs assessment (Goetsch and Davis, 2010; Criado and Calvo-Mora, 2009).

Previous studies results have shown that training is positively related to operational performance (Phan et al., 2011; Kaynak, 2003), employee performance (MacKelprang et al., 2012; Fuentes et al., 2006), customer results (Phan et al., 2011; Das et al., 2000), and aggregate firm performance (MacKelprang et al., 2012; Tari et al., 2007), while others report negative/insignificant results (Rungtusanatham et al., 1998). Thus, based on the literature reviewed, the following hypothesis was proposed.

H4: Training is positively related to performance.

Customer Focus: TQM firms focus on serving the external customers. They first should know the customers expectations and requirements and then should offer the products/services, accordingly. When customer expectations are met, their satisfaction will be increased, and the firm's sales and the market share will increase. Previous studies results have shown that customer focus positively affects operational performance (Phan et al., 2011; Tari and Claver, 2008; Terziovski et al., 2003), employee performance (Tari and Claver, 2008; Samson and Terziovski, 1999), customer satisfaction/results (Phan et al., 2011; Tari and Claver, 2008), and aggregate firm performance (Zehir and Sadikoglu, 2012; Joiner, 2007). Thus, based on the literature reviewed, the following hypothesis was proposed.

H5: Customer focus is positively related to performance.

Strategic Quality Planning: Strategic quality planning includes vision, mission, and values of the firms. They are formed by taking into account the quality concept. With effective strategic quality planning efforts employees

are taken as an input in developing the vision, mission, strategies, and objectives. This facilitates acceptance and support of strategic quality plans by the employees.

Previous studies results have shown that strategic quality planning is positively associated with operational performance, inventory management performance (Phan et al., 2011; Ittner and Larcker, 1997), customer results, and market performance (Macinati, 2008). However, strategic quality planning is not statistically related to perceived performance in the computer industry (Ittner and Larcker, 1997). Thus, based on the literature reviewed, the following hypothesis was proposed.

H6: Strategic quality planning is positively related to performance.

Information and Analysis: Managers should make decisions based on analysis of relevant data and information. Organizations measure, analyze, and review data and information to achieve strategic objectives and to anticipate and respond to any organizational or external changes. Managers in a total quality setting provide reliable, high-quality, and timely data and information for all key users, including employees and suppliers, to improve organizational efficiency, effectiveness, and innovation. Business needs and strategy determine the measures that will provide the critical data and information for decision-making (National Institute of Standards and Technology, 2006). Thus, based on the literature reviewed, the following hypothesis was proposed.

H7: Information and analysis is positively related to performance.

3. THEORETICAL BACKGROUND

After thoroughly reviewed the literature, the TQM factors developed in the questionnaire were leadership (LS), training (TR), supplier management (SM), customer focus (CF), strate-gic quality planning (SQP), and information analysis (IA), and the performance measures were quality performance (QP), operational performance (OPP), and industry performance (IP), these factor areas have often been considered the critical factors of TQM (Farish et al., 2017, Sila, 2007; Fuentes et al., 2004; Kaynak, 2003).

4. RESEARCH METHODOLOGY

4.1. Measurement Instrument

Based on the literature review eight factors (i.e., Independent variables) viz., leadership (LS), training (TR), supplier management (SM), customer focus (CF), strategic quality planning (SQP), and information analysis (IA), were taken as the TQM practices. Under performance, dependent variables include three performance factors, viz, quality performance (QP), operational performance (OPP), and industry performance (IP), to cover aspects of industry performance. Also, TQM index (TQMI) was used as a composite variable of TQM practices (Sadikoglu and Zehir, 2010). Items in the questionnaire were adopted from various studies discussed in literature review part of this study.

The initial questionnaire included 90 TQM practices items and 33 performance items, respectively. Thirty-three items for the TQM practices and 16 items for the performance measures remained after exploratory factor analysis (EFA) and reliability analysis. Questionnaire items were based on a five point Likert - type scale anchored from strongly disagree - 1 to strongly agree - 5, which indicates respondents' disagreement or agreement with each item, respectively.

4.2. Population and Sample

Cross-sectional survey methodology was used and the unit of the sample was at the six operational department's level under industry. Two hundred fifty questionnaires (in Amharic and English languages) were distributed during the working hours of the industry.

4.3. Data Collection Process

Questionnaire was modified based on the suggestions and comments given by the industry representatives (respondents), managers, and academicians. Questionnaire pilot study was also conducted to revise the questionnaire and feedback was also collected from respondents to make it simple, clear, understandable, and easy-to-follow.

Respondent's confidentiality has been maintained to improve accuracy of responses and response rate. Questionnaires were administered as per the guidelines of the follow-up stages given by Saunders et al. (2007) in order to increase response rate. Questionnaire survey was conducted as follows. First, recipients were informed about the survey and questionnaire by face-to-face conversation. Second, survey was conducted with a cover letter during working hours of industry, when the recipients were likely to be receptive. Finally, questionnaires were collected back within short period of time and cross checked whether filled properly or not to increase the response rate. Two hundred forty four usable questionnaires were obtained, with a good response rate of 97.6 percent.

4.4. Statistical Analysis

Before performing principal component analysis, the homogeneity of the data for sample adequacy was measured. The Kaiser-Meyer-Olikin (KMO) measure of sampling is greater than the "middling" value of 0.7 and the result of Barlett's test is less than 0.05 (Tables 1 and 2). Thus, the data have homogeneity and adequacy for principal component analysis.

EFA was conducted to establish factorial validity and to confirm whether or not the theorized dimensions emerge. EFA analysis showed that the factors were logic and reflected accurately what was intended to be measured. Principle components extraction with varimax rotation was used to identify factors with Eigen values of at least one in order to obtain more easily interpreted factor loadings. A bi-variate correlation analysis was also performed to identify the correlation of TQM factors with each other and with the measures of industry performances. Multiple regression analysis was used for each performance measure to figure out the relationship between TQM practices and performance. The TQM index (TQMI) equals the aggregate of all TQM factors (Sadikoglu and Zehir, 2010).

5. RESULTS

5.1. Results of the EFA, Reliability, Descriptive Statistics, and Correlations

EFA was performed for TQM practices and performance measures separately. After EFA and reliability analysis, the final measurement instrument included 33 TQM items and 16 performance measurement items. As clearly noticed from Tables 1 and 2, the TQM items explained 61.968 percent of the total variance, and performance measurement items explained 61.539 percent of the total variance, with the Eigen value of more than one, respectively. Specifically, leadership included eight items that explained 14.616 percent of the total variance, supplier management included seven items that explained 13.896 percent of the total variance, training included six items that explained 11.230 percent of the total variance, customer focus included six items that explained 9.225 percent of the total variance, strategic quality planning included three items that explained 6.648 percent of the total variance, and information analysis included five items that explained 6.353 percent of the total variance.

Table 2 shows that quality performance (QP) had six items that explained 23.651 percent of the total variance, operational performance (OPP) had six items that explained 22.247 percent of the total variance, and industry performance (IP) had four items that explained 15.641 percent of the total variance. The factors had content validity, since the questionnaire items were adapted from previous research studies.

As shown in Tables 1 and 2, all factor loadings and communalities of TQM practices scale and performance measures exceed the 0.50 threshold.

Table 3 show descriptive statistics, Cronbach's alpha values, and Pearson correlations for the variables in the study model. As all the factor loadings values were greater than 0.40, therefore unidimensionality and construct validity of the measures were satisfied. Cronbach's alpha values of the factors were between 0.703 and 0.948, which surpasses the 0.70 threshold. This showed that all TQM practices and performance scales had acceptable reliabilities.

Table 1: Rotated factor matrix of the TQM practices

Variables	Component						Communalities	
	1	2	3	4	5	6	Initial	Extraction
LS1	0.797						1.000	0.721
LS2	0.742						1.000	0.622
LS3	0.737						1.000	0.671
LS4	0.680						1.000	0.606
LS5	0.675						1.000	0.565
LS6	0.656						1.000	0.633
LS7	0.608						1.000	0.570
LS8	0.576						1.000	0.544
SM1		0.751					1.000	0.677
SM2		0.748					1.000	0.692
SM3		0.745					1.000	0.705
SM4		0.682					1.000	0.600
SM5		0.666					1.000	0.625
SM6		0.646					1.000	0.497
SM7		0.612					1.000	0.560
TR1			0.761				1.000	0.685
TR2			0.737				1.000	0.630
TR3			0.714				1.000	0.645
TR4			0.604				1.000	0.576
TR5			0.591				1.000	0.608
TR6			0.572				1.000	0.538
CF1				0.711			1.000	0.619
CF2				0.677			1.000	0.661
CF3				0.648			1.000	0.548
CF4				0.601			1.000	0.633
CF5				0.526			1.000	0.539
CF6				0.428			1.000	0.528
SQP1					0.692		1.000	0.674
SQP2					0.686		1.000	0.735
SQP3					0.683		1.000	0.737
IA1						0.719	1.000	0.630
IA2						0.663	1.000	0.646
IA3						0.587	1.000	0.530
Eigen value:	12.506	2.717	1.666	1.280	1.207	1.074		
Percentage variance explained by factor:	14.616	13.896	11.230	9.225	6.648	6.353		
Percentage total variance explained:	14.616	28.512	39.742	48.967	55.615	61.968		
Extraction Method: Principal Component Analysis. Rotation Method: Varimax with Kaiser Normalization.								
a. Rotation converged in 7 iterations								
KMO = 0.930, Barlett's Test of Sphericity: Chi-Square = 4344.426, df = 528, Sig. = 0.000								

In this study, a company achieving a level of TQM practices implementation above the mean value of 3 is regarded as having a 'positive' level of implementation. This means that the company has taken conscientious efforts to practice TQM or to implement TQM systems; whereas a company with a level of TQM implementation below the mean value of 3 would indicate that it lacks the effort to practice TQM or to implement TQM systems (Lai et al., 2002).

Table 3, show that the mean values of TQM practices were less than three. This means that the industry, in general, have implemented less TQM practices (Lai et al., 2002). As per Table 3, study has found that all factors are positively correlated with each other at the significance level of $p < 0.01$ (2-tailed). The measures have face validity because the

Table 2: Rotated factor matrix of the industry performances

Variables	Component			Communalities	
	1	2	3	Initial	Extraction
QP1	0.778			1.000	0.689
QP2	0.759			1.000	0.667
QP3	0.745			1.000	0.687
QP4	0.734			1.000	0.615
QP5	0.636			1.000	0.497
QP6	0.592			1.000	0.465
OPP1		0.784		1.000	0.695
OPP2		0.772		1.000	0.698
OPP3		0.757		1.000	0.691
OPP4		0.681		1.000	0.682
OPP5		0.609		1.000	0.533
OPP6		0.609		1.000	0.488
IP1			0.802	1.000	0.745
IP2			0.677	1.000	0.552
IP3			0.626	1.000	0.563
IP4			0.611	1.000	0.577
Eigen value:	7.362	1.441	1.043		
Percentage variance explained by factor:	23.651	22.247	15.641		
Percentage total variance explained:	23.651	45.898	61.539		
Extraction Method: Principal Component Analysis. Rotation Method: Varimax with Kaiser Normalization.					
a. Rotation converged in 6 iterations.					
KMO = 0.923, Barlett's Test of Sphericity: Chi-Square = 1933.088, df = 120, Sig. = 0.000					

Table 3: Descriptive statistics, Cronbach's alpha, and bi-variate correlation for the variables in the research model

Variables		1	2	3	4	5	6	7	8	9	10
1.	LS	0.890									
2.	SM	0.490	0.867								
3.	TR	0.505	0.598	0.861							
4.	CF	0.674	0.547	0.616	0.839						
5.	SQP	0.419	0.604	0.589	0.518	0.840					
6.	IA	0.422	0.559	0.561	0.485	0.559	0.703				
7.	QP	0.529	0.590	0.531	0.531	0.604	0.530	0.864			
8.	OPP	0.465	0.619	0.607	0.516	0.506	0.510	0.619	0.870		
9.	IP	0.419	0.697	0.613	0.515	0.567	0.606	0.634	0.644	0.782	
10.	TQMI	0.699	0.815	0.807	0.768	0.771	0.745	0.792	0.783	0.818	0.948
Mean		2.383	2.674	2.663	2.429	2.535	2.431	2.389	2.671	2.852	2.559
Std. Dev.		0.737	0.724	0.801	0.709	0.804	0.706	0.702	0.727	0.823	0.582
No. Items		8	6	6	6	3	3	6	6	4	33

Note: N = 244; all correlations are significant at the p < 0.01 level (2-tailed). Values on the diagonal are Cronbach's alpha

questionnaire was refined with respect to feedback from the manag-ers and academicians and the results of the pilot study. The bi-variate correlations among the TQM factors (i.e., LS, SM, TR, CF, SQP, and IA) range from 0.419 to 0.674. The correla-tions between the TQM practices and performance measures (i.e., QP, OPP, and IP) range from 0.419 to 0.697. The correlations among the performance measures range from 0.34 to 0.66. The measures have discriminant validity since the correlation coefficients between the TQM practices and performance measures are lower than the reliability coefficients. There is a strong criterion-related validity since the bi-variate correlations of the TQM practices with

performance measures are statistically significant. Table 3, revealed that the correlation coef-ficients values of independent variables are less than 0.8, which indicates that results will be close to true value, and their multicollinearity does not have an undue effect on the regression models (Asher, 1983).

5.2. Results of the Regression Analyses between TQM Practices and Performance

Before conducting regression analysis normality assumption was satisfied. Collinearity statis-tics was performed. Tolerance and variance inflation factor (VIF) was measured to assess in-flation in parameter estimates that are due to collineaities among TQM practices (multicolline-arity) in the multiple regression analysis. Since, tolerance and VIF values of all TQM variables were less than 3, their multicollinearity did not have an undue effect.

Table 4 shows the results of the regression analysis between TQMI and the various perfor-mance measures. All regression models are significant ($p < 0.01$) and TQMI is significantly and positively related to performance. This shows that TQM practices, in general, improve industry performance.

Table 4: Results of the regression analysis between TQM index and performance measures

Dependent variable: Performance	Independent variable: TQM index (TQMI)						
	β	t	p	Result	R^2	R^2 Adj.	F
Regression 1: QP	0.657	20.198	0.000	Sig.	0.628	0.626	407.971
Regression 2: OPP	0.627	19.561	0.000	Sig.	0.613	0.611	382.648
Regression 3: IP	0.579	22.163	0.000	Sig.	0.670	0.669	491.177

Table 5: Results of the regression analysis between TQM practices and quality, operational, industry performance

Dependent variables	Independent variable: Quality performance (QP)							
	β	t	p	Result	R^2	R^2 Adj.	F	Sig.
LS	0.195	3.238	0.001	Insignificant	0.510	0.498	41.104	0.000
SM	0.190	3.025	0.003	Insignificant				
TR	0.037	0.639	0.524	Insignificant				
CF	0.054	0.774	0.440	Insignificant				
SQP	0.238	4.306	0.000	Significant				
IA	0.131	2.169	0.031	Insignificant				
Dependent variables	Independent Variable: Operational performance (OPP)							
	β	t	p	Result	R^2	R^2 Adj.	F	Sig.
LS	0.078	1.236	0.218	Insignificant	0.492	0.480	38.315	0.000
SM	0.307	4.617	0.000	Significant				
TR	0.239	3.863	0.000	Significant				
CF	0.062	0.845	0.399	Insignificant				
SQP	0.039	0.670	0.504	Insignificant				
IA	0.109	1.712	0.088	Insignificant				
Dependent variables	Independent Variable: Industry performance (IP)							
	β	t	p	Result	R^2	R^2 Adj.	F	Sig.
LS	-0.041	-0.626	0.532	Insignificant	0.586	0.576	55.927	0.000
SM	0.457	6.728	0.000	Significant				
TR	0.191	3.017	0.003	Insignificant				
CF	0.069	0.918	0.359	Insignificant				
SQP	0.078	1.309	0.192	Insignificant				
IA	0.258	3.979	0.000	Significant				

Table 5 present the results of the regression analysis between the TQM practices and quality performance (QP), operational performance (OPP), and industry performance (IP), respective-ly. In all regression tables, the regression models are statistically significant ($p < 0.001$). The coefficient of multiple determination, R2, shows the proportion of variation of the dependent variable accounted for by the independent variables in the regression model. R2 values of all regression models are greater than 0.35 that can be interpreted strong effect (Cohen, 1988).

5.3. Discussion, Managerial Implications, and Conclusion

5.3.1. Discussion of the Analyses

The study has found that TQM index is positively related to all performance measures (i.e., QP, OPP, and IP). Hence, hypothesis (H1) is accepted. TQM practices, in general, improve performance of the industry. Moreover, the study has found that different TQM practices significantly affect different outcomes. Although leadership and customer focus are not significantly related to any performance measures. Hence, hypotheses (H2) and (H5) are rejected.

It has been found that supplier management is positively related to operational and industry performance (H3-Accpected). An industry cannot improve its performance without the collaboration among the supply chain partners. When suppliers have quality management systems, they are evaluated with respect to quality and delivery performance and participate in quality training, process improvement, and the new product development process.

It has been found that training is positively related to operational performance (H4-Accpected). Educated employees will increase the quality of products and services. Effective training on quality also reduces the time needed for designing and manufacturing products. Educated employees will increase the capacity to meet customer's requirements in time. Effective training increases employee's flexibility skills to adopt production to different volumes of demand.

It has been found that strategic quality planning is positively related to quality performance. Hence, hypothesis (H6) is accepted. Strategic quality planning will keep equipment and processes under statistical quality control on the production shop floor and charts will posted to determine whether manufacturing process are in control or not. Statistical process control is used to monitor the process.

It has been found that information analysis is positively related to industry performance. Hence, hypothesis (H7) is accepted. Industry uses quality data are used as a tool to manage quality to enhance its performance. By using information and analysis product specification are provided to increase performance. Thoroughness of new products and services design reviewed before the products and services are produced and marketed.

5.3.2. Managerial Implications

The positive relationship between TQM practices and performance measures shows the importance of each of these practices to improve sustainability. The reasons of TQM implantations may guide managers on how to motivate employees in these applications in order to improve industry performance.

6. CONCLUSION

TQM is a holistic and ethical approach of the industry to continuously improve their prod-ucts/services or processes involving all stakeholders in order to satisfy their customers and to improve performance and sustainability. The results give that overall TQM practices improve all performance measures. Leadership does not affect performance. This is supported by the results of Choi and Eboch (1998), and Kannan and Tan (2005). It has been found that suc-cessful supplier management enhances operational performance and industry performance. Successful training improves operational performance. A customer focus effort does not af-fect any performance. Effective strategic quality planning enhances quality performance. Al-so, information analysis improves industry performance.

It can be concluded that TQM practices improve various performance measures in the indus-try. All aspects of TQM practices should be effectively managed in an industry because each factor in TQM practices improves different aspects of industry performance. The synergy among the TQM factors brings about exceptional or crucial improvements in the industry per-formances.

REFERENCES

Ahire, S.L. and O'Shaughnessy, K.C. (1998): The role of top management commitment in quality management: An empirical analysis of the auto parts industry. *International Journal of Quality Science*, 3(1): 5-37.

Asher, H.B. (1983): *Causal modeling, Sage Publications*, Beverly Hills, Calif, USA.
Brah, S.A., Tee, S.L., and Rao, B.M. (2002): Relationship between TQM and performance of Singapore companies. International *Journal of Quality and Reliability Management*, 19(4): 356-379.
Chenhall, R.H. (1997): Reliance on manufacturing performance measures, total quality management and organizational performance. *Management Accounting Research*, 8(2): 187-206.
Choi, T.Y. and Eboch, K. (1998): The TQM Paradox: Relations among TQM practices, plant performance, and customer satisfaction. *Journal of Operations Management*, 17(1): 59-75.
Cohen, J. (1988): *Statistical power analysis for the behavioral sciences*. 2nd edn. Lawrence Erlbaum Associates.
Copacino, W.C. (1996): Seven supply-chain principles. *Traffic Management*, 35(1): 60.
Criado, F. and Calvo-Mora, A. (2009): Excellence profiles in Spanish firms with quality management systems. *Total Quality Management*, 20(6): 655-679.
Curkovic, S., Vickery, S., and Droge, C. (2000): Quality-related action programs: their impact on quality performance and firm performance. *Decision Sciences*, 31(4): 885-904.
Das, A., Handfield, R.B., Calantone, R.J., and Ghosh, S. (2000): A contingent view of quality management: The impact of international competition on quality. *Decision Sciences*, 31(3): 649-689.
Douglas, T.J. and Judge Jr., W.Q. (2001): Total quality management implementation and competitive advantage: the role of structural control and exploration. *Academy of Management Journal*, 44(1): 158-169.
Farish, K.A. Anu, P.A., and Satish K.P. (2017): Effect of TQM practices on financial performance through innovation performance in Indian manufacturing context. *International Research Journal of Engineering and Technology*, 04(07): 2650-2655.
Fuentes, M.M.F., Montes, F.J.L., and Fernandez, L.M. (2006): Total quality management, strategic orientation and organizational performance: The case of Spanish companies. *Total Quality Management and Business Excellence*, 17(3): 303-323.
Goetsch, D.L. and Davis, S.B. (2010): *Quality management for organizational excellence*. 6th edn. Pearson, NJ, USA.
Ittner, C.D. and Larcker, D.F. (1997): Quality strategy, strategic control systems, and organizational performance. *Accounting, Organizations and Society*, 22(3-4): 293-314.
Joiner, T.A. (2007): Total quality management and performance: The role of organization support and co-worker support. *International Journal of Quality and Reliability Management*, 24(6): 617-627.
Kannan, V.R. and Tan, K.C. (2005): Just in time, total quality management, and supply chain management: understanding their linkages and impact on business performance. *Omega*, 33(2): 153-162.
Kaynak, H. (2003): The relationship between total quality management practices and their effects on firm performance. *Journal of Operations Management*, 21(4): 405-435.
Krause, D.R. (1997): Supplier development: Current practices and outcomes. *International Journal of Purchasing and Materials Management*, 33(2): 12-19.
Lai, K.H., Weerakoon, T.S., and Cheng, T.C.E. (2002): The state of quality management implementation: A cross-sectional study of quality-oriented companies in Hong Kong. *Total Quality Management*, 13(1): 29-38.
Lee, S.M., Rho, B.H., and Lee, S.G. (2003): Impact of Malcolm Baldrige national quality award criteria on organizational quality performance. *International Journal of Production Research*, 41(9): 2003-2020.
Macinati, M.S. (2008): The relationship between quality management systems and organizational performance in the Italian National Health Service. *Health Policy*, 85(2): 228-241.
MacKelprang, A.W., Jayaram, J., and Xu, K. (2012): The influence of types of training on service system performance in mass service and service shop operations. *International Journal of Production Economics*, 138(1): 183-194.
Mann, R. and Kehoe, D. (1994): An evaluation of the effects of quality improvement activities on business performance. *The International Journal of Quality and Reliability and Management*, 11: 29-44.
Mason, T. (1996): Getting your suppliers on the team. *Logistics Focus*, 4(1): 10-22.
Merino-Diaz de Cerio, J. (2003): Quality management practices and operational performance: Empirical evidence for Spanish industry. *International Journal of Production Research*, 41(12): 2763-2786.
Monczka, R.M., Trent, R.J., and Callahan, T.J. (1994): Supply base strategies to maximize supplier performance. *International Journal of Physical Distribution and Logistics*, 24(1): 42-54.
Nair, A. (2006): Meta-analysis of the relationship between quality management practices and firm performance-implications for quality management theory development. *Journal of Operations Management*, 24(6): 948-975.
National Institute of Standards and Technology: Criteria for performance excellence (2006): Baldrige National Quality Program, /http://www.quality.nist.gov/ *Business_Criteria.htm*, 43-44.
Parast, M.M. and Adams, S.G. (2012): Corporate social responsibility, benchmarking, and organizational performance in the petroleum industry: a quality management perspective. *International Journal of Production Economics*, 139: 447-458.

Phan, A.C., Abdallah, A.B., and Matsui, Y. (2011): Quality management practices and competitive performance: Empirical evidence from Japanese manufacturing companies. *International Journal of Production Economics*, 133(2): 518-529.

Prajogo, D.I. and Hong, S.W. (2008): The effect of TQM on performance in R and D environments: A perspective from South Korean firms. *Technovation*, 28(12): 855-863.

Prajogo, D.I. and Sohal, A.S. (2006): The integration of TQM and technology/R and D management in determining quality and innovation performance. *Omega*, 34(3): 296-312.

Ragatz, G.L., Handfield, R.B. and Scannell, T.V. (1997): Success factors for integrating suppliers into new product development. *Journal of Product Innovation Management*, 14(3): 190-202.

Rungtusanatham, M., Forza, C., Filippini, R., and Anderson, J.C. (1998): A replication study of a theory of quality management underlying the Deming management method: Insights from an Italian context. *Journal of Operations Management*, 17(1): 77-95.

Sadikoglu, E. and Zehir, C. (2010): Investigating the effects of innovation and employee performance on the relationship between total quality management practices and firm performance: An empirical study of Turkish firms. *International Journal of Production Economics*, 127(1): 13-26.

Sadikoglu, E. (2004): Total quality management: context and performance. *The Journal of American Academy of Business*, 5(1-2): 364-366.

Samson, D. and Terziovski, M. (1999): Relationship between total quality management practices and operational performance. *Journal of Operations Management*, 17(4): 393-409.

Saunders, M., Lewis, P., and Thornhill, A. (2007): *Research methods for business students*. 4th edn. Prentice Hall.

Sharma, B. (2006): Quality management dimensions, contextual factors and performance: An empirical investigation. *Total Quality Management and Business Excellence*, 17(9): 1231-1244.

Sila, I. (2007): Examining the effects of contextual factors on TQM and performance through the lens of organizational theories: An empirical study. *Journal of Operations Management*, 25(1): 83-109.

Tari, J.J. and Claver, E. (2008): The individual effects of total quality management on customers, people and society results and quality performance in SMEs. *Quality and Reliability Engineering International*, 24(2): 199-211.

Tari, J.J., Molina, J.F., and Castejon, J.L. (2007): The relationship between quality management practices and their effects on quality outcomes. *European Journal of Operational Research*, 183: 483-501.

Terziovski, M., Power, D., and Sohal, A.S. (2003): The longitudinal effects of the ISO 9000 certification process on business performance. *European Journal of Operational Research*, 146(3): 580-595.

Watts, C.A. and Hahn, C.K. (1993): Supplier development programs: An empirical Analysis. *International Journal of Purchasing and Materials Management*, 24(2): 10-17.

Zehir, C. and Sadikoglu, E. (2012): Relationships among total quality management practices: An empirical study in Turkish Industry. *International Journal of Performability Engineering*, 8(6): 667-678.

Zu, X., Fredendall, L.D., and Douglas, T.J. (2008): The evolving theory of quality management: the role of Six Sigma. *Journal of Operations Management*, 26(5): 630-650

Wind Resource Potential Assessment and implication for climate change mitigation: the case of Bale Zone, South Eastern Ethiopia

Mekuria Tefera[1,*] and Kassahun Ture[2]

[1]*Department of Environmental Science, Wollega University, Ethiopia*
[2]*Department of Physics, Addis Ababa University, Addis Ababa, Ethiopia*
**Corresponding author, e-mail: mekutefera2005@gmail.com*

ABSTRACT

Wind power assessments as well as forecast of wind energy production potential are key issues in the wind energy industry. One of the necessary conditions for the development of wind power generation is to choose the optimal site. Alternative energy plays a great role for climate change mitigation, environmental protection and sustainable development. The objective of this study is to assess the distribution of wind resource based on WRF (Weather Research and Forecasting) model and its implication on climate change mitigation in Bale zone, south eastern Ethiopia. In this study, one year wind speed and wind direction at 6 hr intervals at a height of 10, 50 and 100 m from National Centers for Environmental Prediction (NCEP) were used. In addition to the model observational ground based data is obtained from National Meteorological Agency (NMA) of Ethiopia. The analysis result of the NCEP and NMA data by downscaling the model to 20 km by 20 km spatial resolution enabled to map the wind resource potential sites of Bale Zone applicable for wind mill installation. The study shows that most of the Bale zone areas have significant wind power potential to augment its current power generation. We found that wind resource potential is high during summer than winter season. Have a potential to install 10,329MW wind capacity in Bale zone. If this potential wind resource will installed, so far environment as an estimation of about more than 5 thousand hectare of forest land per year would be preserved, and subsequently, equivalent amount of about 66,294 of CO_2 would be stored per year.

Keywords: *Wind speed; Wind direction; Wind power; WRF model; Bale zone*

1. INTRODUCTION

Wind power, as an alternative clean energy source, supports environmental sustainability and possibly provides part of the solution to our energy insecurity problem (Pryor et al., 2011). Increasing the value of wind generation through the improvement of the performance of prediction systems is one of the priorities for wind energy research in the coming years (Karimiotakis et al., 2004). From the point of view of wind energy, the most striking characteristic of the wind resource is its variability. Wind is highly variable, both geographically and temporally. Furthermore, this variability persists over a very wide range of scales, both in space and time. The application of numerical weather prediction (NWP) models for the simulation of wind conditions in a given area is one of important methods. WRF is a numerical weather prediction (NWP) system designed to serve both atmospheric research and operational forecasting needs. NWP refers to the simulation and prediction of the atmosphere with a computer model, and WRF is a set of software for this. Mesoscale NWP models are essential to the forecast process, provides operational forecasting a flexible and robust platform, while offering advances in physics, numerics, and data assimilation contributed by the many research community developers (Ma et al., 2009). One of the main advantages of WRF modeling for wind resource assessment is creating of wind maps, generating of 'virtual' wind climates, and to assist in generation of synthesized long term data sets by combining observations and WRF. Since accurate assessment of local wind resources is vital for the planning and the management of wind farms, where in-situ measurements are scarce and expensive, the validated mesoscale wind field simulations can provide a suitable alternative dataset. Growing interest in harvesting wind energy requires the development of reliable methodology for estimating the wind resources. In this study, we propose a methodology for the wind resource and site assessment studies at the Mesoscale level using numerical simulations and in-situ metrological data. The aim of this work is to assess wind resource potential sites of Bale zone, Ethiopia and its implication for mitigation of climate change. We have downscaled the model in a special resolution of 20 km by 20 km in the area of interest to map areas according to their wind resource potential. Despite the course special resolution of

the model, we are able to identify wind resource potential regions of the zone. The paper is divided into the following sections. Section 1 is the introduction part. Next, in section 2 we will see the materials and methods. In this section description of the study site, the WRF model, the data used and the methodology are explained in greater detail. Section 3 presents results and discussion. Finally conclusion and recommendations are given in section 4.

2. MATERIALS AND METHODS

2.1. Study Area Descriptions

Bale zone is the second largest zone of Oromia regional state of Ethiopia (Figure 1). It has total area of 63,555 km^2 and covers 17.5% of the total area of the region. The zone has 18 districts, 33 towns, 349 rural villages. The altitude range is 300 m to 4389 m above sea level. The energy share from electricity is 10% while 90% is from traditional source such as fire wood, charcoal, kerosene, dung, crop residue based on the report of Bale Zone Finance and Economic Development Office (2013).

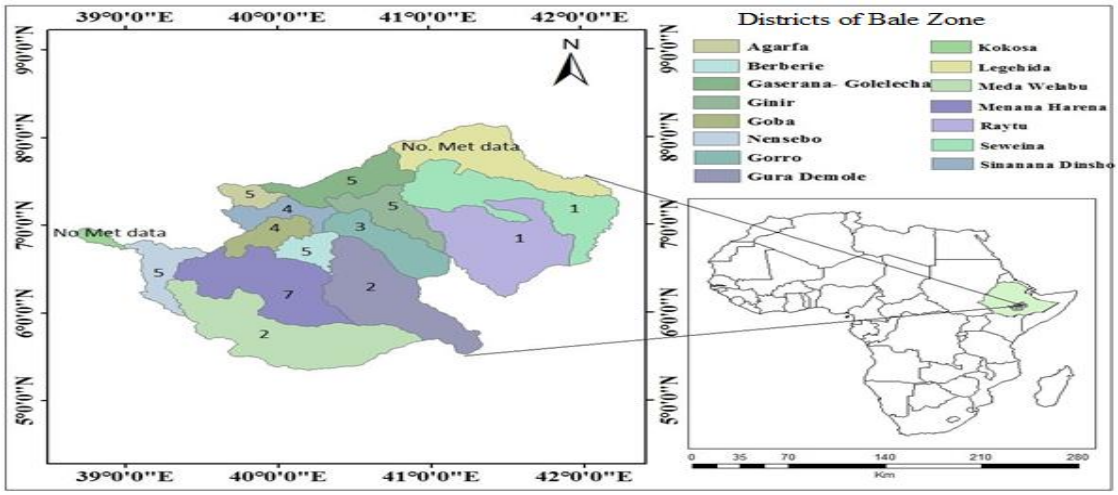

Figure 1: Geograpical map of bale zone with its districs (Numbers 1-7 show wind energy resource potentials of the districts, No Met data, indicates districts with no merological data)

Bale zone climate is highly variable from district to district. The annual average temperature of 17.5°c, maximum annual temperature 32°c and minimum annual temperature 3.5°c and receives 550 mm- 1200 mm amount of annual rainfall. The zone is characterized by a great diversity of thermal zones as a result of its wide range of altitude extent. It has classified as follows, Temperate 14.93%, Subtropical 21.53%, and Tropical 63.53% (BZFEDO, 2013).

2.2. Methodology

2.2.1. Model description

The study is based on the Weather Research and Forecasting Model (WRF, version 3.5), aired in September 2013 (Skamarock et al., 2008). WRF is a limited area meteorological model used for weather forecasting and climatic purposes. It employs an Eulerian mass-coordinate solver with a non-hydrostatic approach, and a terrain following Eta-coordinate system in the vertical. It is a state-of-the-art mesoscale model used in a variety of studies (Clifford et al., 2011; T. Haghroosta et al., 2014; J. J. Gómez-Navarro et al., 2015; P. Jimenez et al., 2013; F. J. Santos-Alamillos., 2013) among others. The WRF model is a numerical weather prediction system for both research and operational forecasting purposes. The Weather Research and Forecast (WRF) model parameters are often used to represent the interaction between different scales in the process of model calculation. Using microphysics, short wave radiation and atmospheric long wave radiation, cumulus parameterization, boundary

layer, and a physical parameterization scheme, the WRF model improves simulation results. In this study, the model used NCEP global 30-s topographic data and NCEP/NCAR (National Center for Atmospheric Research) reanalysis data as initial and lateral boundary conditions. These advanced models have the potential to improve the modeling of the wind flow, particularly in complex terrain. Low computation time to produce forecasts, and as a consequence, they update frequently their outputs.

2.2.2. Data description

Two kinds of data were used. One is observational ground data from Ethiopian National Meteorology head office, Addis Ababa, and the other is simulated data from NCAR by WRF model. The differences between the observed and simulated results were analyzed to see whether the Weather Research and Forecasting (WRF) model is able to capture the wind power resource of this location. In this study, wind speed and wind direction data at 6-hour intervals and average 1 year (2010) observations at a vertical height of 10, 50 and 100 m were used. To assess the wind power density of 1 year trend using the WRF model through dynamical downscaling, National Centers for Environmental Prediction (NCEP) Final (FNL) Operational Global Analysis data was used to verify the results. The required vertical wind speed data is available on 0.5°×0.5° grids every six hours.

2.3. Methods

The statistical analyses of the local distributions of wind speed and wind direction on Bale zone were laid for each 20 km by 20 km special resolution. Later, the wind speed and wind direction distribution maps were constructed. From the map areas of similar wind speed are categorized in one group. The average air density was evaluated from the respective elevations and the average wind power density was estimated for the winter and summer seasons. To assess its magnitude, the average value was thus estimated using the standard deviation of the wind speed normalized by the average wind speed. Finally, the energy yield and the capacity factor from the model data were calculated. Wind speed at turbine hub-height at 50 and 100m is estimated by extrapolating the wind speed from a known height (at 10 m) using the power-law relationship of Eqn1.

To estimate wind speed at turbine hub-height, it is common practice to extrapolate the wind speed from a known height (usually 10 m) using the following power-law relationship:

$$U(z) = \mathrm{Ur}\left(\frac{Z}{Z_r}\right)^{\alpha} \quad \text{.....1}$$

Where *Ur* is the reference (or measured) wind speed at a given height, z_r. *U (z)* is the estimated wind speed at height *z*, and **α** is the shear exponent and can be approximated by the Eqn 2 as stated by (Manwell *et al.*, 2009). According to them the installed capacity per km^2 at height 100 m is 5MW.

$$\alpha = 0.096 \log Z + 0.016 (\log Z)^2 + 0.24 \quad \text{.....2}$$

According to (Antonio et al., 1997) these formulations should be restricted to a height of 200 m; above this height the wind speed can be assumed to be constant.

Then to estimate the vertical profile of wind power densities across the Bale zone wind speed distributions at 50 and 100 m were used. These vertical heights are key levels as most of the wind turbine hub heights are planted around those levels. The wind power density is the energy yield proportional to the area swept by the turbine blade, air density and the velocity cubed. It is given by Eqn3.

$$\frac{P}{A} = \frac{1}{2}\rho v^3 \quad \text{.....3}$$

Where, ρ is the *average density*, *P* is the *Power*, *A* is the *area*, and *V* is the *wind speed*.

The special distribution of the density was calculated at 50 m and 100 m model levels, based on the temperature, pressure and mixing ratio (moisture effect) meteorological parameters, using the ideal gas law. Eqn.4 was used to calculate the moist air density. Dry area density is used in the standard calculations. However to account the density variations due to moisture which can affect the wind power density calculations the moisture

effects included. The temperature, pressure and mixing ratio were first extracted from the WRF model at the two levels specified above and the density was calculated using Eqn 4. Finally, the wind power density was estimated using equation 3.

$$\rho = \frac{P}{RT}\left(\frac{1+w}{1+1.6078w}\right) \ldots\ldots\ldots\ldots\ldots\ldots\ldots\ldots\ldots\ldots\ldots\ldots\ldots\ldots\ldots 4$$

Where, ρ is the average density, P is the pressure, T is the temperature, W is the mixing ratio of the universal gas constant.

3. RESULTS AND DISCUSSION

3.1. Average wind speed, wind direction and wind energy distribution

Based on the WRF model output and statistical analysis of ten year metrological data, districts are classified from super to marginal wind potential. The areas are labeled as shown in Figure 1 and Table1. However, four of wind energy resource potential districts from super to good be chosen. The ratings of the districts are made according to the classification by (Frank, 2014) and (Dennis E., 2007) as shown in Table 2. Daily mean wind speed, wind direction distribution curves of these four districts of the zone are as shown in Fig.2 (A to D). In addition curves of monthly mean wind speed and wind power density of Rayitu, Madawalabu and Robe district are depicted in Figure 3 (A to C) and wind speed is also shown in Figure 4 (A to C). Figure 2.A and Figure 3.A, shows the distribution of wind speed and direction of class1. Rayitu district is in this category. The blue bars are frequency of the wind speed and the red one shows wind direction. The average wind speed lies between 3 and 8 ms^{-1}. Days in the first half segment of the graph are winter time (October to February) while the second half days are for summer (April to August). The magnitude of wind speed in the area is high and extremely variable during summer season than the winter season. The average wind speed is V_m = 6 m s^{-1} for the summer season and 2.25 m s^{-1} for the winter season.

From direction distribution Figure 4.A, east wind and southwest wind play the main role. The main role is played by east wind in winter half years of the Northern Hemisphere and South or Southwest in summer half year of the Northern Hemisphere. This indicates significant characteristics of monsoon climate (McKnight et al., 2000) and (Ritter et al., 2006)

Table 1: Wind potential classification at 10 m

Rating	Wind power class	Wind Power density at 10 m W/m^2	Average wind Speed at 10m/s	Name of districts in similar class
1	Super	196	5.05	Dawekachen, Rayitu and Sewena
2	Outstanding	117	4.25	Beltu and Madawalabu.
3	Excellent	94	3.95	Delosebro, Gololcha, and Sinana
4	Good	43	3.05	Ginnir, Robe, Goba and Daweserer
5	Fair	13	2	Agarfa,Dinsho, Haro and Goro
6	Marginal	5	1.5	Goro, and Dalomena
7	Poor	1.5	1	Angetu, Direshekhusen,

In class 2 (see Figure 2 B), the wind speed lies between 2.5 and 7 m s^{-1}. Beltu and Madawalabu districts are in this class as shown in Table 1. Similarly, Figure 2.B is for Madawalabu district. Seen from the analysis result, there is rich wind resource around this area. In this site too, the average wind speed is not highly variable and the wind direction is more stable than the other area. The annual average model wind speed is V_m = 5 m s^{-1} at the height of 2m. Almost similar to that of the first super class, wind speed is higher from April to September. And also the curves of monthly mean wind speed and wind power density Figure 3B shows the same result. The average wind direction is almost played main role east wind in winter half year of the Northern Hemisphere and southwest wind in summer half year of the Northern Hemisphere as almost similar with the first super wind class.

And also as shown Figure 4B from direction distribution Northeast wind and Southwest wind play the main role. The wind speed distributions shows that summer have good wind distributions. In summer season the average wind direction is almost east wind but in winter the direction of the wind is southwest. Figure 2.D shows the wind

speed and direction for Robe. The wind speed lies between 1 and 5 ms-1 this is categorized under class 4. Districts in this class are Robe, Goba and Daweserer. In these areas wind speed is highly variable. But the wind direction is more variable in winter season than the summer season.

Similarly, Robe is in class 4, category. As Robe city (found in Sinana district) is closer to inland, significant change can been seen in wind speed statistics. High wind occurs from February to May which is almost different from others. For other areas have high wind and occur from April to August. This is because of geographical seasonal climate variability of the area (Jowder, 2009) and (Ashenafi et al., 2008) also found a large variability from one location to the other and also from season to season. It is highly variable, both spatially and temporally and this variability exists over a very wide range of scales. This variability is dependent on the location and weather conditions of the area. Small-scale variation is dictated by factors such as ratio of land to water, terrain, etc.

As seen from direction distribution East wind plays the main role, with Characteristics of monsoon climate which cause a seasonal change in wind direction (McKnight et al., 2000) (Figure 2.D) and Figure 3C. The wind speed lies between 1 and 5 m/s. In this areas wind speed is highly variable in summer season than the winter season. The average model wind speed is $V_m = 3.25$ m s^{-1} for the winter season and 2 m s^{-1} for the summer season.

The rainy season is often called the monsoon in Robe because it is associated with a change in the predominant wind direction; northeast winds prevail during the dry season and westerly to southwesterly winds during the rains.

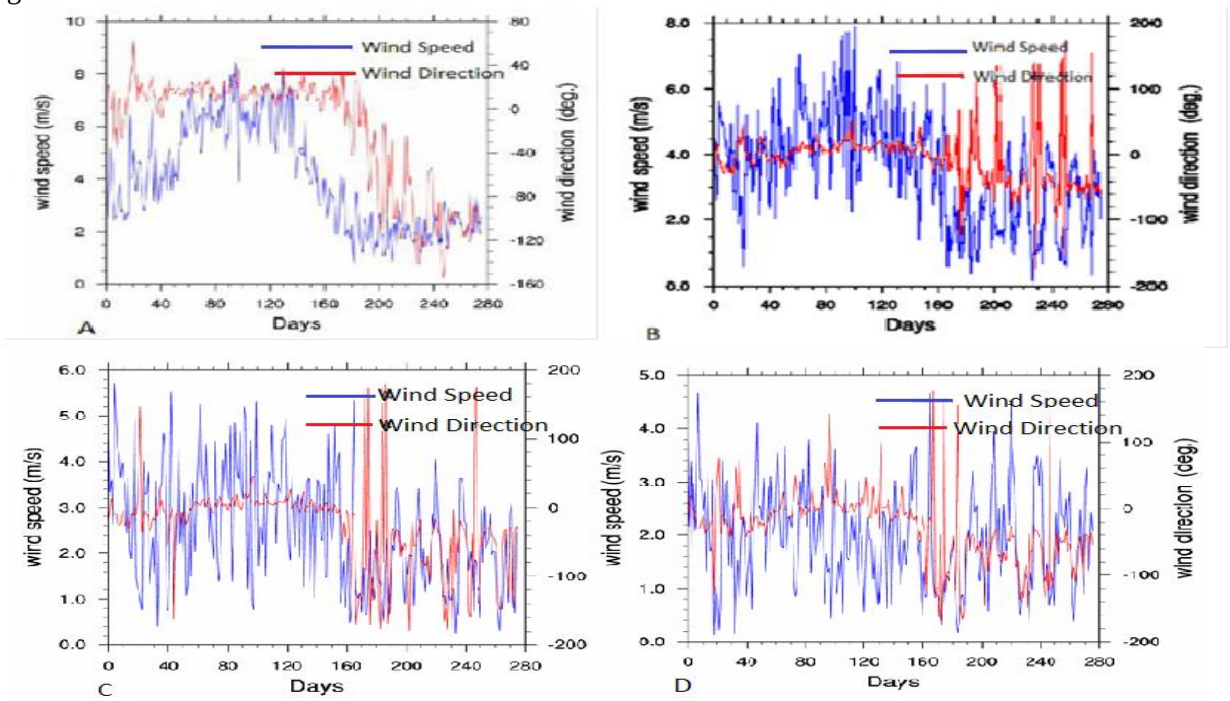

Figure 2: Daily Wind speed (blue bars) and wind direction (red bars) distribution curves of (A) Rayitu, (B) Madawalabu, (C) Meliyu and (D) Robe for the year 2010 from WRF model.

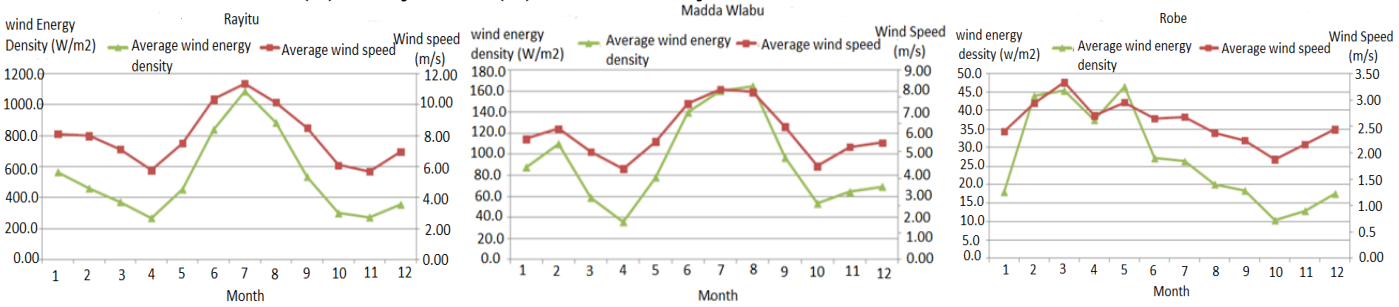

Figure 3: Curves of monthly mean wind speed and wind power density of (A) Rayitu (left), (B) Madawalabu (middle), (C) Robe (right) for the year 2010 from WRF model.

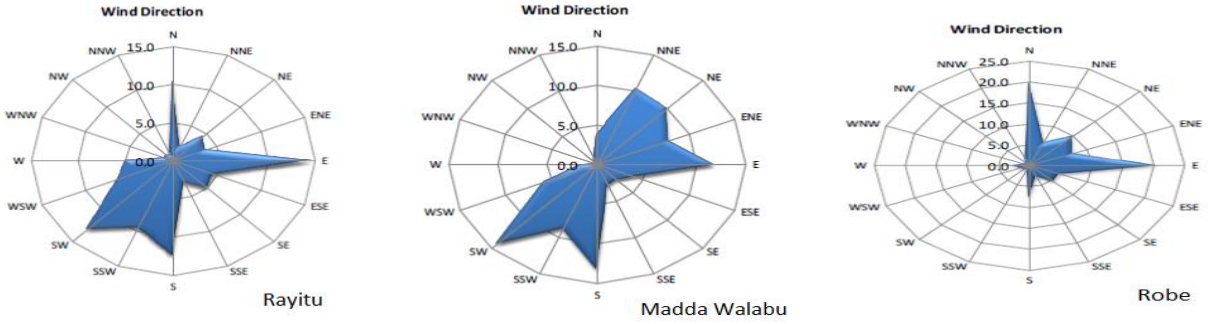

Figure 4: Direction distribution of wind speed of (A) Rayitu (left), (B) Madawalabu (middle) and (C) Robe (right) for the year 2010 from WRF Model.

3.2. Vertical profile of wind speed

Bale zone east plain region mainly Dawekachen, Rayitu, Sewena, Beltu and Madawalabu has richest wind energy resource. Strong wind power under the alternative influence of North- east trade wind zone and Southwest monsoon zone. Hence it's richest in wind energy resource reserve in Bale zone. Mean wind speed of Bale zone in east is higher in the west and southwest. In a similar study, Oumer (2013) and Derbew (2013) investigate as Ethiopia have enormous potential, wind energy resource. The study shows that in most of the Bale zone meets the requirements for assessing macro wind energy.

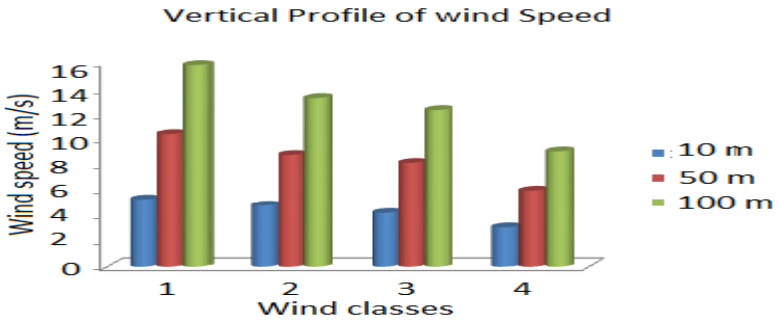

Figure 5: Good to super wind potential classification at 10, 50 and 100 m

The wind speed at 10, 50 and 100 m and the corresponding power potential at 50 m height of the four classes of wind categories are depicted in Figure 5. Our results are clearly coincide with the results obtained by Elhadidy et al., 2005 over coastal region of Saudi Arabia, they observed that wind is faster, less turbulent and yields more energy at 50m or above the ground. Alam et al. (2011) also investigates the wind speed increases with height in each class. As the height of wind speed measurement increase, the percent frequency of occurrence of higher winds also increases.

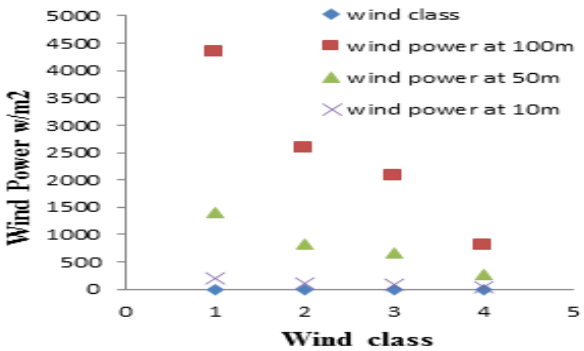

Figure 6: Wind power potential at 10, 50 and 100 m.

Similarly, wind power potential increase with height as shown in Fig 5. The average wind power densities for summer are therefore 328 Wm^{-2}, 190 Wm^{-2}, 138 Wm^{-2} and 52 Wm^{-2} for winter are 17 Wm^{-2}, 17 Wm^{-2}, 12 Wm^{-2} and 12 Wm^{-2} class1, class2, class3 and class4 respectively. The wind speed distributions show that summers have good wind distributions with > 294 W m^{-2} wind power densities. Although these methods are very vital for statistical analysis of observed wind data, mesoscale modeling provides a liberty to use the wind data at several key levels. Dennis et al. (2007) also found similar results in wind power classification for Afganistan and Pakistan. He also included in calculations by assuming installed capacity per km^2 = 5MW at 50m height.

Table 2: Super to Good wind resource. Wind resource capacity calculated at 50 and 100 m

Rating	Wind class	Wind Speed at 50 m (m/s)	Wind Speed at 100m (m/s)	Wind Power at 50 m W/m^2	Wind Power at 100m W/m^2	Land area (Km^2)	% of windy Land	Total capacity at 100 m (MW)
Super	1	10.39	15.8	1392	4331	159	0.25	794
Outstanding	2	8.75	13.3	830	2583	318	0.5	1,590
Excellent	3	8.13	12.36	665	2073	477	0.75	2,385
Good	4	5.95	9.04	261	811	1,112	1.75	5,560
Total						2,066	3.25	10,329

3.3. Total wind power density distribution over Bale zone

To estimate the wind power densities across the Bale zone wind speed distributions at 50 and 100 m were used. These vertical heights are key levels as most of the wind turbine hub heights are planted around those level values. The moist air density at 50 and 100m is 1.013 kg m^3 and 0.912 kg m^3 respectively based on Eqn.5 first by extracting the temperature, pressure and mixing ratio from the WRF model. Then by using Eqn 4 wind power density at 100 m is calculated and the estimation result is given in Table2.

Assumptions to calculate the installed capacity per km^2 = 5 MW (Frank, 2014)

Total land area of Bale zone = 63,555 km^2

Good to Excellent wind resource is 2,066 sq. km almost 3.25 % of Bale zone's total land area of 63,555 sq. km. 10,329 MW of potential installed wind capacity assumes 5MW per sq. km. And also according to Manwell et al. (2009) the installed capacity per km^2 is 5MW.

The average wind power density (Figure 6) is calculated for the class 1, class 2, class 3 and class 4 are 4331, 2583, 2073 and 811 W/m^2 at 100 m vertical heights and 1392, 830, 665 and 261 W/m^2 for the 50 m vertical heights respectively. The result shows that wind power density increases with height.

3.4. The difference between the observed and simulated wind data

The simulated WRF model output and observational ground meteorological wind data are shown in Figure 7. As shown in the figure the first one is the wind speed from simulated data and observational data. In general WRF configured with high resolution in space and time predicts accurately wind speeds over Bale zone. While the work performed was a good representative of the year, more simulations and observations are required to draw a complete confidence level of wind profiles over the study area

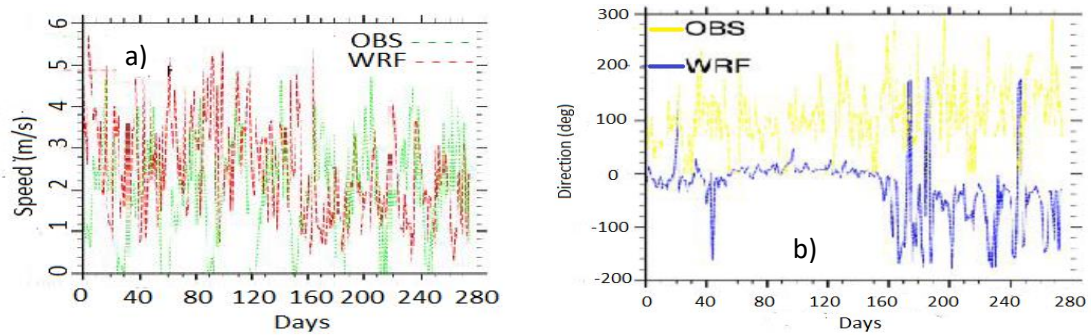

Figure 7: Comparison between observational and WRF model wind speed (a) and wind direction (b).

3.5. Environmental Analysis

Environmental conservation have economic benefits by Providing raw materials such as land, water, minerals and timber for economic production and consumption, income and employment; Generating ecological services such as pollution regulation, climate control and water catchment protection which protect natural and human resources through providing a sink for wastes and residues and maintaining essential life support functions; Giving aesthetic pleasure and holding cultural significance for many different people.

For this study the emission saved (other than carbon) from wood, charcoal and kerosene, controlling pollution by the proper use of slurry, minimization of indoor pollution due to the use of traditional fuels and the decrease of women's load are considered to be intangible, but highly rewarding. The tangible benefits are presented below.

3.5.1. Decrease in deforestation

Deforestation is defined as clearance, or clearing is the removal of a forest or stand of trees where the land is thereafter converted to a non-forest use (SAF net Dictionary, 2008). Deforestation occurs for multiple reasons: trees are cut down to be used for building or sold as fuel (sometimes in the form of charcoal or timber), while cleared land is used as pasture for livestock and plantation.

The removal of trees without sufficient reforestation has resulted in habitat damage, biodiversity loss and aridity. It has adverse impact on bio sequestration of atmospheric carbon dioxide. As of 2005, net deforestation rates have ceased to increase in countries with a per capita GDP of at least US$4,600 (Kauppi et al., 2006; The New York Times, 2009). Deforested regions typically incur significant adverse soil erosion and frequently degrade into wasteland. Deforestation causes extinction, changes to climatic conditions, desertification, and displacement of populations as observed by current conditions and in the past through the fossil record (Sahney, 2010).

This study reveals that because of huge potential wind resource in south eastern Ethiopia deforestation will be reduced. The amount of fire wood will be saved when introduce wind energy estimated and the equivalent number of trees was calculated using literature value i.e. 712 kg of dry wood is equivalent to 6 large trees (USDA forest service 2010), and to produce 1 kg of charcoal 5.21 kg of wood are required (Sepp 2014). Thus using 6trees/712 kg of wood and 1kgcharcoal/5.21 kg of wood as conversion factors, and estimating the total wind energy users into consideration, the yearly decline in deforestation is estimated and showed in Table 3.

Table 3: Annual deforestation decline rate

	Annual deforestation decline rate		
	Fire wood	Charcoal	Save forest
Percentage	59	68	65

3.5.2. Emission saving

A healthy tree stores up to 13 pounds (6 kg) of carbon annually (USDA forest service 2010; Nowak and Crane 2002). Table 3 indicates that 65% (10,549) trees will be saved annually due to wind energy dissemination in South Eastern Ethiopia if replacing some part of the fire wood and charcoal by wind energy. Besides the carbon saved, which otherwise would be released when cutting trees, about 66294 kg of carbon is stored per year.

4. CONCLUSION

In this study wind reanalysis and station metrological wind speed and direction data were analyzed to assess the wind resource potential of Bale zone. The wind speed potential increase with altitude and summer has very good wind potential than winter season. From the five months of April, May, June, July and August the wind speed statistics based on the 10 m model wind speed and direction output showed a high wind potential in June and low in November. September and March are transition months for most of the Bale zone district. The month of November also shows the lowest wind speed from winter seasons of October, November, December, January and February.

The 2D distribution of the 10m wind speed output during June, wind speed distributions of the Bale zone area showed high winds while the low elevations and valleys showed relatively low wind speeds. This will depend on many factors including but not limited to proximity to grid connection, access to area, and land use and land cover among others. In similar studies by E Streevalson et al., 2009, the crest of hills, cliffs, ridges and escarpments, the wind accelerate while near the foot and valley it will decelerate. And also discussed by Lebassi Belay et al. (2013) in wind resource assessment in Dragash-Kosovo he found that the wind close to the low level jet have higher wind resources since they get momentum transfer from the jet by eddy mixing. The valleys are relatively low wind speeds due to winds tipped in the jet toward the hill. The 50 and 100 m wind distributions also analyzed which showed higher wind speeds with similar pattern as expected. The wind power densities of the two heights showed similar patterns as the distribution of wind speeds where the high and medium elevations showed the high wind power densities.

The tropical areas of bale zone relatively have high wind power density. From the Bale zone east plain region mainly Dawekachen, Rayitu, Sewena, Beltu and Medawelabu districts are the areas with super to outstanding wind potential and Daweserer, Gololcha, Delosebro, Maliyu, Goba, Sinana and Robe town have the excellent to good wind potential area when compared with the others. This study showed that most of the Bale zone areas have significant wind power potential to augment its current power generation. Mean wind speed of Bale zone in east is higher than west and southwest wind shares higher in direction distribution. This indicates southeast of Bale zone is highly influenced by low level jet from Somalia. Hence it's richest in wind energy resource reserve in Bale zone. Therefore it meets requirements for assessing macro wind energy resource in most area over the Bale zone. Have a potential of installed 10,329MW wind capacity in Bale zone. If this potential wind resource will installed and only 10% of the population is used, so far environment as an estimation of about more than 5 thousand hectare of forest land per year would be preserved, and subsequently, equivalent amount of about 66,294 of CO**2** would be stored per year. In this study area due to lack of observational data, microscale wind modeling is challenging to accurately reproduce for any location in the area.

Recommendations

Based on the empirical findings of this study, we forward the following recommendations.

To found more accurate result it is necessary to increase spacial resolution and long term analysis is required for better results. Thus more measurements are necessary to acquire temporally high resolution meteorological data at key locations in the area. But we feel that these findings are good starting points for further study to choose optimal wind resource site in Bale zone.

Acknowledgements

We would like to extend our heartfelt thanks to Madawalabu University Research and Community service Directorate for providing financial support. Ethiopian Metrological Service (NMA) and National Centers for Environmental Prediction (NCEP) Final (FNL) Operational Global Analysis data for providing the data free of charge.

REFERENCES

Characteristics at different heights for a wind data collection tower in Saudi Arabia, World renewable energy congress, Sweden.

Antonio C., Guido C., Hans E. and René S. (1997). Vertical profiles of wind, temperature and turbulence, COST Action 710 Preprocessing of Meteorological Data for Dispersion Modelling Report of Working Group3.

AshenafiAbebe, GelanaAmente and GetachewAbebe, (2008). Short-Term Temporal Wind Speed Variability: Case Study of Dubbo Village, Journal of Chemical, Biological and Physical Sciences, an International Peer Review E-3 Journal of Sciences.

BZFEDO (Bale Zone Finance and Economic Development Office). (2013). Bale, Robe.

Clifford, Kevin Thomas. (2011). WRF-Model Performance for Wind Power Forecasting in the Coast Ranges of Central California, Master's Theses Paper 4043.

Dennis E., (2007). Wind Resource Assessment and Mapping for Afghanistan and Pakistan, National Renewable Energy Laboratory Golden, Colorado USA.

Derbew Derese (2013). Ethiopia's Renewable Energy Power Potential and Development Opportunities, Ministry of Water and Energy, Abu Dhabi.

Elhadidy, M.A. and Shaahid, S.M., (2005). Wind Resource Assessment of Eastern Coastal Region of Saudi Arabia, *Journal of the Association of Arab Universities for Basic and Applied Sciences*, 1:1-14.

Frank Kreith, Susan Krumdieck (2014). *Principles of Sustainable energy Systems*. Second edition, CRS Press, Taylor & Francis Group.

Gómez-Navarro J. J, C. C. Raible1, and S. Dierer. (2015). Sensitivity of the WRF model to PBL parameterizations and nesting techniques: evaluation of wind storms over complex terrain. *Geosci Model Dev*, 8: 3349–3363.

Haghroosta T., W. R. Ismail P. Ghafarian, and S. M. Barekati. (2014). The efficiency of the Weather Research and Forecasting (WRF) model for simulating typhoons. *Nat. Hazards Earth Syst. Sci.*, 14: 2179–2187.

Jimenez, P. A., J. Dudhia, J. F. Gonzalez-Rouco, J. P. Montavez, E. Garcia-Bustamante, J. Navarro, J. Vila-Guerau de Arellano, and A. Munoz-Roldan. (2013). An evaluation of WRF's ability to reproduce the surface wind over complex terrain based on typical circulation patterns, *J. Geophys. Res. Atmos*., 118, 7651–7669, doi:10.1002/jgrd.50585.

Jowder F. (2009). Wind power analysis and site matching on wind Turbine generators in Kingdom of Bahrain, Applied Energy.

Karimiotakis P., Pinson K. and Giebel G. (2004). The state or art in short-term prediction of wind power-from an offshore perspective. Sea Technology Week, France.1-13.

Kauppi, P. E.; Ausubel, J. H.; Fang, J.; Mather, A. S.; Sedjo, R. A.; Waggoner, P. E. (2006). Returning forests analyzed with the forest identity. *Proceedings of the National Academy of Sciences*, 103 (46): 17574

Lebassi, B, Berhane T. and Mengisteab A., (2013). Wind Resource Assessment in Dragash – Kosovo, United Nations Development Programme.

Ma Y., Huang M. and Mills G. (2009). Verification of mesoscale NWP forecasts of abrupt cold frontal wind changes. *Weather and Forecasting*, 25.

Manwell F., McGowan J. and Rogers A. (2009). *Wind Energy Explained: Theory, Design and Applications*, 2nd Edition, A John Willey and Sons, Ltd. Publications.

McKnight, Tom L; Hess, Darrel (2000). *Climate Zones and Types: The Koppen System. Physical Geography: A Landscape Appreciation. Upper Saddle River*, NJ: Prentice Hall, pg. 208, ISBN 0-13-020263-0.

Nowak, DJ., Crane, DE. (2002). Carbon storage and sequestration by urban trees in the USA. *Environmental pollution*, 116:381-389

Oumer, (2013). Wind Resource Data Analysis: The case of Myderhu project site, Tigray regional state, Ethiopia, KTH School of Industrial Engineering and Management Energy Technology EGI-2013-051MSC EKV953 Division of Heat & Power SE-100 44 Stockholm 051msc ekv953.

Pryor S. and Barthelmie R. (2011). Assessing climate change impacts on the near-term stability of the wind energy resource over the United States. *Proc Nati Acad Sci (PNAS) U S A.*, 108(20): 8167–8171.

Ritter, Michael E. (2006). The Physical Environment, an Introduction to Physical Geography.

SAFnet Dictionary Definition For deforestation. Dictionary of forestry.org (29 July 2008). Retrieved 2011-05-15.

Sahney, S., Benton, M.J. & Falcon-Lang, H.J. (2010). Rainforest collapse triggered Pennsylvanian tetrapod diversification in Euramerica. Geology 38 (12): 1079 1082. Bibcode: 2010.

Santos-Alamillos. (2013). Analysis of WRF Model Wind Estimate Sensitivity to Physics Parameterization. http://journals.ametsoc.org/doi/abs/10.1175/JAMC-D-12-0204.1, Published Online: 13 July.

Skamarock W. and Coauthors C. A. (2008). Description of the Advanced Research WRF Version 3, MMM division, NCAR Technical Note, NCAR/TN-475+STR.

Streevalsan E. (2009). Wind resource and assessment techniques. *International Journal of wind and Renewable Energy*, 3.

The New York Times (2009). *Use Energy, Get Rich and Save the Planet*, The New York Times.

USDA forest service (2010). Assessing Urban Forest Effects and Values. Chicago's Urban Forest.

Geo- Electrical Resistivity Method in Groundwater Potential Mapping: A Case Study from South Eastern part of Vikarabad District, South India

Sreedhar Kuntamalla[1] and Praveen Raj Saxena[2,*]

[1]*Department of Applied Geochemistry, University College of Science, Osmania University, Hyderabad, India*
[2]*Department of Applied Geology, School of Applied Natural Sciences, Adama Science and Technology University, Ethiopia*
**Corresponding author, e-mail: saxenapraveenraj@gmail.com*

ABSTRACT

An attempt made to identify the subsurface lithology and aquifer zones by geo-electrical resistivity method and delineation of recharge and discharge areas in parts of Vikarabad District, Telangana State, India. The study area consists of Granites, Deccan Traps and Laterites. A total of 148 Vertical Electrical Soundings (VES) were conducted to study the subsurface aquifer zones along the profiles to understand the structures across and along the lineaments. The results of the survey indicated the presence of four to five layers of overburden (0-20 Ω-m-Clay, 20-50 Ω-m- Hard Murram, 50-120 Ω-m Semi-weathered to fractured rock, 100-250 Ω-m - Fractured rock, >250 Ω-m Hard rock. Geo-electrical pseudo cross sections have been prepared based on resistivity of the soundings. From the interpretation of results potential of deeper aquifers is determined by lineaments such as faults and joints and the shallow aquifers is due to geomorphologic features and the integrated studies of geomorphological, geophysical and iso resistivity data were used to prepare a groundwater potential map. The potential for ground water in this area is moderate and the yields of the wells eventually affected by the precipitation and over utilization of water for irrigation purposes in the area.

Keywords: *Aquifers, Resistivity, Vertical Electrical Sounding (VES), Isoresistivity, Recharge and Discharge areas*

1. INTRODUCTION

The present study was carried out at South eastern part of Vikarabad district, Telangana State, South India, geographically bounded by 17° 03' to 17° 28' N latitude and 77° 75' to 78° 00' E longitude covering an area of about 381 km^2 (Figure 1). The altitude of the area ranges between 638 meters to 526 m above sea level. It receives an annual average rainfall of about 946 mm from the south west monsoon during the months of June to September and the climate is semi-arid. The maximum temperature recorded in the summer was 32°C in the summer season. Groundwater is one of the most valuable natural renewable resources and important for sustenance of life. However major population of the area depends on groundwater for day-to-day domestic, agricultural, industrial and commercial water supply depended on the rainfed agriculture. Geologically, the area is underlain by Peninsular Gneissic Complex (PGC) rocks of Precambrian crystalline granites and gneisses along with enclaves of schists (older metamorphic), basic dykes (Proterozoic) and a thin cover of Deccan Traps (Cretaceous to Paleocene) and Laterites (Pleistocene) super group. Hydro geologically, the area belongs to the Precambrian hard rock province. The groundwater occurs in semi-confined to confined conditions in fractures and compartments of aquifer system in hard rock granite (Ahmed et al. 1995; Krishnamurthy et al. 2006; Chandra et al. 2008; Dhakate et al. 2008; Sonkamble 2012; Sreedhar et al., 2018; Sakram et al., 2019). The successful exploitation of groundwater in basement terrain requires a proper understanding of its hydrogeophysical characteristics (Choudhury et al., 2001). The area suffer from acute shortage of water in rabi season effects the yield of the crop, critical irrigation becomes a challenging task for the farmers. Therefore, drilling programme for groundwater development is generally recommended by detailed geophysical investigations. The Vertical Electrical Sounding (VES) had been utilized to portray the diverse sub-surface layers (Ezeh, 2012; Sreedhar et al., 2018; Sakram et al., 2019), aquifer characteristics, the sub-surface characteristics and depth to water table (Okonkwo and Ujam, 2013; Sreedhar et al., 2018; Sakram et al., 2019).This is important in identification of hidden fractures in basement aquifers (Satpathy and Kanungo, 1976; Sreedhar et al., 2018; Sakram et al., 2019). The electrical resistivity method is an efficient and wide spread economical method for exploration of groundwater (Zohdy 1974; Lawrence and Ojo (2012); Arulprakasam et al., 2013; Sreedhar et al., 2018; Sakram et al., 2019). This study was aim at delineating suitable sites for groundwater development in the study area.

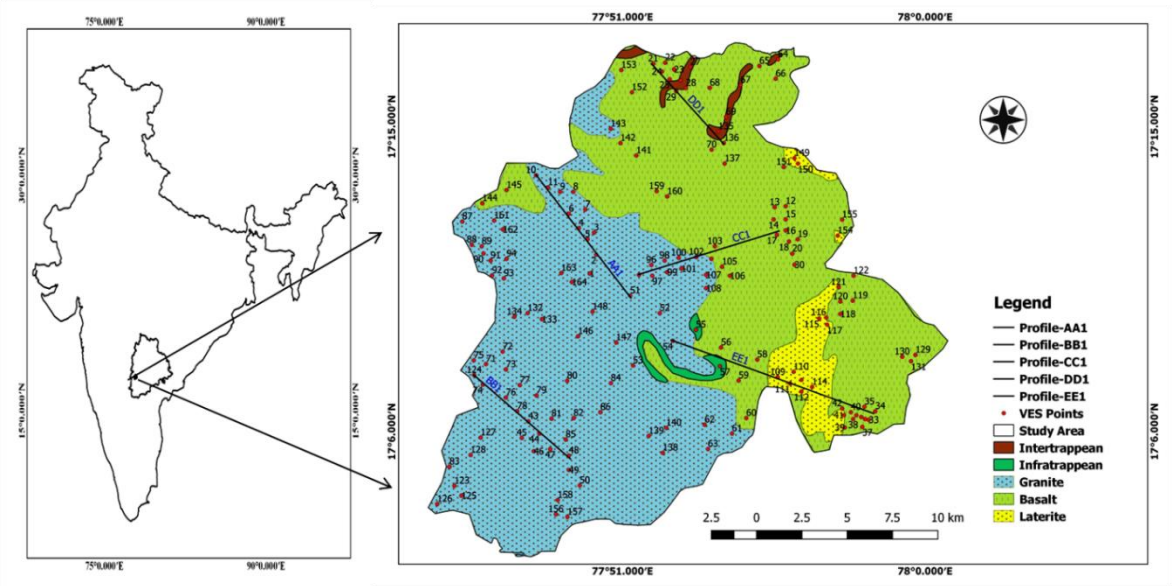

Figure 1: Location Map of the Study Area

2. MATERIAL AND METHODS

Electrical resistivity method is one of the important geophysical techniques for exploration of groundwater. The resistivity is inversely proportional to the porosity of rock and its water content present in the saturation zone. Salinity of water also an important aspect in resistivity decreases with the increase of salinity. Even the resistivity decreases with the presence of clays in the rock (Zohdy, 1974; Telford et al., 1990; Reynolds, 2011, Sreedhar et al., 2018; Sakram et al., 2019).In general for measuring the resistivities of beneath formations, four electrodes are required by passing the current (C1 and C2) two electrodes into the ground, and the resultant voltage difference at potential electrodes (P1 and P2) was determined. From the current (I) and voltage (V) values, resistivity (R) and an apparent resistivity (pa) value is calculated.

$$R = \frac{V}{I} \qquad \rho a = K.\frac{V}{I}$$

Where, V/I is the potential difference between potential electrodes to that of current flowing; and 'K' is the geometric factor which depends on the arrangement of the four electrodes.

3. RESULTS AND DISCUSSION

3.1. Resistivity Survey

The results of the survey indicates the presence of four to five layers of overburden (0-20 Ω-m-Clay, 20-50 Ω-m- Hard Murram, 50-120 Ω-m Semi-weathered to fractured rock, 100-250 Ω-m - Fractured rock, >250 Ω-m Hard rock (Ramanuja chary, 2012; CGWB, 2014-15; Sreedhar et al., 2018; Sakram et al., 2019). The field data were acquired using IGIS DDR3 instrument. About one hundred forty eight vertical electrical sounding (VES) using Schlumberger electrode array system was conducted. Only results for twenty seven VES stations were presented. The acquired data is processed using IPII2 win software programme. The software package was designed to create the layers and the pseudo-cross sections of the sounding. This method helps to eliminate the erroneous interpretations arising from manual techniques. The processed data were presented in the form of 1-D resistivity models, inferred lithologic layers and contoured maps

Table 3. 1: Interpreted model geoelectric layers and curve types from the study area

VES No.	Long.	Lat.	ρ1	h1	ρ2	h2	ρ3	h3	ρ4	h4	ρ5	Probable Composition	Groundwater Prospects
3	77.8358	17.1979	633	3.1	198	10	68.8					h1= top soil, h2=weathered zone, h3= fractured rock	Good
4	77.8282	17.2001	1549	0.8	273	1.9	57.8	19.9	107			h1=top soil, h2= weathered zone, h3= fractured rock	Good
12	77.9308	17.2109	69.6	0.8	1.08	0.5	42.4	2.3	14.8			h1= top soil, h2= clay zone, h3=fractured rock	Good
24	77.8732	17.2733	311	0.8	6.98	0.3	122	30.1				h1= top soil/murram, h2=clay zone, h3= fractured rock	Good
25	77.8787	17.2728	48.4	12	935	33	19.6					h1=top soil, h2= hard rock, h3= fractured rock	Good
26	77.8835	17.2793	32.6	12	92.7	33	0.41					h1=top soil, h2= fractured rock	Good
34	77.96979	17.11226	174	14	207	5.2	391	12	24108			h1= top soil/murram, h2=fractured rock, h3= hard rock	Good
38	77.96006	17.10209	62	11	80	0.8	112	9.9	6466			h1= top soil, h2=clay zone, h3= fractured rock	Good
39	77.96304	17.1096	44	9.1	69	3.3	143	7.5	22732			h1= top soil, h2=clay zone, h3= fractured rock	Good
47	77.8233	17.0812	19.3	2.7	313	1.8	30.7	3.7	111			h1= top soil, h2= fractured rock, h3= clay zone	Good
52	77.8863	17.1501	75	9.8	117	1.5	254	6.6	49624			h1= top soil, h2= fractured rock, h3= hard rock, h4=clay zone	Good
58	77.9042	17.0991	2581	0.8	16.7	0.1	358	35.6	1208			h1= hard rock, h2=clay zone, h3= fractured rock	Good
60	77.8922	17.0915	311	0.8	5.13	0.1	78.3	21.5	16355			h1= top soil/murram, h2= clay zone, h3=fractured rock	Good
61	77.927	17.2831	134	11	130	3.1	242	16	4056			h1= top soil/murram, h2= fractured rock, h3=hard fractured rock	Good
69	77.7905	17.1394	204	0.8	9.32	0.3	288	0.9	26.1	5	50357	h1= top soil/murram, h2= clay zone, h3=hard rock, h4=fractured rock	Good
70	77.7921	17.1306	1281	0.8	45.6	0.3	1178	0.4	147	30	3021	h1= hard rock, h2=weathered rock, h3= hard rock, h4=fractured rock	Good
71	77.7806	17.1232	1179	0.8	223	3.3	106	39.4	17560			h1= hard rock, h2=weathered rock, h3= fractured rock, h4=hard rock	Good

72	77.7881	17.1253	198	0.8	10.2	0.4	183	27.7	1866			h1= top soil/murram, h2= clay zone, h3=fractured rock, h4=hard rock	Good
74	77.799	17.1229	7190	0.8	232	2.4	25.7	2.6	699			h1= hard rock, h2=weathered rock, h3= fractured rock	Good
78	77.8147	17.1064	210	3.7	31.4	3.8	286	46.1	11.5			h1= top soil/murram, h2= weathered rock, h3=fracturedrock	Good
90	77.7911	17.1754	2615	3.2	367	0.6	2414					h1= hard rock, h2=fractured rock, h3= hard rock	Good
100	77.8957	17.1912	13.3	14.3	533	15	55					h1= top soil/clay, h2= hard rock, h3=fractured rock	Good
106	77.9268	17.1268	19	9.5	56	3.5	133	5	2319			h1= top soil/clay, h2= weathered rock, h3=fractured rock	Good
117	77.7665	17.0734	659	3.2	6546	4.8	478	23	59741			h1= top soil/murram, h2= hard rock, h3=fractured rock	Good
142	77.9351	17.2345	68	9.3	115	0.8	337	19	759			h1= top soil/murram, h2= weathered rock, h3=fractured rock	Good
150	77.7862	17.2039	110	3.2	12.3	2.3	747	2.2	58.8			h1= top soil/murram, h2= weathered rock, h3=fractured rock	Good
152	77.8195	17.178	178	3.8	1893	4.6	141	10.3	801			h1= top soil/murram, h2= hard rock, h3=fractured rock	Good

Note: ρ1, ρ2, ρ3, ρ4 and ρ5 are the resistivites in (Ω m) and h1, h2, h3, h4 and h5 are the thickness in (m) of the respective soundings in the area

A total of five pseudo-cross sections were chosen to be representative of the area (viz). AA1, BB1, CC1, DD1 and EE1to generate the hydro-geologic profiles along the assumed sections. Each cross-section has four to five hydro-geologic layers in deccan traps and granites; Top soil; Un-saturated zone; Aquifer zone; and compact basalt, however top soil; Unsaturated zone; Aquifer zone; and hard massive granite respectively.The profile line AA1 (Figure 3.1) made up of four layers the first layer is the thin resistive top soil, it has resistivity range of 39.2 to 3975 Ω m and a thickness range of 0.8 to 10 m. The second layer is interpreted as the weathered rock with lower resistivity value, it has resistivity range of 1.9 to 95875 Ω m and a thickness range of 0.2 to 9.7 m. The third layer is interpreted as the fractured rock with low resistivity and massive rock with high resistivity value; it has resistivity range of 31 Ωm to 88432 Ω m and a thickness range of 2.9 to 19.9 m. The fourth layer which is to infinity also suggests a fresh basement rock and has resistivity range of 75.8 Ω m to 4140 Ω m.

The profile line BB1 (Figure 3.2) revealed that the line is also made up of five layers the first layer has resistivity range of 19.3 to 2820 Ω m and a thickness range of 0.8 to 16 m, composed of thin top soil. The second has resistivity range of 3.9 to 344 Ω m and a thickness range of 0.4 to 12.3 m, interpreted as the weathered rock. The third layer is interpreted as the fractured rock with low resistivity and massive rock with high resistivity value; it has resistivity range of 30.7 Ω m to 42592 Ω m and a thickness range of 1.8 to 27.7 m. The fourth and fifth layer which is to infinity also suggests a fresh basement rock and has resistivity range of 111 Ωm to 1866 Ω m.

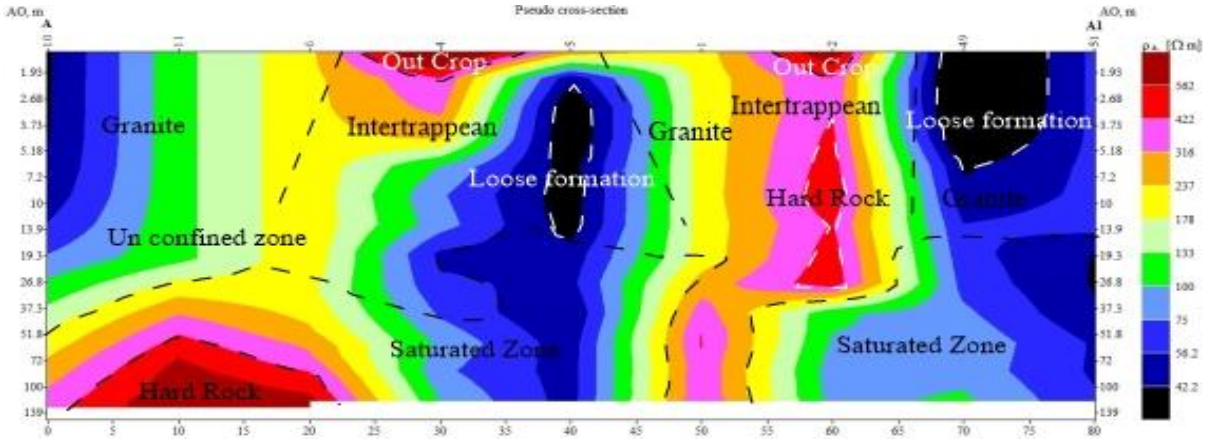

Figure 3.1: Pseudocross section-Profile AA1 in the study area

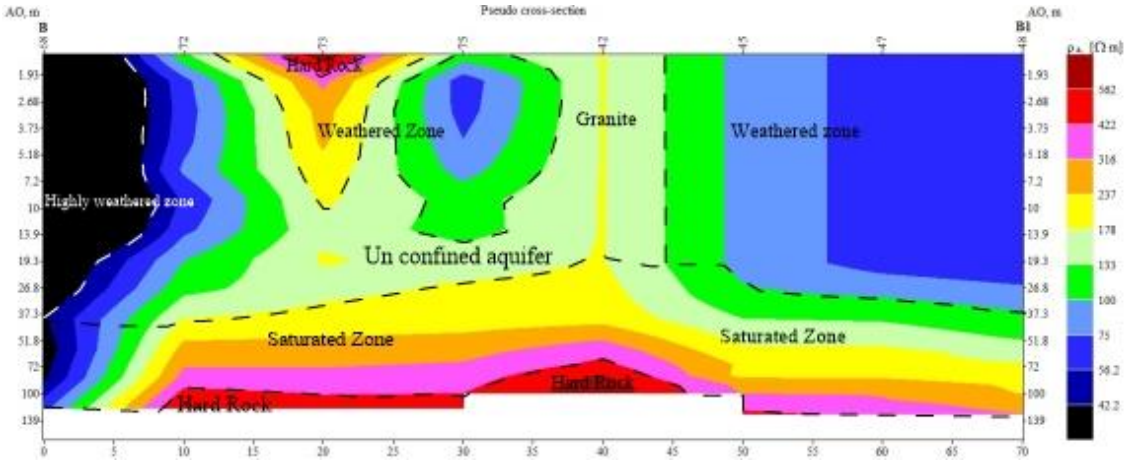

Figure 3.2: Pseudocross section-Profile BB1 in the study area

The profile line CC1 (Figure 3.3) revealed that the line is made up of four layers the first has resistivity range of 234 to 6865 Ω m and a thickness range of 3.15 to 17.4 m, top soil. The second layer is interpreted as the weathered rock with lower resistivity value; it has resistivity range of 12.3 to 44963 Ω m and a thickness range of 1.65 to 48 m. The third layer is interpreted as the fractured rock with low resistivity and massive rock with high resistivity value; it has resistivity range of 6.18 Ωm to 4559 Ω m. The fourth layer which is to infinity also suggests a fresh basement rock and has resistivity range of 21089 Ω m.

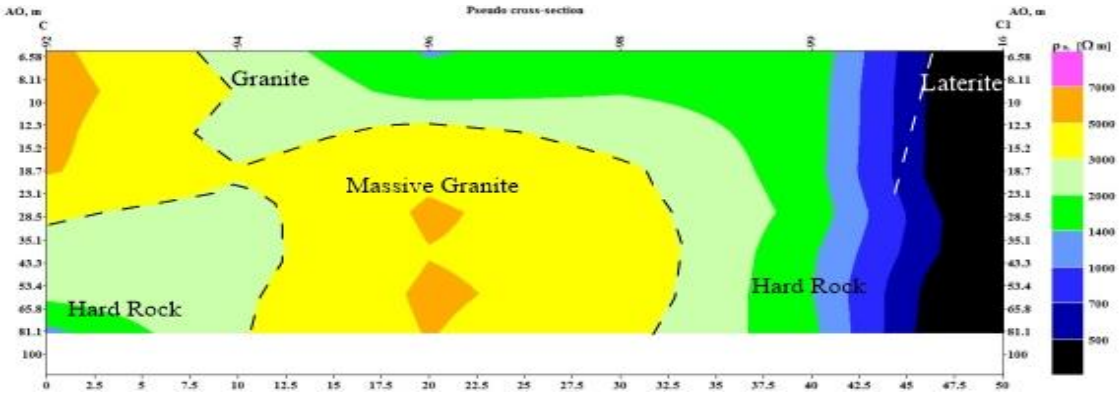

Figure 3.3: Pseudocross section-Profile CC1 in the study area

The profile line DD1 (Figure 3.4) revealed that the line is made up of four layers the first layer is the thin resistive top soil, it has resistivity range of 5.75 to 1505 Ω m and a thickness range of 1.5 to 56 m. The second layer is interpreted as the weathered rock with lower resistivity value; it has resistivity range of 23.3 to 10234 Ω m and a thickness range of 5 to 218 m. The third layer is interpreted as the fractured rock with low resistivity and massive rock with high resistivity value; it has resistivity range of 19.6 Ωm to 45867 Ω m. The fourth layer which is to infinity also suggests a fresh basement rock and has resistivity range of 512 Ω m.

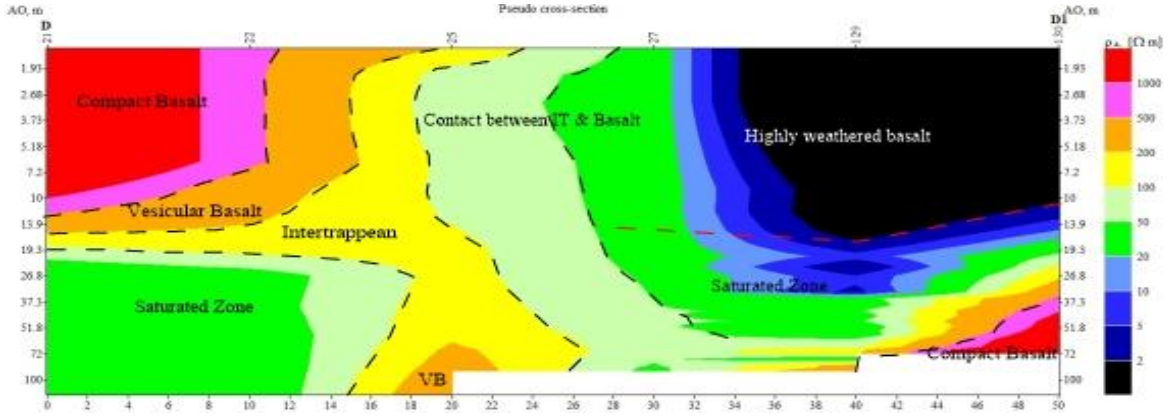

Figure 3.4: Pseudocross section-Profile DD1 in the study area

The profile line EE1 (Fig.3.5) revealed that the line is made up of four layers the first layer is the thin resistive top soil, it has resistivity range of 15.1 to 305 Ω m and a thickness range of 9.1 to 29.9 m. The second layer is interpreted as the weathered rock with lower resistivity value; it has resistivity range of 6.82 to 4153 Ω m and a thickness range of 2.2 to 48 m. The third layer is interpreted as the fractured rock with low resistivity and massive rock with high resistivity value; it has resistivity range of 22.2 Ωm to 150000 Ω m and a thickness range of 5 to 7.5 m. The fourth layer which is to infinity also suggests a fresh basement rock and has resistivity range of 2319 Ω m to 22732 Ω m.

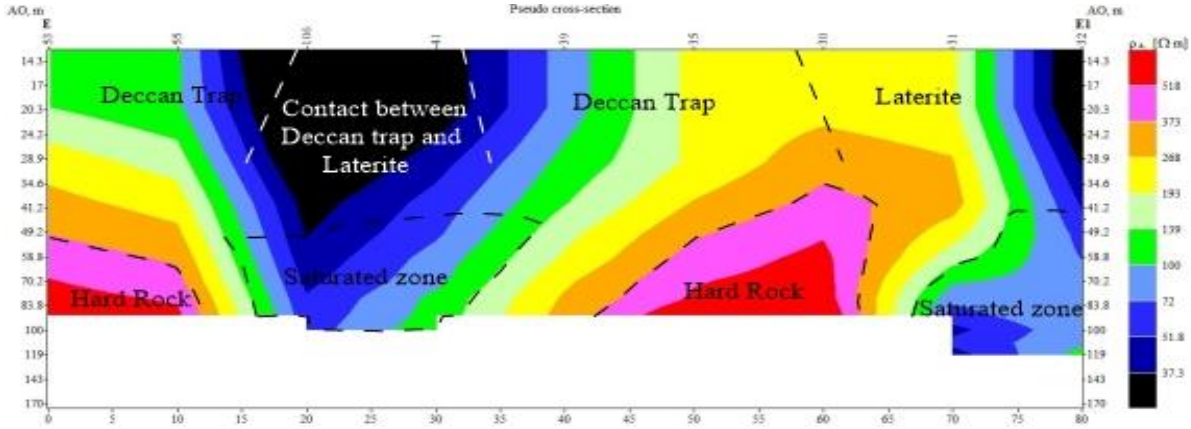

Figure 3.5: Pseudocross section-Profile EE1 in the study area

3.2. Iso-resistivity

The iso-resistivity maps are prepared by using software package (Surfer 11). The resistivity contours map provides pictures of the subsurface, which show variation in bedrock topography, precise location of concealed fractures, and nature and thickness of the overburden (N.C. Mondal et al. 2008; Sreedhar et al., 2018). Low resistivity denotes good conductors and high resistivity values are poor conductors (Figure 3.6).

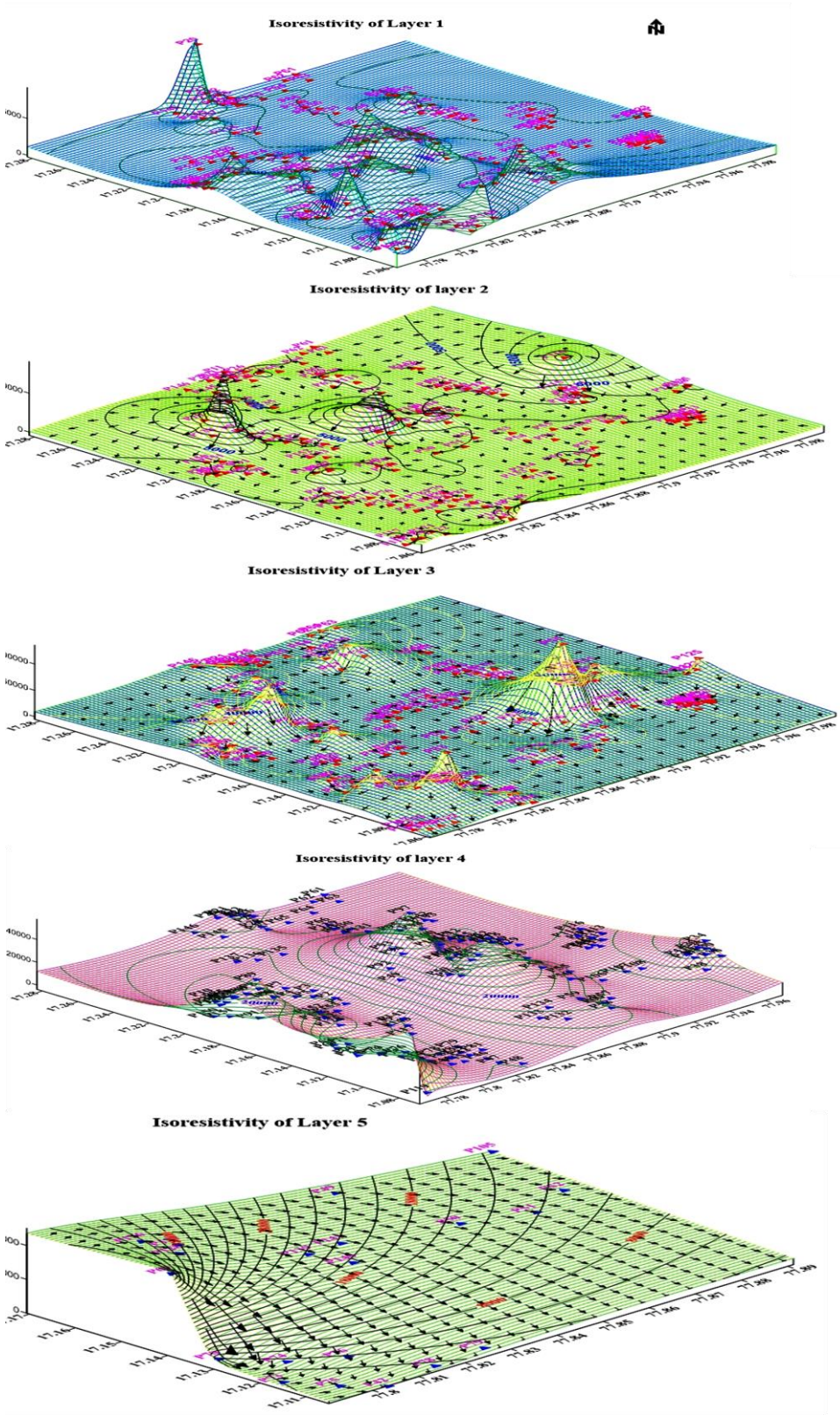

Figure 3.6: Iso resistivity Layer Characteristics of the soundings

3.3. Recharge and Discharge Area

Groundwater recharge, discharge and intermediate zones of the catchment were mapped based on different indicators such as; topography, groundwater flow pattern and static groundwater levels (Afewerk, 2011 and Toth 1963; Fetter, 1994). Among these indicators, topographic elevation is the simplest (Freeze and Cherry, 2002). The flow line on a flow net tends to diverge from recharge areas and converges towards to discharge areas (Fetter, 2001) (Figure 3.7 & 3.8).

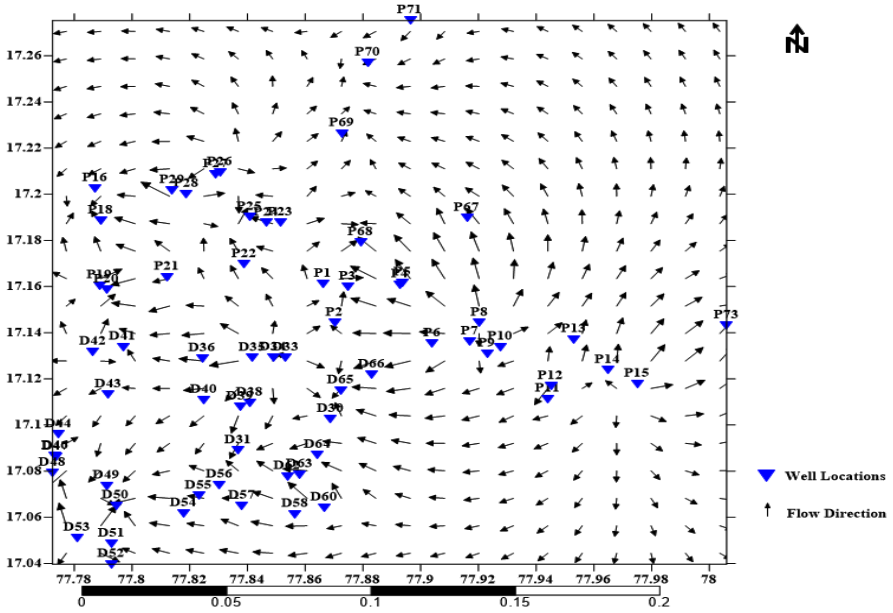

Figure 3.7: Flow direction Map of the area

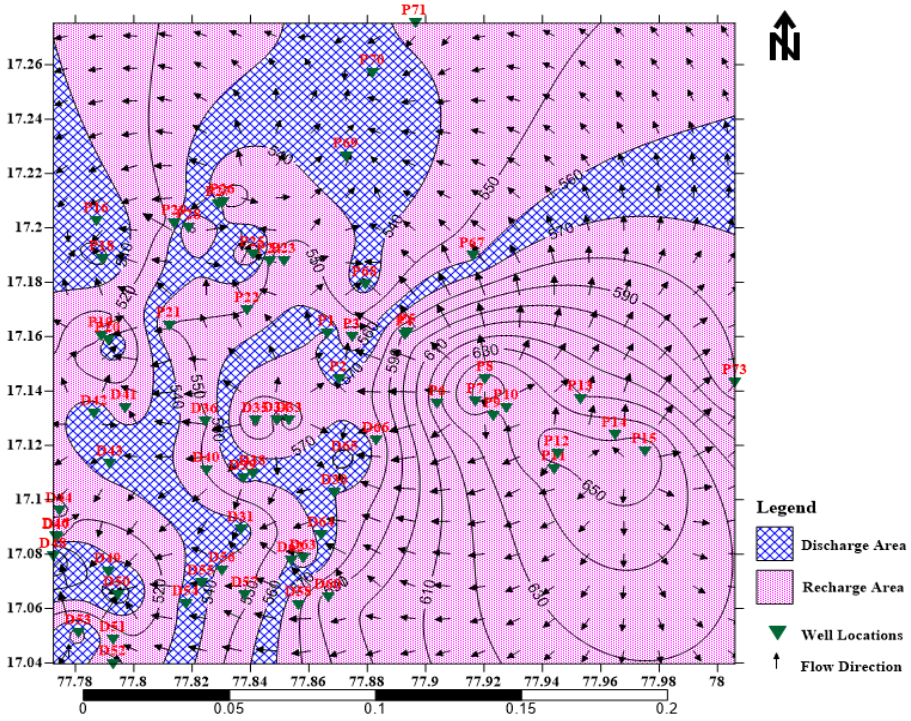

Figure 3.8: Recharge and Discharge Area Map

The water table elevation in the catchment along the Southeastern escarpments of the catchment is defined by 650 m AMSL; however the lowest water table elevation is about 480 m in Southwestern part of the study area. Movement of groundwater flows from high altitude to the lowest in the perpendicular direction to the contour lines. The contour map revealed that groundwater flows downward from the East in a higher hydraulic head towards to Southwestern part of the study area (Figure 3.9).

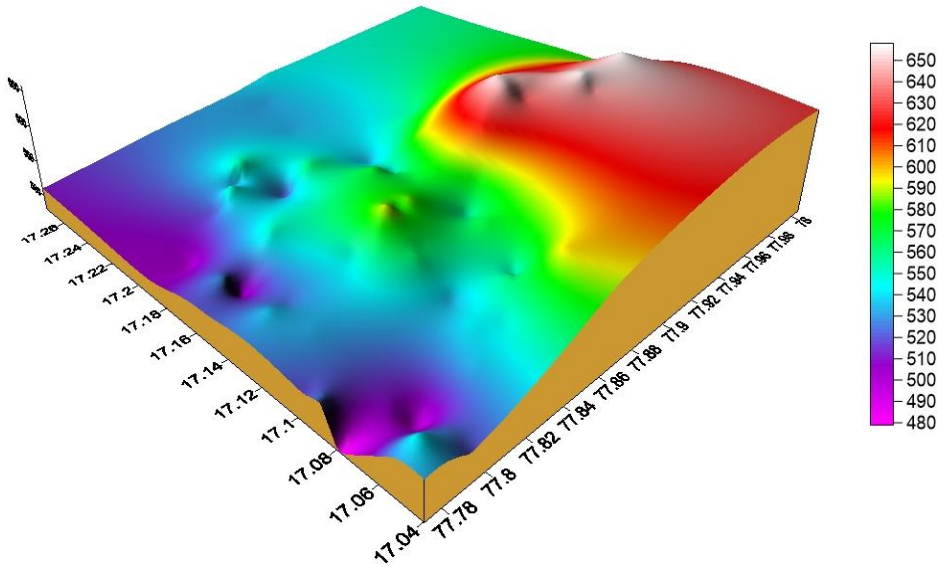

Figure 3.9: 3-Dimensional view map of the area

4. CONCLUSION

Geologically the area comprised of Granites, Deccan Traps and Laterites, electrical resistivity of around 148 soundings were carried out to study the subsurface aquifer characteristics. The results of the survey indicated the presence of four to five layers (viz.) overburden (0-20 Ω-m-Clay, 20-50 Ω-m- Hard Murram, 50-120 Ω-m Semi-weathered to fractured rock, 100-250 Ω-m - Fractured rock, >250 Ω-m Hard rock. Geo-electrical pseudo cross sections have been prepared based on resistivity of the soundings. A total of five Pseudo cross-sections (viz): A-A1; B-B1; C-C1; D-D1 and E-E1 were identified to generate the hydro-geologic profile of the study area. Layer characteristic map generated by the iso-resistivity depicts the understanding of the subsurface, which show variation in bedrock topography, precise location of concealed fractures, and nature and thickness of the overburden. Recharge and discharge area were demarcated based on the flow direction of reduced water levels flow line on a flow net tends to diverge from recharge areas and converges towards to discharge areas. Based on the results drawn from resistivity measurements and their correlation with the existing borewell lithologs more than 90 locations were suggested for borewells as an exploration and 27 locations estimated for high yielding production wells in the area.

ACKNOWLEDGEMENTS

The first author would like to extend sincere thanks to University Grants Commission (BSR), New Delhi for providing financial support and pursing this program.

REFERENCES

A.O. Lawrence, T.A. Ojo (2012). The use of combined geophysical sur- vey methods for groundwater prospecting in a typical basement complex terrain: case study of Ado-Ekiti southwest Nigeria, Res. *J. Eng. Appl. Sci.*, 1: 362–376.

Afework, D. (2011). Groundwater Potential Evaluation And Flow Dynamics of Hormat-Golina River Catchment, Kobo Valley, Northern Ethiopia, Addis Ababa University.

Ahmed S, Sankaran S, Gupta CP (1995). Variographic analysis of some hydrogeological parameters: use of geological soft data. *J Environ Hydrol*, 3(2):28–35

Central Groundwater Board (2014-15), Ground Water Year Book, Telangana State.

Chandra S, Ahmed S, Ram A, Dewandel B. (2008). Estimation of hard rock aquifers hydraulic conductivity from geoelectrical measurements: a theoretical development with field application. *J Hydrol*, 357:218–227

Choudhury K, Saha DK, Chakraborky P (2001). Geophysical study for saline water intrusion in a coastal alluvial terrain. *J. Appl. Geophys.*, 46:189-200.

Dhakate R, Singh V S, Negi B C, Chandra S and Rao V A. (2008). Geomorphological and geophysical approach for locating favourable groundwater zones in granitic terrain, Andhra Pradesh, India; *J. Environ. Manag.*, 88(4):1373–1383

Ezeh CC (2012). Hydrogeophysical studies for the delineation of potential groundwater zones in Enugu state, Nigeria. *Int. Res. J. Geol. Min.*, 2(5): 103-112

Fetter, C.W. (1994). *Applied Hydrogeology*, 3rd ed. Macmillan College Publishing, Inc., NewYork, 616.

Fetter, C.W. (2001). Applied hydrology. Prentice-Hall, inc. upper Saddle River, NewJersey.

Freeze R.A. and Cherry, J.A. (2002). Groundwater. Prentice-Hall: Englewood Cliffs: Englewood Cliffs, NY. 604

Krishnamurthy N S, Dutta S, Girard J F, Rao V A, Chandra S, Kumar D, Marc D, Gouez J M, Baltasat J M, Dewandel B, Gandolfi J M, Voullamoz J M and Ahmed S; (2006). Electrical resistivity tomography and magnetic resonance sounding studies for characterising the weathered-fractured aquifer in A.P., India, NGRI-2006GW-529.

Okonkwo AC, Ujam II (2013). Geoelectrical studies for the delineation of potential groundwater zones at Oduma in Enugu state; southeastern Nigeria. *International Journal of physical science*, 8(35):1761-1771

Ramanuja Chary, K.R. (2012). "Geophysical Techniques for Groundwater Exploration", Professional Book Publishers, 85 p.

Reynolds, J.M., (2011). *An Introduction to Applied and Environmental Geophysics*, second ed.. John Wiley and Sons Ltd., pp. 289–345

Sakram G., Kuntamalla S., Madhusudan N., Dhakate R., Saxena P.R. (2019). Demarcating of Aquifer Zones with Geophysical and Geospatial Approach in South Western parts of Rangareddy District, Telangana State, India. In: Rao P., Rao K., Kubo S. (eds) Proceedings of International Conference on Remote Sensing for Disaster Management. Springer Series in Geomechanics and Geoengineering. Springer, Cham, 978-3-319-77276-9, https://doi.org/10.1007/978-3-319-77276-9-52

Satpathy BN, Kanungo DN (1976). Water exploration on land terrain: A case history. *Geophys. Prospect*., 24: 725-736

Sonkamble S, Sahya A, Mondal NC, Harikumar P (2012). Appraisal and evolution of hydrochemical processes from proximity basalt and granite areas of Deccan Volcanic Province (DVP) in India. *J Hydrol*., 438–439:181–193. doi.org/10.1016/j.jhydrol.2012.03.022

Sreedhar Kuntamalla, Madhusudhan Nalla, Sakram G, and Praveen Raj Saxena (2018). Identification of Groundwater Potential Zones in Granitic Terrrain of Rangareddy District, Telangana State: A Case Study from Pendyala Village, International Journal of Engineering, *Science and Mathematics*, 7(3):27-33.

Telford WM, Geldart LP, Sheriff RE (1990) Applied geophysics II Ed. Cambridge University Press, UK, p 790

V. Arulprakasam, R. Sivakumar, B. Gowtham, (2013). Determination of hydraulic characteristics using electrical resistivity methods—a case study from Vanur watershed, Villupuram District, Tamil Nadu, IOSR J. *Appl. Geol. Geophys*., 1: 10–14.

Zohdy AAR (1974) *Application of surface geophysics to groundwater investigations*. US Dept. Interior, Geological Survey Book No. 2

Session 2

Smart Materials and Construction Technology

Invited Speakers

Dr Ing. Jakub Raček

Brno University of Technology, Czech Republic

Topic: Microwave Torrefaction Process of Sewage Sludge for Biochar Production

Prof. Nagaswarupa H.P.

Director, Research Center, East West Institute of Technology, Bangalore, India

Topic: Multi Functional Applications of Metal Oxide Nano Particles

Third Generation Biodiesel and Biomaterials from Microalgae under Biorefinery Scheme

Asnake Gudisa[1,]*, Luísa Afonso Barreira[2], Katkam N. Gangadhar[2]

[1]*Kotebe Metropolitan University, Ethiopia*
[2]*Centre of Marine Sciences, Portugal*
**Corresponding author, e-mail: astuasnegude@gmail.com*

ABSTRACT

The aim of the present work was to obtain a neutral lipids fraction of microalgae free of polar lipids (i.e., phospholipids and glycolipids) to produce biodiesel and, at the same time, get phospholipids and glycolipids rich fractions as value added products under a biorefinery approach. To achieve this objective, ethanolic extracts of the wet biomass (70.0%, w/w)of two microalgal strains (Nannochloropsisoculata and Phaeodactylumtricornutum) were prepared and partitioned into three fractions, namely hexane, colloidal and water fractions, using a binary solvent mixture (hexane + water), employing a new process called as Liquid Tri-phase System (LTPS). HPLC-ELSD was used to analyse the lipid classes and GC-MS to assess the fatty acid profiles. N. oculata had an ethanolic extract yield of 38.2% (w/w, dry weight) and P. tricornutum of30.3%. Lipid class distribution (% w/w, total lipids) of N. oculata was 45.1, 22.1 and 32.8 for neutral lipids, glycolipids and phospholipids, respectively; and for P. tricornutum it was 23.2, 49.1 and 27.7, respectively. When the LTPS process was applied, lipid distribution was: hexane (27.4%), colloidal (53.4%) and water (19.2%) for N. oculata; and 30.6, 55.4, and 14.0% for P. tricornutum. The colloidal phases in both strains contain more than 23.0% glycolipids and 68.0% phospholipids. HPLC-ELSD confirmed that the neutral lipids fraction was obtained free of glycolipids and phospholipids. The fatty acids composition from GC-MS showed that the neutral lipids fraction or hexane phase of the LTPS is suitable for biodiesel production as it contains more than 83.0% of saturated and monounsaturated fatty acids, which are less prone to oxidation compared to polyunsaturated fatty acids (PUFA). Additionally, a colloidal phase fraction rich in glycolipids, that can be converted into biosurfactants, and phospholipids that can be processed as liposome, aquaculture feed or infant formula additives as it is enriched in eicosapentaenoic acid (EPA) or other long chain poly unsaturated fatty acids, was obtained.

Keywords: *Microalgae, Liquid tri-phase system, Lipid classes, Biodiesel, Bio-refinery*

1. INTRODUCTION

Fossil fuels are the world's primary energy consumption in the transportation sector (Houghton et al., 2001), which are finite and, at current usage rates, are expected to be depleted in this century, and thus not renewable in the short period (Akansu et al.,2004). They are the largest contributor for greenhouse gas emissions (GHGs) (Raupach et al., 2007). Hence, consideration of this issue leads to evolution of biofuel generations.

The first generation biofuels have been mainly generated from food and oil crops .But, competition with food was barriers to their success (Group & Management, 2009; Koh & Wilcove, 2008).The second generation biofuels are from lignocelluloses rather than food crops (Koh & Wilcove, 2008; Moore, 2008). However, infant technology (Koh & Wilcove, 2008).

Third generation biofuels are produced from microalgae biomass. The following are advantages of microalgae: Highest oil productivity (Schenk et al., 2008); needs less water (Dismukes et al., 2008); cultivated on non-arable land (Searchinger et al., 2008); rapid growth potential (Metting , 1996); fixate high amount of CO_2 (Chisti, 2007);nutrients for cultivation(especially nitrogen and phosphorous) can be obtained from wastewater, therefore, apart from providing growth medium, there is a dual potential for treatment of wastewaters(Cantrell et al., 2008); produce valuable co-products such as proteins, β-carotene (Brennan & Owende, 2010; Spolaore et al.,2006); oil yield may be enhanced (Qin, 2005).

However, to make microalgae competitive feedstock for biodiesel and/or biomaterials, it is important to apply the bio-refinery approach. Biorefinery is the use of the whole biomass for fuels and other value added products

such as biosurfactant, biopolymer/bioplastic, aquaculture feed, liposome as drug delivery system, feed or food, biofertilizer or biogas. If we produce only biodiesel from biomass we will lose the by-products or side products that lead to socio-economic and environmental impacts. As a result, the present study is to obtain a neutral lipid rich fraction free of phospholipids and glycolipids to produce biodiesel from microalgae and, at the same time, get phospholipids and glycolipids rich fraction with biomedical, food and/or feed or other industrial applications under a biorefinery scheme, using industrially feasible processes.

2. MATERIALS AND METHODS

2.1. Total Lipid Extraction

Lipids were extracted according to the protocol described in(Yao et al., 2012) with a little modification (Figure 2.1a).

2.2. Lipid Separations

Lipids were separated into Neutral lipids (NLs), Glycolipids (GLs) and phospholipids(PLs) using column chromatography applying the method described at (Wang & Wang, 2012) with little modification (Figure 2.1b).

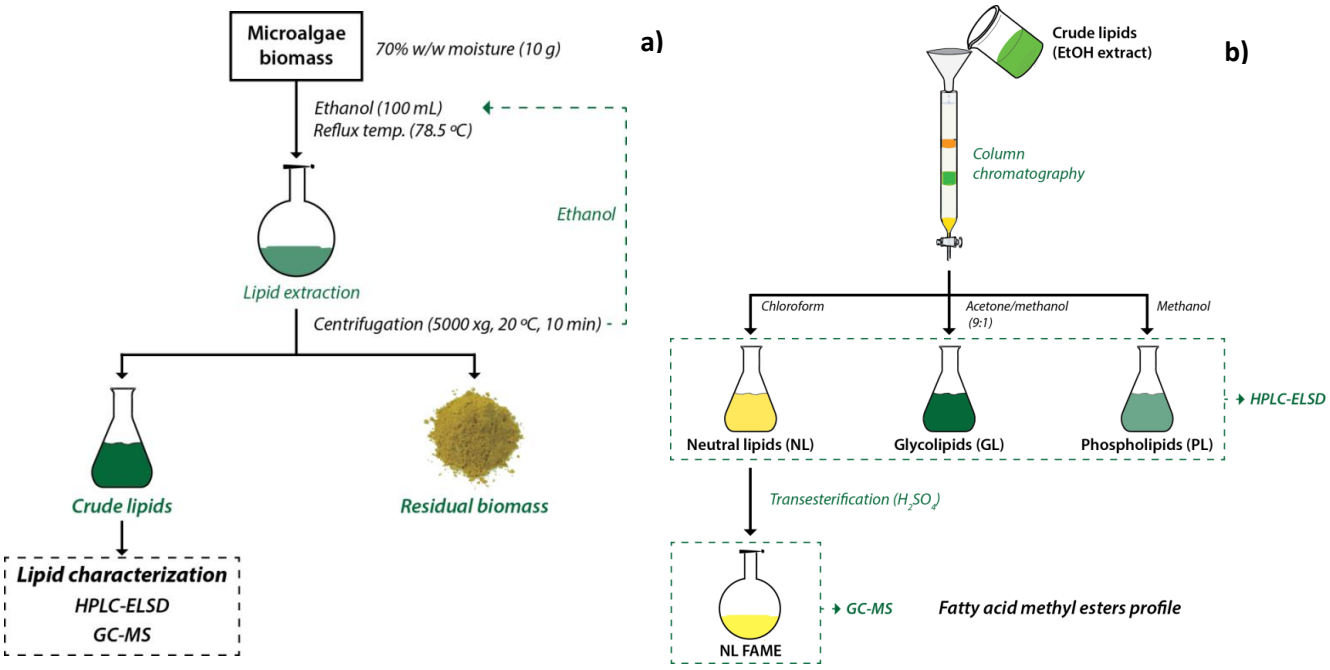

Figure 2.1: Lipids extraction from wet microalgae using ethanol (a) and lipid separation using column chromatography (b)

But, column chromatography is not feasible industrially. Consequently, we develop the new method of lipid separation applying Liquid Tri-phase system (LTPS) .In LTPS, we used binary phase system (hexane + water) and separate the total lipids of microalgae into three major classes with three distinct phases (Figure 2.2). This is unusual chemistry in higher plants lipid where we can find only two phases.

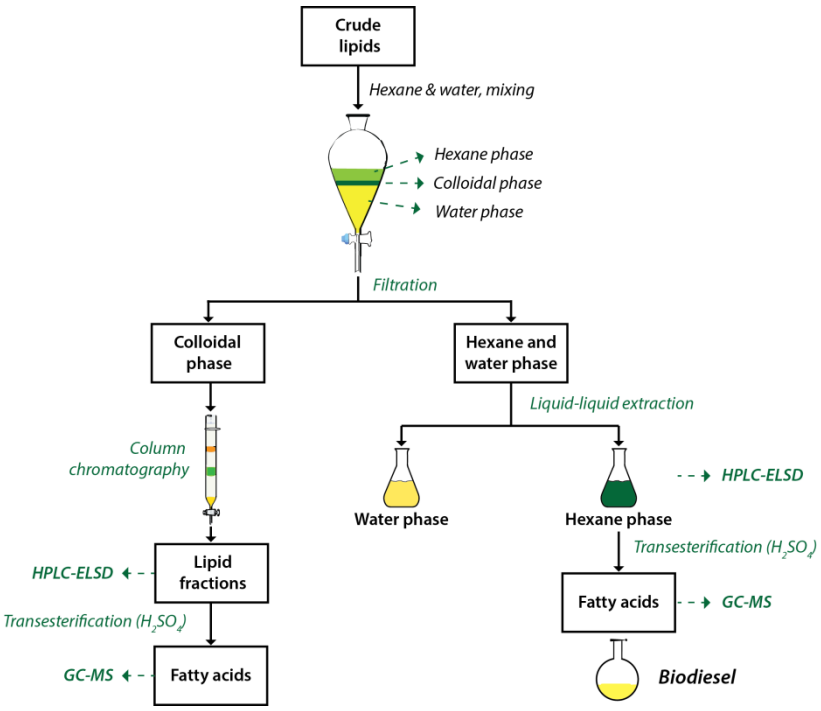

Figure 2.2: Lipid partitioning using LTPS followed by HPLC-ELSD and GC-MS analysis

3. RESULTS AND DISCUSSION

3.1. Lipid Characterization

3.1.1. Lipid Profiles

The total lipids extracted from microalgae were separated into lipid classes (i.e. NLs, GLs and PLs) using silica gel column chromatography**.** Lipid class distribution (% w/w, total lipids (TL)) of *N. oculata* was 45.1, 22.1 and 32.8% for NLs, GLs and PLs, respectively(Fig 3.1).These results are in agreement with the findings of Wang and Wang (2012). And, *P. tricornutum* lipid distribution was 23.2, 49.1 and 27.7% for NLs, GLs and PLs, respectively (Figure 3.1). This result is in line with the report of Miranda et al.(2015).

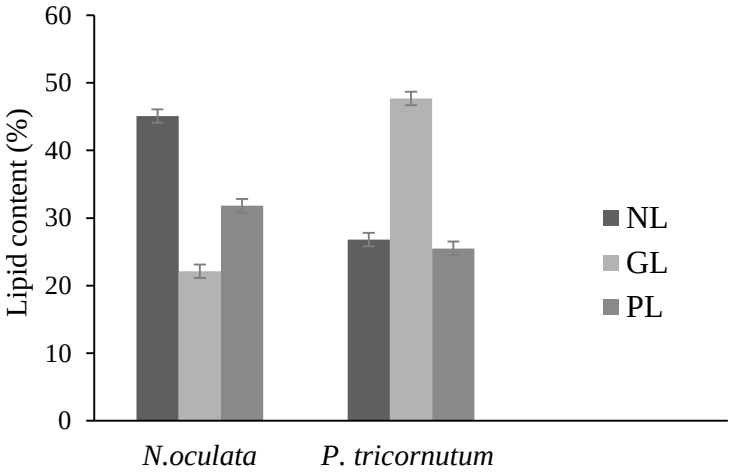

Figure 3.1: *N. oculata* and *P. tricornutum* lipid classes separated by silicagel column chromatography. NL-neutral lipid, GL-glycolipid, PL-phospholipid

HPLC-ELSD was used to determine the lipid fractions present in the microalgae crude extracts and in the fractions. In this regard, we achieved the separation of standards TAG (triacylglycerol), DAG (diacylglycerol), FA (Fatty acid), MG and PLs in just 40 minutes (Figure 3.2). The more non-polar, TAG, was eluted first, followed by DAG, FA and MAG (monoacylglycerol). PLs were the last to elute in our gradient program.

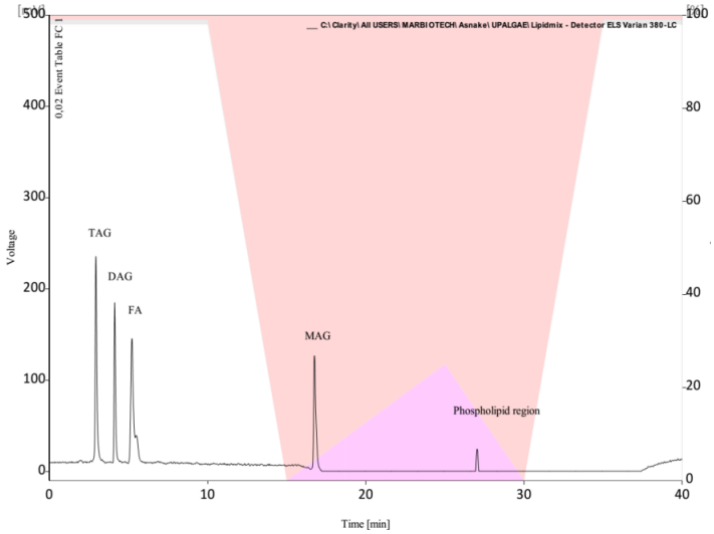

Figure 3.2: Separation of standard lipids by gradient elution on HPLC-ELSD

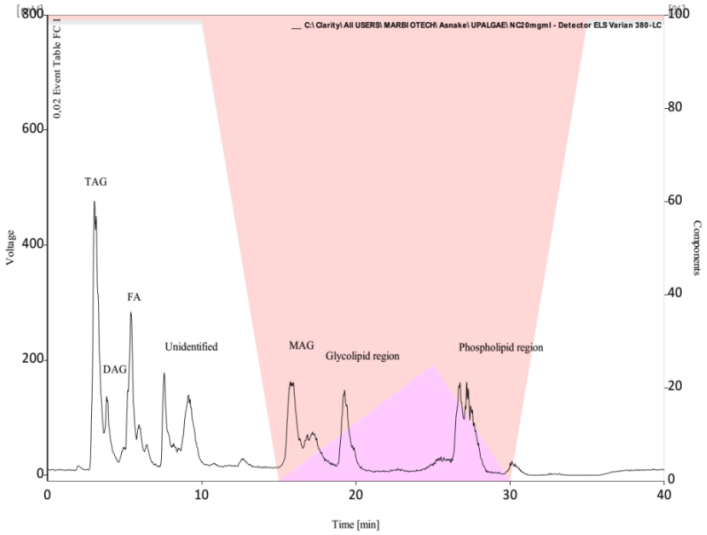

Figure 3.3: HPLC-ELSD chromatogram of *N.oculata* crude extract showing the separation of lipid classes

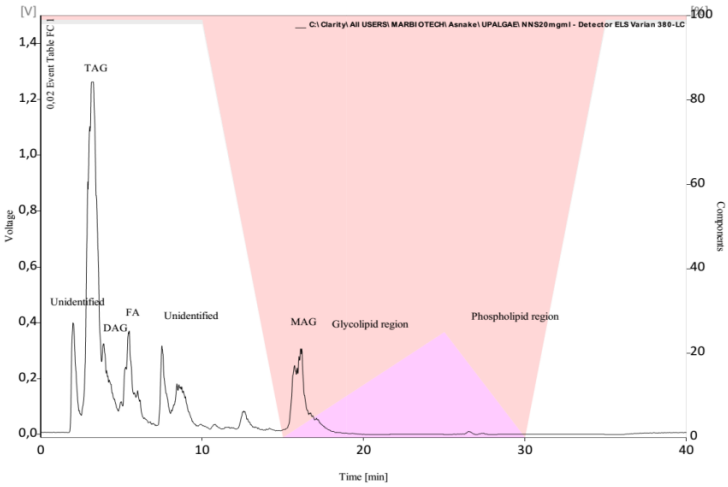

Figure 3.4: HPLC-ELSD chromatogram of the NLs fraction of *N.oculata*

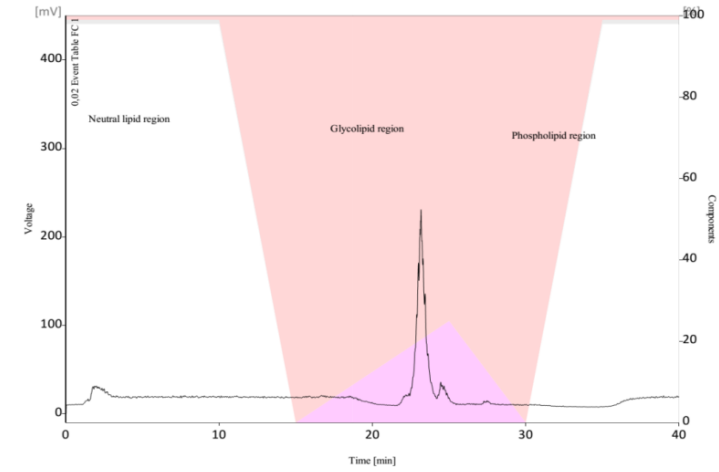

Figure 3.5: HPLC-ELSD chromatogram of the GLs fraction of *N.oculata*

The newly developed program fairly resolved *N.oculata*NLs such as TAG, DAG, FA and MAG (Figure 3.3). Closely related finding was reported for *Chlorella* and *C. kessleri* (Jones et al., 2012; Kobayashi et al., 2013).GLxs was separated well; but necessitates standard to identify the fraction types. The PLs fractions have very close retention times and a full separation would require further method optimization. Despite the peaks need further resolution, it is possible to ascertain that we achieved to obtain a NLs fraction free of polar lipids for biodiesel production; and at the same time, a polar lipids rich fraction for value added chemicals (Figure 3.4 to 3.6).

Figure 3.4 confirms the separation of NLs from both PLs and GLs in the fractions obtained from silica gel column chromatography.

Figure 3.5 confirms separation of the GLs from both the NLs and PLs by silica gel column chromatography. GLs accounted for 22.1% of *N.oculata* total lipids and can be converted to non-ionicbiosurfactants (Abdel-Mawgoud et al., 2011; Kitamoto et al., 2002).

PLs were also well separated from the remaining lipids by silica gel column chromatography and accounted for 33.0% of the whole lipids (Figure 3.6).

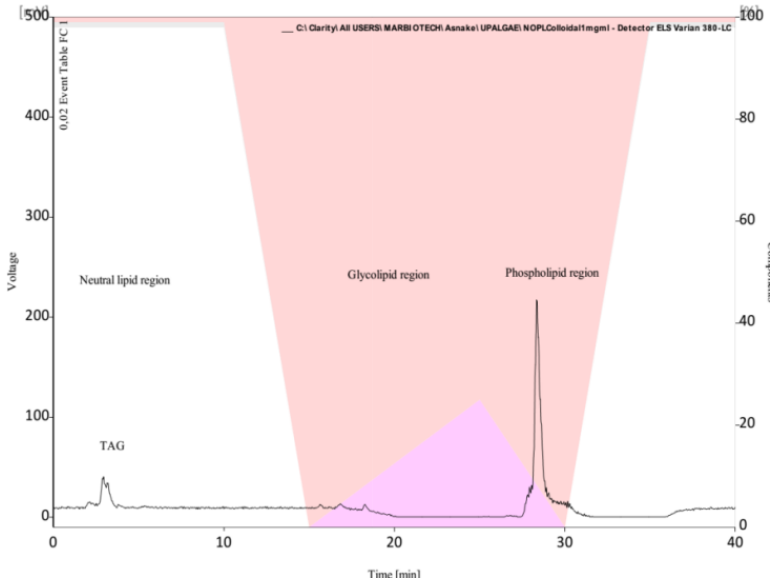

Figure 3.6: HPLC-ELSD chromatogram of the PLs fraction of *N.oculata*

3.1.2. Fatty Acid Composition

FAs composition of the crude lipid extract and the NLs fraction were calculated in terms of total fatty acids (TFA). The main FAs detected in crude extract of *N. oculata* were myristic acid (C14:0), palmitic acid (C16:0), palmitoleic acid (C16:1), and EPA (C20:5) (Table 3.1). This finding is in line with those reported previously (Bellou et al., 2014; Gangadhar et al., 2015). SFAs and MUFAs account for more than 58.0%.These FAs are suitable for biodiesel as they are less susceptible to oxidation. The remaining PUFAs like EPA (30.6%) are needed to be separated and optimized for industrial production for biomedical, feed and/or food as nutritional supplements (Drevon et al., 1993; Simopoulos, 1999).

The major FAs detected in the NLs fraction of *N. oculata* were C16:0, C16:1 and C18:1 (Table 3.1). In this fraction, the sum of SFAs and MUFAs are greater than 86.0%. HPLC-ELSD was used also to analyse the lipid classes of LTPS fractions of *N. oculata* (i.e., hexane, colloidal and water phases) (Figure 3.8 to 3.10). In the hexane fraction (Figure 3.8), more than 93.7% was composed of NLs and the remaining with PLs (6.3%). GLs were not detected and the PLs fractions are not significant. As a result, the hexane phase is suitable aspirant to be used for biodiesel production as it is almost free from polar lipids.

3.2. Liquid Tri-phase System (LTPS)

3.2.1. Lipid Classes

Figure 3.7 shows the partition of the studied microalgae lipids partitioned between the used binary solvent system (hexane and water). The yields of the different fractions were, for *N. oculata*, 27.4, 53.4 and 19.2% for the hexane, colloidal and water phases, whereas for *P. tricornutum*, 30.6, 55.4 and 14.0%, respectively (Figure 3.7).The colloidal phase was further separated using silica gel column chromatography. It was composed of 5.1, 23.4 and 71.5% of NLs, GLs and PLs, respectively for *N. oculata*. Similarly, *P. tricornutum*colloidal consisted of 3.0, 28.7, and 68.3% of NLs, GLs and PLs, respectively. These results reveal that the colloidal phase is a rich source of PLs.

Table 3.1. FAs composition of crude extract and NLs fraction of *N. oculata*. Results are presented as mean ± standard deviation (n = 2)

Fatty acids	Crude extract	NLs fraction
C14:0	8.1 ± 0.9	8.0 ± 0.7
C16:0	20.3 ± 2.1	30.6 ± 1.4
ΣSFA	28.4	38.6
C16:1(n-6)	25.5 ± 1.6	22.2 ± 0.4
C18:1(n-9)	4.1 ± 0.3	25.7 ± 0.6
ΣMUFA	29.6	47.9
C18:2(n-6)	4.1 ± 1.2	5.7 ± 0.7
C20:4(n-6)	7.3 ± 2.1	1.8 ± 1.2
C20:5(n-3)	30.6 ± 0.3	6.0 ± 1.8
ΣPUFA	42.0	13.5

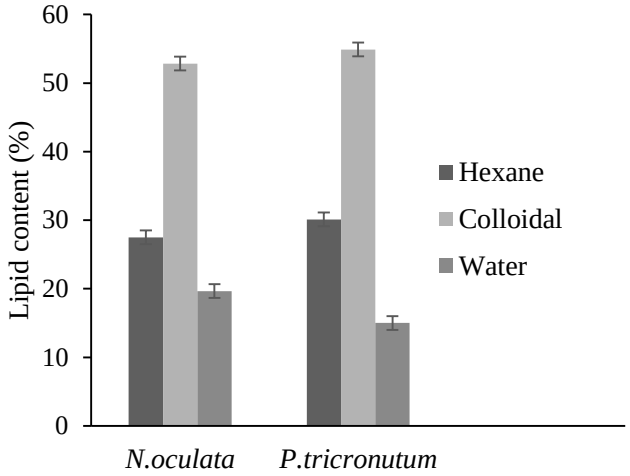

Figure 3.7: Lipid class separation using Liquid tri-phase system (LTPS)

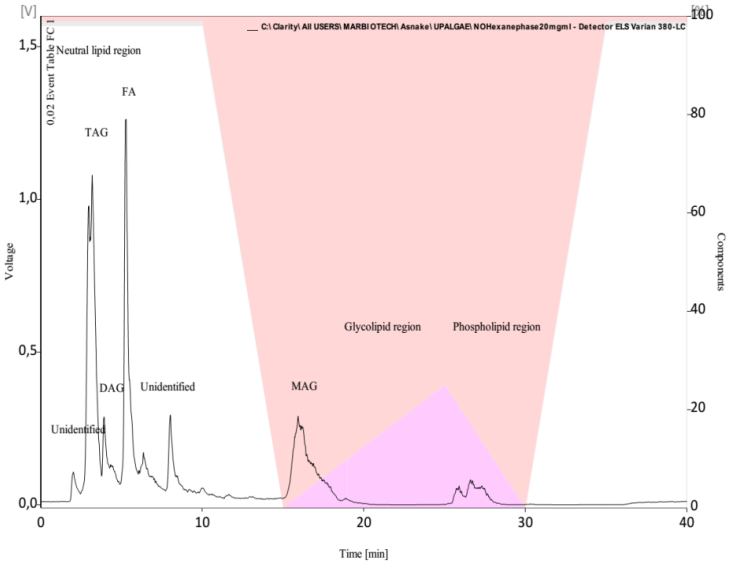

Figure 3.8: Lipid classes composition of the hexane fraction (LTPS) of *N.oculata* tion of *N.oculata*

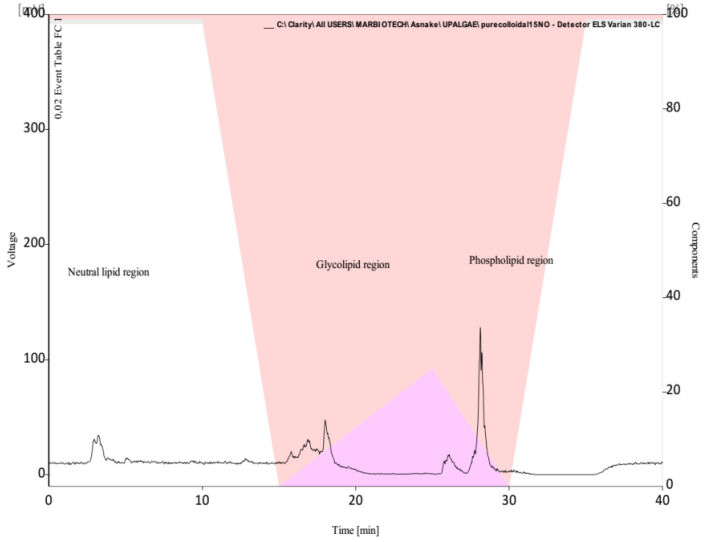

Figure 3.9: Lipid classes composition of the colloidal fraction (LTPS) *N.oculata*

The lipid classes profile of the colloidal fraction is presented in Fig. 3.9.The approximate area percentages were 8.6, 27.8 and 63.5 for NLs, GLs and PLs, respectively. This was a similar to those obtained from column chromatography. This indicates that the colloidal phase was composed of more polar lipids particularly PLs.

The lipid profile of the water phase is presented in Fig 3.10.These fractions appeared only in PLs of the chromatograms. These lipids might be highly hydrolysed PLs fractions (e.g., LPC). It might be sugar and/or peptides. Despite logical conclusion that they are polar (by principle of like dissolves like), scientific conclusion demands concrete evidence. Such polar lipids can be used to produce bioalchols (Chen et al., 2013). However, this has been left for further investigation as standards are essential and attention was given to the two phases (i.e., hexane and colloidal) to study their FAs profiles using GC-MS. But, this is an indication of applying biorefinery scheme by using the whole lipids for several kinds of applications.

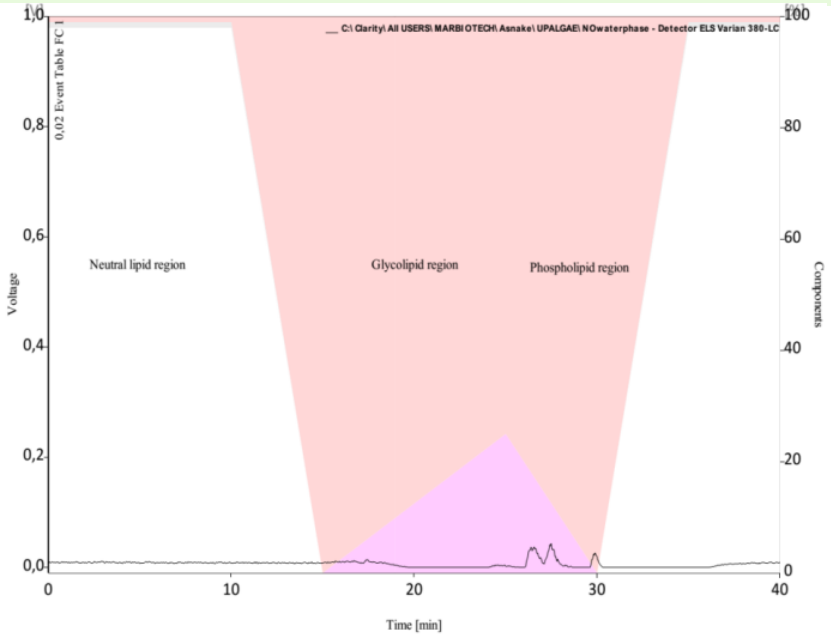

Figure 3.10: Lipid classes composition of the water fraction (LTPS) *N.oculata*

3.2.2. Fatty Acid Composition

Table 3.3 shows the main FAs detected in *N. oculata*. Hexane phase FAs were C14:0, C16:0, C16:1 and C18:1.The sum of SFAs and MUFAs in this phase was more than 88.0%.This has a lot of advantages for biodiesel production from NLs than crude extract. Foley et al.(2011) states highly unsaturated lipids occur more frequently in polar lipid fractions specifically PLs. So, separating the polar lipids from neutral lipids can also enhance the biodiesel quality (i.e., reduce the oxidation) and thus increase the yield of FAMEs (Freedman et al., 1984; Li et al., 2014; Watanabe et al., 2002). Furthermore, it helps to comply with specifications such as EN 14214 and ASTM D6751 standards for phosphorus content should be less than 4ppm according to EN 14214 or 10ppm as per ASTM D6751 specifications(Kaleli, 2001; Tyson & McCormick, 2006).

The colloidal fraction contains some FAs as in hexane phase (Table 3.3**)**. However, it consists of 43.2% of PUFAs such as C20:5, C20:4 and C18:2. As a result, while the hexane phase can be used for biodiesel, the colloidal is able to be used in the treatment of atherosclerosis, cancer, and neurodegenerative diseases such as Alzheimer's because it contains omega-3-Fas (Drevon et al., 1993; Simopoulos, 1999). It can also be used for infant formula nutritional supplement because of arachidonic acid (Sijtsma & De Swaaf, 2004; Simopoulos, 1999) and aquaculture feed (Brennan & Owende, 2010; Pulz & Gross, 2004; Spolaore et al., 2006). In addition, it contains conditionally essential FAs like linoleic acid (C18:2). This is an attempt to apply the bio-refinery scheme so that microalgae can be competitive feedstock for biodiesel.

This finding shows LC-PUFAs occur more frequently in polar lipid fractions specifically colloidal phase containing both PLs and GLs. This is in line with Foley et al.(2011)who reported unsaturated FAs are related to polar lipids specially PLs . For example, EPA in *P. tricornutum* is mainly associated with PLs and GLs (Ryckebosch et al., 2012). Such FAs are available in very few organisms such as fish oil. However, considerable evidences have indicated that n-3-PUFAs in fish oils are actually derived via the marine food chain from zooplankton consuming n-3-PUFAs synthesising microalgae; fish accumulates pollutants up food chain and fish oil is with unpleasant smell (Yongmanitchai & Ward, 1989).Therefore, microalgae are some of the most promising feedstock for biofuels and/or biomaterials. Other applications of PLs fractions include improving intelligence and function of nerve cells (Pepeu et al., 1996). Therefore, it is very important to separate let alone the general lipid

classes even each lipid fractions within the classes to get wider applications from each chemical or compound entity.

In addition, EPA and DHA have the ability to influence cell membrane fluidity and permeability (Burri et al., 2012). These omega-3-FAs are rarely available in higher plants lipids but microalgae PLs are enriched in these FAs (Ryckebosch et al., 2012). This implies that PLs from microalgae can deliver both hydrophilic and hydrophobic drugs to the target site as microalgae contain both non-polar and polar lipids. Such PLs liposomes have many advantages: targeting, tissue compatibility, reducing drug toxicity and improving its stability. Consequently, such liposomes can serve as the carriers of antitumor, antifungal, analgesic, in gene therapeutics and vaccines (Delalat et al., 2015; Li et al., 2015;Pattni et al., 2015).

Table 3.3: FAs composition of *N. oculata* fractions obtained by LTPS. Results are expressed as mean ± standard deviation (n = 2)

Fatty acids	Hexane	Colloidal
C14:0	11.3 ± 0.9	11.0
C16:0	36.4 ± 1.1	16.9
ΣSFA	47.7	27.9
C16:1(n-6)	29.8 ± 2.3	16.0
C18:1(n-9)	11.1 ± 0.3	12.9
ΣMUFA	40.9	28.9
C18:2(n-6)	6.0 ± 2.1	8.8
C20:4(n-6)	1.0 ± 1.2	8.1
C20:5(n-3)	4.4 ± 0.2	26.3
ΣPUFA	11.4	43.2

4. CONCLUSIONS AND RECOMMENDATIONS

4.1. Conclusions

- Ethanol successfully extracts lipids from wet microalgae biomass. This can reduce the high dewatering cost
- Neutral lipids can be obtained free of polar lipids (i.e. colloidal = phospholipids + glycolipids) to produce biodiesel from microalgae and, at the same time, polar rich fractions can be separated for value added products.
- Neutral lipids comprise fatty acids suitable for biodiesel production but the colloidal phase contains fatty acids suitable for biomedical or feed or food applications.

4.2. Recommendations

- Conversion of GLs fraction to non-ionic bio-surfactant and characterization of its suitability for food or pharmaceutical industries.
- Characterization of colloidal phase for liposome as drug delivery system or infant formula additives.
- Carry out life cycle assessment (LCA) or cost benefit analysis (CBA) of microalgae bio-refinery in comparison to petro-refinery.

Acknowledgments

I am unreservedly grateful to the European Commission for the scholarship funded as Erasmus Mundus Category 'A' student of Erasmus Mundus Joint Master Degree in Chemical Innovation and Regulation (EMM ChIR).

First & foremost, I offer my unfeigned and sincerest gratitude to my supervisors-Prof. Luísa Afonso Barreira and Dr. Katkam N. Gangadhar for their eternal support, professional guidance, constructive comments, patience

and diligent help. I attribute the level of my Master Degree to them for this thesis, too, would not have been completed without their support.

My thanks in advance equally go to Hugo Pereira (Research scholar), Dr.Katkam N. Gangadhar (my co-supervisor) and Vera Gomes (CCMAR) who improved my laboratory skills from basic unit operations (extraction, biodiesel production…) to using column chromatography, HPLC-ELSD and GC-MS until I become ous to activities closely related to my present thesis. Without these three professionals and my supervisor, my practical skills should not have been improved.

REFERENCES

Akansu, S. O., Dulger, Z., Kahraman, N., & Veziroğlu, T. N(2004). Internal combustion engines fueled by natural gas—hydrogen mixtures. *International Journal of Hydrogen Energy, 29*(14): 1527-1539.

Brennan, L., & Owende, P (2010). Biofuels from microalgae—a review of technologies for production, processing, and extractions of biofuels and co-products. *Renewable and Sustainable Energy Reviews, 14*(2): 557-577.

Cantrell, K. B., Ducey, T., Ro, K. S., & Hunt, P. G(2008). Livestock waste-to-bioenergy generation opportunities. *Bioresource Technology, 99*(17): 7941-7953.

Chisti, Y. (2007). Biodiesel from microalgae. *Biotechnology Advances, 25*(3): 294-306.

Group, U. N. E. P. B. W., & Management, U. N. E. P. I. P. f. S. R (2009). Towards sustainable production and use of resources: assessing biofuels: UNEP/Earthprin

Houghton, J. T., Ding, Y., Griggs, D. J., Noguer, M., van der Linden, P. J., Dai, X., Johnson, C(2001). Climate change 2001: The scientific basis.

Koh, L. P., & Wilcove, D. S.(2008). Is oil palm agriculture really destroying tropical biodiversity? *Conservation Letters, 1*(2): 60-64.

Metting Jr, F (1996). Biodiversity and application of microalgae. *Journal of Industrial Microbiology, 17*(5-6): 477-489.

Raupach, M. R., Marland, G., Ciais, P., Le Quéré, C., Canadell, J. G., Klepper, G., & Field, C. B (2007). Global and regional drivers of accelerating CO_2 emissions. *Proceedings of the National Academy of Sciences, 104*(24): 10288-10293.

Optimization of Drilling Parameters in Metal Matrix Composites using Genetic Algorithm

G. Somasundaram, and J. Bhaskaran*

Department of Mechanical Engineering, Adama Science and Technology University, P.O.Box 1888, Adama, Ethiopia
**Corresponding author, e-mail: bhaskaranj@gmail.com*

ABSTRACT

A novel drilling process using a friction tool known as Friction drilling is experimented here for making holes in Aluminium Silicon Carbide (AlSiC) Metal Matrix Composites (MMC). Friction drilling is a non-traditional hole-making method that utilizes the heat generated from friction between a rotating conical tool and the work piece to soften and penetrate the work-material and generate a hole in the work piece. In the present study the drilling performance of friction tool is evaluated using reduced surface roughness as the performance indicator. Experiments are conducted using Central Composite of Design of experiments (CCD) under Design of Experiments (DOE) technique. Optimization of the process parameters is carried out using Genetic Algorithm (GA). The optimized results could be useful for selecting the level of drilling parameters which result in saving machining time and by this the product cost can be economised.

Keywords: *AlSiC composites, Friction Drilling, Surface roughness, Central Composite of Design of experiments (CCD), Optimization, Genetic algorithm*

1. INTRODUCTION

Aluminium Matrix Composites (AMC) is replacing Cast Iron (C.I) as an alternative construction material due to its corrosion resistant and light weight. AlSiC composites are widely used in industry, particularly in automotive applications. Despite the superior mechanical and thermal properties of particulate metal-matrix composites, their poor machinability has been the main deterrent to their substitution for metal parts. The hard abrasive reinforcement phase causes rapid tool wear during machining and, consequently, high machining costs.

Paulo Davim and ConceicaoAnto´nio (2001) found out that the wear of conventional twist drills are mainly due to cutting the abrasive SiC particles and hence a novel drilling process where the tool will not cut the material but plasticizes and deforms the material to form a hole is experimented here. They used experimental data to develop a numerical model based on a genetic search and the model proved to be effective in optimizing the cutting conditions in drilling of particulate metal matrix composites. Miller et al. (2006) observed that in friction drilling there is a formation of bushing in-situ from the thin-walled work piece and is a clean, chip less process. TeroStjernstoft (2004) developed a self-propelled rotary cutting tool made up of titanium nitride (TiN) coated sintered Carbide as an alternative to Poly Crystalline Diamond (PCD) tools, for machining composites and some other difficult-to-cut materials, and found out that rotary cutting tool provide higher material removal rate than conventional cemented carbide and PCD tooling. Machined surface changing into recast structure was observed by Yanming Quan and Bangyan Ye (2003) when machining AlSiC composites and its hardness was lower than that of normal. Lin et al. (1998) studied the chip formation in machining AlSiC-MMC and noticed that the addition of SiC particle reinforcement into the aluminum matrix has caused a reduction in its ductility and makes the material ideal for producing semi-continuous chips.

Effect of cutting fluid on the machinability of aluminum- based matrix composites reinforced with SiC/Al_2O_3 particles was studied by Hung et al. (1997) and they found that the surface finish and the cutting forces are insensitive to cutting fluid and cutting speed when machining with new diamond tool, but deteriorate with greater tool wear. Existing coated tools, such as those coated with titanium nitride or titanium carbide which had shown advantages in the cutting of steel showed poor performance in machining AlSiC was the inference made by Durante et al. (1997) after conducting machining tests. Tosun and Muratoglu (2004) conducted experiments with tool materials HSS (High Speed Steel), TiN coated HSS and solid carbide drills and concluded that the drilling

of AlSiC composites is suitable with solid carbide drills, with 130° point angles, at a speed of 1330 rpm. Riccardo Polini et al. (2003) conducted dry turning tests of alumina /aluminum composites with Chemical Vapour Deposited (CVD) diamond coated Co-cemented tungsten carbide tools and suggested the usage of CVD carbide tools as an alternative to the expensive PCD tools for machining MMC.

Ibrahim Ciftci et al (2004) evaluated tool wear when machining AlSiC composite and noticed that uncoated carbides produced better surface finish than coated carbides. The higher Ra values in the case of coated cutting tools can be attributed to the formation of a larger built-up-edge on the coated cutting tools than that formed on the uncoated cutting tools. Wear and damage of cutting tools in dry machining of aluminum alloys were studied by Nouari et al. (2005) and they noticed that the damage is caused by adhesion of the machined material on the tool surface. They concluded that tool geometry can seriously change machined surface quality and the required geometrical tolerances.

Paris et al. (2008) observed ploughing effect while drilling Crank shaft steel using cemented tungsten carbide drill. Ploughing effect happens when the flank face is in contact with the machined surface. Effect of particles size in AlSiC was studied by Chen and Tokaji (2004) and they concluded that the 5 and 20 μm composites exhibited nearly the same fatigue strength as the unreinforced alloy, while the 60 μm composite showed significantly lower fatigue strength.

Hung et al. (1996) used analytical models developed by modifying the Taylor's equation to study the machinability of aluminum matrix composites reinforced with SiC or Al_2O_3 particles and concluded that CBN and PCD tools are better than WC tools in terms of wear resistance. A mathematical models to predict some properties of holes such as cylindricty, roundness, perpendicularity values was developed Pirtini and Lazoglu (2005) for drilling Aluminum (Al7039) using Carbide drills.

Wang and Zhang (2008) developed predictive models for the thrust force and torque in drilling operations using the modified plane rake faced twist drills using the unified-generalized mechanics of cutting approach. They developed empirical type thrust, torque and power equations to facilitate practical applications. Audy (2008) made computer-assisted analysis of effects of drill geometry and surface coating on forces and power in drilling and reported that the predicted values and trends matched reasonably well with the experimental data, and the force tests have confirmed the advantage of various single layer coatings over unprotected/uncoated tool substrate material. Lee et al. (1998) modelled drilling operations using self-organized abductive networks and applied simulated annealing for searching optimal drilling process parameters.

Satishkumar and Asokan (2008) developed a mathematical model for the selection of optimal conditions for Computer Numerical Control (CNC) multi tool drilling system and concluded that minimum production cost is obtained in two stage drilling rather than single stage drilling. Tash (2006) obtained experimental correlations between the metallurgical parameters and the machinability values for Heat-Treated 319 Alloys (mean total drilling forces and moments as well as heat build-up on the cutting tool edge) and analyzed them using factorial analysis.

Palanikumar (2007) applied response surface methodology to analyze the influence of four important input variables such as cutting speed, feed rate, depth of cut and fiber orientation angle in machining of Glass Fibre Reinforced Plastics (GFRP) composites and concluded that the surface roughness increases with the increase of fibre orientation angle. Somasundaram et al. (2012 & 2015) obtained an empirical secondorder model describing the friction drilling process using the RSM and finding the optimal set of model coefficients.

Mustafa Kurt et al. (2009) applied Taguchi methods to optimize surface finish and hole diameter accuracy in the dry drilling of Al2024 alloy. They obtained minimum surface finish value as 3.58 μm and minimum hole diametric error value as 36.5403 μm by using Taguchi's optimization method. Erolkilickap et al. (2011) conducted experiments for drilling AISI 1045 using TiN coated HSS tool. They modelled the process using Response Surface Model (RSM) and optimized using Genetic Algorithm (GA) in order to find the optimum values of independent variables. They reported optimum drilling parameters for the minimum surface roughness (Ra=1.89μm) value as cutting speed of 7.62m/min, feed of 0.1mm/rev, and MQL (1).

2. EXPERIMENTAL WORK

Central composite rotatable design (CCD) of second order has been found to be the most efficient tool in design of experiments (DOE) technique. Based on the literature and trial work done on these cutting parameters for friction-drilled aluminum alloy by author the independently controllable predominant drilling parameters that have greater influences on the surface roughness of the friction drilled Al/SiCp MMC plates have been identified. The factors considered and their levels used for the experimentation are given in Table 1. The experiments were performed on VMC-100 CNC machine. A five level, central composite, rotatable design matrix as shown in Table 2, is used for experimentation. The five different levels of spindle speed are chosen as 2000, 2500, 3000, 3500 and 4000 rpm. Similarly, feed variations are 40, 50, 60, 70 and 80 mm/min and the variations for weight percentage of SiC are 5,10,15,20 and 25 % and thickness of work piece is varied as 2, 2.5, 3, 3.5 and 4 mm.

Table 1: Experimental factor and their levels

S. No.	Factors	Unit	Levels				
			(-2)	(-1)	0	(+1)	(+2)
1.	Spindle speed	rpm	2000	2500	3000	3500	4000
2.	Tool feed rate	mm/min	40	50	60	70	80
3.	Weight % of SiC	%	5	10	15	20	25
4.	Plate thickness	mm	2	2.5	3	3.5	4

Table 2: Layout of central composite rotatable design and observed values of surface roughness

S. No	Spindle speed, rpm	Feed rate, mm/min	Wt. % of SiC, %	Thickness of plate, mm	Surf rough, µm
1	-1	-1	-1	-1	1.54
2	1	-1	-1	-1	1.63
3	-1	1	-1	-1	1.97
4	1	1	-1	-1	1.76
5	-1	-1	1	-1	1.16
6	1	-1	1	-1	1.16
7	-1	1	1	-1	1.22
8	1	1	1	-1	0.94
9	-1	-1	-1	1	0.99
10	1	-1	-1	1	1.01
11	-1	1	-1	1	1.95
12	1	1	-1	1	1.68
13	-1	-1	1	1	1.31
14	1	-1	1	1	1.25
15	-1	1	1	1	1.94
16	1	1	1	1	1.42
17	-2	0	0	0	1.43
18	2	0	0	0	0.89
19	0	-2	0	0	1.05
20	0	2	0	0	1.97
21	0	0	-2	0	2.15
22	0	0	2	0	1.23
23	0	0	0	-2	1.13
24	0	0	0	2	1.34
25	0	0	0	0	1.54
26	0	0	0	0	1.45
27	0	0	0	0	1.95
28	0	0	0	0	1.26
29	0	0	0	0	1.45
30	0	0	0	0	1.34
31	0	0	0	0	1.64

Every machining operation leaves characteristic evidence on the machined surface. This evidence is in the form of finely spaced micro irregularities left by the cutting tool. Each type of cutting tool leaves its own individual pattern, which therefore can be identified. This pattern is known as surface finish or surface roughness. Surface roughness is also one of the important concerns in machining and the surface finish of the work piece only improves the quality of manufactured part and precision fits. The average surface roughness (Ra) was taken for the present study and is defined on the basis of ISO 4287 standard. The surface roughness of the holes was measured at three positions with40˚ interval using a stylus-type instrument. The measurements were repeated three times and the average values were used for the analysis. Since the probe diameter of the tester is larger than the diameter of the hole, the work piece is cut with wire cut Electric Discharge Machining (EDM) in such a way that the friction drilled holes are cut into two halves.

3. OPTIMIZATION OF MACHINING PARAMETERS USING GENETIC ALGORITHM

The Optimization of machining processes is essential for the achievement of high responsiveness to production, which provides a preliminary basis for survival in today's dynamic market conditions. The complexity of cutting process management increases with each different single or combined influence of the cutting tool and work piece material. On the other hand, engineers have limited time for production setting, and therefore, the popularity of reliable and quick experimental methods of production is increasing. In the present work, Genetic algorithms (GA) optimization method is applied for the drilling process. Genetic algorithms (GA) are an evolutionary optimization approach which is an alternative to traditional optimization methods. GA is most appropriate for complex non-linear models where location of the global optimum is a difficult task. It may be possible to use GA techniques to consider problems which may not be modelled as accurately using other approaches.

Genetic Algorithm follows the concept of solution evolution by stochastically developing generations of solution populations using a given fitness statistic (for example, the objective function in mathematical programmes). They are particularly applicable to problems which are large, non-linear and possibly discrete in nature, features that traditionally add to the degree of complexity of solution. Due to the probabilistic development of the solution, GA does not guarantee optimality even when it may be reached. However, they are likely to be close to the global optimum. This probabilistic nature of the solution is also the reason they are not contained by local optima.

3.1. Procedure Adopted for Optimizing using GA

The GA consists of four main stages: evaluation, selection, crossover and mutation (Figure 1). The *evaluation* procedure measures the fitness of each individual solution in the population and assigns it a relative value based on the defining optimization (or search) criteria. Typically in a non-linear programming scenario, this measure will reflect the objective value of the given model. The *selection* procedure randomly selects individuals of the current population for development of the next generation. Various alternative methods have been proposed but all follow the idea that the fittest have a greater chance of survival. The *crossover* procedure takes two selected individuals and combines them about a crossover point thereby creating two new individuals. Simple (asexual) reproduction can also occur which replicates a single individual into the new population. The *mutation* procedure randomly modifies the genes of an individual subject to a small mutation factor, introducing further randomness into the population.

This iterative process continues until one of the possible termination criteria is met: if a known optimal or acceptable solution level is attained; or if a maximum number of generations have been performed; or if a given number of generations without fitness improvement occur. Generally, the last of these criteria applies as convergence slows to the optimal solution. Genetic algorithms are blind without the fitness function. The fitness function drives the population toward better solutions and is the most important part of the algorithm.

The fitness function for optimizing the friction drilling process is the mathematical model of the process concerned. In any machining process, there will be two or more process variables that are inherently related and it is necessary to explore the nature of their relationship. A model has been proposed relating the process parameters with the output response. This model can be used for prediction, process optimization or control purposes.

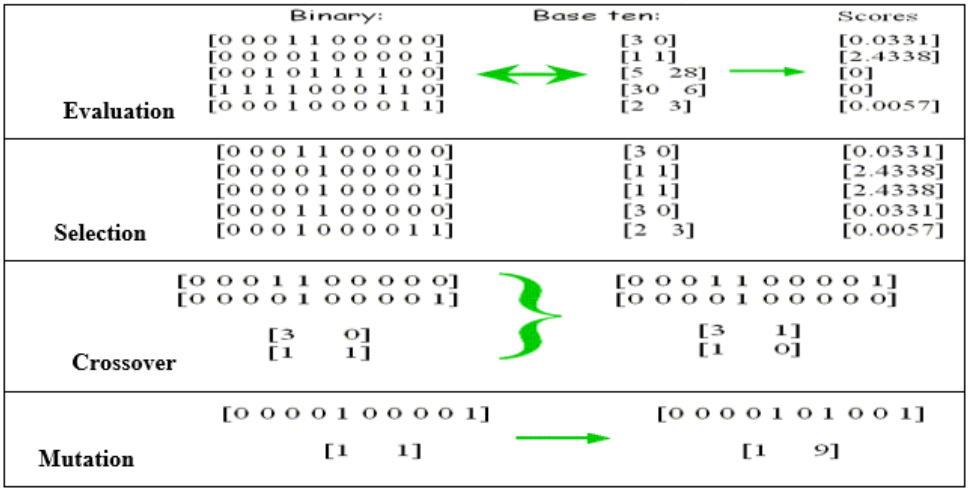

Figure 1: Schematic explanation of procedure adopted for optimizing using GA

The results of the experiments were used by the authors to fit response surface model to the response, surface roughness, as a function of four particular controllable factors of the friction drilling process. Two factors were spindle speed (measured in rpm), feed rate (measured in mm/min) of the machine and the other two factors were weight percentage composition of SiC (measured in percentage) and the thickness (measured in mm) of the work piece material, AlSiC composite.

By using the RSM and finding the optimal set of model coefficients, an empirical second-order model is obtained. Using the significant terms' coefficients from regression statistics, the relevant mathematical model fitted for Surface roughness was obtained and is represented by the quadratic equation (1), describing the process, in coded units.

1.5186-0.0639*s+0.1938*f-0.1157*w-0.0829*s*f-0.0976*f*w-0.1362*s*s+0.1201*w*w+0.1274*f*p+0.1686*w*p (1)

Using this equation surface roughness for any values of process parameters, namely, spindle speed (s), feed (f), weight percentage of SiC (w) and plate thickness (p) within the respective minimum and maximum limits can be predicted. This mathematical model represented by the quadratic equation (1) developed by the authors separately is used as the fitness function for the GA. Table 3 shows the optimized machining parameters in coded as well as in standard values obtained by GA.

Table 3: Optimized machining parameters

Machining parameters	Spindle speed	Feed rate	Wt. % of SiC	Thickness of plate	Surf roughness, µm
Optimized values in coded values	1.981	-1.242	1.812	-1.98	0.830128
Optimized values in standard values	3990.698 rpm	47.585 mm/min	24.561 %	2.14	

4. RESULT AND DISCUSSION

Analysis of drilling parameters for the responses surface roughness in friction drilling of AlSiC-Metal Matrix Composites is carried out by using analysis of variance (ANOVA). The purpose of the analysis of variance is to

investigate which drilling parameters significantly influence the performance characteristic. The influence of factors and their interaction are evaluated through the coefficients of the postulated model.

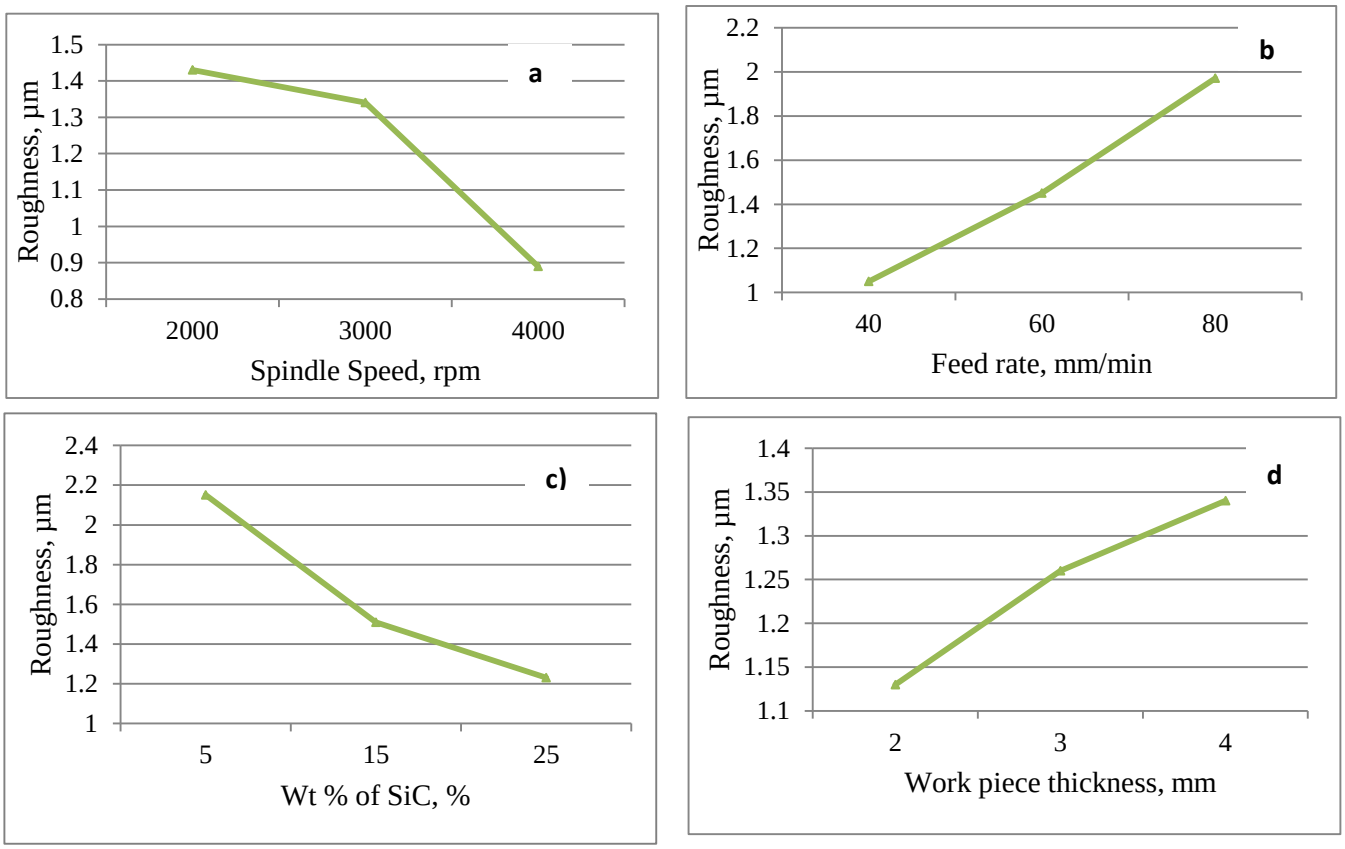

Figure 4: Influence of various parameters, (a) spindle speed, (b) feed rate, (c) wt% of SiC particles and (d) work piece thicknesses, on surface roughness of the holes made

Influence of spindle speed on surface roughness is presented in Figure 4(a). General trend is as the speed increases the surface roughness values are decreasing gradually. Tool penetration was difficult at the lower spindle speeds where the associated heat generated is not sufficient for plasticization of the work piece and the vibration level is higher which reflects in higher surface roughness. Influence of feed rate on surface roughness is presented in Figure 4(b). General trend is as the feed rate increases the surface roughness values are increasing. This may be due to the act of unbalancing of thrust forces which destabilizes the process and increases tool vibration

Influence of wt% of SiC particles on surface roughness is presented in Figure4(c). General trend is as the wt% of SiC particles increases the surface roughness values are decreasing. Tosun and Muratoglu, (2004) believed that thermal softening is taking place in machining of Al/SiC composites where the work piece material becomes softer due to the heat generated and SiC particles become pressed into the work piece. This may be the reason for minimal surface roughness values for the higher range of composition of wt% of SiC particles.

Influence of work piece thicknesses on surface roughness is presented in Figure 4(d). General trend is that surface roughness increases gradually with increase of work piece thickness The major reason must be due to the instability of the tool while penetrating thicker plate. Better performance of Coated HSS tool is because of the easy penetration of the tool with less vibration which is mainly due to the sliding action of the coating material TiN. This unique phenomenon is the characteristic of the TiN coating which is having coefficient of friction ranging from 0.4 to 0.9 versus itself (non-lubricated) and Vickers hardness of 18-21 GPa.

5. CONCLUSION

Main contribution of the study is to minimize surface roughness and to find out optimum drilling condition using GA. Genetic algorithms have been very useful in optimization of the response variable and also in multi-response cases. The RSM based surface roughness model can be optimized using a genetic algorithm in order to find the optimum values of independent variables. The given model can be utilized to select the level of drilling parameters. Using this model, a noticeable saving in time and cost has been obtained.

Genetic algorithm was used for optimizing the machining process with multiple performance characteristics. The successful implementation of this technique for friction drilling of AlSiCp - MMC composite material was achieved with a lower number of experimentation instead of many tedious machining trials.

REFERENCES

Audy. J, (2008); A study of computer-assisted analysis of effects of drill geometry and surface coating on forces and power in drilling, *Journal of Materials Processing Technology*, (204): 130–138.

Chen Z.Z, K. Tokaji, (2004). Effects of particle size on fatigue crack initiation and small crack growth in SiC particulate-reinforced aluminium alloy composites, *Materials Letters*, (58):2314– 2321.

Durante. S, G. Rutelli, F. Rabezzan, (1997). Aluminum-based MMC machining with diamond-coated cutting tools, *Surface and Coatings Technology*, (94-95): 632-640.

Erol Kilickap, Mesut Huseyinoglu, Ahmet Yardimeden (2011). Optimization of drilling parameters on surface roughness in drilling of AISI1045 using response surface methodology and genetic algorithm. *International Journal of Advanced Manufacturing Technology*, (52): 79–88.

Hung N.P, C.H. Zhong, (1996). Cumulative tool wear in machining metal matrix composites part-I: modeling, *Journals of Materials Processing Technology*, (58): 109-113.

Hung N.P, S.H.Yeo, B.E.Oon, (1997). Effect of cutting fluid on the machinability of metal matrix Composites, *Journal of material processing technology*, (67): 157-161.

Ibrahim Ciftci, Mehmet Turker, UlviSeker, (2004). Technical report, Evaluation of tool wear when machining SiCp-reinforced Al-2014 alloy matrix composites, *Materials and Design*, (25): 251–255.

Kanagaraju.T, Rajendra Boopathy.S, Somasundaram.G, (2009). Optimisation of drilling parameters for thrust force and torque in Friction drilling of aluminium 6061-T6 alloy, *National Conference on Recent Trends in Manufacturing Technology, Chennai*, pp 43-49.

Lee B.Y, H.S.Liu,Y.S. Tarng, (1998). Modeling and optimization of drilling process, *Journal of Materials Processing Technology*, (74): 149–157.

Lin J.T, D. Bhattacharyya, W. G. Fergusod, (1998). Chip formation in the machining of sic-particle reinforced, Aluminium-matrix composites, *Composites Science and Technology*, (58): 285-291.

Miller Scott F, Jia Tao, Albert J.Shih, (2006). Friction drilling of cast metals, *International Journal of Machine Tools & Manufacture*, (46): 1526–1535.

Mustafa Kurt, Eyup Bagei, Yusuf Kaynak, (2009). Application of Taguchi methods in the optimization of cutting parameters for surface finish and hole diameter accuracy in dry drilling process, *International Journal of Advanced Manufacturing Technology*, (40): 458-469.

Nouari M, G.List, F.Girot, D.Gehin, (2005). Effect of machining parameters and coating on wear mechanisms in dry drilling of aluminium alloys, *International Journal of Machine Tools & Manufacture*, (45): 1436–1442.

Palanikumar.P, (2007), Modelling and analysis for surface roughness in machining glass fiber reinforced plastics using response surface methodology, *Materials and Design*, (28): 2611-2618.

Paris.H, D.Brissaud, A.Gouskov, N.Guibert, J.Rech, (2008). Influence of the ploughing effect on the dynamic behavior of the self-vibratory drilling head, CIRPAnnals, *Manufacturing Technology*, (57): 385–388.

Paulo Davim.J, C.A.ConceicaoAnto´nio, (2001). Optimal drilling of particulate metal matrix composites based on experimental and numerical procedures, *International Journal of Machine Tools & Manufacture*, (4): 21–31.

Pirtini.M, I.Lazoglu, (2005). Force and hole quality in drilling. *International Journal of Machine Tool & Manufacture*, (45): 1271-1281.

Riccardo Polini,FabrizioCasadei, PierangeloD'Antonio, Enrico Traversa, (2003). Dry turning of alumina/aluminum composites with CVD diamond coated Co-cemented tungsten carbide tools, *Surface and Coatings Technology*, (166): 127–134.

Satishkumar.S, P. Asokan, (2008). Selection of optimal conditions for CNC multitool drilling system using non-traditional techniques, *Int. J. Machining and Machinability of Materials*, (3): 190–207.

Somasundaram, G, Maniravindran, Rassayiah, (2015) "Modelling of the friction drilling process for making holes in Aluminum Silicon Carbide Metal Matrix Composite", *International Journal of Applied Engineering Research, 10(68)*: 611-614.

Somasundaram, G., Rajendra Boopathy, S. and Palanikumar, K (2012). "Modeling and analysis on roundness error in friction drilling of Aluminum Silicon Carbide Metal Matrix Composite", *Journal of Composite Materials*, 46 (2): 169-181.

Tash.M, F.H. Samuel, F. Mucciardi, H.W. Doty, S. Valtierra, (2006). Effect of metallurgical parameters on the machinability of heat-treated 356 and 319 aluminum alloys, *Materials Science and Engineering A*, 434: 207–217

Tero Stjernstoft (2004). Ph.D Dissertation- Department of Production Engineering, The Royal Institute of Technology, KTH.

Tosun.G, M. Muratoglu, (2004). The drilling of Al/SiCp metal–matrix composites. Part I: *microstructure*, *Composites Science and Technology*, (64) 299-308.

Wang.J, Q.Zhang, (2008) A study of high performance plane rake faced twist drills. PartII: Predictive Force models, *International Journal of Machine Tools & Manufacture*, (48): 1286–1295.

Yanming Quan, Bangyan Ye, (2003). The effect of machining on the surface properties of SiC/Al composites, *Journal of Materials Processing Technology*, (138): 464–467.

Structural and Electrical Properties of Ytterbium and Samarium Co-doped Ceria as a Solid Electrolyte for Intermediate-Temperature Solid Oxide Fuel Cell

Lemessa Asefa Eressa*, PV Bhaskara Rao

Wollega University, Department of Physics, Nekemte, Ethiopia
**Corresponding author, e-mail: lemessaphys@gmail.com*

ABSTRACT

Solid oxide fuel cells (SOFCs) have received much recent attention as next-generation alternative energy conversion devices because of their high efficiencies, good fuel flexibility and eco- friendly manner. However, the high-temperature operation results in a number of challenges that needs to be overcome, including degradation of SOFC components resulting in reduction of SOFC useful life and cost of fabrication. One approach to overcome the bottle-neck of operating temperatures of SOFCs is finding an alternate electrolyte exhibiting high performance at intermediate temperature SOFCs (IT-SOFC) applications. Hence, the study was aimed on the preparation of Ytterbium and Samarium co-doped Ceria materials $(Ce_{1-x-y}Sm_xYb_yO_{2-\delta})$ $(YbSDC)$ *with concentrations* $(x = 0.05, y = 0.05{,}0.1)$ *by Sol-Gel method to investigate its structural and electrical properties for use as an electrolyte for IT-SOFCs applications. The crystal structure, microstructure and ionic conductivity have been determined by X-ray diffraction (XRD), Scanning electron microscopy (SEM), Energy dispersive X-ray spectrometer (EDX), Raman Spectroscopy (Raman) and impedance spectroscopy respectively. The XRD result reveals that all the samples are single phase with cubic fluorite-type structure. The relative densities of samples sintered at 1400^{0}C are about 98% of theoretical density. The average grain sizes of YbSDC- samples found from SEM image are in the range of 474-680nm. The Raman spectra result showed formation of three distinctive peaks in the YbSDC- lattice. An intense peak at 464cm^{-1} and two weaker peaks at 260cm^{-1} and 552cm^{-1}. Based on the impedance spectroscopy results, the composition $Ce_{0.85}Sm_{0.05}Yb_{0.1}O_{1.925}$ exhibited greater conductivity of 4.4 x10^{-3} S/cm than that of composition $Ce_{0.85}Sm_{0.05}Yb_{0.05}O_{1.95}$ which exhibited a conductivity of 1.88 x10^{-3} S/cm at 500^{0}C in air atmosphere. All the results confirmed that Yb and Sm co-doped ceria is a promising alternative electrolyte for intermediate temperature solid oxide fuel cell (IT-SOFCs) applications.*

Keywords: *IT-SOFCS, electrolyte, co-doped ceria, ionic conductivity*

1. INTRODUCTION

One of society's current ambitions is to achieve the clean and efficient generation of electricity from renewable sources, together with the reduction of emissions of both atmospheric polutants and carbon dioxide emissions. To achieve this goal, alternative energy conversion devices need to be searched. Solid- oxide fuel cells(SOFCs) play a major role in this transition from a high- carbon economy to a low- carbon economy and ultimately to a zero-carbon economy. These devices offer operational flexibility and fuel processing so that the transition from fossil fuels to synthetic hydrocarbons derived from biomass and other renewable sources to a fully renewable energy economy is possible (Dönmez et al., 2015; Gan et al., 2015; Kobi et al., 2016; Kumar et al., 2017; Kumar et al., 2016; Raharjo et al., 2017; Shajahan et al., 2018; Venkataramana et al., 2017; Yang et al., 2016). Despite these advantages, however, SOFC still has marketing problems, such as its manufacturing costs at high temperatures and the durability of cell components. One of the strategies which is supposed to be addressed to overcome the bottle-neck of operating temperatures of SOFCs is finding an alternate solid electrolyte for intermediate SOFCs (IT-SOFCs) (IT- SOFCs) (Kim et al., 2013; Molenda et al., 2007; Omar et al., 2007; Tarancón, 2009). Ceria-based oxides for intermediate temperature applications are explicitly investigated due to their various advantages over ZrO_2-based materials (Accardo et al., 2016; Daza et al., 2018; Spiridigliozzi et al., 2015). Samaria doped ceria(SDC) has received considerable attention as a potential IT- SOFC electrolyte because of its high ionic conductivity among the various dopants studied (Arabaci, 2015a; Arabaci, 2015b; Dell'Agli et al., 2017; Karaca et al., 2010; Kosinski and Baker, 2011).

However, the results of the literature showed that single- doped ceria- based oxides have limits on their application as solid electrolytes because of the tendency to reduce Ce^{4+}(ionic conduction) to Ce^{3+} (electronic conduction) (Koteswararao et al., 2015; Sandhya et al., 2017; Singh et al., 2012; Wu and Lin, 2014). In addition, low temperatures (500^0C-700^0C) are still not suitable for single doped ceria as an SOFC electrolyte due to its high grain resistance(Singh et al., 2012).

In particular, the structural, microstructure and electrical properties of single doped ceria with Yb for IT-SOFC application as an electrolyte were not well studied (Bondioli et al., 2005; Jeyanthi et al., 2015; Ye et al., 2007). In addition, a low ion conductivity value for single doped ceria with ytterbium has been reported (0.34x 10^{-3}S/cm at 500^0C) (Stojmenović et al., 2015) due to the aforementioned factors.

In literature, the co- doping method was reported to be a new principle for improving the structural, electrical and thermal stability of ceria- based electrolytes at intermediate temperatures (Daza et al., 2018; Li et al., 2010; Ramesh et al., 2014; Roy, 2012; Wu et al., 2017; Zając and Molenda, 2008). To date, there are no clear reports for the ionic conductivity properties of the co- doped ceria electrolyte with Yb.

The author therefore aimed at the synthesis of $Ce_{1-x-y}Sm_xYb_yO_{2-\delta}$ $(x = 0.05, Y = 0.05,0.1)$materials using the Sol- Gel method to investigate its structural and electrical properties for use as an electrolyte for IT-SOFC applications.

2. EXPERIMENTAL METHODS

The samples with the general formula $Ce_{1-x-y}Sm_xYb_yO_{2-\delta}$ $(x = 0.05, Y = 0.05,0.1)$ were synthesized through sol-gel method. High purity cerium (III) nitrate hexahydrate ($Ce(NO_3)_3$.$6H_2O$, 99.9%, Otto, India), Samarium (III) nitrate hexahydrate ($Sm(NO_3)_3$.$6H_2O$,99.9%, Otto, India) and Ytterbium (III) nitrate Pentahydrate ($Yb(NO_3)_3$.$5H_2O$, 99.9%, Otto, India) were used as the starting materials.

Stoichiometric amounts of all nitrates were dissolved in distilled water under continuous stirring. Citric acid was added to the whole mixture of precursors in 1:1 molar ratio to maintain the total molar ratio of metal to citric acid. In order to adjust the *p*H to ≈7, ammonium hydroxide was added drop by drop to the solution.

After adjusting pH value, the whole mixture was stirred at 80^0C for 2-3h and a homogenous solution was then formed. After 2-3h, a yellowish viscous gel was formed. The gel was placed in an oven to form ash. As the gel was put in an oven, slowly the gel started to foam, swell and finally burn with glowing flints and the evolution of large amounts of gas occurred. This auto ignition was slowly propagated until the whole sample was fully burnt to produce a yellowish colored ash. Ash was calcined at 700ºC for 2 h to remove the carbonaceous materials and the most stable mixed oxide phase was found. The resultant ash was ground continuously for 1h in agate mortar to get a fine homogeneous powder. The powders were pressed with the help of a hydraulic press under a pressure of 200MPa into a circular pellet (8mm in diameter and 2 mm in thickness). Finally, the pellets were sintered in furnace at 1400ºC for 2h and prepared for density and other measurement techniques.

3. RESULTS AND DISCUSSIONS

3.1. XRD Analysis

Figure 1 shows the XRD patterns obtained from YbSDC- samples that were prepared by sintering at 1400ºC for 2 h. Eight symmetrical diffraction peaks were observed in the XRD spectra (111, 200, 220, 311, 222, 400, 331 and 420). This XRD pattern matches with standard single-phase cubic fluorite structure with space group Fm3m (JCPDS File No.:34-0394) (Accardo et al., 2018; Anjaneya and Singh, 2017; Bhabu et al., 2016; Kahlaoui et al., 2013). Also, the diffraction pattern exhibits that the nanoparticles possess good crystalline nature. Secondary peaks were not observed in the XRD pattern. The lattice parameter of the YbSDC- sample increases slightly with increasing dopants content, as depicted in Table 2. This increase can be attributed to the substitution of the smaller Ce^{4+} (r = 0. 97A^0 by the larger Yb^{3+} (r = 0.985A^0) and Sm^{3+} (r = 1.08A^0) (Stojmenović et al., 2015).

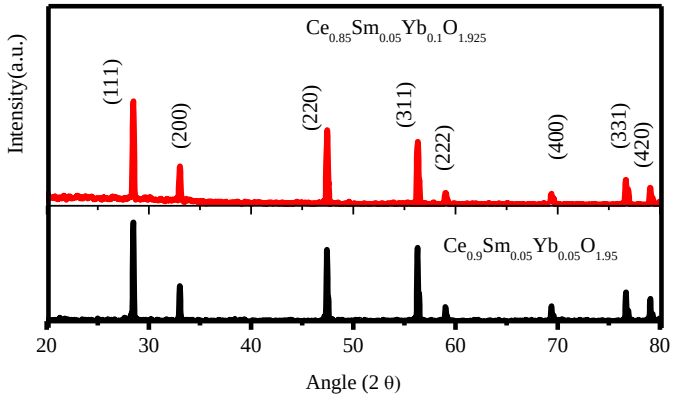

Figure 1: XRD Patterns of YbSDC- Samples

In this study, the theoretical lattice parameter of Yb and Sm codoped ceria is calculated using Hong and Vikar formula as(Anjaneya et al. 2013):

$$a = \frac{4}{\sqrt{3}}[(xr_{Re}) + (1-x)r_{Ce} + (1-0.25x)r_O + (0.25)x(r_{VO})]0.9971 \quad (1)$$

Where x is the average concentration of Yb and Sm dopants, r_{Re} is effective radii of Yb^{3+} and Sm^{3+}(1.0325A^0), r_{Ce} is radius of Ce^{4+}(0.97A^0), r_O is radius of O^{-2}(1.38A^0) and r_{Vo} is radius of oxygen vacancy(1.164A^0) respectively. Accordingly, the theoretical lattice parameter of $Ce_{1-x-y}Sm_x\,Yb_yO_{2-\delta}$ system with ionic radii (Ce^{4+} = 0.97A^0, Sm^{3+} = 1.038A^0, Yb^{+3} = 0.985A^0) are given in Table 1.

Table 1: Theoretical lattice parameter of Yb and Sm Co-doped ceria

Sample	Theoretical lattice parameter (A^0)
$Ce_{0.9}Sm_{0.05}Yb_{0.05}O_{1.95}$	5.421
$Ce_{0.85}Sm_{0.05}Yb_{0.1}O_{1.925}$	5.423

The experimental lattice parameter 'a' can be calculated from the equation:

$$a = d.\sqrt{h^2 + k^2 + l^2} \quad (2)$$

Where, 'd' the inter planner distance and '*hkl*' are the Miller indices of the plane obtained in XRD measurement. Using Eq.2, the experimental lattice parameters of $Ce_{0.9}Sm_{0.05}Yb_{0.05}O_{1.95}$ and $Ce_{0.85}Sm_{0.05}Yb_{0.1}O_{1.925}$ calculated were 0.5417 *nm* and 0.5419 *nm*, respectively and depicted in Table 2. These values are slightly larger than lattice parameter of pure CeO_2 (0.5411 *nm*) (Dos Santos et al. 2008), as expected from the effective ionic radii of Yb^{3+} and Sm^{3+} (0.10325 *nm*).

In this study, the density measurement was carried out to determine the extent of porosity in prepared samples. Theoretical density was calculated using the formula which is given as (Yang et al. 2016):

$$D_t = \frac{4}{N_A a^3}[(1-x)M_A + xM_B + (2-0.5x)M_O] \quad (3)$$

Where, '*x*' is the average mass of samarium and ytterbium content, '*a*' the lattice parameter at room temperature of samples, N_a the Avogadro number (6.023x10^{23}), M_A, M_B, and M_O refers to atomic weights of cerium, average weights of samarium and ytterbium, oxygen respectively.

The relative density η is calculated as a relation in percentage of the sample density (D_e) to the theoretical density (D_t):

$$\eta = \frac{D_e}{D_t} X\ 100\% \quad (4)$$

The theoretical, experimental and relative densities of YbSDC-samples were shown in Table 2. As it can be observed from Table 2, the calculated relative densities of YbSDC- samples were about 98% of the theoretical densities and these findings were supported by SEM images.

Table 2: Crystallite Size, grain size, lattice parameter and relative densities of YbSDC-samples.

No.	Compositions	Grain size (nm)	Experimental Lattice parameter (nm)	Theoretical Density (g/cm^3)	Experimental Density (g/cm^3)	Relative density (%)
1	$Ce_{0.9}Sm_{0.05}Yb_{0.05}O_{1.95}$	474	0.5417	7.28938	7.17825	98.5
2	$Ce_{0.85}Sm_{0.05}Yb_{0.1}O_{1.925}$	680	0.5419	7.42467	7.3292	98.7

3.2. SEM and EDX Analysis

Sintering directly affects the material properties such as density and grain size. The morphology and chemical composition of $Ce_{0.9}Sm_{0.05}Yb_{0.05}O_{1.95}$ and $Ce_{0.85}Sm_{0.05}Yb_{0.1}O_{1.925}$ samples presented in Figure 2 and Figure 3 respectively. It can be seen that the surface of the samples shows high densification with few invisible pores indicating relative density less than 100%.

The microstructure of all sintered pellets was examined using SEM. SEM micrograph clearly shows the presence of uniform grains with clean and distinct grain boundaries. As shown in Table 2, the average grain sizes of YbSDC-samples found from SEM image are in the range of 474-680nm. However, literature results indicated that the average grain size value was 10800nm for pure ceria(Arabacı et al., 2017). Hence, doping Yb and Sm in ceria depresses the grain growth of CeO_2. It also depicts that the grain sizes of YbSDC-samples increased with Yb amount at constant amount of samarium. The smaller grain size was obtained for the concentration(x = y = 0.05). This finding is consistent with the result reported in the previous literature for single doped ceria with Yb content(Ye et al. 2007). It can be seen from Figure 3, the EDX graph confirmed the presence of elements Yb, Sm, Ce and O in the YbSDC- lattice and no other elements were observed. Moreover, Figure 3 indicated the atomic weight of elements Yb, Sm, Ce and O found in each sample is as per stochiometry and their atomic percentage is depicted in Table 3.

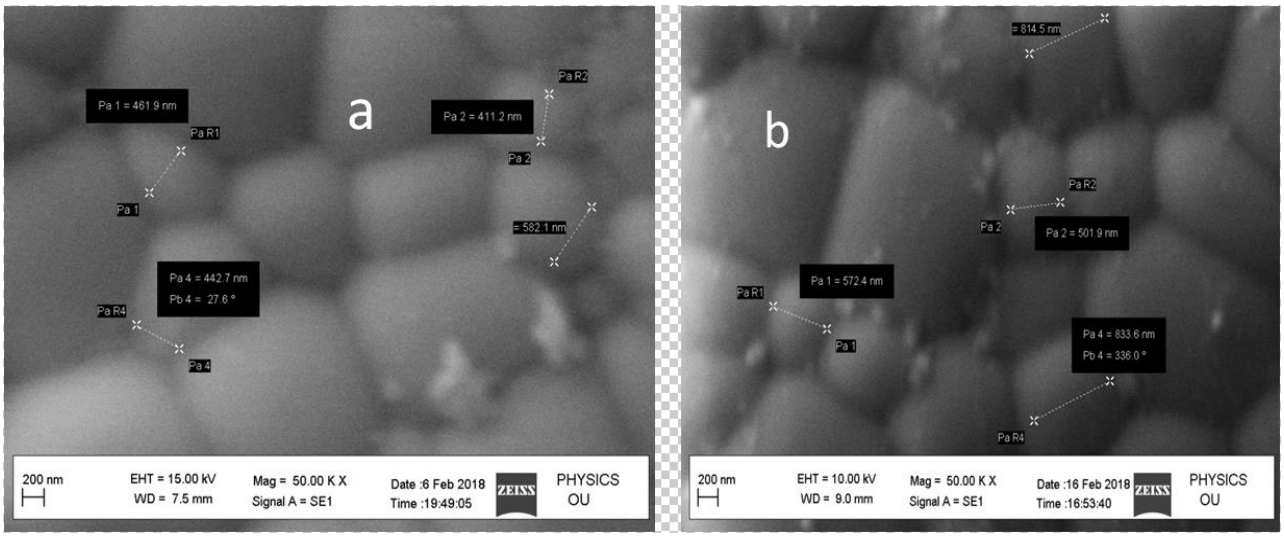

Figure 2: SEM graphs of (a) $Ce_{0.9}Sm_{0.05}Yb_{0.05}O_{1.95}$ (b) $Ce_{0.85}Sm_{0.05}Yb_{0.1}O_{1.925}$

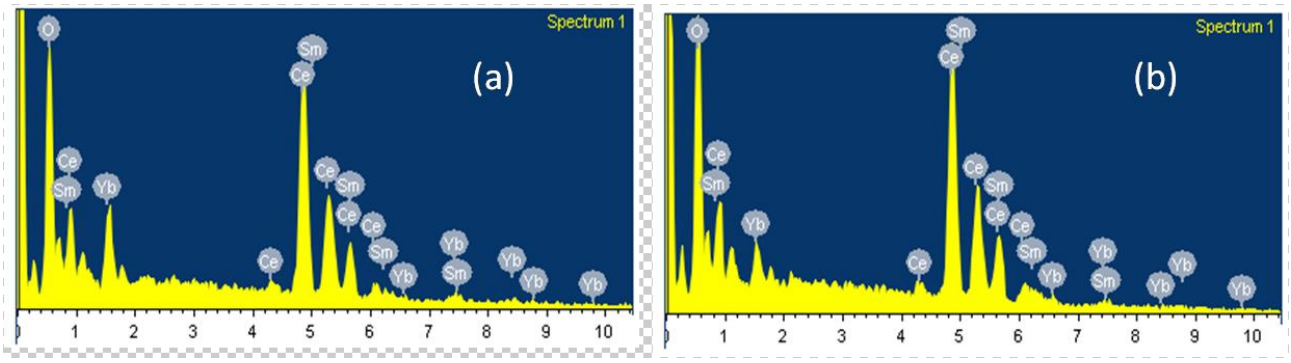

Figure 3:.EDX analysis of (a) $Ce_{0.9}Sm_{0.05}Yb_{0.05}O_{1.95}$ (b) $Ce_{0.85}Sm_{0.05}Yb_{0.1}O_{1.925}$

Table 3: EDX quantitative analysis of elements O, Ce, Sm and Yb

No	Co-doped Ceria	Weight (%)				Atomic (%)			
		O K	Ce L	Sm L	YbM	O K	Ce L	Sm L	YbM
1	$Ce_{0.9}Sm_{0.05}Yb_{0.05}O_{1.95}$	21.4	68.86	4.89	4.85	68.2	28.2	1.9	1.7
2	$Ce_{0.85}Sm_{0.05}Yb_{0.1}O_{1.925}$	18.1	69.56	4.32	8.02	69.9	26.52	1.7	3.15

3.3. Raman Spectroscopy Analysis

Figure 4 shows the Raman spectra of the $Ce_{0.9}Sm_{0.05}Yb_{0.05}O_{1.95}$ and $Ce_{0.85}Sm_{0.1}Yb_{0.05}O_{1.925}$ samples sintered at 1400^0C. It can be seen that each Raman spectrum consists of three distinctive peaks. The strong intensive peak observed at 464 cm^{-1} is attributed to first order Raman mode with F_{2g} symmetric vibration of ceria cations surrounded by oxygen anions, which confirms the formation of YbSDC- solid solution (Filtschew et al., 2016; Guo et al., 2011). The second weak peak observed at 260 cm^{-1} can be assigned to the higher order modes of ceria, namely to the second order transverse acoustic mode, that is, 2TA (Piumetti et al., 2017; Spanier et al., 2001; Swatsitang et al., 2016). The second weak peak appeared at 552 cm^{-1} is due to the oxygen vacancy created by the replacement of Ce^{4+} with Sm^{3+} and Yb^{3+} in order to maintain the charge neutrality in the lattice. This band became stronger with increasing Yb^{3+} content in the YbSDC- samples.

Recently, it was reported that the concentration of oxygen vacancies in ceria can be calculated by the intensity ratio of strong intense peak to the weak intense peak (i.e. I_{552}/I_{464}). It is also reported that the oxygen vacancy concentration in ceria solid solution can be estimated by the ratio of area of strong peak to the area of weak peak (i.e. A_{552}/A_{464}) (Li et al. 2009; López et al. 2015; Pu et al. 2007). In the present study, the values of intensity ratios (i.e. I_{552}/I_{464}) found for $Ce_{0.9}Sm_{0.05}Yb_{0.05}O_{1.95}$ and $Ce_{0.85}Sm_{0.05}Yb_{0.1}O_{1.925}$ are 0.10, 0.13, 0.19 and 0.18, respectively.

The higher value of I_{552}/I_{464} was obtained for $Ce_{0.85}Sm_{0.05}Yb_{0.1}O_{1.925}$ sample than $Ce_{0.9}Sm_{0.05}Yb_{0.05}O_{1.95}$. This confirmed that the formation of higher concentration of oxygen vacancies which causes the mobilization of ions in the $Ce_{0.85}Sm_{0.05}Yb_{0.1}O_{1.925}$ lattice resulting in the higher total ionic conductivity with less activation energy than in $Ce_{0.9}Sm_{0.05}Yb_{0.05}O_{1.95}$ sample. In this study, the Raman observation confirms the formation of single phase YbSDC- solid material supporting X-ray diffraction patterns indicated in Figure 1.

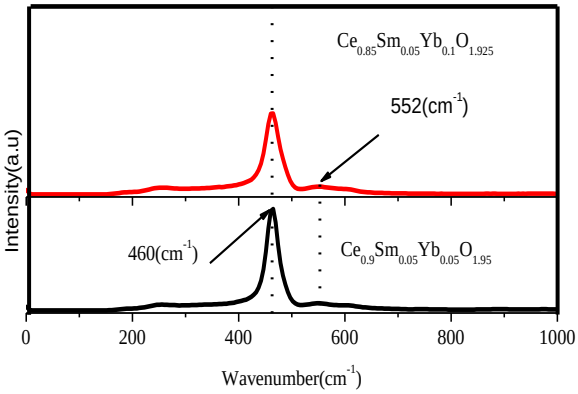

Figure 4: Raman spectra of YbSDC- samples sintered at 1400°C.

3.4. Impedance Spectroscopy

Impedance plots of YbSDC-samples recorded at different temperatures are shown in Figure 5a-d.The impedance spectra collected showed an arc for grain boundary resistance and incomplete depressed arc for electrode resistance behavior only as shown in Figure 5a-d. However, the arc in the high frequency range which represents the grain resistance is not displayed because of the limited frequency of measuring equipment (1Hz - 1MHz). Starting from the origin, the arc was not displayed for high frequency range. This length of real axis for which the arc is not displayed represented as the grain resistance. Hence, the grain resistance (Rg) was represented with the left horizontal axis (arc is not displayed), whereas Rgb was determined from fitting medium frequency arc intercept on the real axis. This behavior of impedance was also reported for doped ceria in previous literatures (Ali et al., 2017; Jais et al., 2017; Matović et al., 2014; Singh et al., 2010; Xiaomin et al., 2015).

The equivalent circuit model used to fit the impedance spectra includes a series of parallel resistances *R* and capacitances *C*. Considering the inhomogeneity of microstructure within the sintered sample, the capacitance *C* was substituted by constant phase element (CPE). This consists the grain resistance *R*g, the parallel connection of grain boundary resistance *R*gb and grain boundary constant phase element (*C*PE$_1$), and the parallel connection of electrode resistance *R*e and constant phase element (*C*PE$_2$).

The total resistance is given by

$$R = R_g + R_{gb} \qquad (5)$$

Where, *R*g and *R*gb stand for the resistance of grain interior and grain boundary respectively.
Then, the ionic conductivity (σ) of each sample was calculated using the equation:

$$\sigma = \frac{l}{RA} \qquad (6)$$

Where, *l* is the thickness of sample and A is the cross-sectional area. Through curve fitting a circle to the semi circles on the impedance spectra, the sample resistances were obtained using (Eq.5).The conductivity values of samples were then calculated from the resistance values using (Eq.6). This result is presented in Tables 4 and 5.

Table 4: Rg, Rgb, R and Conductivities of $Ce_{0.9}Sm_{0.05}Yb_{0.05}O_{1.95}$ at different measuring temperatures.

Temperature(^{0}C)	$Rg(\Omega$	$Rgb(\Omega$	$R(\Omega$	$\sigma(S/cm)$
300	548.76	27163.29	27712.05	2.58x10^{-5}
350	297.58	8826.22	9123.8	7.82x10$^{—5}$
400	98.99	2547.5	2646.49	2.69x10^{-4}
450	50.32	962.38	1012.70	7.05x10^{-4}
500	28.52	351.02	379.54	1.88x10^{-3}

Table 5: Rg, Rgb, R and conductivities of $Ce_{0.85}Sm_{0.05}Yb_{0.1}O_{1.925}$ at different measuring temperatures

Temperature(^{0}C)	$Rg(\Omega$	$Rgb(\Omega$	$R_T(\Omega$	$\sigma(S/cm)$
300	567.58	10219.21	10786.79	6.62 x10^{-5}
350	353.74	3133.13	3486.87	2.04 x10^{-4}
400	140.79	957.11	1097.9	6.5 x10^{-4}
450	75.37	329.8	405.17	1.76 x10^{-3}
500	46.64	115.64	162.28	4.4 x10^{-3}

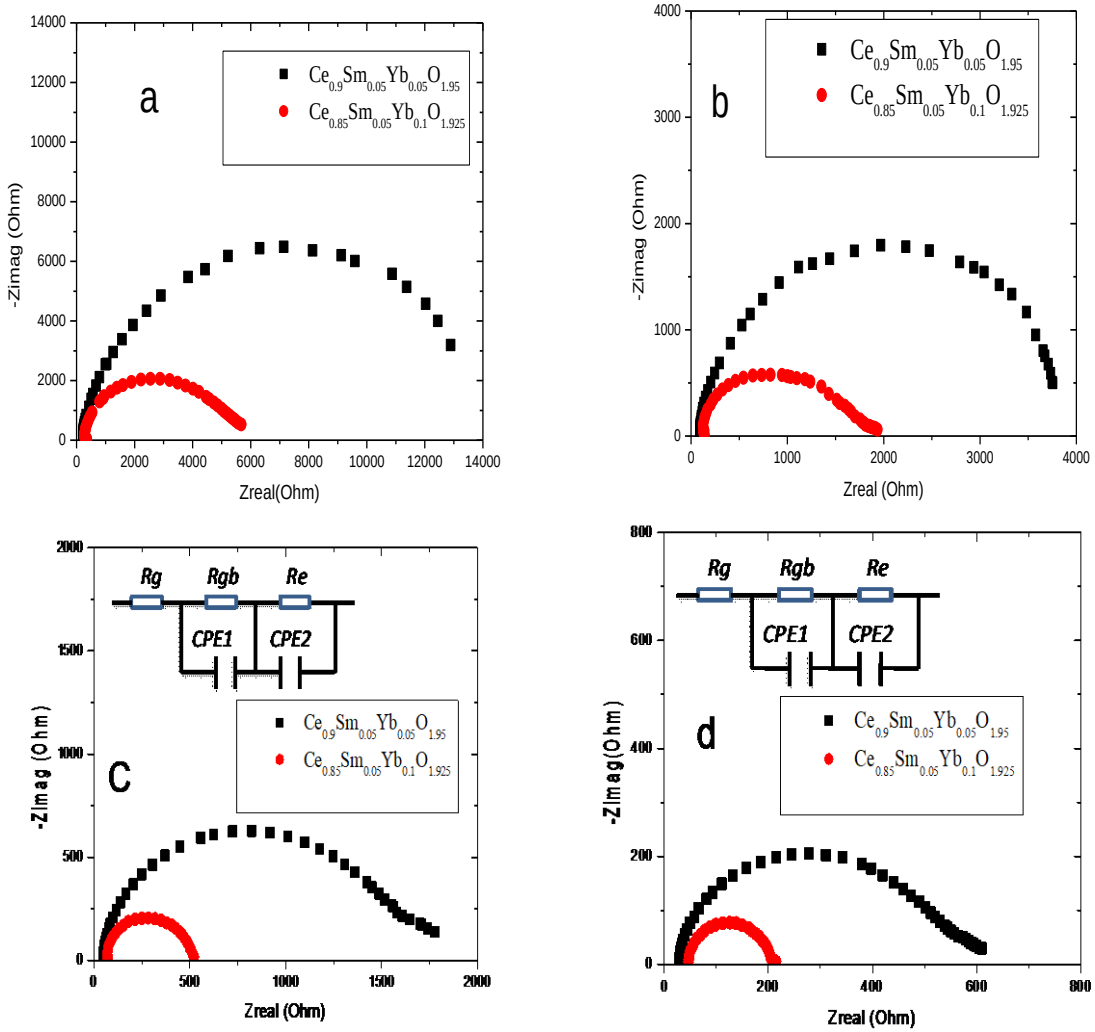

Figure 5: Impedance plots of YbSDC- samples measured in air at (a) 350^{o}C, (b) 400^{0}C,(c) 450 ^{0}C and (d) 500^{0}C.

As shown in Tables 4 and 5, the grain boundary resistance of $Ce_{0.85}Sm_{0.05}Yb_{0.1}O_{1.925}$ sample was dramatically decreased as compared to $Ce_{0.9}Sm_{0.05}Yb_{0.05}O_{1.95}$ with rise in measuring temperature. This shows that the increase in the concentration of Yb at constant amount of Sm has significant effect on the size of grain boundary resistance. It was observed in Table 2, the grain size of $Ce_{0.85}Sm_{0.05}Yb_{0.1}O_{1.925}$ sample is larger than that of $Ce_{0.9}Sm_{0.05}Yb_{0.05}O_{1.95}$. Consequently, this greater grain size resulted in the greater conductivity of $Ce_{0.85}Sm_{0.05}Yb_{0.1}O_{1.925}$ sample than that of $Ce_{0.9}Sm_{0.05}Yb_{0.05}O_{1.95}$. The increase in conductivity with increase in grain size is supported with the results reported in previous literatures(Xiaomin et al., 2015). Moreover, the increase in conductivity with increase in ytterbium doping is consistent with the results reported previously for single Yb doped ceria(Matović et al., 2014) .

As indicated in Tables 4 & 5, the conductivity of compositions $Ce_{0.9}Sm_{0.05}Yb_{0.05}O_{1.95}$ and $Ce_{0.85}Sm_{0.05}Yb_{0.1}O_{1.925}$ obtained are 1.88 x10^{-3} S/cm and 4.4 x10^{-3} S/cm respectively at 500^{0}C in air atmosphere. The conductivity of $Ce_{0.9}Sm_{0.05}Yb_{0.05}O_{1.95}$ is smaller than that of $Ce_{0.85}Sm_{0.05}Yb_{0.1}O_{1.925}$. This indicates that conductivity is increased with increase in the amount of ytterbium at constant amount of samarium.

As reported in literatures, the grain and grain boundary arcs of doped ceria electrolytes are associated with the capacitances in the 30 to 60*pF* and 7 to 25*nF* ranges respectively(Bucevac et al., 2013; Jaiswal et al., 2015). These are determined from the relation $2\pi f_{max}RC=1$, where f_{max} is the applied frequency at the arc maximum, R is the resistance, and C is the capacitance of a particular contribution.

In this study, the values of Cgb calculated for the middle range frequency semicircles obtained at 450^{0}C (Figure 5c) and at 500^{0}C (Figure 5d) are 36.64nF, 31.65nF for $Ce_{0.9}Sm_{0.05}Yb_{0.05}O_{1.95}$ and 11.8nF, 13nF for $Ce_{0.85}Sm_{0.05}Yb_{0.1}O_{1.925}$ respectively. The calculated values of Cgb found are almost close to the expected values for grain boundary response. This confirmed that the middle range frequency semicircle in the impedance spectra measured at 450 and 500^{0}C in YbSDC- samples is almost associated with the grain boundary resistance.

The temperature dependence of ionic conductivity often follows an Arrhenius relation:

$$\sigma T = \sigma_o e^{-Ea/KT} \qquad (7)$$

Where, *Ea* is the activation energy for conduction, *T* is the absolute temperature, *K* is the Boltzmann's constant and σ_o is a pre-exponential factor. The total ionic conductivities of YbSDC- samples sintered at 1400^{0}C for 2h was presented in Figure 6 in the form of $\ln(\sigma T)$ versus$\left(10^3/_T\right)$. The value of *Ea* and σ_o were found from the slope and intercept of the graph, respectively.

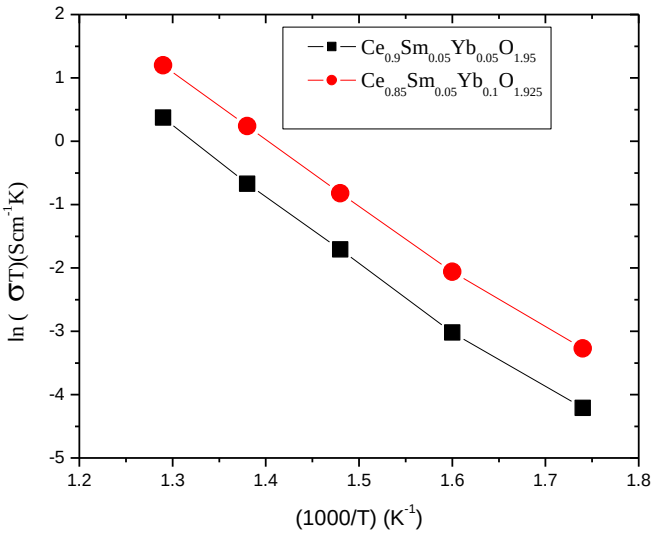

Figure 6: Arrhenius plots of total conductivity of $Ce_{0.9}Sm_{0.05}Yb_{0.05}O_{1.95}$ and $Ce_{0.85}Sm_{0.05}Yb_{0.1}O_{1.925}$ samples

The Arrhenius plot described in Fig.6 reveals that the conductivity of YbSDC- samples increased linearly with temperature. This was possibly because of thermal excitation which enhances the kinetic energy of carriers and force oxygen ions to pass through oxygen vacancies in a higher speed. As the temperature rises, there exists stronger diffusion ability of oxygen ions, which ultimately lead to the enhancement of conductivity.

As it can be observed from Fig.6, the conductivity of $Ce_{0.85}Sm_{0.05}Yb_{0.1}O_{1.925}$ sample is higher than that of $Ce_{0.9}Sm_{0.05}Yb_{0.05}O_{1.95}$. This could be due to formation of more number of oxygen vacancies and suppression of ordering of oxygen vacancies in $Ce_{0.85}Sm_{0.05}Yb_{0.1}O_{1.925}$ than in $Ce_{0.9}Sm_{0.05}Yb_{0.05}O_{1.95}$ which leads to a decrease in the activation energy for diffusion of O^{2-} ions (Wang et al., 2005).

The Arrhenius plots of YbSDC- samples show a change in the slope at 350°C.This indicates that a transition from associated defect pairs (regions where oxygen vacancies are bound to cation defects) to dissociated defects (regions where oxygen vacancies are free).

Table 6.shows that the activation energy of YbSDC- samples obtained by fitting of the data in Figure 6 to Arrhenius relations (Eq.7).

Table 6: Activation energy of YbSDC-samples obtained by slope fitting.

No	Sample	Ea(*eV*)
1	$Ce_{0.9}Sm_{0.05}Yb_{0.05}O_{1.95}$	0.93
2	$Ce_{0.85}Sm_{0.05}Yb_{0.1}O_{1.925}$	0.92

Literature result indicated that for the lanthanide series, the combinations of rare earth dopants producing an average atomic number between 61 and 62 should be the right choice to get the lowest activation energy (Ea) in doped ceria (Andersson et al., 2006). In this regard, the combinations of Nd/Sm and Pr/Gd show low activation energy and enhanced ionic conductivity.

As it can be observed in Table 6, the activation energy of Yb and Sm codoped ceria reported in this work is smaller than single doped ceria with Yb (1.18eV) and greater than single doped ceria with Sm(0.76eV) reported in previous literatures(Dos Santos et al., 2008; Matović et al., 2014). This is possibly due to improvement in the dopants (Sm/Yb) average atomic number (66) which is closer to the ideal dopants effective atomic number 61(Pm) and 62(Sm) than that of Yb (70) atomic number. Moreover, it may be due to increase in the effective ionic radii of co dopants which is close to the critical ionic radii (0.1038nm) for doped ceria (Omar et al., 2009). As the ionic radii of dopant cations is closer to critical ionic radii of host, the lower activation energy effect to the diffusion of oxygen vacancies and the greater the conductivity of the electrolyte.

The high densities with negligible pores of YbSDC- samples observed in SEM micro graph leads to the increase in the ionic conductivity. It can be concluded that the codoping of Yb and Sm in ceria restrict the reduction of Ce^{4+} (ionic conductivity) to Ce^{3+}(electronic conductivity). Therfore, the above result indicated that co-doping Yb and Sm in ceria lowered activation energy and enhanced its electrical properties. Moreover, the conductivity of codoped YbSDC- samples obtained at 500^0C in this work was greater than that of single Yb doped ceria previously reported literatures(Tarancón, 2009; Wang et al., 2005). Furthermore, all the results confirmed that co-doping method of Yb and Sm increases the conductivity of ceria at intermediate temperature.

4. CONCLUSION

Ytterbium and Samarium co-doped ceria samples were successfully prepared through sol-gel method. In order to obtain dense ceramics, the sample pellets were sintered at 1400^0C for 2h. The XRD result reveals that all the samples are single phase with cubic fluorite-type structure. The calculated relative densities were about 98% of the theoretical densities. SEM micrograph clearly showed the presence of uniform grains with clean and distinct grain boundaries. The EDX graph revealed that all elements like Yb, Sm, Ce and O are entered in the lattice as per stochiometry. The Raman spectra result showed three distinctive peaks. An intense peak at 464cm^{-1} and two weaker peaks at 260cm^{-1} and 552cm^{-1}. Raman spectroscopy analysis showed that the values of intensity ratios (i.e. I_{552}/I_{464}) found for $Ce_{0.85}Sm_{0.05}Yb_{0.05}O_{1.95}$ and $Ce_{0.85}Sm_{0.05}Yb_{0.1}O_{1.925}$ are 0.10 and 0.13 respectively. The conductivity of YbSDC- increased with the increase in the ytterbium substitution with constant samarium dopant. The composition $Ce_{0.85}Sm_{0.05}Yb_{0.1}O_{1.925}$ showed higher ionic conductivity and minimum activation energy of (4.4 x10^{-3}S/cm, Ea = 0.92eV) than composition $Ce_{0.85}Sm_{0.05}Yb_{0.05}O_{1.95}$ which showed a conductivity and activation energy of (1.88 x10^{-3}S/cm, Ea = 0.93eV) respectively at 500^0C in air atmosphere. From the experimental results, all YbSDC-samples showed conductivity higher than 10^{-3}S/cm at temperature of 500^0C. Therefore, the results

confirmed that the material prepared from $Ce_{1-x-y}Sm_xYb_yO_{2-\delta}$ $(x = 0.05, Y = 0.05, 0.1)$ can be used as an electrolyte for intermediate temperature SOFC applications.

ACKNOWLEDGEMENTS

The authors are very much thankful to Material Research Laboratory, Department of Physics, Osmania University, and Hyderabad, India for giving opportunity to do experimental work. Also, the authors thank Department of Physics, Wollega University, Ethiopia for providing financial support to visit Osmania University, Hyderabad, India.

REFERENCES

Accardo G, Ferone C, Cioffi R, Frattini D, Spiridigliozzi L, and Dell'Agli G. (2016). Electrical and microstructural characterization of ceramic gadolinium-doped ceria electrolytes for ITSOFCs by sol-gel route. *Journal of applied biomaterials & functional materials*, 14(1):35-41.

Accardo G, Frattini D, Ham H, Han J, and Yoon S. (2018). Improved microstructure and sintering temperature of bismuth nano-doped GDC powders synthesized by direct sol-gel combustion. *Ceramics International*, 44(4):3800-3809.

Ali SM, Anwar M, Abdalla AM, Somalu MR, and Muchtar A. (2017). Ce0. 80Sm0. 10Ba0. 05Er0. 05O2-δ multi-doped ceria electrolyte for intermediate temperature solid oxide fuel cells. *Ceramics International*, 43(1):1265-1271.

Andersson DA, Simak SI, Skorodumova NV, Abrikosov IA, and Johansson B. (2006). Optimization of ionic conductivity in doped ceria. *Proceedings of the National Academy of Sciences*, 103(10):3518-3521.

Anjaneya K, Nayaka G, Manjanna J, Govindaraj G, and Ganesha K. (2013). Preparation and characterization of Ce1− xSmxO2− δ (x= 0.1–0.3) as electrolyte material for intermediate temperature SOFC. *Solid State Sciences*, 26:89-96.

Anjaneya K, and Singh MP. (2017). Synthesis and properties of gadolinium doped ceria electrolyte for IT-SOFCs by EDTA-citrate complexing method. *Journal of Alloys and Compounds*, 695:871-876.

Arabaci A. (2015a). Effect of Sm and Gd dopants on structural characteristics and ionic conductivity of ceria. *Ceramics International*, 41(4):5836-5842.

Arabaci A. (2015b). Synthesis and Characterization of Samarium-Doped CeO2 Powders as a Solid Electrolyte by Using Pechini Method. *Acta Physica Polonica A*, 127(4):888-890.

Arabacı A, Der M, Öksüzömer M, and Altınçekiç T. (2017). Characterization of Nd and Sm Co-Doped CeO 2-Based Systems.

Bhabu KA, Theerthagiri J, Madhavan J, Balu T, Muralidharan G, and Rajasekaran T. (2016). Cubic fluorite phase of samarium doped cerium oxide (CeO 2) 0.96 Sm 0.04 for solid oxide fuel cell electrolyte. *Journal of Materials Science: Materials in Electronics*, 27(2):1566-1573.

Bondioli F, Ferrari AM, Lusvarghi L, Manfredini T, Nannarone S, Pasquali L, and Selvaggi G. (2005). Synthesis and characterization of praseodymium-doped ceria powders by a microwave-assisted hydrothermal (MH) route. *Journal of materials chemistry*, 15(10):1061-1066.

Bucevac D, Radojkovic A, Miljkovic M, Babic B, and Matovic B. (2013). Effect of preparation route on the microstructure and electrical conductivity of co-doped ceria. *Ceramics International*, 39(4):3603-3611.

Daza PCC, Meneses RAM, Rodrigues ACM, and da Silva CRM. (2018). Ionic conductivities and high resolution microscopic evaluation of grain and grain boundaries of cerium-based codoped solid electrolytes. *Ceramics International*.

Dell'Agli G, Spiridigliozzi L, Marocco A, Accardo G, Frattini D, Kwon Y, and Yoon S. (2017). Morphological and crystalline evolution of Sm-(20 mol%)–doped ceria nanopowders prepared by a combined co-precipitation/hydrothermal synthesis for solid oxide fuel cell applications. *Ceramics International*, 43(15):12799-12808.

Dönmez G, Sarıboğa V, Gürkaynak Altınçekiç T, and Öksüzömer MAF. (2015). Polyol Synthesis and Investigation of Ce 1− x RE x O 2− x/2 (RE= Sm, Gd, Nd, La, 0≤ x≤ 0.25) Electrolytes for IT-SOFCs. *Journal of the American Ceramic Society*, 98(2):501-509.

Dos Santos M, Lima R, Riccardi C, Tranquilin R, Bueno PR, Varela JA, and Longo E. (2008). Preparation and characterization of ceria nanospheres by microwave-hydrothermal method. *Materials Letters*, 62(30):4509-4511.

Filtschew A, Hofmann K, and Hess C. (2016). Ceria and its defect structure: new insights from a combined spectroscopic approach. *The Journal of Physical Chemistry C*, 120(12):6694-6703.

Gan Y, Cheng J, Li M, Zhan H, and Sun W. (2015). Enhanced ceria based electrolytes by codoping samaria and scandia for intermediate temperature solid oxide fuel cells. *Materials Chemistry and Physics*, 163:279-285.

Guo M, Lu J, Wu Y, Wang Y, and Luo M. (2011). UV and visible Raman studies of oxygen vacancies in rare-earth-doped ceria. *Langmuir*, 27(7):3872-3877.

Jais AA, Ali SM, Anwar M, Somalu MR, Muchtar A, Isahak WNRW, Tan CY, Singh R, and Brandon NP. (2017). Enhanced ionic conductivity of scandia-ceria-stabilized-zirconia (10Sc1CeSZ) electrolyte synthesized by the microwave-assisted glycine nitrate process. *Ceramics International*, 43(11):8119-8125.

Jaiswal N, Kumar D, Upadhyay S, and Parkash O. (2015). Preparation and characterization of Ce 0.85 La 0.15− x Sr x O {2−(0.075+ x/2)} solid electrolytes for intermediate temperature solid oxide fuel cells. *Ionics*, 21(2):497-505.

Jeyanthi CE, Siddheswaran R, Kumar P, Chinnu MK, Rajarajan K, and Jayavel R. (2015). Investigation on synthesis, structure, morphology, spectroscopic and electrochemical studies of praseodymium-doped ceria nanoparticles by combustion method. *Materials Chemistry and Physics*, 151:22-28.

Kahlaoui M, Chefi S, Inoubli A, Madani A, and Chefi C. (2013). Synthesis and electrical properties of co-doping with La3+, Nd3+, Y3+, and Eu3+ citric acid-nitrate prepared samarium-doped ceria ceramics. *Ceramics International*, 39(4):3873-3879.

Karaca T, Altınçekiç TG, and Öksüzömer MF. (2010). Synthesis of nanocrystalline samarium-doped CeO2 (SDC) powders as a solid electrolyte by using a simple solvothermal route. *Ceramics International*, 36(3):1101-1107.

Kim G, Lee N, Kim K-B, Kim B-K, Chang H, Song S-J, and Park J-Y. (2013). Various synthesis methods of aliovalent-doped ceria and their electrical properties for intermediate temperature solid oxide electrolytes. *International Journal of Hydrogen Energy*: 38(3):1571-1587.

Kobi S, Jaiswal N, Kumar D, and Parkash O. (2016). Ionic conductivity of Nd^{3+} and Y^{3+} co-doped ceria solid electrolytes for intermediate temperature solid oxide fuel cells. *Journal of Alloys and Compounds*, 658:513-519.

Kosinski MR, and Baker RT. (2011). Preparation and property–performance relationships in samarium-doped ceria nanopowders for solid oxide fuel cell electrolytes. *Journal of Power Sources*, 196(5):2498-2512.

Koteswararao P, Suresh MB, Wani B, and Rao PB. (2015). Studies on Structural, Morphological and Electrical Studies of Gadolinium Doped Ceria. Materials Today: *Proceedings*, 9(2):4353-4359.

Kumar AS, Balaji R, and Jayakumar S. (2017). Thermal, structural and electrical properties of samarium doped barium cerate electrolyte for SOFCs. *Materials Chemistry and Physics*, 202:82-88.

Kumar AS, Balaji R, Jayakumar S, and Pradeep C. (2016). Microwave assisted sintering of gadolinium doped barium cerate electrolyte for intermediate temperature solid oxide fuel cells. *Materials Chemistry and Physics*, 182:520-525.

Li B, Liu Y, Wei X, and Pan W. (2010). Electrical properties of ceria Co-doped with Sm^{3+} and Nd^{3+}. *Journal of Power Sources*, 195(4):969-976.

Li S-P, Lu J-Q, Fang P, and Luo M-F. (2009). Effect of oxygen vacancies on electrical properties of Ce0. 8Sm0. 1Nd0. 1O2− δ electrolyte: an in situ Raman spectroscopic study. *Journal of Power Sources*, 193(1):93-98.

López JM, Gilbank AL, García T, Solsona B, Agouram S, and Torrente-Murciano L. (2015). The prevalence of surface oxygen vacancies over the mobility of bulk oxygen in nanostructured ceria for the total toluene oxidation. *Applied Catalysis B: Environmental*, 174:403-412.

Matović B, Stojmenović M, Pantić J, Varela A, Žunić M, Jiraborvornpongsa N, and Yano T. (2014). Electrical and microstructural properties of Yb-doped CeO_2. *Journal of Asian Ceramic Societies*, 2(2):117-122.

Molenda J, Świerczek K, and Zając W. (2007). Functional materials for the IT-SOFC. *Journal of Power Sources*, 173(2):657-670.

Omar S, Wachsman ED, Jones JL, and Nino JC. (2009). Crystal structure–ionic conductivity relationships in doped ceria systems. *Journal of the American Ceramic Society*, 92(11):2674-2681.

Omar S, Wachsman ED, and Nino JC. (2007). Higher ionic conductive ceria-based electrolytes for solid oxide fuel cells. *Applied Physics Letters*, 91(14):144106.

Piumetti M, Bensaid S, Andana T, Dosa M, Novara C, Giorgis F, Russo N, and Fino D. (2017). Nanostructured Ceria-Based Materials: Effect of the Hydrothermal Synthesis Conditions on the Structural Properties and Catalytic Activity. *Catalysts*, 7(6):174.

Pu Z-Y, Lu J-Q, Luo M-F, and Xie Y-L. (2007). Study of oxygen vacancies in Ce0. 9Pr0. 1O2-δ solid solution by in situ X-ray diffraction and in situ Raman spectroscopy. *The Journal of Physical Chemistry C*, 111(50):18695-18702.

Raharjo J, Aninda RS, and Lestari NA. (2017). Synthesis and Characterization of La, Sc, Yb and Nd co-doped Gadolinium doped Cerium (GDC) Composite Electrolyte for IT-SOFC. Journal of Physics: Conference Series: IOP Publishing. p 012077.

Ramesh S, RAJU KJ, and Reddy CV. (2014). Preparation and characterization of Ce1–xDyx–ySryO2–δ system. *Transactions of Nonferrous Metals Society of China*, 24(2):393-400.

Roy J. (2012). The effect of strontium doping on densification and electrical properties of Ce 0.8 Gd 0.2 O 2− δ electrolyte for IT-SOFC application. *Ionics*, 18(3):291-297.

Sandhya K, Chitra Priya N S, Aswathy P K, Rajendran DN, and Thappily P. (2017). Enhanced structural and electrical properties due to the effect of co-doping ceria electrolyte. *American Institute of Physics Conference Series*.

Shajahan I, Ahn J, Nair P, Medisetti S, Patil S, Niveditha V, Babu GUB, Dasari HP, and Lee J-H. (2018). Praseodymium doped ceria as electrolyte material for IT-SOFC applications. *Materials Chemistry and Physics*.

Singh NK, Singh P, Kumar D, and Parkash O. (2012). Electrical conductivity of undoped, singly doped, and co-doped ceria. *Ionics*, 18(1-2):127-134.

Singh V, Babu S, Karakoti AS, Agarwal A, and Seal S. (2010). Effect of submicron grains on ionic conductivity of nanocrystalline doped ceria. *Journal of nanoscience and nanotechnology*, 10(10):6495-6503.

Spanier JE, Robinson RD, Zhang F, Chan S-W, and Herman IP. (2001). Size-dependent properties of CeO_{2-} y nanoparticles as studied by Raman scattering. *Physical Review B*, 64(24):245407.

Spiridigliozzi L, Dell'Agli G, Marocco A, Accardo G, Ferone C, and Cioffi R. (2015). Hydrothermal synthesis at low temperature of gadolinium-doped ceria. *Proceedings of the 6th European Fuel Cell*.

Stojmenović M, Žunić M, Gulicovski J, Bajuk-Bogdanović D, Holclajtner-Antunović I, Dodevski V, and Mentus S. (2015). Structural, morphological, and electrical properties of doped ceria as a solid electrolyte for intermediate-temperature solid oxide fuel cells. *Journal of Materials Science*, 50(10):3781-3794.

Swatsitang E, Phokha S, Hunpratub S, and Maensiri S. (2016). Modification of Ce valence states by Sm/Sr co-doping of CeO_2 nanoparticles for improved magneto-electrochemical properties. *Materials & Design*, 108:27-33.

Tarancón A. (2009). Strategies for lowering solid oxide fuel cells operating temperature. *Energies*, 2(4):1130-1150.

Venkataramana K, Madhuri C, Reddy YS, Bhikshamaiah G, and Reddy CV. (2017). Structural, electrical and thermal expansion studies of tri-doped ceria electrolyte materials for IT-SOFCs. *Journal of Alloys and Compounds*, 719:97-107.

Wang F-Y, Wan B-Z, and Cheng S. (2005). Study on Gd^{3+} and Sm^{3+} co-doped ceria-based electrolytes. *Journal of Solid State Electrochemistry*, 9(3):168-173.

Wu Y-C, Chien C-H, and Xu G. (2017). Conductivity and microstructure analysis of ceria materials doped with multiple elements. *Ceramics International*, 43:S747-S757.

Wu Y-C, and Lin C-C. (2014). The microstructures and property analysis of aliovalent cations (Sm^{3+}, Mg^{2+}, Ca^{2+}, Sr^{2+}, Ba^{2+}) co-doped ceria-base electrolytes after an aging treatment. *International Journal of Hydrogen Energy*, 39(15):7988-8001.

Xiaomin L, Qiuyue L, Lili Z, and Xiaomei L. (2015). Synthesis and characterization of Ce0. 8Sm0. 2–xPrxO2–δ (x= 0.02–0.08) solid electrolyte materials. *Journal of Rare Earths*, 33(4):411-416.

Yang J, Ji B, Si J, Zhang Q, Yin Q, Xie J, and Tian C. (2016). Synthesis and properties of ceria based electrolyte for IT-SOFCs. *International Journal of Hydrogen Energy*, 41(36):15979-15984.

Ye F, Mori T, Ou DR, Takahashi M, Zou J, and Drennan J. (2007). Ionic conductivities and microstructures of ytterbium-doped ceria. *Journal of the Electrochemical Society*, 154(2):B180-B185.

Zając W, and Molenda J. (2008). Electrical conductivity of doubly doped ceria. *Solid State Ionics*, 179(1-6):154-158.

Properties of Leed Certified Eco Friendly Pervious Concrete

P.M.Shanmugavadivu*, Brook Abate, Seifu Sisay, Habtamu Eskezia

College of Architecture and Civil Engineering, Addis Ababa Science and Technology University, Addis Ababa, Ethiopia
**Corresponding author, e-mail: shanmugavadivu.marimuthu@aastu.edu.et*

ABSTRACT

Pervious concrete is a LEED certified porous concrete and gap graded concrete which enhanced the porosity of concrete. It is a green material that helps to reduce water run-off and pollution. It is a LEED certified product controls storm water pollution and storm water run-off. The term "pervious concrete" is a performance – engineered concrete made with controlled amounts of cement, coarse aggregate, admixtures and water. The combinations of these ingredients will produce a hardened material with connected pores ranging size from 2mm to 8mm and void content ranges from 18% to 35% that allows water to pass through easily. The drainage rate of pervious concrete pavement varies with aggregate size and density of the mixture. This Eco-friendly material reduces pollution by the degradation of oils from the vehicles due to the presence of aerobic bacteria's in its pores and also save the natural water reservoirs. In this paper we have discussed the properties of pervious concrete.

Keywords: *Pervious concrete, Permeability, LEED certified concrete, Eco – friendly material*

1. INTRODUCTION

The term "pervious concrete" typically describes an open graded material consisting of Portland cement, coarse aggregate, admixtures, water and little or no fine aggregate. Carefully controlled amounts of water and cementitious materials are used to create a paste that forms a thick coating around aggregate particles without flowing off during mixing and placing. Using just enough paste to coat the particles maintains a system of interconnected voids. It is the pavement material which reduces the impact of development by reducing run-off rates and protecting water supplies. Water percolates into the ground beneath recharging the natural water table instead of running off and causing erosion, it carries away 90% of pollutants found on pavements; it can percolate 120 to 320 liters of water per minute to pass through each square metre. The aggregate size employed here is 10 mm to 20 mm. It reduces the glare associated with conventional concrete pavement. Its compressive strength is 3.5 MPa to 28 MPa and flexural strength 1MPa to 3.8MPa. Pervious concrete pavements offer an eco friendly solution to water runoff and associated water pollution problems. Pervious concrete also helps to achieve LEED points of the Green Building Council. Pervious concrete has been recognized by the EPA as a best management practice (BMP) to address this most vital environmental concern. The open-cell structure of pervious concrete provides a medium for aerobic bacteria that break down many of the pollutants that seep from parked cars. Pervious concrete also contributes to enhanced air quality by lowering atmospheric heating through lighter colour and lower density, decreasing the impact of heat island effects.

1.1. Advantages of pervious concrete

- Reducing glare effects on the road surfaces to a great extent.
- Reducing the interaction noise between the tyre and the pavement.
- Its light- coloured surface both reduces "heat island" effects and lowers lighting costs due to its lighter reflectance than asphalt, thus boosting safety for vehicles and pedestrians.
- Light colors also help to earn LEED points.
- It is considered also "green" because it supports recycling in that it can be made using by- products from manufacturing and power plants, reducing landfills needs.
- Produces no toxic run-off and due to this it adds additional LEED point.

2. REVIEW OF LITERATURE

Although pervious concrete has been used for paving for more than 20 years in the U.S, only a few investigations have been carried out to determine the performance (Ghafoori, 1995). These investigations have been based primarily on laboratory tests with little data from actual field installations obtained. Currently, few standard procedures exist for fabricating and testing pervious concrete specifications in the laboratory or field. Vernon et al (2006) investigated "Mix Design Development for Pervious Concrete in Cold Weather Climates". In this research, concrete mixes were designed with various sizes and types of aggregates, binder contents, and admixture amounts. The engineering properties of the aggregates were evaluated. Additionally, the porosity, permeability, strength, and freeze-thaw durability of each of these mixes was measured. Results indicate that Portland cement pervious concrete (PCPC) made with single-sized aggregate has high permeability but not adequate strength. Adding a small percent of sand to the mix improves its strength and freeze-thaw resistance, but lowers its permeability (Wang et al, 2006). In this research PCPC mixes made with various types and amounts of aggregates, cementitious materials, fibres, and chemical admixtures were evaluated. The results indicated that the PCPC made with single-sized coarse aggregates generally had high permeability but not adequate strength. Addition of a small amount of fine sand (approximate 7% by weight of total aggregate) to the mixes significantly improved the concrete strength and freezing-thawing resistance while maintaining adequate water permeability. Addition of a small amount of fibre to the mixes increased the concrete strength, freezing-thawing resistance as well as void content. Dale P. Bentz (2008) presents various virtual pervious concrete micro structural models and compares their percolation characteristics and computed transport properties to those of real world pervious concretes. Finally he concluded that potential extensions of the virtual pervious concrete to exploring durability issues such as freezing-and-thawing resistance and clogging have been introduced. Subramanian (2008) reported that pervious concrete pavements can store large quantities of rainwater, allow it to percolate into the underlying soils and at the same time reduce the entrance of pollutants in stormwater systems. Hence, it is the best solution for rainwater runoff and pollution problems in urban areas. Pratt et al. (1999) at the Coventry University School of Science and the Environment focused on the effect of hydrocarbon runoff, since permeable pavement had already been shown to retain suspended solids. Runoff was then measured from simulated rainfall events and the results were compared with the results from normal concrete and asphalt test sections. Three rainfalls per week were simulated, with an intensity of 0.5 inches per hour for 28 minutes, yielding 0.28 inches of rain per simulated storm event. Oil was applied to the surface before each storm event. Over the course of the study, 0.32 liters of oil were applied to each section, and retention was measured by the difference between the oil concentration applied to the surface and the concentration in the runoff. The pervious pavement retained 99.6% of the oil, while standard concrete and asphalt retained only 70.2% and 49.6%, respectively. The biological treatment capacity of pervious pavement was also evaluated by Pratt et al. (1999). The test specimens were seeded with microorganisms, and nutrient deficiencies were prevented by applying a slow-release, commercially available fertilizer. Oil was then applied as before and the effluent runoff concentration was measured, along with the respiration of the microorganisms. It was found that after 1,150 days, the runoff concentration of oil in the effluent remained negligible. A similar study performed at the University of Florida evaluated the effects of using PCPC for water purification (Park and Tia, 2004). PCPC sections were submersed in a stream for three months to allow a microorganism population to become established. Water with known concentrations of chemicals was then passed through the seasoned PCPC sections, and the effluent concentration of total phosphorus and total nitrogen was measured. The maximum reduction was 47% for total nitrogen and 96% for total phosphorus.

3. EXPERIMENTAL INVESTIGATION

3.1. Materials Used

The materials used are Portland pozzolana cement, 20 mm down size Coarse aggregate and water. Initial Properties of materials are shown in Table 3.1 and 3.2.

Table 3.1: Properties of cement

S. No	Description	Values
1	Specific gravity	3.16
2	Fineness(by sieve analysis)	4.50%
3	Consistency	30.00%
4	Bulk density of cement	1411 kg/m^3

Table 3.2: Properties of coarse aggregate

S. No	Description	Values	
		12.5 mm Size	20 mm size
1	Specific gravity	2.75	2.73
2	Bulk density	1684 kg/m^3	1653.06 kg/m^3
3	Surface moisture	0.091%	0.0865%
4	Water absorption	1.00%	1.00%

3.2. Testing Details

3.2.1. Compressive Strength Test

In most structural applications, concrete is employed primarily to resist the compressive stresses. Therefore, concrete making properties of various ingredients of mix are usually measured in terms of the compressive strength. Compressive strength is also used as a qualitative measure for other properties of hardened concrete. The compressive strength of concrete cube was determined based on IS: 516 –1959. Three cubes of size 150mm x 150mm x 150mm were tested using a compression testing machine which is shown in Figure 3.1.

Figure 3.1: Compressive strength test

3.2.2. Flexural Strength Test

Flexural strength of the concrete was measured by the prism specimens of size 100 mm x 100 mm x 500 mm and tested as per IS: 516-1959. The bed of the testing machine was provided with two steel rollers of 38mm in diameter on which the specimen was supported, and these rollers were mounted at the distance of 40mm from center to center. The system of loading was symmetrical two point loading which is shown in Figure 3.2.

3.2.3. Void ratio

The most important features of pervious concrete is it's ability to percolate water through it. The percolation rate is directly dependent on the void ratio. It also depends on other factors like aggregate gradation, cementitious

material content w/cm and compaction. The void ratio is calculated by taking the concrete specimen of height 120mm and diameter 90mm and weighed it. Then the specimen was placed in a wire basket and attached with a spring balance at top. The basket along with the specimen was immersed in water and the saturated weight under (W_1) water was found. Then the specimen was kept for drying in an oven at 100°C for 24 hours and the dry weight (W_2) was found as shown in Figure 3.3.

The void ratio of pervious concrete was determined by calculating the difference in weight between the oven dry sample and the saturated under water sample and using Equation 3.1.

$$V_r = (1- ((W_2 – W_1)/\rho_w * vol))*100 \quad \text{..... (Eq. 3.1)}$$

Where, ρ_w = density of water, kg/m^3

V_r = total void ratio, % W_1 = weight under water, kg

W_2 = oven dry weight, kg Vol = volume of sample, m^3

Figure 3.2: Flexural strength test

Figure 3.3: Void Ratio test

4. RESULTS AND DISCUSSION

4.1. Compressive Strength Test

Table 4.1 and Figure 4.1 shows the Compressive strength of the pervious concrete with different size of aggregate. From the Figure 4.1, it was found that, the compressive strength is increased while reducing the size of the coarse aggregate. So, the compressive strength depends upon the size of aggregate and the bond between the aggregate and cement paste.

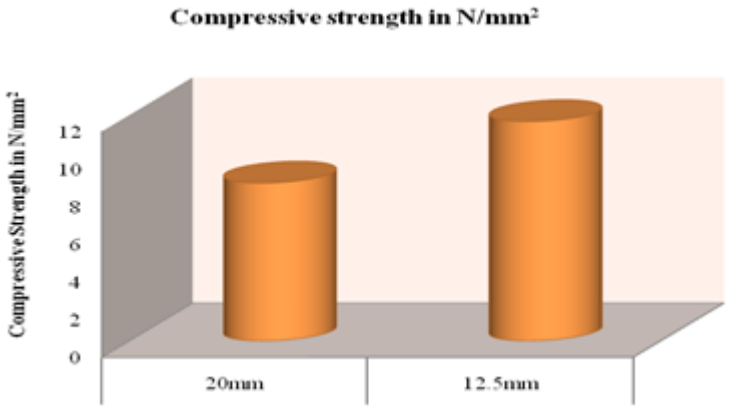

Figure 4.1: Compressive Strength Test Results

4.2. Flexural Strength Test

Figure 4.2 shows the flexural strength of the pervious concrete with different size of aggregates. From the Table 4.2 and Figure 4.2, it was found that, the flexure strength of the pervious concrete is increased while

reducing the size of the coarse aggregate. This is due to the better interlocking between the aggregate and cement paste.

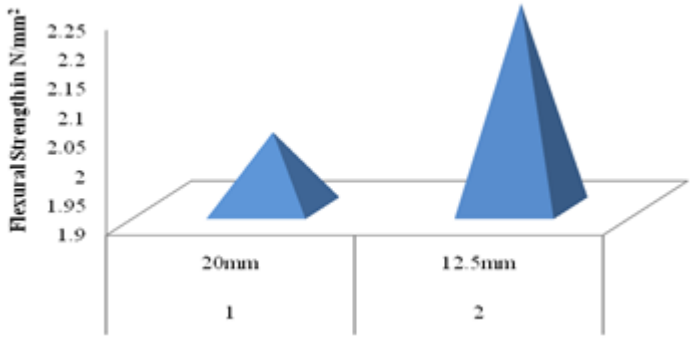

Figure 4.2: Flexural Strength Test Results

4.3. Void ratio

The void ratio of the pervious concrete with different size of aggregate is shown in Figure 4.3. From the Figure 4.3, it was noticed that, the void ratio is reduced while reducing the size of the coarse aggregate. The reason behind is the reduction in size of the aggregate creates better interlocking between the aggregate and paste, which reduces the void content in the concrete.

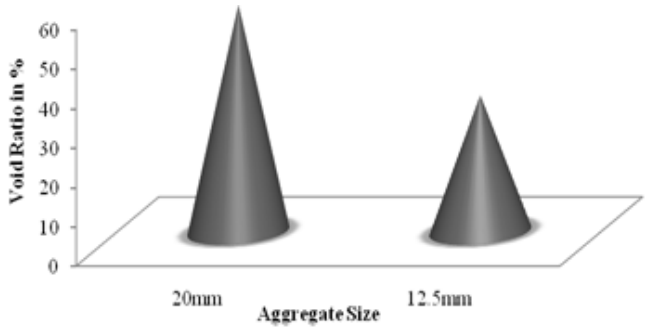

Figure 4.3: Void ratio test results

4.4. Permeability test

The permeability of the concrete with different size of aggregate is shown in Figure 4.4. From the Figure 4.4, it was observed that, the flow rate is reduced while reducing the size of the coarse aggregate. This is due to the presence of fewer voids, while reducing the size of the coarse aggregate.

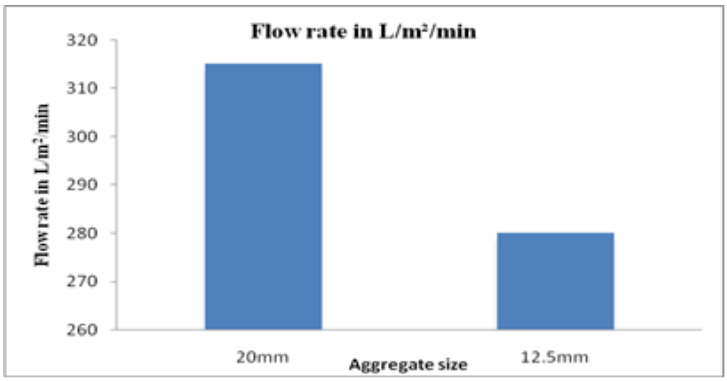

Figure 4.4: Permeability test results

5. CONCLUSION

The various properties of pervious concrete are studied and the conclusions are as follows.

- The compressive strength of the pervious concrete is increased while reducing the size of the aggregate and the maximum compressive strength of 11.67N/mm^2 is obtained for 12.5mm aggregate size.
- The flexural strength of the pervious concrete is increased when reducing the size of the aggregate and the maximum flexural strength is obtained as 2.25N/mm^2 for 12.5mm aggregate size.
- The void ratio is reduced while reducing the size of the aggregate and it is obtained as 34.67% for 12.5mm aggregate size.
- The permeability depends upon the void ratio. The flow rate is obtained as 280 L/m^2/min in 12.5mm aggregate concrete specimen.
- So, the pervious concrete can be used as the pavement material for foot path and parking lot.

ACKNOWLEDGEMENT

The authors acknowledge the lab technicians of Construction materials Laboratory.

REFERENCES

ACI Committee 522, Specifications for pervious concrete pavement, (ACI522R-08), American Concrete Institute, Farmington Hills, MI, pg.7.

ACI Committee 522, Pervious concrete, (ACI522R-08), American Concrete Institute, Farmington Hills, MI, pg.25.

A thirst world, http://www.unesco.org/courier/2001_10 uk/doss02.htm

Ashley, E., (2008). Using pervious concrete to achieve LEED points, *Concrete In Focus, A Publication of NRMCA.*

Brown, H.J. (2008). Pervious concrete research compilation: Past, present and future, Concrete Industry Management Program, RMC Research & Education Foundation, Middle Tennessee State University.

Concrete Technology Today December 2004

Dale P. Bentz (2008): Virtual Pervious Concrete: Microstructure, Percolation, and Permeability.

http://www.rmc-foundation.org/newsite/images/PCRC%20Final%206-08.pdf

Jain, O.P., (1996): Proportioning no-fines concrete, The Indian Concrete Journal, May 1966, Vol.20,No .5, pp.183-189.

Meninger, R.C., (1988): No-fine pervious concrete for paving, Concrete International, American Concrete Institute, August 1988, Vol.10, No. 8, pp.20-27.

Naik, T.R., Kraus, R.N. and Siddique, R., (2002): No-fines concrete using non-specification flyash, Report No, CBU-2002-37, Centre for By-Products Utilization, University of Wisconsin-Milwaukee.

Subranmanian.N. (2008): Pervious Concrete – A green material that helps reduce water run – off and pollution, The Indian Concrete Journal.

Vernon R. Schaefer et al., (2006): Mix Design Development for Pervious Concrete in Cold Weather Climates, Final Report, Iowa Department of Transportation, National Concrete Pavement Technology Iowa State

www.nrmca.org/certifications/pervious

www.perviouspavement.org/

Wang, K.1, et al., (2006). Development of Mix Proportion for Functional and Durable Pervious Concrete.

Design of Plasmonic Core-Shell Nanocomposites for Energy Conversion by Photocatalysis

Getaneh Diress Gesesse[1,*], Thomas Le Neel[2], Zhenpeng Cui[1], Guillaume Bachelier[2], Hynd Remita[1], Christophe Colbeau-Justin[1], Mohamed Nawfal Ghazzal[1]

[1]*Laboratoire de Chimie Physique, UMR 8000 CNRS, Université Paris-Sud,Université Paris-Saclay, 91405 Orsay, France*
[2] *Université Grenoble Alpes, CNRS, Institut Néel, 38000 Grenoble, France*
**Corresponding author, e-mail: getaneh-diress.gesesse@cnrs-orleans.fr*

ABSTRACT

Designing materials with high photoefficiency are the major challenges for green energy conversion (e.g. H_2 production). Heterogeneous photocatalysts (e.g. TiO_2) are among the promising materials for such applications. However, the limited ability of light harvesting and fast recombination of photogenerated charge-carriers reduces its photoefficiency. Therefore, the objective of this research was to design a novel material in core-shell system with plasmonic nanoparticles (SiO_2@Au@TiO_2) to enhance the performance of TiO_2 for hydrogen production by photocatalytic process. A spherical SiO_2 (as a core) with different diameter was synthesized by Stöber method, then gold nanoparticles (AuNPs) was loaded on the surface of the core followed by coated with TiO_2 shell to form a ratio of 0.25 wt. % of Au/TiO_2. The synthesized materials were characterized by different techniques. The size of SiO_2 (ranged from 70 to 450 nm diameter), AuNPs (5-7 nm) and uniform TiO_2 shell with a thickness of 10 nm were determined by TEM. Diffuse reflectance spectra shows that AuNPs containing composites exhibited a localized surface plasmon resonance (LSPR) at maximum wavelength 541 nm, where as there is no absorption for AuNPs free core-shell composites. The LSPR maximum wavelength was found to have a direct relation to the diameter of spherical silica core. For further understanding of the effect of SiO_2@TiO_2 core-shell size on LSPR, the field distribution was numerically simulated at the corresponding LSPR absorption maximum. The photocatalytic activity of the synthesized materials was evaluated for hydrogen (H_2) production from aqueous methanol solution (1:3 v/v ratio, methanol/water) under UV-Vis and Vis irradiation. The production of H_2 was analyzed by gas chromatography equipped with thermal conductivity detector. According to the obtained results, plasmonic core-shell nanocomposites have been highly improved the H_2 generation compared to AuNPs free core-shell composites. The silica core diameter and LSPR intensity of AuNPs was found the key parameters for the kinetics of the H_2 generation. In order to obtain a direct evidence for electron transfer of the process, time resolved microwave conductivity (TRMC) technique was employed to measure the photogenerated charge-carriers density and their lifetime. The TRMC signal was much more intense for the plasmonic core-shell nanocomposites which shows a better photoefficiency of H_2 production that is in a good agreement with LSPR intensity of AuNPs.

Keywords: *Plasmonic core-shell, gold nanoparticles, photocatalysis, H_2 production*

1. INTRODUCTION

Sunlight is a reagent to be select for green energy and sustainable environment due to its abundance, absence of cost, and environmentally friendly nature. However, the development of materials for absorption of light energy to convert photon-to-chemical reaction is one of the challenge in research and industrialized sectors. Heterogeneous photocatalysts based on semiconductors (e.g. TiO_2) are widely used for different application such as catalysis, water depollution, air purification, hydrogen production, solar cells and so on. Despite the fact that TiO_2 have many applications, the limited ability of light harvesting and fast recombination of photogenerated charge-carriers reduces its photoeficiency (Luna et al., 2016). In order to overcome to the solution, many approaches has been proposed. Among those methods, coupling TiO_2 with other semiconductor having narrow band-gap, doping with metal and non-metal elements, and sensitizing with organic dyes was explored. Most of those methods can slightly extended the photoresponse of TiO_2 to visible region (Butburee et al., 2014). Recently, plasmonic nanoparticles (e.g. Au, Ag) coupled with TiO_2 becomes a promising approach to improve the photoefficiency due to they have extremely large absorption/scattering cross-sections and can strongly focus light

close to the metal surface (Schuller et al. 2010). Gold and silver nanoparticles show localized surface plasmon resonance (LSPR), i.e., collective oscillations of free electrons in response to an incident electromagnetic field. The plasmon-excited energetic electrons (hot electrons) can be transferred from the NPs to the conduction band of the adjacent semiconductor (Linic et al., 2011). Then, metal NPs act as electron scavengers or/and co-catalysts under UV-visible and visible illumination, leading to a significant improvement in the photocatalytic efficiency of TiO_2 (Wang et al., 2017). Several researchers has been reported that the incorporation of plasmonic NPs as core–shell nanostructures to TiO_2 enhanced their light harvesting behavior for photocurrent generation in DSSCs, photoanode and others (Jang et al., 2014). However, there are only a few works done for hydrogen production using plasmonic core-shell nanostructure. In this context, the objective of this research was to design a novel material in core-shell system with plasmonic nanoparticles for hydrogen generation by photocatalysis. Particularly for this experiment, spherical nanoparticles synthesized by Stöber method having different diameter were used as a core. A small amount of gold nanoparticles was loaded on the surface of silica core. Afterwards, a thin layer TiO_2 shell were coated around the silica-gold surface to form a final ratio 0.25 wt. % of Au/TiO_2. The synthesized plasmonic core-shell nanocomposite were characterized by different techniques, and finally the photoefficiency was tested for hydrogen generation.

2. EXPERIMENTAL

2.1. Materials

In this work reagents in analytical grade such as; Tetraethyl ortho silicate (TEOS), titanium isopropoxide (TTIP), $HAuCl_4 \cdot 3H_2O$, 3-aminopropyltrimethoxy silane (APTMS), chloroauric acid trihydrated, tetrakis (hydroxymethyl) phosphonium chloride (THPC), and ammonium hydroxide (NH_4OH) were used without further treatment. For characterization of synthesized materials, diffusion reflectance spectrophotometer (DRS), transmission electron microscopy (TEM), time resolved microwave conductivity (TRMC) were used. Gas chromatograph (GC) was used to follow the hydrogen production.

2.2. Synthesis of spherical SiO_2 (core) nanoparticles

The Stöber method were used to synthesize spherical SiO_2 nanoparticles [W. Li and D. Zhao, 2013]. Silica nanoparticles with variable size were synthesized by adjusting the ratio of reagent used (table 1). Briefly, the required amount of distilled water and ethanol absolute were mixed, and stirred for 10 minutes at room temperature. In order to adjust the pH of the solution NH_4OH were added and the temperature was raised to 40 °C under magnetic stirring for 10 minutes. Afterwards, TEOS as a source of silica were added dropwise and stirred for 1 h at constant temperature, 40 °C. The synthesized silica nanoparticles were separated by centrifugation, washed with distilled water (3 times), and then dried in the oven at 70 °C overnight.

Table 1: Type and amount of reagents used for preparation of SiO2 nanoparticles.

Size (nm)	TEOS (mL)	Ethanol (mL)	NH_4OH (mL)	H_2O (mL)
70	4.5	15	5	20
150	4	42	15	35
300	6.2	56.1	15	22.5
450	6.2	64.2	15	14.4

2.3. Gold nanoparticles (AuNPs) loaded on surface SiO_2 nanoparticles

In this experimental part, gold nanoparticles (AuNPs) were loaded on the surface of synthesized SiO_2 nanoparticles. In order to have a homogeneous loading of gold nanoparticles, first SiO_2 nanospheres has been functionalized with APTMS. Briefly, 200 mg of SiO_2 nanospheres were dispersed in 10 mL ethanol while stirring

vigorously, followed by sonication for 30 minutes for complete dispersion. Then, a 0.1 mL APTMS was added dropwise at room temperature and continued stir for 6 hours. The functionalized SiO_2 nanoparticles was separated by centrifugation, washed with ethanol (3 times). On the other hand, gold nanoparticle containing solution were prepared separately following the procedure reported elsewhere [M. G. Méndez-Medrano, 2016]. Briefly, a 1.5 mL (0.2 mol L^{-1}) NaOH solution was added to 45 mL of water and stirred for 5 minutes. While stirring the above solution the 1 mL of THPC (0.05 mol L^{-1}) was added, followed by the addition of a required amount of $HAuCl_4 \cdot 3H_2O$ solution. The color of solution was changed to red-purple color that is due to the reduction of Au (III) to Au (0), and kept stirred for 30 more minutes. Afterwards, the APTMS-functionalized SiO_2 nanoparticles were dispersed in gold nanoparticles containing solution and stirred for 4 h. The obtained SiO_2@Au nanoparticles was then collected by centrifugation, washed with absolute ethanol (3 times) and dried in oven at 60 °C for 48 hours.

2.4. TiO_2 (shell) coated on synthesized SiO_2/Au nanocomposites

The synthesized SiO_2@Au nanoparticles were further functionalized with APTMS using the same procedure as explained above. Next, a mixture of 1.5 mL $Ti(OiPr)_4$ and 50 mL absolute ethanol were added dropwise while stirring, and continued stirred for 2 h at room temperature. The quantity of the $Ti(OiPr)_4$ precursor was fixed to form a final weight ratio of Au/TiO_2: 0.25 wt.% for all samples. The synthesized plasmonic core-shell SiO_2@Au@TiO_2 nanocomposites were collected by centrifugation, washed with absolute ethanol (3 times) and dried at 80 °C overnight. Finally, the synthesized nanoparticles was calcined at 500 °C for 2 hours in air with 2 °C min^{-1}.

2.5. Characterization

The optical response of the synthesized plasmonic core-shell nanocomposite were studied by diffusion reflectance spectroscopy (DRS) using a Cary-5000 spectrophotometer (Agilent) equipped with a Cary 4/5 diffuse reflection sphere. Transmission electron microscopy (TEM) observations were performed on a JEOL JEM 100 CXII equipped with LaB6 filament microscope. The electronic property, the photogenerated charge carrier density and lifetime was measured by a contactless technique of time resolved microwave conductivity, TRMC. Last but not lease, for further understanding of the effect of core–shell size on the enhancement of LSPR of AuNPs, the field distribution inside the SiO_2@Au@TiO_2 nanostructure was numerically simulated.

2.6. Photocatalytic test

In order to test the performance of the synthesized plasmonic core-shell nanostructure, photocatalytic hydrogen production from an aqueous methanol solution was performed. First, the solution of water/methanol (3:1 v/v; total volume of 30 mL) was placed in a closed Pyrex glass reactor and stirred under a flow of nitrogen for 30 minutes to remove the dissolved oxygen. Then, 30 mg of the synthesized plasmonic core-shell nanostructure photocatalyst was added to the solution, followed by illuminated using a Xenon lamp (300 W) as artificial light sources to simulate the entire solar spectrum. A visible light experiment was performed using a cut-off filter ($\lambda > 450$ nm). The production of hydrogen was measured by gas chromatography (GC) on an Agilent gas chromatograph, equipped with a thermal conductivity detector.

3. RESULTS AND DISCUSSION

Spherical SiO_2 nanoparticles with a diameter of 70 nm, 150 nm, 300 nm and 450 nm were successfully synthesized by adjusting the reagents molar ratio. Gold nanoparticles with an average size of 5-7 nm were efficiently formed and loaded on the silica surface. Figure 1 shows the TEM images of synthesized nanocomposites with controlled size of the silica core and loaded AuNPs nanoparticles on the surface of silica core (SiO_2@Au@TiO_2). A uniform TiO_2 shell with a thickness of 10 nm (Figure 1a) was coated around the SiO_2@Au nanoparticles. The functionalized step that form a nucleation sites on silica-gold surface helps for the formation of homogenous TiO_2 thin shell during the hydrolysis and polycondensation of TTIP precursor.

According to HR-TEM images, an anatase crystalline form of TiO_2 (101) face with an interplanar spacing of 0.3699 nm were obtained.

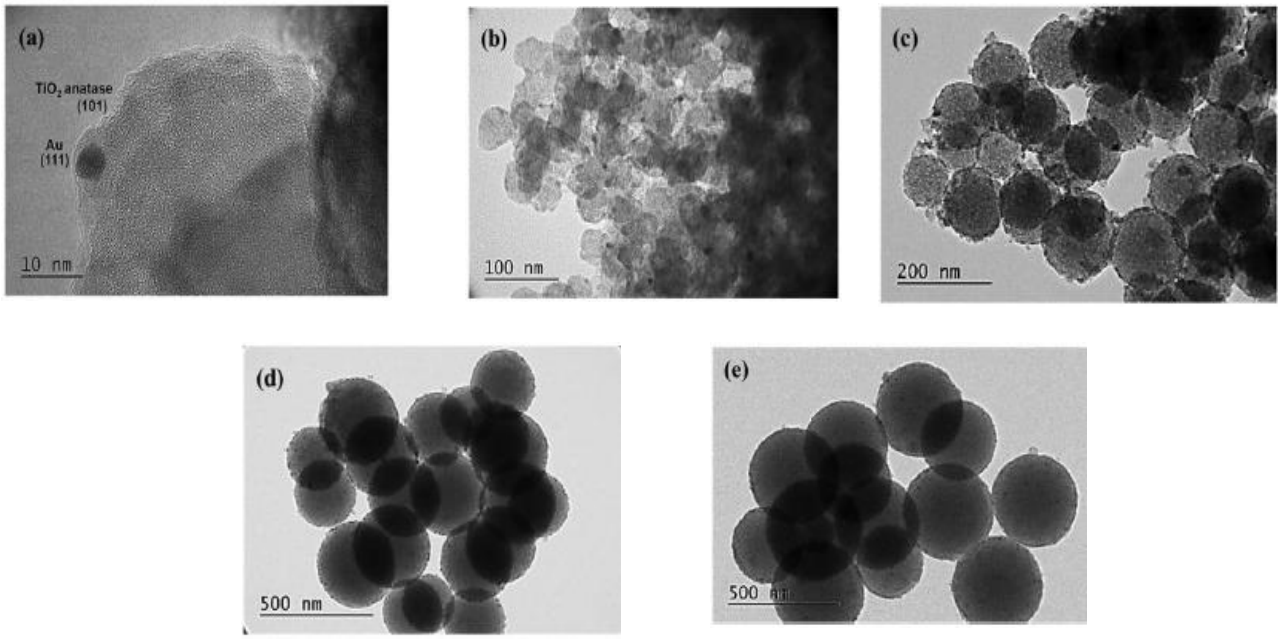

Figure 1: TEM images of synthesized plasmonic core–shell nanostructure with variable size of the silica core (a) HR-TEM image: TiO_2 shell and Au, (b) 70 nm, (c) 150, (d) 300 nm and (e) 450 nm

UV–visible diffuse reflectance spectroscopy was used to study the localized surface plasmon resonance (LSPR) properties of the core shell SiO_2@Au@TiO_2 nanocomposite systems with identical Au loading (0.25 wt. %) and variable SiO_2 nanosphere diameter size (Figure 2). In the plasmonic core–shell system, AuNPs containing nanostructure exhibited LSPR at maximum wavelength of 541 nm, whereas the non-plasmonic core–shell (SiO_2@TiO_2) have no absorption in the visible region. The absorbance sp

ectra showed that, when the SiO_2 diameter increased from 70 to 150 nm the absorption intensity increased at LSPR maximum wavelength. However, the absorption intensity decreases as the diameter of silica increased to 300 nm and 450 nm. Generally, a red-shifted were observed at the maximum wavelength of the LSPR band when the diameter of SiO_2 increased, reach up to 580 nm for SiO_2 core with 450 nm diameter.

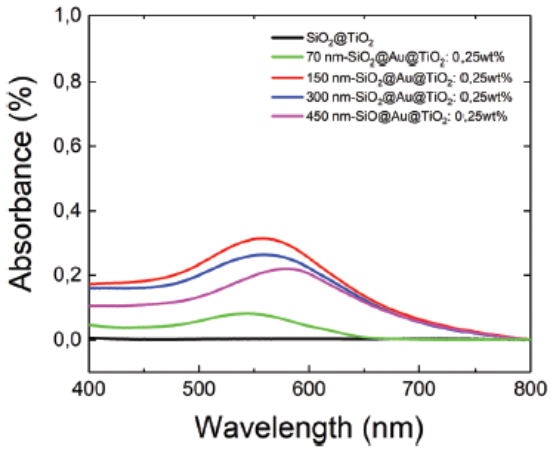

Figure 2: UV-visible absorption spectra of SiO_2@TiO_2 and SiO_2@Au@TiO_2 with variable silica core size and AuNPs loading (0.25 wt. %) in the 400–800 nm wavelength range

In order to understand the effect of SiO_2@TiO_2 core–shell size on the improvement of LSPR of AuNPs, the field distribution inside the SiO_2@Au@TiO_2 nanostructure was numerically simulated. The simulation were conducted at a wavelength of λ = 544 nm, corresponding to the localized surface plasmon resonance (LSPR) absorption maximum. The study was mainly to track the variation in the electric field distribution in the core–shell nanostructures for different diameters of the silica core. This core–shell nanostructure was modeled inside water as the surrounding medium to mimic the experimental conditions.

Figure 3 presents field distribution patterns, which the scattering effect is strongly dependent on the nanoparticles diameter and the refractive index of each medium. When the diameter of silica nanoparticles increases, the scattering field intensity increases with a more intense forward lobe. These behavior designated that the core–shell nanostructure behaving as a convex nanolens starting for diameters as small as $dSiO_2$ = 150 nm. Moreover, at larger sizes ($dSiO_2$ = 300 nm and $dSiO_2$ = 450 nm) a clear "beaming effect" was shown with an electromagnetic field enhancement at the outer surface, even leading a focus point at the surface of the core–shell. The nano-focusing was superior when the TiO_2 shell coated on the surface of the silica core, due to the changing of refractive index of the surrounding medium.

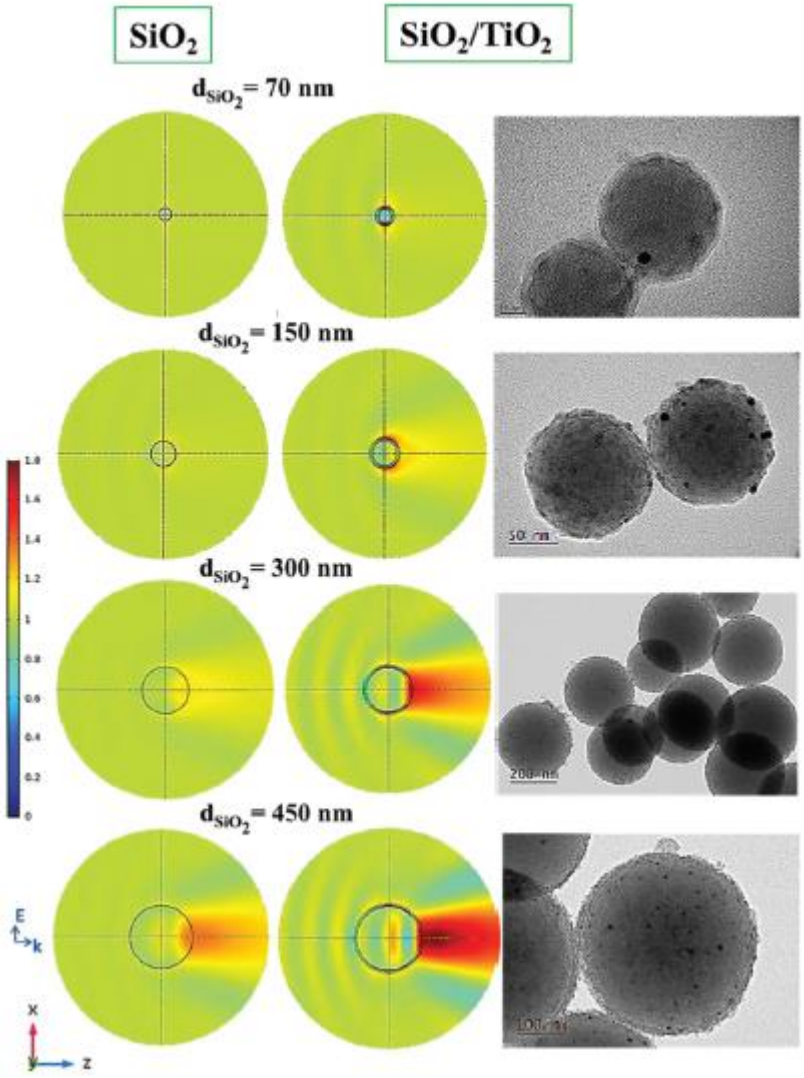

Figure 3: Near-field distribution of the square of electric field intensity for different diameters of silica core before (left) and after (right) shell coating and the corresponding TEM images of plasmonic core–shell nanoparticles.

For further understanding of the influence of the beaming effect on the final performance of the plasmonic core-shell nanolens, the squared electric field amplitude was averaged over the inner surface of TiO_2 where the AuNPs were located, which is directly proportional to the amount of energy absorbed in the metal. Figure 4 depicted an enhancement of 44.3% of the energy absorbed in the AuNPs when the core–shell size increased from 70 nm to 150 nm, whereas less increment was observed for silica core particles with larger diameters (up to 450 nm). Hence, the beaming effect was directly correlated to an enhancement of the electromagnetic energy density to excite the AuNPs and consequently boost the creation of hot electrons assisted by LSPR.

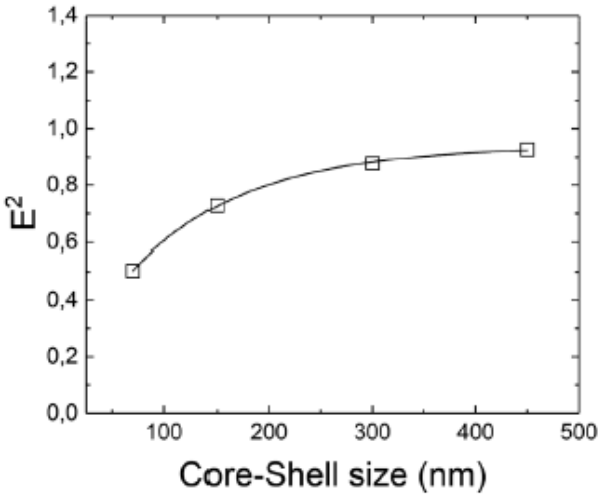

Figure 4: Size dependence of the squared electric field amplitude, averaged over the inner surface of TiO_2 where the AuNPs are located.

Hydrogen production

The photocatalytic property of the synthesized plasmonic core–shell nanocomposite materials was tested for hydrogen production from aqueous methanol solution (methanol: water; 1:3 v/v ratio) under UV-visible and visible ($\lambda > 420$ nm) light illumination. Figure 5c present that, plasmonic SiO_2@Au@TiO_2 nanostructure shows higher photocatalytic activity for hydrogen production under visible irradiation, whereas no activity for non-plasmonic SiO_2@TiO_2 composite for the same silica core diameter. Figure 5a shows the kinetics of hydrogen production for plasmonic core-shell system at different core diameter. A maximum of hydrogen was produced with silica core size of 150 nm, which is 5-fold higher compared to that of silica core with 70 nm diameter. However, the kinetics decreased as the silica core increases to 300 and 450 nm.

The obtained photocatalytic hydrogen production followed exactly the same trends of the LSPR intensity of AuNPs. Briefly, the LSPR maximal absorbance intensity and the enhanced rate of the hydrogen production was observed at SiO_2@Au@TiO_2 system with 150 nm core diameter. The AuNPs could assist the photocatalytic reaction through energy transfer or mediate the sensitization of TiO_2 in the visible range by injecting energetic electrons in the case of oxidation reactions (Erwin et al., 2016).

In order to obtain a direct evidence for electron transfer from the excited TiO_2 to the AuNPs, TRMC technique was employed to which measured the photogenerated charge carrier density and lifetime. Fig 5b shows, the TRMC signal was much more intense for plasmonic core shell nanostructure with silica core diameter 150 nm, and then decreases as the diameter increases to 300 nm and 450 nm. This observation was in a good agreement for both LSPR intensity of AuNPs and photoefficiency of H_2 production. The fast decay of TRMC signal was observed, indicating the disappearance of electrons from the TiO_2 surface (<10 ns) due to trapped by AuNPs, which decreases the charge carrier recombination. Besides, the photo-excited electrons trapped by AuNPs from the conduction band could transferred to the hydrogen ions for the formation of H_2 (Murdoch et al., 2011).

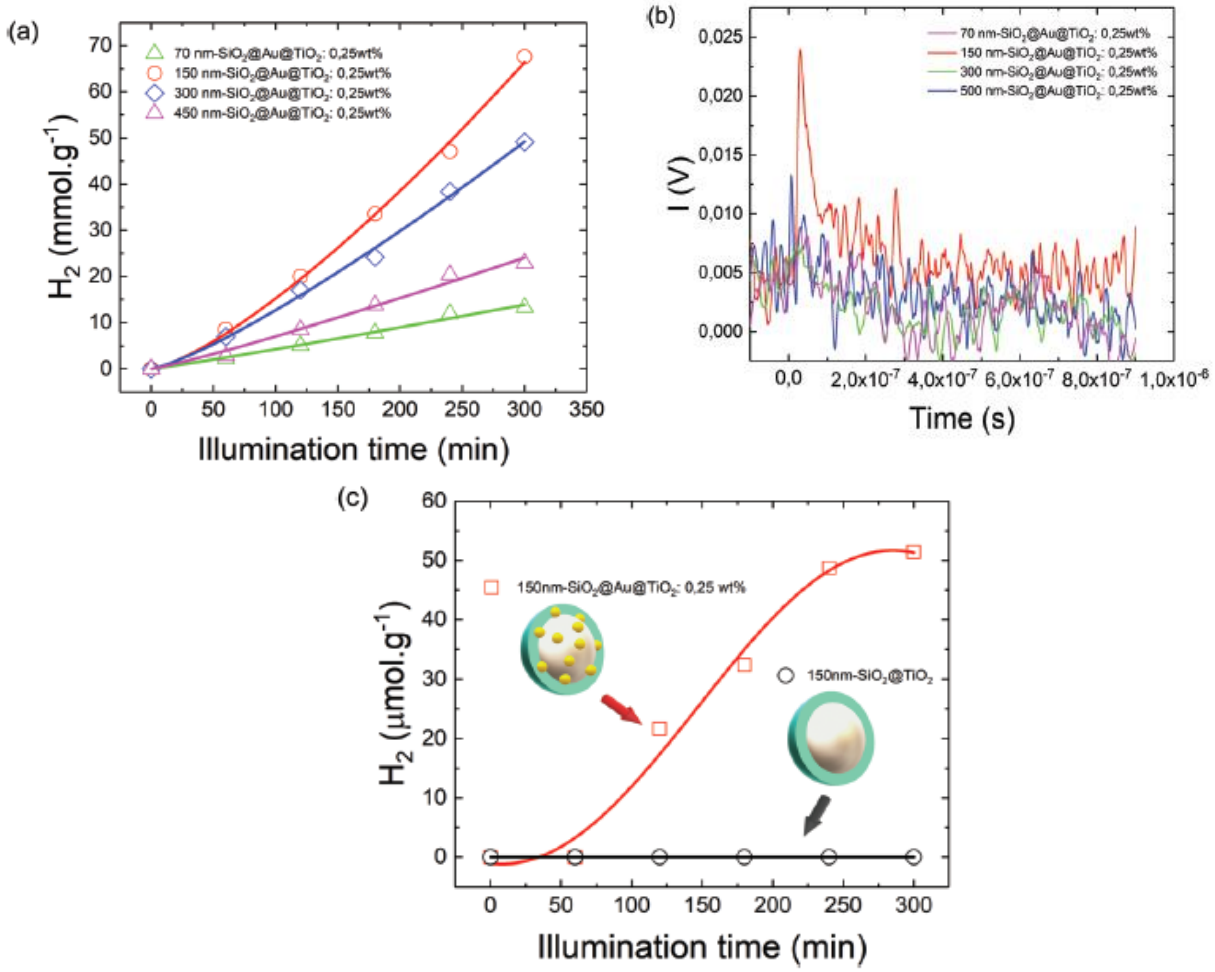

Figure 5: (a) Hydrogen production under UV-visible light illumination and, (b) TRMC signal of synthesized plasmonic core–shell nanoparticles with variable core size. (c) Hydrogen production under visible light irradiation ($\lambda > 420$ nm) for plasmonic and non-plasmonic core-shell with a core size of 150 nm.

Figure 5c presents the hydrogen production under visible light illumination for both plasmonic and non-plasmonic core-shell nanocomposites. In this part, a core-shell with 150 nm diameter that shows a better performance under UV-Vis irradiation was selected. The plasmonic core-shell system (embedded with very low amount of AuNPs; 0.25 wt. %) exhibited a very good activity in the visible range, while no hydrogen was measured for the SiO_2@TiO_2 core-shell. In this regard, the exclusive mechanism of hydrogen production is the reduction of hydrogen ions by the LSPR (hot electrons) at the AuNPs surface since TiO_2 was not active. When the methanol adsorbed at the surface of TiO_2 shell, electrons rising from LSPR were able to overpass the shell and reach the hydrogen ions to complete the reduction reaction and form hydrogen molecule [P. M. Jayaweera, et al., 2007].

4. CONCLUSIONS

In summary, a successful method have been followed to design a plasmonic core-shell nanostructure to enhance light harvesting and hydrogen production. The diameter of silica core was found a key parameter, which influences the optical response, beaming effect, TRMC signal and finally the photocatalytic hydrogen production. In plasmonic core-shell system, an enhanced performance was observed compared to non-plasmonic core-shell nanocomposite.

ACKNOWLEDGMENTS

The authors are grateful to "Agence Nationale pour la Recherche (ANRUpPhotoCat)" for finantial support of this research. The authors acknowledge Bertrand Busson for his help and valuable discussions throughout this study.

REFERENCES

T. Butburee, Y. Bai, J. Pan, X. Zong, C. Sun, G. Liu and L. Wang, (2014). *J. Mater. Chem*. A, 2: 12776.
W. R. Erwin, H. F. Zarick, E. M. Talbert and R. Bardhan, (2016). *Energy Environ. Sci*., 9: 1577–1601.
Y. H. Jang, Y. J. Jang, S. T. Kochuveedu, M. Byun, Z. Lin and D. H. Kim, (2014). *Nanoscale*, 6: 1823–1832
P. M. Jayaweera, E. L. Quah and H. Idriss, (2007). *J. Phys. Chem. C*, 111: 1764–1769.
W. Li and D. Zhao, (2013). *Adv. Mater*., 25: 142–149.
S. Linic, P. Christopher and D. B. Ingram (2011). *Nat. Mater*., 10: 911–921
A. L. Luna, E. Novoseltceva, E. Louarn, P. Beaunier, E. Kowalska, B. Ohtani, M. A. Valenzuela, H. Remita and C. Colbeau-Justin (2016). *Appl. Catal., B*, 191: 18–28.
M. G. Méndez-Medrano, E. Kowalska, A. Lehoux, A. Herissan, B. Ohtani, S. Rau, C. Colbeau-Justin, J. L. Rodríguez-López and H. Remita, (2016). *J. Phys. Chem. C*, 120: 25010–25022.
M. Murdoch, G. I. N. Waterhouse, M. A. Nadeem, J. B. Metson, M. A. Keane, R. F. Howe, (2011). *J. Llorca and H. Idriss, Nat. Chem.*, 3: 1–4.
J. A. Schuller, E. S. Barnard, W. S. Cai, Y. C. Jun, J. S. White and M. L. Brongersma, (2010). *Nat. Mater.*, 9: 193–204
S. Wang, Y. Gao, S. Miao, T. Liu, L. Mu, R. Li, F. Fan and C. Li, (2017). *J. Am. Chem. Soc*., 139: 11771–11778.

The Experimental Investigation on Performance of Cotton Seed Biodiesel with Nano Additive in Single Cylinder Diesel Engine

Megersa Lemma[1,*], Ramesh Babu Nallamothu[2]

[1]*Mechanical Engineering Department, Mizam Teppi University, Etihiopia*
[2]*Mechanical Systems and Vehicle Engineering Department, Adama Science and Technology University, Adama, Ethiopia.*
**Corresponding author, e-mail: megersalemma77@gmail.com*

ABSTRACT

Biodiesel made from the vegetable oils found to be one of the most promising alternative to petro diesel in solving the issues like depletion of petroleum sources, environmental pollution etc. For a country like Ethiopia with large trade gap producing home grown and eco-friendly fuel is an urgent necessity. For Ethiopia with wide cultivation of cotton seed oil which is non-edible would be smart feedstock for preparation of biodiesel. Biodiesel has several drawbacks like higher viscosity, low calorific value, cold flow issues, higher emission, shorter storage life etc. In recent days with the development of nanotechnology, addition of nano particles for improving the performance of fuels attracting the attention of researchers. In this work it is aimed to test the performance of cotton seed oil biodiesel with cerium oxide (CeO_2) nano particles as additive. This work goes through the various stages like production of biodiesel, addition of nano particles with the biodiesel-diesel blends in different proportion using ultrasonicator, testing the effect of nano additives on physiochemical properties of the fuel blend, testing the stability of fuel blend with nano particles, testing the performance and exhaust emission in diesel engine. The blends B10 (90% diesel and 10% biodiesel in volume), B20 (80% diesel and 20% biodiesel in volume), B20+50ppm (80% diesel and 20% biodiesel and 0.05 gm/l cerium oxide) in volume, B20 + 100ppm (80% diesel and 20% biodiesel and 0.1 gm/l cerium oxide) in volume, B25 (75% diesel and 25% biodiesel) in volume were prepared. From the performance test results, the cotton seed oil fuel blended with cerium oxide shows increment in brake power 4.5kW 4.68kW and brake torque of 18.43Nm and 18.52Nm with 50 ppm and 100 ppm respectively. Addition of CeO_2 improved exhaust emission compared to pure diesel (B0). The brake specific fuel consumption of cotton seed fuel blended with cerium was decreased compared to the diesel. Generally, it may be concluded from the experimental investigation that the cotton seed oil biodiesel fuel blended with cerium oxide nanoparticle can become a good alternative to petro-diesel.

Keywords: *Biodiesel, CeO_2 Nanoparticles, Performance and Emission, Stability of the blend, Ultrasonicator*

1. INTRODUCTION

The growing industrialization and moralization of the world has led to a step up for the demand of petroleum-based fuel. The petroleum based fuels are obtained from restricted reserves. These finite reserves are highly targeted in certain areas of the world. Therefore, those countries not having these resources face energy/foreign exchange crisis, principally because of the import of crude petroleum. Hence, it's necessary to appear for alternative fuels which might be produced from resources accessible domestically among the country such as alcohol, biodiesel, vegetable oils etc. (Agarwal, 2007). To solve this issue, many researchers established with results that biodiesel is an alternate fuel.

It's evident that two things are necessary, one is process of vegetable oil to biodiesel and the alternative is testing obtained biodiesel in diesel engine for its compatibility as fuel to diesel engine particularly the blend percentage which will offer results almost like diesel. Biodiesel is outlined as mono-alkyl esters of long chain fatty acids derived from renewable biolipids via transesterification method, that conform to ASTM D6751 specifications to be used in diesel engines (Agarwal, 2007) . The method of elimination all glycerol and fatty acid from the vegetable oil within the presents of catalyst are called as transesterification. It's basically a written record reaction. Triglycerides are first reduced to di glycerides. The di glycerides are afterwards reduced to mono glycerides. The mono glycerides are finally reduced to fatty acid esters (Akhtar, 2011).

The properties of biodiesel typically has higher density, viscosity, cloud point, cetane number, lower volatility and heating value The properties of biodiesel typically has higher density viscosity cloud point cetane number

lower volatility and heating value compared with diesel fuel that affecting on engine performance and emissions. However, using optimised blend of nano particles and diesel will help to reduce these high properties or its blends could also be used in the present diesel engines with very little or no modification to the engine (Benjumea, 2008, Selvan, 2009). With the following goals and method this work has been completed through fuel additives (nanofuel). Nanofuel could be a renewable and ecofriendly alternative diesel fuel for CI engine. What are more additives are an important a part of these days fuels, along with the carefully developed fuels composition. They contribute to efficiency responsibility associated long lifetime of an engine like using optimised blend of nano particles and diesel rather than conventional diesel fuel considerably reduces emission of particulate matters (PM), carbon monoxide (CO), sulphur oxides (SOx), and unburned hydrocarbons (HC). With the utilization of fuel additives within the blend of nanoparticles and diesel improves performance, combustion and additionally improves fuel properties that enhance the combustion characteristics. The impact of mixture of cerium oxide (CeO_2) and carbon nanotube (CNT) in single cylinder four-stroke water-cooled inconstant compression ratio engine using castor biodiesel blend with ethanol. When blended at 25ppm, 50ppm and 100 ppm of 32 nm sized CeO_2 and 100 nm sized CNT, brake thermal efficiency and cylinder pressure is increased. Moreover, such a blend of nano particles resulted in forward-looking peak pressure incidence with cleanser combustion means reducing emission (Selvan, 2009). This work study was designed to analyze the result of CSME blended with diesel beside cerium oxide (CeO_2) nanoparticle on the performance and exhaust gas characteristics of diesel engine. For investigation varied blends of cotton seed biodiesel with diesel were taken. The cerium oxide (CeO_2) nano particle was added with various proportions. (Ghanshyam, 2015). The researchers are targeted on single biodiesel with Nano fuels blends like soybean oil, rapeseed oil, pongamia pinnata oil, Cotton seed oil, Neem oil, Castor oil, Mahua oil, Mahua oil,jatropha oil, lineed oil, rice bran oil etc. and its blended with diesel (Ghanshyam, 2015, Mekhilef, 2011). The stability of nano fluid is increase by ultrasonic bath stabilization or by adding chemical agent within the fluid (Sajeevan, 2013).

Nanoparticles acts as a fuel accepted catalyst that improves specific properties of fuel once value-added to the base fuel depending upon the dosage level of it (i.e., flash point, fire point, kinematic viscosity, heating value and cetane number). This can be because of its better thermo physical properties. Particles that have size in between one nm to one hundred nm are thought-about as nanoparticles. The size of nanoparticles varies from 1 to 100 nm (Selvan, 2014). The experimental on emission characteristics, performance with Hinge oil methyl ester (HOME) biodiesel fuel blended with multi walled carbon tube (MWCNT) at 25 ppm and 50 ppm concentration in single cylinder four stroke direct injection diesel engine (Tewari, 2013). In addition, the investigation of emission characteristics and performances of pure diesel and diesel-biodiesel blend and ethanol blends with 25 ppm cerium oxide (CeO_2) (Arul Mozhi Selvan, 2009).

2. MATERIALS AND METHODS

2.1. Materials

The cotton seed was obtained from awash. Methanol, potassium hydroxide, and distilled water were purchased from chemical marketing and suppliers companies (Ranchem chemicals Plc, Addis Ababa) for laboratory scale amount. Cerium oxide (CeO_2) nanoparticle were purchased from Nano Research Lab, India; diesel fuel was purchased from Oil Libya Adama. All chemicals used for the research were analytical grade. Characterisation of fuel blends were tested at Ethiopian petroleum supply and enterprise while the performance and exhaust emission test was conducted at Dilla University Mechanical Engineering laboratory on CT 110 Test Stand Diesel Engine (single cylinder, 4-stroke engine).

2.2 Extraction of cotton Seed oil

The raw Cotton seed were obtained from cotton ginning factory Awash and separated the seed from the lint before the oil extracted from the seed. The lint goes to textile industry and the seed for the oil extraction to Hundaf

Engineer Food oil production Plc. There are some core procedures to be followed for extracting crude oil from cotton seed. The steps are like collection of all cotton seeds, de hulling and separation of the hulls (husk), cleaning the seed and drying, mechanical press, heat treatment and cooking and filtering. Figure 1 shows the pressing of cotton seed using screw press.

Figure 1: Extraction of oil from cotton seed by screw pressing

After the crude oil was extracted using screw press, the transestification was done at Adama Science and Technology University, Chemistry Department Laboratory.

2.3.1. Determination of acid value

3.3.1 Titration

In order to determine the percent of FFA in the oil, a process called titration is used. The vegetable oil is first mixed with methanol. Next, a mixture of sodium hydroxide (NaOH) and water is added till all of the FFA has been reacted. This can be confirmed by checking the pH of the mixture. If the oil samples have high FFA content (more than 1%) then the reaction consumes more alkali catalyst to neutralize the FFA. The FFA content in the oil was found as 0.59. The FFAs < 1, therefore transestirification process was used to prepare biodiesel. Fig. 2 shows the titration of crude oil.

Figure 2: Titration to find FFA in the oil

2.3.2. Laboratory Preparation of Biodiesel (Transestirification Process)

The biodiesel production using transesterification process involves various stages.

Figure 3: Transesterification

Figure 4: Glycerol Separation from methyl ester

Figure 5: Washing biodiesel (soap is at bottom)

Figure 6: Final washing of biodiesel

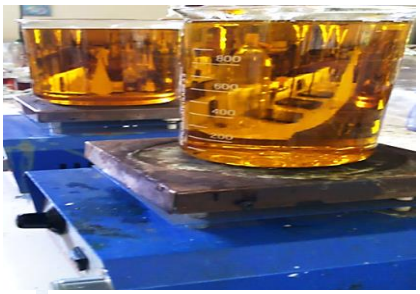

Figure 7: Drying of biodiesel

Figure 8: Prepared biodiesel

The Figure 3 to Figure 8 show the statges of biodiesel production like transesterification using hotplate with magnetic stirrer, separation of glycerine, washing of biodiesel with water (First washing and Final washing), biodiesel drying and finally the prepared biodiesel.

2.3.3. Mixing nanoparticles with fuel blend

The cerium oxide nanoparticles were mixed with B20 at a proportion of 50 ppm and 100 ppm using magnetic stirrer and ultrasonic cleaner for homogeneous dispersion of nanoparticles in the blend. Stable mixture was obtained adding CTAB surfactant.

Figure 9: Ultrasonicator and fuel blends

Figure 10: Prepared biodiesel blends

Blending of nanoparticles was done using ultrasonic cleaner with a frequency of 40 kHz for about 30 mnts. Figure 9 shows the ultrasonic cleaner and the prepared blends. Figure 10 shows all fuel blends prepared.

3. EXPERIMENTAL SETUP

The performance and exhaust emission tests were conducted on CT 110 Test Stand for Small Combustion Engine. The specifications of the test stand are given in the Table 1. Figure 11. Shows the picture of the experimental setup.

Table 1: Specification of the CT 110 Test Stand with engine

Engine model	1B30-2
Number of cylinders	1
Length x Width x Height	370 mm x 330 mm x 450 mm
Company	Hatz
Weight	35 kg
Fuel	CT 100.22 Diesel
Bore	80 mm
Stroke	69 mm
Crank length	34.5 mm
Rod length	114.5 mm
Output power at 3500 min-1	5.5 kW
Oil capacity	1.1 L
Stop solenoid	12 V
Compression ratio	22: 1
Engine type	Air-cooled single cylinder 4-stroke Diesel Engine

Figure 11: Experimental setup

4. RESULT AND DISCUSSION

5.1. Characterization Results

The characterization results of the biodiesel produced from cotton seed oil and blend fuels that were certified from Ethiopian petroleum supply enterprise are shown in Table 2.

Table 2: The properties of biodiesel and blends

SN.	properties	Test method ASTM	EPSE Diesel limits	Results					
				B100	B10	B20	B25	B20+ 50ppm CeO_2	B20+ 100ppm CeO_2
1	Density@15°C (g/ml)	D4O52	Report	0.8563	0.8425	0.8467	0.8488	0.8477	0.8464
2	Density@20^{0}C (g/ml)	D4052	Report	0.8465	0.8389	0.8432	0.8454	0.8442	0.8458
3	Flash Point (PMCC, ^{0}C)	D93	Min.60	182	85	86	89	87	86
4	Cloud point (^{0}C)	D2500	Max.+5	+3	+1	-1	+2	+1	+1
5	Total acidity (mgKOH/g)	D974	-	0.0985	0.0852	0.1009	0.0918	0.0930	0.1005
6	Viscosity@40^{0}c (cSt)	D445	1.9-6	3.67	3.29	3.32	3.33	3.32	3.31

4.2. Engine brake power (kW)

From the Figure 12, it is observed that, the maximum brake power was developed at 2808 rpm for the fuels tested. The highest values of brake power for B0, B10, B20, B25, and B20 + 50ppm CeO2, B20 + 100ppm CeO2 are 5.18 kW, 4.67 kW, 4.60 kW, 4.31 kW, 4.53 kW and 5.21 kW respectively.

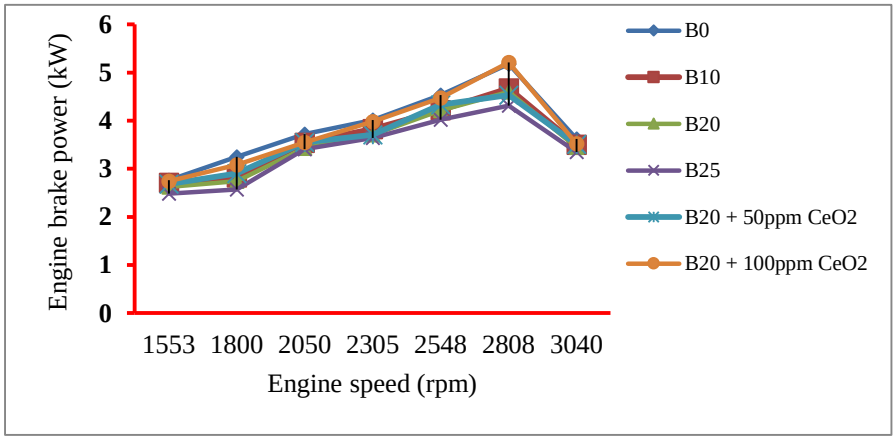

Figure 12: Variation of Brake power (kW) with Engine speed (rpm)

4.3. Engine Brake Torque (Nm)

From Figure 13, given below, it is observed that all fuel samples producing maximum torque at a speed of 2548 rpm. The maximum brake torque for the fuel samples B0, B10, B20, B25, B20 + 50 ppm CeO2 and B20 + 100 ppm CeO_2 are 18.48 Nm, 18.35 Nm, 18.12 Nm, 17.83 Nm, 18.43 Nm, and 18.52 Nm respectively. B20 + 100 ppm CeO_2 had higher brake torque than other fuel blends. It is clearly observed that the addition of CeO2 caused higher brake torque.

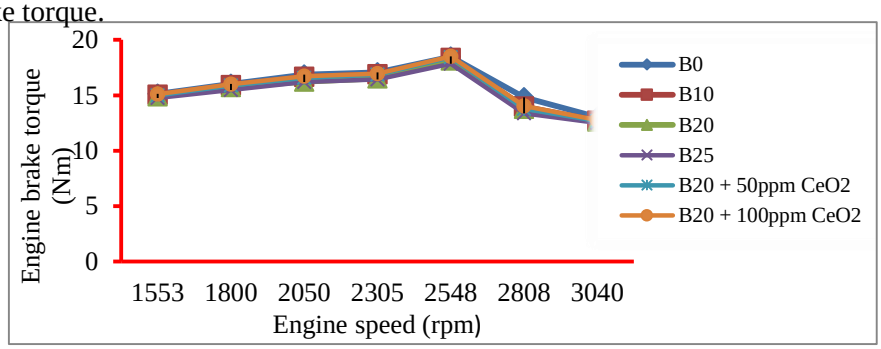

Figure 13: Variation of Brake torque (Nm) with Engine speed (rpm)

4.4. Brake Specific Fuel Consumption bsfc (kg/kWh)

Figure 14 shows that there is a reduction of brake specific fuel consumption with addition of nanoparticles engine speed for neat diesel, biodiesel blend fuel and biodiesel blend fuel plus cerium oxide nano particles. The bsfc was observed to be reducing from 1553 rpm to 2548 rpm later starts increasing.

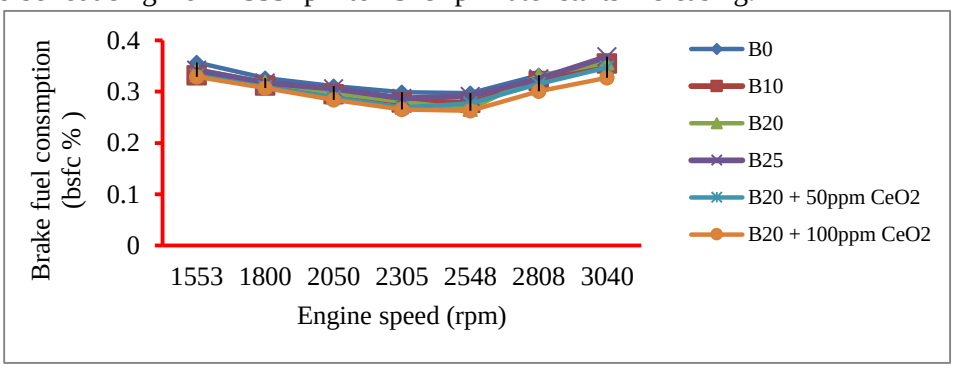

Figure 14: The variation of brake specific fuel Consumption (kg/kWh) with engine speed (rpm)

4.5. Carbon monoxide emission (CO %)

Figure 15 shows the variation of CO emission with speed for different fuel blends. Reduction of CO with the addition of CeO_2 is clearly indicated. At higher speeds there is a reduction tendency of CO with CeO_2 addition.

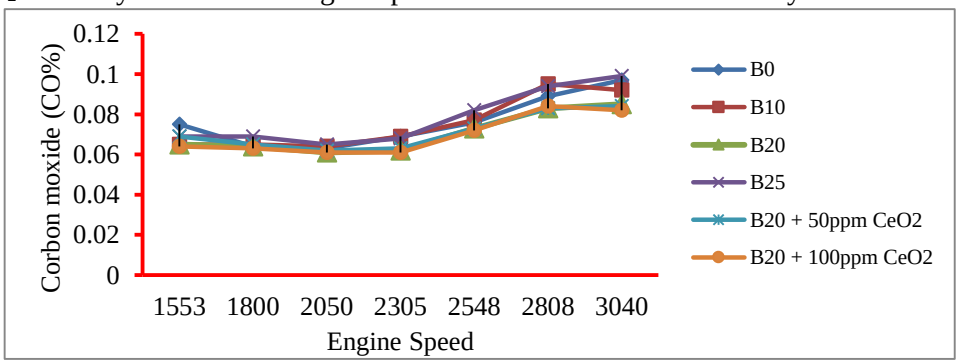

Figure 15: Variation of carbon monoxide (%) with respect to engine speed (rpm)

4.6. Carbon Dioxide emission (CO_2%)

From Figure 16, it can be seen that CO_2 emission is less for all biodiesel blends compared to diesel fuel. Especially in B20 + 100ppm CeO_2 the reduction of CO_2 is more than others blends. The reduction of CO_2 at low engine speed 1553 rpm is 2.53%, 2.38%, 2.47% 2.52%, 2.32% and 2.28% respectively compared to diesel.

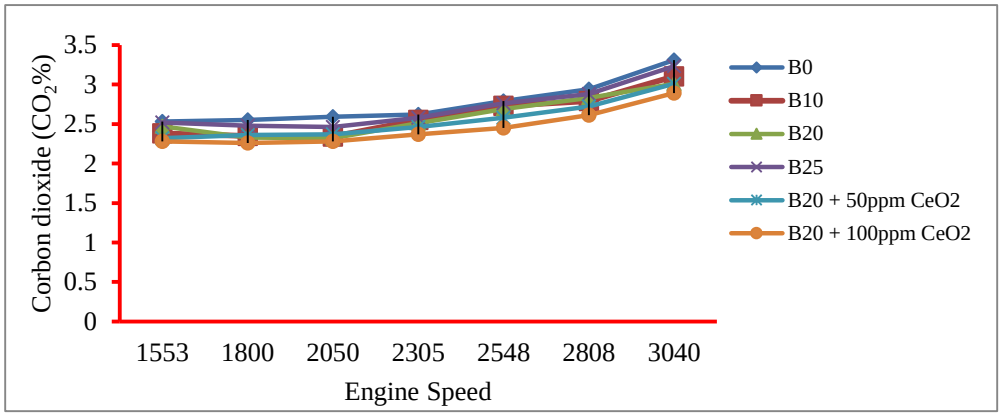

Figure 16: Variation of carbon dioxide (%) respect to engine speed (rpm)

4.7. Hydrocarbon emission (HC ppm)

B20 + 50ppm CeO_2 and B20 + 100 ppm CeO_2 fuel blends had less HC emission than others Figure 17.

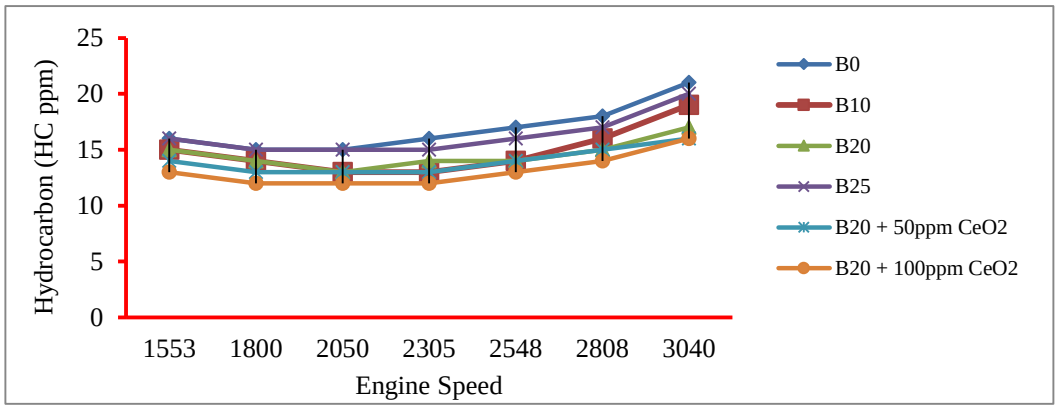

Figure 17: Variations of Hydrocarbon (HC) respect to Engine speed (rpm)

4.8. Emission Test for (O_2 %)

The oxygen (O_2) in case of fuel blended with cerium oxide nano particle is somewhat higher than other fuels. For a blend of B20 + 100 ppm CeO_2 the O_2 emission is 17.56%, 17.55%, 17.49 %, 17.33%, 17.29%. 17.18%, 16.99% higher for engine speeds 1553 rpm, 1800 rpm, 2050 rpm, 2305 rpm, 2548 rpm, 2808 rpm, and 3040 rpm respectively, than diesel fuel.

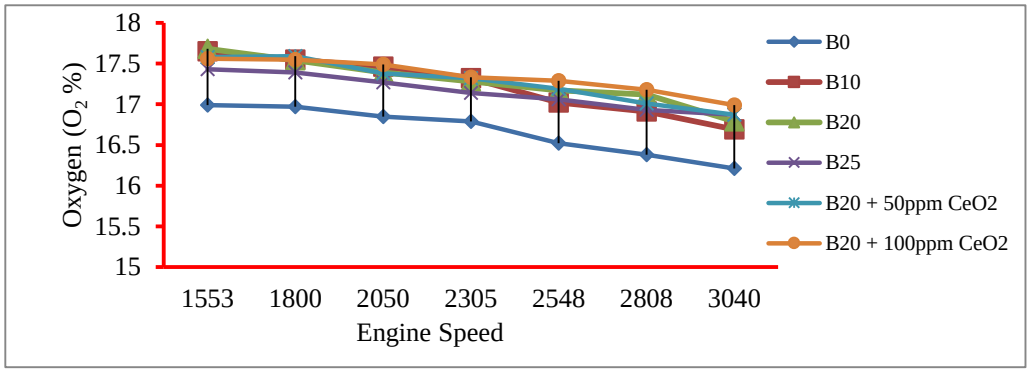

Figure 18: Variations of oxygen (O2) respect to Engine speed (rpm)

5. CONCLUSION

Based on engine performance and exhaust emission tests, it can be concluded that diesel biodiesel fuel blends with CeO_2 can be used satisfactorily in diesel engine without any modifications of the engine. Transesterification reduced the viscosity of the oil considerably and addition of CeO2 also caused slight reduction in viscosity (3.67cSt, 3.29cSt, 3.32cSt, 3.33cSt, 3.32cSt, and 3.31cSt for biodiesel, B10, B20, B25, B20 + 50ppm CeO_2, and B20 + 100ppm CeO_2 respectively). These results were nearly close to diesel and confirm with the biodiesel standards (ASTM D6751). From the engine performance test and emission test, it is clearly observed that the addition of CeO2 caused better performance and less harmful emissions compared to conventional diesel.

REFERENCES

Agarwal, A. K. (2007). "Biofuels (alcohols and biodiesel) applications as fuels for internal combustion engines". *Progress in energy and combustion science*, 233-271.

Akhtar, T. (2011). "Synthesis of biodiesel from triglyceride oil" (Master's thesis,).

Arul Mozhi Selvan, V. R. A. (2009). "Effects of cerium oxide nanoparticle addition in diesel anddiesel-biodiesel-ethanol blends on the performance and emission characteristics of a CI engine". 4, 1-6.

Benjumea, P. A. (2008). "Basic properties of palm oil biodiesel diesel blends". *Fuel*. (10)(87): 2069-2075.

Ghanshyam S. Soni, P. D. (2015). "Goswami (Performance and emission characteristics of CI engine using diesel and biodiesel blends with nanoparticles as additive" - A review study), *3*(4): 2321-9939.

Mekhilef, S. S. (2011). "A review on palm oil biodiesel as a source of renewable fuel. Renewable and Sustainable Energy" Reviews. *(4)*(15), 1937-1949.

Sajeevan, A. C. (2013). Diesel Engine Emission Reduction Using Catalytic Nanoparticles: An Experimental Investigation.

Selvan, B.V. A. M., Anand, R. & Udayakumar, M. (2009). "Effects of cerium oxide nanoparticle addition in diesel and diesel biodiesel ethanol blends on the performance and emission characteristics of a CI engine". *(7)*(4), 1819-6608.

Selvan, V. A. (2014). "Effect of Cerium Oxide Nanoparticles and Carbon Nanotubes as fuel-borne additives in Diesterol Blends on the performance, combustion and emission characteristics of a variable compression ratio engine". Fuel. 160-167.

Tewari, P. D. (2013). Experimental investigations on a diesel engine fuelled with multi-walled carbon nanotubes blended biodiesel fuels. *3*, 72-76.

Influence of Cu-Cr Substitution on Structural, Morphological, Electrical and Magnetic Properties of Magnesium Ferrite

Yonatan Mulushoa S.*, N.Murali[2], Tulu Wegayehu M.[3], K.Samatha[3]

[1]*Department of Physics, Assosa University, Assosa, Ethiopia*
[2]*Advanced Analytical Laboratory, Andhra University, Visakhapatnam, India*
[3]*Department of physics, Andhra University, Visakhapatnam, India*
**Corresponding author, e-mail: tafe.mule06@gmail.com*

ABSTRACT

Cu-Cr substituted magnesium ferrite materials ($Mg_{1-x}Cu_xCr_xFe_{2-x}O_4$ with x = 0.0 -0.7) have been synthesized by the solid state reaction method. XRD analysis revealed the prepared samples are cubic spinel with single phase face centered cubic. A significant decrease of ~ 41.15 nm in particle size is noted in response to the increase in Cu-Cr substitution level. The room temperature resistivity increases gradually from 0.553×10^5 Ωcm (x=0.0) to 0.105×10^8 Ωcm (x=0.7). Temperature dependent DC-electrical resistivity of all the samples, exhibits semiconductor like behavior. Cu-Cr doped materials can be suitable to limit the eddy current losses. VSM result shows pure and doped magnesium ferrite particles show soft ferrimagnetic nature at room temperature. The saturation magnetization of the samples decreases initially from 34.5214 emu/g for x=0.0 to 18.98 emu/g (x=0.7). Saturation magnetization, remanence and coercivity are decreased with doping, which may be due to the increase in grain size.

Keywords: *Solid state reaction, X-ray diffraction, Crystalite size, Magnetic and electrical properties, saturation magnetization*

1. INTRODUCTION

Now a days spinel ferrites are seeking an enormous attention by scientist being having different structural development and encouraging physical properties. Because of these ferrite materials shows a variety of unique and improved characteristics, these materials is significant for sophisticated technological use. Ferrites are very applicable in technological fields with regards to fine size distribution and its identical particle size. Ferrites are more applicable as a good dielectric material and very useful for microwave devices also [1]. Composition, method of preparation, temperature, sintering conditions and cation distribution among tetrahedral and octahedral sites are very critical and fundamental parameters used to study the properties of ferrite materials [1]. The chemical composition of a spinel ferrite can be written as MFe_2O_4 where M = Mg, Zn, Ni, Cu, Co, Mn etc. These ferrite materials, i.e. MFe_2O_4, combined with M divalent ion considered as key materials which is used for current technologies due to their attractive properties. These material shows high electrical conductivity, high specific heating, high corrosion resistance, high thermodynamic stability, low melting points and low magnetic transition temperature [2]. Spinel ferrite materials can also described by its higher efficiency, low cost and have an appropriate dielectric loss which can be used in microwave devices and memory cores [3].

Among a number of Fe-based ferrites, magnesium ferrite ($MgFe_2O_4$) is the promising candidate for various applications due to their high electrical resistivity as well as magnetic and low dielectric losses [4,5] and possesses spinel cubic structure having octahedral site occupancy with Mg^{2+} ions and ferric Fe^{3+} ions residency on tetrahedral sites.. Magnesium ferrite with substitution for Mg^{2+} and Fe^{3+} ions has attracted attention of a number of research workers who attempted to explain the magnetic properties on the basis of the distribution of the only magnetic ion Fe^{3+} in tetrahedral (A) and octahedral (B) sites, which makes the analysis reliable [6]. Study of DC-electrical, dielectric and magnetic properties of ferrite materials provide valuable information about the conduction mechanism and magnetic state of the ions.

In recent years a number of synthesis methods have been established like physical and chemical methods. Some these are ceramic methods, micro-emulsion method, hydrothermal method, sol-gel method and co-

precipitation method. Due to low-cost starting materials, easy to understand the chemistry of the reaction and to produce a high dense sample, ceramic methods was selected for synthesis.

The structural, electrical and magnetic properties of $MgFe_2O_4$ have been investigated by means of different characterization methods with the substitution of metal cation like Co-Cr [7], Ni-Cd [8], Ti^{4+} [9] and Al^{3+} [10]. Substituting of $MgFe_2O_4$ with one or several transition metals is one of the best method to enhance the properties of ferrites as studied with Cr substitution [11]. But a study of physical, electrical and magnetic properties of Cu-Cr doped magnesium ferrite using solid state methods is not yet reported. So the present work is an investigation of structural, electrical and magnetic properties of magnesium ferrite which is substituted by Cu-Cr metal cation.

In the present study, Mg^{2+} and Fe^{3+} were substituted by copper and chromium ions simultaneously. The ceramic or solid state method was used to synthesize these materials. The purpose of this study is to explore the effect of Cu-Cr substituted on the structural, morphological, magnetic and electrical properties of magnesium ferrite and their use in recording media.

2. EXPERIMENTAL

2.1. Synthesis of $Mg_{1-x}Cu_xCr_xFe_{2-x}O_4$ ferrite material

In this study, MgO (99% purity, Himedia, India), Fe_2O_3 (98% purity, Himedia, India), CuO (98% purity, Himedia, India) and Cr_2O_3 (99% purity, CDH, India), PVA (99% purity, Merck, India) and Acetone (99.5% purity, Himedia, India) were used as the starting chemicals. The oxides in their weight proportion were mixed thoroughly and well ground using acetone. Magnesium ferrite sample doped simultaneously with Cu and Cr was prepared by the solid state method with the details of the procedure given below. The following four series of chemical reaction used to prepare each sample with respect to its concentration using the solid state method.

$$0.9MgO + 0.1CuO + 0.05Cr_2O_3 + 0.95Fe_2O_3 \Rightarrow Mg_{0.9}Cu_{0.1}Fe_{1.9}Cr_{0.1}O_4 + gas\uparrow$$
$$0.7MgO + 0.3CuO + 0.15Cr_2O_3 + 0.85Fe_2O_3 \Rightarrow Mg_{0.7}Cu_{0.3}Fe_{1.7}Cr_{0.3}O_4 + gas\uparrow$$
$$0.5MgO + 0.5CuO + 0.25Cr_2O_3 + 0.75Fe_2O_3 \Rightarrow Mg_{0.5}Cu_{0.5}Fe_{1.5}Cr_{0.5}O_4 + gas\uparrow$$
$$0.3MgO + 0.7CuO + 0.35Cr_2O_3 + 0.65Fe_2O_3 \Rightarrow Mg_{0.3}Cu_{0.7}Fe_{1.3}Cr_{0.7}O_4 + gas\uparrow$$

The solid state reaction synthesis method includes two steps. First, the precursors are well mixed and thoroughly ground with agate mortar, then subjected to heat treatment at a temperature of 800 ^{0}C to dry the samples free of gases and impurities. Then, this powder was cooled at the rate of 5 ^{0}C/min. Finally, the mixture is reground and calcined at temperatures 1000^{0}C for 6 hours to complete the chemical reaction in air using a muffle box furnace. This final powder was used for study structural, morphological study and magnetic properties.

For electrical and dielectric study, pellets with a size of around 13.52, 14.19, 13.81 and 14.42 mm in diameter and 2.28, 2.29, 2.36 and 2.33 mm in thickness are used respectively with respect to concentration. The powder samples added with polyvinyl alcohol (PVA) as a binder and ground for one hour, then pressed at 7 tons / 5 minutes pressure into a circular disk shaped pellet. The pellet is then sintered at 1150^{0}C for 7 hours in air at heating and cooling rates of 5^{0}C/min. The surface layers of the sintered pellet are carefully polished and washed with acetone and then the pellet is coated with silver paste on the opposite faces which act as electrodes.

2.2. Characterization

The TG/DTG measurement is conducted using Mettler Toledo TG/DTG 851^e instrument from room temperature to 1000^{0}C in a Nitrogen atmosphere at a heating rate of 10 ^{0}C /min. The TGA curves are plotted with the percent weight change against temperature. The powder X-ray diffraction (XRD) data of the sample are collected on a PANalytical X-pert pro diffractometer with diffraction angles of 20^0 and 80^0 in increments of 0.008^0. The unit cell lattice parameter is obtained by the unit cell software from the 2θ and (hkl) values. Further, the crystallite size of the sample is obtained by applying the Scherrer's equation from XRD pattern. The particle morphology and elemental analysis of the powders are observed using scanning electron microscopy (SEM) and

energy dispersive spectra (EDS) taken from JEOL JSM-6610LV connected with Inca-Penta FETx3.JPG, Oxford Instruments. Fourier transform infrared (FT-IR) spectra are obtained on a Shimadzu IR-Prestige21 spectrometer using a KBr as a binder and studying the wave number range between 400 and 4000 cm^{-1}. Electrical characterizations measured interns of DC-electrical resistivity. The electrical resistivity was measured at a temperature range 300-500 K by using two probe method. Magnetization, coercivity and remanence for all the samples were measured by vibrating sample magnetometer (VSM) at room temperature.

3. RESULT AND DISCUSSION

3.1. Thermal Analysis

The TGA and DTG measurements are carried out in nitrogen atmosphere by heating the powdered samples from room temperature to 1000^0C at a heating and cooling rate of 10^0C/min as shown in Figure 1. One representative sample with a composition of x = 0.1 from each of the four series is selected for thermal analysis.

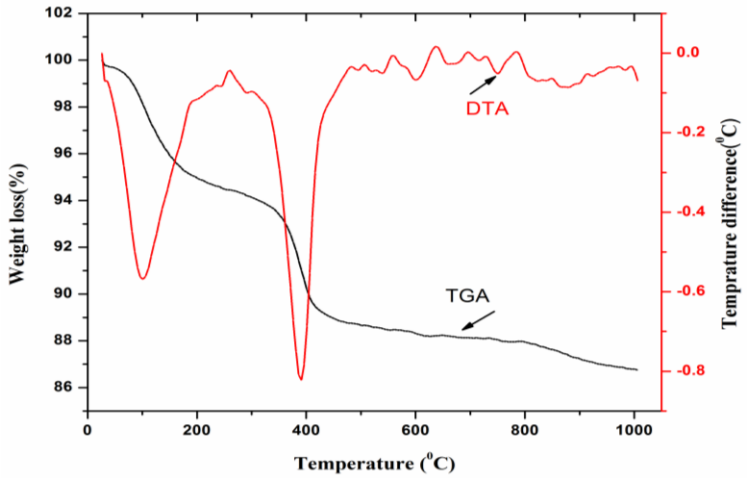

Figure 1: TG/DTG curve for $Mg_{0.9}Cu_{0.1}Cr_{0.1}Fe_{1.9}O_4$

As can be seen from the curves, there is an initial weight loss in the temperature range from room temperature to 300^0C (~ 6%). This corresponds to the evaporation of methanol used during grinding to homogenize the mixture and the moisture absorbed during storage [12]. The TGA curve of $Mg_{1-x}Cu_xCr_xFe_{2-x}O_4$ shows more weight loss (~ 7%) between the temperatures 300 ^{0}C and 600 ^{0}C. This loss may be due to the decomposition of the precursors MgO, CuO, Cr_2O_3 and Fe_2O_3 the reaction between the decomposed materials thereby to produce crystalline and $Mg_{1-x}Cu_xCr_xFe_{2-x}O_4$. This is confirmed by sharp peak observed at 390 ^{0}C on the DTG curve. There is minor weight loss observed up to the temperature of 800 ^{0}C to 900 ^{0}C is due to complete decomposition of any interfering phases [13]. The desired complete single-phase cubic spinel structure formation has been formed at 1000^0C.

3.2. Structural Analysis

3.2.1. X-ray diffraction (XRD) analysis

XRD patterns of the Cu-Cr doped magnesium ferrite $Mg_{1-x}Cu_xCr_xFe_{2-x}O_4$ samples (x = 0.0, 0.1, 0.3, 0.5 and 0.7) is shown in Figure 2 calcined at 1000^0C for 7 hour. The X-ray diffraction (XRD) studies confirm the formation of cubic spinel phase. The formation of single phase was confirmed by comparing X-ray diffraction line corresponding to (220), (311), (222), (400), (422), (511), (440), (620), (533) and (444) planes with standard diffraction plot (JCPDS card number 17-464). As can be seen from the diffraction peaks, the obtaining samples are quite similar to the results of N.M.Deraz and Omar H. Abd Elkader [14]. This confirms that the dopant must have simply replaced the Mg^{2+} - Fe^{3+} ions without distortion of the cubic symmetry of the host magnesium ferrite. All the diffraction peaks are fitted well with those for cubic spinel crystal structure and belongs to the Fd-3m space

group. It can be seen that highest peak in this diffraction pattern (311) at 2θ ≈ 35.0665 value belongs to typical ferrites highest diffraction.

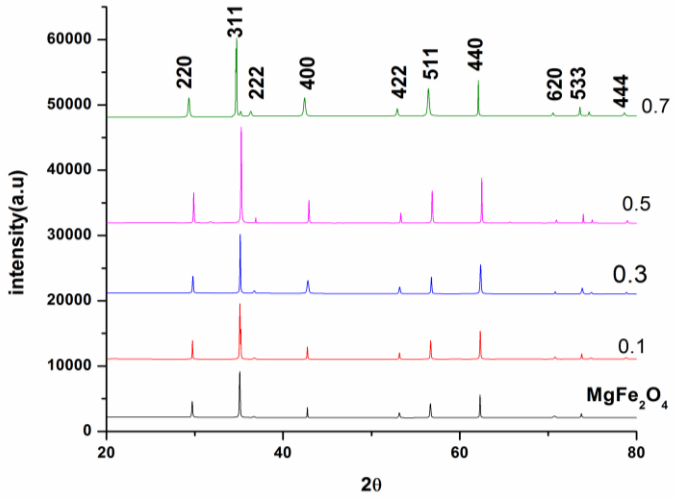

Figure 2: XRD patterns of Mg-ferrite doped with Cu-Cr contents (x = 0.0-0.7)

Lattice constant and Crystallize size can be calculated using Bragg's law that was combined with the full width at half maximum (FWHM) into a web-based crystallite calculator [15] and Debye-Scherrer formula [16] respectively. The lattice parameters were calculated from the XRD data using UNITCELL software and the crystallize size is found to be in the range 34.5-75.65 nm. Crystallite size can be extracted by applying a highest diffraction pattern, i.e., (311). A significant decrease of ~ 41.15 nm in particle size is noted in response to the increase in Cu-Cr substitution level. It has been reported that a crystalline size of < 50 nm is needed for obtaining switching applications [17]. It is clear from the Fig. 3 that the lattice constant decreases with increases in Cu-Cr content.

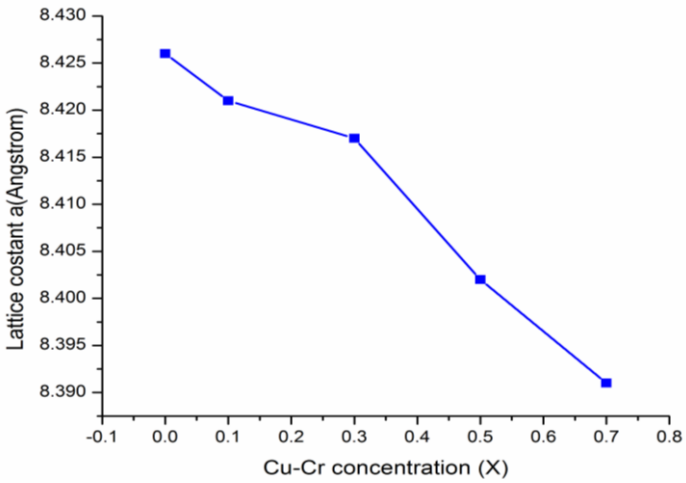

Figure 3: Plot showing lattice parameters Vs Cu-Cr concentration for $MgFe_2O_4$

The value of lattice constant (a) and cell volume (V_{cell}) decreased with the increase in Cu-Cr substitution level as shown in Table 1. The dopant ions Cu^{2+}(0.73Å), Cr^{3+}(0.63Å) have comparable ionic size with those of host ions, i.e. Mg^{2+} (0.72Å) and Fe^{3+} (0.64Å). The lattice constant and cell volume both have performing decreasing tendency with the increase in the Cu-Cr concentration. The main reason for the decreasing tendency is a negligible decrease in the lattice constant value which is most likely due to comparable ionic size between host ion and doped metallic ion. The observed increase in the value of X-ray density (d_x) and bulk density (d_b) with the substitution

of dopant ion is due to (a) Larger molar mass of the doped metal cations compare to that of host material. (b) Shrinkage of lattice that leads to the observed decrease in the value of V_{cell}. The increase in d_x is a direct consequence of the decrease in lattice constant, as predicted from x-ray density equations [18]. Bulk density is lower than x-ray density, i.e., $d_b < d_x$ due to some unavoidable pores created during sintering.

Table 1: Crystallite size (D), lattice constant (a), cell volume (V cell), X-ray density (d_x), bulk density (d_b) and Porosity of $Mg_{1-x}Cu_xCr_xFe_{2-x}O_4$ (x = 0.0 - 0.7)

Parameters	0.0	0.1	0.3	0.5	0.7
D(nm)	44.94	63.73	35.14	75.65	34.5
a(Å)	8.426	8.421	8.417	8.402	8.391
V_{cell} (Å^3)	598	597.2	596.3	593.18	590.84
d_x (g/cm^3)	4.44	4.529	4.693	4.877	5.055
d_b (g/cm^3)	3.95	4.394	4.552	4.639	4.636
Porosity	11.03	3.07	3.09	5.13	9.03

3.2.2. Scanning Electron Microscopy (SEM) Analysis

SEM images of all the samples are shown in Fig. 4 (a) to (e). The morphology of all synthesized samples was observed and analyzed by using a scanning electron microscope. As shown in Fig. 4, the microscopic structure and morphology of the Cu-Cr substituted Mg-ferrite materials have been presented. As can be seen from the SEM images, the synthesized materials are irregular shaped group of grains and rough and porous surface morphology are also observed in almost all samples synthesized. The SEM micrograph shows that the grains have non uniform grain size distribution. The particle sharpness is more or less spherical indicating the crystallinity as confirmed by XRD pattern except at higher concentration. And also it is clear from the images that non uniformly distributed; agglomerated and inhomogeneous grains have been formed. However, some unusually large particles are observed in addition to the smaller particles and also more agglomeration is existed. The grain sizes measured using software associated with theSEM which is displayed in the ranges of 251 nm-3.07 µm for all samples. The grain size increases with the increase of Cu-Cr concentration. Ferrite materials are considered as good for application if they have small grain size, the fraction of grain occupied by the domain wall increase also increasing eddy current and hysteresis loses [18].

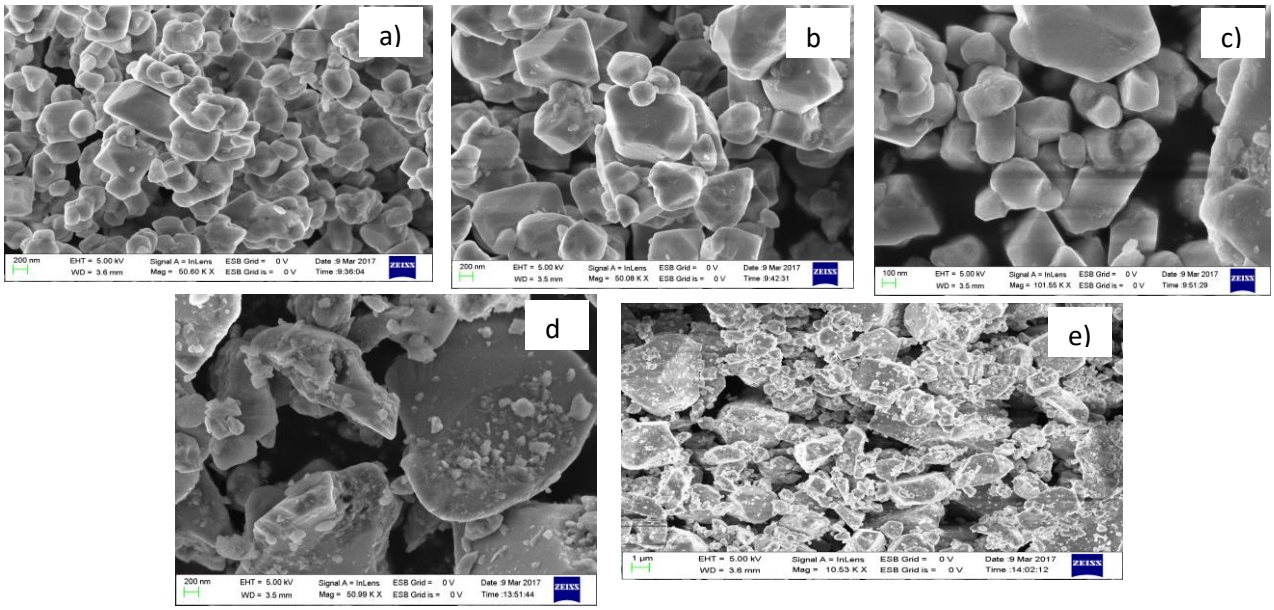

Figure 4: FESEM images of Mg ferrites doped with Cu-Cr contents (x = 0.0, 0.1, 0.3, 0.5, 0.7 a) to e), respectively)

3.2.3. EDS Analysis

Energy Dispersive spectroscopy (EDS) gives a useful analysis of elemental composition, thus it can be used to determine the stoichiometry of the material. The EDS spectra of all prepared samples were shown in Figure 5. EDS is more of quantitative result which shows the presence of Mg, Fe, O, Cr and Cu. These percentages of elements were well matched with the calculated weight percentage of all elements as per stoichiometric equation.

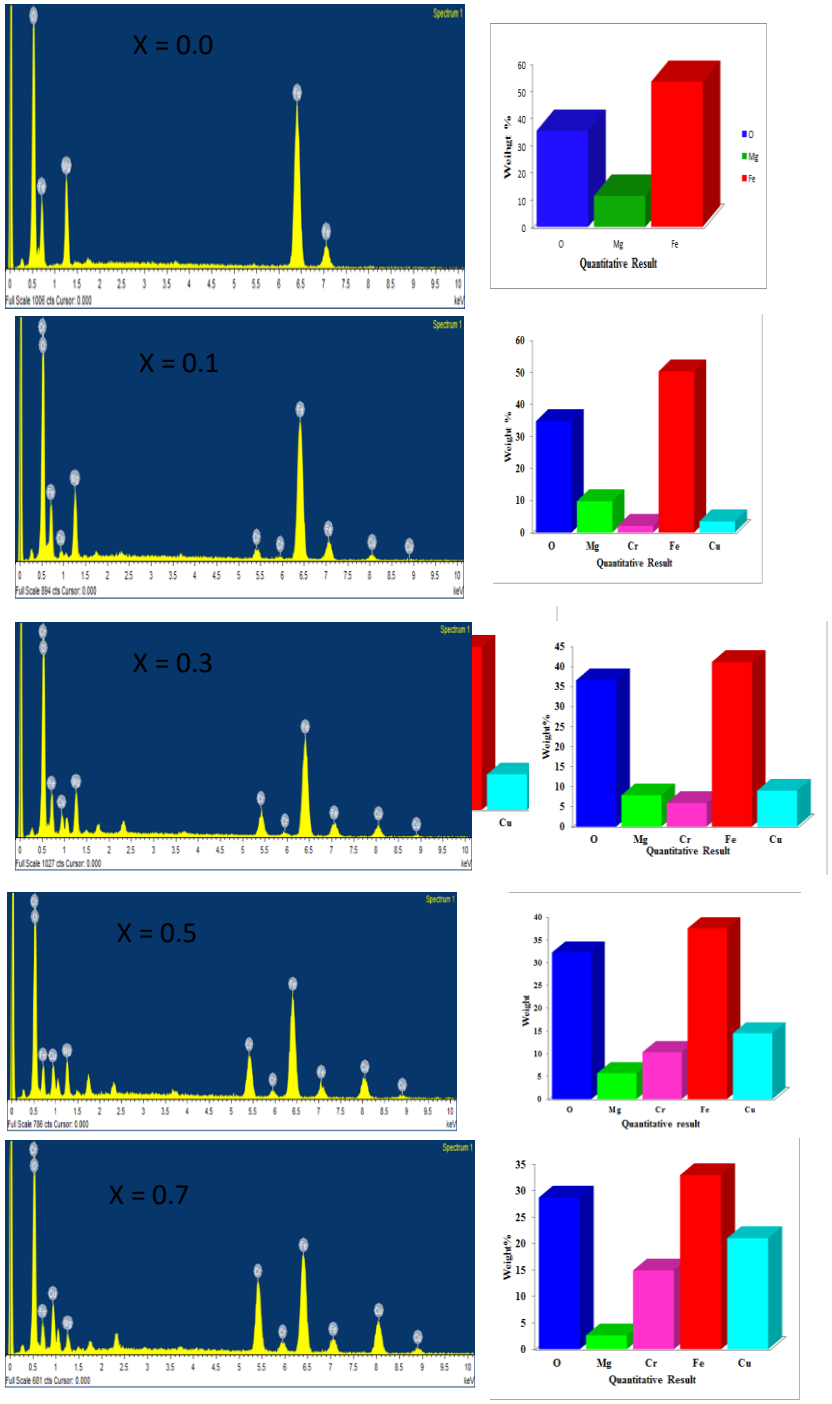

Figure 5: EDS spectra and histogram of elemental weight composition of Mg-ferrite doped with Cu-Cr contents (x =0.0-0.7)

3.2.4. FT-IR SPECTROSCOPY STUDIES

Typical FT-IR spectra of $Mg_{1-x}Cu_xCr_xFe_{2-x}O_4$ (x = 0.0, 0.1, 0.3, 0.5 and 0.7) materials synthesized by the solid state reaction method are shown in Figure 6. The spectra of all the powders in Figure 6 displayed the existence of two principal absorption bands, the one which is concentrated in the wave number range around ~ 600 and ~ 400. The higher frequency band (ν_1) is due to the stretching vibration of unit cell of the spinel in the tetrahedral (A) site and lower band (ν_2) is caused by metal-oxygen vibration in octahedral (B) site. According to Waldron [19], ferrites can be considered continuously bonded crystals, that is the atoms are bonded to all nearest neighbors by equivalent forces (ionic, covalent or Van Der Waals).

It has been observed that substitution of Cu^{2+} and Cr^{3+} in to Mg^{2+} - Fe^{3+} host materials causes shifts towards higher frequency (higher wave number) side, which may be due to changes that occurred to decrease in bond length at B-sites and cation distribution of the spinel lattice [20]. This can be explained as an increase of the concentration Cu^{2+}-Cr^{3+}cations in the A-sites and B-site contributes to the decrease of ionic radii of the A-site and B-site site. Therefore, a slight shifting of ν_1 bands toward high frequency is expected, because a decrease in site radius increases the fundamental frequency.

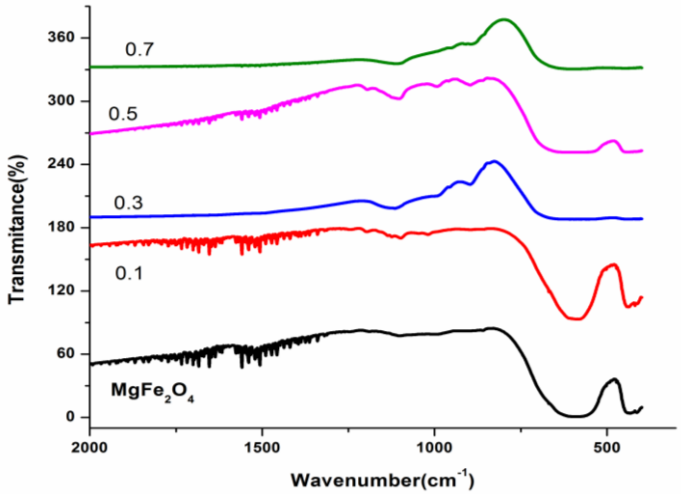

Figure 6: Infrared spectra of $Mg_{1-x}Cu_xCr_xFe_{2-x}O_4$ sample at (x = 0.0 - 0.7)

3.3. DC-ELECTRICAL PROPERTIES

In this present work DC resistivity of the Cu-Cr-substituted magnesium ferrite materials synthesis was conducted using a two-probe technique in the temperature ranges of 300–500 K. The resistance of each sample was measured at 5 K interval of temperatures. The DC resistivity for each sample was calculated from the resistances and the dimensions of the pellets using the formula,

$$\rho = R \times \frac{A}{t}\ \Omega.cm$$

Where, *R* is the resistance of the pellet, *A* is the surface area of the pellet, and *t* is the thickness of the pellet.

The DC electrical resistivity of the Mg ferrite system was found to increase from 0.553×10^5 (Ω-cm) to 0.105×10^8 (Ω-cm) at room temperature with the increase in Cu-Cr concentration from 0.0 to 0.7 as given in Table 2. The DC resistivity in all concentration varies between 10^5 and 10^8 Ω-cm. This increase in the resistivity due to the reason that substitution of Cr^{3+} for Fe^{3+} results in the reduction of Fe ions at B-site. Thus, it decreases an electron hopping between the Fe^{2+} to Fe^{3+} ions and as a result increases the resistivity. And also substitution of Cu^{2+} at the B-site might generate holes by the following exchange reaction, which can also be involved in conduction. The electron hopping, however, would mainly contribute in conduction and the overall effect of doping of Cu-Cr is the enhancement of resistivity. By doping calcium and Nickel on spinel ferrite at room temperature the resistivity found to be order of 10^6 to 10^7 [21, 22].

Table 2: DC-electrical resistivity (ρ^{RT}), activation energy (E_a) and drift mobility (μ_d) of $Mg_{1-x}Cu_xCr_xFe_{2-x}O_4$(x = 0.0-0.7).

Parameters	x=0.0	x=0.1	x=0.3	x=0.5	x=0.7
ρ^{RT}(Ω-cm)	0.553×10^5	0.147×10^6	0.634×10^6	0.188×10^7	0.105×10^8
E_a(eV)	0.0391	0.0432	0.1482	0.4472	0.45
μ_d $cm^2V^{-1}S^{-1}$	3.03×10^{-11}	1.096×10^{-11}	2.5216×10^{-12}	8.481×10^{-13}	1.667×10^{-13}

The temperature dependence of DC-electrical resistivity of Cu-Cr doped $MgFe_2O_4$ ferrite is shown in Figure 7. From the figure it can be seen that the resistivity of $Mg_{1-x}Cu_xFe_{2-x}Cr_xO_4$ (x = 0, 0.3, 0.5, and 0.7) increases with concentration. At the highest concentration of Cu-Cr the resistivity is greater than the parent material and this might be related to the increase in grain boundaries besides the nature of the dopant material and therefore the Cu-Cr-substitution is applicable for microwave device. It is evident that the DC-electrical resistivity of all samples exhibits semiconductor like behavior, i.e. decreasing resistivity with increasing temperature for all the samples. In ferrites, this behavior with increasing temperature is due to thermal mobility of charge carriers, but not due to the increased number of charge carriers at higher temperatures. Since, at higher temperatures relatively small amount of energy is sufficient for hopping of electron between octahedral sites [23].

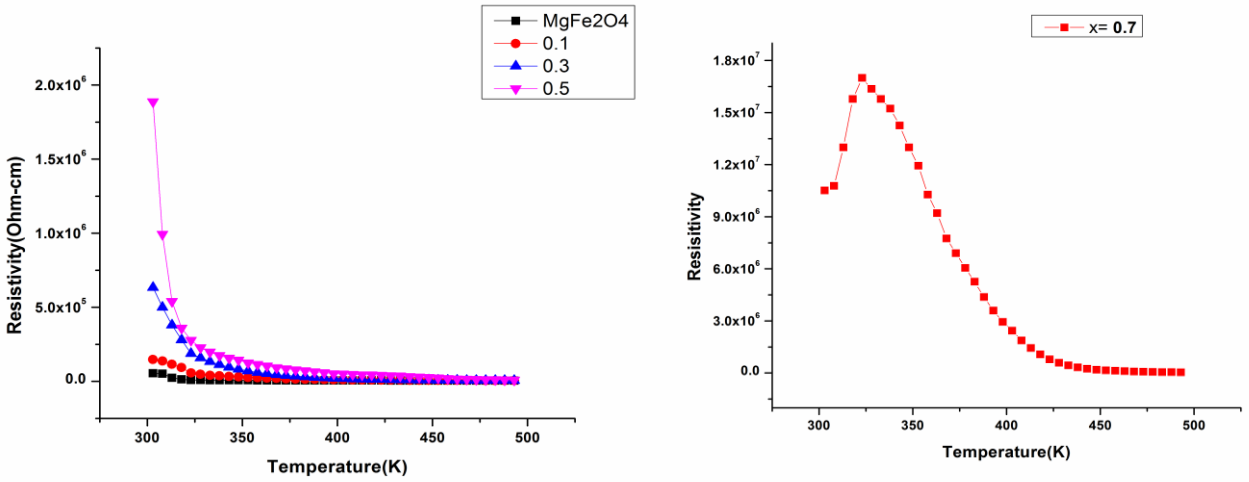

Figure 7: Resistivity Vs Temperature of Cu-Cr doped in $MgFe_2O_4$ at x = 0.0 (left) and 0.7 (right)

The values activation energy against Cu-Cr content shows increases activation energy from 0.0391 eV to 0.45 eV (Table 2). It can be observed that by increase resistivity, the values of activation energy are also increasing. Because it can also be been that samples having low resistivity have low activation energy and vice versa as reported by Islam and El-Shabasy in their work [24, 25].

The drift mobility and resistivity have an inverse relationship since $Mg_{1-x}Cu_xCr_xFe_{2-x}O_4$ ferrite can have increasing electrical resistivity so they have decreased mobility of their charge carriers. The room temperature value of drift mobility (Table 2) shows that it increases from 3.03×10^{-11} $cm^2V^{-1}s^{-1}$ to 1.667×10^{-13} $cm^2V^{-1}s^{-1}$, due to electron hopping suppressed at the B-sites causing the increase in resistivity. It can be seen that samples having higher resistivity have low mobility and vice versa [23] (Figure 8).

3.4. MAGNETIC PROPERTIES

Magnetic properties of the given samples were characterized by vibrating sample magnetometer at room temperature (300 K) with maximum applied field of -15 to 15KOe. The relation between the Magnetization (*M*) and the applied field (*H*) is given by Hysteresis loops. Typical magnetic hysteresis loop of $Mg_{1-x}Cu_xCr_xFe_{2-x}O_4$ samples with 'x' values from 0.1 to 0.7 with step size 0.2 is shown in Figure 9. The M-H hysteresis curve shows the magnetic behavior of parent and Cu-Cr doped magnesium ferrite material. These materials show soft ferrimagnetic nature.

This is confirmed by soft magnetic material have small the area inside the loop which shows small amount of energy is dissipated in reversing the magnetization.

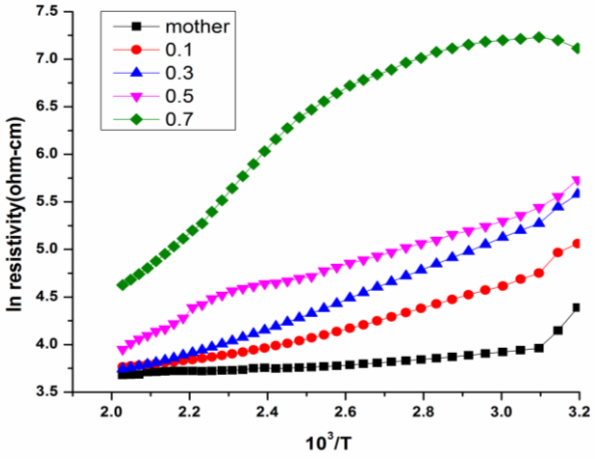

Figure 8: Plot of DC-electrical resistivity of $Mg_{1-x}Cu_xFe_{2-x}Cr_xO_4$ (x = 0.0 -0.7) versus temperature.

The saturation magnetization (M_s), coercivity (H_c), remanence (M_r) and remanent ratio ($R=M_r/M_s$) of sample with different Cu-Cr content is tabulated in Table 3. Cu-Cr substituted sample shows decrease in M_s, M_r and H_c values. The magnetic properties of soft ferrites are influenced by the composition and microstructure of the materials. Among these factors the microstructure has great effect on the magnetic properties. Mainly saturation magnetization depends on grain size, that means the material having smaller the grain size expected to have the highest saturation magnetization [26]. With the increase in Cu-Cr concentration the grain size increased, hence the saturation magnetization values decreased. The other reason trend for decreasing in M_s value also explained due to the fact that the Fe^{3+} (i.e., magnetic moment 5.92 μB) are replaced by lesser magnetic Cr^{3+} ions (i.e., magnetic moment 3.87 μB) in the octahedral (B) sites of the ferrite sub lattice. The same result has shown by the substitution of Cr ion in host material $MgFe_2O_4$ synthesized by Citrate-Gel auto combustion method [27]. A similar variation in H_c is shown by magnesium ferrite material with Cu-Cr co-substitution which is evidence that the coercivity of ferrites depends on the sintering temperature and the grain size [28, 29]. The value of coercivity (H_c) decreased from 146.33 to 38.201 G and this may be also due to a decrease in anisotropic field, which in turn decreases the domain wall energy [32].

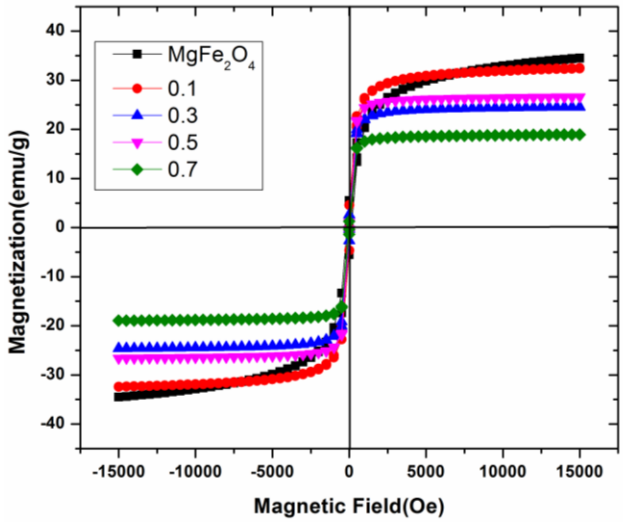

Figure 9: Hysteresis loops of $Mg_{1-x}Cu_xFe_{2-x}Cr_xO_4$ sample doped with x= 0.0 - 0.7

The remanent ratio $R=M_r/M_s$ shows the ease with which the direction of magnetization reorients to the nearest easy axis direction after the field is removed. Similar to H_c variation, R values are also showing a decreasing trend with an increase in grain size. So we conclude that the low value of R indicates the isotropic nature of the sample [30]. The magnetic recording media requires the saturation magnetization value as high as possible and moderate coercivity values [31]. So Cu-Cr substituted ferrite material is used for magnetic recording media.

Table 3: The saturation magnetization (M_s), coercivity (H_c), remanance (M_r) and remanant ratio ($R = M_r/M_s$) of $Mg_{1-x}Cu_xCr_xFe_{2-x}O_4$(x = 0.0-0.7).

Content	grain size(nm)	Ms (emg/g)	M_r (emg/g)	H_c(Oe)	$R=M_r/M_s$
0.0	251 nm to 414 nm	34.5214	5.522	146.33	0.1599
0.1	121.3 nm to 1.366 μm	32.44	4.629	92.447	0.142
0.3	344 nm to 1.524 μm	24.58	2.664	61.177	0.108
0.5	545.4 nm to 2.883 μm	26.58	1.129	24.941	0.042
0.7	183.2 nm to 3.070 μm	18.98	1.027	38.201	0.054

4. CONCLUSION

The $Mg_{1-x}Cu_xCr_xFe_{2-x}O_4$ (x = 0.0, 0.1, 0.3, 0.5 and 0.7) ferrite materials are successfully synthesized by solid-state reaction method. On the basis of observations and experiments, it is concluded that the substitution of Cu-Cr in the Magnesiumferrites produces appreciable changes in its structural, electrical and magnetic properties. XRD analysis revealed the prepared samples are cubic spinel with single phase in all concentration, this confirms that the dopant must have simply replaced the Mg^{2+} - Fe^{3+} ions without distortion of the cubic symmetry of the host magnesium ferrite. The DC resistivity increases continuously with increasing Cu-Cr concentration of 0.553×10^5 Ω-cm to 0.105×10^8 Ω-cm. Reason for increase resistivity in Cu-Cr doped samples, substitution of Cr^{3+} for Fe^{3+} results in the reduction of Fe ions at B-site, thus it decreases an electron hopping between the Fe^{2+} to Fe^{3+} ions and consequently increases the resistivity. The magnetic behavior of pure and doped magnesium ferrite particles show soft ferrimagnetic nature. With the increase in Cu-Cr concentration the grain size increased hence the saturation magnetization values decreased. In general $MgFe_2O_4$ doped with Cu-Cr content used for the magnetic recording area.

REFERENCES

[1]. Rabinder D. and K. Latha., (1999). Dielectric behaviour of mixed Mg-Zn ferrites at low frequencies, *Mat. Lett.*, 41:247-253.
[2]. Xu Q, Wei Y, Liu Y, Ji X, Yang L, Gu M., (2009). Preparation of Mg/Fe spinel ferrite nanoparticles from Mg/Fe-LDH microcrystallites under mild conditions, *Solid State Sci.* 11(2):472–478.
[3]. J. Judith Vijaya, G. Sekaran, M. Bououdina, (2015). Effect of Cu^{2+} doping on structural, morphological, optical and magnetic properties of $MnFe_2O_4$ particles/sheets/flakes-like nanostructures, *Ceram. Int.* 41:15–26.
[4]. L. B. Kong, Z. W. Li, G. Q. Lin, and Y. B. Gan, (2007). Magneto-Dielectric Properties of Mg–Cu–Co Ferrite Ceramics: II. Electrical, Dielectric, and Magnetic Properties, *J. Am. Ceram. Soc.*, 90: 2104-2112
[5]. Y. Konseoglu, H. Kavas, and B. Aktas, (2006). Surface effects on magnetic properties of superparamagnetic magnetite nanoparticles, *Phys. Status Solidi A.*, 203,1595-1601
[6]. S.D.Chhaya,M.P.Pandya,M.C. Chhantbar,K.B.Modi,G.J. Baldha, and H. H. Joshi, (2004). Study of substitution limit, structural, bulk magnetic and electrical properties of Ca^{2+} substituted magnesium ferrite, *Journal of Alloys and Compounds*, 377(1-2):155-161
[7]. Muhammad Javed Iqbal, Zahoor Ahmad, Turgut Meydan, and Yevgen Melikhov, (2012). Magnetization and Mossbauer studies of the Mg-Zn ferrite system, *Journal of Applied Physics*, 111:033906
[8]. M. M. Eltabey, A. M. Massoud, and Cosmin Radu, (2014). The magnetic properties of the Mg-Cd ferrite system by Mossbauer spectroscopy, *Journal of Nanomaterials*, 2014:7

[9]. R. A. Brand, H. Georges-Gibert, J. Hubsch, and J. A. Heller, (1985). Ferrimagnetic to spin glass transition in the mixed spinel $Mg_{1+t}Fe_{2-2t}Ti_tO_4$: a Mossbauer and DC susceptibility study, *Journal of Physics F: Metal Physics*,15(9):1987-2007

[10]. K. B. Modi, H. H. Joshi, and R. G. Kulkarni, (1996). Magnetic and electrical properties of A^{l3+}-substituted $MgFe_2O_4$,
Journal of Materials Science, 31(5):1311-1317

[11]. P. P. Hankare, V. T. Vader, N. M. Patil, S. D. Jadhav, U. B. Sankpal, M. R. Kadam, B. K. Chougule, and N. S. Gajbhiye, (2009). Synthesis, characterization and studies on magnetic and electrical properties of Mg ferrite with Cr substitution, *Mater. Chem. Phys*., 113:233

[12]. S. Jouanneau, J.R. Dahn, (2003). Preparation, Structure, and Thermal Stability of New $Ni_xCo_{1-2x}Mn_x(OH)_2(0 \leq x \leq {}^1/_2)$ Phases, *Chem. Mater.*, 15(2):495-499

[13]. Iqbal, M.J.; Ahmad, Z.; Melikhov, Y.; Nlebedim, (2012). Effect of CuCr co-substitution on magnetic properties of nanocrystalline magnesium ferrite, *J. Magn. Magn. Mater*., 324:1088-1094

[14]. N.M.Deraz and Omar H. Abd-Elkader, (2013). Investigation of Magnesium Ferrite Spinel Solid Solution with Iron-Rich Composition, *International J. Elecrochem.Sci.*, 8:9071-9081

[15]. B.D. Cullity (1978). "*Elements of X-ray diffraction*", Philippines, Addision Wesley Publishing Company, Inc., 2nd Edition. California.

[16]. Dodrill, B.C. (2004). *Low Moment Measurements with a Vibrating Sample Magnetometer*, LakeShore Cryotronics, Inc. 575 McCorkle Blvd. Westerville, Ohio.

[17]. Che, S.; Wang, J.; Chen, Q., (2003). Soft magnetic nanoparticles of $BaFe_{12}O_{19}$ fabricated under mild conditions *J. Phys.: Condens. Matter*., 15:335-339

[18]. A. Goldman (1990). "*Modern Ferrite Technology*", Van Nostrand Reinhold, New York.

[19]. R. D. Waldron, (1955). Infrared Spectroscopy of ferrites, *Phys. Rev*. 99:1727

[20]. H. M. Zaki, H. A. Dawoud, (2010). Far-infrared spectra for copper–zinc mixed ferrites, *Physica B*, 405:4476-4479

[21]. S. D. Chhaya, M. P. Pandya, M. C. Chhantbar, K. B. Modi, G. J. Baldha, and H. H. Joshi, (2004). Study of substitution limit, structural, bulk magnetic and electrical properties of Ca^{2+} substituted magnesium ferrite, *J. Alloys Compd*., 377:155-161

[22]. P. K. Roy and J. Bera, (2008). Characterization of nanocrystalline NiCuZn ferrite powders synthesized by sol–gel auto-combustion method, *J. Mater. Process. Technol*., 197:279

[23]. I. H.Gul, F. Amin; A. Z. Abbasi, M. A. Rehman, Maqsood, (2007). Physical and magnetic characterization of co-precipitated nanosize Co–Ni ferrites, *J. Scripta Materialia*, 56:497-300

[24]. M.El-Shabasy, (1997). DC electrical properties of Zn-Ni ferrites, *Journal of Magnetism and Magnetic materials*, 172:.188-192

[25]. M. U. Islam, M. Ashraf Chaudry, T. Abbas, M. Umar, (1997). Temperature dependent electrical resistivity of Co–Zn–Fe–O system, *Materials chemistry and Physics*, 48:227-229

[26]. X. Qi, J. Zhou, Z. Yue, Z. Gui, and L. Li, (2002). Effect of Mn substitution on the magnetic properties of MgCuZn ferrites, *Journal of Magnetism and Magnetic Materials*, 251:316–322

[27]. M. Raghasudha, D. Ravinder, and P. Veerasomaiah, (2013). Effect of Cr Substitution on Magnetic Properties of Mg Nanoferrites Synthesized by Citrate-Gel Auto Combustion Method, *Journal of Chemistry*, 2013:.6

[28]. A.Ghasemi, A. Morisako, (2008). Static and high frequency magnetic properties of Mn–Co–Zr substituted Ba-ferrite
J. Alloys Compd., 456:485-491

[29]. Ghasemi, A.; Hossienpour, A.; Morisako, A.; Saatchi, A; Salehi, M. (2006). Electromagnetic properties and microwave absorption characteristics of doped barium hexaferrite, *J. Magn. Magn. Mater*., 302(2006):429-435

[30]. Shirsath S E, Toksha B G and Jadhav K M , (2009). Structural and magnetic properties of In^{3+} substituted $NiFe_2O_4$ *Mater. Chem. Phys*. 117(2009):163

[31]. Yadong Li, Renmao Liu, Zude Zhang, Caoshui Xiong, (2000). Synthesis and characterization of nanocrystalline $BaFe_{9.6}Co_{0.8}Ti_{0.8}M_{0.8}O_{19}$ particles, *Mater. Chem. Phys*., 64:256-259

[32]. P.N. Anantharamaiah, P.A. Joy, (2017). Tuning of the magnetostrictive properties of cobalt ferrite by forced distribution of substituted divalent metal ions at different crystallographic sites, *J. Appl. Phys*. 121:093904

Development of Recycled Reactive Powder Concrete through Partial Replacement of Cement by Teff Straw Ash and Waste Brick Powder

Belachew Asteray Demiss[1,*], Walter Odhiambo Oyawa[2], Stanley Muse Shitote[3]

[1]*Civil Engineering Department, Addis Ababa Science and Technology University; P.O. Box 16417, Addis Ababa, Ethiopia*
[2]*Civil Engineering Department, Jomo Kenyatta University of Agriculture and Technology, Nairobi, Kenya*
[3]*Civil and Structural Engineering Department, Moi University, Eldoret, Kenya a*
**Corresponding author, e-mail: belachew.asteray@aastu.edu.et*

ABSTRACT

The rapid rise in concrete raw material usage has led to serious environmental effects. Moreover, to meet the global infrastructure developments, the production of cement involves high energy consumption and consumes a significant amount of non-renewable raw materials which leads to continuous degradation of natural resources which in turn makes the cement industry unfit in the contemporary picture of a sustainable industry. The objective of this study was to develop recycled reactive powder concrete (RRPC) through partial replacement of cement by teff straw ash and waste brick powder. In this study, recycled reactive powder concrete were developed from cement, waste ceramic powder, fine sand, superplasticizer, water, steel fiber, waste glass powder, teff straw ash and waste brick powder. Silica fume was fully replaced by waste glass powder. In addition to this, cement was replaced partially by teff straw ash versus waste brick powder by 5%, 15% and 25% by weight. Within each partial replacement percentages, 25% teff straw ash and 75% waste brick powder were utilized. The performances of RRPC mixes were appraised in terms of its mechanical strength properties (compressive, split tensile and flexural strengths) and microstructure investigation using XRD analysis. The experimental results indicated that development of RRPC through partial replacement of cement by teff straw ash and waste brick powder at standard curing was a viable approach to solve raw material shortage for the current generation structural concrete. Through partial replacement of cement, 54.32 MPa maximum mean compressive strength, 4.8 MPa tensile splitting strength and 6.7 MPa flexural strength were observed using 5% replacements of cement by teff straw ash and brick powder combinations after 28 days standard curing. Furthermore, maximum mineralogical compositions (% mass) for Quartz, Microcline, Albite and Portlandite, which are good indicators for improved quality, were observed from the XRD analysis. By far, reutilizing waste ceramic, teff straw and waste glass will help for an ecofriendly construction and to reduce consumption of raw materials from biomass.

Keywords: *Recycled Reactive Powder Concrete, Recycling, Waste Ceramic Powder, Teff Straw Ash, Ecofriendly Construction*

1. INTRODUCTION

In the current construction-related research, the potential use of recycled materials in concrete is a growing interest (Jang et al., 2015). Moreover, to meet the global infrastructure developments, the production of cement involves high energy consumption and consumes a significant amount of non-renewable raw materials which leads to continuous degradation of natural resources which in turn makes the cement industry unfit in the contemporary picture of a sustainable industry.

Today, the cement industry is responsible for emitting between 6% and 7% of all the CO_2 emission into the atmosphere. Therefore, it is essential to seek alternative binders to provide environmentally friendly materials (Shojaei, Behfarnia, & Mohebi, 2014).

Much more energy is required for the production of cement which is not cost-effective. According to Ivanov, Chu, & Stabnikov (2015), temperature above 950^{o}c is required for conversion of limestone to cement clinker which represents 20–40 % of energy from the total cost of cement production (Ivanov, Chu, & Stabnikov, 2015). However, for the conservation of natural resources, energy saving and environmental approachability, the use of substitute materials from waste products has become the main focus of researchers in engineering (Ling & Teo, 2013).

According to Ghosh et al. (2015), as cement industry is one of the most polluting industry, cement can be replaced fully or partially by waste materials (Ghosh et al., 2015) to reduce the pollution and cost of concrete. As per Imbabi et al. (2013), the cement industry faces a number of challenges since every tonne of Ordinary Portland Cement produced releases on average a similar amount of CO_2 into the atmosphere, or in total roughly 6% of all man-made carbon emissions. Improved production methods and formulations that reduce or eliminate CO_2 emissions from the cement manufacturing process are thus high on the agenda. In this regard, locally available minerals, recycled materials, and industry, agriculture and domestic waste may be suitable for blending with OPC as a substitute, or in some cases replacement, binders (Imbabi, Carrigan, & Mckenna, 2013). It also indicated that the growing concern for the environment all over the world, as well as the high cost of Portland cement, has placed a limitation on its use as the sole binding material in concrete (Arum, Ikumapayi, & Aralepo, 2013). As a solution, supplementary cementitious materials (SCMs) have been proposed by many scholars to partially replace Portland cement in concrete as a value-added approach to address the environmental concerns, for reduction of solid waste disposal and landfills (Du & Tan, 2017).

One possible alternative is the application of concrete from finely dispersed local waste raw materials such as recycled reactive powder concrete. Reactive powder concretes were developed by careful control of aggregates and additives. RPC compositions vary, but commonly consist of siliceous sand, Portland cement, pozzolanic additives such as silica fume, and other fine particulates such as ground quartz powder (Dham et al., 2010) to gain superior mechanical and physical properties, exhibiting excellent ductility and durability characteristics (Ipek et al., 2011), super-high-strength, extreme durability and superior toughness (Yanzhoua et al., 2015).

Helmi et al. (2016) also developed RPC that comprises cement with quartz sand, superplasticizer, silica fume, and water which is processed by heat curing and/or pressure. The processing of an RPC mixture by static pressure treatment (during setting), followed by heat curing (during hardening), resulted in a multiscale transformation with respect to microstructural composition and pore geometry (Helmi et al., 2016).

According to Yazici et al. (2008), cement dosage of Reactive Powder Concrete is generally over 800–1000 kg/m^3 that affects the production costs, but also has negative effects on the heat of hydration and may cause shrinkage problems. Replacing cement with mineral admixtures may positively affect the durability of concrete and a feasible solution (Yazici et al., 2008).

Following these, sustainable construction has received much attention throughout the world over the last few years (Yeheyis et al., 2013). In concrete production, sustainability can be achieved by innovations in substitutions of material used. Cement-based materials are the most abundant materials in the world. Due to the high demand of natural resources, engineers and architects have growing interests in sustainable development by choosing sustainable material for eco-friendly construction and to save the environment by utilizing waste products generated by industries (Anwar et al., 2015). Hence, the use of locally available materials, as well as the use of industrial and agricultural waste in the building industry, has become a potential solution to the economic and environmental problems of developing countries in particular (Le, Nguyen, & Ludwig, 2014).

Therefore, to fulfil the above gaps, recycled reactive powder concrete were developed through partial replacement of cement by teff straw ash and waste brick powder as a proper construction material in the emerging concrete technology for future Civil Engineering applications.

2. MATERIALS AND METHODS

In this study, Portland cement, fine sand, silica fume, finely dispersed waste ceramic tile powder, finely dispersed waste glass powder, teff straw ash, waste brick powders, steel fibers, superplasticiser and water available around Nairobi area were used for the development of RRPC mix and for the entire tests. The physical and chemical properties of the raw materials in this study were identified and described in each section.

2.1. Materials

The raw materials used in this study were described as follows.

Portland cement: The cement used in this study were Portland cement Type I PowerPLUS 42.5 N Portland cement from Bamburi Cement Limited in Nairobi fulfilling the criteria for the European Norm Standard EN 197. The properties of cement used in this study were shown in Table 1. The chemical compositions of cement in this study were also presented in Table 2.

Table 1: properties of cement used in this study

Parameters	Specific Surface (cm^2/g)	Water Demand (%)	Setting Time (Minutes)		Soundness (mm)	Compressive Strength (Mortar Prism) (N/mm^2)	
			Initial	Final		At 2 days	At 28 days
Results	3197	25.65	160	252	0.3	19.3	48.94

Table 2: The chemical compositions of Portland cement in this study

Material	Silica (SiO_2)	Alumina (Al_2O_3)	Calcium Oxide (CaO)	Magnesium Oxide (Mgo)	Sodium Oxide (Na_2O)	Potassium Oxide (K_2O)	Titanium Dioxide (TiO_2)	Manganese Oxide (MnO)	Iron Oxide (Fe_2O_3)	LOI
Cement	18	4.7	60	0.6	0.4	0.51	0.53	0.01	4	2.63

Silica Fume: In order to develop the control mix for this study, MasterRoc MS 610 type densified Silica fume was used from BASF East Africa LTD in Nairobi. Table 3 also shows the chemical compositions of silica fume in this study.

Table 3: The chemical compositions of Silica fume in this study

Material	Silica (SiO_2)	Alumina (Al_2O_3)	Calcium Oxide (CaO)	Magnesium Oxide (Mgo)	Sodium Oxide (Na_2O)	Potassium Oxide (K_2O)	Titanium Dioxide (TiO_2)	Manganese Oxide (MnO)	Iron Oxide (Fe_2O_3)	LOI
Silica fume	96.18	0.106	0.372	1.465	0	0.629	0	0.202	0.463	2.1

Fine Sand: Locally available natural sand as fine aggregate from Meru, Kenya, were used in the preparation of all test specimens. Fine aggregates were sieved using 600µm standard sieve size and were used in the dry condition. Moreover, particle size distribution of fine sand was determined based on British Standard (BS812-103.1, 1995). The grading of fine sand used for the entire mixtures is shown in Table 4. The physical properties of fine sand in this study were also shown in Table 5.

Table 4: Grading of Fine Sand for this study.

Sieve No	Cumulative % Retained	% Passing
4.75 mm	0.00	100.00
2.4 mm	0.00	100.00
1.2 mm	0.00	100.00
600 um	0.00	100.00
300 um	14.17	85.83
150 um	91.13	8.87
75 um	99.37	0.63

Table 5: Physical properties of Fine Sand in this study.

Parameters	Result
Specific Gravity	2.42
Loose Density (Kg/m^3)	1438.25
Bulk Density (Kg/m^3)	1612.75
Fineness Modulus	3.0

Steel Fibres: For this study, locally available waved wire steel fibres of 50 mm length with 0.22 mm thickness from Steel Wall Africa in Nairobi were used for development of RRPC. By using steel fibres in concrete, greater

flexural strength was observed instead of direct tension and compression (ACI Committee 544, 1988). The reinforcing effect of steel fibres is especially critical to the mechanical properties of RPC under tension (Chan & Chu, 2004).

Admixtures: Commercially available superplasticiser supplied by SIKA® Company Kenya Limited in Nairobi under the commercial name Sika Viscocrete-10 were used in this study to attain workability.

Water: The ordinary drinking water was also used for the preparation of the desired concrete mix following British Standard (BS EN 1008, 2002).

Teff Straw Ash: In this study, teff straw ash was one of the raw materials prepared for this study to replace cement partially combined with brick powder.

Teff (Eragrostis tef) is the smallest cereal grain in the world that has been cultivated and used for human consumption in Ethiopia for centuries. It is composed of complex carbohydrates, protein content, well-balanced amino acid composition and good concentrations of lysine. Teff is a comparatively good source of essential fibre, fatty acids, phytochemicals, and minerals especially calcium and iron (Baye, 2014). Teff is grown in almost all regions of Ethiopia since it is the preferred grain for local consumption (Kebede, 2009). Ethiopia is the only country in the world that uses teff as a cereal crop to prepare the best kind of "Ingera" from teff flour (Mengesha, 1965). Teff is a reliable and low-risk cereal that grows on a wider ecology under moisture stress and waterlogged areas with few plant diseases and grain storage pest problems. Processing of teff for different foods is usually done by traditional ways (Gebremariam, Zarnkow, & Becker, 2012) on which this process produces teff straw. Nationally, teff ranks first in total cropland and quantity of production among other cereals. In 2003-2004, it occupied about 2 million hectare (ha) which accounts for 28.5% of the total cereal crops grown in Ethiopia (Kebede, 2009).

In support, Seyfu (1997) quotes the Ethiopian Central Statics Agency report (CSA 1995) and explains that teff is cultivated in about one million hectares of land each year. During the 1994/95 cropping season, teff occupied 32% of the cultivated land under cereals, while maize occupied 19%, sorghum 16%, barly 15%, wheat 13%, millet 4% and oats 1% (Seyfu, 1997). Crymes (2015) has also observed that the domestic demand for teff is increasing with an increase in the population. Even worldwide, given the increasing global popularity of teff, the international demand for this grain has also increased (Crymes, 2015).

The above information shows that as teff is produced in larger quantities, there will be a large amount of straw with potential for recycling in concrete. Figure 1 shows the teff plant and its straw.

Figure 1: Teff Plant (left) and its Straw (right)

In Ethiopia, teff straw is one of the major field crop residues that have great potential to serve as animal feed (Habte, 1998). Traditionally, teff straw is used as a fibre to make the mud mortar when Ethiopian people construct local housing. The presence of iron, manganese, calcium and zinc in teff straw with high quantity were given a chance to use the straw for concrete production through the preparation of teff straw ash (TSA).

For this study, teff straw samples were collected from Ethiopian farms and ashes were prepared by burning the straw in the field. After burning the straw, it was left for 72 hours by covering thin metallic sheets on the top till

getting cold. Then, the ashes were collected and sieved with a 300µm standard sieve. Figure 2 shows the preparation of teff straw ash for this study.

Waste Glass Powder: Glass is an amorphous solid that has been found in a wide variety of forms, from plain clear glass to tempered and tinted varieties and used in many applications. However, after its usage, it is generally dumped in landfills as a non-biodegradable material that does not provide a friendly environment (Dubey & Dhakre, 2016). It comprises several chemical varieties including binary alkali-silicate glass, borosilicate glass, and ternary soda-lime silicate glass (Shayan & Xu, 2006). It is also indicated that million tons of waste glass have been produced every year in the world due to the improvement of living standards, the rapid population growth, industrialization and urbanization. Therefore, it has become a critical problem around the world to utilize the waste glass. Hence, development of new technologies were one of the necessary requirements for utilization of waste glass (Khan & Khan, 2017).

Figure 2: Preparation of teff straw ash in Ethiopia.

Waste Ceramic Powder: Ceramic waste is one of the non-biodegradable wastes where its recycling is a big problem. One of the natural ways of reusing inorganic industrial wastes is their use in the production of building materials, especially as raw materials in the concrete manufacture for positive impact on the environment (Halicka, Ogrodnik, & Zegardlo, 2013). In the ceramic industry, nearly 15%-30% waste material is generated from the full production in which the industries are dumping the wastes in any nearby pit or vacant spaces which contributes to severe environmental pollution (Anwar et al., 2015). In concrete production, the ceramic waste can be used to alter concrete properties, reduce raw material cost and waste disposal. As a cement replacement ingredient, 20-30% fine ceramic waste can be replaced without compromising strength (Aditya & Lakshmayya, 2016). It is also indicated that concrete with ceramic waste powder has minor strength loss that is dependent on the pozzolanic reactivity of the different ceramic wastes (Pacheco-Torgal & Jalali, 2011).

Waste Clay Brick Powder: Waste clay brick is silicate solid waste that accounts for 50%-70% of the construction waste produced by urban redevelopment, and 30%-50% by building operations. With the speeding up of urban construction and improvement, a large amount of waste clay brick from the demolition of old buildings has been produced. Hence, its recycling has great environmental and social significance (Cheng, 2016). In the past, the brick bodies of used brick products or rejects usually crushed to a grain size of about 1 mm and were utilized as a pozzolan. Currently, brick dust is a by-product of the production of calibrated brick components that are treated by grinding to achieve precise dimensions for mortar-free walling. This very fine dust is used as a filler material in the raw mix at some brick- kilns (Navrátilová & Rovnaníková, 2016). It is also suggested that cement technology should assess for utilization of brick powder in cement-based materials such as mortar and concrete. Additional investigations may be necessary to improve activation of brick powder at high blending level for cement at early ages (Kirgiz, 2015).

2.2. Methods

2.2.1. Methods for Preparation of Finely Dispersed Local Waste Brick, Ceramic and Glass Powders

Waste brick, waste ceramic and waste glass were collected from construction sites and crushed both by manpower and using a crushing machine at Jomo Kenyatta University of Agriculture and Technology Engineering

Workshops. Initially, the collected wastes were crushed with a sludge hammer using manpower. Then, the crushed products were taken to the crushing machine to make them very fine and to produce pozzolanic powders. After getting finely grained powder products, the products were sieved through manpower using a 150µm standard sieve to get finely dispersed glass powder and 300µm standard sieve to get finely dispersed ceramic powder and brick powder. Preparation of finely dispersed local waste powders including waste glass, waste ceramic and waste brick were shown in Figure 3.

Figure 3: Preparation of Waste glass, waste ceramic, waste brick.

2.2.2. Physical and Chemical Properties

In this study, physical properties such as specific gravity, loose density, bulk density, colour and particle size distribution (for sand, silt and clay content) were investigated based on British Standards. The particle size distribution of raw materials by laser diffraction (LA950) for sand, silt and clay content were analyzed in World Agroforestry Centre (ICRAF), Nairobi.

Moreover, X-ray fluorescence (XRF) spectrometry analysis was also conducted in Kenya Ministry of Mining to characterize the chemical composition of raw materials. After XRF analysis, the results of the chemical analysis for local waste materials used in this study were compared with the minimum requirement for a standard pozzolana quality as per ASTM C618. The overall chemical composition of a pozzolan is considered as one of the parameters governing long-term performance (e.g. compressive strength) of the blended cement binder, ASTM C618 prescribes that a pozzolan should contain SiO_2 + Al_2O_3 + Fe_2O_3> 70 wt.%.

2.2.3. Proposed Mix Design for Recycled Reactive Powder Concrete, Specimen Preparation and Curing

For this study, RRPC was developed based on the existing mix proportions of RPC (Ahmad, Zubair, & Maslehuddin, 2015; Bayard & Plé, 2003; Kushartomo, Bali, & Sulaiman, 2015; Richard & Cheyrezy, 1995) through preliminary tests by replacing cement partially by local waste materials. Since the mix design was employed using these local waste materials together with other core raw materials, the name "Recycled Reactive Powder Concrete" was given for the concrete mixture.

In this study, partial replacement of Cement was designed using two mix series to replace cement by 5%, 15% and 25% by weight. In the first mix series, cement was replaced partially by teff straw ash versus waste brick powder. Within each partial replacement percentage (5%, 15% and 25%), 25% teff straw ash and 75% waste brick powder were utilized. For all mixes, hand mixing, standard water curing and the uniform water-binder ratio of 0.25 were used.

The control mix was developed from finely dispersed waste glass powder, Portland cement, finely dispersed waste ceramic powder, superplasticizer, fine sand, water and steel fibre. As shown in Table 6, four mixes were utilized including the control mix.

For this study, the mix propositions designed in Table 6 were applied for the research program. Then, by preparing watertight and non-absorbent 100X100X100 mm3 cube, 100x200 mm3 cylinder and 150x150x550mm3 prism moulds, RRPC specimens were prepared based on British Standard, the methods for making and curing test specimens for strength tests (BS 5328: Part 1, 1997; BS EN 12390-1, 2000; BS EN 12390-2, 2000).

Table 6: Mix Design for 1 m^3 RRPC

	Ingridients	Mix No and Content (kg/m^3)			
		Control	Mix 1	Mix 2	Mix 3
1	Cement	842	799.9	715.7	631.5
2	Waste Ceramic Powder	168	168	168	168
3	Fine Sand	926	926	926	926
4	Super plasticizer	56	56	56	56
5	Water	306	306	306	306
6	Steel Fiber	116	116	116	116
7	waste glass powder	210	210	210	210
8	Teff Straw ash		10.53	31.58	52.63
9	waste Brick Powder		31.58	94.73	157.88

In order to prepare specimens, dry mixing of ingredients was done for 3 minutes. After that, wet mixing was done by adding 80% of the water and all of the superplasticiser into the mixed dry materials and was mixed for another 7 minutes. Then, the remaining water was added and mixing was done again until a visually suitable mix was obtained. Hand mixing was employed throughout the entire specimen preparations.

After getting a uniform mix and placing layer by layer on moulds, compaction was employed in two layers by steel compacting rod of circular cross-section having 16 mm diameter and length 600 mm with rounded ends. Once levelling of the surface was made with steel floats, the specimens were left in the moulds for one day till getting dry. After removal of specimens from the mould, the specimens were marked without damaging them. Then, standard curing of the test specimens was done till testing days for 7, 14 and 28 days in water at a temperature of 20°C ± 2°C instead of steam curing at a high temperature in conventional RPC.

2.2.4. Mechanical Properties

For testing, before placing the test specimens centrally in the testing machine, any excess moisture from the surface of the specimen was wiped. Then, three specimens were tested for the mechanical properties of RRPC (compressive, tensile splitting and flexural strength) as per the British Standard testing procedure for hardened concrete (BS EN 12390-3, 2002; BS EN 12390-4, 2000; BS En 12390-5, 2000; BS EN 12390-6, 2000) in Jomo Kenyatta University of Agriculture and Technology Structural Engineering laboratory.

Figure 4: The experimental setup for testing Mechanical Properties

2.2.5. Microstructural Analysis

Beyond the mechanical performance, microstructural studies of the developed recycled reactive powder concrete at different percentages were the other main objective of this study. For this purpose, samples were taken from each variable that was prepared at different percentages by mass to replace cement partially including the controls and taken for mineralogical characterization/analysis after 28 days standard curing.

To observe the microstructure which enables the spatial distribution of ingredients and particles, this study used Bruker's X-ray Diffraction D2 Phaser in World Agroforestry Center (ICRAF), Nairobi for detailed analysis of minerals within the RRPC powder specimen. The samples for XRD analysis were collected from each test variables made from different percentages and were then processed using the procedures described in Figure 5.

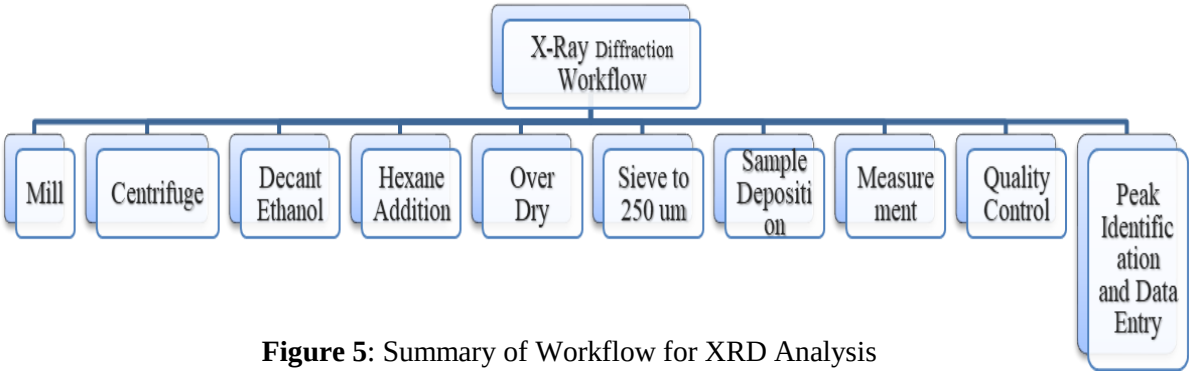

Figure 5: Summary of Workflow for XRD Analysis

3. RESULTS, ANALYSIS AND DISCUSSION

3.1. Physical and Chemical Properties

The physical properties of finely dispersed local wastes such as specific gravity, loose density, bulk density, colour and particle size distribution (for sand, silt and clay content) were investigated in this study. Additionally, the overall chemical composition of selected finely dispersed local wastes for this study was determined. Table 7 describes the physical properties and chemical compositions of local waste raw materials in this study.

Table 7: Physical properties and Chemical Compositions of local waste raw materials in this study

Parameters	Finely Dispersed Glass Powder	Teff Straw Ash	Finely Dispersed Ceramic Powder	Brick Powder
Silica (SiO2)	80	90	66	67
Alumina (Al2O3)	0.7	1	16.6	15.2
Calcium Oxide (CaO)	9.4	0.61	2.5	0.74
Magnesium Oxide (Mgo)	0.9	0.3	0.53	0.31
Sodium Oxide (Na2O)	6	0.23	3.36	1.71
Potassium Oxide (K2O)	0.22	0.73	1	3
Titanium Dioxide (TiO2)	0.1	0.76	0.72	1.1
Manganese Oxide (MnO)	0.01	0.15	0.01	0.5
Iron Oxide (Fe2O3)	0.27	0.6	6.7	7.73
Loss of Ignition	1.1	1	1	0.7
Specific Gravity	2.61	1.14	2.3	2.11
Loose Density (kg/m^3)	959.75		1263.75	1007.25
Bulk Density (kg/m^3)	1229.25		1507.75	1196.50
Colour	White	Black	reddish white	Red

The laser analysis results of local waste raw materials in this study are illustrated in Figure 6. The major composition in each local waste is sand content followed by silt and clay.

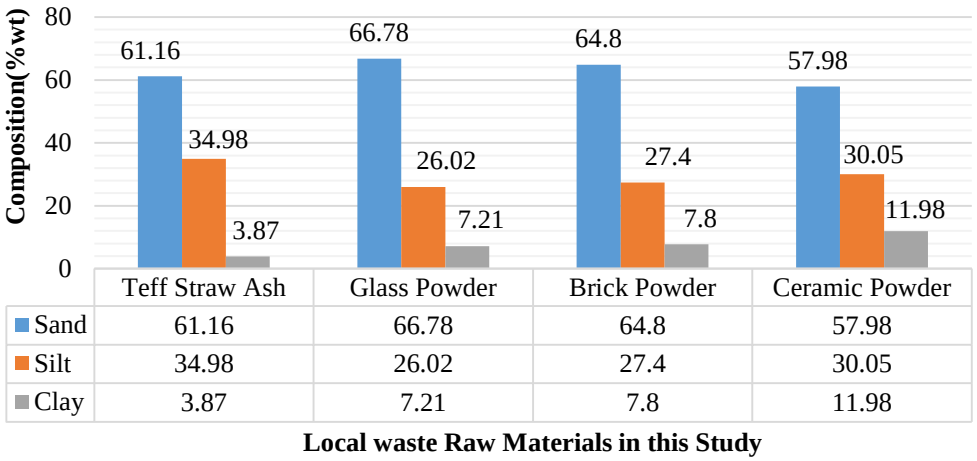

	Teff Straw Ash	Glass Powder	Brick Powder	Ceramic Powder
Sand	61.16	66.78	64.8	57.98
Silt	34.98	26.02	27.4	30.05
Clay	3.87	7.21	7.8	11.98

Local waste Raw Materials in this Study

Figure 6: Particle size distribution by laser diffraction for local wastes in this study

Figure 7 shows the chemical compositions of silica, alumina and iron oxide content for selected local wastes in this study after XRF analysis

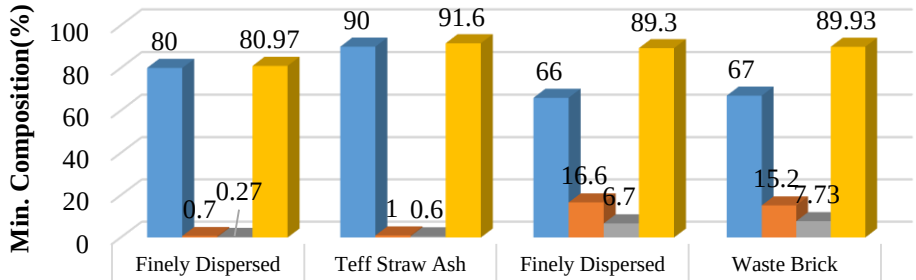

	Finely Dispersed Glass Powder	Teff Straw Ash	Finely Dispersed Ceramic Powder	Waste Brick Powder
Silica	80	90	66	67
Alumina	0.7	1	16.6	15.2
Iron Oxide	0.27	0.6	6.7	7.73
Min. req	80.97	91.6	89.3	89.93

Local Waste raw materials

Figure 7: Minimum requirement for the Pozzolanic property of waste raw materials in this study

As evaluation criteria, the sums of the three mineral components (silica, alumina and iron oxide content) in each local waste were compared with the requirement of ASTM C618 as a pozzolan.

In view of that, finely dispersed glass powder contains 80.97%; teff straw ash 91.6%, finely dispersed ceramic powder 89.3 % and waste brick powder 89.93% by weight. Hence, the chemical compositions for the proposed local waste raw materials were greater than 70 (by weight %). Accordingly, as per the minimum requirement for a pozzolan, the proposed local waste raw materials will be nice pozzolanic additives which can play a micro-filler role within the concrete matrix. Hence, the local waste materials used in this study revealed good pozzolanic property that can greatly affect the long-term performance of recycled reactive powder concrete product.

3.2. Properties of Fresh Recycled Reactive Powder Concrete

Figure 8 (a and b) shows the fresh property of recycled reactive powder concrete. Due to the minimum amount of water-to-powder ratio, the fresh mixtures were prepared with zero slumps.

However, when it was compacted with tamping rod within the moulds during casting, the hardened RRPC mixture releases water and becomes plastic. Then, the specimens were dried after one day.

Figure 8: Property of fresh RRPC by slump test

3.3. Mechanical Properties of RRPC

The main task in this study was development of RRPC by partial replacement of cement by local wastes containing teff straw ash (TSA) and brick powder (BP) at 5%, 15% and 25% replacement.

Table 8 shows the density of RRPC cubes containing TSA and BP at testing ages. Based on the results, cubes with 5% replacement were observed better densities but less than the control.

Table 8: Density of RRPC Cubes containing TSA and BP at testing ages

Percentage	Density (g/cm3)		
	7 Days	14 Days	28 Days
5 % Replacement	2366.33	2377.33	2380.00
15 % Replacement	2279.67	2318.00	2345.67
25 % Replacement	2310.67	2336.00	2346.67
Control	2388.00	2418.67	2507.00

Moreover, the mechanical properties of RRPC containing TSA and BP were evaluated as follows.

Figure 9 shows the compressive strength of RRPC containing TSA and BP at different standard curing ages. In this regard, a maximum compressive strength of 54.32 MPa was observed after 28 days standard curing using 5% replacement of cement in series 1. However, this strength was 1.8% less than the control mix. On 15% replacement at series 2, the compressive strength was reduced by 24% compared to the first series. Additionally, on 25% replacement at series 3, 26.5% strength was reduced compared to the first series. Hence, the compressive strength was reduced as the replacement percentage increases.

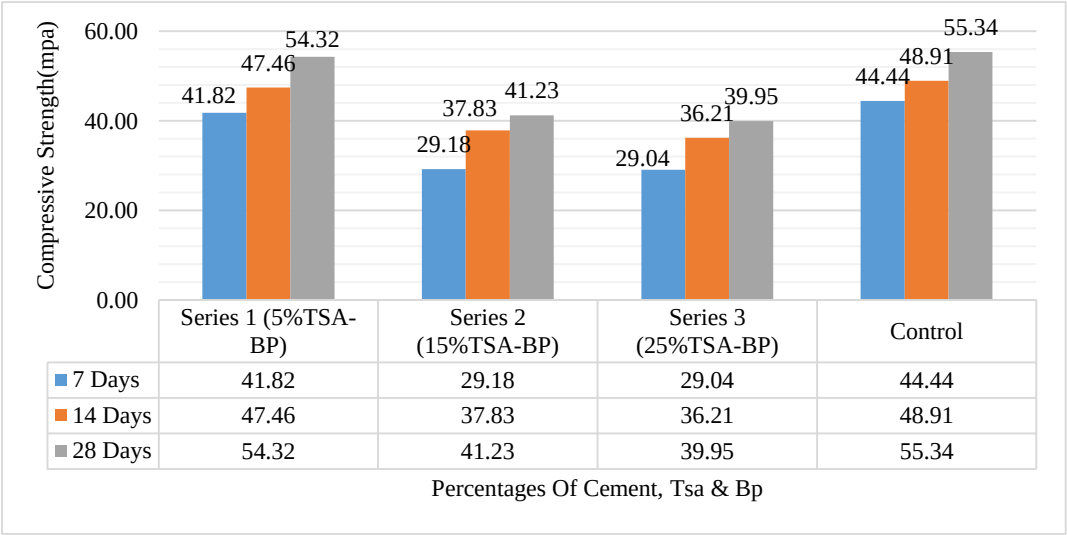

Figure 9: Compressive Strength of RRPC containing TSA and BP at different standard curing ages

Moreover, the tensile splitting Strength of RRPC containing TSA and BP at different standard curing ages was described in Figure 10

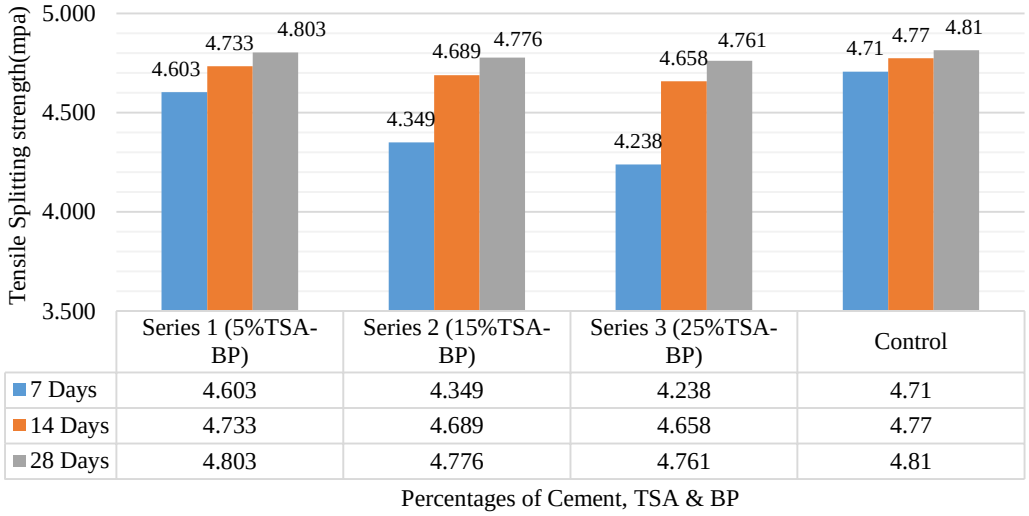

Figure 10: Tensile Splitting Strength of RRPC containing TSA and BP at different standard curing ages

A maximum tensile splitting strength of 4.8 MPa was observed at 28 days standard curing using 5% replacement in series 1. Compared to the control, it was less by 0.2%.

Additionally, Figure 11 shows the flexural strength of RRPC beams containing TSA and BP at 28 days standard curing ages.

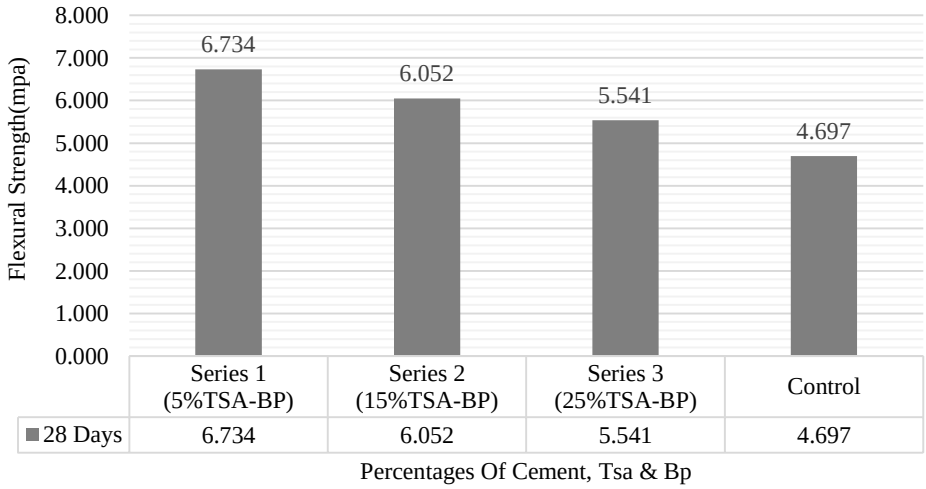

Figure 11: Flexural Strength of RRPC containing TSA and BP at 28 days standard curing ages

Accordingly, 6.7 MPa flexural strength was observed as a maximum strength using 5% replacement. Compared to the control, this value is 30.3% greater in strength.

3.4. Microstructural Analysis of Recycled Reactive Powder Concrete Structure Containing Teff Straw Ash and Waste Brick Powder

The mineralogical compositions of RRPC containing TSA and BP (mass %) were studied as it is stated in Table 9 and the XRD pattern diagrams as shown in Figure 12 to 15.

Table 9: Mineralogical Compositions of RRPC containing Teff Straw Ash and Waste Brick Powder (mass %)

Mineral	5TSA-BP	15TSA-BP	25TSA-BP	Control
Albite, $NaAlSi_3O_8$	21.4	26.4	31	29.2
Calcite, $CaCO_3$	8.3	8.2	7.8	5.5
Diopside, $CaMgSi_2O_6$	5.2	4.6	5.2	4.1
Halloysite, $Al_2Si_2O_5(OH)_4$	1.5	1.7	1.4	0
Hatrurite, Ca_3SiO_5	3.8	3.6	3.6	5.2
Margarite, $CaAl_2(Al_2Si_2)O_{10}(OH)_2$	0	0	0	2.5
Microcline, $KAlSi_3O_8$	15	14.9	12.1	15
Nacrite, $Al_2Si_2O_5(OH)_4$	1.1	1.4	0	1.4
Portlandite, $Ca(OH)_2$	10.7	8.9	6.9	10.7
Quartz, SiO_2	27.9	25.6	25.4	26.9

From Table 9, Quartz, Microcline and Albite were observed as a maximum composition in RRPC containing TSA and BP followed by Portlandite, Calcite and Diopside.

Accordingly, 27.9 maximum mineralogical compositions by mass (%) of Quartz content were observed using 5% TSA-BP mix combinations. Compared to the control, this value is greater than by 3.6%. For Microcline, 15 was observed using 5% a TSA-BP mix combination which has equal mass (%) with the control Microcline composition. Moreover, for Albite, 31 compositions by mass (%) were observed using 25% TSA-BP mix which has 1.8 more mass (%) compared to the control.

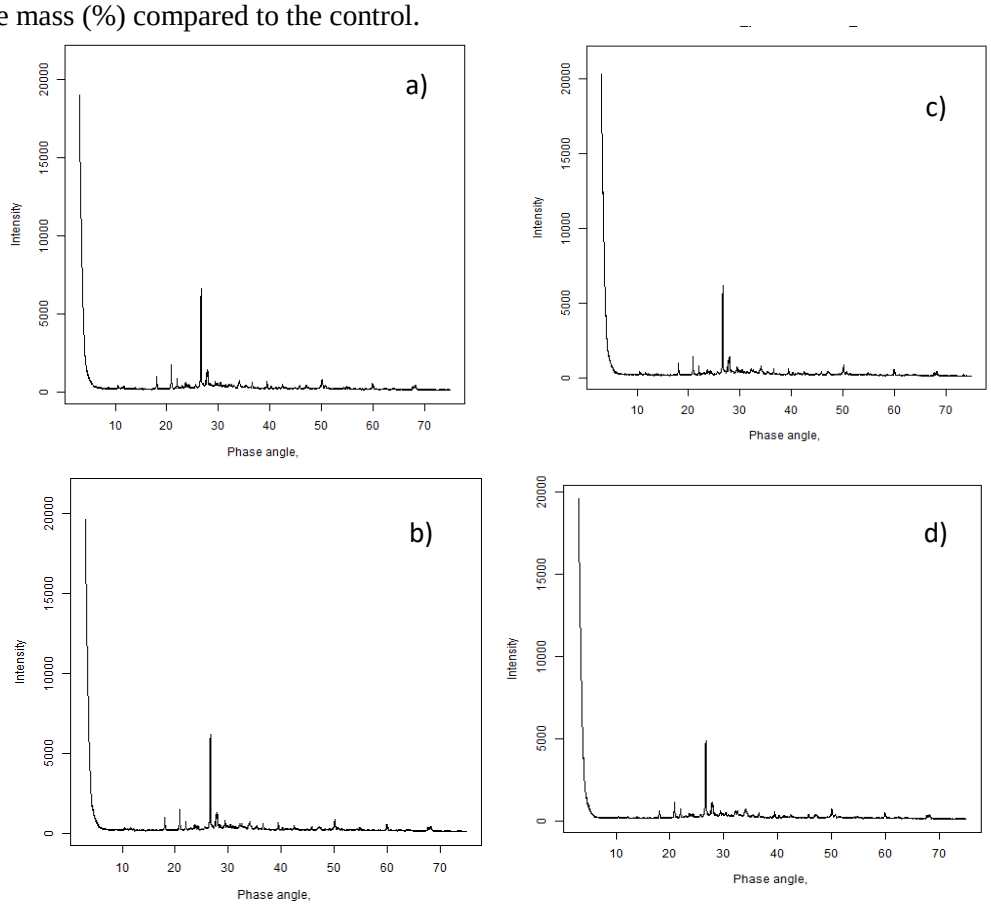

Figure 13: XRD pattern of RRPC Mix containing (a) 5% TSA-BP, (b) 15%TSA-BP, (c) 25%TSA-BP and (d) control

4. CONCLUSIONS

From this study, the following conclusions can be drawn:

- The local waste materials used in this study revealed extensive pozzolanic property in relation ASTM requirements that may be utilized to enhance the long-term performance of RRPC product. In this regard, finely dispersed glass powder contains 80.97%; teff straw ash 91.6%, finely dispersed ceramic powder 89.3 % and waste brick powder 89.93% by weight. The chemical compositions for the proposed local waste raw materials were greater than 70 (by weight %). Hence, they fulfill the requirement of ASTM C618 as a pozzolan.
- In all mix proportion series, higher early mechanical strengths were observed which increased with curing age.
- For partial replacement of cement by teff straw ash (TSA) and brick powder (BP) combinations, 54.32 MPa maximum mean compressive strength; 4.8 MPa tensile splitting strength and 6.7 MPa maximum flexural strength were observed using 5% replacements after 28 days standard curing.
- For partial replacement of cement by local wastes, Quartz, Microcline and Albite were observed as a maximum composition in RRPC containing TSA and BP followed by Portlandite, Calcite and Diopside. 27.9 maximum mineralogical compositions by mass (%) of Quartz content were observed using 5% TSA-BP mix combinations. For Microcline, 15 was observed using 5% a TSA-BP mix combination which has equal mass (%) with the control Microcline composition. Moreover, for Albite, 31 compositions by mass (%) were observed using 25% TSA-BP mix. The presence of Albite, Quartz, Portlandite and Microcline within the RRPC composition were an indicator of bind ability, hardness, the degree of hydration and filling ability of the minerals within the concrete matrix.

This study recommends that the rapid recycling of local waste materials that have pozzolanic nature can produce an eco-friendly structural concrete that can help for the current generation concrete. By far, recycling local waste materials will help to save our environment by avoiding utilization of biomass raw materials for construction and to reduce associated costs of waste disposal.

REFERENCES

ACI Committee 544. (1988). Design Considerations for Steel Fiber Reinforced Concrete: Manual of Concrete Practice (Vol. 88). Retrieved from http://www.concrete.org/Publications/InternationalConcreteAbstractsPortal.aspx?m=details&i=3144

Aditya, G., & Lakshmayya, M. T. S. (2016). Effective Utilization of Various Industrial Wastes in Concrete for Rigid Pavement Construction – A Literature Review. International Journal for Innovative Research in Science & Technology, 3(3), 65–73. Retrieved from www.ijirst.org

Ahmad, S., Zubair, A., & Maslehuddin, M. (2015). Effect of key mixture parameters on flow and mechanical properties of reactive powder concrete. Construction and Building Materials, 99, 73–81. https://doi.org/10.1016/j.conbuildmat.2015.09.010

Anwar, A., Ahmad, S., Husain, S. M. A., & Aqeel, S. (2015). Salvage of Ceramic Waste and Marble Dust for the Refinement of Sustainable Concrete. International Journal of Civil Engineering and Technology, 6(9), 79–92.

Arum, C., Ikumapayi, C. M., & Aralepo, G. O. (2013). Ashes of Biogenic Wastes — Pozzolanicity, Prospects for Use, and Effects on Some Engineering Properties of Concrete. Materials Sciences and Applications, 4(September), 521–527. https://doi.org/10.4236/msa.2013.49064

Bayard, O., & Plé, O. (2003). Fracture mechanics of reactive powder concrete: Material modelling and experimental investigations. Engineering Fracture Mechanics, 70(7–8), 839–851. https://doi.org/10.1016/S0013-7944(02)00153-4

Baye, K. (2014). Teff : nutrient composition and health benefits. Ethiopia Strategy Support Program; Center for Food Science and Nutrition, College of Natural Sciences, Addis Ababa University.

BS812-103.1. (1995). British standard for Testing aggregates —Part 103: Methods for determination of particle size distribution — Section 103.1 Sieve tests.

BS 5328: Part 1. (1997). British Standard for Concrete -Guide to specifying Concrete. British Standard Institution, London, UK.

BS EN 1008. (2002). British Standard for Mixing water for concrete. Specification for sampling, testing and assessing the suitability of water, including water recovered from processes in the concrete industry, as mixing water for concrete" (Vol. 3). British Standard Institution, London, UK.

BS EN 12390-1. (2000). British Standard for Testing hardened concrete — Part 1: Shape, dimensions and other requirements for specimens and moulds. British Standard Institution, London, UK.

BS EN 12390-2. (2000). British Standard for Testing hardened concrete — Part 2: Making and curing specimens for strength tests. British Standard Institution, London, UK.

BS EN 12390-3. (2002). British Standard for Testing hardened concrete — Part 3: Compressive strength of test specimens. British Standard Institution, London, UK.

BS EN 12390-4. (2000). British Standard for Testing Hardened Concrete - Part 4: Compression strength- Specification of test machines. British Standard Institution, London, UK.

BS En 12390-5. (2000). British Standard for Testing hardened concrete - Part 5: Flexural strength of test specimens. British Standard Institution, London, UK.

BS EN 12390-6. (2000). British Standard for Testing hardened concrete Part 6: Tensile splitting strength of test specimens. British Standard Institution, London, UK.

Chan, Y. W., & Chu, S. H. (2004). Effect of silica fume on steel fiber bond characteristics in reactive powder concrete. Cement and Concrete Research, 34(7), 1167–1172. https://doi.org/10.1016/j.cemconres.2003.12.023

Cheng, H. (2016). Reuse Research Progress on Waste Clay Brick. Procedia Environmental Sciences, 31, 218–226. https://doi.org/10.1016/j.proenv.2016.02.029

Crymes, A. R. (2015). The international footprint of teff: Resurgence of an ancient Ethiopian grain. Arts and Sciences Electronic Theses and Dissertations. WASHINGTON UNIVERSITY IN ST, LOUIS, University College, International Affairs The. https://doi.org/10.1007/s13398-014-0173-7.2

Dham, M., Rushing, T. S., Helferich, R., Marth, T., Sengupta, S., Revur, R., … Cummins, T. K. (2010). Enhancement of Reactive Powder Concrete via Nanocement Integration. Transportation Research Record: Journal of the Transportation Research Board, 2142(1), 18–24. https://doi.org/10.3141/2142-03

Du, H., & Tan, K. H. (2017). Properties of high volume glass powder concrete. Cement and Concrete Composites, 75, 22–29. https://doi.org/10.1016/j.cemconcomp.2016.10.010

Dubey, S., & Dhakre, S. S. G. O. S. (2016). Feasibility of study on effect of waste glass Powder as a partial replacement of cement on compressive strength of concrete, 4(5), 38–41.

Gebremariam, M. M., Zarnkow, M., & Becker, T. (2012). Teff (Eragrostis tef) as a raw material for malting, brewing and manufacturing of gluten-free foods and beverages: a review. Journal of Food Science and Technology, 51(11), 2881–2895. https://doi.org/10.1007/s13197-012-0745-5

Ghosh, S. K., Chaudhury, A., Datta, R., & Bera, D. K. (2015). A Review on Performance of Pervious Concrete Using Waste Materials. International Journal of Research in Engineering and Technology, 4(13), 105–115. Retrieved from http://www.ijret.org

Habte, T.-Y. (1998). The Nutritive Value of Teff Straw and its Response to Chemical Treatment with Alkali. Ethiopian Journal of Science, Faculty of Science, Addis Ababa University, 21(1), 145–151.

Halicka, A., Ogrodnik, P., & Zegardlo, B. (2013). Using ceramic sanitary ware waste as concrete aggregate. Construction and Building Materials, 48(May), 295–305. https://doi.org/10.1016/j.conbuildmat.2013.06.063

Helmi, M., Hall, M. R., Stevens, L. A., & Rigby, S. P. (2016). Effects of high-pressure/temperature curing on reactive powder concrete microstructure formation. Construction and Building Materials, 105, 554–562. https://doi.org/10.1016/j.conbuildmat.2015.12.147

Imbabi, M. S., Carrigan, C., & Mckenna, S. (2013). Trends and developments in green cement and concrete technology. International Journal of Sustainable Built Environment, 1(2012), 194–216. https://doi.org/10.1016/j.ijsbe.2013.05.001

Ipek, M., Yilmaz, K., Sümer, M., & Saribiyik, M. (2011). Effect of pre-setting pressure applied to mechanical behaviours of reactive powder concrete during setting phase. Construction and Building Materials, 25(1), 61–68. https://doi.org/10.1016/j.conbuildmat.2010.06.056

Ivanov, V., Chu, J., & Stabnikov, V. (2015). Biotechnologies and biomimetics for civil engineering. In Biotechnologies and Biomimetics for Civil Engineering (pp. 1–437). Springer International Publishing, Switzerland. https://doi.org/10.1007/978-3-319-09287-4

Jang, H., Jeon, S., So, H., & So, S. (2015). Properties of different particle size of recycled TFT-LCD waste glass powder as a cement concrete binder. International Journal of Precision Engineering and Manufacturing, 16(12), 2591–2597. https://doi.org/10.1007/s12541-015-0331-7

Kebede, Z. (2009). Levels of essential elements in three tef [Eragrostis tef (Zucc.)Trotter] varieties. MSc Thesis: Department of Chemistry, Addis Ababa University, Addis Ababa, Ethiopia.

Khan, A. G., & Khan, B. (2017). Effect of Partial Replacement of Cement by Mixture of Glass Powder and Silica Fume Upon Concrete Strength. International Journal of Engineering Works, 4(7), 124–135. Retrieved from www.kwpublisher.com

Kirgiz, M. S. (2015). Strength gain mechanisms of blended-cements containing marble powder and brick powder. KSCE Journal of Civil Engineering, 19(1), 165–172. https://doi.org/10.1007/s12205-014-0557-4

Kushartomo, W., Bali, I., & Sulaiman, B. (2015). Mechanical behavior of reactive powder concrete with glass powder substitute. Procedia Engineering, 125, 617–622. https://doi.org/10.1016/j.proeng.2015.11.082

Le, H. T., Nguyen, S. T., & Ludwig, H.-M. (2014). A Study on High Performance Fine-Grained Concrete Containing Rice Husk Ash. International Journal of Concrete Structures and Materials, 8(4), 301–307. https://doi.org/10.1007/s40069-014-0078-z

Ling, I. H., & Teo, D. C. L. (2013). EPS RHA concrete bricks - A new building material. Jordan Journal of Civil Engineering, 7(4), 361–370.

Mengesha, M. H. (1965). Chemical Composition of Teff. Economic Botany. Undiscussed portion of a Ph.D. research project at Purdue University, Agronomy Department, West Lafayette, Indiana.

Navrátilová, E., & Rovnaníková, P. (2016). Pozzolanic properties of brick powders and their effect on the properties of modified lime mortars. Construction and Building Materials, 120, 530–539. https://doi.org/10.1016/j.conbuildmat.2016.05.062

Pacheco-Torgal, F., & Jalali, S. (2011). Compressive strength and durability properties of ceramic wastes based concrete. Materials and Structures, 44(1), 155–167. https://doi.org/10.1617/s11527-010-9616-6

Richard, P., & Cheyrezy, M. (1995). Composition of reactive powder concretes. Cement and Concrete Research, 25(7), 1501–1511. https://doi.org/10.1016/0008-8846(95)00144-2

Seyfu, K. (1997). Eragrostis tef (Zucc.) Trotter: Promoting the conservation and use of underutilized and neglected crops. The International Plant Genetic Resources Institute (IPGRI). Biodiversity Institute, Addis Abeba, Ethiopia.

Shayan, A., & Xu, A. (2006). Performance of glass powder as a pozzolanic material in concrete: A field trial on concrete slabs. Cement and Concrete Research, 36(3), 457–468. https://doi.org/10.1016/j.cemconres.2005.12.012

Shojaei, M., Behfarnia, K., & Mohebi, R. (2014). Application of alkali-activated slag concrete in railway sleepers. Materials and Design (Vol. 69). Elsevier Ltd. https://doi.org/10.1016/j.matdes.2014.12.051

Yanzhoua, P., Jun, Z., Jiuyan, L., Jin, K., & Fazhou, W. (2015). Properties and microstructure of reactive powder concrete having a high content of phosphorous slag powder and silica fume. Construction and Building Materials, 101, 482–487. https://doi.org/10.1016/j.conbuildmat.2015.10.046

Yazici, H., Yiğiter, H., Karabulut, A. Ş., & Baradan, B. (2008). Utilization of fly ash and ground granulated blast furnace slag as an alternative silica source in reactive powder concrete. Fuel, 87(12), 2401–2407. https://doi.org/10.1016/j.fuel.2008.03.005

Yeheyis, M., Hewage, K., Alam, M. S., Eskicioglu, C., & Sadiq, R. (2013). An overview of construction and demolition waste management in Canada: A lifecycle analysis approach to sustainability. Clean Technologies and Environmental Policy, 15(1), 81–91. https://doi.org/10.1007/s10098-012-0481-6

Interference based Call Admission Control of Secondary User in Cognitive Radio Network

Suresh Kumar Balam*, Ararso Taye, Derara Senay, Gurmessa Meribo Bora

Department of ECE, Bule Hora University, Bule Hora, P.O. Box-144, Ethiopia
**Corresponding author, e-mail: sureshnit415@gmail.com*

ABSTRACT

In this paper, an analysis has been done to evaluate performance of an interference based call admission control algorithm in CDMA based cognitive radio networks in the presence of an increased number of primary receivers (PRs). Different performance metrics like interference and blocking probabilities have been evaluated/simulated using matlab for secondary users (SUs) in an uplink scenario of CDMA based cognitive radio network consisting of SUs and a base station (BS) in the presence of four PRs. In our network model both primary radio network and cognitive radio network coexist and the BS computes instantaneous signal to interference ratio (SIR) of a SU. The uplink SIR of a SU should be above an SIR threshold level and also the instantaneous interference at all PRs to be below a predefined interference threshold for the SU to be allowed into the network

Keywords: *Cognitive Radio, blocking probability, CAC algorithm, CDMA*

1. INTRODUCTION

In modern wireless communication system the number of wireless licensed users is increasing rapidly with the advent of various new high speeds wireless technologies that results a necessary demand for radio spectrum. Since the spectrum is finite resource the efficient utilization of the same spectrum is absolutely necessary to solve spectrum scarcity. Under the observation of the federal communication commission (FCC), it is shown that 70% of the allocated spectrum is not used at a given time even in a crowded area where the spectrum usage is intensive [8]. To enhance the efficient utilization of RF spectrum, cognitive radio (CR) technology is an innovative solution for the spectrum scarcity.

Cognitive Radio is a dynamic adaptive system that has periodically sensing capacity and dynamically adjusting its physical parameters based on interaction with the radio environment as per requirement. The development of software defined radios is a radios control and operating spectrum to be dynamically configurable in accordance with the directions contained in the software in embedding device [6], [7]. CR is based on software defined radio.

Any CR network consists of two types of users, primary users (PUs) and secondary users (SUs). A PU is authorized users of a channel for whom the spectrum is allocated for exclusive use in wireless network such as cellular network, TV and Radio broadcast etc. The SUs are unauthorized users of a channel. The SUs are also known as cognitive users, which scans the channels periodically for identifying the currently unused channels and accesses the channel opportunistically in case of dynamically sharing spectrum. Dynamic spectrum sharing is divided into horizontal sharing and vertical sharing [8], [9], [10].

Horizontal sharing: It refers to the sharing within networks those have the same regulatory status, i.e., licensed spectrum or unlicensed spectrum. The coexistence of networks operating in unlicensed spectrum, i.e., WLAN 802.11and Bluetooth 802.15.1 is an example of heterogeneous horizontal sharing. Frequency hopping spread spectrum (FHSS) is used in Bluetooth PHY to cope with coexistence with WLAN 802.11. In FHSS, transmission of data moves between different channels. Thus, the harmful interference with WLAN 802.11 can be avoided.

Vertical sharing: It assumes the existence of primary and secondary users in which the license of the spectrum has only been given to the primary user but the secondary user can opportunistically access the spectrum without harmful interference to the primary user. There are two approaches for secondary user to make use of the licensed spectrum while keeping the interference under the acceptable level, overlay sharing and underlay sharing.

In overlay sharing, the PUs owns a band of spectrum but is not using all of it at the same time. The SUs equipped with cognitive radios can seek available spectrum, known as spectrum holes or white space, for their transmissions. Once the PUs has returned to the channel, the secondary user vacates the channel immediately and may access another available channel instead, if any. This approach is also called opportunistic spectrum access (OSA).

In underlay sharing, all SUs may transmit all the time, in presence of PUs, maintaining a predefined interference threshold at primary receiver. In this paper we consider a system model which comes under the type of underlay sharing spectrum. Here we see how the licensed spectrum is shared by SUs in the presence of primary receivers in radio environment by maintaining a predefined interference threshold. The system model consists of one Base Station (BS), several SUs and four Primary Receivers (PRs). The SUs can access the spectrum only if the interference to all PRs is less than the predefined threshold [2]. At the same time SUs should adapt their transmission powers in order to satisfy their own SIR. Here we assume Code Division Multiple Access (CDMA) as the multiple access mechanism, where all SUs can access the same spectrum band simultaneously.

1.1. Contribution of the paper

We consider an algorithm for controlling the admission of a new SU. This algorithm is used to reduce interference to PR as a new call is admitted on the basis of the interference threshold. Admission of a SU depends also on the required SIR threshold of SU. We assume that all users in network are in active and each SU is interfering with every other SU in our CDMA based CR network. The basic principle of call admission control is that the interference at all PRs due to the new SU (which seeks admission into the network) should be less than the interference threshold assumed beforehand. Here, the four PR are sharing information with the BS. If the overall tolerable interference limit is exceeded, the PR would notify the BS by sending an alarm. The interference scenario for CR network may be degraded by a new SU. Hence, a new SU would be admitted in the network only if overall interference to all PRs remains below the interference threshold and SIRs for all PRs including the new one remain within the acceptable limits. Our present work shows that there is always some room for SUs in the licensed spectrum to utilize. Our present work is an extension of our earlier work [10].

2. SYSTEM MODAL

2.1. Network Scenario Description

We consider a network consisting of one BS at the centre of the hexagonal cell and surrounded by several SUs. The four PR located near the cell are considered. Here all SUs are trying to transmit data in uplink to the BS and all PRs will receive the interference from SUs [3, 4].

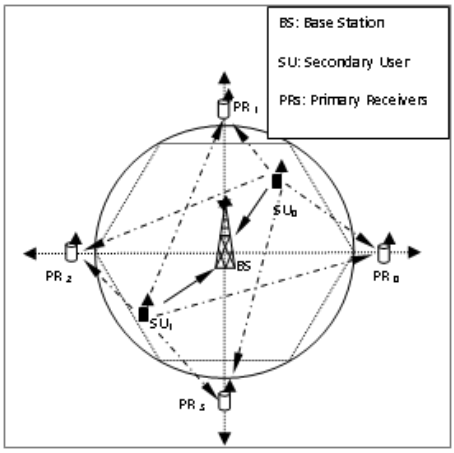

Figure 1: Simulation Model for Four Primary Receivers

The SUs can only be admitted to the BS, if the interference caused by all SUs to all PRs should be less than the predefined threshold and at the same time SUs should adapt their transmission powers in order to satisfy their own SIR [2].

2.2. Power Control

In order to avoid near far problem in CDMA systems, the received power at BS is kept at a constant value and if the mobile station (MS) is situated far away from the BS then the MS need to transmit with high power, which drains the battery quickly and leads to health hazard. In order to increase the battery life and decrease health hazards the transmitting power of MS must be limited to a maximum allowable transmit power level. That's why if the required transmit power level is greater than the maximum allowable transmitted power then transmitted power is fixed at a maximum allowable transmitted power.

$$If\ P_t > P_{max}\ then\ \ P_t = P_{max} \tag{1}$$

Here we assume shadowing and path loss exponent in our model is 4. Each PR will receive interference from all SUs and assuming that each PR is situated at a distance d_{PR} from the BS and the received power at PR is expressed as

$$P_r' = P_t 10^{\zeta/10}\left(\frac{d_0}{d'}\right)^{\alpha} \tag{2}$$

Where ζ in decibel has a normal distribution with zero mean and standard deviation (σ), 5~12 dB the following symbols are used in this paper

d'_{xy} : distance between SU_x and PR_y
d : distance between MS and BS
θ : angle of SU from BS with respect to reference line
θ_{PR} : angle of PR from BS with respect to reference line
P_t : transmit power of a MS.
P_{max} : maximum allowable transmit power.
P_r : received power at the BS
P_r': received power at the PRs.
d_o : close in reference distance
α : path loss exponent
n : number of SUs

The distance of the SU_x from the PR_y is expressed as

$$d'_{xy} = \sqrt{(d\sin(\theta) - d_{PR}\sin(\theta_{PR}))^2 + (d\cos(\theta) - d_{PR}\cos(\theta_{PR}))^2} \tag{3}$$

The distance between SU_0 and PR_0 is

$$d'_{00} = \sqrt{(d\sin(\theta))^2 + (d_{PR} - d\cos(\theta))^2} \quad \text{for } \theta_{PR} = 0 \tag{4}$$

The distance between SU_0 and PR_1 is

$$d'_{01} = \sqrt{(d_{PR} - d\sin(\theta))^2 + (d\cos(\theta))^2} \quad \text{for } \theta_{PR} = \pi/2 \tag{5}$$

The distance between SU_0 and PR_2 is

$$d'_{02} = \sqrt{(d\sin(\theta))^2 + (d_{PR} + d\cos(\theta))^2} \quad \text{for } \theta_{PR} = \pi \tag{6}$$

The distance between SU_0 and PR_3 is

$$d'_{03} = \sqrt{(d_{PR} + d\sin(\theta))^2 + (d\cos(\theta))^2} \quad \text{for } \theta_{PR} = 3\pi/2 \tag{7}$$

2.3. Signal to Interference Ratio of the SUs:

The SIR of a SU is nothing but the ratio of received power at the BS from a particular SU to the summation of received powers of all other SUs except that particular SU. Therefore, the SIR of i^{th} SU may be expressed as

$$SIR(i) = \frac{P_r(i)}{\sum_{j=1, j\neq i}^{n} P_r(j)} \quad (8)$$

Here the processing gain of SIR is not considered and the additional number of SUs that a base station can serve is defined as the residual capacity [5] and given as

$$R(i) = \left\lfloor \frac{1}{SIR_{th}} - \frac{1}{SIR(i)} \right\rfloor \text{ If } \left\lfloor \frac{1}{SIR_{th}} - \frac{1}{SIR(i)} \right\rfloor > 0$$

$$= 0 \quad \text{otherwise} \quad (9)$$

$$R = \min(R)$$

2.4. Interference Power

Here we calculate interference at each of the four PR and referred them as interference0, interference1, interference2, interference3 respectively for PR0, PR1, PR2 and PR3 respectively. Always the interference power is caused by all SUs to PR and the total interference is equal to the summation of all interference power.

$$I_{total} = \sum_{i=1}^{n} P'_r(i) \quad (10)$$

2.5. Network Performance:

The performance of the CR network is measured by two parameters viz. the blocking probability and outage probability. The Outage probability is defined as

$$P_{out} = \text{Prob}\{SIR < SIR_{th}\}$$

The Blocking Probability is defined as $P_{blk} = \text{Prob}\{R=0\}$.

3. CALL ADMISSION CONTROL ALGORITHM

1. Input: n, int_{th} , SIR_{th} ,P_r ,P_{max}, Radius, Iteration
2. Initialize iteration
3. Loop for iteration
4. Generate: d (i), dPR, ζ_i , ζ_i'
5. Calculate: d' (i), Pt (i)
6. if P t(i) > Pmax
   Pt (i) = Pmax
   end if
7. Calculate: P_r' for each of the primary receivers
8. Calculate: Interference0, interference1, interference2, interference3
9. Calculate: SIR (i)
10. Calculate: R (i)
11. Calculate: R
12. Loop for arrival calls
    if (R > 0) then
    if (Interference 0> int_{th} or Interference 1> int_{th} or Interference 2> int_{th} or Interference 3>int_{th})
    Call block due to more interference at PU
    block counter=block counter+1

```
            else
                Call admitted
            end if
        else
            Call block due to low SIR.
            block counter=block counter+1
        end if
```

13. End of the loop
14. End of the loop
15. Blocking probability=block counter/ (iteration*new call)

4. SIMULATION MODEL

We did all simulation by using MATLAB and our simulation model consists of several SUs within the hexagonal cell. Four PR are present outside the hexagonal cell, at fixed positions as shown in Fig.1. The distance and angle of the SUs with respect to the BS are generated randomly as per uniform distribution within the cell. We calculate the distances between PRs and SUs using equation (3) and the SUs power is controlled by the BS. According to the requirement for simulation, (i) the numbers of SUs, (ii) the value of interference threshold and (iii) the value of SIR threshold are chosen. Since CDMA is interference limited, noise term in the SINR expression has been neglected in our simulation.

5. SIMULATION RESULTS

In our simulation model, a BS is located at the center of a hexagonal cell with a radius of 1000m. The distance between a SU and BS is randomly chosen from 100m to 1000m and angle of a SU is randomly generated between [0,2π].Four PR are located at fixed positions outside the cell each at a distance of 1500m as shown in Fig. 1. Two different allowable values of maximum transmission powers are assumed to be 0.5mW and 0.005mW. We assume propagation model with path loss exponent, α = 4 and standard deviation, σ = 8 dB.

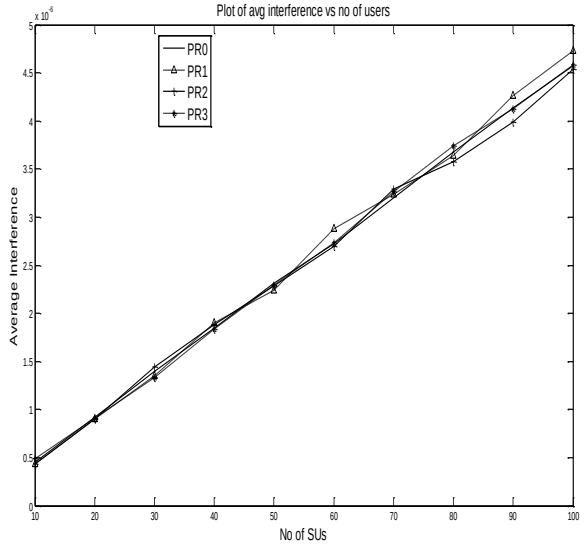

Figure 2: Average Interference vs. Number of SUs

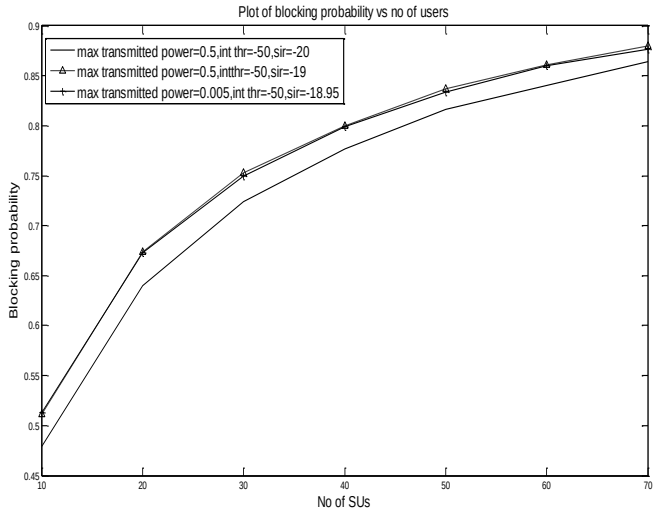

Figure 3: Blocking Probability vs. Number of SUs

Figure 2 shows the plot of average interference at each PR caused by all SUs. The number of SUs in the network is determined by the interference caused by them on the PRs, to allow a new SU in the primary radio network the interference caused must be below a certain threshold interference level which is -50dB in our simulation model. We can see that when the number of SUs is 100 the interference caused is -53dB, this is less

than the threshold value, so our model allows large number of SUs in the primary radio network. However the SIR caused by the new user should be above the threshold SIR value to allow it to enter into the network.

In Figure 3 blocking probability of SUs is shown as a function of number of SUs in the network. The blocking probability is increasing as number of users is increasing in the network. We consider three different cases (i) maximum transmitted power=0.5mW, interference threshold = -50 dB, SIR threshold= -19dB, (ii) maximum transmitted power=0.005mW, interference threshold= -50dB, SIR threshold= -18.95dB, (iii) maximum transmitted power=0.5mW, interference threshold= -50dB, SIR threshold= -20dB. For first case the maximum allowable transmitted power is 0.5mW and SIR threshold is more than the third case having the same limit on maximum transmitted power, hence interference created by SUs will be more than any other case causing less number of users to stay in the network and thus has the highest blocking probability. For the third case it has the least SIR threshold value, hence will allow more number of SUs in the primary radio network even if the interference level is increased and thus it offers the least blocking probability.

In Figure 4 blocking probability of a SU is varied against the variation of SIR threshold level. Here again we are considering three different cases, (i) maximum transmitted power= 0.5mW, interference threshold= -50dB, (ii) maximum transmitted power=0.005mW, interference threshold= -50dB, (iii) maximum transmitted power= 0.005mW, interference threshold= -40dB. For the two cases with having same limit of 0.005mW on the transmitted power, the network will have same total interference on a primary receiver, but to allow a new SU into the network the total interference should be less than the threshold interference level, so the case having less threshold interference level will have more blocking probability. For the first case having the maximum possible transmitted power of 0.5mW, interference to the PR caused by the SUs will be more and thus will have the highest blocking probability for a new SU in the network.

In Figure 5 the behavior of the outage probability of SUs over the SIR threshold in dB is shown. Outage probability also depends upon both SIR threshold and number of SUs. The outage probability is increasing exponentially with increase in SIR threshold. We consider three different cases. (i) Users=20, interference threshold=-50dB (ii) users=30, interference threshold=-50dB (iii) users=40, interference threshold=-50dB. From the plot we observe that for the three cases the outage probability increases with increase in SIR threshold and number of SUs. Hence all these results show that there is a room for SUs in the licensed spectrum to utilize.

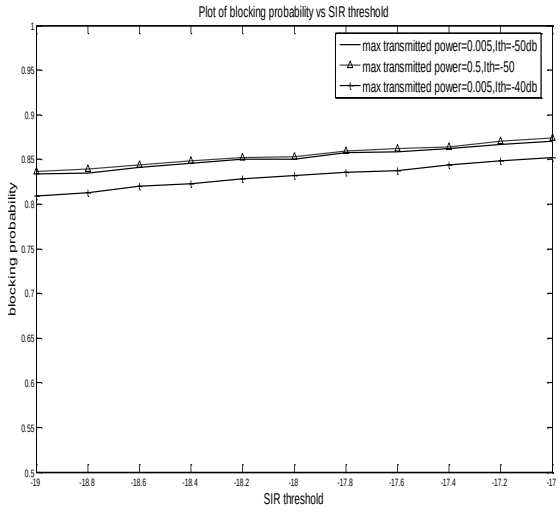

Figure 3: Blocking Probability vs. SIR threshold

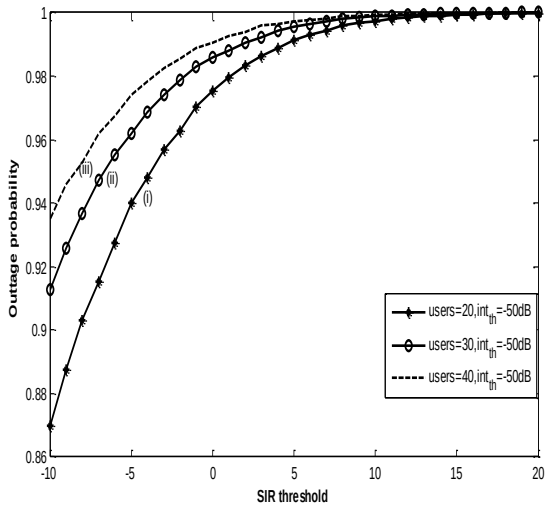

Figure 4: Outage probability vs SIR threshold

6. CONCLUSION

This paper shows the influence of number of SUs, SIR threshold, and interference threshold on the admission of a new SU in CDMA based CR network in the presence of an increased number of PRs. The simultaneous satisfaction of the SIR of SUs and interference conditions forms the basis of the algorithm. We have also evaluated blocking probability of SUs with respect to number of SUs and SIR threshold in the presence of four primary receivers placed symmetrically in the hexagonal cell. The blocking probability increases with increase in number of SUs as well as with increasing value of SIR threshold. However the rate of increase in blocking probability with increase in SIR threshold is slow. In the algorithm, the SIR threshold can be selected so as to satisfy a desired requirement for outage performance without sacrificing too much in blocking performance. The outage probability increases exponentially with increase in number of SUs as with increase in value of SIR threshold.

REFERENCES

[1] J.Mitola and G.Maguire, (1999). "Making Software radios more personal," *IEEE Personal Communications*., 6:13-18.
[2] Ki Tae and Seong Keun Oh, (2008). "Cognitive Ad-hoc Networks under a Cellular Networks with an Interference Temperature Limit," *ICACT*, 879-882.
[3] Karama Hamdi, Wei Zhang, and Khaled Ben Letaief, (2007). "Uplink Scheduling with QoS Provisioning for Cognitive Radio Systems," *WCNC*, 2594-2598
[4] Tevfik Yücek and Hüseyin Arslan, (2009). "A Survey of Spectrum Sensing Algorithms for Cognitive Radio Applications," *IEEE communications surveys & tutorials*, 11:1.
[5] Z. Liu and M.E. Zarki, (1994). "SIR based call admission control algorithm for DS-CDMA system," *IEEE journal on selected areas of Communication*, 12,:638-644
[6] Youping Zhao, Joseph Gaeddert, Kyung K. Bae, and Jeffery H. Reed, (2007). "Radio Environment Map Enabled Situation-Aware Cognitive Radio Learning Algorithm," in 2nd IEEE symposium on New Frontiers in Dynamic Spectrum Access Network.
[7] Peter G. Cook, Stephen R. Hope, (2006) "An Application Independent Model of Cognitive Radio Domain," in SDR Forum Technical Conference, 2006.
[8] Hui Wang; Hang Qin; Li Zhu; (2008) State Key Lab. of Software Eng., Wuhan Univ., Wuhan, "A Survey on MAC Protocols for Opportunistic Spectrum Access in Cognitive Radio Networks," in International Conference on Computer Science and Software Engineering.
[9] S. Pollin, "Coexistence and Dynamic Sharing in Cognitive Radio Networks", Cognitive Wireless Communication Networks, pp 84-96.
[10] Roy, S.D.;Mondal, S.;Kundu, S.; (2011). ECE Dept., NIT, Durgapur, Durgapur, India "A New Algorithm for Admission Control of Secondary Users in CDMA based Cognitive Radio Network" *International Conference on Computer and Communication Technology*, 35-39.

Synthesizing lanthanum doped cadmium sulfide thin films for photovoltaic application

Tizazu Abza*, Fekadu Gashaw Hone

Department of Physics, Hawassa University, Hawassa, Etihiopia
**Corresponding author, e-mail: zabishwork2@gmail.com*

ABSTRACT

In this work Lanthanum doped cadmium sulfide (La:CdS) thin films have been deposited by chemical bath deposition technique (CBD) to tune the electrical and optical properties of the films suitable for photovoltaic application. The thin films were deposited from chemical baths containing cadmium acetate, tartaric acid, lanthanum chloride and thioacetamide at a bath temperature of 333 K and pH of 2.35 for a period of one hour. The resulted films were greenish yellow, smooth and reflective. The samples were characterized by powder X-ray diffraction for structural analysis, UV-VIS spectrometer for optical analysis, scanning electron microscopy (SEM) for surface morphology and two probe electrical measurements. The structural analysis of the doped and undoped CdS thin films showed the hexagonal structure with preferred orientation along (002) plane and crystallite size in the range 30 - 40 nm. The SEM micrograph revealed spherical grains covering the substrates. The band gaps of the films decreased from 3.39 to 1.8 eV as the lanthanum concentration increased from 0- 2%. The electrical resistivity of the films also decreased with increasing the lanthanum concentration. The doping of La has significant influence on the structural, optical and electrical properties of the films. The films have suitable optical properties to be used as the window layer of thin film solar cells.

Keywords: *Cadmium sulfide, doping, lanthanum, electrical properties, crystal structure*

1. INTRODUCTION

CdS is an important II-VI group semiconductors material owing to its optical properties, photoconductivity, high transparency, high electron affinity and stability (Pandya, 2016). It exhibits n-type conductivity because of native defects such as sulfur vacancies and interstitial cadmium (Anbarasi et al., 2015). Currently the standard technique of mass-producing Cu(In,Ga)Se2 (CIGS) thin film solar cells includes a chemical bath deposited CdS as a buffer layer due to its good optical and electrical properties (Hashimoto et al., 1998; Abou-Ras et al., 2005). However the quantum efficiency of a CdS/CIGS solar cell drops at short wavelengths due to loss of optical absorption from the relatively small band gap CdS (Eg = 2.45 eV) layer (Long et al., 2008; Qi et al., 2008). The use of wider band gap semiconductors as a window layer is expected to solve this problem (Nakada et al., 2001). With the current knowledge and technology the performance CdS buffer in CIGS and CdTe thin film solar cells is still at the front despite many attempts to replace it by other wider band gap buffer materials (Tsuji et al., 2000; Kamada et al., 2016). However, the attained efficiency of thin film solar cells is far below the theoretical efficiency (Chopra and Das, 1983). This implies that further investigation is to be carried out on each layer of the thin film solar cell and the interface between these layers to improve the solar cell conversion efficiency.

CdS thin films can be prepared by many different techniques such as closed space sublimation, chemical bath deposition (CBD), vacuum evaporation, magnetron sputtering and spray pyrolysis (Jun Young et al., 1998). CBD deposition of CdS is a common practice since 1960s (Hodes, 2002). However many of the depositions were carried out in alkaline medium. There are only few reports on acidic bath deposited CdS thin films (Abza et al., 2017). The band gap of most of chemical bath deposited CdS thin films is not greater than 2.5 eV. In addition, chemical bath deposited CdS thin films have high electrical resistance due to the highly stoichiometry of the films. The window materials should have high conductivity and a large band gap in order to transmit the incident radiation and to minimize the sheet resistance of the solar cell to collect photogenerated electron-hole pairs to the external circuit. Quite recently chemical bath deposited CdS thin films with band gap as high as 4 eV were reported from acidic bath which is promising material to solve the problem of low incident radiation transmittance (Abza et al.,

2017). However the films have high resistivity. In situ doping with group III elements such as Lanthanum, Aluminium, Indium and Gallium are the most suitable approach to tackle this problem (Rubel and Podder, 2015; Khallaf et al., 2008; Bhushan et al., 2001; Bhushan and Sharma, 1990; Khallaf et al., 2009). In this work we report on the effect of lanthanum doping on structural, optical and electrical properties of acidic bath deposited CdS thin films so that the material is suitable as a window layer of thin film solar cells.

2. EXPERIMENTAL PROCEDURE

The reaction bath used for the deposition La:CdS thin films consisted of 0.1 M (20 ml) cadmium acetate, 0.01 M (0, 1, 2, 3, and 4 ml) lanthanum chloride, 2 ml (60 %) hydrazine, 1 M (7.5 ml) tartaric acid, 1M (7.5 ml) thioacetamide and deionized water to make the total volume 70 ml. The LA:CdS thin films were deposited on glass substrates at a pH of 2.35 and temperature of 60°C for 1 hr. The depositions were doubled to increase the thickness of the films. The films were greenish yellow in colour. The films were characterized by X-ray diffraction (XRD), UV-VIS spectrometer and two probe electrical measurements to study the structure, optical and electrical properties.

3. RESULT AND DISCUSSION

3.1. Reaction Mechanism

Hydroxide ion is normally responsible for film growth through cluster-by-cluster mechanism. However deposition in acidic medium normally takes place through ion-by-ion mechanism due to the presence of very limited hydroxide ion in acidic chemical bath. Thioacetamide can release S^{2-} either through the formation of H_2S by hydrolysis decomposition or directly by complex decomposition. Thioacetamide in pure water is fairly stable and demands deposition temperature reater than the room temperature to to hydrolyze and release S^{2-}.

A general irreversible thioacetamide decomposition reaction for sulphide formation is

$$H_3C.C(S)NH_2 + 2H_2O \rightarrow CH_3COOH + H_2S + NH_3 \quad (1)$$

In strongly acidic bath, decomposition of thioacetamide results in the formation of H_2S as shown in equation (1). This process is followed by the formation of hydrosulphide ion by dissolving H_2S in water as

$$H_2S + H_2O \leftrightarrow HS^- + H_3O \quad (2)$$

The hydrosulphide ion again dissolves to sulphur ion

$$HS^- + H_2O \rightleftharpoons H_3O + S^{2-} \quad (3)$$

The Cd^{2+} ion is released from Cadmium acetate dihydrate

$$Cd(CH_3COO)_2.2H_2O \leftrightarrow Cd^{2+} + 2CH_3COO^- + 2H_2O \quad (4)$$

The Cd^{2+} ion released from the cadmium acetate dihydrate should be complexed by appropriate ligand(s) in order to control the precipitation of CdS.

In the present work the Cd^{2+} ion was complexed by hydrazine and tartaric acid. The ionic reaction of S^{2-} which is released from the hydrolysis of thioacetamide and the Cd^{2+} released from the complexes forms a solid phase CdS either as a thin film on the substrate or a CdS precipitate within the stock solution.

$$Cd^{2+} + S^{2-} \longrightarrow CdS \quad (5)$$

The formation of CdS by complex decomposition of thioacetamide can be represented as

$$[Cd\text{-}(CH_3CSNH_2)]^{2+} \leftrightarrow CdS + H_2 + CH_3CN$$

3.2. Optical properties

The optical properties of the films were carried by measuring absorbance using Perkin Elmer Lambda 950UV/VIS/NIR spectrometers for the wavelength range of 300-800nm. The band gap of the films was obtained by using Stem (1963) relation (Abza *et al.*, 2018).

$$A = \frac{[k(h\nu - E_g)]^{\frac{n}{2}}}{h\nu} \quad (6)$$

where A is absorbance, k is a constant, ν is the frequency of the radiation, h is the Planck's constant, and n is 1 for the direct transition which true for almost all compound semiconductors and 4 for the indirect transition. In the case of direct transition $(Ah\nu)^2$ and the photon energy ($h\nu$) (Eqn.1) has linear relation in the region next to the onset of fundamental absorption (Nasr et al., 2006) which is true for almost all compound semiconductors. The band gap energy (E_g) was obtained by extrapolating the linear portion of the $(Ah\nu)^2$ vs ($h\nu$) curve towards $h\nu$ axis (Figure 1). From the Fig. 1 it can be observed that the band gap of undoped, 0.5%, 1%, 1.5% and 2% La-doped CdS thin films are 3.39, 2.57, 2.35, 2.3, and 1.8 eV respectively. Abdelhameed and El Radaf (2018) observed red shift from 2.45 to 2.09 eV of CdS up on La doping. The unusual band gap of pure CdS is explained in our previous work (Abza et al., 2017). However the decreased band gap of the pure CdS thin film compared to the our previous report could be due change in 60% hydrazine volume from 5 ml to 2 ml and double deposition of the films. Manthrammel et al. (2018) also reported a slight red shift from 2.47 to 2.3 eV in the band gap of La doped CdS thin films.

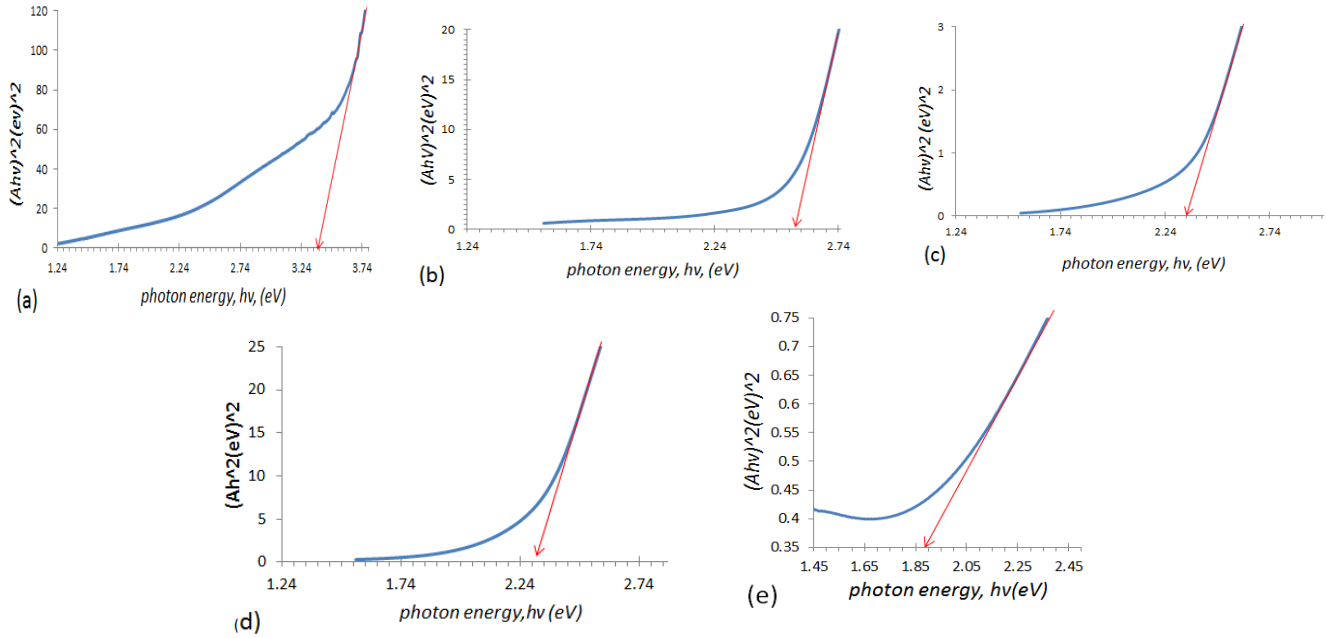

Figure 1: Plot of $(Ahv)^2$ vs hv for (a) undoped, (b) 0.5 %, (c) 1%, (d) 1.5 % and € 2% La-doped CdS thin films.

3.3. Structural properties

The structural analyses of the films were carried by Shimadzu X-ray diffractometer. The XRD pattern is shown in Fig. 2. The undoped CdS thin film has three visible peaks at 25.0, 26.74 and 28.32° which are indexed to (100), (002) and (101) planes of hexagonal CdS (JCPDS 01-07-2553) with preferred orientation long the (002) plane. It has also four very weak peaks along (102), (100), (103) and (112) planes. All these peaks almost disappeared for La-doped CdS, however the peaks along (100), (002) and (101) planes appeared in all samples with a continuous decrease in peak intensity up to 1.5% La doping and then increased for 2% La doping. Similar result is reported by Agrawal and Khare (2015).

The crystallite size of the films were calculated using the Scherrer equation:

$$D = \frac{k\lambda}{\beta cos\theta} \quad (7)$$

where, D = average crystallite size, $k =$ 0.9 is particle shape factor, λ =1.5406 nm is wavelength of the X-ray used, β = full width half maximum of the diffraction peaks and θ is the Bragg diffraction angle. The obtained crystallites size along the (002) plane were 40 nm for pure, 30 nm for 0.5%, 1% and 1.5 % La-doped and 32 nm for 2% La-doped CdS thin films. The results show that no structural phase change was observed on doping lanthanum except a slight change in a crystallite size and a decrease in intensity of the peaks.

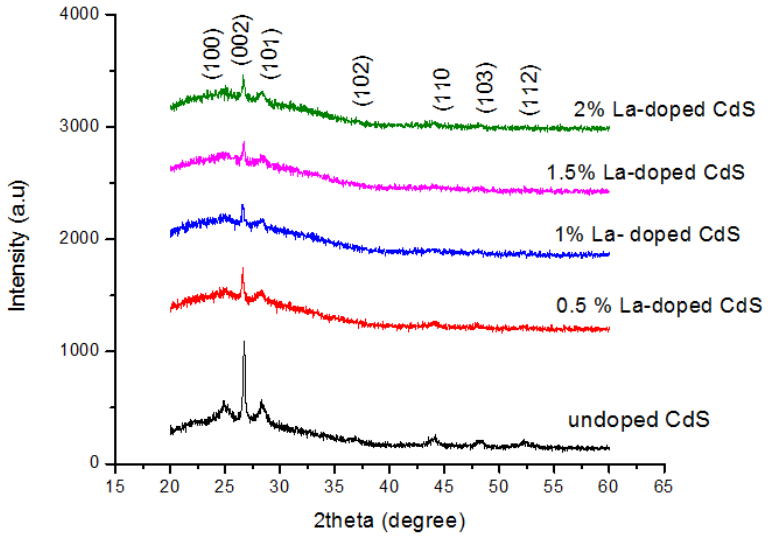

Figure 2: The XRD pattern of pure and La-doped CdS thin films

3.4. Surface Morphology

The surface morphology of the La:CdS thin films were investigated using a field emission scanning electron microscopy (FESEM, Zeiss, sigma). Fig. 2 represents the surface morphology of the pure, 1% La doped, 2% La doped CdS thin films. The pure CdS thin film has a uniformly covered surface morphology formed by compact spherical shaped grains. It is free from cracks and pinholes. For 1% and 2% La doped CdS thin films the surface morphology is nearly the same as that of pure CdS, however few pinholes were observed in both cases.

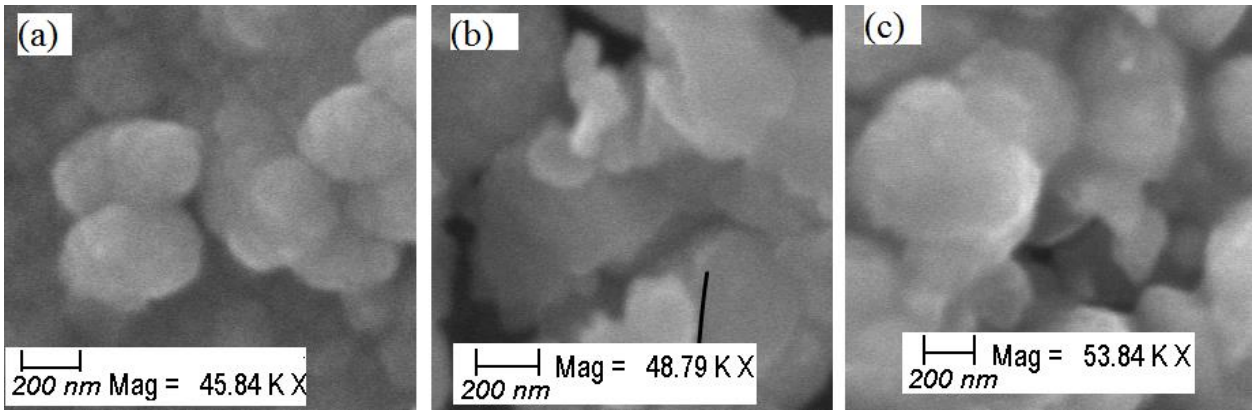

Figure 3: Surface morphology of (a) CdS (b) 1% La dope CdS and (c) 2% Ladoped CdS thin films

3.5. Electrical properties.

The electrical properties of the films were measured using two-probe method. The resistance drastically decreased upon 0.5% La doping (Fig. 4), and continues to decrease gradually up to 1.5% La doping. For 2% La doping, the resistance begins to increase again. One of the reasons for the decrease in resistance up to 1.5 % La-doping could be owing to the substitution of the group II cadmium by less electronegative and large atomic radius

group III element, La, which releases one free electron per La atom. This free electron increases the conductivity of the films. The other reason could be the formation of lanthanum sulfide phase, which has higher conductivity than CdS (Khomane, 2010; Kariper *et al.*, 2011; Bagde *et al.*, 2000; Cahay *et al.*, 2006). An improved electrical conductivity of CdS thin films by La-doping was reported by Abdelhameed and El Radaf (2018). This variation of the band gap energy and the electrical conductivity up on the doping of La on CdS thin films can be used to design a suitable window material in the fabrication of thin film solar cells.

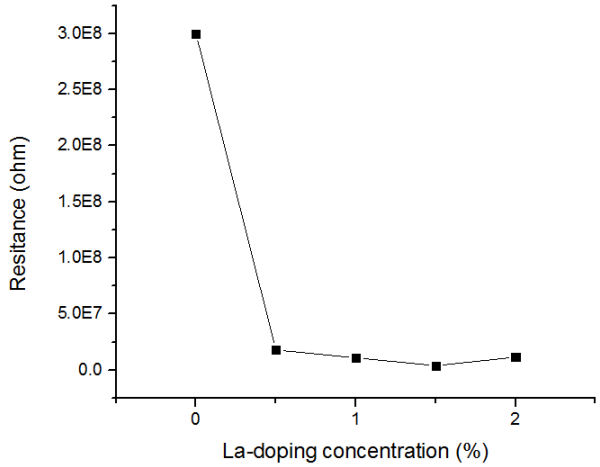

Figure 4: Variation of electrical resistance with La-doping concentration

4. CONCLUSION

0- 2% lanthanum doped CdS thin films were successfully deposited on a glass substrate by chemical bath deposition techniques from a solution containing cadmium acetate, hydrazine, tartaric acid and thioacetamide. The films were crystalized in hexagonal structure with preferred orientation along the (002) plane of cadmium sulfide. The crystallinity and the band gap of the films decreased with increasing doping concentration. However, the conductivity of the films increased by the order of 100 up on doping of lanthanum. The films' surface morphology is free from cracks except few pinholes. The current investigation has shown that doping of lanthanum has significant influence on the structural, optical, electrical and surface morphology of the CdS thin films deposited from acidic chemical baths.

REFERENCES

Abdelhameed, R. M., and El Radaf, I. M. (2018). Self-cleaning lanthanum doped cadmium sulfide thin films and linear/nonlinear optical properties. *Materials Research Express*, *5*(6), 066402.

Abou-Ras, D., Kostorz, G., Romeo, A., Rudmann, D., and Tiwari, A. (2005). Structural and chemical investigations of CBD-and PVD-CdS buffer layers and interfaces in Cu (In, Ga) Se2-based thin film solar cells. *Thin solid films*, *480*, 118-1

Abza, T., Ampong, F. K., Hone, F. G., Nkrumah, I., Nkum, R. K., and Boakye, F. (2017). A New Route for the Synthesis of CdS Thin Films from Acidic Chemical Baths. *Int. J. Thin Films Sci. Technol.*, *6*(2), 67-71.

Abza, T., Ampong, F. K., Hone, F. G., Nkum, R. K., and Boakye, F. (2018). Preparation of cadmium zinc sulfide (Cd1−xZnxS) thin films from acidic chemical baths. *Thin solid films*, *666*, 28-33.

Agrawal, S., and Khare, A. (2015). Effect of La on optical and structural properties of CdS–Se films. *Arabian Journal of Chemistry*, *8*(4), 450-455.

Anbarasi, M., Nagarethinam, V., and Balu, A. (2015). Studies on the physical properties of undoped AND Zn-doped CdS thin films prepared by spray pyrolysis technique using perfume atomizer. *Indian J. Sci*, *13*(38), 48-52.

Bagde, G., Yermune, V., and Lokhande, C. (2000). Preparation and characterization of lanthanum sulphide thin films deposited by Spray Pyrolysis Technique.

Bhushan, S., Mukherjee, M., and Bose, P. (2001). Photoconductivity of chemically deposited lanthanum/neodymium doped (Cd-Pb) S films. *Radiation effects and defects in solids, 153*(4), 367-377.

Bhushan, S., and Sharma, S. (1990). Photoconductive properties of chemically deposited CdS: La films. *Journal of Physics D: Applied Physics, 23*(7), 909.

Cahay, M., Garre, K., Wu, X., Poitras, D., Lockwood, D., and Fairchild, S. (2006). Physical properties of lanthanum monosulfide thin films grown on (100) silicon substrates. *Journal of applied physics, 99*(12), 123502.

Chopra, K. L., and Das, S. R. (1983). Why thin film solar cells? *Thin Film Solar Cells* (pp. 1-18): Springer.

Hashimoto, Y., Kohara, N., Negami, T., Nishitani, N., and Wada, T. (1998). Chemical bath deposition of Cds buffer layer for GIGS solar cells. *Solar Energy Materials and Solar Cells, 50*(1-4), 71-77.

Hodes, G. (2002). *Chemical solution deposition of semiconductor films*: CRC press.

Jun Young, C., Kang-Jin, K., Ji-Beom, Y., and Donghwan , K. (1998). Properties Of Cadmium Sulfide Thin Films Deposited By Chemical Bath Depositionwith Ultrasonication. *Solar Energy, 64*(1-3), 7.

Kamada, R., Yagioka, T., Adachi, S., Handa, A., Tai, K. F., Kato, T., and Sugimoto, H. (2016). *New world record Cu (In, Ga)(Se, S) 2 thin film solar cell efficiency beyond 22%.* Paper presented at the 2016 IEEE 43rd Photovoltaic Specialists Conference (PVSC).

Kariper, A., Güneri, E., Göde, F., Gümüş, C., and Özpozan, T. (2011). The structural, electrical and optical properties of CdS thin films as a function of pH. *Materials Chemistry and Physics, 129*(1-2), 183-188.

Khallaf, H., Chai, G., Lupan, O., Chow, L., Park, S., and Schulte, A. (2008). Investigation of aluminium and indium in situ doping of chemical bath deposited CdS thin films. *Journal of Physics D: Applied Physics, 41*(18), 185304.

Khallaf, H., Chai, G., Lupan, O., Chow, L., Park, S., and Schulte, A. (2009). Characterization of gallium-doped CdS thin films grown by chemical bath deposition. *Applied Surface Science, 255*(7), 4129-4134.

Khomane, A. (2010). Morphological and opto-electronic characterization of chemically deposited cadmium sulphide thin films. *Journal of Alloys and Compounds, 496*(1-2), 508-511.

Long, F., Wang, W.-M., Cui, Z.-k., Fan, L.-Z., Zou, Z.-g., and Jia, T.-k. (2008). An improved method for chemical bath deposition of ZnS thin films. *Chemical Physics Letters, 462*(1), 84-87.

Manthrammel, M. A., Ganesh, V., Shkir, M., Yahia, I., and Alfaify, S. (2018). Facile synthesis of La-doped CdS nanoparticles by microwave assisted co-precipitation technique for optoelectronic application. *Materials Research Express, 6*(2), 025022.

Nakada, T., Mizutani, M., Hagiwara, Y., and Kunioka, A. (2001). High-efficiency Cu (In, Ga) Se2 thin-film solar cells with a CBD-ZnS buffer layer. *Solar Energy Materials and Solar Cells, 67*(1-4), 255-260.

Nasr, T. B., Kamoun, N., Kanzari, M., and Bennaceur, R. (2006). Effect of pH on the properties of ZnS thin films grown by chemical bath deposition. *Thin solid films, 500*(1-2), 4-8.

Pandya, S. G. (2016). Preparation and characterization of cadmium sulphide nanocrystalline thin film grown by chemical method. *International Journal of Recent Scientific Research, 7*(12), 14887-14890.

Qi, L., Mao, G., and Ao, J. (2008). Chemical bath-deposited ZnS thin films: preparation and characterization. *Applied Surface Science, 254*(18), 5711-5714.

Rubel, A. H., and Podder, J. (2015). Optical properties of spray pyrolysis deposited Cds: Al thin films. *Journal of Bangladesh Academy of Sciences, 39*(1), 25-30.

Tsuji, M., Aramoto, T., Ohyama, H., Hibino, T., and Omura, K. (2000). Characterization of CdS thin-film in high efficient CdS/CdTe solar cells. *Japanese Journal of Applied Physics, 39*(7R), 3902.

A Realistic Approach to Save Passenger lives in Case of Vehicle Accidents Using Arm7 Processor

N.SuthanthiraVanitha*, Tilahun Weldcherkos, Aderajew Ashagrir, Elizabeth Girma

Department of Electrical and computer engineering, Addis Ababa Science and Technology University, Ethiopia
**Corresponding author, e-mail: varmans03@gmail.com*

ABSTRACT

Currently, Air buses are the new era of public transport system with high speed, luxury and comfort but while considering safety issues it lacks behind with the development of Automobile industries. People have started to look towards the safety factors of these luxurious vehicles but it is not taken in greater account. Due to the negligence in the safety factors of these buses they have become luxurious confines which destroy the precious lives of many people. As per the latest news at Bangalore in a Volvo bus accident lots of people have died with a lots suffering. Now industrialists understand the necessities of safety factors of these buses but they could not identified a proper solution for this problem. Government has made some set of safety measures at the time of journey but these measures will not be that much efficient solution for this disaster. With a view to change this scenario, we wish to make the bus which will be controlled by a system that has lot of sensors to sense the vital functions of it and it continuously sends a input signal to the controller which controls the basic functions of the bus. Since the driver is fully responsible to handle the hurdles at the time of driving, he has to be subjected to certain test until which the system will not allow him to start the bus. After the system gets started it starts to analyze the several factors of the bus, if any of the factors gets fails alarm unit is turned on and fuel supply to the engine is blocked leading to the prevention of disaster. Similarly some of the sensors are connected to the external surface of the bus to prevent collision with the nearer vehicles. The result of our research idea is done in Auto Cad and the simulations are shown in this paper. Since this research paper is just a proposed system, In future this concept will be implemented with the help of Air Bus Company.

Keywords: *Arm 7 processor, Air bus, GSM module, IR sensor, Vibration Sensor, Speed sensor and Fire sensor*

1. INTRODUCTION

Now a day's people wish to use the public transports than of their personal transports for long distance because of the rise in petrol cost and other economic reasons. Most popular of all transport means bus, now as technology develops the buses have evolved by means of latest technology. In city's people wish to have a fast and more comfortable bus. This leads to the introduction of Volvo buses. These buses are provided with lot of comfort and they are faster than other buses. But at the same time they become the source for the loss of many lives, due to the lack of safety measures and there is no advancement in the technical side of the bus for safety. A few days back in Bangalore, an accident which was happened due to the lack of technical support in the Volvo bus, most of the people died due to the fire in the bus and they have no way to get out of the bus, around 22 people died in this accident. Until this accident has happened none of them have thought of safety measures in these buses. They have brought out some solutions but none of them where technically supported the safety measures which could prevent before the accident could happen.

The first and fore most problem is that it is completely closed. There is only one exit in these buses and they can't rush out at the times of crisis. If they attempt to get out they will harm others and they can't get out. If they try to break the glasses it's not that much possible they are made out of thick glasses. So we have decided to change the fate of this travel into pleasure with safety. We have brought out with clubbed functions of lot of methods, which will prevent the accidents in many ways as possible and it will save many lives. We have big scope of protection in these methods. This not only changes the mode of luxury bus transport this will make a new era in the public transport system. We are going to implement lot of sensors that will sense lots of characteristics of the bus and the driver activities which can be analyzed by the processor and it will give commands to the system accordingly which will make counter actions for the malfunction. There are four different types of sensors used for the sensing and these signals are fed into the processor and if any of the predetermined condition fails the entire system gets shut down.

Several steps have been taken by the government on safety aspects but only very few are following that which will not prevent the accidents in a very high manner. Steps needs to be taken by the Gov. are : 1) Promoting safety videos before starting journey, 2) Drivers must have gone training on safety measures,3) Drivers should be changed for in regular intervals of 150 Km and 4) Bus shouldn't exceed the speed limit of 80km/hr. But at the time of driving driver or anyone could not analyze any of these factors. So we have developed a system that could analyze all these factors and prevent the bus from any accident that may happen. It consists of list of sensors like IR sensor, vibration sensor, speed sensor and fire sensor. Each has separate actions to perform at the time when the system is turned on. This is controlled by the Arm 7 controller if the condition gets fails the fuel supply to the engine is blocked. After starting the engine driver must wear a glass with IR sensor which detects the motions of the eye lids of the driver. If he is in drowsy state his eyelids will stay closed for very long period (for a period of above 3 to 4 sec) by using this data the processor can sends a warning signal through the voice alarm and a new driver has to take his position to drive if not the system will not allow him to drive. If the driver is good enough to handle the condition then almost 70% of the accidents can be reduced.

2. LITERATURE SURVEY

AS per the REF of Hindu News paper reported by Namas Bhojani, Two Gruesome Bus Accidents In India Put Spotlight On Bus Maker Volvo: A 'luxury' bus operated by the state-owned road transport corporation in Bangalore .Two back-to-back bus infernos in recent weeks in India that led to 52 deaths have both involved buses of Swedish bus maker, Volvo. The ghastly accidents have raised questions about safety measures followed by bus operators, as well as the suitability of the European-made buses for Indian conditions. The gruesome disasters have come at a time when buses are becoming an increasingly popular mode of intercity transport in India. "Luxury" buses with comfortable seats and air conditioning are preferred by young, upper-middle classmigrant professionals who travel to and fro between their hometown and their workplace. In both accidents, passengers were burned alive inside, unable to flee the raging flames as the buses burnt down to a carcass. Surviving passengers alleged that they could not spot or access emergency exits. Neither bus had hammers available for passengers to break glass and escape, they said.

Precautions taken to avoid Volvo bus accidents: Road accidents are common on India's highways and claim hundreds of lives each year but rarely do buses burn down at the speed seen in these recent incidents. The accidents have dented the image of Volvo, the foreign bus maker with the highest market sharein India with some 5,000 buses on the roads. Its gleaming, multi-axle, low-chassis buses are favored by both private bus operators as well as regional, state-owned transport corporations. Following the accidents, the government in the southern Karnataka state, of which Bangalore is the capital, ruled that bus operators will have to install emergency exits within three months. The accidents brought to light private bus operators' unscrupulous ways — such as doing away with emergency exits to accommodate extra seats in the 45-to 50-seater buses to increase profitability, with Volvo itself looking the other way. Investigations into the two accidents are currently on. But preliminary studies throw up a multitude of possible reasons – from over speeding by drivers to the use of adulterated fuel that could have accelerated the fire. Volvo said that its own investigation by its global experts is underway. "The investigation will be deep and will cover all aspect around the accident including the circumstances and conditions – external and internal – human aspects, among others," the bus maker said in an email response. It will engage with operators and authorities to take collective measures towards better transport safety, the email said.

As per the Ref Volvo bus accident, Haveri District, Bangalore-Mumbai bus accident, Haveri district hospital, Volvo bus fire. Passenger blames "reckless" driving for Volvo bus accident: A passenger who escaped unhurt from the accident of Mumbai-bound Volvo bus from Bangalore blamed it on the driver for reckless driving. "It was at around 3 a.m., when we were in sleep, we heard a loud noise and then an explosion followed," said Ismail Sheikh (41), a resident of Mumbai Central who had gone to Bangalore to meet his "religious guru" along with three other friends. Thanking his "guru" for saving him, the small scale businessman added: "It was

nothing less than a miracle. I jumped out of the broken window as soon as I sensed that the bus was on fire. Others also tried to break the glass," he told The Hindu over the phone. According to him, many passengers were injured while desperately trying to jump out of the bus. "The driver almost climbed on the road divider. It is possible that he lost his control over the wheel while speeding up," he said.

"**Diesel tank catches fire after rear of the bus hits a bridge**": Seven persons, including five of a family, died and 30 were injured when a multi-axle Volvo bus operating between Bangalore and Mumbai rammed a road median on National Highway 4 near Haveri and caught fire. Forty-two passengers, including two foreign nationals, managed to get out by breaking the glass windows. The toll could well have been higher had it not been for two youngsters who woke up sleeping passengers and smashed the window panes to help them escape. The driver jumped out and is absconding. The second driver, Nawaz, who was asleep in the trunk, was charred to death. The bus belonging to National Travels, owned by a former Minister and Janata Dal (Secular) legislator B.Z. Zameer Ahmed, had left Bangalore around 8 p.m. The accident occurred sometime after 3 a.m. The bus is believed to have veered to the left and hit a bridge at Kunimellihalli village, off Bankapura Cross, rupturing the fuel tank in the process. The fuel spill presumably caused the fire. The accident bears a striking resemblance to the one at Mahbubnagar a fortnight ago in which 45 passengers were charred to death. According to the passengers, the bus was filled with smoke and there was fire on all sides by the time it came to a halt. Some residents of Kunimellihalli village rushed out of their homes on hearing the noise, but could do little as the highway is located at a higher altitude. They saw a few passengers breaking windows and jumping out. Some reached the top through the ventilators and jumped down. It took a while for the fire services personnel to arrive. But by then, the bus was totally gutted. The injured passengers were initially rushed to the district hospital at Haveri. Five with severe burns were later shifted to the Karnataka Institute of Medical Sciences (KIMS) Hospital at Hubli. The condition of two of them is stated to be serious. The identity of all but one of the deceased has been established. Later in the day, 26 passengers left for Mumbai in a bus arranged by the KSRTC. Ten returned to Bangalore.

Posted By Karthick M V on Nov 15, 2013 at 01:49 IST. Accidents will always happen (the law of averages) however, lives can always be saved. He blamed the poor 'exit' design of Volvo bus cabin. You cannot expect people to Jump down six to nine feet. There should be an emergency door on the rear end.

Posted by Shiva on Nov 15, 2013 at 00:45 IST. Back when I was in under-grad, these luxurious buses with comfortable reclining seats, TVs were just popping up. I used them frequently as they were convenient and easy to book. Getting a train ticket is a herculean task when trip is planned in a short span of time. Most of them operate during nights, which is scary. There was always a lingering thought on what would happen if the bus driver fell asleep or was a reckless. It is sad to see that even after ten years of their existence, proper norms aren't enacted by the government. Passengers should at least be educated on emergency exits, when they are aboard. Else panic will reign with co-passengers pushing, hustling and shouting endangering everyone life .Drivers should be well trained and should get enough rest every 4 hours. Depending on the distance, there should be back-up drivers. Proper redressal measures should be put in place when unfortunate things happen. Licenses should be revoked for those found in violation of norms.

Posted by Subramaniam on Nov 14, 2013 at 14:57 IST. There have been 3 such incidents of recent involving Volvo buses, which should be investigated thoroughly. At the same time Govt should ensure that all Volvo's are stopped from operating till adequate safety measures are in place, drivers trained properly, no loading of goods in the lower carriage meant only for passenger goods. I have seen all Volvo's whether PVT or Govt flouting such rules and regulations blatantly. In the safer interest of all passenger's Govt should immediately intervene and act with an iron hand on all operators (Pvt or Govt) owned.

Posted by Rahul on Nov 14, 2013 at 14:57 IST. Main problem is now-a-days there's only 1 driver in bus even for such long distance and many times the helper also drives in between though he doesn't have skills to control/handle the huge vehicle. I have also noticed if there are 2 drivers then there wont be any helper so basically none of the driver get proper sleep.

Posted by sankar on Nov 14, 2013 at 14:54 IST. Speed is the main villain. There should be speed limit of 100 km/h. Our drivers treat the vehicle as a toy and put the passengers to risk. Can't blame the vehicle but speed arresters should be installed. I recently travelled across Europe, around 3500 km in seven days; I never felt that there could be an accident. Speed was never more than 100 km/h.A limit of 8 hours for the driver.. Do we follow any norm. Every time I travel from chennai to madurai or any other place, am scared when the road is very good... because drivers drive at 100 km+ only. Governments should wake up.

The Hindu The accident occurred at around 3.20 a.m. near Kunimelli bridge, off Bankapura Cross in Haveri district. Photo: Sanjay Ritti

The Hindu The bus, operated by Bangalore-based National Travels, was on its way from Bangalore to Mumbai. Photo: Sanjay Ritti

Special Arrangement In this file photo, a Volvo bus burns after its diesel tank burst into flames after hitting a road divider at Palem near Mahbubnagar district of Andhra Pradesh. 45 were killed in the accident

The Times of India, The accident occurred at early morning near Bangalore highway due to the over speed

The Hindu, a Volvo bus burns near Bangalore due to the over speed of the bus catches fire and burst

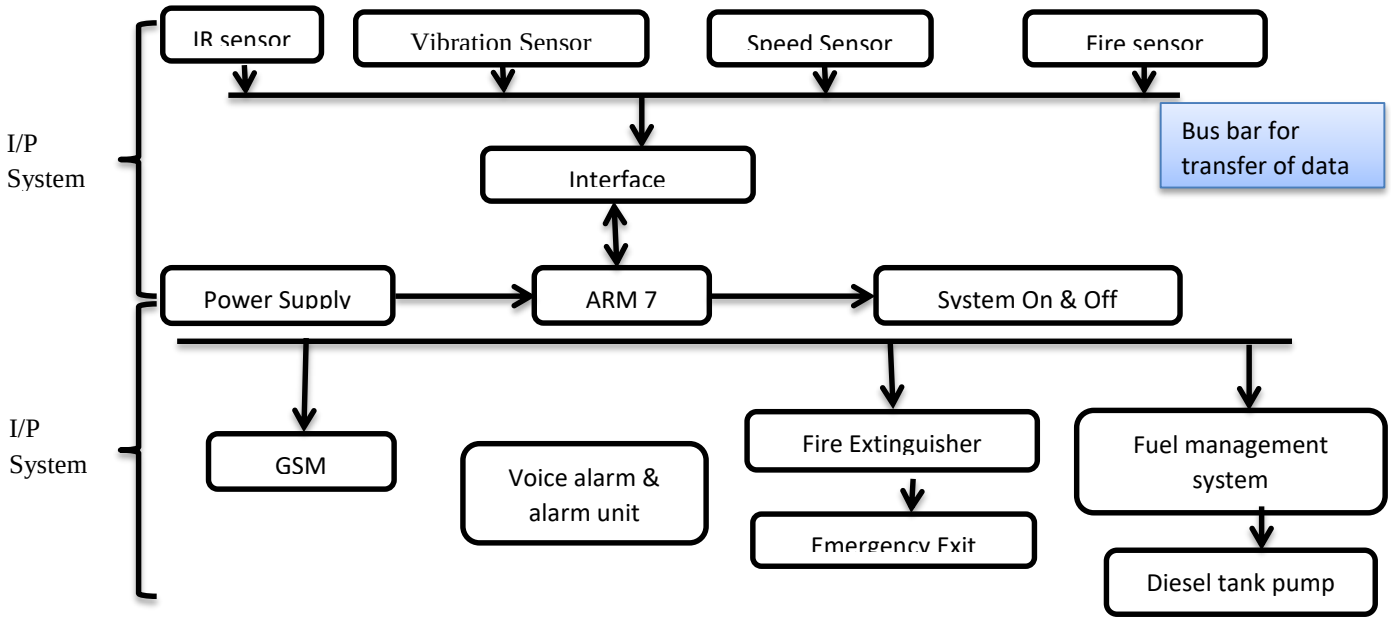

Figure1: Block Diagram of the Proposed system

The Figure 1 depicts the overall functioning of the module and the proposed system incorporates Arm 7 based bus accident prevention system. The proposed system, which is installed at the bus consists of four sensors namely Vibration sensor, Speed sensor, Fire sensor and IR sensor. This four sensors performs four different operations and the input is given to the Arm processer. Vibration sensor has to be attached to the vital parts of the bus. If the vibration get exceeds the predefined range then there is a possibility of getting accident or destroying a part of the bus so it has to be taken into account. This will continuously transmit the signal to the input system and it immediately stop the vehicle by cutting the fuel going to the engine. With in a mean time emergency exit open step by step, First top and followed by side window. Similarly IR sensor also do the same operation as vibration sensor.IR sensor is placed in the front of driver, which senses the eye lid movement of the driver. If the driver is in drowsy state automatically the bus stop by cutting the fuel. In case of fire accident, fire sensor senses the fire and then it gives the input to the arm processer then automatically fire extinguisher turn on and emergency exit open. Voice alarm turn on during above said situations for guiding the passengers by voice instructions. Speed sensor is connected to the speedometer of the bus to analyze the speed of the bus using the counts of rotation per minute. The speed of the bus is monitored frequently in ordered to maintain the stability of the bus if not there is a chance of getting the collision. If the speed gets exceeded then the ARM processor sends a signal to the driver by turning on the alarm to reduce the speed of bus and then speed of the bus gets reduced. If not then automatically the speed of the bus is send to the company IP address or government via GSM module and also cut the fuel to the engine. In several conditions if driver gets panic he may press the accelerator hardly than to press break at the times like that this will efficiently regulate the speed of the bus and it will prevent the bus from getting into the accident. Similarly with the help of same GSM module we can communicate to the near by ambulance, police station, fire rescue and fire service incase of emergency and during accidents. This will help to save the passengers life with in the mean time and communicate to the passengers relative and company IP address during the emergency and accidents.

3. RESULT AND ANALYSIS

AutoCAD is a general purpose Computer Aided Design and Drafting (CAD) program which can be used to create all kinds of line drawings. available since 1982 as a desktop application and since 2010 as a mobile web and cloud-based app, currently marketed as AutoCAD 360.Developed and marketed by Autodesk, Inc AutoCAD was first released in December 1982 having been purchased a year prior in its original form by Autodesk founder John Walker. The software is currently marketed in its eighteenth generation. Emphasis is placed on efficient and accurate drawing techniques incorporating the features, commands, and techniques for creating, editing, and printing 2D production drawings. The latest AutoCAD releases are AutoCAD 2014 and AutoCAD 2014 for Mac. The 2014 release marked the 28th major release for the AutoCAD for Windows. The simulations of the Volvo bus structure is shown in the Auto CAD 2014.

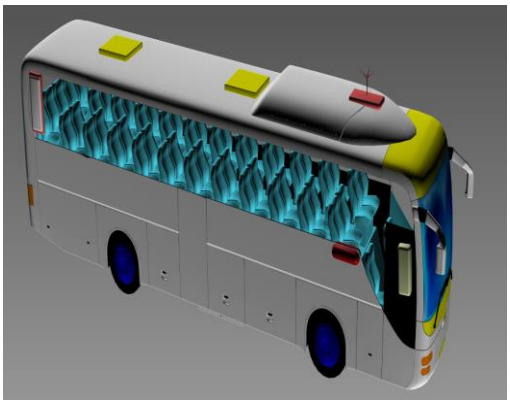

Figure 2: Model of proposed bus system in Auto Cad

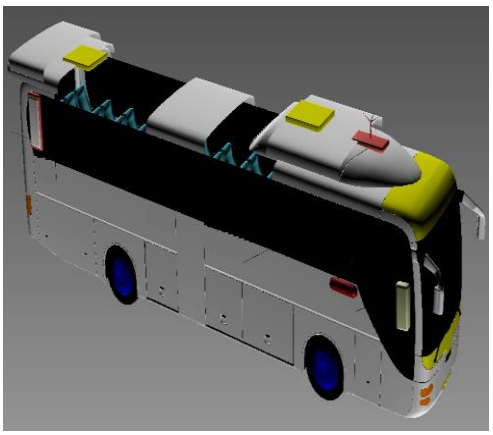

Figure 3: Top view of the Emergency exit open and close in Auto Cad

Figure 2 shows the proposed volvo bus system which consists of the four different types of sensor namely Vibration sensor, IR sensor, Speed sensor and Fire sensor is placed inside the bus inorder to avoid the accident and so ensure safety.These four sensors are controlled by the ARM processor and the decisions are taken according to the inputs received by the ARM processor.

Figure 3 shows a operation of the emergency exit open at the top of the bus in volvo during accident in order to prevent the passenger from injuries. At the time of emergency, there is a need of another exit called emergency exit.In our system we are using the either side of the bus as a exit.This above said process takes place with in a fraction of seconds after the inputs from the sensors given to the ARM processor.The emergency exit open and close after the volvo bus is out of motion (i.e. stopped).

Figure 4 Depicts the function of side window doors open and close during the time of accident. During the accidents people are moving towards a single door side in order to save their life .But they faces a lot of troubles to open the door because the door may struck during the accidents, some times the door was closed outside by the bus operator. There is no way for the passengers to escape outside. They simply fight with others to escape and even break the glass window, which cause injuries to others. To avoid mesh between the passengers and to avoid injuries our proposed system is provided with more ways for exit by opening the side window.

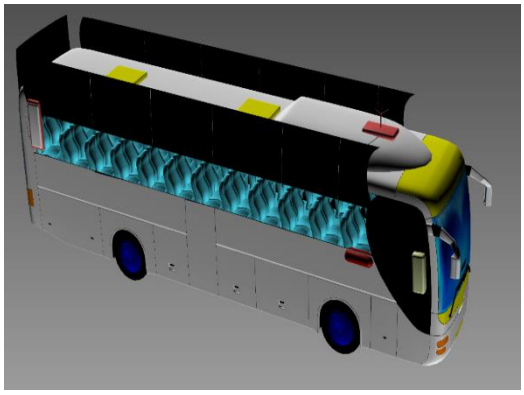

Figure 4: Side view of the glass open and close in Auto Cad

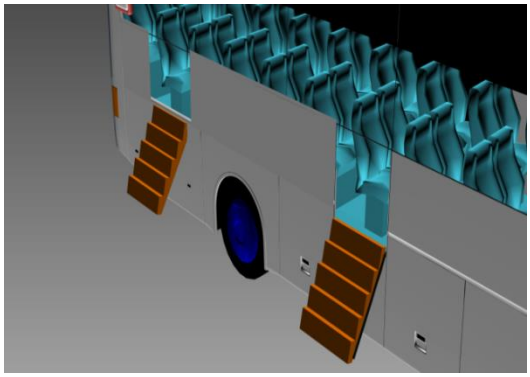

Figure 5: Cross sectional view of Steps opening Auto Cad

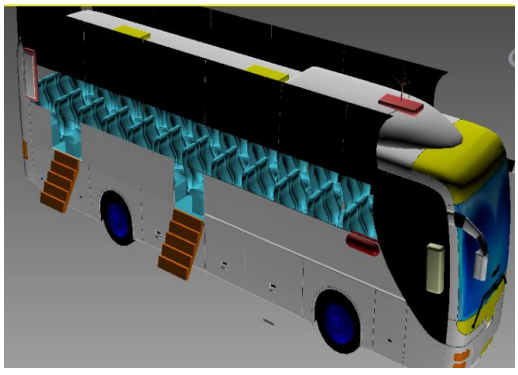

Figure 6: Steps open during the emergency in Auto Cad

Figure 5 shows the process of opening of side steps, which is similar to the opening of steps in the airplanes. This proposed step model overcomes the traditional emergency exit system. In traditional emergency system, emergency exit is placed at the end of the bus. This exit is not opened automatically instead opened by the passenger or conductor. But this is risk, some times the emergency exit get struck and not opened. Other case if we opened the door we want to jump from the bus. This will cause injuries to the passenger and also old people

find it very difficult to jump. So in order to safeguard the passengers and help the old people. Here we placed the step model of emergency exit to escape during accident with out any injury.

Figure 6 depicts the steps open and close during the time of accident. Here we are using sensors at the vital parts of the bus and they send the signal to the ARM processor, which control the entire system It activates the motors to lift the shutters and move the side walls down and it gives a way for the passenger to exit from the bus. Due to the large space to exit they can get out without any trouble.

4. CONCLUSION

In this paper, from our above work, We can conclude that this proposed system can provide a safe, secure and efficient way for avoiding accidents in Airbus. The proposed system, which is installed at the bus consists of four sensors namely Vibration sensor, Speed sensor, Fire sensor and IR sensor. This four sensors performs four different operations and the input is given to the Arm processor under critical condition and it automatically stop the bus and our proposed idea can give benefit to the passenger by saving their life during accidents using the automatic emergency exit and fire extinguisher. GSM is placed inside the bus in order to send the up to date information about the vehicle to the company IP address .During the emergency cases like accidents we can communicate to the near by ambulance, police station, fire rescue and fire service. By implementing this modern transport system in actual practice, due to more safety, government can not only gain more benefits, but also, we can bring our national transport system towards global standards.

REFERENCES

Fouracre PR and Jacobs GD (1976). Comparative Accident costs in developing countries.

TRRL Supplementary Report 206. Crowthorne: Transport Research Laboratory Ghee C, Silcock D, Astrop A, Jacobs GD (1997). Socio-economic aspects of road accidents in developing countries.

TRL Report 247, TRL, Crowthorne, UK. Jacobs G and Aeron Thomas A and Astrop A (2000). Estimating Global Road Fatalities. TRL Report 445, TRL, Crowthorne, UK.

Maunder DAC and Mbara TC (1995). The initial effects of introducing commuter omnibus services in Harare. TRL Report 123, TRL, Crowthorne, UK.

Maunder DAC and Mbara TC (1993). *The effect of ownership on the performance ofstage bus services in Harare*, Zimbabwe. PR25, TRL, Crowthorne, UK.

Maunder DAC and Mbara TC (1996). Liberalisation of urban public transport services: What are the implications? *Indian Journal of Transport Management*, 20:2.

Yamamura Y, Tabe M, Kanehira M. (2001). Development of an adaptive cruise control system with stop and go capability. SAE World Congress [C]. Detroit, Michigan, US.

Li Keqiang, Wang Yuejian, Gao Feng (2006). Vehicle Driving Safety Assistant System Based on ITS Technologies. *Automotive Technology*, 8:32-35, 94.

Shao Yiming, Gao hongbo (2009). Study of active speed control system of autobus. *Highways&Automotive Applications*, (6):10-13

Wu Youling, An Yu (2005). Design of the intelligent alarm system in controlling the automobile speed. *Journal of Chongqing University (Natural science edition)*, 28(12):85-86.

Jansson J, Johansson J. (2002) Decision Making for Collision Avoidance System [A]. 2002 Society of Automotive Engineers. Pennsylvania: *World Headquarters*.

Liu Wei, Xie Xuhui, Li Shengyi (2003). Present state and perspectives of micromachined inertial sensors. *Optics and Precision Engineering*, 11(5):426-430.

Session 3

Energy, Manufacturing & Computational Science

Invited Speakers

Prof. Boris Mordukhovich

Wayne State University

Topic: Variational Analysis: New Trends and Developments

Prof. Priyadarshi Kanungo

C. V. Raman College of Engineering, Bhubaneswar Odisha, India

Topic: Fusion of Temporal and Spatial Segmentation Information for Slow Moving Object Detection

A Survey on Separation of Blood Vessels for Detecting Retinal Vascular Disorders

V. Ellappan*, Satyasis Mishra, and Tadesse Hailu hyana

School of Electrical Engineering & Computing, Adama Science and Technology University, P.O.Box 1888, Adama, Ethiopia
**Corresponding author, e-mail: ellappan.venugopal@astu.edu.et*

ABSTRACT
Separating vascular from the retinal image is essential for detecting many retinal vascular disorders. Diseases which are all affecting the blood vessels of the eye are known as Retinal vascular disorders. Vessel separation of retinal image is a fundamental step in finding the affected area of vascular. Retinal Blood Vessel Separation (RBVS) is necessary for identifying diseases and changes in the retina. For segmenting the blood vessel and early detection of these disorders many different approaches and algorithms have been developed; few of them were discussed in this paper. In this paper, various existing techniques, methodologies, and algorithms for separating the vessels from the retinal image were analyzed. This paper also provides the summary of various existing techniques based on Segmentation methodology, performance matrices, and databases used.

Keywords: *Segmentation, Retina, Blood vessel, Techniques, summary*

1. INTRODUCTION

Eyesight is one of the most important and valued senses in Human Beings. Some eye diseases have no symptoms in their early stages. Some of the disorders of retinal vascular are Diabetic Retinopathy (DR), Hypertensive Retinopathy, Retinal Vein Occlusion (RVO), Central Retinal Artery Occlusion (CRAO), and Glaucoma. Diabetic retinopathy (DR) is a retinal blood vessel disorder of patients who are affected by diabetes mellitus. Diabetes affects the eyes and reduces the strength of blood vessels in the retina. Because of Strength loss, vessels may break down and that may lead to leakage of fluid into the center of the retina (macular edema) or growth of some abnormal blood vessels over the retina surface may lead to bleed and scar. This may cause loss of vision.

DR creates new blindness in adults of developed countries, including India. Almost 31.7 million Indians affected by Diabetic and related complications like vision loss, stroke, and heart failure. DR screening is important for reducing disease burden reported World Health Organization (WHO).The regular direct visual examination is useful for detecting other retinal membrane disorders. In diabetic retinopathy diagnosis blood vessel structure of retina has an important role. For segmenting blood vessel several methods are available.

Features of blood vessels like abnormal branching, tortuosity, entropy, and neovascularization are highlighted during Vessel segmentation. Using automatic RBVS, specialized physicians can provide speed diagnosis and increase their diagnostic performance. Screening image processing highlights anomalies situation compares this image to the previous images and demonstrates the transformation of the retina [20].

Analysis of various section described in this paper as follows. Section II is for providing some information about RBVS. Section III is for giving the descriptive study of few existing works. Section IV is focused on giving a summary of various existing techniques and approaches to RBVS. Section V presents the conclusion.

2. VESSEL SEPARATION TECHNIQUES FOR RETINAL IMAGE

Blood vessel structure of retina has an important role in diabetic retinopathy diagnosis. Various approaches used for segmenting the vessels. Categorization is performed based on the algorithms, and the methodologies used for an image-processing. These methods use distinct techniques for image processing, and each has different merits and demerits in segmenting the blood vessel [1]. Hybrid algorithms are developed because of this property.

Detecting blood vessel of the retina from an image is a continuous process; If it is not executed properly we cannot obtain best-segmented result image. Before performing segmentation, the image should be pre-processed

for removing the noise and for enhancing the contrast between blood vessel of the retina and its background. The segmentation process is fed with an enhanced image for obtaining the segmented image which is further applied to thresholding to obtain the threshold image. Finally, post-processing applied to an image for removing false pixels and obtains the edge map.

3. DESCRIPTIVE STUDY OF FEW EXISTING WORKS

3.1. Robust Vessel Segmentation Based on Reinforcement Local Descriptions

Meng Li et al. [27] proposed segmentation of vessel, based on reinforcement local descriptions. At first, separation of the green channel is performed in the color retinal image. After that features of an image like the local intensity, line sets-based feature, and multi-scale morphology features are extracted.

The local shape of the vessels is expressed using the gray information of the local area revealed by local intensity feature, the line set based features, and the local edge of small vessels enhanced by the morphology gradient feature, which made the reinforcement local description more robust.

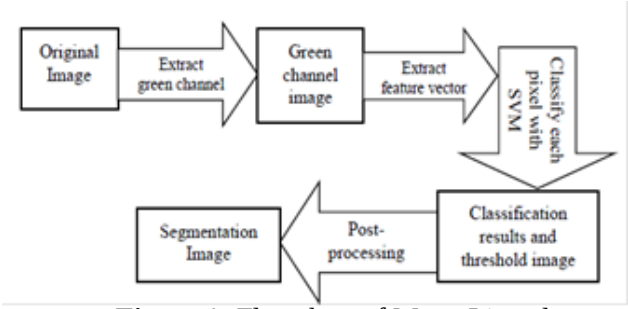

Figure 1: Flowchart of Meng Li et al.

Then the extracted features are combined into the reinforcement local descriptions for each pixel. After feature extraction, SVM used for vessel segmentation which is trained based on the reinforcement local descriptions. Finally, some discontinued thin vessels exist after vessel segmentation by SVM.

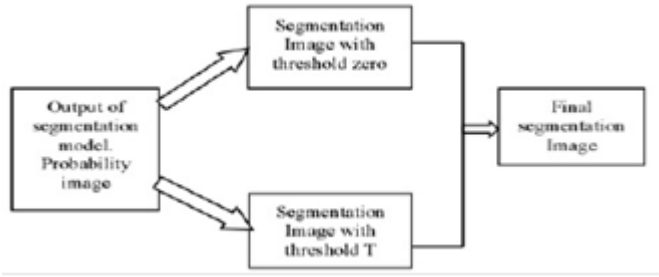

Figure 2: Flowchart of post-processing

For connecting the discontinuous vessels and getting more accurate segmentation image post-processing based on the morphological reconstruction was proposed. It can connect discontinuous vessels without introducing noise. Because of that, the post-processing achieves more accurate segmentation result.

Meng Li et al. randomly selected 1000-pixel samples from each image. Sensitivity is high on STARE database and is accessible on DRIVE database. This gives high accuracy for both databases, which is important for the clinical application.

Table1. Result of Meng Li et al.

Testing Dataset	Training Dataset	Accuracy (Acc)
DRIVE	STARE	0.9626
STARE	DRIVE	0.9626

3.2. Fuzzy C-Mean and Neutrosophic Approach for Disease Detection and Segmentation

Ishmeet and Lalit Singh [10] proposed approach contains three steps for segmenting the blood vessels. That is 1) Image preprocessing 2) Unsupervised approach 3) Image post-processing.

Image preprocessing used for enhancing the quality of the image and making further calculation simple. This step includes extraction of the color channel, enhancing the contrast, unsharp masking and calculating magnitude of the image. Unsupervised approach gets input from above Preprocessing stage.

The unsupervised approach is the clustering process it uses two algorithms, fuzzy c-mean clustering and neutrosophic. This step applied for further differentiation of the image pixels into vessels, non-vessels and indeterminate. Mathematical morphological operations are included in post-processing phase, and the final segmented image is obtained.

Table 2: Result of Ishmeet Kaur and Lalit Mann Singh

Dataset	Average		
	Accuracy (Acc)	**Sensitivity (SN)**	**Specificity (SP)**
DRIVE	98.74%,	98.38%,	94.78%

With the above result, they detected affected portion in a DIARETDB1 dataset with 99.6% of sensitivity. It provides better exactness in vessel segmentation; this may be the powerful tool for diagnosis and useful in early detection of DR.

3.3. Computerized Image Analysis Using Data Mining

Geetha Ramani & Balasubramanian proposed techniques included three stages in vessel segmentation. 1) Pre-processing of an Image, 2) Learning and 3) Post-processing of an Image. The image pre-processing contains the steps of cropping the image, transforming the color space and Extracting the color channel, Enhancing contrast, half-wave rectification, and Gabor filtering.

Here, color space transformation was performed and the color channels (G, Y, L, G1) which exhibited the maximum contrast in each color model was chosen. CLAHE was applied for increase the variance of the pre-processed image.

The output image of this step is given as input to the learning stage. It includes supervised and unsupervised learning. This is a data mining approach; it includes feature vector formulation, PCA application, clustering followed ensemble classification. At this stage, the vessel segmentation problem is viewed as a categorization problem. An image pixel should be categorized based on the pixel of the vessel or not.

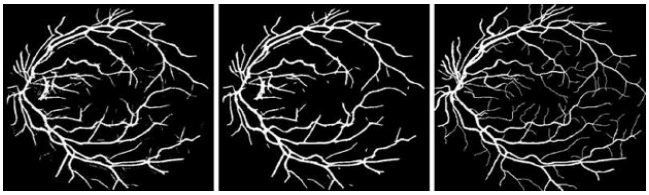

Figure 3: Outcome of data mining phase, post-processing phase and the corresponding sample image (left eye image).

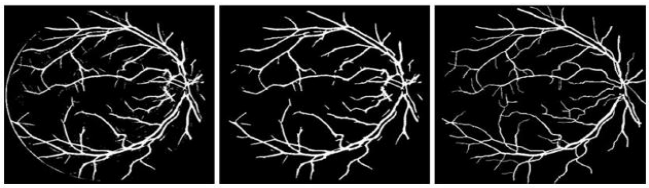

Figure 4: Outcome of data mining phase, post-processing phase and the corresponding sample image (right eye image).

The Post-processing stage done using mathematical morphology techniques and connected component analysis. This step is useful for eliminating unwanted arc. After elimination, isolated vessel pixels and spurs are removed by applying cleaning.

Table 3: Result of Geetha Ramani & Balasubramanian proposed

Matrices Values	Acc	SN	SP	PPV
Average value of normal image	95.36%,	70.79%	97.78%	75.76%
Diseased image	94.70%	74.08%	96.65%.	-
Mean value of normal image	95.52%	69.97%	98.06%	-

Acc – accuracy; PPV- positive predictive value; SN – sensitivity;

3.4. Neural Network Used For Artery/Vein Classification

Binooja & Nisha [1], proposed vessel classification of retinal images is useful for finding changes in the vascular. The proposed method consists of 1) Graph generation 2) Graph Analysis 3) A/V classification 4) Disease Identification.

Graph generation algorithm steps followed by authors a) Vessel Segmentation – this step of assigns a label to all pixels in the image and locate boundaries. b) Vessel centerline extraction - used for obtaining minimally connected centerline vessel graph. c) Graph Extraction - finding the intersection points and terminal points and removing intersection point from vessel centerline graph with its neighbors. d) Graph Modification – identifies the error using i) Node splitting ii) Missing a link and iii) False link and modifies the graph if the error identified.

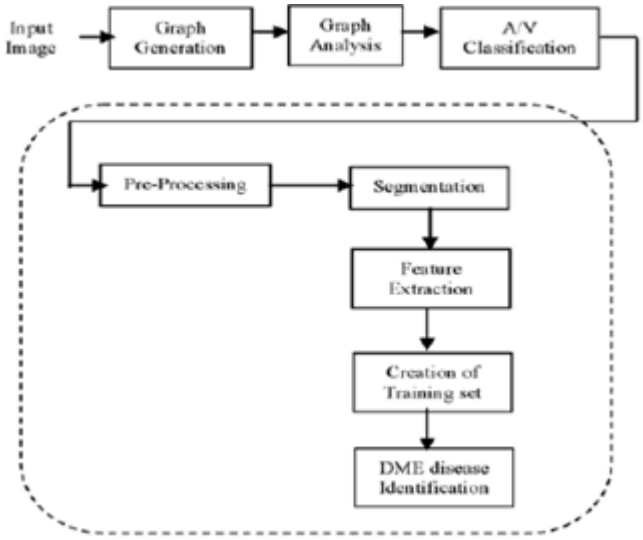

Figure 5: Block Diagram of Disease Identification.

Graph Analysis analyzes various numbers of intersection points and extracts node's information using node classification method. Then every sub-graph is labeled using suitable algorithm till covering the whole retinal image. Using this step, graph with various labeling to its every disjoint sub-graph obtained.

Next step, Disease Identification using Feed Forward Neural network (FFN) to distinguish disease. The framework proposed by Binooja & Nisha has better accuracy, speed, and great execution.

Table 4 (a): Result of Binooja & Nisha

Dataset	Accuracy (Acc)
DRIVE	90%,
VICAVR	92%
INSPIRE-AVR	98%

This system classifies the retinal images as severe and moderate. Result of that is shown in Table 4 (b).

Table 4 (b): Result of Binooja & Nisha

Matrices	Acc	SN	SP
Retinal image	≥	≥	≥
Severe image	0.965	0.800	0.993
Moderate image	0.966	0.802	0.992

3.5. Vessel Localization Using FCM, PS & Bee Colony

Hassanien et al. proposed approach contains three basic building phases. That are 1) Image preprocessing 2) Segmentation 3) Image post-processing. These three phases are explained in figure 6.

At first brightness of green band in the retinal image has been enhanced in preprocessing because it has most contrast. In segmentation, Bee Colony optimization with FCM compactness is used for finding clusters. Then, for refining these clusters PS with thinness function used. After that, segmentation accuracy is improved in the Post-processing phase by removing the gap filling and non-thin connected components.

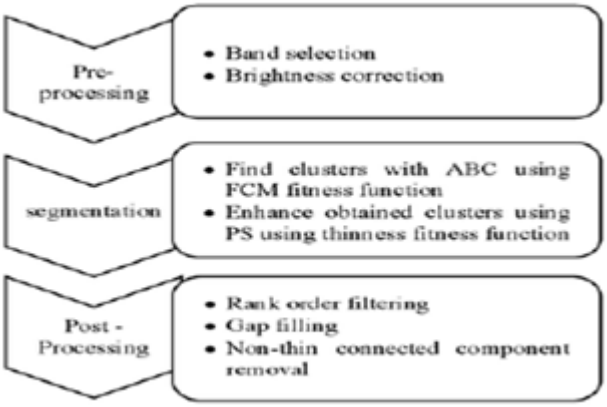

Figure 6: The overall vessel localization algorithm

Vessel segmentation algorithm (ABC-PS) in segmentation phase gets retina image as input and gives vessel segmentation as output. It contains the following steps: 1) Apply ABC algorithm for minimizing the fuzzy compactness function in the image data. 2) Black and white image is constructed using Cluster centers. 3) Clusters are obtained using fitness function of PS algorithm. After each iteration center of the clusters are updated and reconstruction of the binary image performed.

Table 5. Result of Hassanien et al.

Dataset	Accuracy (Acc)	Sensitivity (SN)	Specificity (SP)
DRIVE	0.945	0.868	0.987
STARE	0.961	0.802	0.997

3.6. Vessel Segmentation Algorithm Using Fuzzy Segmentation

In Razieh Akhavan et al. [17] proposed algorithm contains four main parts: 1) Preprocessing, 2) Processing with two phases, 3) Combining. Processing include, 1) Vessel centerline detection, and 2) Fuzzy vessel segmentation. Before extracting, two results obtained from previous steps are combined and then complete pixels belonging to the retinal vessels are extracted.

For making segmentation process easier and reducing the computational time the green channel is obtained from the retinal color image because it contains clear information and provides a maximum contrast. For detecting noise pixels locations within the image Noise Adaptive Fuzzy Switching Median Filter (NAFSM) applied and the noise to be eliminated.

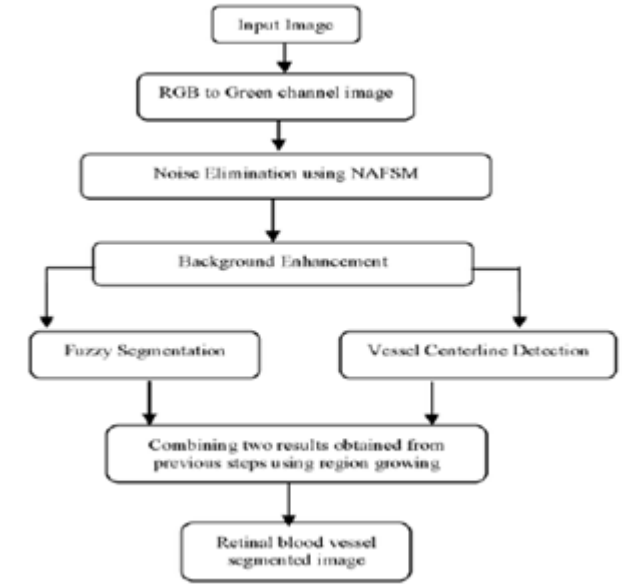

Figure 7: Retinal vessel segmentation functional diagram

After this step, to achieve complete segmentation, retinal vessels filled from start to the detected Centre-lines. For this, Fuzzy C-Means (FCM) clustering technique used. In region growing, pixels of fuzzy segmentation image are connected for filling the vessel centerline pixel which is used as a primary point.

Table 6: Result of Razieh Akhavan et al.

Dataset	Accuracy (Acc)	Sensitivity (SN)	Specificity (SP)
DRIVE	95.13%	75.52%	97.33%
STARE	95.30%	77.60%	96.80%
STARE	95.30%	77.60%	96.80%

3.7. FCM Based Segmentation

Nilanjan Dey et al. [15], proposed Fuzzy C-Means (FCM) based segmentation. Initially, the retinal image's green channel is converted into a grayscale image.

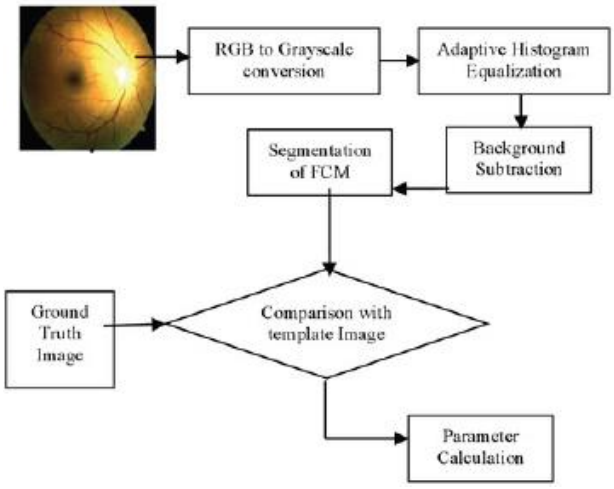

Figure 8: Blood vessel segmentation method

On the gray image, Adaptive histogram equalization is performed. Then, median filter technique is applied for subtracting background from the foreground of the image. After completing binarization and filtering techniques, FCM applied on the image.

Finally, the resulting image and ground truth image are compared for identifying the corresponding disease. For identifying diseases all the measures have been calculated for the resulting image.

This paper deals with the ground truth and FCM segmented retinal blood vessel. For proper segmentation, this algorithm expects good quality (sharpness, contrast, focus etc.) images. Adaptive local thresholding technique is used for detecting thick vessels in a normalized image.

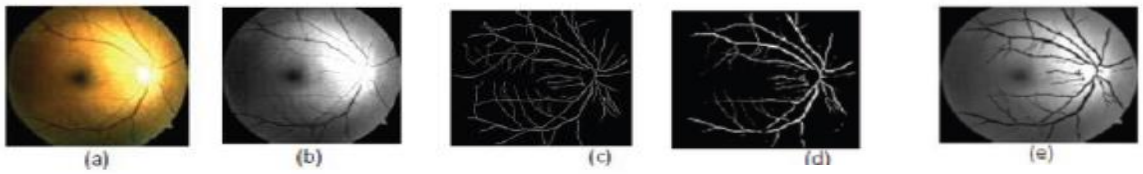

Figure 9: (a) Retinal image, (b) Image of grayscale, (c) Ground truth image, (d) Detected Vessel, (e) Image of the detected vessel.

This proposed algorithm has given a very good performance. This algorithm gives importance to all finer information about blood vessels without referring thick or thin. However, this algorithm gives low Specificity.

Table 7: Result of Nilanjan Dey et al.

Matrices	Values
Accuracy (Acc)	95.03%
Sensitivity (SN)	95.03%
Specificity (SP)	~54.66%
Positive Predictive Value (PPV)	95.08%
Positive Likelihood Ratio (PLR)	219.72

3.8. Semi-Supervised Vessel Segmentation Using SVM

You et al. [43] proposed pre-processing algorithm contains two stages: 1) Enhancement procedure. 2) Vessel pixel selection procedure.

After that Location of the vessel centerlines detected using Radial projection. Radial projection is applied for detecting the low contrast vessel. Pixels come under ROI (Region of Interest) are analyzed using Radial projection for deciding vessel pixel. Then Semi-supervised technique used for extracting Vessel's major structures. For building classifiers, both labeled and large unlabeled examples were used together.

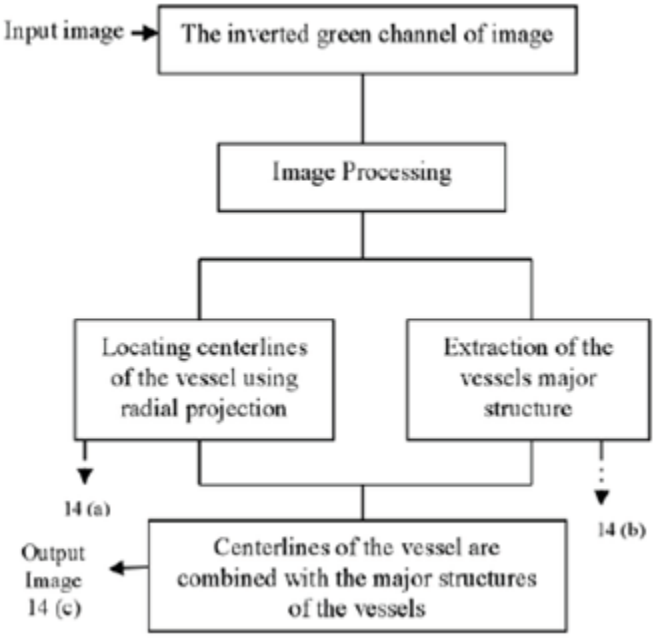

Figure 10: Flowchart of proposed by You et al.

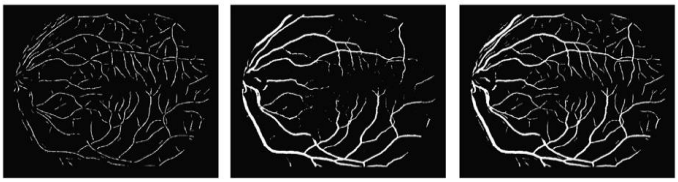

Figure 11: (a) Centerlines of the Vessel (b) Vessel's major structures (c) Vessel segmentation result.

Table 8: Result of You et al.

Dataset	Accuracy (Acc)	Sensitivity (SN)	Specificity (SP)
DRIVE	0.9473	0.7761	0.9773
STARE	0.9516	0.8949	0.9810

The disadvantage of this method is detecting some spots falsely as vessels that may be the optic disc's border and some pathological regions. This method has another drawback also. That is, it overestimates some noises like narrow vessels.

3.9. Clustering and Morphological Process for Image Analyzing

Radha et al. [16]. Proposed method first performs Retina Blood Vessels Detection for Plane separation, Contrast Enhancement, Morphological Process. Then, segmentation technique was used for exudates Detection.

The first, color image is converted into a grayscale image. After that bit plane separation, contrast enhancement and morphological processes like dilation, erosion, closing, and opening are used for extracting the blood vessel. Next, Discrete Wavelet Transform (DWT) & Energy feature coefficients were applied to extract feature.

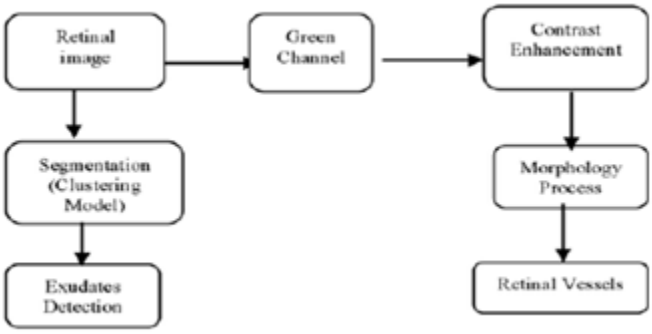

Figure 12: Block diagram proposed by Radha et al.

Then, the extracted features were taken for training with Probabilistic Neural Networks (PNN). For differentiating the hard and soft exudates, K-means Clustering method was applied to segmentation.

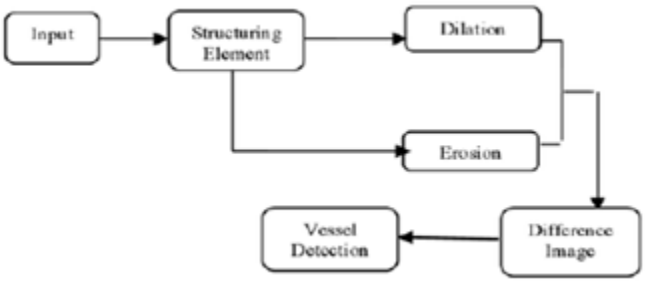

Figure 13: Flow diagram of vessel detection proposed by Radha et al.

After that, the morphological process is applied for smoothing the exudates. Final image helped to determine whether the retina was in normal condition or not.

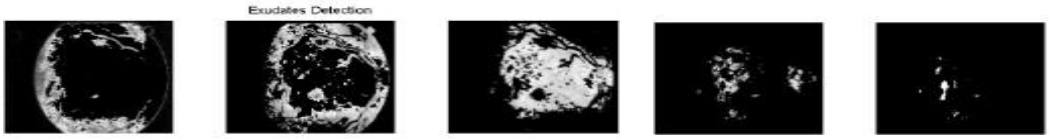

Figure 14: Extracted detection

Here, the Process time was faster while comparing with another clustering with more number of data points. 110 images were tested and trained for producing a better result. It also provided better contrast enhancement, precise detection of retinal vessel and execute.

However, the disadvantage this clustering algorithm is, the number of clusters K must be determined; it yields the different result for each time the algorithm is executed. Also, simple thresholding method was used, therefore, there was missing of some thin vessels.

3.10. Vessel Segmentation Using Moment Invariants and Gray-Level Based Features

Marin et al. proposed method contains following steps. Pre-processing is used for vessel enhancement. Then for identifying a numerical representation of pixels Feature extraction step is performed. After that, classifier used to identify vessel pixels. Finally, to fill pixel gaps and removing falsely-detected isolated pixels post-processing is applied.

Preprocessing contains the following steps: 1) central light reflection is removed from the vessel, 2) background homogenization and 3) enhancing the blood vessel. This step reduces the fault vessels and creates more a suitable image for next step.

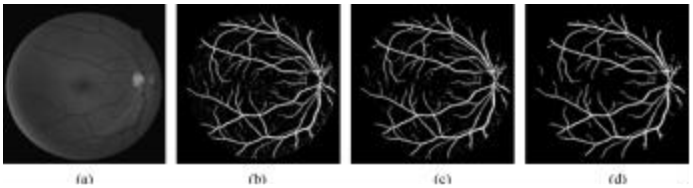

Figure 14: (a) Original image's green channel. (b) An image representation of obtained probability map. (c) Threshold image. (d) Image after Postprocessing.

Feature extraction aims to characterize pixels based on some features, and some quantity measurements are used for representing pixels. This helps to identify the vessel pixels. Here, moment invariants and gray-level based features are used.

They used two stages of classifications. The design stage decides the configuration of NN and training of NN. The application stage uses the trained NN and classifies pixels and creates a binary image of vessels. The performance of Classifier is enhanced using two steps. 1) pixel gap filling and 2) falsely detected vessels removal.

Table 9: Result of Marin et al.

Dataset	Average value					
	TV	Accuracy (Acc)	Sensitivity (SN)	Specificity (SP)	AUC	PPV
DRIVE	0.63	0.9452	0.7076	0.9801	0.9588	0.8433
STARE	0.91	0.9526	0.6944	0.9819	0.9769	0.8227

3.11. Automated Vessel Separation Using Region Features

Fan et al. proposed vessel separation method depends on blood vessel's region feature. In this vessel separation is performed as follows: 1) Vessel enhancement, 2) Vessel segmentation, 3) Vessel combination.

At first, two vessels enhanced binary images are obtained from the color image by thresholding method. In these, one image is preprocessed using IUWT (Isotropic Undecimated Wavelet Transform) and other image is preprocessed using morphological reconstruction. For removing the reflex of vessel central light, morphological top-hat transformation is applied before IUWT.

Figure 15: (a) Vessel improved image; (b) Threshold image; (c) Final image after combining.

Next, vessel's initial images are separated, according to region features of vessel. Area, Bounding Box, Extent, VB Ratio, Convex Area, Solidity, and VC Ratio are used as the region features. These are used to decide whether it is vessel region or not. After that common region of two images are extracted. These are considered as major vessels.

Two initial vessel image's rest of the pixels are processed using simple linear iterative clustering (SLIC) and skeleton extraction. Finally, the processed vessel pixels linked with the major vessels. This method evaluated on STARE and DRIVE datasets. Fan et al. achieved segmentation in less time and consistent accuracy when compared with other methods.

Table 10: Result of Fan et al.

Dataset	Accuracy (Acc)	Sensitivity (SN)	Specificity (SP)	Time
DRIVE	0.9578 (0.0038)	0.7408 (0.0569)	0.9788 (0.0063)	9.7080 (0.7892)
STARE	0.9580 (0.0075)	0.7880 (0.1268)	0.9716 (0.0121)	14.5802 (1.7566)
STARE Normal	0.9600 (0.0063)	0.8400 (0.1083)	0.9689 (0.0112)	15.2403 (1.7185)
STARE Abnormal	0.9561 (0.0084)	0.7360 (0.1274)	0.9743 (0.0129)	13.9200 (1.6101)

4. CONCLUSION

This paper presents different techniques used for segmenting the blood vessel and classifies existing blood vessel segmentation techniques. Blood vessel structure of retina has an important role in diabetic retinopathy diagnosis. RBVS is used to identify DR at an earlier stage. The accurate result of vascular segmentation is necessary for effectively screening and diagnosis most of the eye diseases. Many algorithms and techniques for segmenting the vessels have been proposed and developed, but still, it requires advanced techniques for accurate detection different eye diseases.

REFERENCES

[1]. Early Treatment Diabetic Retinopathy Study research group. Early photocoagulation for diabetic retinopathy. ETDRS Rep. 9. Ophthalmology. 1991; 98(5 suppl):766–785. [PubMed: 2062512].

[2]. Behdad Dashtbozorg, Ana Maria Mendonca [2014], Senior Member, IEEE, and Aurelio Campeche, Member, IEEE An Automatic Graph-Based Approach for Artery/Vein Classification in Retinal Images, vol. 23, NO. 3, March.

[3]. Binooja. B.R, Nisha. A.V, (2015) "Diabetic Macular Edema Detection by Artery/Vein Classification Using Neural Network neural network", International Journal of Engineering and Technical Research (IJETR) ISSN: 2321-0869 (O) 2454-4698 (P), Volume-3, Issue-7, July.

[4]. Cheng.J, J. Liu, Y. Xu, F. Yin, D. Wong, N.-M. Tan, D. Tao, C.-Y. Cheng, T. Aung, and T. Y. Wong [2013], "Super-pixel classification based optic disc and optic cup segmentation for glaucoma screening," IEEE Transactions on Medical Imaging, vol. 32, no. 6, pp. 1019–1032, June.

[5]. Condurache A.P. and A. Mertins. 2012. Segmentation of retinal vessels with a hysteresis binary-classification paradigm. Computerized Medical Imaging and Graphics, 36(4): 325–335.

[6]. Fathi, A. and A.R. Naghsh-Nilchi. 2013. Automatic wavelet-based retinal blood vessels segmentation and vessel diameter estimation. Biomedical Signal Processing and Control, 8(1): 71–80.

[7]. Fan.Z, J. Lu, and Y. Rong,[2016] "Automated blood vessel segmentation of fundus images using region features of vessels," in Computational Intelligence (SSCI), 2016 IEEE Symposium Series on. IEEE, , pp.1–6.

[8]. Fraz, M.M., S.A. Barman, P. Remagnino, A. Hoppe, A. Basit, B. Uyyanonvara, A.R. Rudnicka and C.G. Owen. [2012a]. An approach to localize the retinal blood vessels using bit planes and Centreline detection. Computer Methods and Programs in Biomedicine, 108(2): 600–606.

[9]. Fraz, M.M., S.A. Barman, P. Remagnino, A. Hoppe, A. Basit, B. Uyyanonvara, A.R. Rudnicka and C.G. Owen. [2012b]. Blood vessel segmentation methodologies in retinal images—A survey. Computer Methods and Programs in Biomedicine, 108(1): 407–433.

[10].Fraz, M.M., P. Remagnino, A. Hoppe, B. Uyyanonvara, A.R. Rudnicka, C.G. Owen and S.A. Barman. [2012c]. An ensemble classification based approach applied to retinal blood vessel segmentation. IEEE Transactions on Biomedical Engineering, 59(9): 2538–2548.

[11].Fraz, M.M., P. Remagnino, A. Hoppe, B. Uyyanonvara, C. Owen, A.R. Rudnicka and S.A. Barman. [2011]. Retinal vessel extraction using first-order derivative of Gaussian and morphological process¬ing. Advances in Visual Computing. Springer: Berlin, pp. 410–420.

[12].Fraz, M.M., A. R. Rudnicka, C. G. Owen, and S. A. Barman,[2014] "Delineation of blood vessels in Paediatric retinal images using decision trees-based ensemble classification," International Journal of Computer Assisted Radiology and Surgery, vol. 9, no. 5, pp. 795–811.

[13].Gegundez-Arias, M.E., A. Aquino, J.M. Bravo and D. Marin. [2012.] A function for quality evaluation of retinal vessel segmentations. IEEE Transactions on Medical Imaging, 31(2): 231–239.

[14].Geetha Ramani.R and L. Balasubramanian, [2016]. "Retinal blood vessel segmentation employing image processing and data mining techniques for computerized retinal image analysis", Biocybernetics and Biomedical Engineering, vol. 36, no. 1, pp. 102-118.

[15].Giachetti.A, L. Ballerini, and E. Trucco, [2014]"Accurate and reliable segmentation of the optic disc in digital fundus images," Journal of Medical Imaging, vol. 1, no. 2, p. 024001.
[16]. Hassanien.A.E, E. Emary, and H. M. Zawbaa, [2015] ―Retinal blood vessel localization approach based on bee colony swarm optimization, fuzzy c-means and pattern search, Journal of Visual Communication and Image Representation, vol. 31, pp. 186–196.
[17]. Hou. Y, [2014]. "Automatic Segmentation of Retinal Blood Vessels Based on Improved Multiscale Line Detection," in Journal of Computing Science and Engineering, vol.8, pp. 119 - 128,
[18]. Ishmeet Kaur & Lalit Mann Singh[2016] "A Method of Disease Detection and Segmentation of Retinal Blood Vessels using Fuzzy C-Means and Neutrosophic Approach" Vol-2, Issue-6,.
[19]. Kanski, J.J. and B. Bowling. [2011]. Clinical Ophthalmology: A Systematic Approach. 7th ed. London: Elsevier Health Sciences.
[20]. Klein R, Klein B.[1995] "Vision disorders in diabetes." In: National Diabetes Data Group, ed. Diabetes in America. 2nd ed. Bethesda, MD: National Institutes of Health, National Institute of Diabetes and Digestive and Kidney Diseases;, pp. 293-337.
[21]. Li. Q., J. You and D. Zhang. [2012]. Vessel segmentation and width estimation in retinal images using mul¬tiscale production of matched filter responses. Expert Systems with Applications, 39(9): 7600–7610.
[22]. Liskowski. P and K. Krawiec,[2016.] "Segmenting retinal blood vessels with deep neural networks," IEEE Transactions on Medical Imaging, vol. 35, pp. 1–1,
[23]. Marin. D, M. E. Gegundez-Arias, A. Suero, and J. M. Bravo[2015], "Obtaining optic disc center and pixel region by automatic thresholding methods on morphologically processed fundus images," Computer Methods and Programs in Biomedicine, vol. 118, no. 2, pp. 173 –185,.
[24]. Marin, D., A. Aquino, M.E. Gegundez-Arias and J.M. Bravo. [2011] A new supervised method for blood vessel segmentation in retinal images by using gray-level and moment invariants-based features. IEEE Transactions on Medical Imaging, 30(1): 146–158.
[25]. Mehrotra.A et. al, [2014] Blood Vessel Extraction for Retinal Images Using Morphological Operator and KCN Clustering", IEEE International Advance Computing Conference (IACC).
[26]. Mendonca.A, B. Dashtbozorg, and A. Campilho,[2013] "Segmentation of the vascular network of the retina," in Image Analysis and Modeling in Opthalmology, E. Y. K. Ng, U. R. Acharya, J. S. Suri, and A. Campilho, Eds. Boca Raton, FL, USA: CRC Press.
[27]. Meng Li, ZhenshenMa, Chao Liu, Guang Zhang, and Zhe Han. [2017]. Robust Retinal Blood Vessel Segmentation Based on Reinforcement Local Descriptions. Hindawi, BioMed Research International Volume 2017, Article ID 2028946, 9 pages. https://doi.org/10.1155/2017/2028946
[28]. Miri, M.S. and A. Mahloojifar. [2011] Retinal image analysis using curvelet transform and multi-struc-ture elements morphology by reconstruction. IEEE Transactions on Biomedical Engineering, 58(5): 1183–1192.
[29]. Moghimirad, E., S. Hamid Rezatofighi and H. Soltanian-Zadeh. [2012] Retinal vessel segmentation using a multi-scale medialness function. Computers in Biology and Medicine, 42(1): 50–60.
[30]. Nilanjan Dey, Anamitra Bardhan Roy, Moumita Pal, Achintya Das,[2012] ―FCM based blood vessel segmentation method for retinal image‖, International Journal of Computer Science and Network (IJCSN), Volume 1, Issue 3, June, ISSN 2277-5420.
[31]. Ocbagabir.H, I. Hameed, S. Abdulmalik and D. B. Buket,[2013] "A Novel Vessel Segmentation Algorithm in Color Images of the Retina", IEEE Applications and Technology Conference in Systems, pp. 1-6, May..
[32]. Orlando.J.I, E. Prokofyeva, and M. B. Blaschko,[2017] "A discriminatively trained fully connected conditional random field model for blood vessel segmentation in fundus images," IEEE Transactions on Biomedical Engineering, vol. 64, no. 1, pp. 16–27,.
[33]. Quellec, G., M. Lamard, M.D. Abràmoff, E. Decencière,[2012],B. Lay, A. Erginay, B. Cochener and G. Cazuguel.. A multiple-instance learning framework for diabetic retinopathy screening. Medical Image Analysis, 16(6): 1228–1240.
[34]. Radha R and Bijee Lakshman, ―Retinal image analysis using morphological process and clustering technique, SIPIJ Vol.4, No.6, December 2013.
[35]. Roychowdhury. S, D. D. Koozekanani , Keshab K and Parhi, (2014). "Blood Vessel Segmentation of Fundus Images by Major Vessel Extraction and Sub -Image Classification, " in Biomedical and Health Informatics, IEEE Journal, pp. 2168-2194,
[36]. Sangmesh Biradar, A.S.Jadhav [2015]"A Survey on Blood Vessel Segmentation and Optic Disc Segmentation of Retinal Images",. International Journal of Advanced Research in Computer and Communication Engineering, Vol. 4, Issue 5, May.
[37]. Salazar- Gonzalez.A, D.l Kaba, Y. Li and X. Liu,[(2014) "Segmentation of Blood Vessels and Optic Disc in Retinal Images," in IEEE Journal of Biomedical and Health Informatics, pp. 2168-2194,.

[38]. Saffarzadeh.V.M, A. Osareh, and B. Shadgar, [2014] "Vessel segmentation in retinal images using multi-scale line operator and K-means clustering," Journal of Medical Signals and Sensors, vol. 4, no. 2, p. 122,.
[39]. Singh, G., Krishna, V., & Chakraborty, C. (2012). Expert Systems with Applications. 2-D Gabor filter followed by hysteresis thresholding
[40]. Shijian, L. and L. Joo Hwee. [2011]. Automatic optic disc detection from retinal images by a line opera-tor. IEEE Transactions on Biomedical Engineering, 58(1): 88–94.
[41]. Sivakumar B, Srilatha.K,"[2016] A Survey Based on Blood Vessel and Optic Disc Segmentation" Research Journal of Pharmaceutical, Biological and Chemical Sciences, ISSN: 0975 – 8585, July– August, RJPBCS 7(4), Page No. 63.
[42]. Tagore M.R.N, Giri Babu Kande, E.V.Krishna Rao, and B.Prabhakar Rao,[2013]"Segmentation of Retinal Vasculature using Phase Congruency and Hierarchical Clustering", International Conference on Advances in Computing, Communications and Informatics (ICACCI).
[43]. Wang. Y, G. Ji, P. Lin, and E. Trucco, "Retinal vessel segmentation using multiwavelet kernels and multiscale hierarchical decomposition," Pattern Recognition, vol. 46, no. 8, pp. 2117– 2133, 2013.
[44]. Xiao. Z, M. Adel, and S. Bourennane, "Bayesian method with spatial constraint for retinal vessel segmentation," Computational and Mathematical Methods in Medicine, vol. 2013, Article ID 401413, 9 pages, 2013.
[45]. Xu, X., M. Niemeijer, Q. Song, M. Sonka, M.K. Garvin, J.M. Reinhardt and M.D. Abràmoff. [2011] Vessel boundary delineation on fundus images using graph-based approach. IEEE Transactions on Medical Imaging, 30(6): 1184–1191.
[46]. Yin. Y, M. Adel, and S. Bourennane, [2013] "Automatic segmentation and measurement of vasculature in retinal fundus images using probabilistic formulation," Computational and Mathematical Methods in Medicine, vol. 2013, Article ID260410, 16pages.
[47]. Yin. Y., M. Adel and S. Bourennane. [2012] Retinal vessel segmentation using a probabilistic tracking method. Pattern Recognition, 45(4): 1235–1244.
[48]. You. X., Q. Peng, Y. Yuan, Y.-M. Cheung and J. Lei. [2011] Segmentation of retinal blood vessels using the radial projection and semi-supervised approach. Pattern Recognition, 44(10–11): 2314–2324.
[49]. Yuan. Y., L. Yishan and A.C.S. Chung. [2011] VE-LLI-VO: Vessel enhancement using local line inte-gralsandvariationaloptimization.

Magnetohydrodynamic Boundary Layer Flow of Nanofluid Past a Wedge Embedded in a Porous Medium

Ayele Tulu[1,*], Wubshet Ibrahim[2]

[1]*Department of Mathematics, Wollega University, Nekemte, Ethiopia*
[2]*Department of Mathematics, Ambo University, Ambo, Ethiopia*
**Corresponding author, e-mail: ayeletulu@ymail.com*

ABSTRACT

The problem of two-dimensional steady laminar Magnetohydrodynamic (MHD) boundary layer flow past a wedge with heat and mass transfer of nanofluid embedded in a porous medium is presented in this study. An incompressible viscous fluid in the presence of a transverse magnetic field with viscous dissipation, Brownian motion and thermophoresis effect is considered. Using suitable similarity transformations, the governing partial differential equations have been transformed into nonlinear higher order ordinary differential equations. The transmuted model is shown to be controlled by a number of thermophysical parameters, viz. the pressure gradient, magnetic, permeability, Prandtl number, Lewis number, Brownian motion, Thermophoresis and Eckert number. The problem is solved numerically using the recently developed numerical technique known as spectral quasilinearization method (SQLM). The accuracy of the method is checked against the previously published results and an excellent agreement has been obtained. For different thermophysical parameters, the numerical results of the velocity, temperature and nanoparticle concentration profiles are presented in graphical form. Furthermore, the skin friction coefficient, local Nusselt number and local Sherwood number are presented in tabular form. The result of the study reveals that, the thickness of velocity boundary layer reduces with an increase in pressure gradient, permeability and magnetic parameters. Thermal boundary layer thickness increases with an increase in Eckert number, Brownian motion and thermophoresis parameters. Greater the value of Prandtl number, Lewis number, Brownian motion and magnetic parameter reduce the nanoparticles concentration boundary layer. Moreover, the result shows that the skin-friction at the surface enhances with an increase in pressure gradient, permeability and magnetic parameters. The local Nusselt number is a decreasing function of the pressure gradient parameter, magnetic parameter, permeability parameter, thermophoresis parameter and Eckert number. Finally, following the obtained results, conclusions are indicated.

Keywords: *Wedge flow, Nanofluid, Porous medium, viscous dissipation, Spectral quasilinearization*

1. INTRODUCTION

Fluid flows with heat and mass transfer over a wedge shaped bodies is ensured in many thermal engineering applications like crude oil extraction, geothermal systems, thermal insulation, heat exchangers and the storage of nuclear waste, etc. (Nagendramma et al., 2015). A model of steady laminar fluid flow over a wedge has developed for the first time by Falkner and Skan (1931) to illustrate the application of Prandtl's boundary layer theory. Late, Hartree (1937) investigated the same problem with similarity transformation and gave numerical results for wall shear stress for different values of the wedge angle. Eckert (1942) also solved Falkner-Skan flow along an isothermal wedge and presented the first wall heat transfer values. Afterward, the variety of applications and understanding of the physical features of laminar boundary layer flow past a wedge have motivated many researchers.

Magnetohydrodynamic (MHD) is the study of fluid flow in electrically conducting fluids with magnetic properties that affect fluid flow characteristics. When a magnetic field is incident in an electrically conducting fluid, current is induced. This effect polarizes the fluid and as a result the magnetic field is changed. Due to extensive practical applications of MHD in technological processes such as plasma studies, petroleum industries, MHD power generator designs, design for cooling of nuclear reactors, construction of heat exchangers and on the performance of many other systems, there are many studies that considered MHD fluid flow past a wedge. These include the work of Abbasbandy et al. (2014) who examined the effects of MHD in the Falken-Skan flow of

Maxwell fluid, and Khan et al. (2014) analyzed MHD laminar boundary layer flow past a wedge with the influence of thermal radiation, heat generation and chemical reaction.

In the past few years, MHD boundary layer flow with heat and mass transfer of nanofluids has become a major topic of modern-day interest. Nanofluids have a significant role in enhancing the heat transfer properties of fluids. The most important properties of nanofluids are enhanced effective fluid thermal conductivity and heat transfer coefficient. Some recent studies on MHD boundary layer flow of nanofluid include the work of the Srinivasacharya et al. (2015) who analyzed the steady laminar MHD flow in a nanofluid over a wedge in the presence of a variable magnetic field, and Rasheed et al. (2017) investigated MHD boundary layer flow of nanofluid over a continuously moving stretching surface.

Viscous dissipation effect changes the temperature distribution by playing a role like energy source, which leads to affected heat transfer rate and hence needs to be considered in heat transfer problems. The analysis of MHD boundary layer flows in porous media with and without the effect of viscous dissipation has been a subject of several recent papers. Arthur et al. (2014) analyzed hydro magnetic stagnation point flow over a porous stretching surface in the presence of radiation and viscous dissipation. Ramesh et al. (2017) studied the MHD boundary layer flow past a constant wedge within porous media. Heat and mass transfer of MHD flow of nanofluids in the presence of viscous dissipation effects is numerically analyzed by (Eshetu Haile and Shankar, 2015). Majesty et al. (2016) also studied the effect of viscous dissipation on MHD boundary layer flow past a wedge through porous medium. They concluded that viscous dissipation produces heat due to drag between the fluid particles, which cause an increase in fluid temperature.

Most of the standard methods of solving the boundary layer problems are the numerical approach based on the shooting algorithm with the Runge-Kutta scheme, finite difference method, spectral homotopy analysis method, and Newton-Raphson based methods such as the quasilinearization method and the successive linearization method. Recently, spectral based numerical techniques such as the spectral quasilinearization method and spectral relaxation method have been developed (see Motsa, 2013; Motsa et al. 2014). As indicated by Motsa et al. (2013b) Chebyshev spectral collocation methods are easy to implement, adaptable to various problems and provide more accurate approximations with a relatively small number of unknowns. Furthermore, Motsa et al. (2014a) stated that the interest in using Chebyshev spectral collocation methods in solving nonlinear PDEs stems from the fact that these methods require less grid points to achieve accurate results and efficient compared to traditional methods like finite difference and finite element methods.

The objectives of the present study is to investigate MHD boundary layer flow past a wedge with heat and mass transfer of Nanofluid embedded in a porous medium with viscous dissipation, Brownian motion and thermophoresis effects. Using appropriate similarity transformation, the governing nonlinear partial differential equations are reduced to non-linear higher order ordinary differential equations. These equations are then numerically solved by Spectral quasilinearization method. The effects of different parameters on velocity, temperature and concentration fields are investigated and analyzed with the help of their graphical representations.

2. MATHEMATICAL FORMULATION AND METHOD OF SOLUTION

We consider steady two-dimensional, laminar boundary layer flow past a wedge with heat transfer of incompressible electrically conducting nanofluid embedded in a porous medium with viscous dissipation effects. The coordinate system is chosen with x coordinate pointing parallel to the plate in the direction of the flow and y coordinate pointing towards the free stream, as shown in the Fig. 1 below. The wall of the wedge is maintained with uniform and constant temperature T_w and nanoparticle concentration C_w. T_w and C_w are respectively, greater than the ambient temperature T_∞ and ambient nanoparticle concentration C_∞. The fluid is assumed to have constant physical properties. It is also assumed that a constant magnetic field B_0 is applied in the positive y-direction, normal to the walls of the wedge. The induced magnetic field caused by the motion of electrically conducting fluid is neglected, as it is very small compared to magnetic field (Ullah et al., 2016).

We use the general model of the conservation equation for a general scalar variable φ which can be expressed as (see Versteeg and Malalasekera, 2007)

$$\frac{\partial(\rho\varphi)}{\partial t} + \nabla.(\rho\boldsymbol{u}\varphi) = \nabla.(\Gamma\nabla\varphi) + S_{\varphi} \qquad (1)$$

Where, the velocity vector given by $\mathbf{u} = < u, v, w >$, ρ is density of the fluid, Γ is the diffusion coefficient and S_{φ} is the source term. Equation (1) is the so-called transport equation for property φ, and it clearly highlights the various transport processes. By setting φ equal to 1, **u**, temperature of fluid T, and nanoparticle concentration C in equation (1), and selecting appropriate values for diffusion coefficient Γ and source terms S_{φ}, we obtain special forms of PDEs (Navier-Stokes equations).

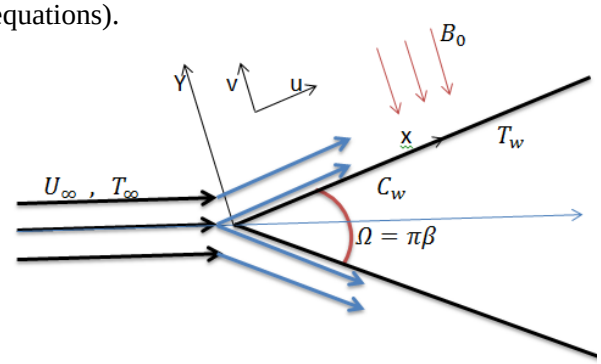

Figure 1: Physical model of flow configuration and coordinate system.

With the above assumptions and the boundary layer approximations, the continuity, momentum, energy and nanoparticle concentration equations governing steady two dimensional MHD boundary layer flow past a wedge embedded in a porous medium with viscous dissipation effects and constant fluid properties are given as (see Srinivasacharya et al., 2015; Haile and Shankar, 2015; Alam et al., 2017).

$$\frac{\partial u}{\partial x} + \frac{\partial v}{\partial y} = 0 \qquad (2)$$

$$u\frac{\partial u}{\partial x} + v\frac{\partial u}{\partial y} = -\frac{1}{\rho}\frac{\partial p}{\partial x} + \nu\frac{\partial^2 u}{\partial y^2} - \left(\frac{\sigma {B_0}^2}{\rho} + \frac{\nu}{K}\right)u \qquad (3)$$

$$u\frac{\partial T}{\partial x} + v\frac{\partial T}{\partial y} = \alpha\frac{\partial^2 T}{\partial y^2} + \frac{\nu}{c_p}\left(\frac{\partial u}{\partial y}\right)^2 + \tau\left\{D_B\left(\frac{\partial T}{\partial y}\frac{\partial C}{\partial y}\right) + \frac{D_T}{T_\infty}\left(\frac{\partial T}{\partial y}\right)^2\right\} \qquad (4)$$

$$u\frac{\partial C}{\partial x} + v\frac{\partial C}{\partial y} = D_B\frac{\partial^2 C}{\partial y^2} + \frac{D_T}{T_\infty}\frac{\partial^2 T}{\partial y^2} \qquad (5)$$

The appropriate boundary conditions are given as:

$$u = 0; \quad v = 0; \quad T = T_w; \quad C = C_w \quad at\ y = 0$$
$$u \to U(x) = U_\infty x^m; \quad T \to T_\infty; \quad C \to C_\infty \quad as\ y \to \infty \qquad (6)$$

Where, u and v are respectively, the x and y velocity components. ρ, ν, α and c_p, are respectively, density, kinematic viscosity, thermal diffusivity and specific heat capacity of the base fluid. K is the permeability of porous medium, D_B is the Brownian diffusion coefficient, D_T is the thermophoresis diffusion coefficient, τ is the ratio of the effective specific heat capacity of the nanoparticle material and the specific heat capacity of base fluid.

We assume that $U(x) = U_\infty x^m$ is the fluid velocity at the wedge outside the boundary layer, where U_∞ is the free stream velocity. For a uniform stream, the momentum equation (3) becomes (see Falkner and Skan, 1931).

$$-\frac{1}{\rho}\frac{\partial p}{\partial x} = U\frac{dU}{dx} + \left(\frac{\sigma {B_0}^2}{\rho} + \frac{\nu}{K}\right)U \tag{7}$$

Substituting (7) in (3), the momentum equation written as

$$u\frac{\partial u}{\partial x} + v\frac{\partial u}{\partial y} = U\frac{dU}{dx} + \nu\frac{\partial^2 u}{\partial y^2} + \left(\frac{\sigma {B_0}^2}{\rho} + \frac{\nu}{K}\right)(U-u) \tag{8}$$

Here, x is measured from the tip of the wedge, m is the Falkner-Skan power-law parameter, $\beta = \frac{2m}{1+m}$ is the Hartree pressure gradient parameter corresponding to $\beta = \frac{\Omega}{\pi}$ for the total angle Ω of the wedge (see Figure 1). Physically, $m < 0$ corresponding to an adverse pressure gradient (often resulting in boundary layer separation) while $m > 0$ represents favorable pressure gradient (Nagendramma et al., 2015). In the Blasius solution $m = 0$ corresponding to an angle of attack of zero radians, where $m = 1$ corresponding to stagnation point flow.

In order to transform the governing equations (2)-(6) into a set of ordinary differential equations, we introduce the stream function $\psi(x,y)$ such that $u = \frac{\partial \psi}{\partial y}$; $v = -\frac{\partial \psi}{\partial x}$ and, we use the following transformation variables:

$$\eta = y\sqrt{\frac{1+m}{2}\frac{U_\infty}{\nu}}\,x^{\frac{m-1}{2}}; \quad \psi(x,\eta) = y\sqrt{\frac{2}{1+m}\nu U_\infty}\,x^{\frac{m+1}{2}}f(\eta); \quad \theta(\eta) = \frac{T-T_\infty}{T_w-T_\infty}; \quad \phi(\eta) = \frac{C-C_\infty}{C_w-C_\infty}$$

Where, η is a dimensionless similarity variable, $f(\eta)$ non-dimensional stream function, $f'(\eta)$ is non-dimensional velocity, $\theta(\eta)$ is non-dimensional temperature, $\phi(\eta)$ is non-dimensional nanoparticle concentration. We find that continuity equation (2) is identically satisfied, and upon substituting similarity variables into equations (3)-(6), we obtain the following system of ordinary differential equations:

$$f''' + ff'' + \beta[1-(f')^2] + \frac{1}{1+m}(M+K)[1-f'] = 0 \tag{9}$$

$$\theta'' + Pr[f\theta' + Ec(f'')^2 + Nb\theta'\phi' + Nt(\theta')^2] = 0 \tag{10}$$

$$\phi'' + LePr(f\phi') + \frac{Nt}{Nb}\theta'' = 0 \tag{11}$$

The transformed boundary conditions are:

$$\begin{aligned} f &= 0; \quad f' = 0; \quad \theta = 1; \quad \phi = 1 \ \ at\ \eta \\ f' &\to 1; \quad \theta \to 0; \quad \phi \to 0 \ \ as \ \ \eta \to \infty \end{aligned} \tag{12}$$

with

$$M = \frac{2\sigma {B_0}^2 x^{1-m}}{\rho U_\infty}; \quad \kappa = \frac{2\nu x^{1-m}}{KU_\infty}; \quad Ec = \frac{U^2}{c_p(T_w-T_\infty)}; \quad Pr = \frac{\nu}{\alpha}$$

$$Nb = \frac{\tau D_B(C_w-C_\infty)}{\nu}; \quad Nt = \frac{\tau D_T(T_w-T_\infty)}{\nu T_\infty}; \quad Le = \frac{\alpha}{D_B}; \quad Re_x = \frac{u_w x}{\nu}$$

Where, M is magnetic parameter, Re_x is local Reynolds number, Pr is Prandtl number, Ec is Eckert number, κ is the permeability parameter, Le is Lewis number, Nb is the Brownian motion parameter, Nt is the thermophoretic parameter, and prime (') denotes derivative with respect to η.

The physical quantities of engineering interest in the present study are the skin friction coefficient C_f, local Nusselt number Nu_x and local Sherwood number Sh_x; and respectively, defined as:

$$C_f = \frac{2\tau_w}{\rho U^2(x)}; \quad Nu_x = \frac{xq_w}{k(T_w-T_\infty)}; \quad Sh_x = \frac{xM_w}{D_B(C_w-C_\infty)} \tag{13}$$

Where, τ_w, q_w and M_w are the surface shear stress, the surface heat flux, and surface mass flux; and respectively, they are given as:

$$\tau_w = -\mu\left(\frac{\partial u}{\partial y}\right)_{y=0}; \quad q_w = -k\left(\frac{\partial T}{\partial y}\right)_{y=0}; \quad Sh_x = -D_B\left(\frac{\partial C}{\partial y}\right)_{y=0} \tag{14}$$

Here, the non-dimensional skin friction coefficient, local Nusselt number and local Sherwood number are respectively given as:

$$\sqrt{\frac{1}{2(1+m)}}\, C_f\sqrt{Re_x} = -f''(0); \quad \sqrt{\frac{2}{1+m}}\frac{Nu_x}{\sqrt{Re_x}} = -\theta'(0); \quad \sqrt{\frac{2}{1+m}}\frac{Sh_x}{\sqrt{Re_x}} = -\phi'(0) \tag{15}$$

The system of non-linear ODE (9)-(11) subject to the boundary conditions (12) have been solved numerically using spectral quasilinearization method (SQLM). The main idea behind this approach is identifying univariate and multivariate nonlinear terms of function and its derivative in each of the equations of the system (9)-(11), linearizing the terms and applying Chebyshev pseudo-spectral collocation method (see Motsa, 2013a).

3. RESULT AND DISCUSSION

Numerical solutions are obtained using SQLM for the velocity, temperature and concentration profiles across the boundary layer for different values of the parameters. The number of collocation points in the space *x* variable used to generate the results is $N = 40$ in all cases. To ensure the numerical accuracy of the numerical method used, the skin friction coefficient $-f''(0)$ and local Nusselt number $-\theta(0)$ have been calculated for different values of Falkner-Skan power-law parameter *m*. From table 1, it is observed that the data produced by the SQLM code and those reported by (Ashwini and Eswara, 2012; Watanaba, 1990; Ullah et al., 2016) are excellent agreement. Thus, we are very much confident that the present results are accurate.

Table 1: Comparison of the SQLM results of skin friction coefficient $-f''(0)$ and local Nusselt number $-\theta'(0)$ for various values of *m* for $\kappa = 0$, M=0, Ec=0, Pr=0.73, Nb=10^{-5}, Nt=0, and Le=0.

	$-f''(0)$				$-\theta'(0)$	
m	Ashwini G.	Watanaba T.	Ullah I.	Present	Watanaba T.	Present
0.0	0.4696	0.46960	0.4696	0.46960	0.42015	0.42016
0.0141	0.5046	0.50461	0.5046	0.50461	0.42578	0.42578
0.0435	0.5690	0.56898	0.5690	0.56898	0.43548	0.43548
0.0909	0.6550	0.65498	0.6550	0.65498	0.44730	0.44730
0.1429	0.7320	0.73200	0.7320	0.73200	0.45693	0.45694
0.20	0.8021	0.80213	0.8021	0.80213	0.46503	0.46503
0.3333	0.9277	0.92765	0.9277	0.92765	0.47814	0.47814
1.0	1.2326		1.2326	1.23258		

Table 2 illustrates the influence of non-dimensional governing parameters on the skin friction coefficient, local Nusselt and local Sherwood numbers. The skin friction coefficient enhances with increase in pressure gradient, permeability and magnetic parameter. The local Nusselt number is a decreasing function and a local Sherwood number is an increasing function of the pressure gradient parameter, magnetic parameter, Permeability parameter, Prandtl number, Lewis number, thermophoresis parameter and Eckert number.

Figure 2(a) shows the variation of velocity profiles for different values of pressure gradient parameter β. It clearly demonstrates that the velocity profile increases with an increase in pressure gradient parameter. This is because of the increment of wedge angle, the fluid moves much slower and decreases velocity boundary layer

thickness. Figure 2(b) shows the effect of permeability parameter κ on the velocity profile. It is observed that increase in κ leads to increase the velocity of the nanofluid on the porous surface and decrease its boundary layer thickness. It is also noticed that both pressure gradient parameter β and permeability parameter κ have no significant effect on both nanofluid temperature and concentration.

Table 2: Computations of the skin friction coefficient $-f''(0)$, local Nusselt number $-\theta'(0)$ and local Sherwood number $-\phi'(0)$ for various parameters

β	M	κ	Pr	Ec	Le	Nb	Nt	$-f''(0)$	$-\theta'(0)$	$-\phi'(0)$
0.5	2.0	0.5	0.71	0.5	1.5	0.4	0.2	1.64926	0.15931	0.67917
1.0								1.66202	0.15452	0.68732
0.5	5.0							2.22828	0.08382	0.79196
	2.0	8.0						1.71589	0.15117	0.69231
		0.5	1.5					1.64926	-0.05294	1.03077
			0.71	1.0				1.64926	-0.10049	0.79817
				0.5	2.0			1.64926	0.15483	0.76246
					1.5	0.6		1.64926	0.12881	0.66467
						0.4	0.3	1.64926	0.14915	0.71774

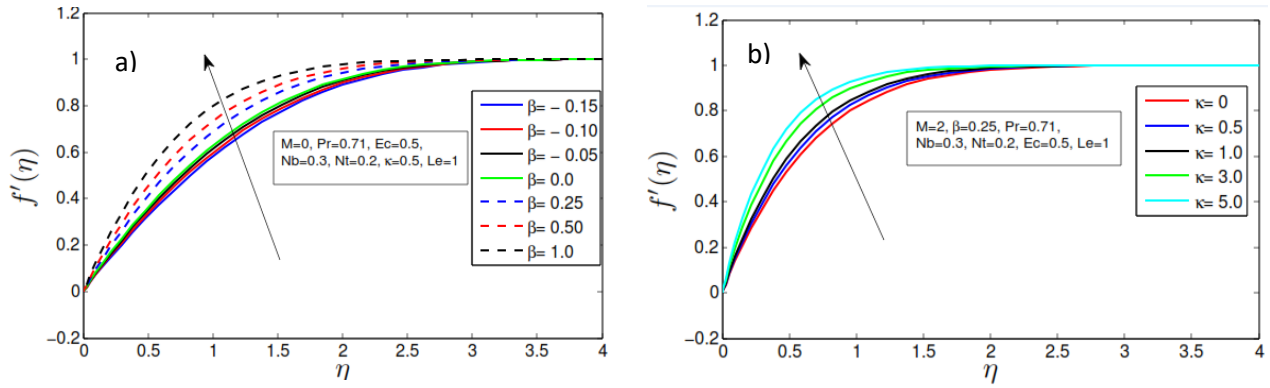

Figure 2: a) Velocity profiles for various values of β and b) Velocity profiles for various values of K.

Figure 3(a), 3(b) and 4(a) illustrate the influences of magnetic parameter M on the velocity, temperature and concentration profiles respectively. Fig. 3(a) reveals that the velocity boundary layer thickness decreases with an increase in magnetic parameter. This is due to the fact that the presence of transverse magnetic field sets in Lorentz force, which results in retarding force on the velocity field. Consequently, as the values of magnetic parameter increase, so does the retarding force and hence the velocity profile increase.

Figure 3(b) evident that the thermal boundary layer thickness decreases with increases in magnetic parameter. This is due to additional work expended in dragging the fluid in the boundary layer against the action of the Lorentz force and energy is dissipated as thermal energy which heats the fluid. This makes reduce in temperature. It is also observed that the concentration profile and its boundary layer thickness decrease with an increase in magnetic parameter as shown in Figure 4(a). Figure 4(b) descries the concentration profile for different values of Lewis number Le. It is clearly observed that the concentration profile and its boundary layer thickness reduce considerably as the Lewis number increases.

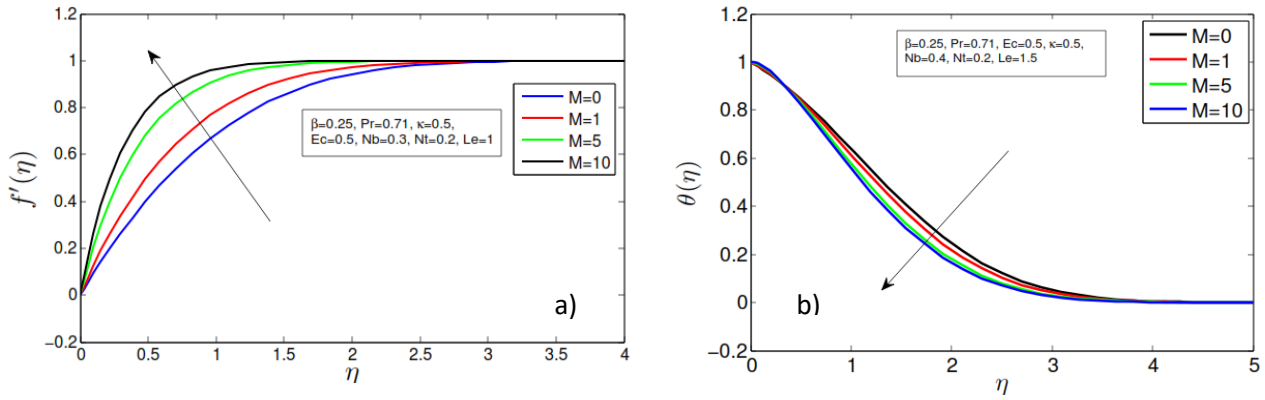

Figure 3: a) Velocity profiles for various values of M and b) Temperature profiles for various values of M.

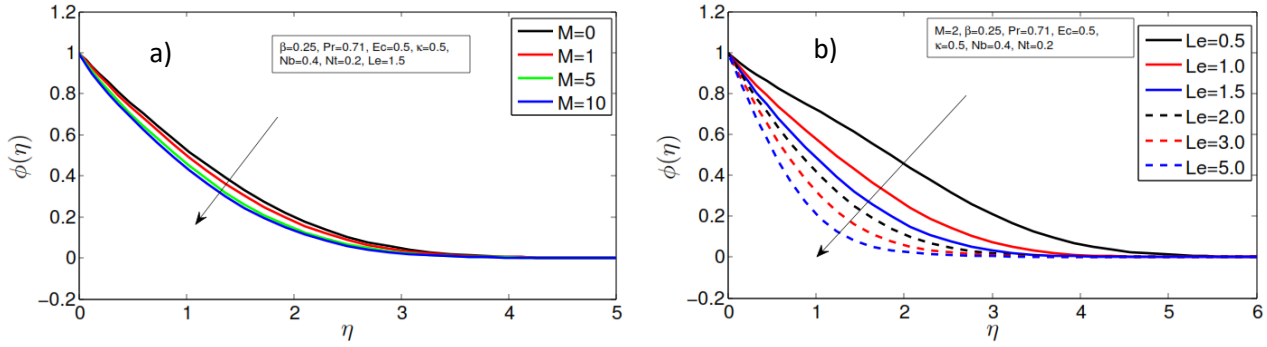

Figure 4: a) Concentration profiles for various values of M and b) Concentration profiles for various values of Le.

The effect of the Prandtl number on the temperature and concentration is shown in Fig. 5 (a) and 5(b) respectively. It is depicted that the temperature and concentration profiles and their boundary layer thickness reduce significantly as the Prandtl number increase. Because increasing the Prandtl number tends to reduce the thermal diffusivity of the fluid and causes weak penetration of heat inside the fluid. However, in the region near to the boundary surface, the heat transfer rate increases with an increase in Pr. This is due to the fact that the temperature gradient at the surface increase.

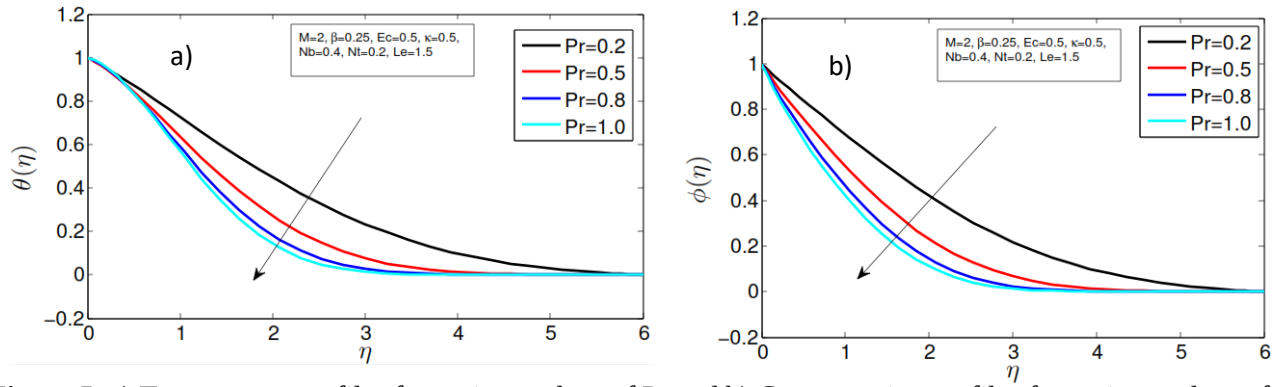

Figure 5: a) Temperature profiles for various values of Pr and b) Concentration profiles for various values of Pr.

The effect of viscous dissipation parameter Ec on the temperature and concentration profiles is presented in Figure 6(a) and 6(b) respectively. The Eckert number expresses the conversion of kinetic energy into internal energy by work done against the viscous fluid stress. It is observed that the temperature increases significantly from the surface and attains a peak value around η=0.5, and then decreases in the rest of the region as given in Figure 6(a). This implies that the thermal boundary layer becomes thicker with large Eckert number. The

concentration profile gradually reduces near the surface up to η=1 and then it increases with an increase in the viscous dissipation parameter Ec as highlighted in Figure 6(b).

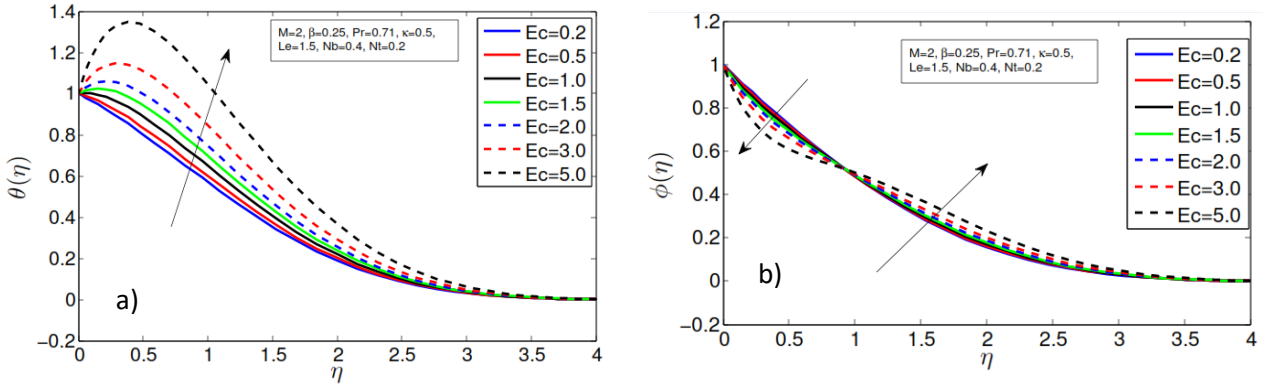

Figure 6: a) Temperature profiles for various values of Ec and b) Concentration profiles for various values of Ec.

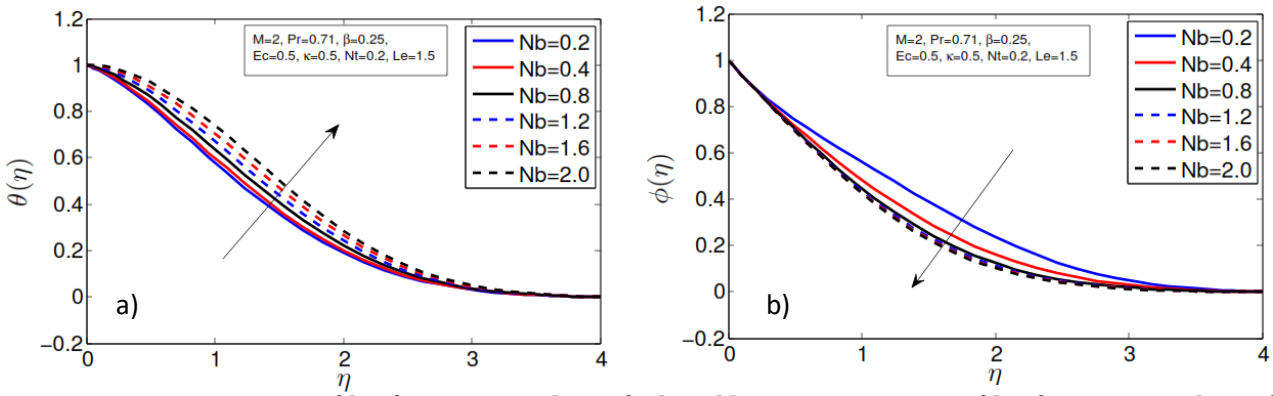

Figure 7: a) Temperature profiles for various values of Nb and b) Concentration profiles for various values of Nb.

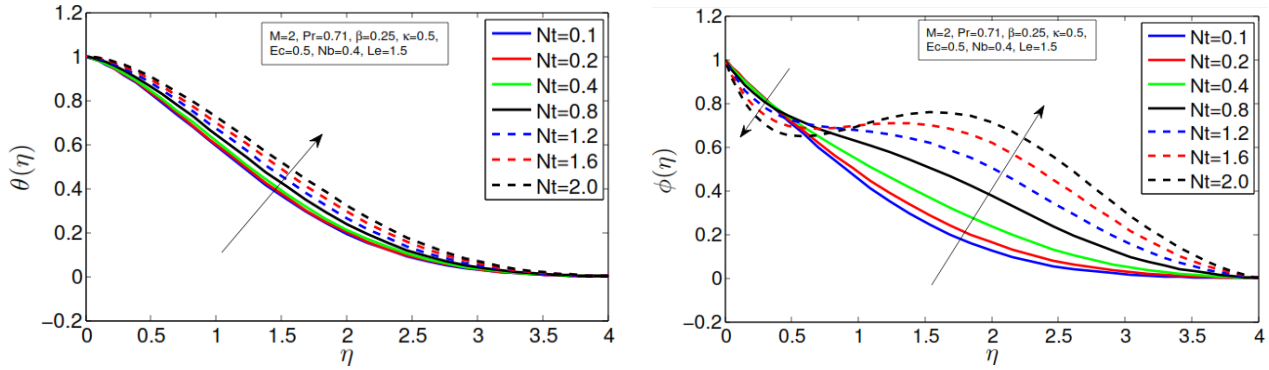

Figure 8: a) Temperature profiles for various values of Nt and b) Concentration profiles for various values of Nt

The influence of the Brownian motion parameter Nb on the nanofluid temperature and concentration profiles is presented in Figure 7(a) and 7(b) respectively. Figure 7(a) reveals that the temperature profile increases with an increase in Nb, particularly in the region close to the surface. The physics behind this phenomenon is that the increased Nb increases the thickness of thermal boundary layer, which finally enhances the temperature. Figure 7(b) remarks that increasing the Nb tends to decrease the concentration profile near the surface. Figure 8(a) and 8(b) respectively reveal the usual temperature and concentration profiles for various value of thermophoresis parameter Nt. The thermophoresis force generated by the temperature gradient produces a fast flow and more fluid

is heated away from the surface. Consequently, the higher the value of Nt increase temperature profile and its boundary layer thickness as given in Figure 8(a)

Figure 8(b) reveals that concentration profile decline near the boundary surface until η=0.5 and afterward it increases with an increase in thermophoresis parameter Nt.

4. CONCLUSION

The problem of two-dimensional steady laminar MHD boundary layer wedge flow with heat and mass transfer of nanofluid past a porous media with viscous dissipation, Brownian motion and thermophoresis effects has been studied. Using suitable similarity transformations, the governing equations are transformed into a system of non-linear ordinary differential equations and solved numerically employing Spectral quasilinearization method. From the above discussions the following conclusions are given:

- The thickness of velocity boundary layer reduces with an increase in pressure gradient, permeability and magnetic parameters.
- Thermal boundary layer thicker with an increase in Eckert number, Brownian motion and thermophoresis parameters.
- Greater the value of Prandtl number, Lewis number, Brownian motion and magnetic parameter reduce the nanofluid concentration profile.
- The skin-friction at the surface enhances with an increase in pressure gradient, permeability and magnetic parameters.
- The local Nusselt number is a decreasing function and a local Sherwood number is an increasing function of pressure gradient parameter, magnetic parameter, permeability parameter, thermophoresis parameter and Eckert number.

ACKNOWLEDGMENT

The authors wish to express their very sincere thanks to Prof. S.S. Motsa for his valuable contribution in usage of Spectral quasilinearization method (SQLM) for the solution of the paper.

REFERENCES

Abbasbandy, S., Naz, R., Hayat, T., and Alsaedi, A. (2014). Numerical and analytical solutions for Falken-Skan flow of MHD Maxwell fluid. *Applied Mathematics and Computation*, 242:569-575.

Alam, M.S., Ali, M., Alim, M. A., Munshi, M.J., and Chowdhur, M. Z. (2017). Solution of Falkner- Skan unsteady MHD boundary layer flow and heat transfer past a moving porous wedge in a nanofluid. *Science Direct Procedia Engineering*, 194:414-420.

Arthur, E. M., and Seini, I. Y. (2014). Hydromagnetic stagnation point flow over a porous stretching surface in the presence of radiation and viscous dissipation. *Applied and Computational Mathematics*, 3(5):191-196.

Ashwini, G., and Eswara, A.T. (2012). MHD Falkner-Skan boundary layer flow with internal heat generation or absorption. *International Journal of Mathematical and Computational Sciences*, 6(5): 556-559.

Eckert, E. R. G. (1942). Die berechnungs/des warmeuberganges in der laminaren grenzschichtum stomter korper. *VDI-Forschungsheft*, 416:1-24.

Eshetu Haile, and Shankar, B. (2015). Boundary-layer flow of nanofluids over a moving surface in the presence of thermal radiation, viscous dissipation and chemical reaction. *Journal of Applied Mathematics*, 10(2):952-969.

Falkner, V.M., and Skan, S.W. (1931). Some approximate solutions of the boundary layer equations. *Philos. Mag*, 12:865-896.

Hartree, D.R. (1937). On an equation occurring in Falkner and Skan's approximate treatment of the equations of the boundary layer. *Procedia Cambridge Philos. Soc*, 33:223-239.

Khan, M.S., Karim, I., Islam, M.S., and Wahiduzzaman, M. (2014). MHD boundary layer radiative, heat generating and chemical reacting flow past a wedge moving in a nanofluid. *Nano Convergence*, 1:20-28.

Majety, S.S., and Gangadhar, K. (2016). Viscous dissipation effects on radiative MHD boundary layer flow of nano fluid past a wedge through porous medium with chemical reaction. *IOSR Journal of Mathe*matics, 12(5):71-81.

Motsa, S. S. (2013a). A new spectral local linearization method for nonlinear boundary layer flow problems. *Journal of Applied Mathematics*, doi:10.1155/2013/423628.

Motsa, S. S. (2013b). A new spectral relaxation method for similarity variable nonlinear boundary layer flow systems. *Chemical Engineering Communications*, 201(2):241-256.

Motsa, S. S., Magagula, V. M., and Sibanda, P. (2014a). A bivariate Chebyshev spectral collocation quasilinearization method for nonlinear evolution parabolic equations. *Scientific World Journal*, doi:10.1155/2014/581987.

Motsa, S. S., Makukula, Z. G., and Shateyi, S. (2013). Spectral local linearization approach for natural convection boundary layer flow. *Mathematical Problems in Engineering*, doi:10.1155/2013/765013.

Motsa, S. S., Sibanda, P., Ngnotchouye, J. M., and Marewo, G. T. (2014). A spectral relaxation approach for unsteady boundary-layer flow and heat transfer of a nanouid over a permeable stretching/ shrinking sheet. *Advances in Mathematical Physics*, doi:10.1155/2014/564942.

Nagendramma, V., Sreelakshmi, K., and Sarojamma, G. (2015). MHD heat and mass transfer flow over a stretching wedge with convective boundary condition and thermophoresis. *Science Direct, Procedia Engineering*, 127:963 - 969.

Nicholas, A. (2010). *An Introduction to Magnetohydrodynamics*. Battista Stony Brook University, New York, 11794-3600.

Ramesh, B. K., Shreenivas, R. K., Achala, L. N., and Bujurk, N. M. (2017). Similarity solutions of the MHD boundary layer flow past a constant wedge within porous media. Hindawi, *Mathematical Problems in Engineering*, doi:10.1155/2017/1428137

Rasheed, H., Rehman, A., Sheikh, N., and Iqbal, S. (2017). MHD boundary layer flow of nanofluid over a continuously moving stretching surface. *Applied and Computational Mathematics*, 6(6):265-270.

Srinivasacharya, D., Mendu, U., and Venumadhav, K. (2015). MHD boundary layer flow of a nanofluid past a wedge. *Science Direct, Procedia Engineering*, 127:1064 - 1070.

Trefethen, L. N. (2000). Spectral methods in MATLAB. *Society for Industrial and Applied Mathematics*, 10

Ullah, I., Khan, I., and Shafie, S. (2016). Hydro magnetic Falkner-Skan flow of Casson fluid past a moving wedge with heat transfer. *Alexandria Engineering Journal*, 55: 2139-2148.

Versteeg, H. K., and Malalasekera, W. (2007). *An introduction to computational fluid dynamics*; the finite volume method. Second Edition, Pearson Education Limited, 24.

Watanabe, T. (1990). Thermal boundary layer over a wedge with uniform suction and injection in forced flow. *Acta Mechanica*, 83:119126.

Development and Performance Test of a Mechanical Sugarcane Planter

Cherinet Gosaye[1,*], Ermiyas Feliche[2], Abraha Hailu[3], Zenebe Mengiste[1]

[1]*Ethiopian Sugar Corporation R&D Center, Addis Ababa, Ethiopia*
[2]*Sugar Corporation Training Academy*
[3]*Wolkayit Sugar Development Project*
**Corresponding author, e-mail: cherinet22@gmail.com*

ABSTRACT

Ethiopian Sugar Estates use manual sugarcane planting system. Manual sugarcane planting is an arduous job which requires high labor force. Finding enough skilled labor at peak planting seasons have become a challenge in some sugar estates as other sectors of the economy grow and laborers shift to high paying less arduous jobs. A mechanical sugarcane planter was developed with the objective of mechanizing the manual sugarcane planting operation and reducing labor dependence in the Ethiopian Sugar Estates. The machine was developed in such a way that it could execute three operations (furrow opening, seed cane placement, and seed cane covering) simultaneously in a single pass. The mechanical planter requires two laborers to feed the seed cane from a hopper down through a chute which drops the seed cane in to the opened furrows. Field testing of the planter showed that it opened furrows at 1.45 m spacing and 30 cm depth which conforms to the conventional practice. The work rate of the machine was found to be 0.24 ha/hr with an average working speed of 1.5 km/hr. The mechanically planted plot showed a 63% germination rate while the manual plot showed 65%. The stalk population and stalk weight data were also found to be comparable to those of mechanical planting. The economic analysis showed that it is possible to gain a financial saving of about 341.66 Birr/ha by using the mechanical planter instead of the conventional manual planting. Finally the planter was promoted for large scale verification and use by the Ethiopian Sugar Estates.

Keywords: *Mechanical planter, furrow opening, seed cane placement*

1. INTRODUCTION

Sugar cane grows from a stem, into a tall upright plant. Unlike most stems that are planted upright, a sugar cane stem has to be furrowed and placed on its side in order for it to grow. The cane field is prepared very well by using different tillage implements. Tractor drawn ridgers are used to open furrows. Furrow to furrow spacing of 145 cm is currently used in the Ethiopian Sugar Estates. Laborers are employed to cut the sugarcane into two or three budded pieces, which is called sets. The huge amounts of sets are transported to field and then dropped in furrows. Then sets are covered with soil.

In conventional method of planting sugarcane in Ethiopian Sugar Estates, furrows are opened mechanically; cane sets are manually conveyed to the field and planted manually in furrows, followed by manual covering. Manual sugarcane planting is an arduous and labor-intensive operation executed outdoors. Most of the sugar estates are located in dry and arid areas where the air temperature reaches up to 40^{o}C. The availability of manual labor willing to work on sugarcane planting especially in harsh environmental conditions is decreasing from time to time.

The new sugar development projects of the country are located in remote and harsh environmental areas where getting cheap labor force has become more difficult. The severity of the problem increases due to the fact that big farm sizes need to be planted in a short period of time. Therefore, there is a need to mechanize the cane planting unit operations and reduce its drudgery.

Experiences from other countries indicate that using mechanical cane planters could reduce cost of cane planting. One clear reasoning for instance is that the cane planter does furrow opening and fertilizer application simultaneously which otherwise would have been two separate operations. Labor costs for cane planting are also highly reduced.

Different types of mechanical sugarcane planters have been developed worldwide. These machines are broadly categorized in to two depending on the type of cane they can use as seed material. Some of them use whole stock cane while others use chopped cane. Those using whole stock cane as seed material have cane metering and cutting

mechanism and are hence more complex than those using chopped cane. Planters which use chopped cane are less complex.

According to Pandev (1997), comparative studies conducted on two types of sugarcane planters showed semi automatic sugarcane planters where by pre prepared cane setts are used as planting material are cheaper to produce and less complex to operate than whole stalk planters. The cheapness of its construction comes from the fact that these types of planters do not require complex cane metering and cutting mechanisms which require a number of precision machined parts.

This research was initiated to develop and test the performance of a semi automatic mechanical sugarcane planter to be used in the Ethiopian Sugar Estates (ESE). The machine was designed in such a way that it can cover the following operations in a single pass: furrow opening, cane placement, and cane covering. Chemically treated cane setts are used as seed material.

2. MATERIALS AND METHODS

2.1. Description of the study area

The study was conduction at Wonji Shoa Sugar Estate which is located at $8^0$31' N and $39^0$12' E with an altitude of 1500 m.a.s.l. The area has annual rainfall of 830 mm, with mean air temperature of 20.8 ^{0}C and relative humidity of 56 %. In general, it has a sub-humid climate having single rainy season in summer, from July to September.

2.2. Methodology

Different types of planters developed in cane producing countries were considered and literature review was made before deciding on which type of machine to develop. The theory followed here is to produce a less complicated design which could be easily produced in workshops equipped with basic metal working tools. As a result complex and expensive gearing and power transmission mechanisms were omitted. The best option which fulfils the above points is a machine which uses seed canes previously prepared thus avoiding the need for cane metering. After developing the machine, field testing was carried out to check the uniformity of planting, germination percentage, and ease of use. Comparison was made between planting by the machine and the conventional manual planting to check the savings in labor, time and cost.

2.3. Design Approach

The design philosophy is to go for a sturdy, low cost and low level of technology requiring design that could be manufactured in a workshop equipped with basic metal working tools. The design features no machined parts which require complex and expensive machinery. The number of moving parts is minimized as much as possible to reduce the wear and tear during operation. The hopper was designed to carry about 4 quintals of seed cane at a time thus allowing lesser refill times without endangering the stability of the tractor. The schematic and isometric views of the planter are shown in Figures 1 and 2.

2.3.1. Determination of Major Forces Exerted on the Planter

The major force exerted on the planter comes from the reaction between the furrowing bottoms and the soil. To determine the force exerted at the furrow bottoms, analytical method stated by the American Society of Agricultural Engineers (ASAE) is used. The planter has 2 bottom furrowers which open the soil for planting operation. The tillage depth is 30 cm while the recommended working speed is 6.3 km/h and the soil type is fine textured soil.

a) Draft force

According to ASAE (2000), the draft power requirement of the implement as calculated by:

$$D = Fi\,[\,A + B\,(S) + C\,(S)^2\,]\,WT$$

Where: D = implement draft, N;

F = a dimensionless soil texture adjustment parameter;
i = soil factor and it is = 1 for fine, 2 for medium and 3 for coarse texture soils;
A, B & C = machine – specific parameters referred from table;
S = forward speed, km/h;
W = machine working width, m;
T = tillage depth (cm)

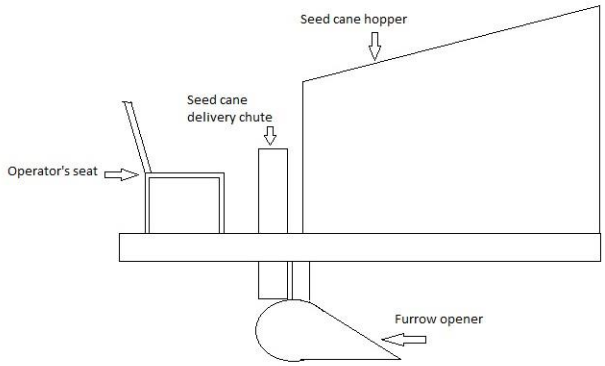

Figure 1: Schematic representation of the planter

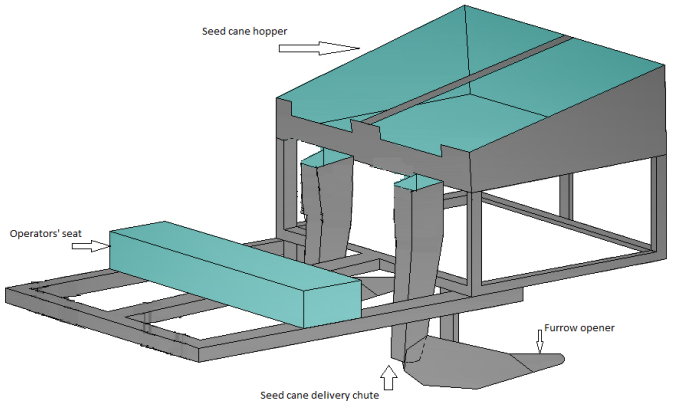

Figure 2: Isometric view of the proposed planter design

Since our soil is fine textured soil, we shall take F_i to be F_1. The operation is a secondary tillage operation carried out by ridger and hence, we can consider it as a minor tillage tool. The implement used in the operation is a ridger / furrower /bedder. By using these facts, and extracting the values from ASAE 2000, the draft is estimated to be 20.57 kN.

b) Drawbar power required by the implement

Drawbar power required to power the implement was determined using the following formula obtained from ASAE (2003) and as used by Mai (2009).

$$P_{db} = \frac{D \times S}{3.6}$$

Where; D = 20.57 kN and S = 6.3 km/ h

$$\text{Therefore } P_{db} = \frac{20.57 \times 6.3}{3.6} = 36\ kW$$

c) Tractor power determination

According to ASAE (2000), the maximum drawbar power developed by a 4WD wheeled tractor on tilled surface will be given by $Net\ Flywheel\ Power \times 0.9 \times 0.75$. The Net Flywheel Power is unknown while we know that the tractor should be able to produce at least 36 kW drawbar power. Therefore, the net flywheel power of the tractor required for the operation is at least 53.33 kW which equates to 72 hp. Thus, tractor of at least 80 hp should be used.

2.3.2. Stress Analysis

After determining the major force exerted on the planter stress distribution analysis was done using CATIIA software as shown in Figure 3. The analysis showed that the maximum stress is induced at the point where the furrowing bottoms are attached to the toolbar.

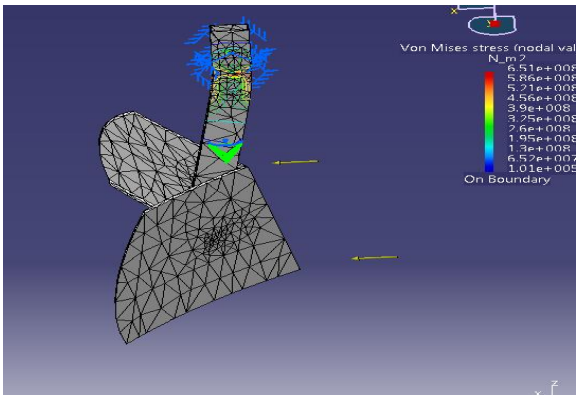

Figure 3: Stress analysis of furrow opener using CATIA

3. RESULTS AND DISCUSSION

3.1. Fabrication of the Mechanical Planter

The mechanical planter was fabricated at Shoa Training Center Workshop based on the developed design. The development process of the planter is shown in Figures 4 and 5.

Figure 4: Different stage of the planter development

Figure 5: The completed planter ready for field testing

3.2. Testing Furrow Opening Potential of the Planter

After developing in the workshop, the mechanical sugarcane planter was tested for its performance capacity in the field. First the ability of the planter to open cane planting furrows was observed and it was found that the machine opened cane planting furrows with the right dimension and at the right spacing (Figure 6).

Figure 6: Checking the furrow spacing and depth created by the planter

After confirming that the machine operates at the proper depth and creates furrows at the correct spacing, cane planting was executed and performance measures were taken (Figure 7). The results obtained from the field testing are listed as follows:

Figure 7: Planting cane with the developed planter

3.3. Work Rate Determination

After confirming that the machine could open furrows at the correct spacing and depth, field testing was continued to determine the work rate and observe the planting potential of the machine. The average working speed during planting was 1.5 km/hr. The theoretical working rate with this speed was found to be 0.435 ha/hr. Assuming a field efficiency of about 55% the expected work rate to be attained is 0.24 ha/hr.

A two row mechanical sugarcane planter developed by Vasantadada Sugar Institute (VSI) showed average work rate of 0.245 ha/hr when planting at 0.90 m spacing and 0.304 ha/hr when working at 1.2 m spacing.

3.4. Cane Performance

The mechanically planted plots had 63% germination rate while the manually planted plots had 65% germination (table 1). Due to the poor field condition of the test plot the germination percentage of both the mechanically planted and manually planted plots was low although comparable to each other. In contrast the VSI developed mechanical planter had average germination of 72.16% and 72% with furrow spacing of 0.90 m and 1.2 m was as against 67.11% and 67% respectively under conventional manual planting.

The mechanically planted plot showed a stalk population comparable to the manually planted plot. The population of mechanically planted plot is expected to increase as the labor force gets familiar with the mechanical planting practice.

As shown in table 2, the mechanically planted plot showed a stalk population comparable to the manually planted plot. The population of mechanically planted plot is expected to increase as the labor force gets familiar with the mechanical planting practice.

Although the developed planter has achieved most of its design objectives, some gaps were observed during field testing. The first gap was that seed cane was dropped in v-shaped pattern instead of lying in the furrow. Thus the cane dropping chute needs design modification so that dropped seed cane directly lies in the furrow. There was also gap between the dropped cane sets which was resulted due to delay in cane drop. Properly training the planting laborers and modifying the hopper design could solve this gap.

Using pre-manufactured farm machinery tool bars and standard mould boards / ridgers for future mass production and use of the machine is recommended to reduce time delays and to come up with durable planter.

Table 1: Field testing results

Parameter	Mechanically planted	Manually planted	Remark
Germination percent (%)	63	65	
Stalk count ('000/ha)	82.02	83.45	
Stalk weight (kg)	0.91	1.16	
Brix %	19.77	18.94	
Pol%	18.29	17.42	
Purity	92.72	91.96	
Sucrose yield%	12.96	12.26	

5.5. Economic Analysis

The economic analysis was made to compare planting with the developed planter and the conventional manual planting.

The average fuel consumption of the tractor is 8 lt/hr. By considering the work rate of 0.24 ha/hr, about 33.33 liters of diesel fuel is required per hectare. Assuming a retail price of 17 Birr / liter of diesel fuel the fuel cost would be 566.61 Birr/ha. Lubrication cost is assumed to be 5% of the fuel cost and hence would be about 28.33 Birr/ha.

Four laborers are required to load seed cane and to operate the machine. By taking the current rate of 34.32 Birr/ day, the labor cost will be about Birr 137.28. Assuming that about 2 hectares of land would be planted in an eight hour day, the labor cost will be about 68.64 Birr/ha. Assuming the monthly salary of the tractor operator to be 3500 Birr, and assuming there are 26 working days per month and he can plant 2 hectares per day, the operator expense per hectare would be about 58.33 Birr. The owning cost of the mechanical planter is estimated to be about 150,000 Birr and it is expected to operate for 10 years. Assuming the planting season lasts for 3 months and assuming that there are 26 working days per month, the daily rate for using the machine would be about 192.31 Birr. Since the machine could plant 2 hectares daily, the rate would be 96.15 birr per hectare. Thus, the overall cost of using the mechanical sugarcane planter would be about 818.06 Birr/ha.

Regarding the conventional manual planting, furrowing cost is 480 Birr/ha and we need about 679.73 Birr in labor cost for manual planting. Thus, the total cost of opening furrows and manually planting a hectare of field will be about 1159.73 Birr.

The above analysis shows that there is a net gain of about 341.66 Birr per hectare by using the mechanical planter over the conventional manual planting (table 2). The economic benefit is expected to increase as further modifications are made to the machine and as the personnel get familiar with its operation. Assuming the sugar estate plants about 1500 ha per year, the annual cost saving would be about 512,499.23 Birr.

Table 2: Summary of estimated financial benefit of using mechanical planting

Developed planter		Conventional manual planting	
The diesel fuel required for mechanical sugarcane planter 33.33 liters	566.61	Furrowing cost is	480 Birr/ha
Lubrication cost 5% of the fuel cost	28.33	Labor cost	679.73 Birr
Labor cost (birr/ha)	68.64	total cost	1159.73 Birr
Operator expense per hectare	58.33		
Planter use rate per hectare	96.15		
Overall cost mechanical planting (Birr/ha.)	818.06		
Net gain Birr per hectare			341.66

6. CONCLUSIONS AND RECOMMENDATIONS

6.1. Conclusions

The developed mechanical sugarcane planter was found to create furrows at the correct spacing and depth as recommended for cane planting in the Ethiopian Sugar Estates. The work rate of the machine was found to be 0.24 ha/hr and it is expected to increase as the planter is further modified and as the labor force get familiar with the machine. The performance of the machine was also found to be comparable to those developed abroad. The mechanically planted plot showed a 63% germination rate while the manual plot showed 65%. The stalk population and stalk weight data were also found to be comparable to those of mechanical planting. The economic analysis showed that it is possible to gain a financial saving of about 341.66 Birr/ha by using the mechanical planter instead of the conventional manual planting. The economic benefit is expected to increase as further modifications are made to the machine and as the personnel get familiar with its operation. The gaps of the mechanical planter which hinder operation and reduce its productivity are identified and they are expected to be rectified through progressive improvements.

6.2. Recommendations

- The identified gaps of the planter should be rectified to improve its productivity.
- After rectifying its gaps, the planter should be tested in large area for verification.
- After the planter is verified, the final design should be mass produced and used to replace the current manual planting practice in the Ethiopian Sugar Estates.

ACKNOWLEDGMENTS

The authors would like to acknowledge Sugar Corporation Research and Development Center for sponsoring the research work. In addition, we would also like to thank Shoa Traininc Center for letting us use their workshop facilities. Last but not least our acknowledgement goes to Wonji Shoa Sugar Factory Land Preparation and Cultivation Team and Cane Plantation Team for assigning the tractor used in the test and for giving us fields on which the tests were conducted respectively.

REFERENCES

Ariel, M.C., Rouverson P.S., Carlos E.A.F., Fabio A.C., and Fernando H.A. (2017). Operational uniformity for a sugarcane planter. *African Journal of Agricultural Research*, 12(12): 953-962.

ASAE (2000). ASAE Standards D497.4 Agricultural Machinery Management Data. In: ASAE Standards 2000, (372-380) St. Joseph, MI.

ASAE (2003). ASAE Standards EP 496.2 Agricultural Machinery Management. In ASAE Standards, (366-372). St. Joseph, MI.

Mai, M.A. (2009). Evaluation of Some Standards for Tillage Implement's Draft Requirements in Soba Area, Khartoum State, Sudan. M.Sc. Thesis. Department of Agricultural Engineering, University of Khartoum.

Pandev MM., Majumdar KL., (1997). *Farm Machinery Research Digest*, Central Institute of Agricultural Engineering, Nabi Bah, Bhopal-462 038, India

Oscar, A.B., Paulo S.G.M. (2014). Technological Evaluation of Sugarcane Mechanization, p.451-464. In Luis Augusto Barbosa Cortez (Coord.). Sugarcane bioethanol — R&D for Productivity and Sustainability, São Paulo: Editora Edgard Blücher.

Robotham, B.G. (2004). *Sugarcane Planters: Characteristics of Different Types, Soil Disturbance And Crop Establishment*. Proc. Aust. Soc. Sugar Cane Technol., 26. BSES Limited, Bundaberg.

S. Mandal and P. Maji (2008). Design Refinement of Two Row Tractor Mounted Sugarcane Cutter Planter". Agricultural Engineering International: the CIGR Ejournal. Manuscript PM 06 020. Vol. X.

Vaibhav, V. R., Siddharam, V. B., Varuneshwar, R. R., and Bhushan R. K. (2016). Design and Fabrication of Multipurpose Machine for Sugarcane Planting. International Journal of Current Engineering and Technology E-ISSN 2277 – 4106, P-ISSN 2347 – 5161 ©2016

VSI https://www.vsisugar.com/india/agriculture_divisions/agriengineering/mechanical-sugarcane-planter.htm

Coffee Parchment as Potential Bio-fuel for Cement Industries of Ethiopia

Eshetu Bekele Wondemagegnehu*, and Elias Habtu

[1]*Adama Science and Technology University, Adama, Ethiopia*
**Corresponding author, e-mail: eshetu.bekele@astu.edu.et*

ABSTRACT

The present investigation explores the potential of coffee parchment as alternate energy source to supplement the current energy demand of cement industries of Ethiopia. This study estimated quantity of coffee parchment generated from different wet coffee processing facility, established optimum route for collection, characterized the quality of raw and pelletized biomass fuel with respect to combustion properties and quality of the ash product used in clinker production. The raw and pelletized coffee parchment was characterized by CNHS analyzer for elements, ICP-AES for heavy metals, GPS and Arc-GIS software to choose optimized collection routes and IFD for oxide analysis of the ash following ASTM standard procedures. In addition, calorific value and proximate analysis were also carried out following standard procedures. The analytical results revealed that the quantity of coffee parchment generated was estimated to be in the range of 10,583.5 to 12,460.5 tons per year. However, this parchment has been used inefficiently and irregularly by the local population as a cooking fuel. It was also found that within a radius of 41.6 km around the city Addis Ababa, the samples contained higher percentage of C and H (45.5 and 6.5) and lower percentages of N and S (0.4 and 0.1%) in the coffee parchment pellet as compared to the commonly used biomass fuel and also meet the standards specified for non-wood pellets. Moisture content (11.2%) and ash content (5.97%) of the pellet was found to be lower than the amount specified for most of the biomass fuels and is in accordance with ISO 17225-6 standard for non-wood pellets. Calorific value (CV) of coffee parchment was found to enhance from 18.56 and 27.95 MJ/kg after pelletization. The obtained values are on par with common fuels such as wood and coal. These results signify that coffee parchment can serve as a potential alternative energy source, especially as cheap and eco-friendly biofuel for cement industries of Ethiopia.

Keywords: *Microalgae, Liquid tri-phase system, Lipid classes, Biodiesel, Bio-refinery*

1. INTRODUCTION

Cement is considered as one of the most important building materials around the world. Today, the world cement market represents over three billion tons per year (Global Cement Directory 2016). Similarly, Cement industry is flourishing in Ethiopia due to the rapid economic growth, increase in population and the change in living style, and the availability of raw material in the region (Mahlet Mesfin., 2011). On the other hand Cement production naturally consumes non-renewable raw materials and it is an energy-intensive process consuming thermal energy of the order of 3.3 GJ/tonne of clinker produced (Giddings, et al, 2000; European Commission [EC], 2001). Moreover, the energy (principally coal and heavy fuel oils) consumed by the Cement industry, is estimated at about 2% of the global primary energy consumption and contributes 5% of global anthropogenic CO_2 emissions (Hendriks et al., 1998; Battelle, 2002; Murray, & Price, 2008). As a result, the viability and prospects of future existence of cement industry depend on the development of alternative fuels to partially/fully substitute fossil fuels used to heat its kilns.

The level of alternative fuel use is widely variable between countries. Most European countries used Paper waste, Paper sludge, spent solvents, Sewage sludge, Rubber Waste, woods and Plastics in their cement industry. These alternative fuels provided about 18% of the thermal energy consumption in the European Cement industry, substituting/saving approximately 5 million tonnes of coal per year (CEMBUREAU, 2013). Country specific data showed for instance the proportion of alternative fuels used in cement kiln systems of France are 52.4 percent, Switzerland 25 percent, Italy 4.1 percent, and Sweden 2 percent (Mokrzycki et al., 2003; Murray & Price, 2008). Many different potential sources of biomass fuel proposed for developing countries, such as cereal husk, cotton waste, wheat straw, paper waste, sawdust, wood chips, palm fiber, Coffee husk, sugarcane straw, groundnut shells, Rice husk, and maize residues (Pattiya, 2015; IFC, 2017). These and other by-products with recoverable calorific

value can be used as fuels in a cement kiln, replacing a portion of conventional fossil fuels, like coal, if they meet strict specifications (Lechtenberg, 2008; CSI, 2002). For instance, Biomass can substitute for approximately 20% of process heat requirements of cement industry in Ethiopia (Yisehak Seboka, 2009). However, information about their quantity, levels of pellet production, characteristics and application in the developing countries were not well documented.

Because biomass waste is made of 100 percent renewable organic matter, it has high potential for mitigating carbon dioxide emissions from the cement industry. However some challenges remain such as high and variable moisture content, low energy density per unit volume resulting in difficulties in its storage, distribution/transportation and suppresses its energy density (Arranz, 2012; Miranda, et. al., 2015; Bilhat Chala et al. 2015). Moreover, the elemental composition, moisture content, ash content and size of biomass is diversified depending on harvest dates and methods, weather conditions, and plant genetics, which limit their use as it is appeared and exhibit different behaviors in thermal processes (Lewandowski & Kicherer, 1997; Paula et al., 2011; Fagan et. al., 2012; Everard et. al., 2012; Henrich et al.2014; Kyauta et al 2015; de Almeida et al, 2017). These properties causes some problem for combustion process such as Poor heat distribution, unstable precalciner operation, blockages in the preheater cyclones, buildups in the kiln riser ducts, higher SO_2, NOx, and CO emissions, and on the quality of clinker produced (Smidth & Co., 2000; Hewlett, 2004; Taylor et al., 2006; Azad Rahman et al., 2013). Moreover, potentially high collection expenses because of scattered resources and low biomass density of the alternative fuels remain also the main influencing factors for their choice and need to be studied (IFC, 2017). Consequently, selection of the proper type of fuel and upgrading to meet the required quality is vital for optimum efficiency.

Important step in the processing of biomass for energy purpose is reducing the moisture content, size of the biomass and densification in order to obtain denser fuels, with homogeneous properties and size (Poddar et al., 2014). Pelletizing is currently the most extended densification method to ensure the required quality of the final product/pellet so that it is convenient for use in the households, industry and heating plants (Tumuluru et al., 2011; Duca et al., 2014). The pellet has a diameter vary between 3 and 25 mm and the length generally varies between 5 and 40 mm (Morten et al., 2009). It occupies 10-30 times less space than fresh material so that its use decrease transport and storage cost. Global pellet production has considerably increased for the past years and between 2006 and 2012, pellet production worldwide grew from 7 to 19 million tons, with Europe and North America take the lion share, in the production and consumption of these densified products (Duca et. al., 2014; Miranda, et. al., 2015). The most important characteristics that needs to be analyzed for the evaluation of biomass fuel from different sources and became optimized to meet the standards sated includes: calorific value, moisture content, ash and sulfur content, bulk density, specific melting temperature of ash, volatile matter content, alkali metal content and grain size (Obernberger, et.al., 2004; Gillespie et al., 2013; Biswas, et al., 2014; Japhet et al., 2015).

Coffee is the second most traded legal commodity next to petroleum. Millions of people from developing countries rely on their livelihood on coffee production (Bilhat Chala et al., 2015). Ethiopia is the fifth largest coffee producing country and estimated total area covered by coffee is approximately 400,000 hectares, with a total production of about 200,000 tonnes of clean coffee per year (Gemechu, 2009; ICO, 2017). Coffee processing removing outer layers of the freshly picked red cherries of the coffee plant which is comprised of about 68 percent pulp, 6-10 percent parchment, and 26 percent clean coffee beans. Coffee residue has an estimated potential of more than 280,000 tonnes produced annually in Ethiopia equivalent to 360,218 tonnes fuel wood (Bilhat Chala et al., 2015; ESMAP, 1986). From this total coffee residue coffee parchment (which is composed of 54% cellulose, 27% pentosans and 19% lignin) constitutes about 16,800 tonnes per year which is available elsewhere near the washed coffee processing plant (where the endocarp is removed prior to export) located in Addis Ababa. But they were used inefficiently by the local citizen causing extensive pollution to the environment. Moreover, methods for effective utilization of the coffee parchment were not well developed. Therefore, this study was carried out to

investigate the fuel and material characteristics of coffee parchment to be used as alternatively energy source of cement industry.

2. MATERIALS AND METHODS

2.1. Estimation of coffee parchment quantity by weight

The actual quantity of coffee parchment generated were calculated after determining the amount of coffee parchment disposed per kilogram of wet coffee processing delivered to the facility, and by considering the amount lost and diverted for different reasons by the sector that produces the waste. The data collection were conducted in a daily bases and extended for over one month for three consecutive year. Moreover, secondary sources such as previous recordings found in the processing industry and respective government organizations were also used to estimate waste generation per annum. Data on its seasonal variability was also collected by making interview with the respective personnel, as it is one of the major factors in the amount of waste generated in biomass production.

2.2. Establishing an effective collection routes

The collection routes of coffee parchment from various coffee processing plants in Addis Ababa and the nearest transfer station were identified based on the information obtained on the existing sources of the waste, collection and transfer center, the possible route between the source and to the transfer station and having taken in to account the restrictions to the road conditions and topography. About 37 source points available within Addis Ababa were identified for the network analysis study. Distance between these sources were identified according to their position located using GPS. Finally with the help of the Arc-GIS, the routes were chosen in a way that the resources used for collection, the length of route and time taken to complete the collection is minimized (Bhambulkar, 2011; Aremu, 2013). The route optimization process is described in Figure 1 below.

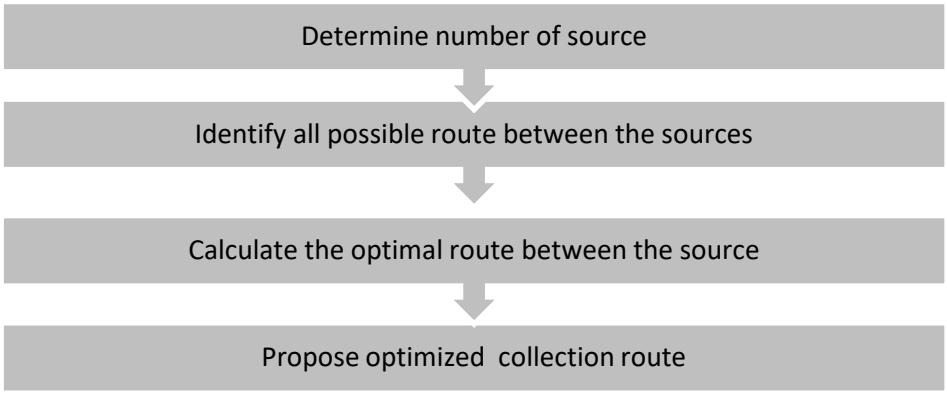

Figure 1: Schematic representation of the phases of the methodology followed

2.3. Pelletizing coffee parchment

In this study coffee parchment was pelletized after drying in an oven for one hour and grinded to pass a mush screen size of 1.46 mm and using the optimum additive (molasses) to water ratio of 2:1 to get proper bulk density and enhance pellets aggregate stability. The quantity of additives used to bind the dried coffee parchment were in accordance with the EU standards, which states additives that improve fuel quality, decrease emissions, or boost burning efficiency can make up to a maximum of 2% of the total mass of the pellets (EPC, 2011). Pellet formation phases done according to Bhattacharya et al. (1989) and pelletizing machine used in this study are indicated in Figure 2.

2.4. Characterization of coffee parchment

2.4.1. Proximate analysis

Ash, volatile matter, fixed carbon and moisture content of the biomass are key parameters determined for estimating the energy value of coffee parchment. They were determined in ASTU chemistry laboratory following

ASTM standard procedure: Moisture content ASTM (D3173), ash content ASTM (D3174), volatile matter content ASTM (D3175), fixed carbon content ASTM (D3172) (Akowuah, 2012). Each parameter was determined in triplicates.

Figure 2: pellet formation phases from coffee parchment and pelletizing machine used

Percentage moisture content

The percentage moisture content (MC %) was found by weighing 2g of the sample (I) and oven drying it at 105°C until the mass of the sample was constant (A). The change in weight (I-A) was then used to determine the sample's percentage moisture content using the Equation below:

$$\text{MC (\%)} = \frac{[Initial\ Mass - Moisture\ Mass]}{[Initial\ Mass]} \times 100 \text{----------1}$$

Percentage volatile matter (VM %)

The percentage of volatile matter was determined by heating 2g of the samples in a crucible and placing it in a furnace to 925 °C for seven minutes in the absence of air and weighed after cooling in a desiccator. The percentage of volatile matter was calculated from the loss in mass of the sample after reducing the loss in mass due to moisture using the equation below:

$$\text{VM (\%)} = \frac{[A-B]}{A} \times 100 \text{----------2}$$

Where, A is the weight of the oven dried sample and B is the weight of the sample after 7min in the furnace at 925°C.

Percentage ash content

The percentage ash content (AC %) was also determined by heating 2g of the sample in the furnace at a temperature of 550°C for 4h and weighed after cooling in a desiccator. to obtain the weight of ash (C). The percentage of ash content was then calculated using the Equation below:

$$\text{AC (\%)} = [C/A] \times 100 \text{----------3}$$

Percentage fixed carbon

The percentage of sample mass that remained after removal of volatile matter and ash content was used to determine the fixed carbon content and the percentage fixed carbon (FC %) was computed by subtracting the sum of VM (%) and AC(%) from 100 as shown in the Equation below:

$$\text{FC (\%)} = 100 - [\text{A(\%)} + \text{VM(\%)}] \text{----------4}$$

2.4.2. Heating or calorific values

Heating value which is the amount of fuel energy that can be released per unit mass or volume when the fuel is completely burned (in units of MJ/kg), of both the raw coffee parchment and pellet produced was examined at

Addis Ababa, ministry of water, irrigation and energy laboratory in accordance with the ASTM procedure. The apparatus used was oxygen bomb calorimeter (model: CAB001.AB1.C). For this analysis loading of biomass samples of about 1 g in to the bomb calorimeter was made and allowed to burn in the presence of oxygen pressurized to 30 bar inside a sealed container (bomb). The heat released from combustion was transferred to a mass of working fluid (water) that surrounds the container, allowing the heating values to be calculated, as the product of the mass and specific heat of the fluid and the measured temperature rise.

2.4.3. Ultimate and Chemical analysis

The raw coffee parchment and pelletized coffee parchment were analyzed in duplicate for the oxide contents according to specification of ASTM C 114/00 using XRF (model) at Mugger cement industry, heavy metal analysis using ICP-AES (model---) after the sample were air dried and digested with HNO_3-HCl (aqua regia). And important chemical elements that makes up biomass, namely percentage Carbon, Hydrogen, Nitrogen and Sulfur, were determined using elemental analyzer (EA 1112 Flash CHNS- analyzer) available at Addis Ababa University. The oxygen content was determined by difference according to the formula below:

$$0xygen\ (\%) = 100 - [\text{Carbon}(\%\ \text{Dry Basis}) + \text{Hydrogen}(\%\ \text{Dry Basis}) + \text{Nitrogen}(\%\ \text{Dry Basis}) + \text{Sulphur}(\%\ \text{Dry Basis}) + \text{Ash}(\%\ \text{Dry Basis})] \text{----------} 5$$

4. RESULT AND DISCUSSION

4.1. Coffee parchment Generation and Management practice

As shown in Figure 3, the total biomass (coffee parchment) amounts generated in three consecutive years 2014, 2015, and 2016 were about 14,361 tonnes, 15,576 tonnes, and 13, 229 tonnes, respectively. This is found to be 20% of the processed coffee cherry transported to wet coffee processing facility in Addis Ababa. And its generation reaches peak during the months of February to July.

The result clearly showed the amount generated per year is huge and if it is not properly managed or used inefficiently, it has potentially causes environmental pollution. The estimated amount of coffee parchment found in this study was supported by recently reported data of about 16,800 tonnes per year (Bilhat Chala et al., 2015). Moreover, increasing emphasis on the production of washed coffee in Ethiopia due to its attractive premium might lead to increase amount of coffee parchment in the next 5 years (ICO, 2017).However, this huge amounts of waste generated mostly seen as waste and managed inefficiently and accumulated at source (near the washed coffee processing plant) or at the transfer station. Very recently individuals started sale the parchment for 25 Birr per 50 kg sack to the local population who irregularly utilize the loose parchment as a cooking fuel.

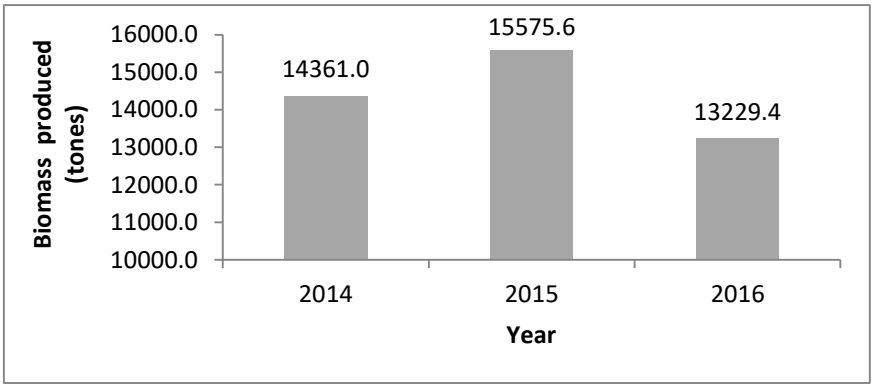

Figure 3: Estimated amount of biomass generated in Addis Ababa wet coffee processing facility in three consecutive years

4.2. Establishment of effective waste collection route

The collection route that minimize the length of each waste collection were proposed based on distance, topography, condition of the roads as shown in Figure 4. All possible routes between biomass source (wet coffee processing facilities) and the existing transfer station were marked with black and the shortest route between the source and transfer station was marked by red (Fig. 4). Total distance calculated from each road length considering that all start the journey from a source and visit the various sources located at different sites, transportation of the biomass covers a total distance of 117.6 km (Table 1, Figure 4). Whereas the optimized route calculated after identified the position of the transfer station using Arc-GIS software were shown in Figure 4 and covers a total distance of 41.6 km from the biomass source to the transfer station.

Table 1: Road distance of each path between the sources and proposed transfer station

path	Distance (m)	path	distance	path	distance
R8	1099.58	R21	2021.36	R71	741.96
R17	2010.40	R18	5306.01	R72	1027.81
R38	1498.19	R9	229.37	R86	1222.48
R39	3135.87	R65	1581.49		
R69	861.46	R24	1110.15		
R97	1359.46	R32	2868.57		
R1	6401.86	R33	1853.91		
R11	1338.99	R36	688.74		
R16	519.35	R44	599.81		
R19	2254.86	R50	1853.53		

4.3. Characterization of coffee parchment, and its pellet.

4.3.1. Proximate analysis

The result of proximate analysis of the raw and pelletized coffee parchment calculated on a dry weight basis was presented in Table 2.

Table 2: Proximate Analysis and heating value of coffee parchment pellet and raw coffee parchment measured in dry weight basis

Sample code	Moisture content (%)	Volatile content (%)	Ash (%)	Fixed carbon (%)	HHV (cal/g)
CP-Pellet	11.2 ± 0.1	86.1 ± 2.4	5.97 ± 0.7	7.97 ± 2.0	6676.4 ± 60.7
CP-Raw	11.5 ± 0.1	93.3 ± 0.9	0.38 ± 0.04	6.29 ± 0.9	4433 ± 8.7

Moisture Content

As shown in Table 2, the moisture content of raw coffee parchment and its pellet were 11.5% and 11.2 %, respectively. These results obtained for both materials were in accordance with ISO 17225-6 standard for non-wood pellets sated to use as alternative fuel (< 12%) (ISO, 2014b) and meets requirements of cement industry (<30%) specified by different countries (Mokrzycki et al., 2003; EC, 2003). Moreover, the moisture content of the studied samples were lower than the moisture content of cotton stalk (12.0%), rice husk pellet (12.7%), barley straw (30%), wheat straw (16.0), and wood (20%) as reported by Tokan et al.(2016); McKendry (2002); Efomah & Gbabo (2015); Henrich et al.(2014). Thermal conversion usually requires low moisture content feedstock typically (< 50%). Thus, this result indicated that the moisture contained in the studied materials were not hinder ignition, adversely impact the overall energy balance for the conversion process and slow the rate of combustion to a large extent (McKendry, 2002).

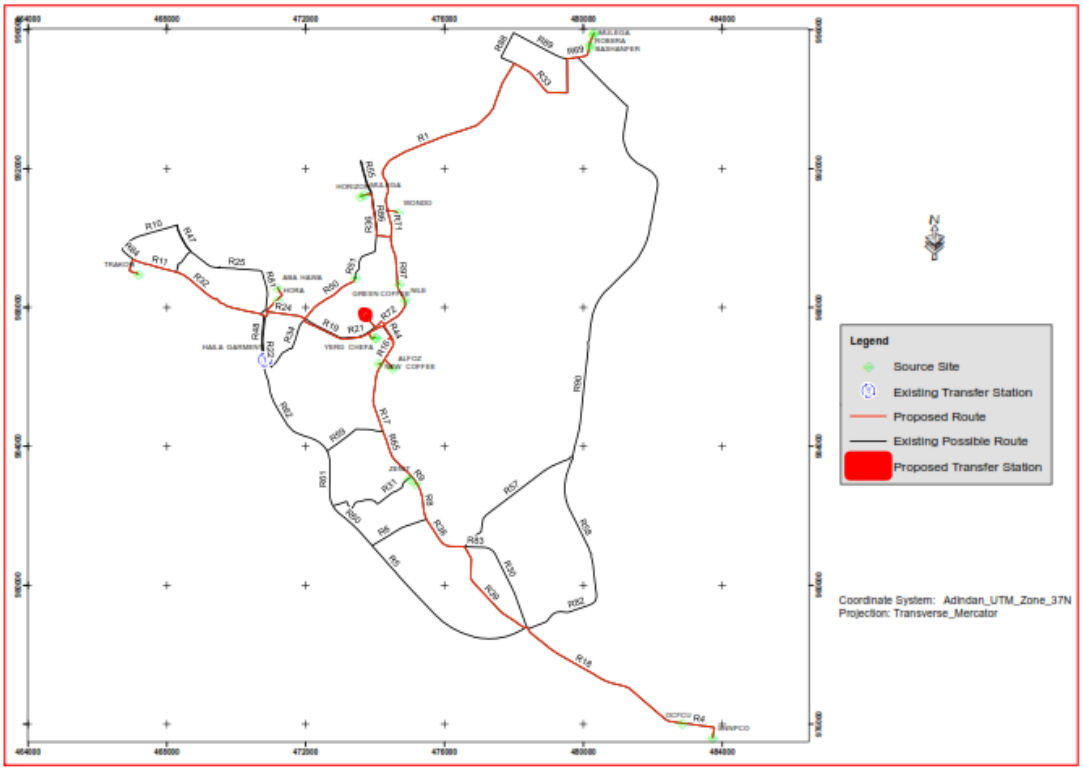

Figure 4: Existing roads and proposed route between biomass sources with identified transfer station

Ash Content

As shown in table 2, the ash content of the studied materials was found to be 5.97% in the pellet formed and 0.38% in the raw coffee parchment. Significantly higher ash content in the pelletized coffee parchment is due to increased elemental composition of the pellet as a result of the binding agent used (molasses), thereby affecting ash content of the final product (Kuokkanen et al., 2011). However, the ash contents of both materials is below ISO 17225-6 standard for non-wood pellets sated to use as alternative fuel (< 6%) (ISO, 2014b). And meets requirements of cement industry (<20%) specified by different countries (Mokrzycki et al. 2003; EC, 2003). This indicated that both the coffee parchment and its pellet are suitable for thermal utilization. Moreover, ash content found in the coffee parchment was lower than reported amount in coal (> 8%) and other woody and non-woody biomass such as sugar cane bagasse (8.7%), wheat straw (4-8%), and Rice husk and its pellet (9.3-26%) (Tokan et al., 2016; Efomah & Gbabo, 2015; Henrich et al., 2014; McKendry, 2002).

Volatile Matter

The volatile content of coffee parchment and its pellet was recorded to be 93.3 %, and 86.1%, respectively (Table 2). This high volatile matter contents was in agreement with the justification that biomass typically has a high volatile matter content (> 80%) (Efomah and Gbabo, 2015) and the result reported by Montenegro Camacho et al. (2016) for coffee pellets (86.1%). The higher volatiles in raw coffee parchment than its pellet may be because of chemical and physical transformation of volatile matters in to volatile gases and fixed carbon up on drying and pelletizing. Comparison of volatile matters in the coffee parchment and other solid fuels confirmed that higher volatile matters were recorded in the coffee parchment than rice husk, cereal straw, sugarcane bagasse and cotton husk, which were found to be in the range of 59.0–83.4% (Sánchez et al., 2014; Henrich et al., 2014; Singh et al., 2013; Mhilu, 2014, Tokan et al., 2016; Efomah & Gbabo, 2015; Domalski et al., 1985). This difference may be due to differences in the chemical composition of the used biomass as well as the operations condition. The higher

volatiles in coffee parchment indicates that coffee parchment can easily ignites under low temperature and give a faster combustion rate while devolatilizing during pyrolysis (Xing Yang et al., 2017).

Fixed Carbon

As shown in table 2 fixed carbon contents of the raw coffee parchment and its pellet are found to be 6.29 ± 0.9 and 7.97 ± 2.0 percent, respectively. The fixed carbon contents was higher than the result reported by Montenegro Camacho et al. (2016) for coffee pellets (5.2%). The observed lower fixed carbon content in coffee parchment than its pellet in table 2 may be because of chemical and physical transformation of volatile matters in to fixed carbon up on drying and pelletizing. This indicated coffee pellet contained higher percentage of carbon available for char combustion during pyrolysis (McKendry, 2002; Mohan et al. 2006).

Heating Value

The heating values of coffee parchment and its pellet indicated in table 2 are the gross heating value in dry basis and they were found to be 4433 ± 8.7 and 6676.4 ± 60.7 cal/g for the raw coffee parchment and its pellet, respectively. Their MJ kg^{-1} equivalent was 18.56 and 27.95, respectively. The higher heating value in pellet than raw coffee parchment mainly attributed to complete combustion of denser materials and more uniform properties of the pellet than the raw biomass. Moreover, high energy value additives (molasses) to facilitate binding may increase the heating value of pelletized coffee parchment. The heating values found in the coffee parchment was higher than reported amount in woody and non-woody biomass such as sugar cane bagasse (17.9-18.4 MJ/kg), wheat straw (17.3 MJ/kg). Rice husk (15.2-17.6 MJ/kg), cotton stalk (17.4 MJ/kg) and saw dust pellet (19.8 MJ/kg (Tokan et al., 2016; Efomah & Gbabo, 2015; Henrich et al., 2014; McKendry, 2002; Sánchez et al., 2014). Moreover, the heating value of the pellet was higher than the result reported by Montenegro Camacho et al. (2016) for coffee pellets (18.4 MJ/kg). The heating value of both materials is above the ISO standards sated to use as alternative fuel (≥ 16.5 MJ/kg) (ISO, 2014a). And meets minimum requirements of cement industry (>15 MJ/kg) specified by different countries (Mokrzycki et al., 2003; EC, 2003). This indicated that both the coffee parchment and its pellet is suitable to be used as alternative energy source and can be used in the clinker sintering zone for proper kiln operation (Duda., 2004).

4.3.2. Ultimate analysis

The ultimate analysis result in table 3 reports the elemental carbon (C), hydrogen (H), Oxygen (O), Nitrogen (N), and sulfur (S) composition in the solid fuel.

Table 3: Percent of organic matter (OM) and ultimate analysis of raw coffee parchment and its pellet form measured in dry weight basis.

Sample code	OM [%]	C [%]	H [%]	O[%]	N [%]	S [%]
CP-Pellet	91.7 ± 0.60	45.5 ± 0.50	6.5 ± 0.02	41.53	0.4 ± 0.04	0.1 ± 0.07
CP-Raw	N.D	43.5 ± 1.50	5.3 ± 0.60	50.12	0.5 ± 0.02	0.2 ± 0.03

N.D-not determined

Table 3 shows high C (43.5% and 45.5%) and H (6.5% & 5.3%) content of both the raw coffee parchment and its pellet, respectively. The materials with a relatively higher C and H percentage have more energy density and higher HHV because of C-C bond release more chemical energy and during combustion hydrogen is converted to H_2O, which significantly contributing to the overall heating value Paula et al. (2011). As compared to other biomass materials, coffee parchment has shown higher carbon percentage than the carbon content reported in rice husk (31.47-39.1%), peanut shell (41.5%), wheat straw (43.5%) and soybean pod (42.5%) (Paula et al., 2011; Braz and Crnkovic, 2014). The result in table 3 also showed that the weight content of H was higher in the studied materials than the H content in rice husk (5.3%), wheat straw (5.9% and saw dust (5.2%) as reported by Singh et

al.(2013) and Demirbas (2004). The lower N and S content of the coffee parchment fuel (Table 3) indicated there will be a minimal release of oxide of sulfur and nitrogen to the atmosphere up on combustion so that the burning of coffee parchment or its pellet will not cause environmental pollution.

4.3.3. Ash oxides contents

The results of the oxide analysis of ash of coffee parchment and its pellet were shown in table 4. The percentage of calcium oxide in the raw and pelletized coffee parchment ash (16.3 and 29.9%, respectively) and iron oxide content in the coffee parchment pellet (1.06%) were higher than coal with the amount appreciated in the coffee parchment pellet (Table 4). The result confirmed that the fuel ash can also contribute to supplement the CaO required from limestone for clinker formation which constitutes about 63-67%. Higher content of calcium oxide in the pellet than raw parchment might be due to the molasses added to facilitate binding of particles during pellet formation. The analysis result with respect to magnesium oxide indicated coffee parchment pellet contained higher percentage as compared to coal (Table 4). This confirmed that the studied material can also be a good source of MgO. However, careful design of the fuels and the raw materials is required to influence the final clinker composition. An excessive amount of magnesia (usually above 5 % as a whole), in the clinker can crystallize out from the flux as a periclase, in which its presence has been associated with long term unsoundness and causes delayed expansion (Hewlett, 2004).

The silica content of the coffee parchment and its pellet (6.38% and 8.76%), respectively was much lower than coal. However, it has an implication that the fuel ash may supplement the silica required for clinker usually ranges from 19.7-23.0 % with proper formulation. This in turn can contribute in reducing the need of raw material and making the cement production more economical (Hewlett, 2004). The analysis result in table 4 also showed aluminum oxide percentage in the studied material was much lower than coal, but relative to the percentage required in clinker formation (3-7 %) the amount in coffee parchment (1.02%) would also significantly contribute to reduce the raw material demand in cement industry. Moreover, as shown in table 4, the content of minor oxides referred to as alkalis in cement (Na_2O and K_2O) were found to be 0.01% and 0.36%, respectively in coffee parchment pellet and lower than reported percentage in coal. The content in the studied materials were less than the optimum limit indicated in the clinker composition which is about 0.5% with respect to K_2O and about 0.2 % with respect to Na_2O. This implied the oxides will not causes disruption and pattern cracking and blockages of air ways in the furnace under favorable moisture and temperature (McKendry, 2002).

Table 4: Oxide analysis of coffee parchment pellet and raw coffee parchment in comparison with reported value Coal (Odunayo et al., 2016)

Sample code	CaO (%)	MgO (%°	SiO_2 (%)	Al_2O_3 (%)	Fe_2O_3 (%)	K_2O (%)	Na_2O (%)
CP-Pellet	29.91	5.95	8.76	1.09	1.06	0.36	0.01
CP-Raw	16.32	4.32	6.38	1.12	0.77	0.25	0.00
Coal	0.18	0.12	16.9	11.4	0.37	0.62	0.14

4.3.4. Heavy Metals contents

The result of heavy metals found in the coffee parchment pellet is presented in table 8. The contents of heavy metals in coal as reported by Odunayo et al. (2016) were also included for comparative presentation.

Table 4: Heavy metal analysis result of coffee parchment pellet and in coal as reported by Odunayo et al. (2016)

Sample	**Cr (mg/kg)**	**Cu (mg/kg)**	**Zn (mg/kg)**	**Cd (mg/kg)**	**Ni (mg/kg)**	**Pb (mg/kg)**
CP-pellet	3.8	4.0	10	< 0.05	1.5	0.3
Coal	N.a	32.8	38.6	N.a	20.6	7.02

N.a- not available

Table 4 shows that the levels of heavy metals found in coffee parchment pellet were lower than coal. Moreover the result confirmed coffee parchment pellet meets minimum requirements of cement industry specified by different countries (Mokrzycki et al., 2003; EC, 2003).

5. CONCLUSIONS

The different analysis result of coffee parchment for the first time confirmed that:

- The quantity of coffee parchment generated in Addis Ababa city within a radius of 41.6 Km were on average 14,388.7 tonnes per year, Moreover, this is a wasted resource dumped elsewhere near the washed coffee processing plant and/or has been used inefficiently and irregularly by the local population who utilize the raw coffee parchment as a cooking fuel. However, this could be effectively used for the production of pelletized fuel as substitutes to coal used in Ethiopian cement factories.
- The coffee parchment has relatively better fuel characteristics as compared to many biomass fuels such as rice husk, cereal straw, and sugar cane bagasse. And meet the required quality to be used as alternative solid fuel as most the proximate and elemental analysis result falls in the standards specified by different organization and countries.
- Upgrading of coffee parchment by pelletizing made the feedstock material more denser and have uniform size as result improved heating value (up to 28 MJ/Kg), fixed carbon content, Hydrogen, silica and other oxide contents
- Ash oxides content found in the studied material confirmed that the fuel ash may supplement sufficient oxide of calcium, silica, aluminum, magnesium and iron required for clinker formation up on careful design of the fuels. Overall this may reduce the raw material demand in cement industry in addition to its contribution to supplement fuel demand which rely on imported coal.
- Finally, the observation in this study indicated the effect of molasses added to facilitate binding on the heating value and other properties that demand further investigation.

ACKNOWLEDGMENTS

We would like to Acknowledge ASTU for the full funding of this project and contribution of everyone who technically support for successful completion of the project.

REFERNCES

Akowuah (2012). Physico-chemical characteristics and market potential of sawdust charcoal briquette. *International Journal of Energy and Environmental Engineering*, 3-20.

Aremu, A.S. (2013). In-town tour optimization of conventional mode for municipal solid waste collection. *Nigerian J. Technol.* 32 (3): 443–449

Arranz, J. I. (2011). Analysis of Densified of the Combination from Different Biomass Waste. Doctoral Thesis, University of Extremadura, Badajoz, Spain.

ASTM standard (2004). *Standard test method for gross calorific value of refuse derived fuel by the bomb calorimeter*. USA: ASTM International.

Azad Rahman, Rasul M. G., Khan M. M. K., and Sharma S. (2013). Impact of Alternative Fuels on the Cement Manufacturing Plant Performance: An Overview," *Procedia Engineering*, 56: 393–400, doi:10.1016/j.proeng.2013.03.138.

Battelle (2002). Toward a sustainable cement industry: climate change Sub study

Bhambulkar S.V. (2011). Municipal solid waste collection routes optimized with ARC GIS network analyst. *(IJAEST) International Journal of Advanced Engineering Sciences and Technologie*s, 11(1): 202 – 207

Bhattacharya S.C., Sivasakthy Sett &. Shrestha R. M. (1989). State of the Art for Biomass Densification, *Energy Sources*, 11(3): 161-182

Bilhate Chala, Latif S, Muller J. (2015). Potential of By-Products from Primary Coffee Processing as Source of Biofuels

Biswas, A.K.; Rudolgsson, M.; Broström, M.; Umeki, K. (2014). Effect of pelletizing conditions on combustion behaviour of single wood pellet. *Appl. Energy*, 119: 79–84.

Braz, C. E., Crnkovic, P. (2014). Physical – Chemical characterization of biomass samples for application in pyrolysis process. *Chemical Engineering Transaction*, 4: 523–528.

CEMBUREAU. (2013). Raw material substitution. European Cement Association.
Cement Sustainability Initiative (2002). Our Agenda for Action. Published by the CSI and WBCSD. in available at www.wbcsdcement.org
De Almeida L.F.P., Sola A.V.H., Behainneet J.J.R. (2017). Sugarcane bagasse pellets: characterization and comparative analysis. *Acta Scientiarum*, 39 (4): 461-468.
Demirbas, A. (2004). Combustion characteristic of different biomass fuels. Progress in Energy and Combustion Science.
Domalski, E. S., Jobe, T. L., Jr & Milne, T. A. (1987). Thermodynamic Data for Biomass Materials and Waste Components. American Society of Mechanical Engineers, NY.
Duca, D.; Riva, G.; Foppa Pedretti, E.; Toscano, G. (2014). Wood pellet quality with respect to EN 14961–2 standard and certifications. *Fuel*, 135: 9–14.
Duda, J. (2004). Energy saving and pro-ecological techniques of clinker burning. Polish: Publishing House of Silesian Institute.
Efomah A.N. and Gbabo A. (2005). The physical, proximate and ultimate analysis of rice husk briquettes. *International journal of innovative science, engineering and technology*, 2(5).
ESMAP (1986). Agricultural residue briquetting pilot projects for substitute household and. Industrial fuel. UNDP/World Bank Technical report
European Commission (EC) (2001). Integarted Pollution Prevention and Control. Reference Document on Best Available Techniques in the Cement and Lime Manufacturing Industries.
European Commission directorate general environment (2003). Refuse derived fuel, current practice and perspectives (b4-3040/2000/306517/mar/e3) final report.
European Pellet Council (2011). Handbook for the Certification of Wood Pellets for Heating Purposes, European Pellet Council, Brussels, Belgium,
Everard C.D, Fagan C.C, McDonnell K. (2012). Visible-near infrared spectral sensing coupled with chemometric analysis as a method for on-line prediction of milled biomass composition pre-pelletising. *J Near Infrared Spectrosc*; 20:361–9.
Fagan C.C, Everard CD, McDonnell K. (2011). Prediction of moisture, calorific value, ash and carbon content of two dedicated bioenergy crops using near-infrared spectroscopy. *Bioresour Technol*; 102:5200–6.
Gemechu B. (2009). Efforts at promoting, branding Ethiopia's coffee, The Ethiopian Herald.
Giddings, D.; Eastwick, C.N.; Pickering, S.J. and Simmons, K. (2000). Computational fluid dynamics applied to a cement precalciner. *Proc. Instn. Mech. Engrs*, 214:A.
Gillespie, G.D.; Everard, C.D.; Fagan, C.C.; McDonnell, K.P. (2013). Prediction of quality parameters of biomass pellets from proximate and ultimate analysis. *Fuel*, 111: 771–777.
Hendriks, C.A., Worrell, E., de Jager, D., Block, K., & Riemer, P. (1998). Reduction of Greenhouse Gases from the Cement Industry. IEA GHG Paper presented at GHGT-4 Interlaken, Switzerland.
Henrich E., Stahl R., Gehrmann, H.J., Vodegel S., Koch M. (2014). Definition of a standard biomass. Forschungszentzrum Karlsruhe GmbH. Available at del_sp2_wp1_2-1-1_05-01-10-fzk%20(1).pdf
Hewlett, P.C. (2004). LEA's Chemistry of Cement and Concrete. (Fouth Edition). Elsevier Butterworth-Heinemann.
International Coffee Organization, (2017). World Coffee Production. Available at: http://www.ico.org/prices/po-production.pdf
International finance corporation (IFC) (2017). Increasing the use of alternative fuels at cement plants: international best practice
International Organization for Standardization. (2014a). ISO 17225-2: Solid biofuels - Fuel specifications and classes Part 2: Graded wood pellets. ISO/TC 238. Geneva, SW: ISO.
International Organization for Standardization. (2014b). ISO 17225-6: Solid biofuels - Fuel specifications and classes Part 6: Graded non-woody pellets. ISO/TC 238. Geneva, SW: ISO.
Japhet, J. A., Tokan, A., and Muhammad, M. H. (2015). Production and Characterization of Rice Husk Pellet; *American Journal of Engineering Research (AJER)*, 4(12):112-119
Kuokkanen M., Vilppo T., Kuokkanen T., Stoor T., Niinimaki, J.(2011). Additives in wood pellets, *Bio Resources*, 4(6): 4331–4355, 2011.
Kyauta E. E., Adisa A.B., Abdulkadir L.N. Balogun S. (2015). Production and Comparartive Study of Pellets from Maize Cobsand Groundnut Shell as Fuels for Domestic Use. *American Journal of Engineering Research (AJER)*, 4(1):97102
Lechtenberg D. (2008). Alternative Fuels in Developing Countries, World Cement.
Lewandowski I & Kicherer A. (1997). Combustion quality of biomass: practical relevance and experiments to modify the biomass quality of Miscanthus x giganteus. *Eur J Agron*, 6:163–77.
McKendry, P. (2002). Energy production from biomass (part 1): overview of biomass. *Bioresource* Technol., 83: 37–46

Mhilu C.F. (2014). *Analysis of energy characterstics of Rice and coffee husk blends*. Hindawi publishing corporation. ISRN chemical engineering.

Miranda.T , Montero I., José Sepúlveda F., Arranz J.I., Rojas C.V., and Sergio Nogales S (2005). A Review of Pellets from Different Sources. *Materials*, 8: 1413-1427; doi:10.3390/ma8041413.

Mohan, D. P. (2006). Pyrolysis of wood/biomass for bio-oil: a critical review". *Energy Fuels*, 848–889.

Mokrzycki E., Uliasz-Bochenczyk A' and Sarna M. (2003). Use of alternative fuels in the Polish cement industry, *Applied Energy*, 74: 101-111

Montenegro Camacho Y.S., Bensaid S., Ruggeri B., Restuccia L., Ferro G., Mancini G. and Fino D. (2016). Valorisation of by-Products/Waste of Agro-Food Industry by the Pyrolysis Process. *Journal of Advanced Catalysis Science and Technology*, 3(1):1-11

Morten T. H., Anna R.J., Sandra H. and Patrick B. (2009). English handbook for wood pellet combustion

Murray, A, & Price, L. (2008). Use of Alternative Fuels in Cement Manufacture: Analysis of Fuel Characteristics and Feasibility for Use in the Chinese Cement Sector, Ernest Orlando Lawrence Berkeley National Laboratory, 10 March 2011 http://ies.lbl.gov/iespubs/LBNL-525E.pdf

Obernberger, I., Thek, G. (2004). Physical characterisation and chemical composition of densified biomass fuels with regard to their combustion behaviour. *Biomass Bioenergy*, 27: 653–669.

Odunayo A.R., Omoniyi P., Leslie P., Olorunfemi O. (2016). Comparative chemical and trace element composition of coal samples from Nigeria and South Africa. *American Journal of Innovative Research and Applied Sciences*, 2(9): 391-404

Pattiya, A. (2015). Thermochemical Characterization of Agricultural Wastes from Thai Cassava Plantations. *Energy Sources, Part A*, 33:691–701

Paula et.al. (2011). Characterization of residues from plant biomass for use in energy generation. *Cerne, Lavras*, 17(2):237-246

Poddar, S.; Kamruzzaman, M.; Sujan, S. M. A.; Hossain, M.; Jamal, M. S.; Gafur, M. A. and Khanam, M. (2014): Effect of compression pressure on lignocellulosic biomass pellet to improve fuel properties:Higher heating value. *Fuel*, 131: 43–48.

Sánchez, E. A., Pasache, M. B. and García, M. E. (2014). Development of Briquettes from Waste Wood(Sawdust) for Use in Lowincome Households in Piura, Peru; Proceedings of the World Congress on Engineering, Vol II,WCE 2014, London, U.K.

Smidth F.L. and Co. (2000). Dry process kiln systems, technical brochure.

Singh H., Sapra P.K., and Sidhu B.S. (2013). Evaluation and characterization of different biomass residues through proximate and ultimate analysis and heating value. *Asian journal of engineering and applied technology*, 2(2): 6-10

Taylor, M., Tam, C., Gielen, D. (2006). Energy Efficiency and CO_2 Emissions from the Global Cement Industry. Paper prepared for the IEA-WBCSD workshop: Energy Efficiency and CO2 Emission Reduction Potentials and Policies in the Cement Industry, IEA, Paris, 4–5

Tokan, A., Muhammad, M. H., Japhet, J. A. and Kyauta, E. E. (2016). Comparative Analysis of the Effectiveness of Rice Husk Pellets and Charcoal As Fuel For Domestic Purpose, *IOSR Journal of Mechanical and Civil Engineering* (IOSR-JMCE, 13(15):21-27

Tumuluru J.S., Wright C.T., Hess J.R. and Kenney K.L. (2011). A review of biomass densifi cation systems to develop uniform feedstock commodities for bioenergy application. *Biofuels, Bioprod. Bioref*. 5:683–707; DOI: 10.1002/bbb

Xing Yang, Hailong Wang, Peter James Strong, Song Xu, Shujuan Liu, Kouping Lu, (2017). Thermal Properties of Biochars Derived from Waste Biomass Generated by Agricultural and Forestry Sectors. Energies.

Yisehak Seboka, Mulugeta Adamu Getahun, Yared Haile-Meskel. (2009). Biomass energy for cement production: opportunities in Ethiopia. New York, USA: UNDP.

Optimal Placement of TCSC with Multi Objectives using Self-Adaptive Firefly Algorithm

Selvarasu Ranganathan*, Palanivel. P, Hinsermu Alemayehu

School of Electrical Engineering and Computing Adama Science and Technology University, Adama, Ethiopia
**Corresponding author, e-mail: selvarasunaveen@gmail.com*

ABSTRACT

This paper examines multi objectives for power system performance improvement through optimal placement of Thyristor Controlled Series Compensator (TCSC) with the application of Self-Adaptive Firefly Algorithm (SAFA). The SAFA selects the best positions and parameters for TCSC placement. Three single objectives of Real Power Loss (P_{loss}) minimization, improvement of Voltage Profile (VP), enhancement of Voltage Stability (VS) and one multi objective of $P_{loss,}$ minimization, simultaneously improve the VP besides enhancing the VS are considered. The proposed SAFA approach is performed on IEEE 30 bus system and the simulation results are presented. The results are validated through solutions obtained by other optimization algorithms of HBA and BFA.

Keywords: *FACTS, Power loss, SAFA, TCSC, Voltage Stability*

1. INTRODUCTION

Nowadays the load on the existing power system network is substantially increasing due to growth of industries and modernization of human life style. As a result the existing power system is forced to operate in stressed condition and leads to voltage instability. Also it's a challenge to widen the existing power system to meet the ever increasing power demand by installing new generation and transmission networks due to economical and environmental constraints. An alternate way to overcome this challenge is installing Flexible Alternating Transmission Systems (FACTs) controllers. The series, shunt controlled and combination of both are the classification FACTs devises. TCSC is one of the classifications of series connected FACTs device, which is capable of increasing power transfer capability, loss reduction, voltage profile (VP) improvement and enhance the voltage stability (VS) of power system network [1-3].

The power system researchers are carried out their research work for placement of FACTs devices on power system network and reported in their publications. They used both conventional and nonconventional method of an optimization algorithm for FACTs placement. Since optimization algorithms has many applications in the field of solving optimization problem, it is generally accepted by most of the power system researchers and they have been considered like Differential Evolution (DE), Genetic Algorithm (GA), Honey Bees Algorithm (HBA), Ant Colony Optimization (ACO), Particle Swarm Optimization Algorithm (PSO), Bacterial Foraging Algorithm (BFA) and Gravitational Search Algorithm (GSA) [4-13].

Available transfer capability of the power system has been improved by the FACTs placement using HBA [4]. Evolutionary algorithms such as DE and GA have been proposed to choose the feasible locations and parameters of TCSC for increasing power flow, reduction of losses and enhancement of stability of the system and performances are tested on IEEE 14 bus system [5]. A Fuzzy lag-lead controller has been proposed to control TCSC and SVC for oscillation damping, stability enhancement and ACO used for parameters setting of TCSC and SVC [6]. Particle Swarm Optimization Algorithm (PSO) has been employed for improving power transfer capability and economic power system operation through proper SVC and TCSC placement [7]. A complete review has been reported that the application of PSO for FACTs placement in power system network [8].

Dr. Passino developed BFA to solve optimization problem than later it has been employed for minimizing loss and enhance voltage profile through UPFC placement [9-10]. SVC and TCSC have been considered for security enhancement and the comparative results are presented with BBO, WISPO and PSO [11]. A cumulative Gravitational Search Algorithm (GSA) has been proposed for FACTs placement with objectives of power loss

minimization and VS enhancement [12]. An evolutionary algorithm has been presented for allocating FACTS to improve VS of the system [13]. Recently, Dr. Xin-She Yang has been initiated a Firefly Algorithm (FA) in 2007, for obtaining the solution for optimization problems [14]. The FA has many applications for solving power system optimization problem like economic dispatch and unit commitment etc., [15-16]. Still, due to an unsatisfactory selection of FA parameters anguishes the convergence and directs to sub optimal results. Hence SAFA has been presented for SVC and TCSC placement and only loss minimization is considered as an objective [17-18]. Multi objectives have been considered for multiple FACTs placement [19].

In this work single and multi objectives are taken into consideration for optimal placement of multiple TCSC in IEEE 30 bus system using SAFA.

2. FIREFLY ALGORITHM

Firefly algorithm is one of the nature inspired meta-heuristic algorithms and it employs based on the light intensity among two fireflies [14]. Twenty fireflies are chosen as number of fireflies, *nF*.

The *r*-th firefly light intensity is represented as

$$LI_r = Fitness\ (x_r) \tag{1}$$

$\beta_{r,s}$ is the absorption coefficient between two fireflies (*r* and *s*) and is represented as

$$\beta_{r,s} = (\beta_{\max,r,s} - \beta_{\min,r,s}) \exp(-\gamma_r r_{r,s}{}^2) \tag{2}$$

In the above, $r_{r,s}$ is the Cartesian distance of fireflies and is presented by

$$r_{r,s} = \|x_r - x_s\| = \sqrt{\sum_{v=1}^{nd} \left(x_r^k - x_s^k\right)^2} \tag{3}$$

The movement between two fireflies takes place, when *r-th* firefly light intensity is less than the *s-th* firefly light intensity and their movement at the *k-th* iteration is as follows

$$x_r(\mathrm{k}) = x_r(\mathrm{k}-1) + \beta_{r,s}\left(x_s(\mathrm{k}-1) - x_r(\mathrm{k}-1)\right) + \alpha\left(rand - 0.5\right) \tag{4}$$

2.1. Self-Adaptive Firefly Algorithm (SAFA)

Firefly parameters such as random movement factor (α), Absorption coefficient ($\beta_{\min}$) and attractiveness parameter (γ), are included with each firefly of decision variables. Hence these parameters are controlled over self-adaptive mechanism at each iterative process in SAFA and the firefly is represented as

$$x_r = \left[x_r^1, x_r^2 \cdots, x_r^{nd}, \alpha_r, \beta_{\min,r}, \gamma_r \right] \tag{5}$$

Each firefly with their parameters undergoes whole search process and the equation (2) is thus tailored by the following,

$$\beta_{r,s} = (\beta_{\max,r,s} - \beta_{\min,r,s}) \exp(-\gamma_r r_{r,s}{}^2) + \beta_{\min,r,s} \tag{6}$$

The advantage of SAFA includes less computational effort, avoiding the sub optimal solution and convergence enhancement.

3. MATHEMATICAL MODELLING OF TCSC

The power flow expressions among the buses i and j are as follows [18]

$$\text{Real power, } P_{ij} = \frac{V_i V_j}{x_{ij}} \sin \delta_{ij} \tag{7}$$

Reactive Power, $Q_{ij} = \frac{1}{x_{ij}}(V_i^2 - V_i V_j \cos\delta_{ij})$ (8)

The TCSC is one classification of series connected FACTs device. The static model of TCSC is considered and it can be denoted as static reactance -jX_c, added in series with the transmission line connecting buses i and j as presented in Figure.1. The transfer reactance between buses i and j decreases resulting that power flow increases, as a result there is reduction in reactive power loss and bus voltage improvement. The effective transmission line reactance among the buses i and j with series compensation is expresses as follows,

$$x_{eff} = x_{ij} - x_c \quad (9)$$

$$x_{ij} = (1-k)x_{ij} \quad (10)$$

Where, $k = \frac{x_c}{x_{ij}}$ = Transmission line compensation factor, whose value is chosen between -0.8 and 0.2 to avoid over compensation and x_{ij} is transmission line reactance.

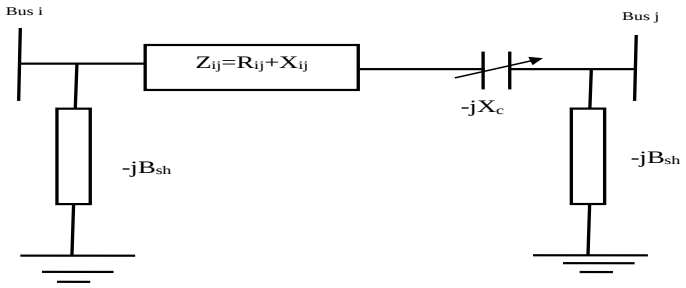

Figure 1: Static Model of TCSC with transmission line

3.1. Proposed Problem

The placement of multiple TCSC is chosen as an optimization problem and an objective is given by following expression,

Minimize $\Phi(x, y)$ (11)

Subjected to $g(x, y) = 0$ (12)

$h(x, y) \le 0$ (13)

In above equations equality constraints are expressed as $g(x, y)$, inequality constraints expressed as $h(x, y)$, x is the state variable, which includes real and reactive power generation at slack bus, reactive power generation at PV buses and real power loss (P_{loss}). y is the control variable, which includes type of FACTs, location and parameters of TCSC.

The equality constraints, $g(x, y)$ are given by the expression as follows

$P(V, \delta) - P^{sp} = 0$ for generator and load buses (14)

$Q(V, \delta) - Q^{sp} = 0$ for load buses (15)

The equality constraints, $h(x, y)$ are defined as follows

$-0.8 \le k \le 0.2$ for TCSC (16)

$$Q_{Gi}^{\min} \le Q_{Gi} \le Q_{Gi}^{\max} \text{ at PV buses} \quad (17)$$

$$V_i^{\min} \le V_i \le V_i^{\max} \text{ at PQ buses} \quad (18)$$

The objective functions are formed with four different cases of three single objectives and one multi objective. Single objectives considered are $P_{loss,}$ minimization, improvement of VP, and enhancement of VS. Multi objectives includes $P_{loss,}$ minimization, simultaneously improve the VP besides enhancing the VS.

Case 1: Real power loss (P_{loss})

Real power loss minimization expression is as follows [18]

$$\text{Minimize } J_1(x,y) = P_{loss} \quad (19)$$

Where,

$$P_{loss} = \sum_{k \in \Im} g_{ij} \left(|V_i|^2 + |V_j|^2 - 2|V_i||V_j|\cos\delta_{ij} \right) \quad (20)$$

Case 2: Bus voltage profile (VP) improvement

The objective function for improvement of bus VP can be obtained by minimizing Total voltage deviation (TVD) as follows [19]

$$\text{Minimize } J_2(x,y) = \sum_{j \in \Phi} |V_j - 1| \quad (21)$$

Case 3: Enhancement of voltage stability (VS)

The enhancement of VS may be achieved by minimizing L-index and its values are in between 0 and 1. The sum of L-indices represented as follows [19].

$$\text{Minimize } J_3(x,y) = \sum_{j \in \Phi} L_j \quad (22)$$

$$\text{Where, } L_j = \left| 1 - \sum_{i=\Omega} F_{ij} \frac{V_i}{V_j} \right| \quad (23)$$

Values of F_{ij} are obtained through bus admittance matrix.

Case 4: P_{loss}, VP and VS.

In this case multi objectives are considered for minimizing P_{loss} at the same time improving the VP also enhancing VS and the objective function as

$$\text{Minimize, } \quad J(x,y) = \sum_{i=1}^{nobj} w_i \, J_i \quad (24)$$

3.2. Illustration of SAFA variables

The firefly is illustrated in Table.1. In which the first row indicates the location for the TCSC, representing transmission line numbers L_k where the TCSC to be placed. The 2nd row represents the compensation factor of TCSC and third row shows the firefly parameters.

3.3. Fitness function

The fitness function is represented by light intensity function (*LI*), which is maximized to get the optimal solution by the SAFA.

$$\text{Maximize } \quad LI = \frac{1}{1+\Psi} \quad (25)$$

Where, $$\Psi = w_1 J(x,u) + w_v \sum_{i=1}^{nload} V_{di} + w_Q \sum_{j=1}^{ngen} \left| Q_{Gi} - Q_{Gi}^{limit} \right|^2 \quad (26)$$

$$V_{di} = \begin{cases} 0 & if\ V_i \in \left[V_i^{min}, V_i^{max} \right] \\ \exp\left\{ \Psi_v \left(|1 - V_i| - 0.05 \right) \right\} - 1 & if\ V_i \notin \left[V_i^{min}, V_i^{max} \right] \end{cases} \quad (27)$$

Table 1. Firefly Illustration for TCSC Placement

L_1	L_2	L_3	⋯	L_{nF}
k_1	k_2	k_3	⋯	k_{nF}
α	β_{min}	γ		

4. SIMULATION RESULTS AND DISCUSSION

The simulation is performed on Matlab software to analyze the feasibility of proposed SAFA for single and multi objectives optimization through TCSC placement in IEEE 30 bus system. Power flow solution is attained using N-R method during the optimization process [20]. The performance of multiple TCSC after their placement is obtained through the SAFA for the four cases, which is described in section 3. The effectiveness of SAFA is compared with the results are attained by HBA and BFA for all considered four cases. The solution for the case 1 is obtained by considering different number TCSCs and is given in Table 2, which helps to select the number of TCSC for remaining cases. It is observed from the Table 2 that P_{loss} reduction is 17.4338 MW from 17.5028 MW when six TCSCs are placed in IEEE 30 bus system. The P_{loss} savings are less for other number of TCSCs. Hence six TCSCs are selected for remaining cases 2-4.

Table 2. P_{loss} with Different Number of TCSC

System	nF	P_{loss}
IEEE 30	0	17.5028
	4	17.4521
	5	17.4485
	6	17.4338
	7	17.4360

The performances obtained through simulation like, P_{loss}, TVD, Maximum Voltage Stability Index (MVSI) and voltage magnitudes limits of IEEE 30 bus system are presented in Table 3 for all four cases of before and after multiple TCSC placement. The case 1 objective is to minimize the P_{loss} and it is noted from this table that P_{loss} minimization is 17.4338 MW by SAFA and concurrently HBA and BFA decrease the P_{loss} to 17.4437 and 17.4519 MW respectively. It is obvious from the solutions that SAFA determines the optimal positions for TCSC placement and suitable VAR support, which reduces the P_{loss} to the minimum feasible amounts than those of HBA and BFA. Figure 2 shows the P_{loss} savings after TCSC placement of case 1.The percentage of P_{loss} saving of HBA and BFA are 0.34 % and 0.29 % correspondingly, though SAFA directs the P_{loss} savings to 0.39 %. The figure shows that SAFA offers higher savings in losses compared to HBA and BFA. The investigation of the Table 3 values also indicates that the SAFA and other algorithms fetch the entire load bus voltages to lie within the considered limits.

Table 3. Performance Solutions for Cases 1-4

	Method	P_{loss} (MW)	TVD	MVSI	V^{low}/V^{high} (pu)
Base Case		17.5028	0.4562	0.1420	0.989/1.082
Case-1	SAFA	17.4338	0.4748	0.1406	1.002/1.050
	HBA	17.4437	0.5501	0.1350	0.991/1.054
	BFA	17.4519	0.4570	0.1414	0.989/1.052
Case-2	SAFA	17.5547	0.4205	0.1422	0.989/1.050
	HBA	17.5093	0.4297	0.1434	0.988/1.052
	BFA	17.5278	0.4310	0.1457	0.991/1.050
Case-3	SAFA	17.6062	0.6083	0.0880	1.008/1.053
	HBA	17.6042	0.5848	0.0886	1.009/1.054
	BFA	17.6870	0.5176	0.0904	1.006/1.054
Case-4	SAFA	17.5012	0.4415	0.1322	0.989/1.051
	HBA	17.5019	0.4487	0.1402	0.987/1.051
	BFA	17.5036	0.4465	0.1358	0.989/1.049

In Case 2, objective is improving VP through minimizing the TVD. It can be observed from Table 3 in case two, the TVD reduced from 0.4562 to 0.4205 by SAFA but the HBA and BFA reduces the TVD to 0.4297 and 0.4310 through multiple TCSC placements. Details of percentage of VP improvement after TCSC placement are shown in Figure 3. HBA and BFA offers the percentage VP improvements are 5.8 % and 5.52 % respectively, but the SAFA presents the percentage VP improvement of 7.82 %. The results clearly indicate that SAFA offers the optimal placements for TCSC and their VAR support, while minimizing the TVD to improve the VP. It should be noticed that the objective of case 2 is to minimize the TVD, which leads all load bus voltage magnitudes closer to 1.0 per unit by maintaining acceptable voltage magnitude limits.

The objective of case 3 is to enhance VS by minimizing MVSI. It can be observed from the Table 3 that the MVSI is reduced from 0.1420 to 0.0880, 0.0886 and 0.0904 over multiple TCSC placements by the application of self -adaptive firefly algorithm, HBA and BFA respectively. Details of percentage of VS enhancement after TCSC placement are shown in Figure.4. The BFA and HBA show the percentage of VS enhancement as 36.34 % and 37.6 % respectively, whereas the SAFA provides 38.02 % VS enhancement. It can be noticed from the solutions that SAFA presents optimal locations with suitable VAR support for TCSCs, which minimize the MVSI to the minimum values, then those of BFA and HBA.

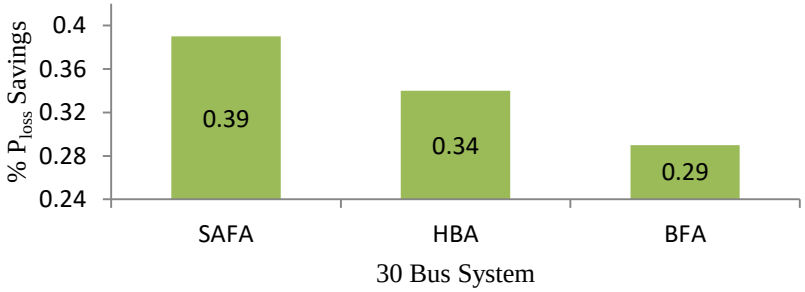

Figure 2: Comparison of % Ploss Savings after TCSC Placement.

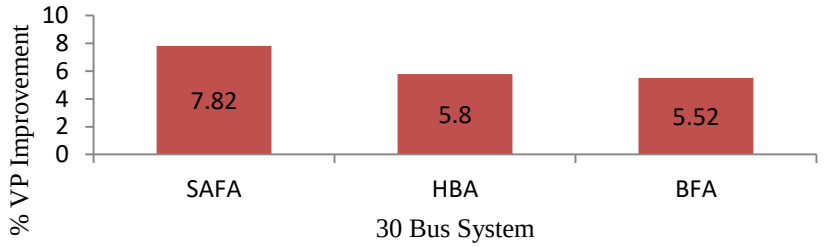

Figure 3. Comparison of % VP Improvement after TCSC Placement

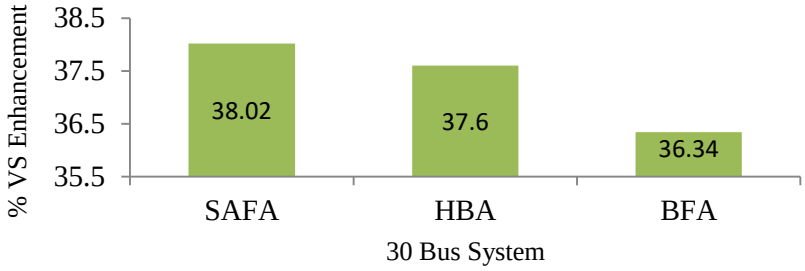

Figure 4. Comparison of % VS Enhancement after TCSC Placement

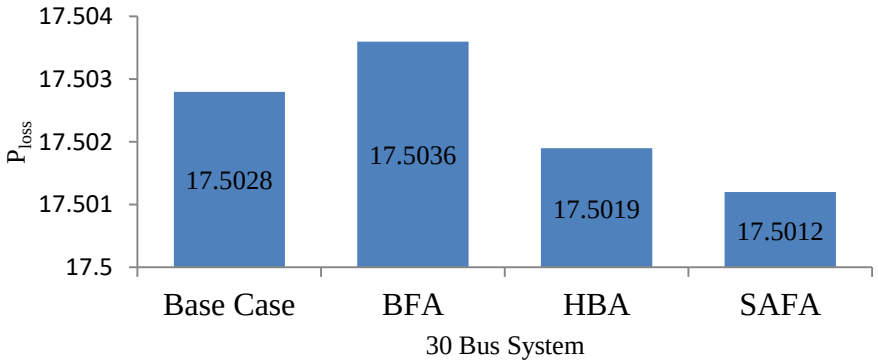

Figure 5. P_{loss} Comparison Obtained through Case 4 after TCSC Placement

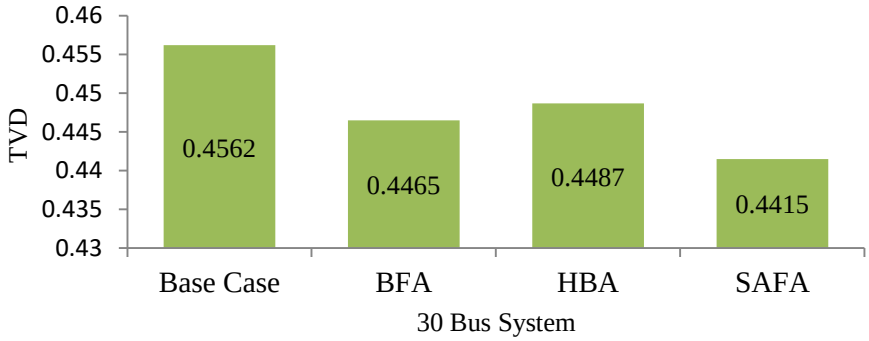

Figure 6. Comparison of TVD Obtained through Case 4 after TCSC Placement

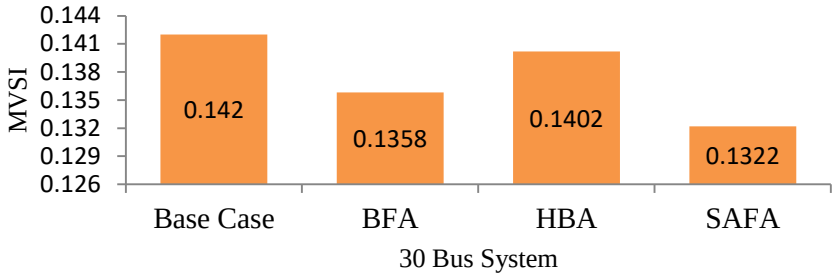

Figure 7: MVSI Comparison Obtained through Case 4 after TCSC Placement

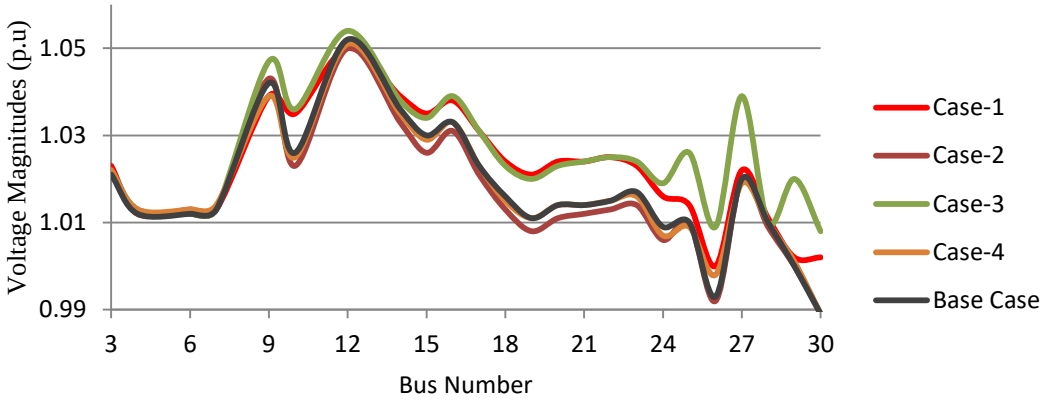

Figure 8: IEEE 30 Bus Systems VP after TCSC Placement

The multi objectives are considered in case 4 and they are minimizing P_{loss}, simultaneously improve the VP also enhance VS. It is observed from Table 3 (case 4) that self-adaptive firefly algorithm reduces P_{loss}, TVD and MVSI are 17.5012 MW, 0.4415 and 0.1322 respectively. The comparison of results obtained through SAFA, HBA and BFA for P_{loss} minimization, VP improvement and VS enhancement are given in Figures 5, 6 and 7 respectively. The presented results obviously shows that the SAFA presents the optimal positions with reactive power values for multiple TCSC placements, which minimizes P_{loss}, improve the VP besides enhancing the VS.

Table 4. Location and parameters of TCSC obtained by SAFA

TCSC No.		1	2	3	4	5	6
Case 1	Line Location	4	9	19	29	31	18
	Compensation factor, (k)	-0.469	0.200	-0.479	0.200	-1.172	-0.240
Case 2	Line Location	14	18	11	15	4	41
	Compensation factor, (k)	0.200	0.200	0.200	0.200	0.057	-0.800
Case 3	Line Location	36	29	25	12	27	11
	Compensation factor, (k)	-0.800	-0.468	-0.575	-0.776	0.037	-0.067
Case 4	Line Location	41	11	37	34	9	29
	Compensation factor, (k)	-0.408	-0.797	-0.722	-0.790	0.200	-0.721

Table 5. Location and parameters of TCSC obtained by HBA

TCSC No.		1	2	3	4	5	6
Case1	Line Location	28	18	25	4	14	7
	Compensation factor, (k)	-0.527	-0.175	-0.800	-0.680	-0.785	0.200
Case 2	Line Location	14	25	34	19	18	30
	Compensation factor, (k)	0.141	-0.003	-0.621	0.163	0.200	0.005
Case 3	Line Location	14	30	29	36	37	26
	Compensation factor, (k)	-0.561	-0.592	-0.416	-0.787	-0.600	-0.406
Case 6	Line Location	11	34	23	4	35	30
	Compensation factor, (k)	-0.800	-0.525	-0.444	-0.163	0.057	-0.401

Table 6. Location and parameters of TCSC obtained by BFA

TCSC No.		1	2	3	4	5	6
Case 1	Line Location	9	41	26	21	4	33
	Compensation factor, (k)	0.147	-0.361	-0.754	-0.005	-0.628	-0.314
Case 2	Line Location	35	37	15	14	30	32
	Compensation factor, (k)	0.175	-0.569	0.195	0.200	0.136	-0.163
Case 3	Line Location	20	41	26	25	36	4
	Compensation factor, (k)	-0.606	-0.687	-0.103	-0.559	-0.773	-0.466
Case 4	Line Location	15	22	36	26	25	11
	Compensation factor, (k)	0.199	0.193	-0.098	0.200	-0.788	-0.770

Load bus voltages of IEEE 30 bus system attained through SAFA for considered all the four cases are presented in Figure 8. Interestingly the values of voltage magnitudes are found to lie in-between 0.95 and 1.1 p.u. It can be observed from the solutions that SAFA identifies optimal positions for multiple TCSC placements for P_{loss} minimization, VP improvement and VS enhancement of the existing system. The locations for TCSC placement and their parameters attained by SAFA, HBA and BFA are given in Tables 4, 5 and 6 respectively.

5. CONCLUSION

Single and Multi objectives of four cases are considered to seek the optimal positions and parameters of TCSC for their placement in IEEE 30 bus system using SAFA. The performances in terms of real power loss, TVD, MVSI and VMs limits are presented and analyzed in terms P_{loss} minimization, VP improvement and VS enhancement. The SAFA identifies the optimal positions and parameter of TCSCs for their placement for existing power system performance improvement. It is obvious from the above discussion that the SAFA presents the feasible solutions than those of HBA and BFA.

REFERENCES

[1]. Taylor, C.W. (1994): *Power System Voltage Stability.* New Delhi: McGraw-Hill.
[2]. Hingorani, N.G., Gyugyi, L. (1999): *Understanding FACTS: Concepts and Technology of Flexible AC Transmission Systems*. US: Wiley, IEEE Press.
[3]. Mathur, R.M., Varma, R.K. (2002): *Thyristor-based FACTS Controllers for Electrical Transmission Systems*. US: IEEE Press.

[4]. Mohamid Idris. R., Khairuddin. A., M. Mustafa. W. (2009): Optimal allocation of FACTS devices for ATC enhancement using Bees algorithm. *World Academy of science Engineering and Technology, 30*, 313-320.
[5]. Ghamgeen I,Rashed., Yuanzhang Sun., Shaheen, H.I. (2012): Optimal location and parameter setting of TCSC for loss minimization based on differential evolution and genetic algorithm. *Physics Procedia, 33*, 1864-1878.
[6]. Chun-Feng Lu., Chia-Hung Hsu., Chia-Feng Juang. (2013): Coordinated control of flexible AC transmission system devices using an evolutionary Fuzzy lead-lag controller with advanced continuous Ant colony optimization. *IEEE Transactions on Power System, 28*(1), 385-392.
[7]. Bhattacharyya, B., Vikash Kumar Gupta., Swapan Kumar Goswami. (2012): Application of DE & PSO algorithm for the placement of FACTs devices for economic operation of a power system. *WSEAS Transactions on Power system, 7*(4), 209-2016.
[8]. Rezaee Jordehi, A. (2015): Particle swarm optimization for allocation of FACTS devices in electric transmission systems: A review. *Renewable and Sustainable Energy Reviews*, *52*(C), 1260-1267.
[9]. Passino, K.M. (2002): Biomimicry of bacterial foraging for distributed optimization and control. *IEEE Control Systems Magazine*, 22(3), 52–67.
[10]. Senthil Kumar, M., Renuga, P. (2012: Application of UPFC for voltage stability improvement and loss minimization using Fast Voltage Stability Index (FVSI). *Archives of Electrical Engineering. 61*(2), 239-250.
[11]. Kavitha, K., Neela, R. (2016): Comparison of BBO, WIPSO & PSO techniques for the optimal placement of FACTS devices to enhance system security. *Procedia Technologies*, *25*, 824-837.
[12]. Packiasudha, M., Suja, S., Jovitha Jerome. (2017): A new cumulative gravitational search algorithm for optimal placement of FACT device to minimize system loss in the deregulated electrical power environment. *International Journal of Electrical Power Energy and System*, *84*, 34–46.
[13]. Sidneo do Nascimento., Maury M, Gouvea, Jr. (2019): Voltage stability enhancement in power systems with automatic facts devices allocation. *Energy Procedia, 107*, 60-67.
[14]. Yang, X.S. (2010): *Nature-inspired meta-heuristic algorithms.* 2 nd ed., Beckington: Luniver Press.
[15]. Yang, X.S., Hosseini, S.S., Gandomi, A.H. (2012): Firefly Algorithm for solving non-convex economic dispatch problems with valve loading effect. *Applied Soft Computing, 12*(3), 180–186.
[16]. Chandrasekaran, K., Sishaj Simon, P. (2012): Network and reliability constrained unit commitment problem using binary real coded firefly algorithm. *International Journal of Electrical Power and Energy System, 43*(1), 921–932.
[17]. Selvarasu, R., Surya Kalavathi, M., Christober Asir Rajan, C. (2013): SVC placement for voltage constrained loss minimization using self-adaptive Firefly algorithm. *Achieves of Electrical. Engineering*, *62*(4), 649–661.
[18]. Selvarasu, R., Surya Kalavathi, M. (2015): TCSC Placement for loss minimization using self-adaptive firefly algorithm. *Journal of Engineering Science and Technology*, *10*(3), 291–306.
[19]. Selvarasu Ranganathan., Surya Kalavathi, M., C. Christober Asir Rajan. (206): Self-adaptive firefly algorithm based multi-objectives for multi-type FACTS placement. *IET Generation, Transmission and Distribution*, *10*(11), 2576-2584.
[20]. Saadat, H. (2004): *Power system analysis.* New Delhi: McGraw-Hill.

Modeling of Heat Transfer and Simulation of Metabolites Formation during Beer Processing: Case Study Harar Brewery Share Company

Bayisa Dame Tesema[1,*], Solomon Workneh[2]

[1]*Chemical Engineering Department, Adama Science and Technology University, Ethiopia*
[2]*Chemical Engineering Department, Bahirdar University, Ethiopia*
**Corresponding author, e-mail: bayisa123@gmail.com*

ABSTRACT

The study focuses on modeling of temperature profile during beer fermentation and selecting modeled temperature to simulate with a growth of a microorganism, ethyl ethanol formation, carbohydrate (glucose, maltose, and malt triose) consumption, and flavor compound formation. The study aimed at how to select best temperature for beer fermentation and how some of biochemical reaction going on with the controlled (selected) temperature. Finite element modeling was used for heat transfer modeling and COMSOL Multiphysics version 5.3 was the used software for the implementation. For simulation of bio-chemical change with the selected temperatures, MATLAB version 17 was used. The simulated results were indicated that at high coolant flow rate, a low-temperature profile was recorded with fermentation time. Accordingly, at 1.2, 1.3 and 1.6 m^3/hrs, 20 ^oC, 18 ^oC, and 12.5 ^oC were the observed temperatures respectively. The modeled vorticity results were also indicated that at 1.2 coolant flowrate uniform flow of fluid was observed around stirring center than other coolant rates. The simulated results were indicated that the initial glucose which were presented in the wort take 6 days and 8hrs for 12.5 ^oC, almost 3 days for 18 ^oC and decreased to 2 days for 20 ^oC to perform its conversion to ethanol and another flavor based by product. Initial glucose concentration (300 mol/m^3*) was finished after 134hrs whereas glucose concentration (200 &100)* mol/m^3 *was finished after 92hrs and 51 hrs respectively. The result indicated that the initial glucose which was presented in the wort take 6 days and 8 hours for 12.5 ^oC, almost 3 days for 18 ^oC and decreased to 2 days for 20 ^oC to finish its conversion to ethanol and another flavor-based by-product. At fermentation temperatures of 12.5^oC, 18^oC and 20^oC to get six percent of alcohol (6.64% (w/w)) content which is alcohol content Harar brewery used currently almost above 250 hrs, 112 hrs and 90 hrs were needed respectively). Both isoamyl alcohol and 2-methyl-1-butanol got their threshold value at lower fermentation time at all three temperatures which is 0.062 mol/m^3.*

Keywords: *Fermentation, Flavor, Modelling, Temperature*

1. INTRODUCTION

Fermentation produces energy from the oxidation of organic compounds. In the case of beer, fermentation is an important process unit operation. The initial chemical reaction pathway is the conversion of sugar into ethanol and carbon dioxide molecule, coupled with exothermic reaction and heat and biomass growth (MacDonald et al., 2008). Concurrently, a number of organic compounds (many of which contribute to or compromise beer flavor) are formed at low concentrations, due to the multitude of side reactions.

Beer fermentation is one of the large-volume industrial processes that are essentially controlled manually. There are several reasons that excluded automation from this process so far. One is that the essential process state variables are difficult to measure on-line. Another is that the fermentation process appears to be a complex system, which had not been modeled precisely enough so far. On the other hand, however, the brew masters make excellent beers with their current technology and any automatic process supervision and control system must compete with these highly skilled human controllers (Sablayrolles and Ball, 2004). Automatic systems would only be of interest to breweries if they would help the brew masters to produce the same quality of beer in a much less expensive way. There are some obvious entry points for further auto-mat ion in beer fermentation. In beer breweries, many tasks presently being performed by men as well as women, such as manual cleaning, filling, pitching, measuring, temperature control, yeast harvesting, pumping into lager vessels, etc., could be automated (Gaurdia, 2001).

The fermentation of alcohol is the most time-consuming step in brewing. It can take up to two weeks to complete. Fermentation progression is sensitive to yeast pitching rate, dissolved oxygen content, batch pressure

and temperature. The system temperature strongly affects yeast growth and metabolic rate: as long as yeast cells are kept below 30ºC and not damaged, higher temperatures accelerate fermentation (Skye and Ling, 2012). Beyond this temperature, ethanol and volatile flavor compound loss rates are too severe, coupled with increased production of undesirable substances and bacterial growth. Brewers control ferment or temperature within a narrow range during batch progression, to accelerate the fermentation while also ensuring that yeast is not deactivated due to denaturation and that no undesirable flavor compounds are produced.

2. MODEL GOVERNING EQUATIONS AND DESCRIPTION.

Diffusion and reaction of temperature flow in beer fermentation tank is integrated to ordinary differential equation as written below. It can be solved by finite element method. The finite element method is a numerical approach by which general differential equations can be solved in an approximate manner. The differential equation or equations, which describe the physical problem considered, are assumed to hold over a certain region. This region may be one-, two- or three-dimensional. It is a characteristic feature of the finite element method that instead of seeking approximations that hold directly over the entire region, the region is divided into smaller parts, so-called finite elements, and approximation is then carried out each element. The collection of all elements is called a finite element mesh. When the type of approximation which is to be applied over each element has been selected, the corresponding behavior of each element can then be determined. This can be performed because the approximation made over each element is fairly simple.

During beer fermentation conduction-convection mode of heat transfer occurs from between beer film and bulk beer, between bulk beer and the coolant. Equations which govern this heat transfer are described as follows. In beer fermentations the governing equation for flow of heat between medium and the growing yeast is derived from energy balance as follows. Basic assumption for the model governing equation:

- ✓ Cooling jacket is well insulated. No heat loss to the surrounding.
- ✓ Specific heat capacity of the wort and the coolant remains unchanged over entire fermentation time.
- ✓ Density of wort and the coolant remains unchanged over entire fermentation time
- ✓ Assume wort is homogeneous liquid.
- ✓ Assume the flow is laminar

Energy balance for fermentation tank

Rate of energy accumulated = rate of energy in- rate energy of out + rate of energy generated– rate of energy lost.

$$\frac{dE}{dt} = 0 - 0 + Egen - Q, \text{ no rate of energy in and out.}$$

$$Q = \mathrm{U} * \mathrm{A} * \Delta \mathrm{T}_{\mathrm{lm}},$$

Hence

$$\frac{d(mCpT)}{dt} = -X(\Delta HFG * \mu 1) * V - U * A * \Delta \mathrm{T}_{\mathrm{lm}}, \ where \ \Delta \mathrm{T}_{\mathrm{lm}} = \frac{T - Tj}{\ln T/Tj}$$

$$m = \rho V$$

$$\frac{d(\rho * V * Cp * T)}{dt} = -X * \Delta HFG * \mu 1 * V - U * A * \Delta \mathrm{T}_{\mathrm{lm}}$$

$$\frac{dT}{dt} = \frac{-X * \Delta HFG * \mu 1}{\rho * Cp} - \frac{U * A * \Delta Tlm}{\rho * Cp * V} \qquad (1)$$

Energy balance for cooling jacket

Following the same procedure from which is energy balance on cooling jacket; $Rate\ of\ energy\ acumulated = Rate\ of\ energy\ in - Rate\ of\ energy\ out + Rate\ of\ energy\ generated - Rate\ of\ energy\ lost$

$$\frac{dE}{dt} = Ein - Eout + 0 + Q$$

$$\frac{d(mj*Cpc*dTj)}{dt} = \rho c * Fc * Cpc * Tc - \rho c * Fc * Cpc * Tj + U*A*\Delta T_{lm}$$

$$m = \rho c * Vj$$

Hence

$$\frac{dT}{dt} = \frac{\rho c*Fc*Cpc*Tc}{\rho c*Vj*Cpc} - \frac{\rho c*Fc*Cpc*Tj}{\rho c*Vj*Cpc} + U * A * \Delta T_{lm}$$

$$\frac{dT}{dt} = \frac{Fc}{Vj}(Tc - Tj) + \frac{U * A * \Delta Tlm}{\rho c * Vj * Cpc} \quad (2)$$

The governing equation for heat flow between film beer and the wall is the conduction-convention heat transfer which is;

$$\rho Cp\left(u\frac{\partial T}{\partial x} + v\frac{\partial T}{\partial y}\right) = k\left(\frac{\partial 2T}{\partial 2x} + \frac{\partial 2T}{\partial 2y}\right)$$, in vector form as follows.

$$dz * \rho * Cp\frac{\partial T}{\partial t} + dz * \rho * Cp * \boldsymbol{u}.\boldsymbol{\nabla T} + \boldsymbol{\nabla}.\boldsymbol{q} = dzQ + qo + dzQp + dzQv \quad (3)$$

For laminar flow the incompressible Naiver stokes equation and continuity equation is used

$$\rho\left(u\frac{\partial u}{\partial x} + v\frac{\partial v}{\partial y}\right) = -\frac{\partial p}{\partial x} + \mu\left(\frac{\partial 2u}{\partial x2} + \frac{\partial 2v}{\partial y2}\right), x\ momentum\ equation$$

$$\rho\left(u\frac{\partial u}{\partial x} + v\frac{\partial v}{\partial y}\right) = -\frac{\partial p}{\partial x} + \mu\left(\frac{\partial 2u}{\partial x2} + \frac{\partial 2v}{\partial y2}\right) + \rho g\beta(T - Tref), \quad y\ momentum\ equation$$

In vector form the two-equation combined as follows.

$$\frac{\rho\partial \boldsymbol{u}}{\partial t} + \rho(\boldsymbol{u}.\nabla)\boldsymbol{u} = \nabla[-\rho\boldsymbol{I} + \mu(\nabla\boldsymbol{u} + (\nabla\boldsymbol{u})^T)] + F \quad (4)$$

$\frac{\partial u}{\partial x} + \frac{\partial v}{\partial y}, contuinity\ equation$, but in vector form

$$\rho\nabla.(\boldsymbol{u}) = 0 \quad (5)$$

For transport of diluted species;

$$\frac{\partial Ci}{\partial t} + \nabla.(-Di\nabla Ci) + \boldsymbol{u}.\nabla Ci = Ri \quad (6)$$

$$\boldsymbol{Ni} = -Di\nabla Ci + \boldsymbol{u}Ci$$

2.1. Model geometry

Most of beer processing industry uses cylindroconical shape of fermentation tank. Therefore, the selected geometry was 2D axial symmetry of cylindro - conical shape with mixing direction and flow direction from upper to lower as shown in Figure 2.1.

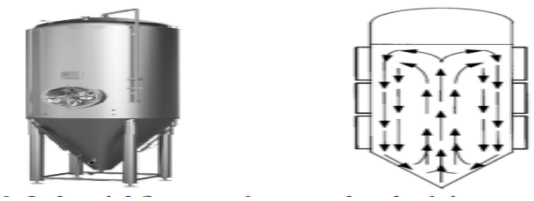

Figure 2. 1: Model geometry for finite element modelling

2.2. Model governing equation for simulation of metabolites

Growth model

Most of growth models in literature have considered total sugar consumption by yeast and here main sugar component known as glucose, maltose and malt triose from hydrolysis of carbohydrate is considered separately.

Glucose consumption

$$\frac{dG}{dt} = -\mu 1 * X \qquad (7)$$

Where, $\mu 1 = \frac{\mu G * G}{KG+G}$

Where, μ_G = Specific uptake of glucose (h^{-1}), K_G = Consumption rate constant of glucose (mol/m^3), G = glucose (mol/m^3)

Maltose consumption

$$\frac{dM}{dt} = -\mu 2 * X \qquad (8)$$

Where, $\mu 2 = \frac{\mu M * M}{KM+M} * \frac{KG'}{KG'+G'}$

Where, μ_M = Specific uptake of maltose (h^{-1}), M = maltose (mol/m^3), K_M = Consumption rate constant of maltose (mol/m^3), K'_G = Consumption rate constant of glucose (mol/m^3), X = Yeast concentration (mol/m^3), G′ = glucose (mol/m^3)

Malt triose consumption

$$\frac{dN}{dt} = \mu 3 * X \qquad (9)$$

Where, $\mu 3 = \frac{\mu N * N}{KN+N} * \frac{KG'}{KG'+G} * \frac{KM'}{KM'+M}$

Where, μ_N = Specific uptake of malt triose (h^{-1}), N = Concentration of malt triose (mol/m^3), K'_M = Consumption rate constant of maltose (mol/m^3). Temperature dependency of specific growth rate and consumption rate of constant are given by:

$$\mu i = \mu o exp\left(\frac{-E\mu i}{RT}\right), where\ i = G, M, N$$

$$Ki = Kio exp\left(\frac{-Eki}{RT}\right), where\ i = G, M, N$$

$$Ki' = Kio' \exp\left(\frac{-Eki'}{RT}\right), where\ i = G, M$$

Where, $E_{\mu i}$ = Arrhenius activation energy for maximum velocity (cal/mol), E_{ki} = Arrhenius activation energy for Michaels constant (cal/mol), R = universal gas constant (cal/mol °C), T = absolute temperature (°C), μ_i = maximum reaction velocity for i^{th} sugar (h^{-1}), K_i = Michaels constant for i^{th} sugar (mol/m^3).

Yeast growth kinetics

$$\frac{dX}{dt} = \mu x * X \qquad (10)$$

Where,

$$\mu x = (YxG * \mu 1 + YxM * \mu 2 + YxN * \mu 3) * \frac{Kx}{Kx+(x-xo)2},$$ is the specific rate of yeast growth.

$\frac{Kx}{Kx+(x-xo)\hat{}2}$ = is the indication of cell growth inhibition from unsaturated fat.

Where, Y_{XG} = Yield coefficient mole X per mole G, Y_{XM} = Yield coefficient mole X per mole M, Y_{XN} = Yield coefficient mole X per mole N, Kx = Empirical yeast growth inhibition constant $(mol/m^3)^2$, X_o = initial yeast concentration (mol/m^3)

N.B in this case of yeast growth kinetics, death phase does not take into consideration.

Ethyl ethanol production kinetics

Ethanol production is assumed to be proportional to the amount of sugar consumed.

$$\frac{dE}{dt} = YEG\frac{dG}{dt} + YEM\frac{dM}{dt} + YEN\frac{dN}{dt} \qquad (11)$$

Where, E = Ethanol concentration (mol/m^3), Y_{EG} = Yield coefficient mole E per mole G, Y_{EM} = Yield coefficient mole E per mole M, Y_{EN} = Yield coefficient mole E per mole N.

Isobutyl alcohol formation kinetics

$$\frac{dIB}{dt} = YIB * \mu V * X \qquad (16)$$

Where $\mu_V = -\frac{1}{X} * \frac{dV}{dt}$, is specific rate of valine uptake, Y_{IB} = Isobutyl alcohol yield, IB = Isobutyl alcohol (mol/m^3).

Methyl butanol formation rate

$$, \frac{dIM}{dt} = YMB * \mu I * X \qquad (17)$$

Where, $\mu I = -\frac{1}{X} * \frac{dI}{dt}$, $is\ specific\ rate\ of\ isoluicine\ uptake$, Y_{MB} = methyl butanol alcohol yield.

n-propanol formation rate

$$\frac{dp}{dt} = YPE(\mu V + \mu I)X \qquad (18)$$

Where, Y_{PE} = n-propanol alcohol yield,

3. RESULT AND DISCUSION

3.1. Effect of coolant flowrate on fermentation temperature and flow condition

The temperature profile, flow conditions and vorticity of flow were discussed in this section at different coolant flowrate. From the modeled results, the temperature profile of beer fermentation was observed with fermentation time (Figure 3.1, 3.2 &3.3). Again, velocity streamline was also solved from naiver stokes equation to see flow condition with a time of fermentation.

The results were also included vorticity field with fermentation time from naiver stokes equation to see the formation of the vortex at a different coolant flow rate. During beer fermentation, the temperature of fermentation is controlled by liquid circulated ammonia (Anderson, 2006). Vortex formation during fermentation controls mass transfer and the rate of dissolved oxygen (Rubenberger, 2006). This liquid ammonia is controlled by its flow rate. The model was tried to relate coolant flowrate to temperature profile from energy balance (eqn 1and 2 above).

The modeled results were indicated that all phenomenon of beer fermentation like air flow (oxygen consumption), temperature profile with time, padic pressure with fermentation time and formation of vortex were influenced by coolant flow rate (Figure 3.1, 3.2 and 3.3). The results were indicated that increasing coolant flowrate decrease temperature profile within the fermentation tank (Figure 3.1, 3.2 and 3.3). This indicates that

increasing coolant flowrate increase heat exchange area hence high amount of heat absorbed or removed by coolant from the tank which produced exothermically as sugar decomposes to ethanol and carbon dioxide with fermentation time.

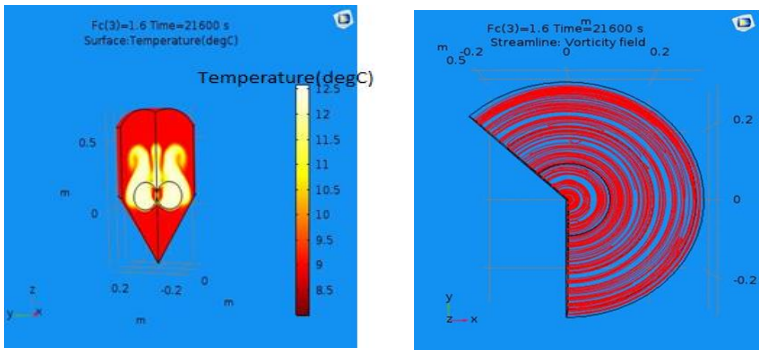

Figure 3. 1: Temperature profile (inner), and vorticity field at 1.6 coolant flowrate

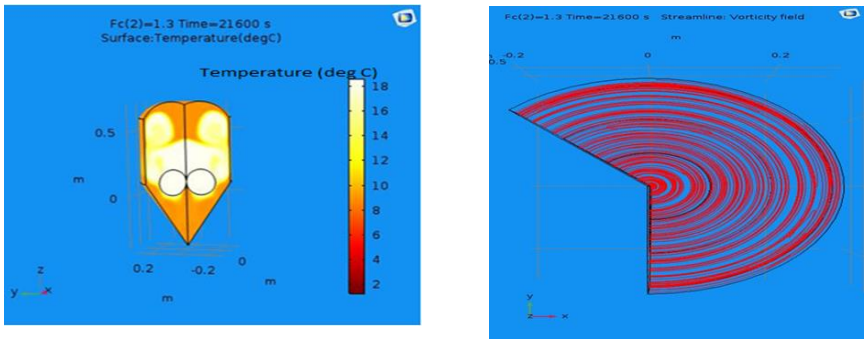

Figure 3. 2: Temperature profile (inner), and vorticity field at 1.3 coolant flowrate

The velocity streamline was indicated that the flow condition of the fermentation was from bottom to top (upside down) at all coolant flowrate and also possible to judge uniformity of flow at these coolant rate which is better at 1.2 m^3/hr and slightly uniformity decreased for the rest flowrate (Figure 3.1, 3.2 and 3.3). This indicated that as coolant flow rate increased, the temperature profile within the fermentation tank cannot form uniform mixing which is not favorable for mass transfer.

The modeled vorticity results were also indicated that at 1.2 m^3/hr coolant flowrate uniform flow of fluid was observed around stirring center than other coolant rates which is responsible for a high transfer rate of dissolved oxygen (Figure 3.1, 3.2 and 3.3).

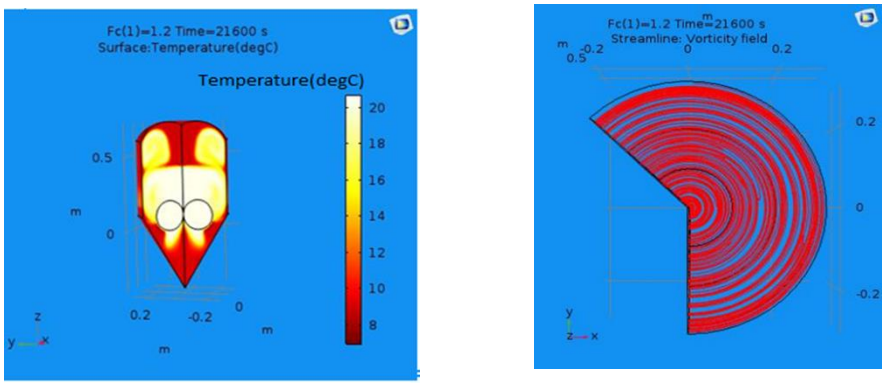

Figure 3. 3: Temperature profile (inner), and vorticity field at 1.2 coolant flowrate

3.2. Effect of temperature on fermentation time and beer flavor quality

The biochemical reaction was simulated at a different temperature which already modeled at different coolant flow rate by the finite element method.

3.2.1. Effect of temperature on carbohydrate (glucose, maltose and malt triose) consumption trend and consumption time

As already indicated in the equation driving case, the temperature was incorporated into the equation through Arrhenius equation-based formula. The simulated results were indicated in (Figure3.4, 3.5 and 3.6) below for carbohydrate (glucose, maltose, and malt triose) consumption trend and time. The result indicated that the initial glucose which was presented in the wort take 6 days and 8 hours for 12.5 ^{o}C, almost 3 days for 18 ^{o}C and decreased to 2 days for 20 ^{o}C to finish its conversion to ethanol and another flavor-based by-product.

Temperature is related to glucose consumption through the specific glucose uptake rate (Jones & Hough, 2006). Maltose is the major sugar of wort, accounting for 50–55% of the total carbohydrate content of wort compared with 10–14% for malt triose (Branyik et al., 2004). Higher fermentation temperature initiates yeast growth and decreases oxygen uptake rate which leads to the production of imbalanced flavor (Jones & Hough, 2006). After glucose consumption was depleted, malt triose was started to consume (Figure 3.4, 3.5 and 3.6).

Both maltose and malt triose also became zero after 200 and 40 hours for 18^{o}C and 200 hrs for 20^{o}C but in the case of 12.5 ^{o}C it was taking a long period of time to depleted to zero (Figure 3.4, 3.5 and 3.6).

3.2.2. Effect of temperature on yeast growth rate and alcohols production rate

During beer, fermentation maltose was converted to glucose, while malt triose was converted to maltose and further converted to glucose which also converted to ethanol (Ayrapa, 2015). Yeast uses glucose as the carbon source and uses amino acid as a nitrogen source during growth (Sablayrolles JM and Ball CB, 2004). At fermentation temperatures of 12.5^{o}C, 18^{o}C and 20^{o}C to get six percent of alcohol (6.64%(w/w)) content which is alcohol content Harar brewery used currently almost above 250 hrs, 112 hrs and 90 hrs were needed respectively which is relatively reduced by 32 hrs at 18^{o}C and 54 hrs at 20^{o}C compared to 16 ^{o}C temperatures (Figure 3.7, 3.8, 3.9).

From the simulated result at the given condition (current company parameters), almost around six days and six hours were needed to get five percent of (6.644% (w/w)) alcohol which is the alcohol content Harar brewery used currently (Fiqadu, 2012).

$$\frac{1040kg/m3}{1500mol/m3} * 1000 = \frac{693.33g}{mol}$$

$$46.09\frac{g/mol}{693.33g/mol} * 100 = 6.64\%(\frac{w}{w})$$

Where, 1040 kg/m^3 is density of original wort, 1500 mol/m^3 is from ethanol graph and 46.09g/mol is molar mass of ethanol. The simulated results of yeast and ethanol were indicated that both of them were increased with time up to all initial glucose were depleted at all the selected temperature. The yeast was still active even though all glucose were depleted (Figure 3.7, 3.8 and 3.9). This indicated that there are maltose and malt triose which make the cell active even though additional time needed for enzyme excretion.

3.2.3. Effect of temperature on higher alcohols (fusel alcohols) production rate

In addition to ethanol, several higher alcohols are synthesized during beer fermentation and contribute most significantly to alcoholic flavor and warm mouth-feel. The formation of these higher alcohols is maximized during amino acid starvation (low FAN levels), unfavorable to beer flavor. Control of higher alcohol formation can therefore be controlled by uptake efficiency of the corresponding amino acid and the sugar utilization rate (Ayrapa, 2001). One identified a biochemical pathway to produce propionyl-CoA is break down of the amino acids Valine

and Isoleucine (Warnasooriy, 2010). Fusel alcohols are alcohols that cause beer flavor to fruity like flavor and cause beer quality to undesirable quality (Engasser, 2001) above thresh hold concentration of 0.15, 0.108 and 0.062 mol/m^3 for propanol, isobutyl, isoamyl and 2-methyl-1-butanol respectively.

Propanol and isobutyl were reached their threshold value after 60 and 81 hrs at 12.5^{o}C, 33 and 42 hrs at 18^{o}C and after 28 and 36 hrs at 20^{o}C which are 0.15 and 0.108 respectively (Figure 3.10, 3.11 and 3.12). Both isoamyl alcohol and 2-methyl-1-butanol got their threshold value at lower fermentation time at all three temperatures which is 0.062 mol/m^3 (Figure 3.10, 3.11 and 3.12). As fermentation time was increased both isoamyl alcohol and 2-methyl-1-butanol maintained constant concentration as mentioned above. The simulated result also indicated that fusel alcohols formations were depended on both initial carbohydrates present in the wort and initial protein content in the wort (Figure 3.4 and 3.10).

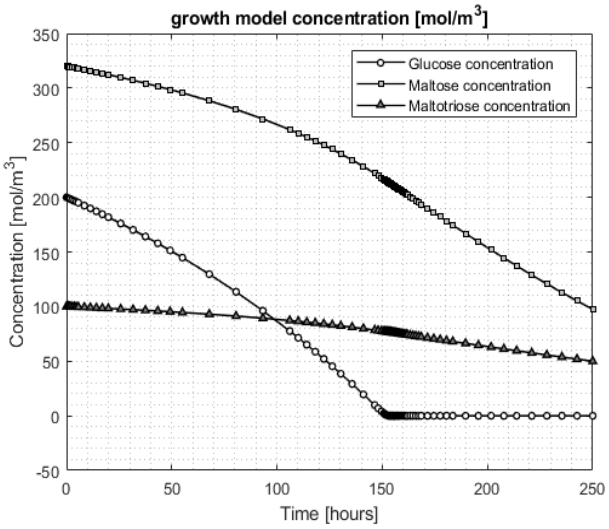

Figure 3.4: Simulated result of carbohydrate concentration at 12.5°C, 50 pitching rate and 200 mol/m^3, 320 mol/m^3, 100 mol/m^3 concentration (initial) for glucose, maltose and malt triose respectively

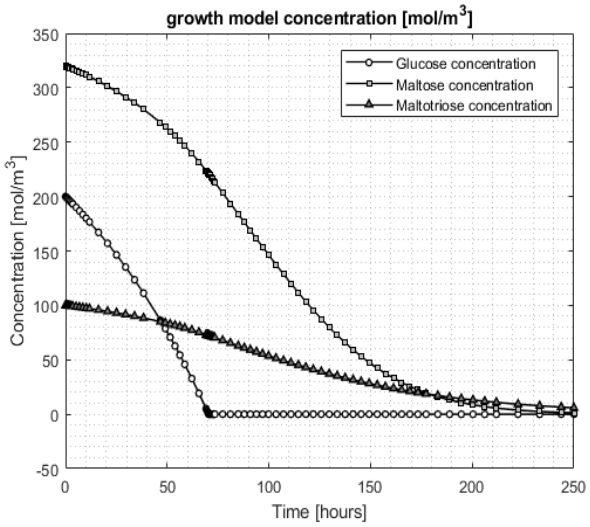

Figure 3.5: Simulated result of carbohydrate concentration at 18°C, 50 pitching rate and 200 mol/m^3, 320 mol/m^3, 100 mol/m^3 concentration (initial) for glucose, maltose and malt triose respectively.

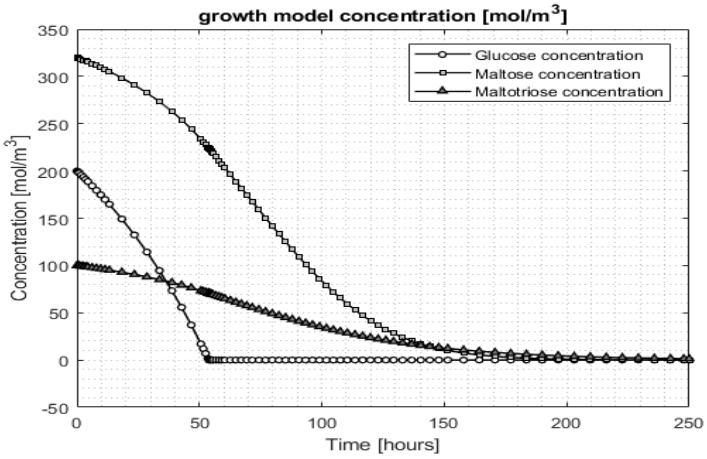

Figure 3.6: Simulated result of carbohydrate concentration at 20 ^{o}C, 50 pitching rate and 200 mol/m^3, 320 mol/m^3, 100 mol/m^3 concentration (initial) for glucose, maltose and malt triose respectively.

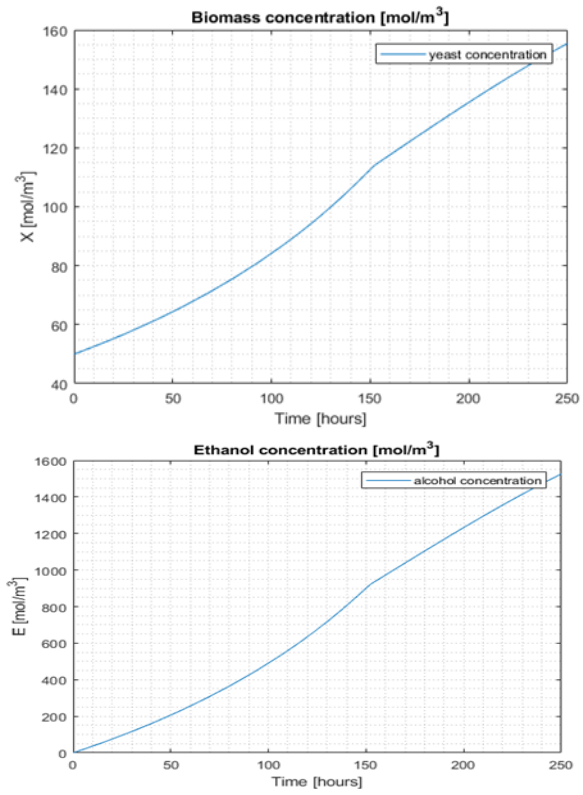

Figure 3.7: Simulated result of yeast and ethanol at 12.5°C, 50 pitching rate and 200 mol/m^3, 320 mol/m^3, 100 mol/m^3 concentration (initial) for glucose, maltose and malt triose respectively

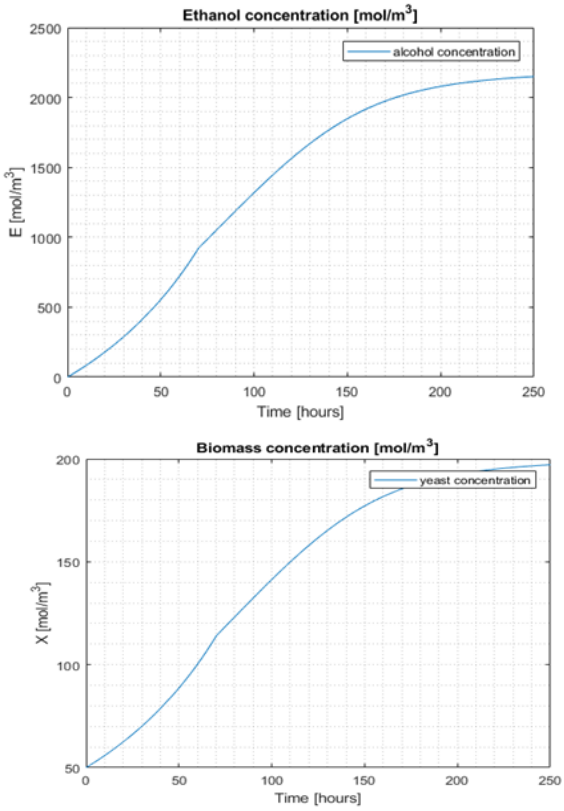

Figure 3.8: Simulated result of yeast and ethanol at 18°C, 50 pitching rate and 200 mol/m^3, 320 mol/m^3, 100 mol/m^3 concentration (initial) for glucose, maltose and malt triose respectively.

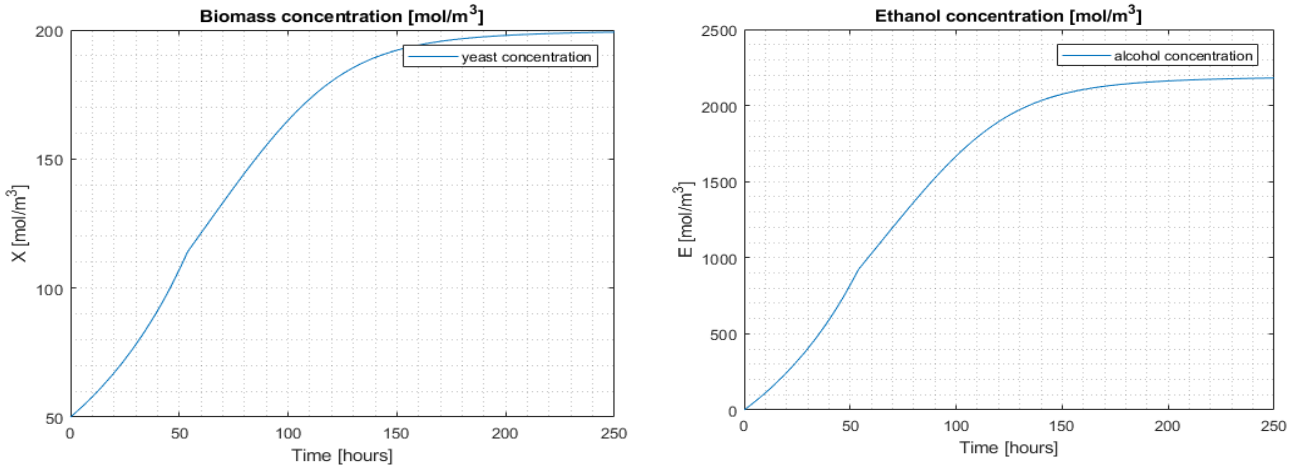

Figure 3.9: Simulated result of yeast and ethanol at 20°C, 50 mol/m^3 pitching rate and 200 mol/m^3, 320 mol/m^3, 100 mol/m^3 Concentration (initial) for glucose, maltose and malt triose respectively

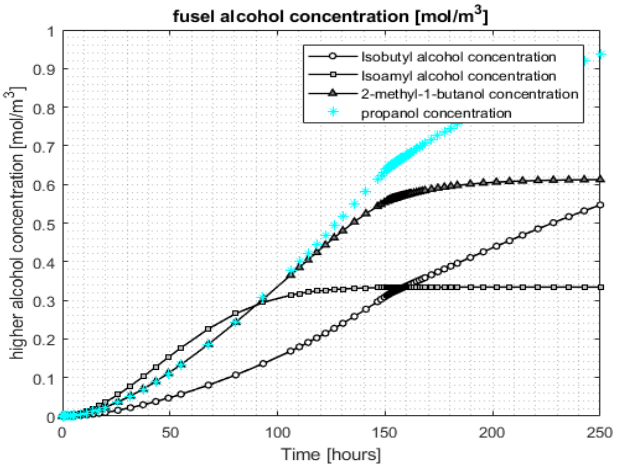

Figure 3.10: Higher alcohol model simulated result at temperature 12.5°C, pitching rate 50 mol/m^3 and 200 mol/m^3, 320 mol/m^3 and 100 mol/m^3 concentration(initial) for glucose, maltose and malt triose respectively.

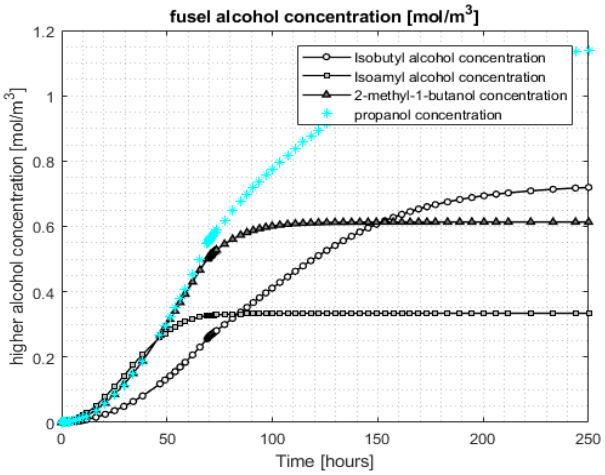

Figure 3.11: Higher alcohol model simulated result at temperature 18°C, pitching rate 50 mol/m^3 and 200 mol/m^3, 320 mol/m^3 and 100 mol/m^3 concentration(initial) for glucose, maltose and malt triose respectively.

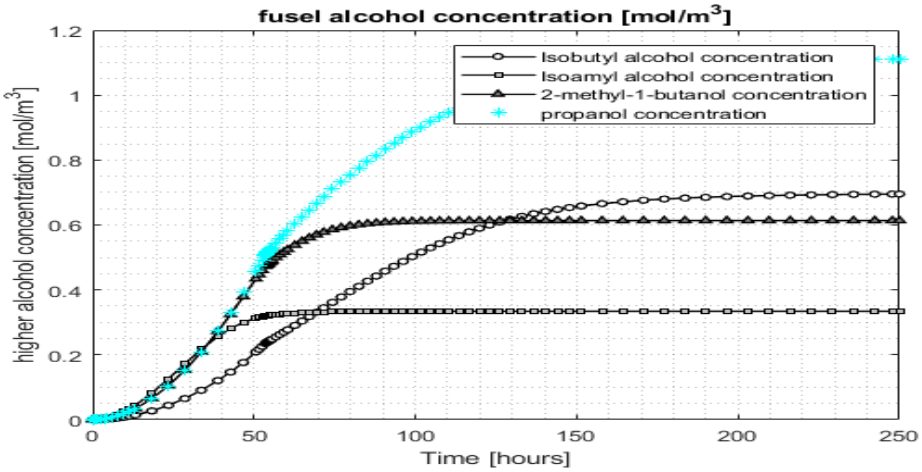

Figure 3.12: Higher alcohol model simulated result at temperature 20 °C, pitching rate 50 mol/m^3 and 200 mol/m^3, 320 mol/m^3 and 100 mol/m^3 concentration (initial) for glucose, maltose and malt triose, respectively.

4. MODEL VALIDATION

To see the accuracy of the generated data, validation of the model was necessary by comparing with already existed data or experimental data. In this case, since the model was a space dependent model, the generated data was compared with the company current value data by using all current company parameter as an input parameter**.** Accordingly, for heat and mass transfer model temperature profile was collected along the arc length of the tank from the mechanical staff at 1.4 coolant flow rate (current coolant flowrate) and compared with the modeled result as follows.

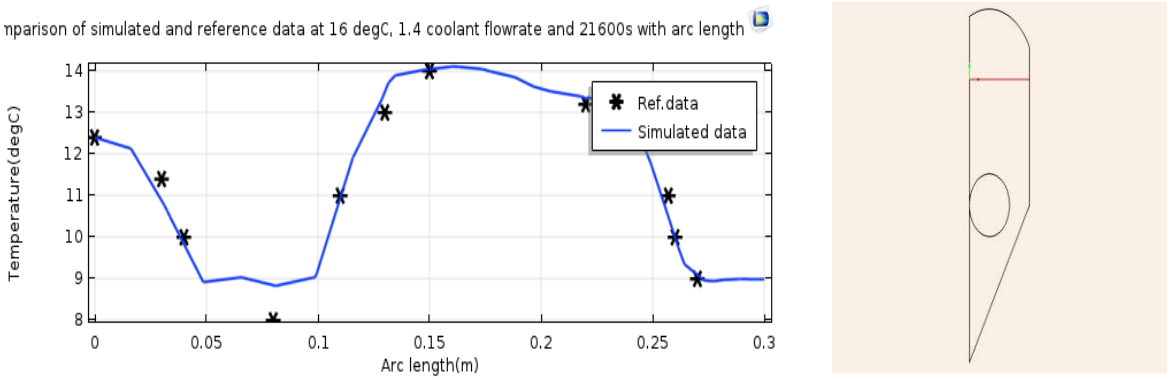

Figure 5. 1: Comparison of simulated and company (reference) data at 16°C, 1.4 coolant flowrate and 21600 second along arc length

5. CONCLUSION

The beer fermentation process has been modeled by having a phenomenon that can be representative of beer fermentation. Mass and energy balance were done to have a temperature profile with fermentation time. Relevant kinetics were developed for growth, and fusel alcohols model and simulated by incorporating operating parameter like temperature.

The finite element method was used to solve energy balance that has solved from mass and energy balance at different coolant flowrate of ammonia coolant. The modeled result was indicated that as coolant flowrate decreased, the temperature profile with fermentation time was increased. 1.2, 1.3, and 1.6 m^3/hr were the selected coolant flowrates to see temperature profile with fermentation time. This is due to of that the study used Harar brewery Share Company as case study which used 1.4 m^3/hr coolant flowrate currently. The temperatures that were observed at 1.2, 1.3 and 1.6 m^3/hr coolant flowrate were 20°C, 18°C and 12.5°C respectively with fermentation time.

The modeled kinetics of flavors and growth model were simulated with the above temperatures to see its effect on fermentation time and beer flavor quality. The simulated results were indicated that at 20°C time to reach flavor threshold value and time of glucose, maltose and malt triose consumption were decreased than the other two temperatures. The current company value was used as a point of reference to discuss the effect of the operating parameter (temperature) on fermentation time and beer flavor quality. Based on this, yeast was highly multiplied at 20°C than the current temperature 16°C and also the other two selected temperatures.

REFERENCES

Almedia, J. B. (2001). Evaluation of fermentation parameters during high gravity beer production. . *Journal of Chemical Engineering,, 18*(4).

Anderson, A. (2000). Direct expansion cooling of ammonia gas on beer fermentation tank. *Institute of brewing*.

Anderson, A. (2006). Capability of liquid ammonia to absorb heat flow. . *Journal of Chemical Engineering,, 20*(6), 30.

Andrews, G. (1997). Area of heat transfer in fouriers law. *Chemical Engineering, 5*.

Ayrapa, T. (2001). Biosynthetic formation of higher alcohols by yeast.Dependence on the nitrogen nutrient level of the medium. *J Inst Brew, 77*, 266–276

Ayrapa, T. (2015). Formation of higher alcohols 14C-labeled valine and luicine. *Institute of brewing*.

Bird RB, Stewart WE, & EN, L. (2002). *Transport phenomena* (2nd ed.). Elsevier: Wiley.

Engasser, J. M. (2001). Kinetic modelling of beer fermentation, Proceedings of the 18th Congress of the European Brewery Convention (579-586), Copenhagen.

Fiqadu, H. (2012). *Assessination of ethiopian beer production capacity and quality evaluation.* Harar Brewery.

Gaurdia, D. (2001). The brewer in control: modern brewery automation. *Brewers Guardian, 120*(3), 17-21.

Gee, D. A., & Ramirez, W. F. (2006). Online state estimation and parameter identification for batch fermentation. *Biotechnology*(12), 132-140.

Gee, D. A., & Ramirez, W. F. (2013). A flavor model for beer fermentation *Institute of brewing, 100*, 321-340.
Henry, A. (2012). Evaluating thermo physical property of ammonia liqiuds. *American Academy of Arts and Science., 55*(8), 325-409.
Horvath, J., & Perry, K. (2015). *Property of water as function of temperature.*
Jones, R. C., & Hough, J. S. (2006). Effect of temperature on the metabolism of yeast growing on continouse culture. . *General Microbiology, 60*, 107.
Macciejowslie., R. a. (2007). Optimal Beer fermentation. . *Journal of Instituete of Brewing, 113*(3), 325-333.
MacDonald J, R. P., Ruddlesden JD and White FH,. (2008). Current approaches to brewery fermentations. *Prog Ind Microbiol, 19*, 47–198.
Miller, N. (2009). "Rising to the top: Brewing up a fermentation science program," College of Agricultural and LifeSciences News, retrieved from http://news.cals.wisc.edu/departments/featured-articles/2011/09/06/rising-to-the-top.
Ramizer , & Macciejowslie. (2007). Optimal Beer fermentation. *Journal of Institue of Brewing, 113*(3), 325-333.
Rodman, A. D., & Gerogiorgis, D. I. (2016). Multi objective process optimization of beer fermentation via Dynamic simulation. *Food Bioproduct.Process., 100*, 255-274.
Rubenberger, K. (2006). Bioreactor with vortex mixing chamber. *Journal of Bioscience and Bioengineering*.
Sablayrolles JM and Ball CB. (2004). Fermentation kinetics and the production of volatiles during alcoholic fermentation. *J Am Soc Brew Chem, 53*, 71–78
Salagnac, P., Glouannec , P., & Lecharpentier, D. (2004). Numerical modeling of heat and mass transfer in porous medium during combined hot air, infrared and microwaves drying. *International Journal of Heat and Mass Transfer, 47*(19-20), 79–89.
Sykes, W. J., & Ling, A. R. (2012). The principle and practice of brewing. *Journal of brewing, 10*.
T.Branyik, Antonio A.Vicente, & Teixiera, P. D. J. A. (2008). A review of flavor formation in continouse beer *Instituete of brewing, 114*(1), 3-13.
Warnasooriy, D. R. (2010). Mathematical modeling and simulation of beer flavor fermentation. *Institue of Brewing,*.
Warnsooriy, D. R. (2011). modeling and simulation of beer fermentation and temperature control. *Institue of brewing*.
Yusuf, C., & Murray Moo, Y. (2003). Aeration and mixing in vortex fermenters. *Journal of Chemical Engineering,, 58*, 331—336.

Design and Analysis of Zero Turning Radius Steering System for Light Vehicles (Bajaj QUTE)

Getachew Fentaw[1,*], Ramesh Babu Nallamothu[2]

[1]*Automotive Engineering Department, Woldia University, Woldia, Ethiopia*
[2]*Mechanical Systems and Vehicle Engineering Department, Adama Science and Technology University, Adama, Ethiopia*
**Corresponding author, e-mail: fentaw50@gmail.com*

ABSTRACT

In this work a two mode steering system which has minimum turning and zero turning configuration has been modeled and simulated in CATIA V5, analyzed in ANSYS 18.1. A detailed conceptual design process was done which helps to evaluate variety of concept variants and select the appropriate and efficient deign path for the developed mechanism which have the two modes in a single car. In this work different assumptions were made appropriately using the data by visiting different websites as well as by measuring directly from the car. To check the strength of the components of the designed steering system, static structural analysis and Eigen value buckling analysis was done with proper mesh size. In addition to this the kinematic analysis of the assembled system was carried out using CATIA DMU kinematics to see how the motion of the mechanism look like and to check whether it can move as required or not. In this work it is found that the turning radius of the bench mark vehicle (Bajaj QUTE) is minimized from 3.5 m to 1.13 m which results a decrement of 62.4% in minimum turning configuration and it has a 100% reduction in zero turning radius mode.That means, using zero turning radius mode, the minimum area required to rotate the vehicle 360^0 is only 7.3 m^2 which can be available everywhere and helps the driver to maneuver easily and drive in the required direction. While reducing the turning radius of a vehicle it is obvious that the critical speed will become less during negotiating a curve due to load transfer. Hence the critical speed during the application of minimum turning configuration is about 43 km/hr and it is 31 km/hr when the driver uses a zero turning mode.

Keywords: *Critical speed, minimum turning, turning radius, zero turning*

1. INTRODUCTION

Many existing cities in the world were not built by considering an increase in the number of cars. Therefore, drivers find it difficult to park their car on crowded city streets and to turn in small radius. However, it is possible to create cars to suit traffic conditions of the cities.

Difficulty of parking in narrow space and at multiplexes, problem of easy removal of vehicle from the traffic jams, difficulty of turning back at narrow roads, wastage of time and fuels during turning and parking and high degree of tire wears are the main problem in current automobiles.

The vehicle will have a zero turning radius when the role center axis passes through the center of gravity of that vehicle and it is achieved by rotating all the four wheels opposite to each other (Lohith et al., 2013). It helps to turn the vehicle with a minimum space possible i.e. a circle with a diameter of the length of the vehicle itself is required to rotate the vehicle fully.

The main consideration in design of the steering system is to produce pure rolling motion of the wheels while maneuvering the tightest turns on the Dirt road tracks. The steering system must also offer adequate feel to the driver while turning. For maximum life of the tires the steering system is designed such that it maintains proper angles between the tires while turning and while braking in corner along with straight ahead position (Arvind, 2013). The driver should be able to turn vehicle with minimum effort but it should not be directionally unstable. The steering system is thus designed in a very unique way by compelling many factors and formulating mathematic model.

2. MATERIALS AND METHODS

2.1. Materials

Different materials like arc welding, Drilling machine, Grinder etc. were used for manufacturing the prototype. In addition to this, some softwares like, CATIA V5, ANSYS 18.1 were used for geometrically modeling and analyzing the stresses induced on individual components.

2.2. Methods

The methodology followed while doing this work has 4 major parts, namely literature review, data collection, design and analysis and manufacturing and assembly of prototype.

2.2.1. ANSYS 18.1 Software Result Verification

The analyzing software used here (ANSYS 18.1) has been verified in the following way. First the analysis was done using the software and the actual analytical solutions were calculated using formulas and then the outcome of the software result is compared with the analytical solutions. Here it is considered a cantilever beam which has a cross-section of 20×20 mm and a length of 100mm in which 1kN force is applied at its free end as shown in Figure 1.

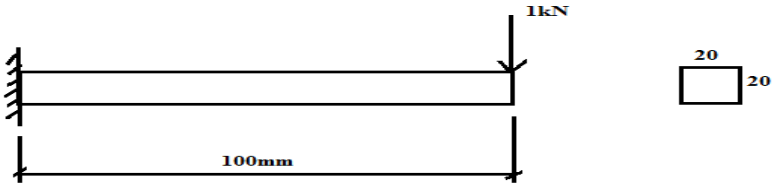

Figure 1: Cantilever beam for software validation

From beam theory, the bending stress is

$$\sigma_b = 75MPa$$

And the ANSYS result for the same problem in different mesh size is shown below in Figure 2a) – c.

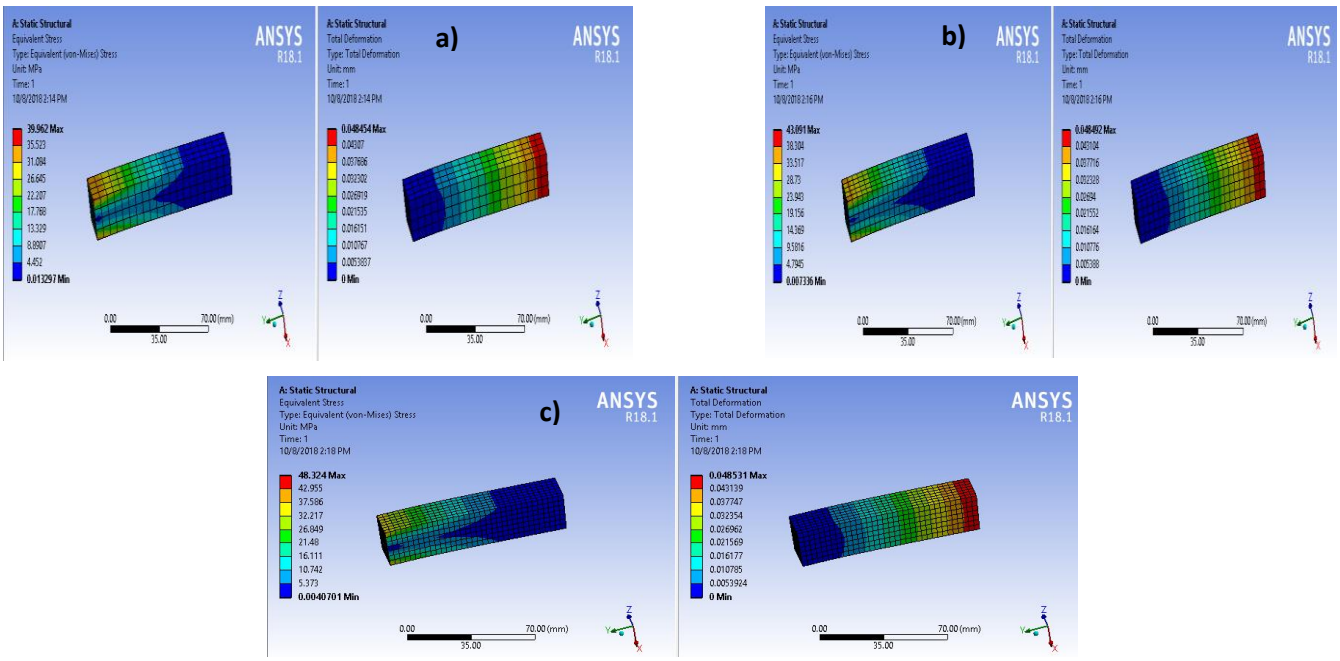

Figure 2: ANSYS Von-misses and normal stress results at different mesh size a) 5 mm, b) 4 mm and c) 3 mm

Similarly, further analyses were done for a mesh size of 2, 1.5, 1, 0.8 and 0.7mm and obtained values are listed on the Table 1.

Table 1: Convergence analysis and software result validation

Mesh size (mm)	Maximum von-misses stress (MPa)	Maximum total deformation (mm)	Nodes	Elements
5	39.962	0.04845	1865	320
4	43.091	0.04849	3396	625
3	48.324	0.04853	8336	1666
2	55.051	0.04856	23441	5000
1.5	58.736	0.048569	173481	40000
1	74.712	0.048572	254352	59248
0.8	74.712	0.048572	333476	78125
0.7	74.712	0.048572	508860	120203

By using the results obtained a convergence graph is plotted in Figure 3 for both mesh size versus von-misses stress and mesh size versus total deformation.

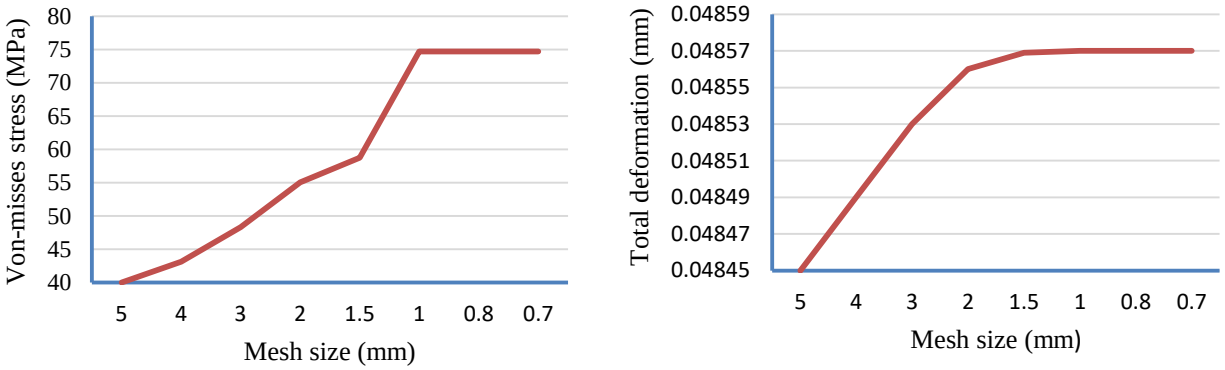

Figure 3: Convergence analysis and ANSYS result validation graph

From table 1 it is clear that the maximum stress is increased from 39.692MPa at a mesh size of 5 mm to 74.712 MPa which is almost equal with the analytical solution of 75 MPa. This shows that as the mesh size becomes finer the software result converges to the exact value of the problem. In von-misses stress software analysis of Figure 3, above, it can be seen that the maximum stress occurs at the fixed end and the stress at the free end is zero which is the same with beam bending theory. In addition to this, figure 3 shows both the total deformation and von-misses stress value increases as the mesh size decreases. After a mesh size of 0.9mm the results become constant which indicates the convergence of the case. Therefore, the software result matches with the analytical result with negligible errors so that ANSYS 18.1 has been validated and used for the other component stress and deformation analysis of the current mechanism.

2.2.2. Manufacturing and Assembly

Once the design and simulation part is end up, the next thing is the method of manufacturing each individual parts and assembling. So the part and assembly drawings is done clearly using CATIA V5.

2.2.3. Concept Generation

The first step is obtaining and identifying the product design specifications which meets the objective of the research work. A black box approach conceptual design process were carried out and the red thick arrows on Table 2 indicates the efficient design path. After the concept is developed the 3D model of the designed mechanism is prepared as shown on Figure 4.

Table 2: Efficient design path

Energy source	Steering mechanism	Transferring mechanism to rear steering system	Torque multiplication
Human	Rack and Pinion	Chain drive	Power assist
	Worm gear type	Belt drive	
	Linkage type	Bevel gear and shaft	Manual

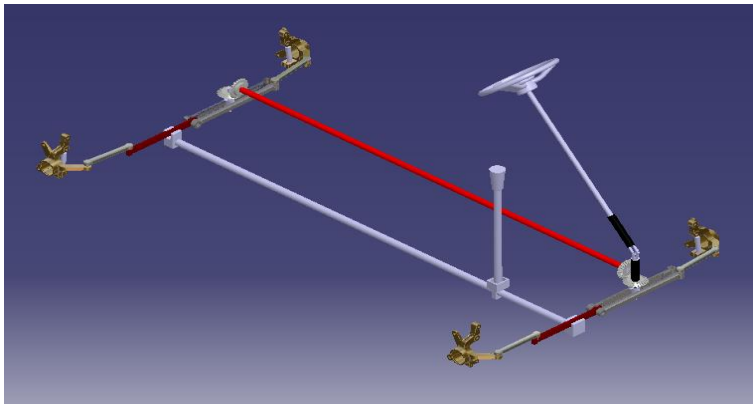

Figure 4: Geometric Model in CATIA V5

3. RESULT AND DISCUSSION

3.1. Component Strength analysis results in ANSYS

The component strength analysis has been done using ANSYS 18.1 and compared with the analytically calculated values and the results of each components are shown on Figure 5 below.

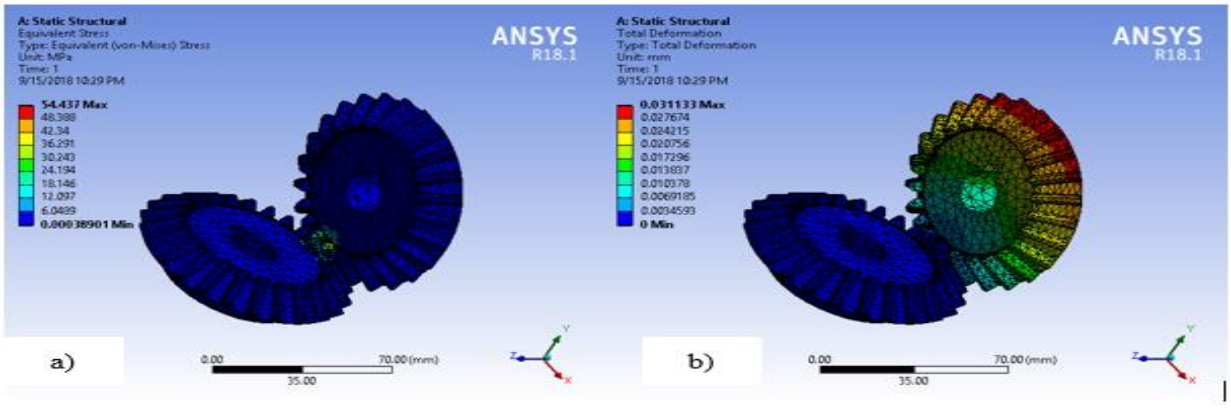

Bevel gear a) Von-misses stress and b) Total deformation

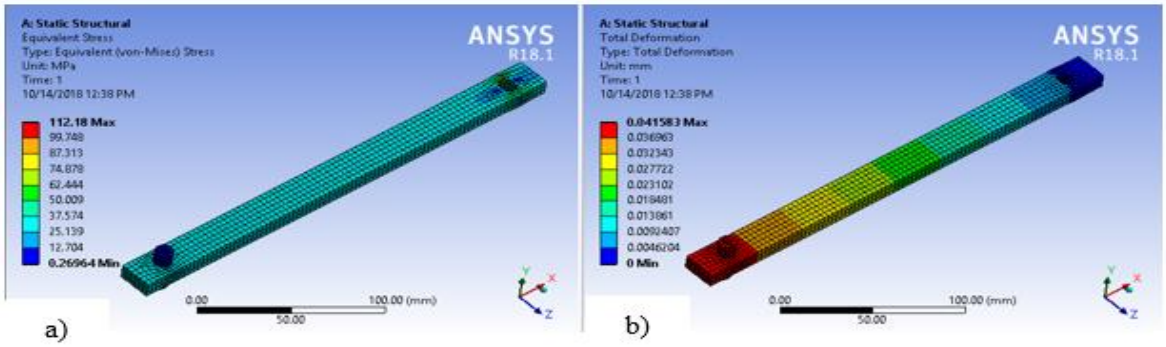

Selector; a) Von-misses stress b) Total deformation

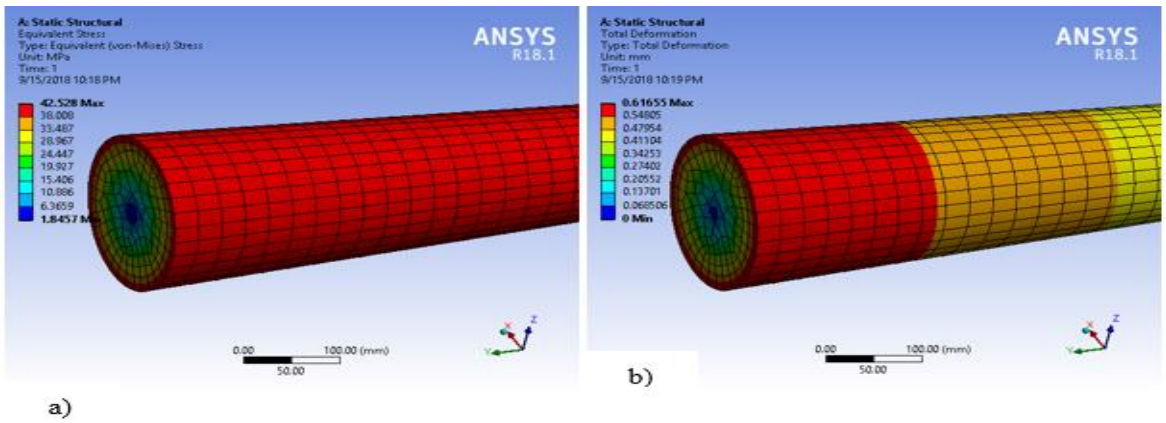

Long Shaft; a) Equivalent stress, b) Total deformation

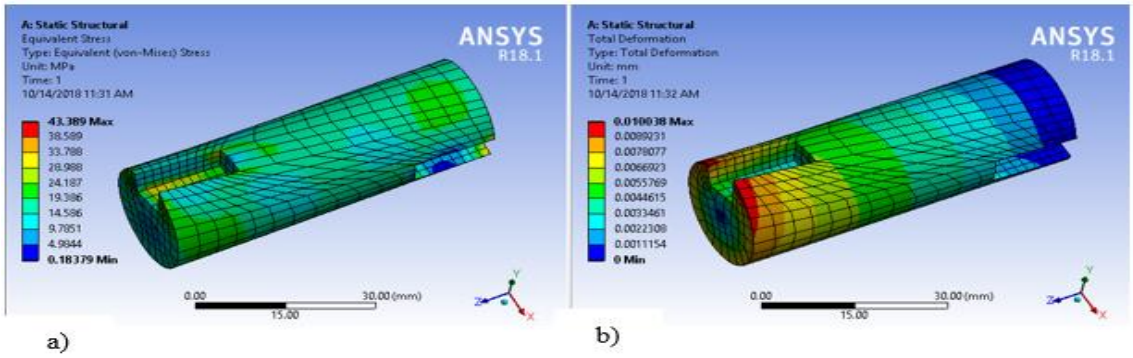

Short shaft; a) Von-misses stress, b) Total deformation

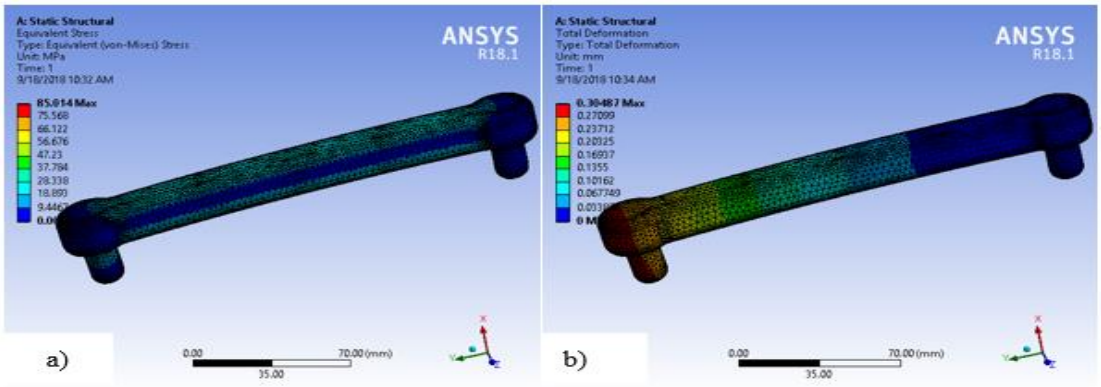

Tie rod; a) Von-misses stress, b) Total deformation

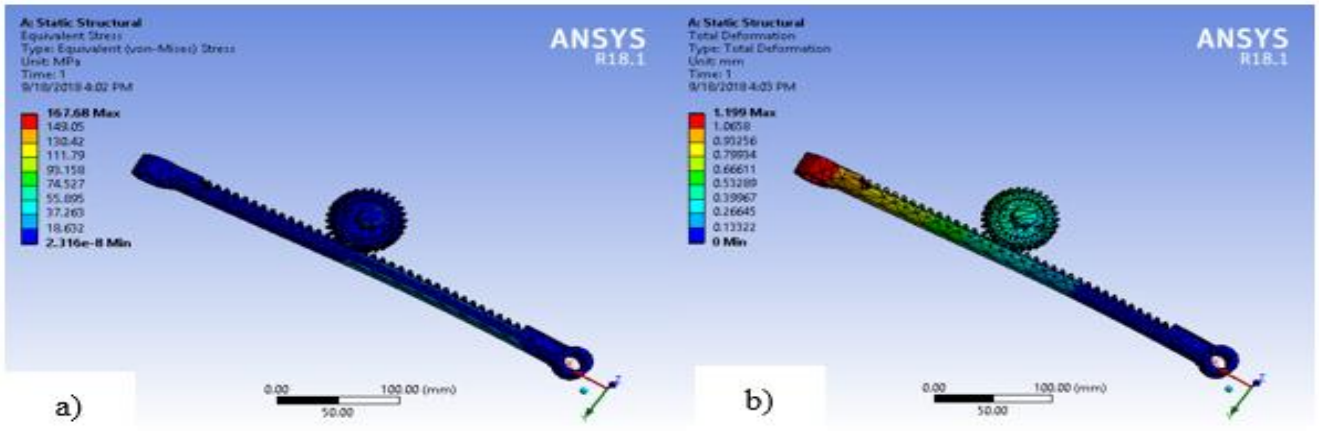

Rack and pinion; a) Von-misses stress, b) Total deformation

3.2. Performance Comparison of the New System with the existing

Here main results of the analysis namely reduction in the turning radius, critical speed for each mode and reduction in required area for 360^0 rotation of the vehicle is discussed one by one as follows. The comparison of the new system with the existing mechanism based on some common criteria's is shown inTable 3.

Table 3: Comparison of the new system with the existing one

Criteria	Conventional	Minimum turning radius mode	Zero turning radius mode
Turning radius (m)	3.5	1.13	0
Critical speed (km/hr)	70	43	31
Area required for 360^0 rotation (m^2)	54.26	19.1	7.3
Turning radius reduction (%)	-	67.8	100
Reduction in area required to rotate the vehicle 360^0 (%)	-	64.8	86.55

The result shows that, using minimum turning configuration will save 62.4% extra radius for maneuvering a vehicle 360^0 in a required direction and during zero turning radius mode it will save almost 100% extra radius spaces which will enable the driver to turn tightly with the minimum space available. The only problem using this configuration is the speed limitation.

The critical speed of the vehicle is reduced to 43 km/hr during the minimum turn configuration at maximum steer angle and 31 km/hr during zero turn configuration mode. That means in driving at speed of more than or equal to 31km/hr the driver should not use zero turning radius mode and when the speed of the vehicle is more than 43km/hr the steer angle should not be maximum otherwise it will lead to vehicle instability. The comparison of the obtained results in turning radius and area requirement is shown on figure 6a-e in the form of bar graph for more clarification.

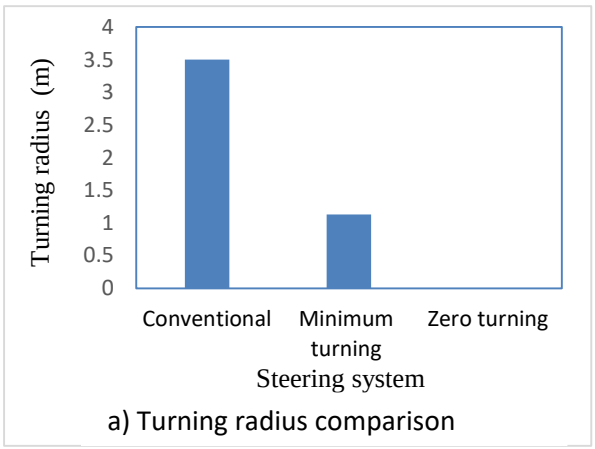

a) Turning radius comparison

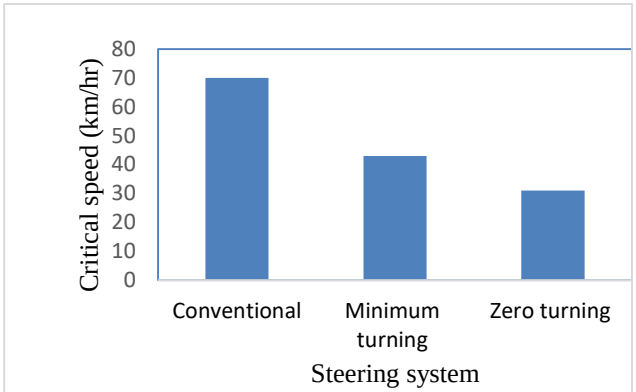

b) Critical speed comparison

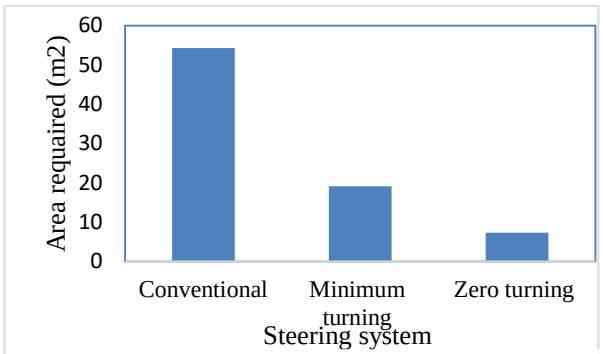

c) Area required comparison

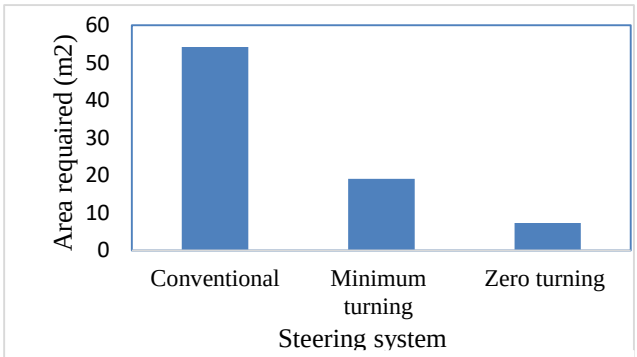

c) Area required comparison

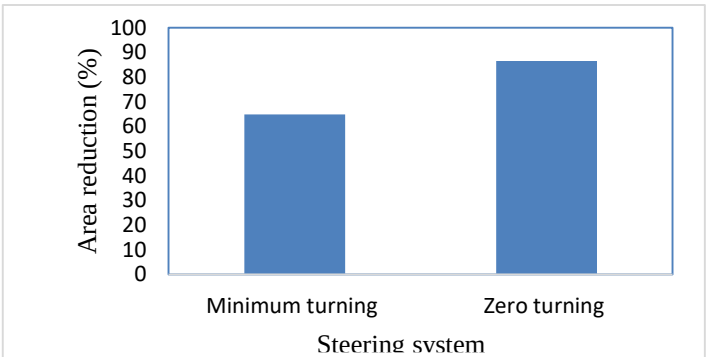

e) Area required reduction comparison

Figure 6: Performance comparison of the new system with the existing

4. CONCLUSION

- The designed steering system has a maximum steer angle of 60^0 in both cases i.e. for the minimum turning as well as zero turning configuration mode and it has a steering ratio of 12:1. The system has a selecting mechanism which is used to shift and select either of the two modes based on the requirement of the driver, road conditions and speed of the vehicle.
- For minimum turning configuration mode, it is found that the turning radius is reduced from 3.5 m to 1.13m which has a total reduction of 67.8% that enables the vehicle to turn in a tight space of approximately 19.1m^2. Although the bench mark vehicle (Bajaj QUTE) can move up to a maximum speed of 70km/hr in normal conditions, while using this mode at its highest value of steer angle i.e. 60^0, the speed of the vehicle

should be kept below 43km/hr otherwise it will cause vehicle instability because of lateral load transfer during cornering.

- For minimum turning configuration, there is a reduction in a turning radius from 3.5 m to 0 m that means during this mode the instantaneous center of rotation lies at the center of gravity. Due to this the reduction in a turning radius is about 100% at its maximum steer angle of 60^0. It is obvious that if the turning radius is very small, its speed should be low for keeping the car stable during cornering. So in this mode the critical speed is found to be 31km/hr which is less than that of the critical speed of minimum turning configuration which has a critical speed value of 43km/hr due to reduction in a turning radius from 1.13 m to 0 m.

REFERENCES

K. Lohith, et al. (2013): Development of Four *Wheel Steering System for a Car*, *Sastech Journal*, 12(1), 90-97.

V. Arvind (2013): Optimizing the Turning Radius of a Vehicle Using Symmetric Four Wheel Steering System, *International Journal of Scientific and Engineering Research*, 4(12), 2177-2184.

Enhancement and Detection of Brain Tumor from MRI Using Water Cycle Algorithm and Relevance Vector Machine Learning Approach

Satyasis Mishra*, M.Ajay Kumar, T.Gopi Krishna, Tadesse Hailu Ayane

Electrical Computing Engineering Department, Adama Science and Technology University, Ethiopia
**Corresponding author, e-mail: satyasismishra@gmail.com*

ABSTRACT

Nowadays, the cancer related deaths are increasing rapidly in Ethiopia, due to brain tumor tissues. The presence of tumor at initial stage is unknown, which cause deaths in large scale. The detection of tumor at its early stage becomes a challenging task for the doctors. To get proper diagnosis of the tumors and its growth from magnetic resonance image (MRI), the enhancement and detection techniques of brain tumor from medical MRI has been proposed in this research work. To enhance the quality of image, a novel nature inspired algorithm, called the water cycle algorithm (WCA) has been proposed for solving problems occurred in gray level medical MRI. The proposed algorithm is designed by simulating the water cycle process in nature. The fundamental concepts which underlie the proposed method which is inspired from the observation of water cycle process in rivers and streams flow in the ocean. A comparative study has been carried out to show the effectiveness of the WCA over other well-known optimizers in terms of entropy and fitness of the image in this paper. Further for the detection of the tumor tissues and remove noise from the MRI the relevance vector machine (RVM) based segmentation technique has been proposed. Image enhancement is mainly done by maximizing the information content of the enhanced image with intensity transformation function. In this research work a parameterized transformation function is used, which uses local and global information of the image. To achieve the best enhanced image the parameters in the transformation function has been optimized with the help of WCA. The parameters of proposed relevance vector machine has been considered for image segmentation. Results obtained using all these techniques are in good agreement and are compared using performance graphs and image based enhancement results. Simulation result proves that WCA based image enhancement and relevance vector machine based segmentation algorithm is superior to the conventional techniques. The comparison results with the proposed WCA has been presented with particle swarm optimization, accelerated particle swarm optimization and the segmentation comparison result has been presented with proposed relevance vector machine algorithm and support vector machine(SVM).

Keywords: *Accelerated particle swarm optimization, Magnetic resonance image, Particle swarm optimization, salt &pepper noise, support vector machine y*

1. INTRODUCTION

The enhancement and manual detection of tumor tissues from MRI becomes a difficult and tedious task for doctors in present days. An automated system for brain tumor detection and segmentation will help the patients for proper treatment planning. Due to complex structure of human brain, a diagnosis of tumor area in brain becomes a challenging task. So detection of such brain tumor location, identification and classification in earlier stage is a serious issue in medical science. So, segmentation of brain tumor from MR images is the most important task as the tumor varies in terms of size, shape, location, and texture. By enhancing the new imaging techniques, it helps the doctors to observe and track the occurrence and growth of tumor-affected regions at different stages.

Bahadure et al. [1] proposed BWT and SVM techniques image analysis for MRI-based brain tumor detection and classification. Joseph et al. [2] proposed segmentation of MRI brain images using K-means clustering algorithm along with morphological filtering for the detection of tumor images. The automated brain tumor classification of MRI images using support vector machine (SVM) was proposed by Alfonse and Salem [3]. For the brain tumor segmentation, Zanaty [4] proposed an approach based on hybrid type, with the combination of seed growing, FCM, and Jaccard similarity coefficient algorithm with the measure of gray and white segmented tissue matter from tumor images. Yao et al. [5] proposed an methodology which included extraction of textures features with wavelet transform and SVM with an accuracy of 83%. For the classification and brain tumor

segmentation, Kumar and Vijaya kumar [6] proposed methodology using principal component analysis (PCA) and radial basis function kernel with SVM and obtained an accuracy of 94% with this method. For the medical image segmentation, a localized fuzzy clustering with the extraction of spatial information was proposed by Cui et al. [7]. The literature survey above gives a clear view of the techniques that were invented only to obtain the segmentation region of interest, some techniques for extracting features and some to train and test using the classifiers. In this research work the RVM is proposed to classify the tumor from the MR images. Many real-world engineering optimization problems, however, are very complex in nature and quite difficult to solve. Meta heuristic algorithms commonly operate with the biological evolutionary process such as genetic algorithms (GAs) proposed by Holland [8] and Goldberg [9], PSO is a recently developed meta heuristic technique inspired by choreography of a bird flock developed by Kennedy and Eberhart [10].

The main objective of this paper is to present a novel meta heuristic WCA for enhancement of biomedical MR images to remove noise from medical MRI. From the literature survey, it is found that the WCA has been applied to different constraint engineering problems to find the optimal number, location, and size of multiple types of distributed generation units in a distribution system. But no researcher has applied WCA algorithm in image processing which motivates us to apply WCA technique to biomedical MR images for enhancement purpose. The enhancement of the MRI plays a vital role to improve image quality. The image quality improvement from magnetic resonance images motivates us to propose a novel nature inspired WCA, which is based on the ecosystem of water cycle.

The rest of the paper is organized as follows: Sect. 2 presents methodology followed by PSO and APSO technique for image enhancement technique, Sect. 3 presents the proposed WCA algorithm technique for enhancement, Sect. 4 presents the support vector machine and proposed relevance vector machine for classification, Sect. 5 presents results and discussion, and finally Sect. 6 contains the conclusion followed by reference.

2. METHODOLOGY

In this study, a computer based brain tumor detection approach in magnetic resonance imaging is proposed. The purpose of this study is to enhance, detect and localize the tumor areas in the brain using proposed RVM learning and WCA techniques. For this study, a special enhancement technique which is based on WCA has been employed on the MRI and compared with PSO and APSO algorithm.

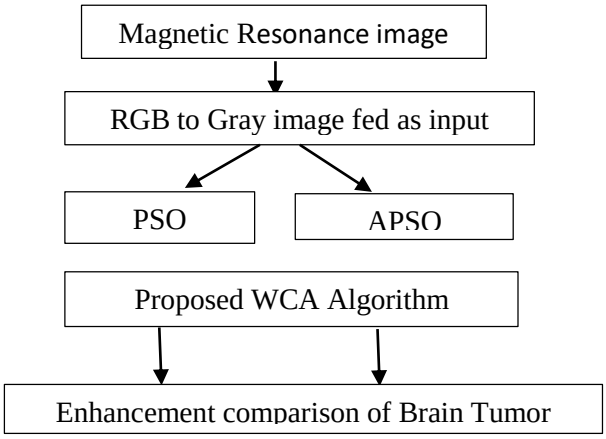

Figure 1: Research flow diagram for image Enhancement

2.1. Particle Swarm Optimization (PSO) and Accelerated Particle Swarm Optimization (APSO)

PSO is a population based stochastic optimization technique inspired by social behavior of bird flocking [11]. PSO uses a population of individuals, to search feasible region of the function space. In this context, each candidate solution is called particle and represents one individual of a population (features). The population is set of vectors and is called swarm (set of feature data points). The particles change their components and move (fly) in a search space.

The standard particle swarm optimization uses both the current global best g^* and the individual best x_i^*. In the accelerated particle swarm optimization (APSO) [12], the velocity vector is generated by a simpler formula

$$v_i^{t+1} = v_i^t + \alpha \in_n + \beta\left[g^* - x_i^t\right] \quad (1)$$

Where $\in_n$ is drawn from N (0, 1) to replace the second term. The update of the position is simply

$$x_i^{t+1} = x_i^t + v_i^{t+1} \quad (2)$$

In order to increase the convergence even further, we can also write the update of the location in a single step

$$x_i^{t+1} = (1-\beta)x_i^t + \beta g^* + \alpha \in_n \quad (3)$$

3. PROPOSED WATER CYCLE ALGORITHM FOR IMAGE ENHANCEMENT

The water cycle algorithm (WCA) mimics the flow of rivers and streams towards the sea and derived by the observation of water cycle process. The idea of the proposed WCA is inspired from nature and based on the observation of water cycle and how rivers and streams flow downhill towards the sea in the real world. It consists of several phases such as evaporation, precipitation, and surface run-off. The WCA [13, 14] has not been used previously by the researchers for Brain magnetic resonance images. In this paper, we have applied the WCA for enhancement which leads to improvement of image quality of MRI.

3.1. Mathematical model for WCA

Let us assume that there are some rain or precipitation phenomena. Starting the optimization algorithm requires the generation of an initial population representing a matrix of streams of size $N_{Population} \times D$, where D is the dimension. Hence, this matrix, which is generated randomly, is given as

$$Total\ population = \begin{bmatrix} Sea \\ River1 \\ River2 \\ River3 \\ \vdots \\ StreamN_{sr+1} \\ StreamN_{sr+2} \\ StreamN_{sr+3} \\ \vdots \\ StreamN_{pop} \end{bmatrix} = \begin{bmatrix} x_1^1 & x_2^1 & \cdots & x_D^1 \\ x_2^1 & x_2^2 & \cdots & x_D^2 \\ \vdots & \vdots & \cdots & \vdots \\ x_1^{N_{pop}} & x_2^{N_{pop}} & \cdots & x_D^{N_{pop}} \end{bmatrix} \quad (4)$$

The rows and column of equation(4) represent the population size ($N_{Population}$) and the number of design variables, D, respectively. In the first step, $N_{Population}$ streams are created. Then, a number of best individuals N_{sr} (minimum values) are selected as the sea and rivers. The stream which has the minimum value (objective function) among the others is considered as the sea. In fact, N_{sr} is the summation of the number of rivers (which

is defined by the user) and a single sea. The rest of the population (N_{Stream}) are considered as streams flowing into the rivers or may alternatively flow directly into the sea.

Atfirststep, $N_{Population}$ streams are created. Some of N_{sr} (good individuals or minimum values) are selected as a sea and rivers. The rest of the population is calculated using the following equation:

$$N_{sr} = No.of\ rivers + 1(sea) \tag{5}$$

$$N_{Stream} = N_{population} - N_{sr} \tag{6}$$

$$NS_n = round\left\{\left|\frac{f(River_n)}{\sum_{i=1}^{N_{sr}} f(River_i)}\right| \times N_{Stream}\right\}, \quad n = 1,2,3 \ldots N_{sr} \tag{7}$$

Where, NS_n is the number of streams which flows into the specific rivers and sea, and f is the evaluation function in the algorithm. The designated streams for each river and the sea are calculated using the following Eq. (7).

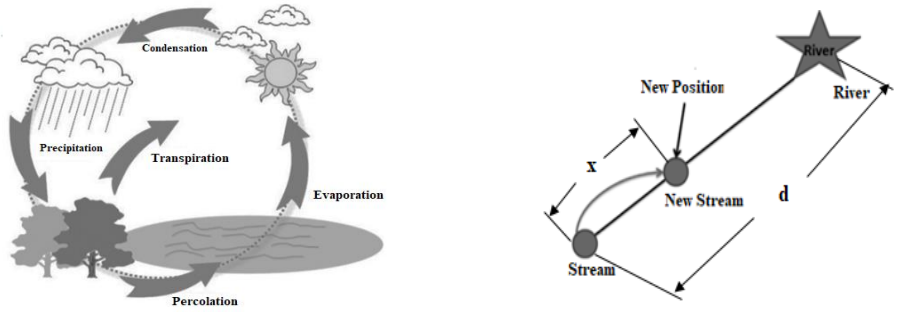

Figure 2: Hydrologic cycle (left) and schematic illustration of streams flowing into a specific river

Figure 3 shows a schematic view of a stream flowing towards a specific river along their connecting line. For the exploitation phase of the WCA, new positions for streams and rivers have been suggested as follows.

$$\begin{aligned}
\vec{X}_{Stream}(t+1) &= \vec{X}_{Stream}(t) + rand \times C \times \left(\vec{X}_{Sea}(t) - \vec{X}_{Stream}(t)\right) \\
\vec{X}_{Stream}(t+1) &= \vec{X}_{Stream}(t) + rand \times C \times \left(\vec{X}_{River}(t) - \vec{X}_{Stream}(t)\right) \\
\vec{X}_{River}(t+1) &= \vec{X}_{River}(t) + rand \times C \times \left(\vec{X}_{Sea}(t) - \vec{X}_{River}(t)\right)
\end{aligned} \tag{8}$$

Where t is an iteration index, 1 < C < 2, and the best value for C may be chosen as 2, and 0 < rand < 1. Basically, evaporation causes sea water to evaporate as rivers/streams flow into the sea. For that purpose, the following criterion is utilized for the evaporation condition between a river and the sea:

$$\text{If } \left\|\vec{X}_{Sea}^{t} - \vec{X}_{River\,j}^{t}\right\| < d_{\max} \quad or \quad rand < 0.1 \tag{9}$$

Where, $j = 1,2,3,\ldots\ldots, N_{sr} - 1$ and perform raining process by uniform random search and the end the process and $d_{\max}$ is a small number close to zero. After evaporation, the raining process is applied and new streams are formed in different locations. Therefore, $d_{\max}$ controls the search intensity near the sea (i.e., best obtained solution). The value of $d_{\max}$ adaptively decreases as follows [15]:

$$d_{\max}(t+1) = d_{\max}(t) - \frac{d_{\max}(t)}{Max.Iteration} \quad t = 1,2,3,\ldots\ldots, Maximum\ \ Iteration \tag{10}$$

3.2 Enhancement results using PSO, APSO and WCA

It is found that the quality of image is much better in visualization from the Fig.4 and Fig.5 using WCA. The PSO, APSO also somehow increases the image quality, but the proposed WCA gives better feature in terms of entropy and gbest value which is presented in table-1 in result and discussion section

4. MAGNETIC RESONANCE IMAGE SEGMENTATION BY SVM AND RVM

In this paper, a fully automatic method for brain tissue segmentation has been proposed, in which the RVM classification algorithm has been employed for tumor extraction successfully. Further, with using the obtained tumor areas, the comparison analysis are presented with using RVM and SVM.

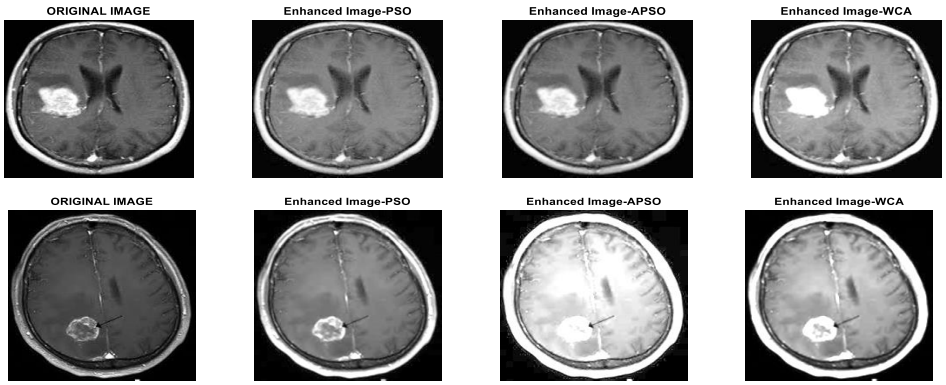

Figure 4: Enhancement result of MRI using PSO, APSO and WCA

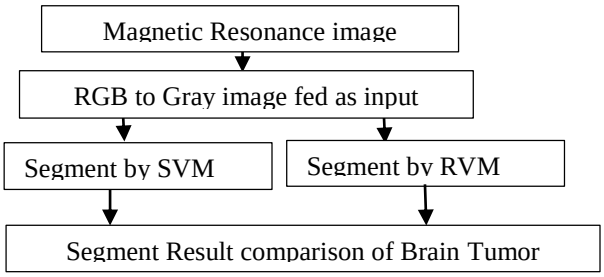

Figure 5: Research flow diagram for image Enhancement

4.1. Support Vector Machine

For binary classification in SVM [16], the Solution for W can be written in a quadratic equation

$$W(\alpha)=\left\{\sum_{i=1}^{N}\alpha_i-\frac{1}{2}\sum_{i=1}^{N}\sum_{j=1}^{N}\alpha_i\alpha_j y_i y_j\left\langle x_i,x_j\right\rangle\right\} \qquad (11)$$

Subject to $\sum_{i=1}^{N}\alpha_i y_i=0$ where, α_i is the hyper parameter or Lagrangian multiplier.

Some advantages of SVM are: (i) it smoothly handles the nonlinear problems, (ii) good prediction accuracy and involved simple mathematical calculations.

4.2. Proposed Relevance Vector Machine (RVM)

The proposed RVM [17, 18] to recast the main ideas behind SVM in a Bayesian context. The RVM decision function can be much sparser than SVM classifier.

Considering a two class problem, for given the input x, the RVM model follow the sigmoid function

$$\sigma(y)=1/\left(1+e^{-y}\right)$$

A RVM classifier model applying the logistic sigmoid function is given by

$$p(t_i = 1, w) = [\sigma(y(x_i; w))] = 1/(1 + e^{-y(x_i;w)}) \quad (12)$$

The RVM classifier function is given by

$$y(x; w) = f_{RVM}(x) = \sum_{i=1}^{N} w_i K(x, x_i) + w_0 = \Phi w \quad (13)$$

Where N is the length of the data and the weight vector $w = [w_0, w_1, w_2, ...w_N]^T$

And Φ is a $N \times (N+1)$design matrix. The matrix Φ has elements $\Phi_{i.j} = K(x_i, x_j)$. The kernel function is given by

$$k(x_i, x_j) = \exp\left(-\frac{\|x_i - x_j\|^2}{2\sigma_k^2}\right) \quad (14)$$

Those training vectors associated with the non-zero weights are called Relevance Vectors and predictions are made based on the posterior distribution over the weights.

4.3. Segmentation results obtained using SVM and RVM

The segmentation results using SVM and RVM has been presented in the Fig.6 and Figure 7. It is found from the Figure 6 and Figure 7 that the noise has been removed and tumor has been detected. In case of SVM the noise removal accuracy is 87.33% and 98.13% in case of RVM which is reported in Table 3. Also the computational time is lesser in RVM than SVM is reported in Table 3.

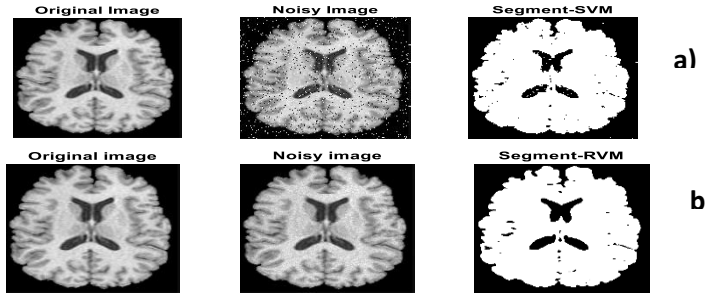

Figure 6: Segment result with a) 30dB salt & Pepper noise using SVM and b) 40dB salt &Pepper noise using RVM

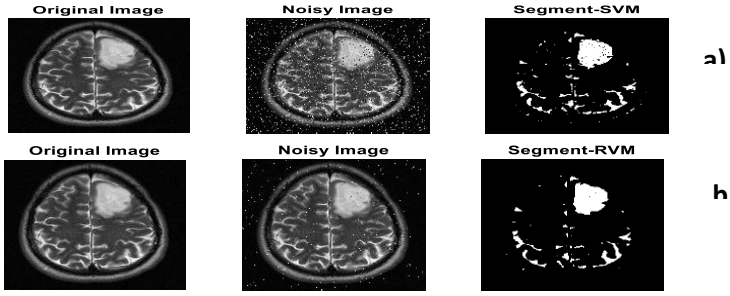

Figure 7: Segment result a) with 30dB salt &Pepper noise using SVM and b) 40dB salt &Pepper noise using RVM

4. RESULTS AND DISCUSSION

The MRI datasets has been collected from the Harvard medical school architecture and Alzheimer's disease Neuroimaging Initiative (ADNI) public database (http://adni.loni.usc.edu/)[1]. In the experimental part of the

study, 75 MRI are used to optimize our system and 25 out-of-sample MRI are also used to test the approach. The comparison of entropy and g_{best} values using PSO, APSO and WCA method for enhancement has been presented in Table-1. It is found that WCA shows good g_{best} and entropy values in comparison to PSO and APSO.

The bar graph shown in Figure 8, depicts the entropy comparisons for individual figure. It is seen that the entropy value obtained using WCA for enhancement of image is better than the other two PSO and APSO method. The bar graph shown in Figure 9, depicts the g_{best} value comparisons for individual images. It is seen that the g_{best} value obtained using PSO is better than APSO and WCA for enhancement of image. But the WCA is preferable as it takes less computational time as compared to PSO and WCA method which is shown in Table 2.

Further, Figure 10 to Figure 11 shows the fitness value of all threes PSO, APSO and WCA method for image enhancement. It is found that the fitness value shown in case of WCA is better in comparison to PSO and APSO method. Magnetic resonance image segmentation has been done by using SVM and RVM with salt & pepper noise. The proposed RVM shows good accuracies than SVM. Further the computational time is lesser in RVM algorithm which is shown in Table 3.

Table 1: Comparison result of Entropy and gbest_value of PSO, APSO and WCA

	PSO		APSO		WCA	
Image	**Entropy**	**g_{best}_value**	**Entropy**	**g_{best}_value**	**Entropy**	**g_{best}_value**
Img-1	0.7008	0.4538	0.7175	0.4511	0.7325	0.4340
Img-2	0.6128	0.4133	0.6266	0.4034	0.6438	0.3825
Img-3	0.6238	0.4250	0.6350	0.4152	0.6578	0.4012
Img-4	0.8815	0.5170	0.8835	0.5142	0.8957	0.5037
Img-5	0.8773	0.5181	0.8853	0.5124	0.8997	0.5041

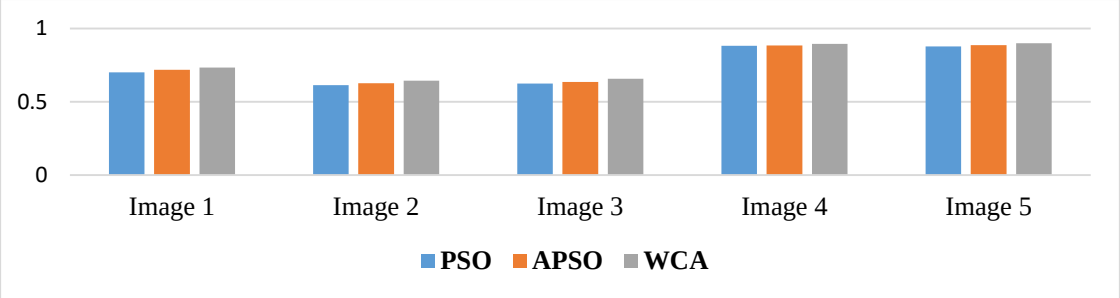

Figure 8: Bar chart for the comparison of Entropy using PSO, APSO and WCA

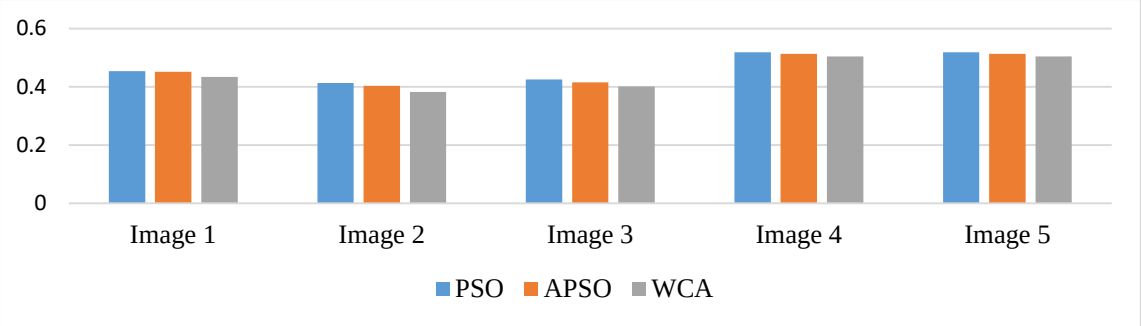

Figure 9: Bar chart for the comparison of gbest value using PSO, APSO and WCA

Table 2: Computational time Comparison using PSO, APSO and WCA

Computational time in Sec (PSO,APSP,WCA)			
Image	**PSO**	**APSO**	**WCA**
Image-1	54.8386	51. 0986	31.3861
Image -2	59.2241	52. 3242	29. 4132
Image -3	57.4485	51.4285	27.4428
Image -4	66.9375	62.9955	26. 7595
Image -5	76.3930	72. 0103	23. 3012

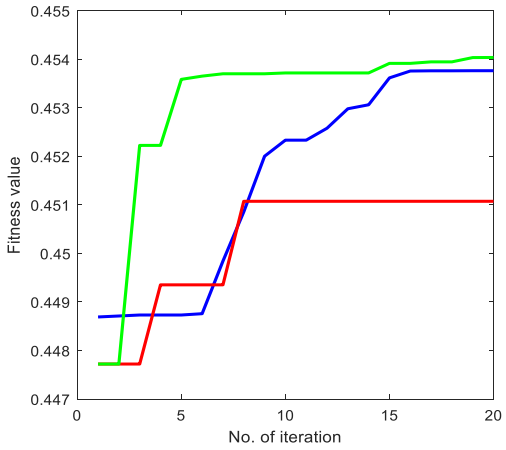

Figure 10: Fitness value curve for image-1

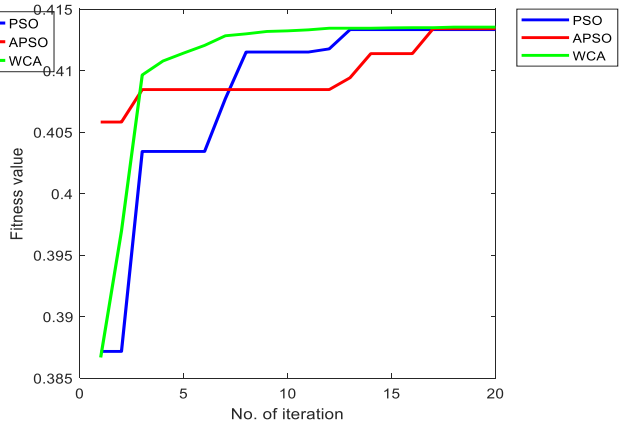

Figure 11: Fitness value curve for image-2

Table 3: Percentage accuracies and Computational time Comparison using SVM & RVM

	Percentage Accuracies (%)		**Computational time in Sec**	
Image	**SVM**	**RVM**	**SVM**	**RVM**
Image-1	84. 86	97. 06	23.3111	12.3221
Image -2	83.21	98. 32	22. 4245	12. 2315
Image -3	87.45	98.28	22.4836	12.4123
Image -4	86.37	97.99	23. 7554	11. 6754
Image -5	**87.33**	**98. 13**	23. 3214	11. 5414

6. CONCLUSION

This paper presented a new optimization technique called the water cycle algorithm. The fundamental concepts and ideas which underlie the method are inspired from nature and based on the water cycle process in real world. In this paper, the WCA with embedded constraint approach is proposed for enhancement of magnetic resonance image and the results containing improvement of quality of image has been reported. The statistical results, based on the comparisons of fitness, entropy and gbest values of the proposed WCA against numerous other optimization methods PSO, APSO illustrate the attractiveness of the proposed method for handling numerous types of constraints. The obtained results show that the proposed WCA algorithm, offers better solutions than PSO, APSO considered in this research which is presented through bar graph, fitness curve and computational time trough

tables. Further, the support vector machine and relevance vector machine based segmentation has been proposed for detection of tumor and removal of noise from magnetic resonance images and results with computational time and percentage accuracies with noisy environment have been reported in this paper. However, further research is required to examine the efficiencies of the proposed WCA, SVM and RVM on large scale medical magnetic resonance imaging problems which leads big data research issues.

REFERNCES

[1] Bahadure NB, Ray AK, Thethi HP (2017), "Image analysis for MRI based brain tumor detection and feature extraction using biologically inspired BWT and SVM", *Int J Biomed Imaging*, Article ID 9749108, 12 pages.

[2] Joseph RP, Singh CS, Manikandan M (2014), "Brain tumor MRI image segmentation and detection in image processing", *Int J Res Eng Technol*, 3: 2321-7308.

[3] Alfonse M, Salem M (2016), "An automatic classification of brain tumors through MRI using support vector machine", *Egypt Comput Sci J*, 40:11–21.

[4] Zanaty EA (2012), "Determination of gray matter (GM) and white matter (WM) volume in brain magnetic resonance images(MRI)", *Int J Comput Appl*, 45:16–22.

[5] Yao J, Chen J, Chow C (2009), "Breast tumor analysis in dynamic contrast enhanced MRI using texture features and wavelet transform. *IEEE J Sel Top Signal Process*, 3(1):94–100.

[6] Kumar P, Vijaya kumar B (2015), "Brain tumor MR image segmentation and classification using by PCA and RBF kernel based support vector machine", *Middle East J Sci Res*, 23(9):2106–2116.

[7] Cui W, Wang Y, Fan Y, Feng Y, Lei T (2013) Localized FCM clustering with spatial information for medical image segmentation and bias field estimation. *Int J Biomed Imaging, Article ID 930301, 8 pages*.

[8] Holland J. (1975) *Adaptation in natural and artificial systems*. Ann Arbor, MI: University of Michigan Press.

[9] Goldberg D. (1989), "Genetic algorithms in search, optimization and machine learning", MA: Addison-Wesley.

[10] Kennedy J, Eberhart R. (1995), "Particle swarm optimization", Proceedings of the IEEE international conference on neural networks. *Perth, Australia*: 1942–1948.

[11] Lu N., Zhou J. Z., He Y., Y., Liu Y(2009)., "Particle Swarm Optimization for Parameter Optimization of Support Vector Machine Model", 2009 Second International Conference on Intelligent Computation Technology and Automation, *IEEE publications*, 283-284.

[12] Yang, X. S., Deb, S., and Fong, S., (2011), "Accelerated Particle Swarm Optimization and Support Vector Machine for Business Optimization and Applications", Networked Digital Technologies (NDT2011), *Communications in Computer and Information Science*, 136: 53-66.

[13] Eskandar H, Sadollah A, Bahreininejad A, Hamdi M. (2012), "Water cycle algorithm - A novel metaheuristic optimization method for solving constrained engineering optimization problems", *Comput Struct*: 151–166.

[14] Shilei Qiao, Yongquan Zhou, Yuxiang Zhou, Rui Wang "A simple water cycle algorithm with percolation operator for clustering analysis", Soft Computing, https://doi.org/10.1007/s00500-018-3057-5, February 2018.

[15] Sadollah A, Eskandar H, Bahreininejad A, Kim JH. "Water cycle algorithm with evaporation rate for solving constrained and unconstrained optimization problems", *Appl Soft Comput*, 30: 58–71.

[16] Sakthivel K, Nallusamy R, Kavitha C. (2014), "Color Image Segmentation Using SVM Pixel Classification Image", World Academy of Science, Engineering and Technology, *International Journal of Computer and Information Engineering*, 8:10.

[17] Ozer S. , Haider M. A. , Langer D. L. , van der Kwast T. H., Evans A. J., Wernick M. N.; Trachtenberg J. (2009) , "Prostate cancer localization with multispectral MRI based on Relevance Vector Machines", *IEEE International Symposium on Biomedical Imaging*: From Nano to Macro.

[18] Wei L., Yang Y., Nishikawa R. M., Wernick M. N. and Edwards A. (2005.), "Relevance Vector Machine for Automatic Detection of Clustered Micro calcifications," *IEEE Trans. on Medical Imaging*, 24: 1278-1285,

Experimental and Statistical Investigation of Al Alloy Welded Joint in Metal Inert Gas Welding

Kishor P. Kolhe[1,*], R. Ramesh[2], M. Sivaraj[2], S. Rajkumar[2]

[1]*Department of Mechanical Engineering, Bahirdar University, Ethiopia*
[2]*Department of Mechanical Engineering, Hawassa University, Ethiopia*
**Corresponding author, e-mail: kishor75@gmail.com*

ABSTRACT

Aluminum and its alloys are having variety of applications in today's industrial scenario. The use of Al and its alloys are increasing day by day due to its specific properties, like light weight, high strength, and excellent corrosion resistance. Present study is planned to analyze and optimize the weld joint quality characteristics like tensile strength, penetration and toughness of aluminum alloy 6061-T6 in metal inert gas (TIG) welding. Welding current, voltage, welding speed are selected as input parameters for conducting experimental runs. Total nine experiments are performed for welding of aluminum 6061 tempered alloy sample using semi-automatic MIG welding model PRO-4200 current range 10 A-420 A and voltage range 10 V-41 V. The welding responses such as tensile strength, penetration and toughness of welded samples were measured for all nine samples Statistical analysis of variance (ANOVA) test was conducted to determine the significant process welding parameters on weld joint responses. From the ANOVA results, it was found that welding parameters were most significant for weld joint strength of aluminum alloy in MIG welding operation. Again, Taguchi methodology was applied on experimental data to obtain the optimum welding input parameters to maximize the penetration, toughness and ultimate tensile strength. Confirmatory tests are validate the optimized conditions by Taguchi method.

Keywords: *MIG welding, Aluminum alloy, Weld strength, Taguchi method, Analysis of variance*

1. INTRODUCTION

Aluminum alloys are alloys in which, aluminum is the predominant metal it includes typical alloying elements, like copper, magnesium, manganese, silicon, tin and zinc [1]. An Al and its alloy play an important role in engineering and metallurgy field because of fabrication and formability [2]. Higher strength 6061 alloy finds broad use in welded structural members such as Truck and marine frames, front and rear suspension frames, and pipelines. The most common temper 6061 aluminum is T6-solution heat treated and artificially aged. Metal inert gas (MIG) welding has been used widely to join pieces of aluminum alloys and other metals in construction of automotive frame, marine frame, and pressure vessels [3]. In the MIG welding process, a gas shield is usually used to protect the arc and the weld from atmospheric contamination, an electric potential is established between the electrode and the work piece that needs to be welded, such electric potential will cause the current to flow and consequently a thermal energy will be generated in the partially ionized inert gas [4]. Welding of aluminum alloy materials is difficult task due to insufficient information about joining of newly developed materials like Al alloy. Metal inert gas (MIG) welding is effective and efficient welding technique to join aluminum alloy sheets [5]. In the present study, weld quality responses of MIG welded aluminum alloy sheets has been made analyzed and optimized by statistical analysis of variance and Taguchi method.

Literature survey has been made to study the effects of process welding parameters in MIG welding of aluminum alloy and other materials by using Taguchi method and analysis of signal-to-noise ratio. The details of the literature survey are given as follows:

Jagtap et al. [4] had been investigated the effects of process welding parameters on quality characteristics of weldment. They had been studied the variations of output responses with varying of input parameters. They stated from their work that welding input parameters had most significant effect for joint quality obtained in MIG welding process. Stathers et al. [6] were found relationship between hardness and tensile properties for HAZ in Al alloy 6061-T651. They used Vickers micro hardness testing machine for measuring hardness and tensile testing by using IN-STRON 8501 Servo-hydraulic testing machine for MIG welded specimens. They were found that

hardness is a sole variable for estimating the yield and tensile strength of the heat affected zone (HAZ) in welding. The relations have been expressed mathematically. Yue et al. [7] were investigated the effect of heat input and preheats on the HAZ and hydrogen induced cracking tendency of BA-160 (Blast resistance steel). Welding of specimens were carried by using GMAW. Miyazaki, et al. [8] were investigated the influence of the grain size on the weld heat affected zone cracking of Gas metal arc (GMA) welds on A 6061. Ambriz, et al. [9] was investigated Local mechanical properties of a weld zone, in a 6061-T6 aluminum alloy subjected to modified indirect electric arc technique. Vargas et al. [10] were also analyzed and optimized the weld response, yield strength in GMAW operation. Researchers were also studied the microstructure of welded samples after experimentation. Finally, they optimized the GMAW process to maximize the yield strength of welded sample. Hooda et al. [11] were identified the empirical relationship of process parameters to predict the yield strength of MIG welded AISI 1040 medium carbon steel samples. The Process parameters such as welding voltage, current, wire speed and gas flow rate were studied and stated that process parameters selection was very important for obtaining desired weld responses. Murat et al. [12] had been performed a research investigation to study the effects of welding input parameters on output responses in arc stud welding using Taguchi method and artificial neural networks.

2. MATERIALS AND METHODS

2.1. Design of Experiments

Pre-selected weld parameters are selected before to the start of the welding process and they cannot be changed during the welding process. These parameters, variables, include the electrode type, size, the torch nozzle size, and the shielding gas type. The indirect weld parameters of the welding process include the arc voltage, arc current, travel speed, shielding gas, and wire feed rate. Indirect weld parameters are parameters that can be modified in process. Once the pre-selected variables are properly chosen, the quality of the weld can be controlled through proper selection and modification of the indirect weld parameters. In any welding process, the input parameters have an influence on the weld joint mechanical properties. By varying the input process parameters combination, the output would be different welded joints with significant variation in their mechanical properties. The input parameters play a very significant role in determining the quality of a welded joint. Generally, most of the researcher uses Taguchi approach for Design of experiment (DOE) because it can significantly reduce time required for experimental investigations but in present investigation the DOE carried out nine experiments as per welding current range from 75A to 275A having nine levels, welding voltage range from 20V to 26V having three levels and welding speed constant. Dr. Taguchi's Signal-to-Noise ratios (S/N), which are log functions of desired output, used as objective functions for optimization, help in data analysis and prediction of optimum results.

The following three types of S/N ratio are employed in practice:

$$\text{Larger-the-Better: S/N ratio} = -10\log_{10}\left(1/n\sum_{i=1}^{n} 1/y_i^2\right) \quad (1)$$

$$\text{Smaller-the-Better: S/N ratio} = -10\log_{10}\left(1/n\sum_{i=1}^{n} y_i^2\right) \quad (2)$$

$$\text{Nominal-the-Best: S/N ratio} = -10\log_{10}\left(\mu^2/d^2\right) \quad (3)$$

Where, n = number of parameters; y = output response; μ= mean; d= standard deviation

2.2. Experimental Procedure

The experiments are carried out on Semi-automatic Metal Inert Gas arc welding machine model PRO-4200 in a single Run which is shown in Figure 1. Argon gas with gas flow rate 25 L/min used as a shielding gas to protect the arc and weld bed from atmospheric contamination. 1.2mm diameter ER 4043 Filler wire used to weld the test specimens. The material chosen for the present study was aluminum alloy 6061-T6. Sample of 150mmx100mmx10mm size has been used as a work piece material. The chemical Composition results are shown in Table 1. The aluminum alloy 6061-T6 Sheet is converted in to nine samples as per desired work piece size by using cutting operation. 60° V edge preparation was made on these specimens as shown in Figure 2. Set up was

made by tack welding. Root gap and root face kept 2mm each. Welding current, Welding voltage varied and Welding speed, Gun Nozzle tip to plate distance, and gas flow rate remained constant. A specific code was made for each welded specimen in which "M" assigned for MIG welded specimen, "A61" assigned for aluminum alloy 6061-T6 and the number followed by this code indicates Experiment number. Total nine experiments were carried out within the welding current range from 75A to 275 A as per fractional factorial design. The welding CVN sample prepared as per ASTM-E-23 standard from the MIG welded specimens shown in Figure 4. Toughness test were made using the Charpy impact test machine, Pendulum impact model- AI-13. Tensile samples were prepared as per ASTM-E8/E8M-09 Standard from the MIG welded specimens which is shown in Figure 5. Tensile test was made using universal testing machine (UTM) with hydraulic grip.

Table 1: Chemical Composition of 6061 AA.

Alloy	Si	Fe	Cu	Mn	Mg	Cr	Zn	Ti	Other		Al
									Each	Total	
Min.	0.40	0.0	0.15	0.0	0.8	0.04	0.0	0.0	0.0	0.0	98.61
Max.	0.8	0.7	0.40	0.15	1.2	0.35	0.25	0.15	0.05	0.15	95.8

Figure 1: Gas Metal Arc Welding machine

3. RESULTS AND DISCUSSION

3.1. Analysis of variance

The purpose of the analysis of variance (ANOVA) is to investigate which design parameters significantly affect the quality characteristic. ANOVA help in formally testing the significance of all main factors and their interactions by comparing the mean square against an estimate of the experimental errors at specific confidence levels. In the present work, Eq. 1 is used to for conducting the analysis of variance for all the responses: penetration, toughness and tensile strength as maximum values of these responses desired. The sum of square (SS), the degrees of freedom (D), the variance (V) and the percentage of contribution to the total variation (P) are used in ANOVA; Results are illustrated in Tables 3-5. The significant contribution of each welding input parameter is calculated as given in Tables 3-5. From the Tables 3-5, it is found that current is the most significant factor all the responses, next is voltage followed by speed.

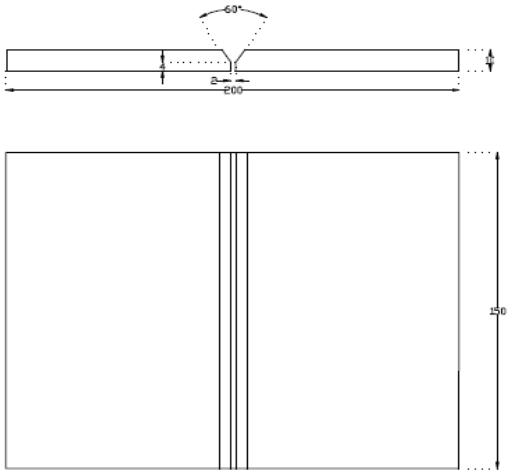

Figure 2: MIG welding sample

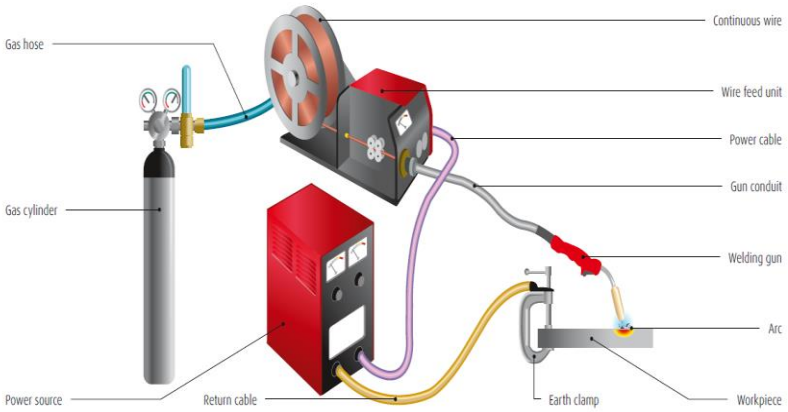

Figure 3: GMAW machine setup

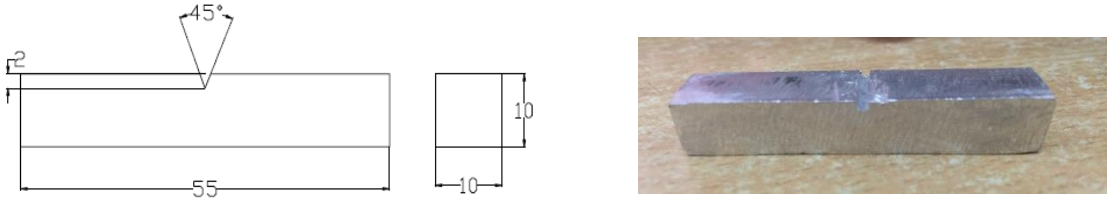

Figure 4: Charpy Impact Test Specimen as per ASTM-E-23

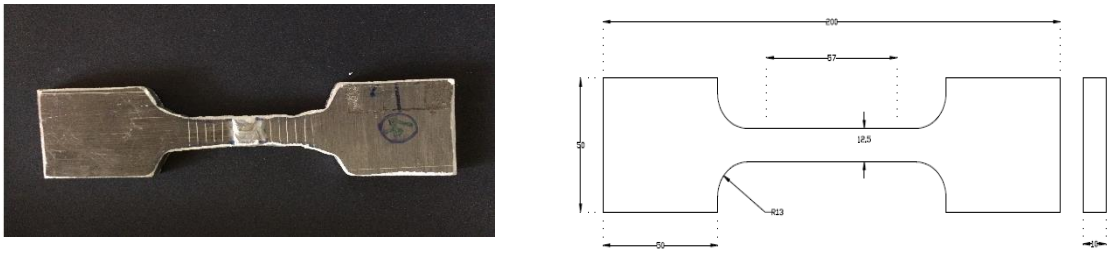

Figure 5: Tensile Testing Sample as Per ASTM-E8/E8M-09

Table 2: Welding parameters and their levels and output responses

Exp No.	Input parameters			Output responses		
	current (A) A	Voltage (B) V	Speed (C) mm/min	Penetration (mm)	Toughness (Joule)	Tensile strength (MPa)
1	75	20	300	5.0	08	84
2	100	20	300	4.0	09	124
3	125	20	300	4.5	14	127
4	150	23	300	6.0	12	152
5	175	23	300	7.0	26	196
6	200	23	300	6.0	14	161.6
7	225	26	300	6.5	04	176
8	250	26	300	4.8	10	118.4
9	275	26	300	3.0	10	122.4

Table 3: Results of ANOVA for Penetration

Welding Parameters	Degrees of Freedom (D)	Sum of Squares (SS)	Variance (V)	Contribution (P%)	Rank
Current	8	26.60	3.32	61.70	1
Voltage	2	15.95	7.97	36.99	2
Speed	0	0.56	0.56	1.30	3
Total	10	43.11		100	

Table 4: Results of ANOVA for Toughness

Welding Parameters	Degrees of Freedom (D)	Sum of Squares (SS)	Variance (V)	Contribution (P %)	Rank
Current	8	80.28	10.03	52.22	1
Voltage	2	71.40	35.7	46.44	2
Speed	0	2.06	2.06	1.34	3
Total	10	153.74		100	

Table 5: Results of ANOVA for Tensile Strength

Welding Parameters	Degrees of Freedom (D)	Sum of Squares (SS)	Variance (V)	Contribution (P%)	Rank
Current	8	28.36	3.54	72.53	1
Voltage	2	15.86	7.93	40.56	2
Speed	0	-5.12	-5.12	-13.09	3
Total	10	39.10		100	

3.2. Optimization of welding responses by Taguchi method

Taguchi methodology from MINITAB 16.2 software is applied on experimental data as given in Table 2, to optimize the responses: penetration, toughness and tensile strength. The larger -is the better criteria (Eq.1) is selected for present case to maximize the all the responses. The obtained optimum responses are shown in Table 6.

Table 6: Optimum process parameters for quality characteristics

Welding parameters	Penetration	Toughness	Tensile strength
Current (A)	175	175	175
Voltage(V)	23	23	23
Speed(mm/min)	300	300	300

3.3. Confirmatory test

The confirmatory tests are conducted for each welding response separately to verify the optimum welding condition obtained by Taguchi method. From the Confirmatory results it is confirms that optimized welding settings for maximizing the weld responses are good agreement with the initial experimental results as shown in Table 2.

4. CONCLUSIONS

The following conclusions were arrived at based on the present investigations:

- Taguchi optimization method was applied to find optimal process parameters for penetration, Toughness and Tensile strength of weld joint. Signal to noise ratio(S/N) analysis and analysis of variance (ANOVA) were used for the optimization of welding parameters.

- The welding current has the most significant influence on the Tensile strength of weld joint, depth of penetration and toughness. Welding Voltage is second most significant factor. The effect of welding Speed is very small in comparison.
- The percentage of contribution of the welding current is 72.53% for Tensile strength, 61.70% for depth of penetration and 52.22% for Toughness. The percentage of contribution of the welding voltage is 46.44% for Toughness, 36.99% for tensile strength, 40.56% for penetration.
- The optimum welding conditions are obtained separately for three responses: penetration, toughness and tensile strength by Taguchi method
- The confirmation test demonstrated good agreement between the predicted and the experimental values of quality characteristics.
- From the present study, it is stated that Taguchi methodology is very useful for optimizing the welding responses in MIG welding aluminum alloy.

REFERENCES

1. Korkmaz, E., Gülsöz, A., Meran, C., (2019): The friction weldability of AA6063 Tube to AA6082 tube plates using an external tool. *Materials Design and Applications*, 98: 427-437.
2. Nima, E., Yannik, H., Alexander, H., Dennis, L., Stefan, B., (2019): Optimization of process parameters for friction stir welding of aluminum and copper using the Taguchi method. *Metals*, 9
3. Rahul, R. C., (2019): Prediction of bead geometry in gas metal arc welding by statistical regression analysis. UWSpace. http://hdl.handle.net/10012/14434
4. Jagtap, M.D., Raut, N., (2019): Parametric optimization of MIG welding on IS 1079 HR 2 by Taguchi method. Lecture Notes in Mechanical Engineering, 81-88.
5. Izeda, A.E., Pascoal, A., Simonato, G., Mineiro, N., Gonçalves, J., Ribeiro, J.E., (2018): Optimization of robotized welding in aluminum alloys with pulsed transfer mode using the Taguchi method. *Proceedings*, 2(8), 426.
6. Stathers, P.A., Hellier, A.K., Harrison, R.P., Ripley, M.I. and J. Norrish, J., (2014): Hardness-tensile property relationships for HAZ in 6061-T651 aluminum. *Welding Journal*, 93: 301-311.
7. Yue, X., Feng, X.L. and Lippold, J.C., (2014): Effect of welding parameters on the heat affected zone hydrogen-induced cracking tendency of blast-resistant steel. *Welding Journal*, 93: 98-105.
8. Miyazaki, M., Nishio, K., Katoh, M., Mukae, S., Kerr, H.W., 1990): Quantitative investigation of heat- affected zone cracking in aluminum alloy A6061. *Welding Journal*, 9, 362-371.
9. Ambriz, R.R., Chicot, D., Benseddiq, N., Mesmacque, G., Torre, S.D., (2011): Local mechanical properties of the 6061-T6 aluminum weld using micro-traction and instrumented indentation. *European Journal of Mechanics A/Solids*, 30: 307-315.
10. Vargas, J. A., Jaime, E.T., Jovanny, A.P., Roque, J.H., (2013): Analysis of heat input effect on the mechanical properties of Al-6061-T6 alloy weld joints: *Materials & Design*, 52: 556-564.
11. Hooda, A., Ashwini, D. and Satpal, S., (2012): Optimization of MIG welding process parameters to predict maximum yield-strength in AISi1040. *International Journal of Mechanical Engineering and Robotics Research*, 1(3):203-213.
12. Murat. O., Engin, E., Ramazan, A., Halil, I.K., Necip, F.Y., (2018): A comparative study on the effect of welding parameters of austenitic stainless steels using artificial neural network and Taguchi approaches with ANOVA analysis. Metals 8

Performance Evaluation of the Ethiopian Leather Industry

Sisay Addis

Institute of Technology, Debre Markos University, Debre Markos, Ethiopia, e-mail: sisayaddis123@gmail.com

ABSTRACT

The government of Ethiopia considers the leather industry as one of the priority sector that is capable of accelerating economic development by creating more employment opportunities and generating income through exports. However, the industry's contribution to the national economy so far is not enjoyable as compared to the country's abundant resource potentials for raw material needs (1st in Africa and 10th in the world in livestock population). The main objective of this study is to evaluate the performance of Ethiopian leather industry (ELI) under the light of critical success factors (CSFs) (such as quality, cost, delivery and flexibility). Also, the study tries to benchmark the performance ELI with leading leather processing countries in the world. Various literature and data were surveyed to examine manufacturing performances. Spider chart is used for the benchmarking. The findings of the study revealed that the ELI is operating at low performance with respect to the CSFs. It is also revealed that there is high deviation between Ethiopia and the competitive countries with respect to the CSFs. Furthermore, the study conducted cause & effect analysis to illustrate the interrelated problems that seem to explain underperformances of the ELI. Also, the SWOT (Strengths, Weaknesses, Opportunities and Threats) analysis is conducted to identify dimensions that are important to upgrade participation of the ELI in global value chain. The industry should alleviate the identified problems to improve performance and realize its vision of becoming globally competitive.

Keywords: *Ethiopia, leather industry, critical success factors, CSFs, performance, competitiveness r*

1. INTRODUCTION

Leather industry is considered as the largest industrial sector in the world. Leather is often cut and assembled into leather goods, clothing, shoes, furniture and many other items of daily use. The leather products are amongst the most widely used and traded commodities in the world. It is compared very well with any internationally traded commodity. According to the 2010 report of FAO, the total value of annual trade of leather items was more than seven times of the trade value of rice, more than six times of coffee and more than two times of meat trade (Netsanet Jote, 2014). At the same time, the leather industry plays a prominent role in the world's economy (contributes approximately USD100 billion/year), out of which Africa's earning amounts to only $4 billion (Mwinyihija and Quiesenberry, 2013). The share of Africa in world leather trade has remained low in the last twenty-five years of the 20th century, irrespective of having 21% of the livestock population in the world to satisfy raw material needs (UNIDO, 2010). In 2011, Africa accounted for total cumulative productivity of only 4.01% of the world's production and 3.31% of the value when compared to the rest of the world (Mwinyihija, 2014). In general, the total production of leather and leather products in Africa is much lower qualitatively, quantitatively and value-wise. A look at Ethiopia, one of the leading leather processing countries in Africa, the export share in the world is negligible. The export share was, on average, only 0.00023% over 2001-2003 (Mekonnen and Gezahegn, 2008) and 0.000597 % in 2010 (Mengstu, 2014).

The leather industry in Ethiopia puts at the forefront of the African leather sector in line with its current comparative advantage for the raw material needs (1st in Africa and 10th in the world in livestock population) (UNIDO, 2010). The livestock population growth trend (cattle, sheep and goat) also shows potential of the sector to be the main economic source of the country in the future. The livestock population escalated from 54.5 million in 1995/96 to 77.5 million in 2005/06 to 103.5 million in 2012/13 (Samson Leta and Firehiwot Mesele, 2014). The resource potential makes the leather industry to be a good candidate for a concerted effort to expand production and achieve competitiveness at the international level. The leather industry is especially significant for the economic development of Ethiopia by reducing the high rate of unemployment caused by the fast growing population and generating income through exports (Sisay Addis et al., 2017b). Despite the above mentioned indigenous resource potentials, the leather industry of Ethiopia is yet to utilize its resources to an appreciable extent. It significantly lags behind many countries that are less abundantly endowed with their indigenous

resources (Netsanet Jote, 2014). The industry faces serious problems, both in the production of raw materials and in the manufacturing stages. The tannery and footwear producers operate at 44.97% and 47.6% of the daily production capacity, respectively. Whereas, the daily installed capacity of leather goods and garment producers is ranging 20-150 pieces/day, but the actual output ranges from 10-60 pieces of garment/day (Sisay Geremew, 2014). Export performance of the industry is also stagnated below average. For the period of 2005-2009, footwear producers performed, on average, only 27.55% of the planned export value. Similarly, tannery's export value was quite below of the projected plan for the same period. Figure 1 shows the plan and actual export value of the Ethiopian leather industry for the period of 2005-2013. Export performance report of the industry for this period was achievable to only 56.89% of the projected export plan. Also, actual average production of the industry is far below the international benchmark standards. For instance, in 2009, the footwear producers perform 4 pairs of shoe/day/person, which characterized low operational performance and production efficiency as compared to best practices (i.e. 16 pairs of shoe/day/person) (Tomas Cherkos, 2011). As a result, the country could not obtain the expected economic return from its huge resource potentials. In the past years, the loss to the Ethiopian economy is estimated to US $14 million per year (Sisay Geremew, 2014).

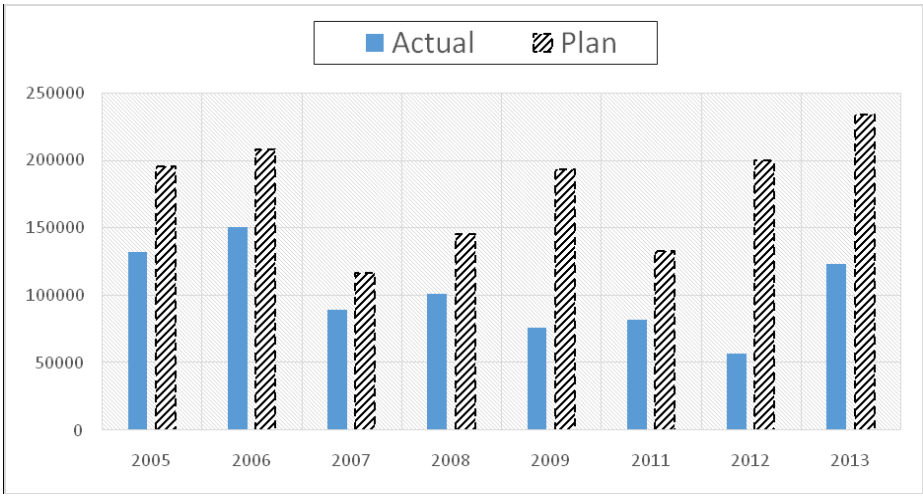

Figure 1: Export performance of the leather industry of Ethiopia (000' USD) (2005-2013) Source: Export performance report from LIDI in 2014

Previous studies revealed that the nature of problems are multifaceted that seem to explain underperformance of the Ethiopia leather industry (ELI) (Sisay Addis et al., 2018). Some of the problems are low utilization of capacity, shortage of raw materials (e.g. processed leather for footwear manufacturers), production delays, bottleneck at workstations, lack of an efficient market structure, financial constraints, lack of latest technologies and lack of human resource management (Netsanet Jote, 2014; Sisay Addis et al., 2019). If Ethiopia has to fully exploit its resource potentials, it is required to address the manifold problems in value chain of the leather industry. Particularly, addressing constraints downstream to the manufacturing stage is critical, because higher stage of manufacturing activity enable organizations achieve increased level of operational performances and meet the challenge of global competition (Sisay Addis et al., 2017a). According to Amrina and Yusof (2011), critical success factors (CSFs) (such as quality, cost, flexibility and delivery) are appropriate strategies to enhance manufacturing performance of organizations. The role of the CSFs is to reflect the current state of manufacturing situation, monitor and control operational efficiency, drive improvement program and gauge the effectiveness of manufacturing decisions. The CSFs are the most commonly cited performance measures to evaluate the manufacturing performance of organizations (El Mola and Parsaei, 2010). They are also recognized as having a relentless impact on the operational performance of the ELI (Sisay Addis et al., 2017a). Accordingly, the main objective of present study is to evaluate the performance of ELI under the light of the CSFs. Also, the study

identifies performance gaps of the industry via benchmarking with competitive leather processing countries in the world.

2. METHODOLOGY

Both primary and secondary data were collected. The study considered high and middle level managers from the leather and leather processing companies in/around Addis Ababa, capital of Ethiopia. Open interviews were used to obtain a deeper understandings of the working conditions of organizations. Senior researchers were also interviewed from the leather industry development institute (LIDI). Moreover, data were composed from literature and documents from LIDI. The data collected from the interviews were analyzed qualitatively that enabled a deeper understanding of organizational performances. A common way to approach qualitative data analysis is the construction of themes or thematic analysis (Bryman, 2004). This kind of analysis is common when the data collection is structured around the predefined themes. In the present study, discussions were conversational and general overall questions were asked about each of the CSFs. After organizing the whole data from the interviews, they were assessed to understand the positive and negative emotion associated with the various themes (Onwuegbuzie et al., 2009).

Tools such as spider chart and cause & effect diagram were used for the data analysis. The spider chart was used to study performance gap analysis between the ELI and the leading leather processing countries in the world. Cause and effect diagram was used to illustrate the interrelated problems that seem to explain the performance of ELI. Moreover, the study conducted SWOT (strength, weakness, opportunity and threat) analysis oriented towards determining dimensions that have impact in upgrading participation of the ELI in global value chain. Finally, concluding remarks are presented based on the outputs of the study.

3. RESULTS AND DISCUSSION

The main objective of this study was to evaluate the performance of ELI under the light of the CSFs. In this section, the results are presented and discussed. Initially, the performance of the ELI is analyzed, followed by benchmarking the ELI with the performance of China and Italy. Subsequently, the cause and effect analysis is conducted, followed by the SWOT analysis.

3.1. Performance evaluation with respect to the CSFs

It is revealed in Section 1 that the performance of the ELI is not comparable with its indigenous resources for the raw material needs. In this section, the current performance ratings of the ELI in the final markets are evaluated with respect to the CSFs (Figure 2).

From the spider chart it is clearly shown that the ELI is conforming to the buyer perception only in price. The price competition is successful for Ethiopia because of the abundance of raw material and cheap labor force. However, there are big gaps in the other CSFs. In low income final markets, price can be a relatively important CSF, but it will not be unique. In higher income final markets, non-price CSFs are generally more important. The major buyers or consumers of leather products of Ethiopia are EU markets like Italy, Germany, Netherlands and France with percent share of 63.17%, 23.54%, 2.87% and 1.04 respectively (Tomas Cherkos, 2011). These markets are very conscience of non-price CSFs. The ELI should focus on the other CSFs for nourishing success in the market. The major and most important CSF for success is the *quality of products*. Ethiopian leather is known for its high reputation in the global market because of its natural quality (Netsanet Jote, 2014). However, the leather products are not performing good quality. It is revealed from the interviews that the ELI is not implementing quality management philosophy yet. For instance:

- quality is not taken as the task of everyone
- no quality targets defined and displayed at work centers
- quality control activities are limited on inspection
- no formal documented way of identifying quality problems and taking corrective actions

- no/limited application of statistical process control techniques
- no determination of quality costs
- no standard procedure for processes.

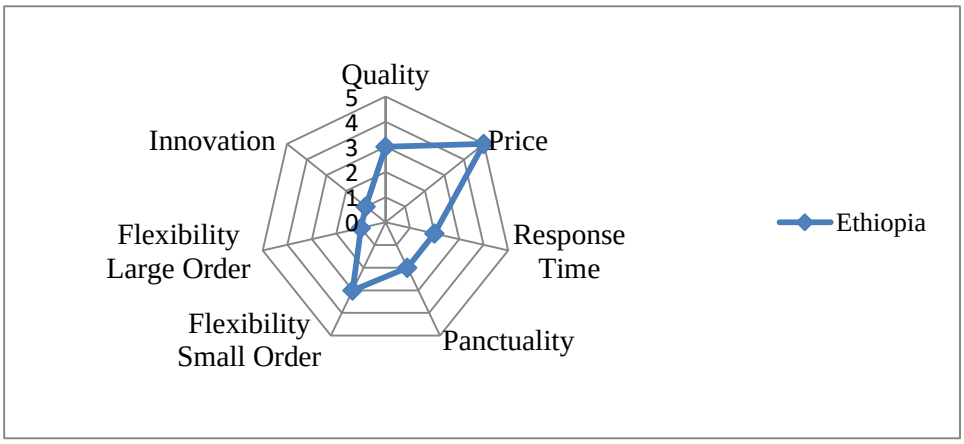

Figure 2: Performance profile of Ethiopian leather

Moreover, there is high rework, scrap, rejection rate, defects, and quality costs, mainly in the footwear manufacturing companies. For instance, the standard benchmark level for scrap and rework is 5% (Tomas Cherkos, 2011). However, the cutting yield of Anbesa shoe S.C is 85% with 15% scrap. Also, Anbesa measures rework level as 11%. Annual cost of rework is determined as around $20,475, which reduces production efficiency of the company (Tomas Cherkos, 2011). In general, the ELI should be committed to design an improvement action plan to improve quality performances as it gratifies crucial values for organizations by satisfying and retaining their customers (De Toni et al., 1995). According to Anderson and Sullivan (1993), customer satisfaction is often regarded as the prime measure of external quality performance.

Delivery is another important CSF for the success of any organizations. According to Hallgren (2007), delivery reliability is sometimes referred to as on-time delivery or delivering according to a promised plan. It can be shown in Fig. 2 that the response and punctuality of the ELI to orders is not satisfactory. The delivery problem basically occurs due to the machines being failed and power interruption in the industry. The downtime increases manufacturing lead time and ultimately influences delivery performance. These problems make manufacturing effectiveness of the ELI (operational planning efficiency) is not well attained (Tesfaye Gezahegn, et al., 2014). The industry should give much attention on planned maintenance management system to increase machines availability. In addition, the major reasons for low delivery performance are:

- delay in raw material supply
- lack of well-designed supply chain network
- workers' efficiency and responsiveness problems
- bottlenecks in the production line (unbalanced production line)
- ineffective motions in the shop floor

Within the manufacturing operations, the ability to adjust production volume and the ability to change between products are the two most influential flexibility types (Hutchison and Das, 2007). Small order flexibility of the ELI is relatively good because of limited batch production capacity of the manufacturers and minimum need of financial stability for the production of small quantities. On contrary, it is very difficult for the ELI to be flexible to large orders as the companies are not large enough to carry out batch production of different designs effectively. Also, flexibility problem exists as there is no practical system for the development of new products based on global demands. In fact, footwear manufacturers try to manage variations in volume and products with large manufacturing lead time. However, the industry in general has to be committed to employ machine flexibility,

systems flexibility, product flexibility, routing/layouts flexibility and volume flexibility. Also, emphasis should be placed on research and development to offer a variety of products based on global demands. Innovation is the least performed CSF for the ELI. This is the effect of low skill of designing, fashioning, less accessibility to fashion forecasts, low skill of product development and research.

3.2. Benchmarking

Benchmarking is a process in which a company compares its performance and practices to industry bests and best practices from other companies (Carpinetti and Oiko, 2007). In this section, benchmarking of the ELI is conducted against two countries with more technically advanced in leather industries in the world. It is clearly shown in Figure 3 and Figure 4 that there is high deviation between the performance of ELI and level of performance of China and Italy with respect to the CSFs. The CSFs are relatively more important for Ethiopia since the major consumers of the leather products are US & EU markets, which are very conscience of the factors. The ELI should alleviate the performance issues to realize the industry's vision of becoming globally competitive and economic benefit of Ethiopia from the industry.

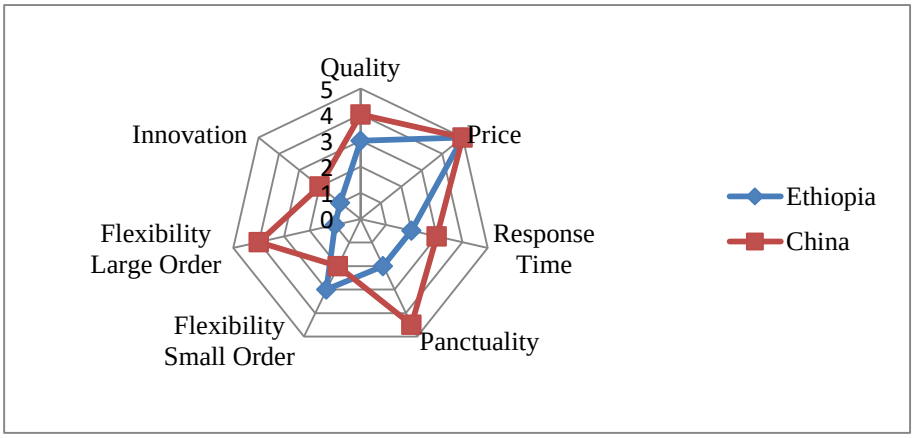

Figure 3: Performance comparison, Ethiopia-China

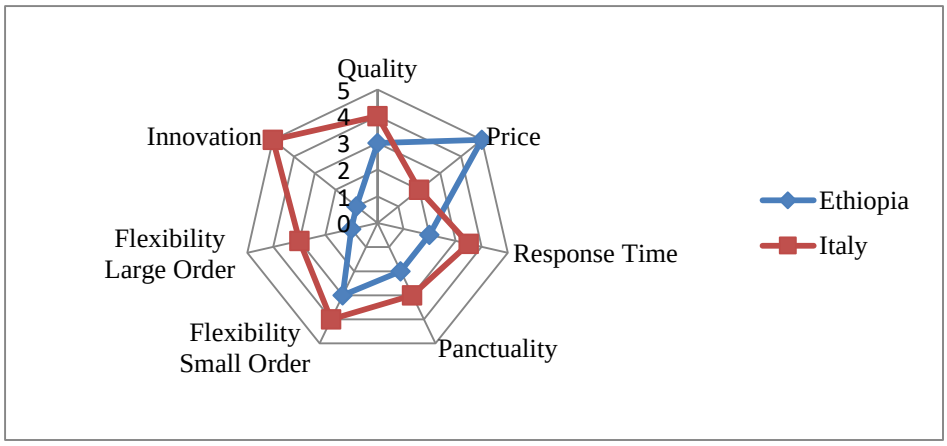

Figure 4: Performance comparison, Ethiopia-Italy

China	Italy	Ethiopia	Recommendation
China is considered as a very cheap source of leather articles with a reliable product quality and strong in coping with massive standardized orders.	Italy is extremely capable of providing innovative designs of products. Buyers who supply the high street boutiques would	The material quality is excellent but the quality of products is poor. The products are very cheap. Other competition factors,	For Ethiopia, the current performance will make no longer competent in the export market. Values should be added to the products to enhance the products

Chinese suppliers extremely suitable to supply the huge price-driven orders from the US retail chains.	look at Italy for small and high fashion orders. Products are expensive and afforded by high class customers.	however, are hardly conformable to customers' perception.	quality. It is wise for Ethiopia to upgrade to China's performance to occupy the market and then proceed to the performance of Italy.

3.3. Cause and effect analysis

Cause and effect diagram (fishbone diagram) was developed by Ishikawa (1976). It is used to determine and break down the main causes of a given problem. In this study, the cause and effect diagram is used to illustrate the relationships between the unsatisfied performances of the ELI and the causes influencing it. The cause and effect analysis is shown in Figure 5.

3.4. SWOT Analysis

The SWOT analysis is oriented towards the external image of the ELI that have impact in upgrading participation in global value chain. In this analysis, Strengths, Weaknesses, Opportunities and Threats have been presented for the leather industry as a whole.

Strengths	**Weaknesses**
✓ Policy initiatives taken by the government to ban export of semi-processed leather ✓ Large raw material base ✓ Good sheep and goatskins properties ✓ Good reputation of finished leather for leather products ✓ Exports of footwear and leather garments ✓ Long and short term training for societies in the industry ✓ Market access through: Common Market for Eastern and Southern Africa (COMESA); European market trade relations with the Africa, Caribbean and Pacific EU/ACP; European Business Association (EBA); African Growth and Opportunity Act (AGOA) ✓ High capital growth of industries ✓ Existence of research and development department ✓ Emergence of large number of enterprises in different regions of the country	✓ Poor resource utilization ✓ Long hides and skin trade supply chain ✓ Deterioration of quality of hides and skins ✓ Shortage of quality leather ✓ Weak advertisement for the products ✓ Lack of marketing strategy ✓ Absence in the global fashion market ✓ Unawareness of international standards ✓ Old technology, obsolete equipment; lack of spare parts ✓ Weak design capabilities ✓ Shortage of differentiated accessories, components, soles and etc. ✓ Poor workmanship ✓ High level of rework and scrap ✓ Lack of introducing modern management systems such as quality management ✓ Unplanned machine maintenance ✓ Small variety of products
Opportunities	**Threats**
✓ Export-oriented industries are supported by the government ✓ Huge internal market for the product ✓ Availability of promotion of joint ventures and foreign direct investment ✓ Negotiations to join the multilateral trading system like AGOA ✓ Competitive advantages for the known Ethiopian sheepskins property ✓ Regional and sub-regional market for leather products like COMESA ✓ The creation of a trade mark as "Made in Ethiopia" to enhance product image	✓ The growing spread of livestock diseases ✓ Uncontrolled imports of second hand leather products like shoes ✓ Competition from Asian and European Countries ✓ Dumping of leather goods from developed countries ✓ Machines expensiveness ✓ International price fluctuation

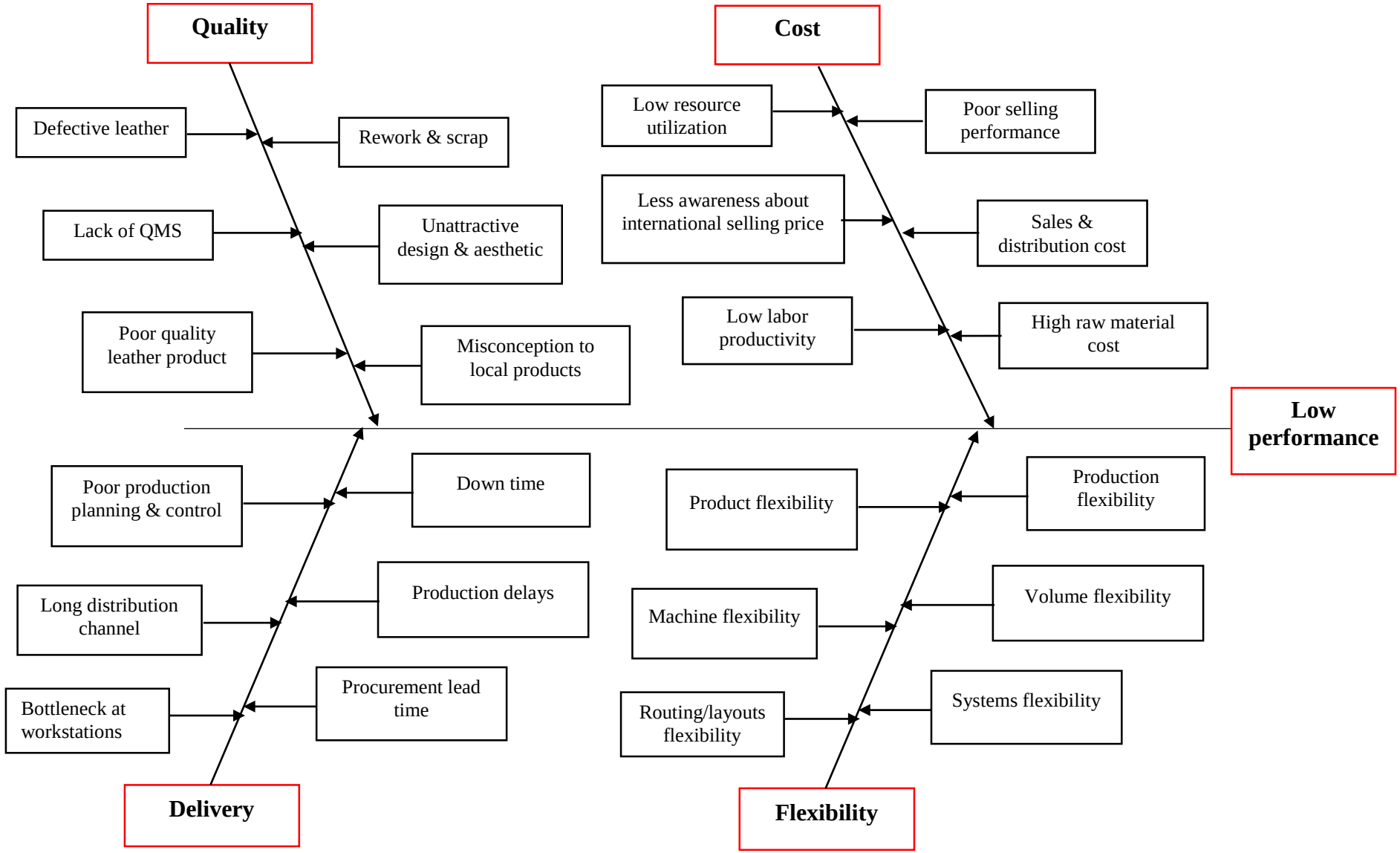

Figure 5: Cause and effect analysis

4. CONCLUSION

Nowadays, there is a need for organizations to measure, analyze and improve performance as they encounter increasing competition from an ever-changing business environment. In this paper, various literature and data were surveyed to examine the current manufacturing performance of the ELI. Further, the study conducted benchmarking of the ELI with the leading leather processing countries in the world (China and Italy). It is revealed that there is high deviation between Ethiopia and the competitive countries with respect to the CSFs. The study also conducted cause & effect analysis and SWOT analysis. Interrelated problems have been identified that seem to explain underperformances of the ELI. Also, different dimensions have been identified that are important to upgrade participation of the ELI in global value chain. The industry should alleviate the identified problems and dimensions to improve organizational performance. It will help to realize the industry's vision of becoming globally competitive and economic benefit of Ethiopia from the industry. As a future research, studies can prioritize the CSFs based on their relative importance. Studies can also develop suitable mathematical models in order to measure the performance of the manufacturing system.

REFERENCES

Altenburg T. (2010): Industrial policy in Ethiopia. German Development Institute, Discussion Paper, Bonn, Germany.

Amrina E. and Yusof S. (2011): Key performance indicators for sustainable manufacturing evaluation in automotive companies. IEEE International Conference, Dec 6, 1093-1097.

Anderson E. W. and Sullivan M. W. (1993): The antecedents and consequences of customer satisfaction for firms. Marketing science, 12(2): 125-143.

Bryman, A. (2004): Social research methods (2nd ed.). Oxford University Press: Oxford.

Carpinetti, L. C. R. and Oiko, O. T. (2007): Benchmarking in Clusters of SMEs: Development and Application of a Data Base. In 19th International Conference on Production Research, Valparaiso, Chile.

De Toni A., Nassimbeni G. and Tonchia S. (1995): An instrument for quality performance measurement. International Journal of Production Economics, 38(2): 199-207.

El Mola, K.G. and Parsaei, H. (2010): Dimensions and measures of manufacturing performance measurement. Computers and Industrial Engineering (CIE), IEEE 40th International Conference, 25 July, 1–6.

Hallgren M. (2007): Manufacturing strategy, capabilities and performance. Ph.D. Thesis, Linköping university, Sweden.

Hutchison J. and Das S.R. (2007): Examining a firm's decisions with a contingency framework for manufacturing flexibility. International Journal of Operations and Production Management, 27(2): 159-180.

Ishikawa, K. (1982). Guide to quality control (Vol. 2). Asian Productivity Organization, Tokyo, Japan.

Leta, S. and Mesele, F. (2014): Spatial analysis of cattle and shoat population in Ethiopia: growth trend, distribution and market access. Springer Plus, 3(1): 310.

Mekonnen B. and Gezahegn A. (2008): The Leather Sector: Growth strategies through Integrated Value Chain. Ethiopian Development Research Institute, Addis Ababa, Ethiopia.

Mengstu A. (2014): Performance of Leather Uppers of Local Footwear products and the Determinants. International Journal of Advancements in Research & Technology, 3(3).

Mwinyihija, M. and Quiesenberry, W. (2013): Review of the challenges towards value addition of the leather sector in Africa. Global advanced research Journal of Management and Business studies, 2(11): 518-528.

Mwinyihija, M. (2014), "Emerging World Leather Trends and Continental Shifts on Leather and Leather goods Production", Advances in Business Management and Administration, Vol. 1(1), pp. 001-013.

Netsanet J. P. (2014): Impact of Supply Chain and Industrial Cluster on the Competitive Advantage of Ethiopian Leather Sector. Ph.D. Thesis, AAU, Ethiopia.

Onwuegbuzie, A. J., Dickinson, W. B., Leech, N. L. and Zoran, A. G. (2009): A qualitative framework for collecting and analyzing data in focus group research. International journal of qualitative methods, 8(3): 1-21.

Sisay G. (2014): Developing Sector Specific VET for the Ethiopian Leather Product Manufacturing Sector (Work-Process Oriented Approach). Ph.D. Thesis, University of Wuppertal, Germany.

Sisay A., Dvivedi, A. and Beshah, B. (2017a): Identifying and prioritising operational performance indicators of the Ethiopian leather industry. International Journal of Productivity and Quality Management, 22(3): 378-394.

Sisay A., Dvivedi, A. and Abebe, B. B. (2017b): Decision-making on job satisfaction improvement programmes using fuzzy QFD model: a case study in Ethiopia. Total Quality Management & Business Excellence, 1-24.

Sisay A., Dvivedi, A. and Beshah, B. (2018): Determinants of job satisfaction in Ethiopia: evidence from the leather industry. African Journal of Economic and Management Studies, 9(4), 410-429.

Sisay A., Dvivedi, A. and Beshah, B. (2019): Quality management practices as a tool for job satisfaction improvement of shop-floor workers: Empirical evidence from the Ethiopian manufacturing organizations. Production Planning & Control. (Accepted for publication).

Tesfaye G., Kitaw D. and Matebu A. (2014): A Total Manufacturing Solutions Technique to Select Appropriate Improvement Strategy: Case Study of a Footwear Factory. International Journal for Quality Research, 8 (3): 371-384.

Tomas C. (2011): Performance Analysis and Improvement of Ethiopian Leather Footwear Factories: With Special Reference to Anbessa Shoe SC. M.Sc. Thesis, AAU, Ethiopia.

UNIDO (2010): Future trends in the world leather and leather products industry and trade. Available at: https://leatherpanel.org/ (Accessed on 13th December 2018).

Green method for generating green energy using Dye Sensitized Solar Cells: Based on some Indigenous plants, Titanium Oxide Nanoparticles

Fedlu Kedir*, Bedasa Abdisa*, Enyew Amare

Department of Applied Chemistry, Adama Science and Technology University, Ethiopia
**Corresponding autors, e-mail: fedlu.kedir@astu.edu.et, bedasa.abdisa@gmail.com, enyewama@yahoo.com*

ABSTRACT

The dye-sensitized solar cell (DSSC) is a third generation photovoltaic device that holds significant promise for the inexpensive conversion of solar energy to electrical energy. The scope of the present study is to evaluate the performance of DSSC based on green synthesized titanium Oxide (TiO_2) and Copper oxide (CuO) nanoparticles (NPs). TiO_2 NPs were synthesized using titanium tetra butoxide as a precursor and ethanolic root extract of indigenous plant kniphofia foliosa as stabilizing and reducing agent. In the same way, CuO NPs were synthesized using tri-hydrated copper nitrate as a precursor and catha edulis extract as reducing and capping agent during the synthesis. Both TiO_2 and CuO NPs were synthesized in different proportions of precursor salt and plant extract. The biosynthesized NPs were characterized by thermogravimetric analysis (TGA-DTA), X-ray diffraction (XRD), scanning electron microscopy-energy dispersive x-ray spectroscopy (SEM-EDS), transmission electron microscopy (TEM), ultraviolet visible spectroscopy (UV-Vis) and Fourier transformer infrared spectroscopy (FTIR). XRD analysis revealed that the biosynthesized NPs of TiO2 have particle size in the range of 8.17 - 10.15 nm. And that of size of CuO NPs is in ranging from 18.2 - 28.5 nm. The results of SEM and TEM exhibited that the green synthesized TiO_2 and CuO NPs were spherical in shape. The pastes of TiO_2 NPs were used as photoanodes and that of CuO NPs were used as counter electrode in the DSSCs. Natural pigments extracted from roosts of kniphofia schemperi were coated on top of the photoanode during fabrication of DSSCs. Effect of variation of proportion of tert-butoxide and extract of roots of Kniphofia foliosa in TiO_2 NPs synthesis for photovoltaic performance of constructed solar cells were evaluated. Fabricated solar cells with TiO_2 PNs synthesized in 1:1 proportion have shown higher power conversion efficiency of 1.3% than other proportions. From the fabricated DSSCs based on green synthesized CuO NPs, maximum power conversion efficiency of 0.165% was achieved. Photovoltaic parameters obtained from the fabricated DSSC shows that bio-synthesized TiO_2 and CuO NPs have a potential application for DSSC in converting solar energy in to electricity using ***kniphofia schemper*** *as light absorbing photoactive material.*

Keywords: *Green synthesis, Dyes sensitized solar cells, indigenous plants extract*

1. INTRODUCTION

A search for a clean and sustainable source of energy free of carbon has therefore become an important issue for scientists and researchers. The primary supply of sustainable and ecofriendly energy is one of the major challenges of the twenty first century. Recent advances in solar energy conversion technologies based on organic semiconductors as light harvesting layer, such as dye-sensitized solar cells and organic solar cells, employ metallic oxide semiconductor (MOS) nanostructures for efficient charge extraction and transportation between the electrodes and organic molecules (Grätzel et al., 2012)

Dye sensitized solar cells (DSSCs) invented by Michael Grätzel since 1991 became a very popular alternative energy sources to silicon based solar cells because of their great potential to convert solar energy into electrical energy at low cost. In the field of photovoltaic research, DSSCs have attracted considerable attention with strong absorption of visible light since it was first developed by Michael Grätzel. Solar cells based on dye sensitized porous nanocrystalline TiO_2 photoanode with attractive performance was first reported by (O´Regan et al., 1991). A dye sensitized solar cell (DSSC) is a low cost and the third generation photovoltaic solar cell belonging to the group of thin film solar cells, which is based on a semiconductor formed between a photo sensitized anode, an electrolyte, and a photo electrochemical systems.

The transition metal oxides (MOSs) such as TiO_2 are well known for their ability to exchange charges with condensed molecules, making them a viable and cost effective candidate to be used in the photovoltaic devices. In dye sensitized, MOSs serve as a scaffold, in photovotaics such as DSSCs and perovskite solar cells, and as a charge transport layer in

organic and DSSCs. The function of scaffold in DSSCs is to facilitate charge separation and charge transport, whereas that of the transport layers is to conduct one type of charge carrier while blocking the other type (Jose et al., 2009).

The synthesis of metallic oxide nanoparticles is an active area of academic and, more importantly application research in nanotechnology. A variety of chemical and physical procedures such as chemical reduction, electrochemical reduction, chemical vapor deposition, thermal decomposition and solvothermal reduction (Tang et al., 2006); have been reported for synthesis of metallicnanoparticles. However, these methods are fraught with many problems including use of toxic solvents, generation of hazardous by-products, and high energy consumption.

A promising approach to achieve high yield, low cost, environment-friendly and sustainable procedures for the synthesis of metal oxide nanoparticles is the one which is based on employing biological resources in nature such as plants, algae, fungi, bacteria, and viruses for production of low cost, energy-efficient, and nontoxic metallic oxide nanoparticles (Taleb et al., 1998). Use of plant extracts for synthesis of nanoparticles could be advantageous over other environmentally benign biological processes as this eliminates the elaborate process of maintaining cell culture (Taleb et al., 1998) and the advantage of using plants for the synthesis of nanoparticles is that they are easily available, safe to handle and possess a broad variability of metabolites that may aid in reduction.

Kniphofia are herbaceous perennials growing from rhizomes. Traditionally the roots of *kniphofia foliosa* have been used for the treatment of different ailments including menstrual pains, infertility, abdominal cramps, wounds, malaria, chest complaint, gonorrhea and hepatitis B (Abate *et al*, 1989). In addition to its traditional medicinal usage for household remedy against various human ailments, roots of *kniphofia foliosa* extracts could also be used for the synthesis of TiO_2 nanoparticles in order to exclude the addition of external stabilizing agents during synthesis process because of the presence of various functional groups within the roots of the plant extracts.

To the knowledge of our research groups, no research work was reported on green synthesis of TiO_2 CuO NPs using indigenous medicinal root extracts of *kniphofia foliosa, and leave extract of Catha edulis (respectively) and kniphofia schemperi* for DSSC application. Therefore, this study was focused on biosynthesis of TiO_2 NPs using titanium tetra butoxide as a precursors and *Kniphofia foliosa* root extract as a reducing and capping agent and then to fabricate DSSCs using sensitizer (*kniphofia schemperi)*.

Accordingly, there is an essential growing need to develop clean, reliable, biocompatible, cost-effective, environmentally benign, and sustainable procedures for synthesis of metallic oxide nanoparticles that do not use toxic chemicals which encouraged more and more researchers to exploit biological systems as possible eco-friendly nano-factories. A promising approach to achieve high yield, low cost, environment-friendly and sustainable procedures for the synthesis of metal oxide nanoparticles is to exploit the array of biological resources in nature. Indeed, over the past several years, plants, algae, fungi, bacteria, and viruses have been used for production of low cost, energy-efficient, and nontoxic metallic oxide nanoparticles (Taleb et al., 989). Use of plant extracts for synthesis of nanoparticles could be advantageous over other environmentally benign biological processes as this eliminates the elaborate process of maintaining cell culture (Taleb et al., 989) and the advantage of using plants for the synthesis of nanoparticles is that they are easily available, safe to handle and possess a broad variability of metabolites that may aid in reduction. Therefore, in this study Copper oxide (CuO) nanoparticle was synthesized using leaf extracts of Khat (*Catha edulis*) and used as cathode/counter electrode for the application of dye sensitized solar cell.

2. METHODOLOGY

2.1. Chemicals and Reagents

Chemicals and reagents used were titanium tetra butoxide (Acros organics, 98%), acetone (Sigma Aldrich), acetonitrile (Sigma Aldrich), sodium hydroxide (Sigma Aldrich), Iodine crystal (Sigma Aldrich), NaI (BDH), 1-ethyl-3-methyl immidazolium iodide (EMIMM-I: Sigma Aldrich), Isopropanol (Riedel-de Haen), PVP (Sigma Aldrich), C_2H_5)4NBF4 (Sigma Aldrich), (ethylenedioxythiophene) (EDOT: Sigma Aldrich), absolute ethanol

(Lab Tech Chemicals), triton X-100 (Sigma Aldrich conductive FTO glass substrate (Sigma Aldrich). Copper (II) nitrate trihydrate (UNI-CHEM Chemical Reagents)

2.2. Instruments Used

Different instruments were used and includes thermo gravimetric analysis (TGA/DTA: DTG-60H Shimadzu Co., South Korea), FTIR (Perkinelmer65), XRD (XRD-7000 X-ray diffractometer, Shimadzu Co., South Korea), UV-Vis spectrophotometer (JASCO V-670UV-Vis spectrophotometer equipped with a diffuse reflectance attachment for powder samples), SEM-EDS (FE-SEM, JEOL-JSM 6500F, made in Japan), TEM (HRTEM, Tecnai F20 G2, Philips, Netherlands), computer controlled electrochemical analyzer (CHI630A).

2.3. Extraction of the root (Broth solution)

Enough amounts of roots of *kniphofia foliosa* were collected and surface cleaned using distilled water and dried under shaded room. The roots were grind using plant grinding machine. The extraction was done by taking 5 gram of the root powder followed by addition of 200 mL of absolute ethanol as a solvent and this was done within a 500 mL erlenmeyer flask. And then it was allowed to boil at 50℃ for about 35 minutes. The final extract of the solution was collected and stored at 4℃ within a refrigerator. The filtrate ethanolic root extract was used as a reducing and capping agent for the biosynthesis of TiO_2 NPs within 1:1 (50 precursor: 50 extract) mL, 2:1 (66.7 precursor: 33.3 extract) mL and 1:2 (33.3 precursor: 66.7 extract) mL (Santosh *et al*, 2014). Following the same procedures, enough amounts of roots of of Catha edulis were collected and surface cleaned using distilled water and dried under shaded room.The measured amounts of dried leaves of Catha eduliswere soacked in diionided wate, and the extract was left at refrigerator for CuO Nps synthesis.

2.4. Biosynthesis of TiO_2 NPs

Titanium tetra butoxide is a chemical compound with the formula of $C_{16}H_{36}O_4Ti$, was used as a precursor for the biosynthesis of TiO_2 NPs in the presence of ethanolic root extract of *kniphofia foliosa*. TiO_2 NPs were biosynthesized in different ratios using 0.4 M of the precursor salt and ethanolic root extract of *kniphofia foliosa* in a separate erlenmeyer flask. In each case the erlenmeyer flask containing the two components was placed on to a plate with magnetic stirrer without applying of heat. The resulting solution was stirred for about 4 and half hours. Then the PH of the solution was measured and after that a small drop of 1 M of sodium hydroxide solution was added as a precipitating agent. Then the formed TiO_2 NPs in different ratio was allowed to stay within a refrigerator for overnight. After that, the formed precipitate for each of the individual ratio was washed with absolute ethanol and again placed within refrigerator for one day. Then appropriate volume of distilled water was added and again placed within a refrigerator for one day. The formed NPs were acquired by centrifugation at 1000 rpm for about 30 minutes followed by washing with absolute ethanol. Again it was subjected to centrifugation at 1000 rpm for about 25 minutes followed by washing with distilled water. The formed TiO_2 NPs were collected using a crucible ceramic dish and placed in to a drying oven for overnight at 100℃ (Santosh *et al*, 2014). After conducting the thermal stability of the biosynthesized TiO_2 nanoparticles in different ratios, it was calcined at 500℃ for about 3 and half hours. Figure 1 shows the schematic synthesis procedure of TiO_2 NPs using root extract of *kniphofia foliosa* and from its precursors (titanium tetra butoxide).

2.5. Biosynthesis of CuO NPs

Fresh leaves of Catha edulis were collected and washed using distilled water to remove the dust particles. The cleaned leaves were let to dry under shade at room temperature and ground into fine powder using mortar. Then, 10 g of Catha edulis powder was taken for synthesis purpose and heated with 150 mL of distilled water for 30 min at 80°C until the color of the aqueous solution changes from watery to light brown. The extract was cooled at room temperature and filtered by Whatman №1 filter paper (Naika et al., 2015). Then three different samples were prepared with different ratios by taking different weight of precursor salt and volume of catha edulis leaf

extract by using the method developed (Jitandra et la., 2015). 10, 30, and 50g of Copper (II) nitrate trihydrate (UNI-CHEM Chemical Reagents) precursor salt was added in to three different 100 mL plant leaf extract each heated at 80°C. Then, for each sample the mixture was stirred continuously with magnetic stirrer at 80°C until the color changes from deep green solution to deep brown precipitate. The precipitate was then centrifuged at 1000 rpm for 30 min and washed three times with deionized water in order to remove the impurities. Finally, the precipitate was dried in an oven at 150°C for 3:30 hrs and was ground to fine powder using agate mortar. The black powder obtained from the above method was calcined at 400°C for 2 hour.

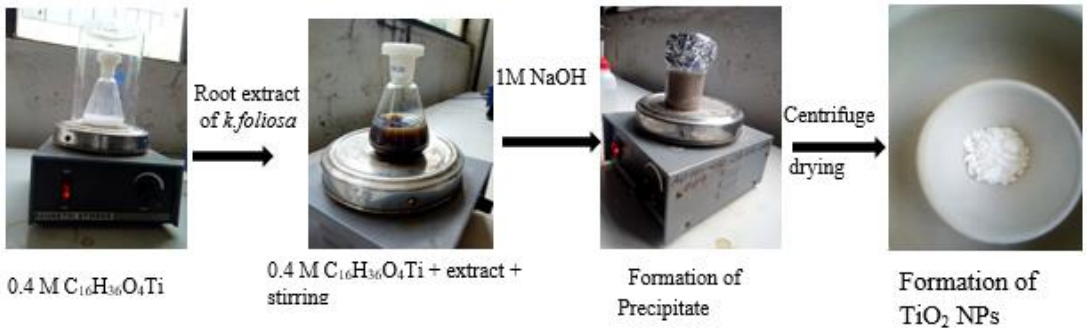

Figure 1: Schematic biosynthetic procedure of TiO_2 NPs using root extract of *Kniphofia foliosa*

2.5. Characterization Techniques of Biosynthesized TiO_2 and CuO NPs

2.5.1. Characterization using TGA

Thermal gravimetric analysis (TGA) of the biosynthesized NPs was carried out using a simultaneous differential thermal analysis DTA-TGA (DTG-60H, Shimadzu Co., South Korea) apparatus to determine the calcination temperature (Ramimoghada *et al*, 2013). Approximately 5.939 mg of the uncalcinated TiO_2 and CuO NPs was taken and placed in to a platinum crucible on the pan of the microbalance and heated from 25°C to 900°C.

2.5.2. Characterization using XRD

The crystalline structure of the biosynthesized titanium oxide NPs were investigated by x-ray diffraction using x-ray diffractometer (XRD-7000 x-ray Diffractometer, Shimadzu Co., South Korea). XRD spectrum was recorded from 10^0 to 80^0 with 2θ angles using CuKα ($\lambda = 1.54056\ A^0$) radiation operated at 40 kV and 30 mA. Debye Scherrer's equation was used to estimate the average crystallite size of the nanoparticles (Xu *et al*, 2008).

$$D = \frac{0.94\ K}{\beta cos\theta} \ldots\ldots\ldots\ldots\ldots\ldots\ldots\ldots\ldots\ldots 1$$

Where D is the crystallite size, $\lambda = 1.54056\ A^0$, is the x - ray source wavelength, β is the full width at half maximum intensity (FWHM) of a peak in terms of radians, and θ is the peak position.

2.5.3. Characterization using SEM-EDS

Biosynthesized TiO_2 and CuO NPs were characterized by field emission scanning electron microscopy-energy dispersive x-ray spectroscopy (FE-SEM, JEOL-JSM 6500F, made in Japan) and provides different informations about the NPs including surface morphology and shape as well as its chemical composition (Pusit *et al*, 2009).

2.5.4. Characterization using TEM

Biosynthesized TiO_2 and CuO NPs were also analyzed using high-resolution transmission electron microscopy (HRTEM, Tecnai F20 G2, Philips, Netherlands) at an accelerating voltage of 200 kV. And provide different informations such as the internal structure and crystalline nature of the biosynthesized nanoparticles (Figgemeir *et al*., 2007).

2.5.5. Characterization using UV-Vis spectroscopy

The UV-Vis absorption spectra of biosynthesized NPs was confirmed using UV-Vis spectroscopy (JASCO V-670UV-Vis spectrophotometer equipped with diffuse reflectance for powder samples) between a wavelength scan of 200 - 800 nm. Band gap energy of the biosynthesized TiO_2 NPs estimated using the formula (equation 2) (Visayalakshmi *et al.*, 2012).

$$E_g = \frac{hc}{\lambda} \quad \ldots\ldots\ldots\ldots\ldots\ldots\ldots\ldots\ 2$$

Where E_g is energy band gap, h is planks constant, c is speed of light and λ is the wavelength at maximum absorbance.

2.5.6. Characterization using FTIR

Fourier transformer infrared (FTIR) spectroscopy of TiO_2 and CuO NPs were NPs was characterized and recorded using a FTIR spectrophotometer (Perkin Elmer65) in order to analyze and detect surface functional groups of the biosynthesized TiO_2 and CuO nanoparticles at the scanning range of 4000 - 400 cm^{-1} (Gao *et al.* 2007).

2.5.7. Extraction and Preparation of Sensitizers

Enough amounts of roots of *kniphofia schemperi* were collected and prepared. Those collected samples were surface cleaned repeatedly and allowed under shadow dry at room temperature. Then it was grind using plant grinding machine followed by packing with a plastic bottle and placed within a dark area. The extract was done by taking 4 g powders of roots of *kniphofia schemperi* powder and socked within 100 mL of absolute ethanol in a 250 mL erlenmeyer flask. The mixture of the solvent and the powder was placed within a dark place by covering with aluminum foil to avoid photo oxidation. And was kept and stored for about 24 hs at room temperature until the required pigment solution was extracted and the solid materials were allowed to settle down overnight and the clear solution of the dye was formed. The clear solutions formed (to be used for sensitization) was separated from solid materials using glass filters (Macht *et al.*, 2002; Calogero *et al*., 2010).

2.6. DSSCs Fabrication Steps

2.6.1. Preparation of the substrate for deposition

The conductive fluorine doped tin oxide (FTO) glass substrate which has an area of (2 cm x 2.5 cm) was cleaned using distilled water and organic solvents such as, acetone, isopropanol and ethanol, sequentially using ultrasonicator for about 20 minutes in each different solvents. The substrates were thoroughly cleaned repeatedly before deposition of film of biosynthesized TiO_2 NPs as working electrode. In the same way the substrate for counter electrode was cleaned with sequence of organic solvents before CuO NPs counter electrode was deposited on.

2.6.2. Semiconductor oxide material paste preparation and deposition

TiO_2 paste was prepared according to the method developed by (Nazeerudin *et al*, 1993). This was done by taking 0.76 g in each of the three ratios of biosynthesized TiO_2 nano powder and ground in a porcelain mortar with drop wise addition of 1 mL of H_2O containing 0.56 mL of 1 M HNO_3 to prevent re-aggregation. After the powder had been dispersed by the high shear forces in the viscous paste, it was diluted by drop wise addition of 1.01 mL of H_2O under continued grinding. Finally 0.025 mL of Triton x-100 also was added as a dispersing agent and grinding the mixture for additional 30 minutes until the paste becomes homogeneous. The prepared paste was deposited near the top edge of FTO glass between the two pieces of the tape and was coated by "doctor blade". This process was continued until the layer became homogenous. The tape was removed carefully without scratching the TiO_2 coating. Figure 2 showed the corresponding paste preparation procedure using biosynthesized TiO_2 NPs and its deposition.

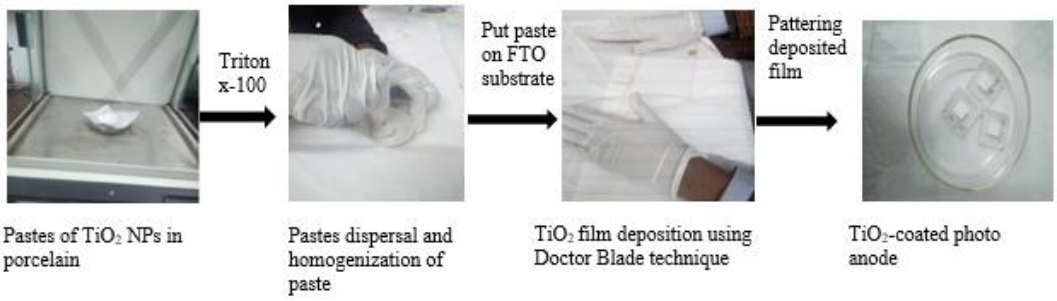

Figure 2: Preparation procedure of photoanode films

The as prepared TiO_2 film was sintered at 450°C in a furnace for about 30 minutes to remove the organic solvents. This process also ensures electrical contact between particles and good adhesion the film to the substrate.

In the same way, 0.5 g of black powder of each synthesized CuO NPs was added in ethanol in different crucibles. After the powder was dispersed by the high shear forces in the viscous paste and few drops of Triton-X100 were added in to the paste preparation to disperse the colloid on the substrate. Afterward, CuO NPs paste was deposited on the cleaned fluorine doped tin oxide (FTO, 8 Ω/sq, 80% transmittance in the visible light) glass by simple casting method using glass rod at room temperature. After natural dry, the CuO NPs deposited FTO glass substrates were heated at 250°C for 15 min to remove the organic solvents and contaminants and CuO NPs based counter electrode was prepared (Murakami and Grätzel, 2008).

2.6.3. Electrode sensitization

Sensitizers obtained from roots of *kniphofia schemperi* and crystal violet synthetic dyes were adsorbed on top of TiO_2 Photoelectrodes as follows. The TiO_2 film coated electrode was immersed into the extracted natural dye solution for about 12 hours and for the crystal violet dye. The film coated was immersed and stayed for about 6 hours until the monolayer of the TiO_2 film became covered with the dye solution. The dye adsorbed film was taken out and was rinsed with the same solvent used to extract and prepare the sensitizer (ethanol absolute, 99.9%, distilled water) to remove the unabsorbed dye and any other remain residues available on the surface (Nazeerudin *et al*, 1993).

2.6.4. Preparation of redox electrolytes

The polymer gel electrolyte was prepared according to the method developed by (Fan *et al*, 2010). This was done by taking 5.3 g of liquid electrolyte which consists of 0.9 M of 1-ethylene-3-methyl immidazolium iodide (EMIM-I) within acetonitrile (high dielectric constant organic solvent) under continuous stirring to form a homogeneous liquid electrolyte. In order to obtain a better conductivity, 0.5 M of sodium iodide was dissolved in the above homogeneous liquid electrolytes and then 0.12 M iodine (I2) and 35% (w/w) of polyvinylpyrrolidone was added. Figure 3 revealed formation of redox electrolyte. The resulting mixture was heated at 70^0C - 80^0C under vigorous stirring to dissolve the added PVP followed by cooling down to room temperature.

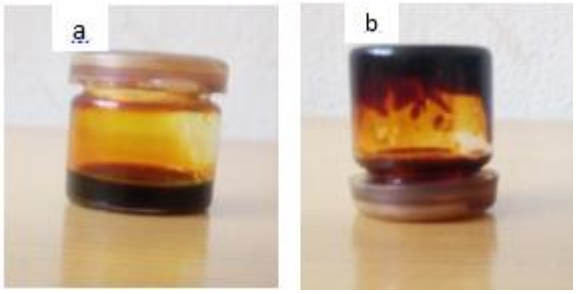

Figure 3: Redox electrolyte formation (in case of b, even if the container containing the redox electrolyte is inverted down it can't flow, indicates the formation of highly gel electrolyte).

2.6.5. Coating counter electrodes

The counter electrode was formed by electrochemical polymerization of 3, 4- ethylenedioxy-thiophene (EDOT) in a three electrode system with one compartment electrochemical cell by using an electrochemical analyzer. The electrochemical cell consists of a pre-cleaned FTO conductive glass which was used as the working electrode, a platinum foil used as the counter electrode, and a quasi-Ag/AgCl was used as the reference electrode. The solution/electrolyte used for polymerization was obtained by mixing 0.1 M EDOT and 0.1 M $((C_2H_5)_4NBF_4)$ in acetonitrile solvent. The polymerization was carried out potentiostatically at +1.8 V for about 2 second (using bulk electrolysis with coulometer). At this potential, the electrode surface was covered with a blue-doped PEDOT film (Chang *et al.*, 2015).

2.6.6. Characterization of fabricated DSSCs

The photoelectrochemical measurements of the cell were performed using a computer controlled electrochemical analyzer (CHI630A). A 250W xenon lamp regulated by an Oriel Power Supply (Model 68830) was used to illuminate the DSSCs. A grating monochromator (Model 77250) placed into the light path and was used to select a wavelength between 300 and 800 nm within a 20 minute interval. The intensity of the incident light was set 100 m Wcm^{-2}. The DSSCs solar cell was then mounted in a sample holder inside a metal box with an area of 1 cm^2 opening to allow light from the source.

3. RESULTS AND DISCUSSION

3.1. TGA Analysis

Thermo gravimetric and differential thermal analysis was made as a function of temperature as it can be shown from Figure 4.

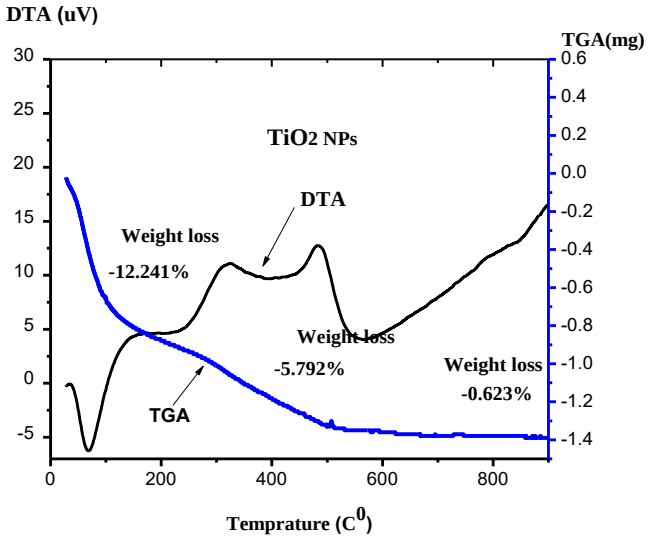

Figure 4: Thermal analysis result for the uncalcinated TiO_2 NPs.

Below 100℃ the weight loss was observed due to the removal of physically and chemically entrapped water molecules. In between the temperature ranges of 100 - 350 degree celsius, the weight loss was also occurred due to evaporation of inorganic materials (Muneer *et al.*, 2012). Weight loss was again continued up to 483.11℃ associated with a strong exothermic peak in the DTA curve, is due to decomposition of organic materials and the complete removal of the sheath of biomass present over the surface of the biosynthesized nano sample. Similar results related to the present study were also reported by (Ramimoghada *et al.*, 2013). After 483.11℃ up to 900^0C no considerable loss was observed. And as a result, 500℃ were used as calcination temperature.

The uncalcinated CuO nanoparticles synthesized was characterized using TGA/DTA. Figure 5 shows the thermal gravimetric analysis/differential thermal analysis (TGA/DTA) data of the given synthesized copper oxide nanoparticle. TGA curve shows mass loss of the sample whereas DTA curve indicates the energy gain or loss during the process. The TGA curve showed a three-step decomposition of the uncalcined nanoparticle. During thermal treatment of the synthesized nanoparticle, mass losses were observed in the temperature range 25 -150 °C, 400-600 °C, and 601-1000 °C. The weight loss of the material observed between the temperatures 25-150 °C was about 11.594% that could be due to vaporization of water content in the material. The weight loss observed in the temperature range of 400-600 °C was about 1.35% that is most probably due combustion of organic compounds from *catha edulis* extract. The weight loss above temperature of 600 °C which was about 2.626% may be due to oxygen loss (Aparna *et al*., 2016).

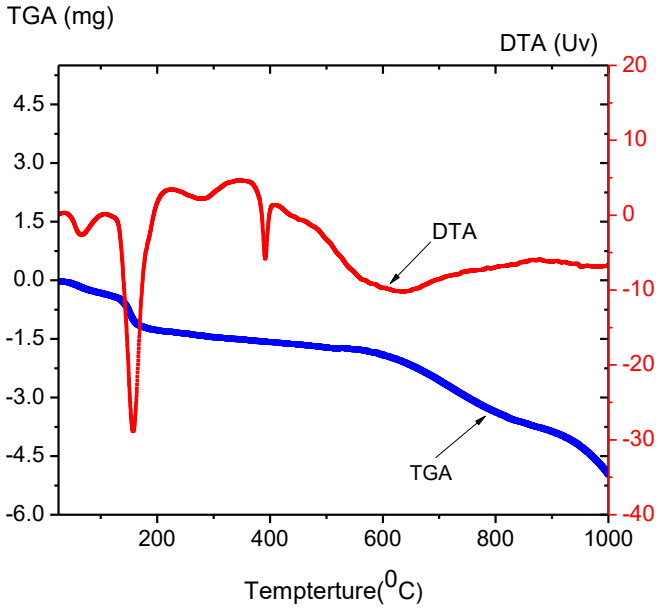

Figure 5: Thermal Analysis result for uncalcinated 1:10 ratio copper oxide nanoparticles

3.2. XRD Analysis

The formation of TiO_2 NPs was analyzed by X-ray diffraction measurements. The diffraction peaks was observed in the samples with 2θ values of ≈ 25.2880, 37.9969, 47.9442, 53.1669, 54.8862, 62.7084, 70.1612 and 75.0294 along with their miller indices values of (101), (004), (200), (105), (211), (204), (220) and (215), respectively. The diffraction peaks was found to be within a good agreement which was reported with JCPDS card number of 21-1272. Diffraction peaks related to impurities were not observed reveals that the formed NPs were pure. The average crystalline size was estimated in the range of 8.17- 10.15 nm for the three different ratios. Figure 6 shows the XRD crystalline nature of the biosynthesized TiO_2 NPs. Similar results related to the present study were reported by (Rao et al, 2015).

As compared to TiO_2 NPs biosynthesized within a 2:1 ratio, XRD result showed that the average crystallite size of TiO_2 (1:1) NPs has relatively smaller average crystalline size (8.17 nm). This difference may be due to the greater amount of root extract used results in a more capping agents/stabilizing agents/ that intern effectively stabilize the biosynthesized TiO_2 (1:1) NPs. As it can be observed from the XRD spectra (a), the biosynthesized nano sample loss its crystalline nature due to the fact that the root extract of the added *kniphofia foliosa* was in excesses which is beyond the coating surface of TiO_2 NPs already available that in turn results in the formation of agglomeration.

The CuO NPs biosynthesized from *Catha edulis* leaf extract were confirmed by the characteristic peaks observed in the XRD patterns as shown in Figure 7 a, b and c with 1:10, 3:10 and 1:2 weight/volume ratios of precursor and plant extract, respectively.

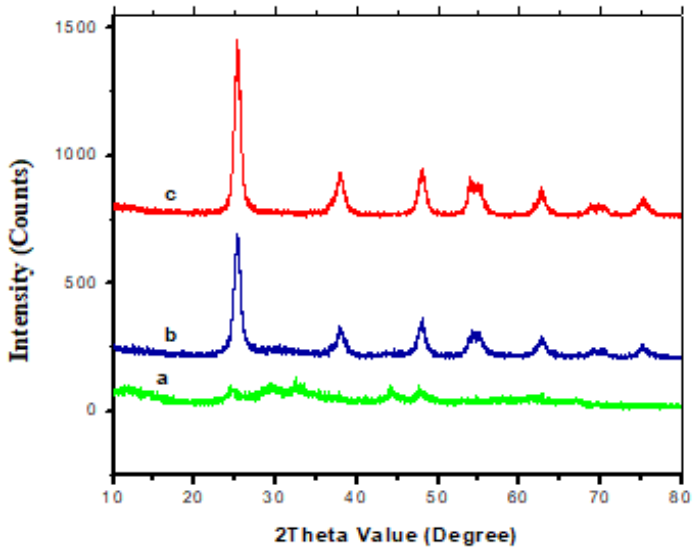

Figure 6: XRD Spectra of biosynthesized TiO_2 NPs a (1:2), b (1:1) and c (2:1).

XRD analysis for Figure 7 a, b and c shows intense peaks at 2θ = 31.4876°, 35.4894°,38.6974°, 48.7540°, 53.4330°, 58.2323°, 61.5322°, 66.2470°, 67.6419°, 72.3621° 75.2398° in Figure a , 32.4911°, 35.5036°, 36.4007°, 38.4007°, 48.8047°, 53.4321°, 58.2223°, 61.5010°, 65.7825°, 67.9854°, 72.3607° and 75.7198° in figure b and 31.6751°, 35.5086°, 38.7159°, 48.8047°, 53.4321°, 58.2223°, 61.5010°, 66.2656°, 67.4820°, 72.3607° and 75.2598° in Figure c corresponding to miller indices of (110), (002), (111), (202), (020), (202), (113), (311), (113), (311) and (222) respectively. The sharp and narrow diffraction peaks indicating highly crystalline structure nature and also phase purity of nanoparticles.

The observed diffraction reflections are comparable with JCPDS card № 048-1548, 048-1548 and 048-1548 for each ratio synthesized respectively, and is attributed to bulk CuO materials. All diffraction peaks can be indexed as the typical monoclinic structure and no extra diffraction peaks of other phases are observed in Figure7 a and c but other two peaks were observed in Figure b at 2θ =36.4° and 44.9° (with reference to ICSD file no. 98-015-4604) indicating the existence of the Cu_2O at the surface. Moreover, the well-defined and sharp CuO reflections in the observed XRD patterns verify the well-crystalline nature of CuO NPs. Similar result was obtained by (Jitendra K .*et al*, 2015; Faheem I. *et al* 2017; Rao A. N. S. et al , 2014) respectively. The crystalline size of the CuO NPs was calculated using Debye Scherer equation. As a result, the crystalline size of CuO NPs corresponds to the highest intense peaks was calculated to be 28.10 nm, 25.30 nm and 18.20 nm respectively for CuO NPs synthesized using 1:10, 3:10, and 1:2 of plant extract to precursor ratios.

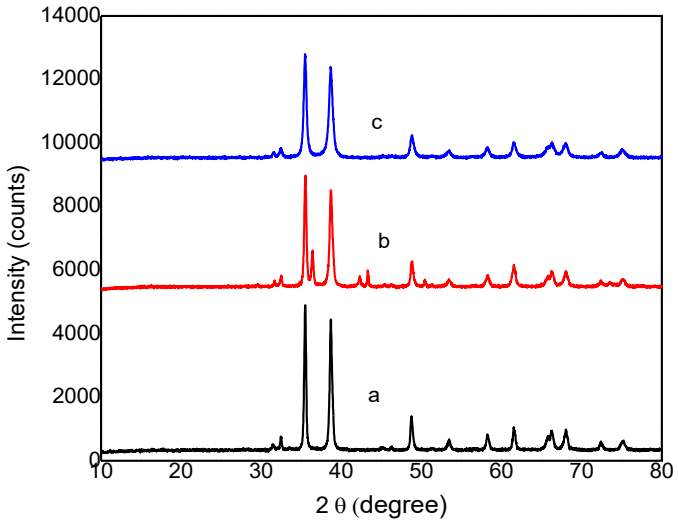

Figure 7: XRD patterns of (a) 1:10, (b) 3:10 and (c) 1: 2 ratios of green synthesized CuO NPs.

3.3. SEM-EDS Analysis

SEM image reveals the surface morphology of TiO_2 NPs and the particles were found to be spherical in shape with distinct edges. SEM image also reveals the increase of particles size with the increase of ethanolic root extract. Figure 8 revealed SEM images of the different ratios of biosynthesized TiO_2 NPs.

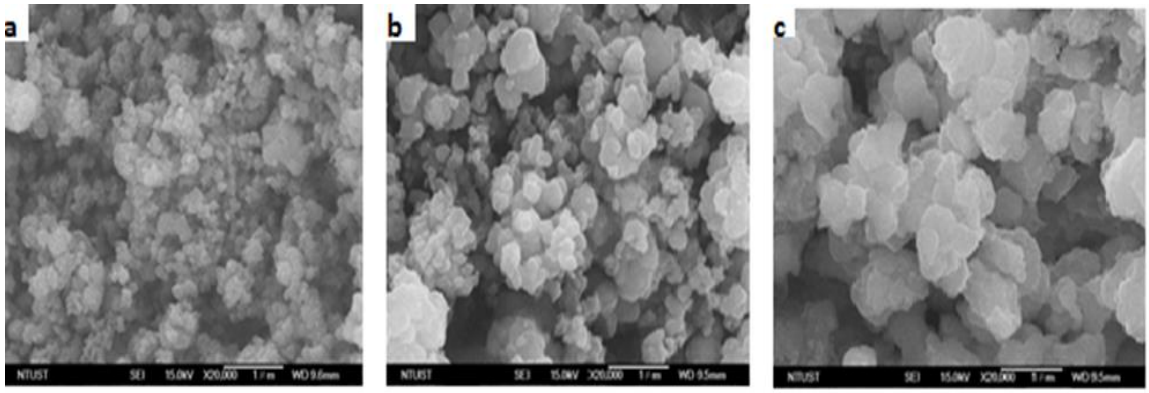

Figure 8: SEM images of TiO_2 NPs for (a) 1:1, (b) 2:1 and (c) 1:2 ratios, respectively.

Previously (Archana *et al*, 2012) reports similar results related to this study. As it can be revealed from Figure 7(c) agglomeration of the particles results in the presence of excess amount of root extract of *kniphofia pholiosa* (Al-Alwani *et al*, 2015). In all cases the SEM image analysis of the biosynthesized TiO_2 nanoparticles were run with a magnification of 1μm.

To gain a further insight about the biosynthesized TiO_2 nanoparticles in different ratios, analysis of the sample was performed using EDS techniques. It is necessary to verify the presence of desired elements in the biosynthesized samples. The absence of any foreign materials other than titanium and oxygen indicates the elimination of water molecules, ethanol molecules and other organic residues (Malarkodic *et al*, 2013). This also

confirms the complete conversion of the starting material, titanium tetra butoxide precursor in to pure TiO_2 NPs. Figure 9 shows EDS analysis result of TiO_2 NPs.

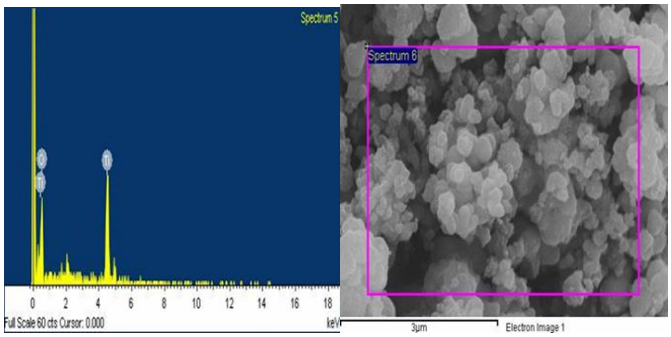

Figure 9: SEM images of selected area for EDS analysis of TiO_2

3.4. TEM Analysis

In order to ascertain and gain further informations about the biosynthesized TiO_2 NPs such as internal surface morphology and crystallinity nature as well as shape, TEM analysis was carried out. Figure 10 showed TEM image analysis result and the analysis reveals that the biosynthesized anatase TiO_2 nanoparticles possess spherical internal structure and have good crystalline nature, as it was also supported by the XRD analysis results.

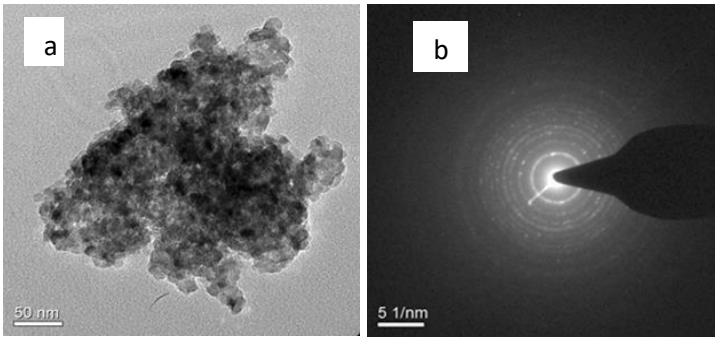

Figure 10: TEM image of TiO_2 (a) NPs and (b) its SAED pattern.

The crystalline nature of the biosynthesized TiO_2 nanoparticles was confirmed by the selected area electron diffraction (SAED) pattern with bright circular spots corresponding to (101), (004), (200), (105), (211), (204), (220) and (215), respectively planes of the anatase lattice of biosynthesized TiO_2 nanoparticles (Figgemeir *et at*, 2017).

Figure 11 a, b and c shows the SEM image of synthesized CuO NPs. Figure 11 a shows SEM image for 1: 10 ratio of the synthesized CuO NPs which showed uniform and define spherical morphology, Figure 11b shows SEM image of 3: 10 ratio of the green synthesized copper oxide nanoparticles. Similar to the 1:10 ratio, the SEM image showed spherical shaped CuO NPs but with some aggregation that could be due to the low concentration of the plant extract that acts as capping agent in addition to reducing agent and Figure c also shows SEM image of 1: 2 ratio of the synthesized copper oxide NPs. The SEM image is similar to the 1:10 ratio. It clearly showed that the particles are small and uniformly distributed over the surface with low aggregation. The low aggregation could also be due to the high fraction of plant extract used which acts as capping/stabilizing agent. It is noticed that green synthesis of CuO NPs produced small and uniform size of spherical particles which is in agreement with previous result reported (Jitendra K. S. et al, 2015;Mahmoud N., S. et al,2015; Sundaramurthy N. et al,2015) respectively.

Figure 11 d shows the TEM images of synthesized 1:10 ratio CuO NPs. The low magnification TEM image reveals almost similar spherical morphology of CuO NPs as seen in SEM image. From the TEM image of CuO NPs as shown in Figure 11, the particles are aggregated and interconnected to each other, resulting in the less visible lattice fringes. Therefore, the morphological characterizations confirm the spherical morphology of CuO NPs biosynthesized from the leaves of *catha edulis* plant (Jitendra *et al.*, 2015).

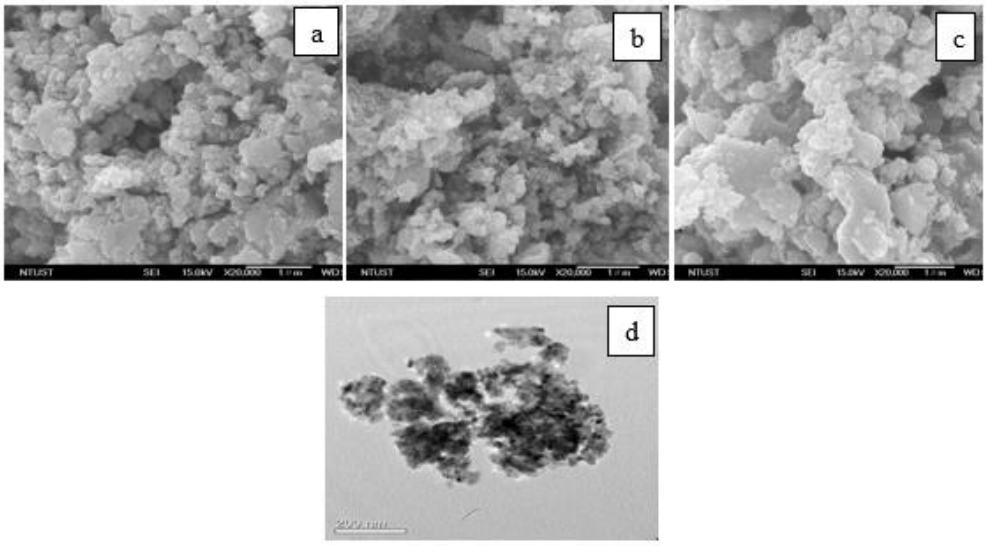

Figure 11: SEM images (a) 1:10, (b) 3:10, (c) 1:2 and (d) TEM image of 1:10 ratios of the synthesized copper oxide nanoparticles

3.5. UV-Vis Analysis

The absorption spectra of biosynthesized TiO_2 nanoparticles reveal the reduction process and formation of TiO_2 which shows excellent agreement with those reported in the literatures. The band gap energy was determined based on the numerical derivative of the optical absorption coefficient and found to be 3.95, 4.16 and 4.05 eV for a 1:1, 2:1 and 1:2 ratio, respectively. The UV-Vis absorption spectra of the biosynthesized TiO_2 NPs in different ratios is indicated in Figure 12.

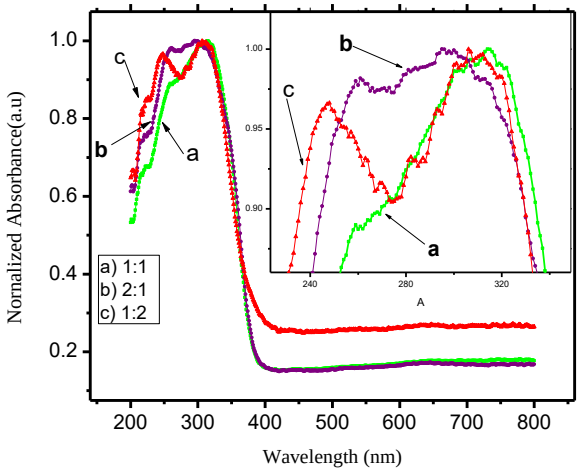

Figure 12: UV-Vis absorption spectra of TiO_2 NPs a (1:1), b (2:1) and c (1:2) ratios.

The absorbance of TiO_2 NPs shows spectral shift following difference in ratio and in addition to this, all the TiO_2 NPs biosynthesized in different ratios exhibit a slight shift of the absorption edge towards the visible region due to their smaller size.

Figure 13 a, b and c shows the UV- Vis spectrum of green synthesized CuO NPs with ratio of 1:10, 3:10, and 1: 2, respectively. The nanoparticle showed high absorbance over visible wavelength range which is one of the indications that the NPs are narrowband gap material.

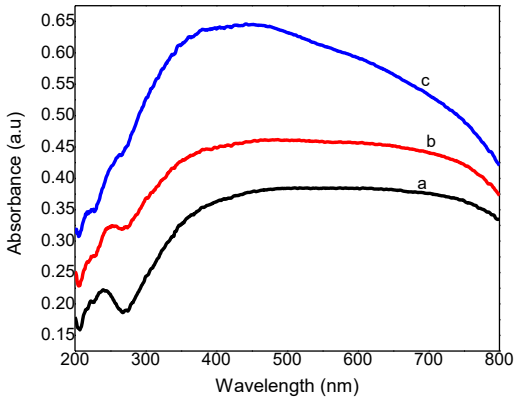

Figure 13: UV-Vis spectra of (a) 1:10, (b) 3:10 and (c) 1:2 ratios of green synthesized CuO nanoparticles

The band gap values of the CuO NPs were determined by analyzing the optical data with the expression for the optical absorbance α and the photon energy hv using Tauc's plot (Zou Z. *et al*, 2015). The band gaps of the CuO NPs was then determined by extrapolating the straight line portion of the $(\alpha h\nu)^2$ versus $(h\nu)$ graphs to the $(h\nu)$ axis until $(ah\nu)^{1/n} = 0$, the linear section of this spectrum as shown in the Figure 14 a, b and c respectively.

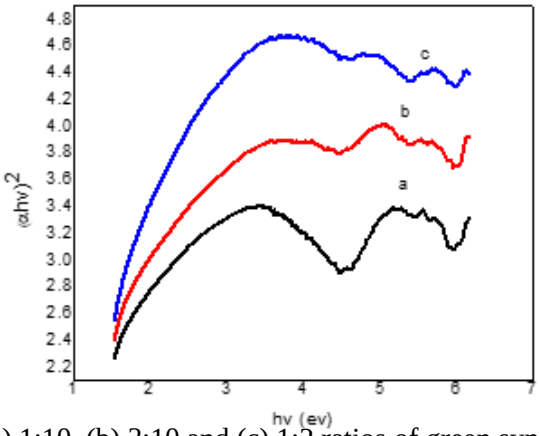

Figure 14: Tauc plots (a) 1:10, (b) 3:10 and (c) 1:2 ratios of green synthesized CuO nanoparticles

Based on Tauc's plot the band gaps of synthesized CuO NPs with ratios 1:10, 3:10 and 1:2 were obtained to be 1.31, 1.39 and 1.45 eV, respectively. The estimated band gap energy of the synthesized CuO NPs was lower than that was reported in the literature reported. This may come due to dense population of the nanoparticles but it was between the intervals that were reported. These findings are similar with previous reports made on these nanoparticles (Rao A.N. *et al*, 2014). This low band gap of CuO NPs made them to be used as counter electrode (cathode), for collection of electrons, in the fabrication of solar cells.

3.6. Fourier Transform Infrared Spectroscopy

The intense peak in Figure 15 shown at 2334.34 cm^{-1} indicates the alkene group with vicinity of C-H bonding. The medium absorption peak at 1627.45 cm^{-1} represents the C=O stretching of primary amide or to C=C groups of aromatic rings. The peak represented by 1354.78 cm^{-1} shows the aromatic ethers of C-O stretching. Those peaks from C=O, and C=C clearly indicates the presence of biomolecules and bio-constituents from roots of *kniphofia foliosa* extract. The peaks corresponding to the broad band centered at 567.13 cm^{-1} represents a characteristic peak of Ti-O-Ti bending mode of vibration which confirms the formation of metal-oxygen bonding (Mahmud *et al*, 2017; Malarkodi *et al*, 2013). The FTIR data confirm the formation of TiO_2 with many surface hydroxyl function groups. The extra peaks from the organic C and O bonds are attributed to a trace amount of extract pyrolytic residues left after a relatively lower temperature firing procedure.

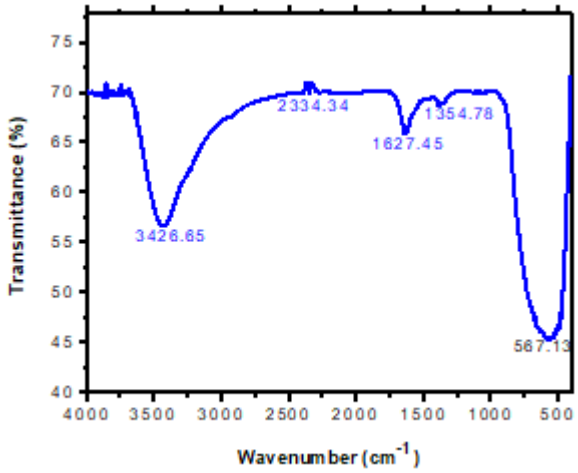

Figure 15: FTIR spectrum of 500°C calcined TiO_2 (1:1) NPs

Figure 16 a and b shows the FTIR spectra of uncalcinated and calcinated CuO NPs. Based on the FTIR spectrum of CuO NPs, the most significant absorption peaks are the one at 531 and 603 cm^{-1}. The phonon bands at correspond to the stretching vibration of Cu–O bond in monoclinic CuO. There is a study reported that CuO (M-O) stretching occurs at 528 cm^{-1} (Mohammed *et al.*, 2015; Sadeghi *et al.*, 2015). The strong peak at (1030 and 1053 cm^{-1}) is due to C-O stretching vibration in carboxylic group and flavanones. The characterized peak observed at (1383 cm^{-1}) is C-N stretching vibration in amine group (Sadeghi. *et al*, 2015).The strong band at (1604 and 1638 cm^{-1}) was due to aromatic C=C bending vibration and absorption peaks at 2875 cm^{-1} and 2884 cm^{-1} were attributed to asymmetric and symmetric C-H stretching mode which caused by the phenolic compounds (Sankar *et al.*, 2014). The broad band at 3439 cm^{-1} was due to O-H stretching vibration in alcohols. This disappeared peak indicates the phytochemical present in the leaf extract, which is involved in reduction and capping of copper oxide nanoparticles.

3.7. Absorption Spectra of Sensitizers

The optical absorption spectrum of *kniphofia schemperi* and crystal violet sensitizers shows an absorption spectrum at 531 and 440 nm, respectively. The absorption of *kniphofia schemperi* ascribes to the component namely, anthocyanin, a group of natural phenolic compounds (Suganya *et al.*, 2014). This result confirms that the pigment extracted from this natural dye can be used as a photosensitizer because it strongly absorbs photons in the UV-Vis region of electromagnetic radiation. Figure 17 reveals the corresponding optical absorption of *kniphofia schemperi* sensitizers. One of the essential requirements of best performing photosensitizer is broad and intense absorption in the UV-Vis and near-IR region of the solar spectrum.

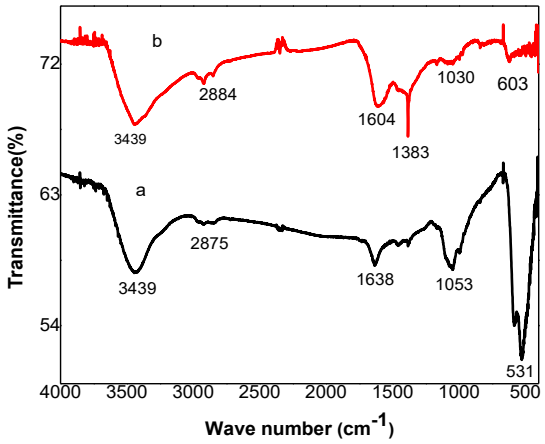

Figure 16: FTIR spectrum of (a) calcinated and (b) uncalcinated 1:10 ratios of synthesized CuO NPs.

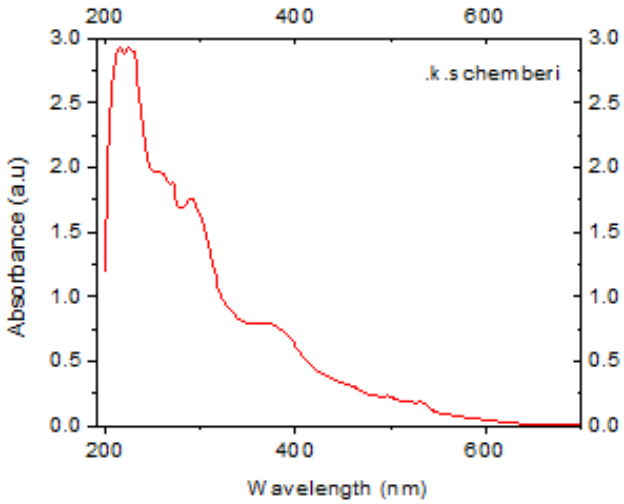

Figure 17: Optical absorption of *kniphofia schemperi (in ethanol extract)*

3.8. Current density -Voltage Characteristics of TiO_2 based DSSCs

The photovoltaic tests of DSSCs prepared using a natural sensitizer extracted from roots of *kniphofia schemperi* and a synthetic sensitizer prepared from crystal violet were performed by measuring the current density-voltage (J-V) characteristic curves by using Oriel Class Solar Simulator under the standard light intensity of illumination (100 mW/cm^2).

The performances of the resulting DSSCs prepared from biosynthesized TiO_2 NPs and the sensitizers were evaluated by different parameters such as short circuit current density, incident Photon to current efficiency also known as quantum efficiency, open circuit-voltage, fill-factor. A typical current density-voltage (J-V) curve of the as prepared DSSCs using roots of *kniphofia schemperi* are shown in Figure 18.

The power conversion efficiency of these DSSCs obtained using ethanolic root extract of *kniphofia schemperi* sensitizer with TiO_2 (2:1) biosynthesized Photoelectrodes shows highest value (1.3%) relative to the remaining two ratios and also it shows the maximum open circuit voltage (161 mV). Figure 16 indicates J-V curve of DSSs prepared using different ratios of TiO_2 NPs in the presence of crystal violet sensitizer.

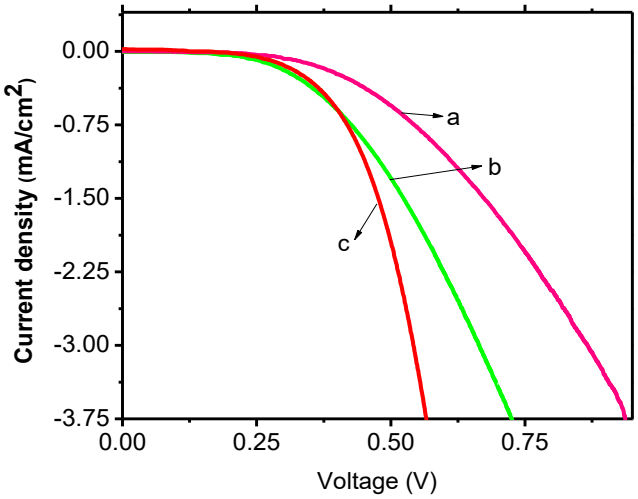

Figure 18: J-V curve of root of *kniphofia schemperi* based DSSCs using TiO_2 a) 2:1, b) 1:1 and c) 1:2.

The improvement in J_{SC} value of TiO_2 (2:1) based DSSC is basically due to the improved absorption of light caused by larger sensitizer coated area of the biosynthesized nanoparticles. As it can be explained from Figure 18, TiO_2 (1:2) based DSSCs shows decrease in J_{SC} which may be attributed to slower electron injection of the extracted sensitizer or due to self-quenching if they undergo aggregation, either before or during dye adsorption process was performed on the biosynthesized metal oxides.

Table 1: Photovoltaic performance of biosynthesized TiO_2 based DSSCs using *kniphofia schemperi*

TiO_2 ratio	J_{SC} (mA/cm^2)	V_{OC} (mV)	J_{max} (mA/cm^2)	V_{max} (mV)	P_{max} (mW/cm^2)	FF %	η%
1:1	$6.05x10^{-3}$	48	$4.17x10^{-3}$	28	$1.17x10^{-1}$	40.3	0.117
2:1	$2.46x10^{-2}$	161	$1.84x10^{-2}$	70.6	1.30	32.8	1.300
1:2	$1.29x10^{-3}$	63	$8.97x10^{-4}$	38	$3.41x10^{-2}$	42	0.034

According to Table 1, maximum DSSCs efficiency was recorded using TiO_2 NPs (2:1), this is due to the more crystalline nature of TiO_2 NPs that allows more dye adsorption and also its larger band gap energy, higher interaction between TiO_2 nano crystalline film and the root extract of the sensitizer which leads to a better charge transfer.

In general the efficiencies of DSSCs not only depend on the molecular structure of the natural pigment, but also depends strongly on the properties of the biosynthesized photoelectrodes such as surface morphology, self-assembly and aggregation of the dye molecules (Wasana *et al*, 2015)). It has been earlier reported that the conversion efficiency of most of the DSSC made from natural dyes and some organic synthetic dyes suffers from low open circuit voltage which is also the case in the present study where the open circuit voltage obtained ranges from 0.029 - 0.161 V.

3.9. IPCE Characteristics of Biosynthesized TiO_2 based DSSCs

Photoaction spectra provided further insights on the photoelectrochemical behavior of biosynthesized photoelectrodes with the presence of sensitizers. Figure 19 shows the IPCE of DSScs with TiO_2 NPs (2:1) photoelectrodes sensitized with *kniphofia schemperi*.

As it can be observed from Figure 19 IPCE% value was obtained using TiO_2 (2:1) in the presence of ethanolic root extract of *kniphofia schemperi* and this value is 8.11% which was located at a wavelength of 340 nm. The improvement of IPCE% for this biosynthesized photoelectrode results from higher electron transportation at the

electrolyte interfaces and good electrocalytic activity of the photoelectrode (O'Regan *et al*, 2005). Again TiO_2 (1:1) with the presence of *kniphofia schemperi* sensitizer possess an IPCE% of 2.66% which occurs at 500 nm. This action spectra response is contributed by sensitizer.

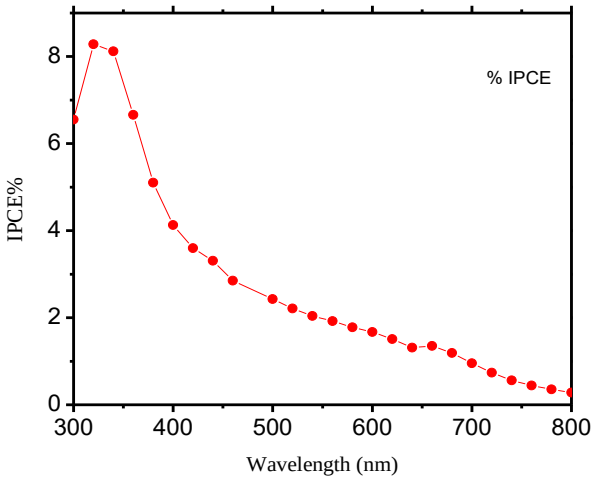

Figure 19: IPCE% spectra of TiO_2 a (2:1) based DSSCs using *kniphofia schemperi*.

3.9.1. Current Density -Voltage Characteristics of CuO NPs Based Dye-Sensitized Solar Cells

The photovoltaic tests of the fabricated DSSCs using the natural sensitizers extracted from kniphofia schemperi and Crystal violet dye were performed by measuring the current density-voltage (J-V) characteristic curves. The performances of the DSSCs were evaluated by using their short circuit current density (Jsc), open circuit voltage (Voc), and maximum power point from the J-V curves and calculated fill factor. The typical current density–voltage (J-V) curves of fabricated DSSCs using natural dyes extracted from kniphofia schemperi and Crystal violet dye for each ratio of the as synthesized CuO NPs paste as a counter electrode were tested and their J-V curves are shown below. Figure 20 and 20 a, b and c shows the J-V curve of DSSCs fabricated using CuO NPs as counter electrode which was synthesized in the ratio of (a) 1:10, (b) 3:10 and (c) 1:2 of precursor mass to volume of catha edulis extract using crystal violet dye and kniphofia schemperi extracted dye photosensitizers ((Figure 21 a-c)) respectively.

The photovoltaic parameters, short circuit current (Jsc) and open circuit voltage (Voc), were determined from the J-V curve and fill factor (FF) and power conversion efficiency (η) were calculated from the corresponding parameters. The average short circuit current for the cells is higher in the DSSC where small band gap energy copper oxide based counter electrodes in 1:10 ratio of synthesized CuO NPs was used.

The higher Jsc in small band gap energy copper oxide based counter electrode solar cell is due to good energy levels alignment that facilitates charge dissociation (Gao et al., 2015). In this ratio the synthesized CuO NPs resulted in maximum conversion efficiency in both *kniphofia schemperi* and crystal violet photosensitizers.

Table 2 shows the summary of photovoltaic parameters of DSSCs fabricated using CuO NPs as counter electrode which was synthesized using different ratios of precursor mass to volume of *khat edulis*

As it can be observed from Table 2, the current density generated from the fabricated DSSCs using CuO NPs as counter electrode is low. The low current generation of the devices could be due to inefficient light harvesting efficiency (LHE) by the dye, inefficient charge injection into TiO_2, or inefficient collection of injected electrons.

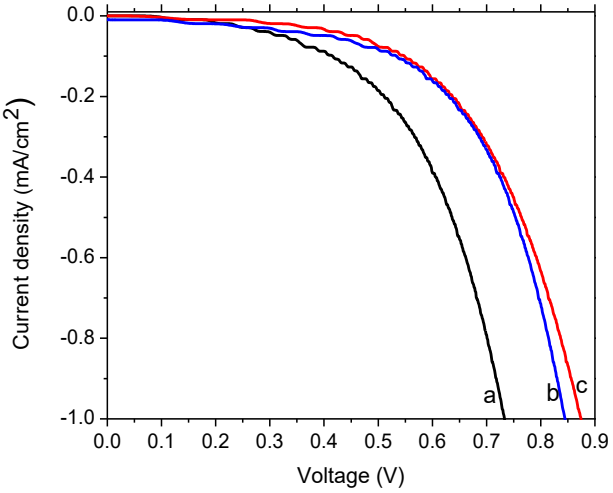

Figure 20: J–V curve of DSSC fabricated with counter electrode based on (a) 1:10, (b) 3:10 and (c) 1:2 ratios synthesized CuO NPs using crystal violet dye.

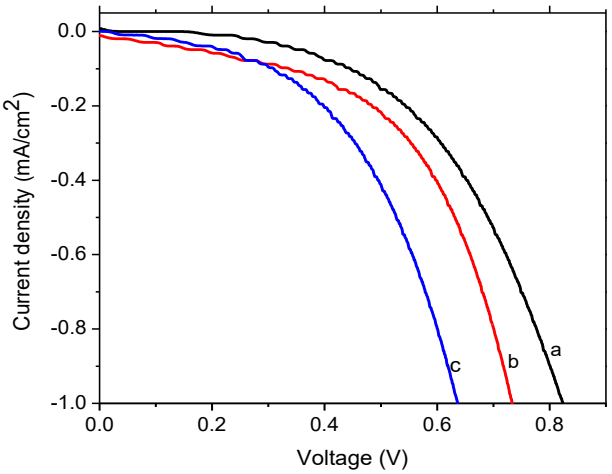

Figure 21: J–V curve of DSSC fabricated with counter electrode based on (a) 1:10, (b) 3:10 and (c) 1:2 ratios synthesized CuO NPs using *Kniphofia schemperi* dye.

Table 2: Photovoltaic parameters of the DSSCs fabricated using CuO NPs as counter electrode and sensitized with natural dyes extracted from *kniphofia schemperi* root and commercial crystal violet dye.

Dyes Used	Solvent	Ratios	J_{sc} (mA/cm^2)	V_{oc}(mV)	P_{max}(mW/cm^2)	FF (%)	η (%)
		1:10	3.03×10^{-3}	68	1.2×10^{-1}	58.2	0.12
Crystal Violet Dye	Distilled Water	3:10	1.29×10^{-3}	46	3.05×10^{-2}	51.4	0.031
		1:2	1.52×10^{-4}	34	2.38×10^{-3}	46.1	0.0024
		1:10	2.03×10^{-3}	139	1.65×10^{-1}	67	0.165
Kniphofia Schemperi Dye	Ethanol	3:10	1.09×10^{-3}	154	7.25×10^{-2}	43.2	0.0725
		1:2	4.04×10^{-4}	110	2.47×10^{-2}	55.6	0.0247

Furthermore, low LHE can be due to a low dye absorption coefficient over the solar spectrum, a low dye concentration, a thin TiO_2 film to support large concentration of adsorbed dye which absorbs a significant fraction of the incident light, insufficient light scattering within the film, absorption of light by TiO_2 or the redox electrolyte, and dye degradation (Halme J. et al , 2015).

3.9.2. Incidence Photon to Current Conversion Efficiency (IPCE)

The incident photon to current conversion efficiency (IPCE) of natural and synthetic pigments sensitized DSSCs with TiO_2 photoelectrode and CuO nanoparticles based counter electrode was calculated using Equation 2.2 from experimentally generated data. Figure 22 and 23 show the action spectra for the DSSCs sensitized using Kniphofia schemperi and crystal violet dyes respectively.

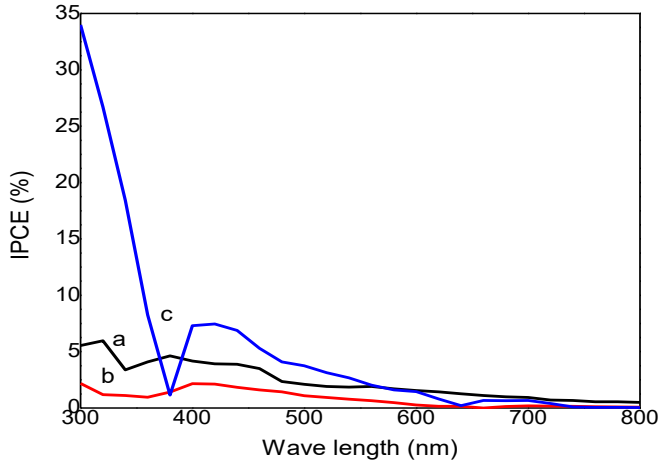

Figure 22: IPCE of CuO (a) 1:10, (b) 3:10 and (c) 1:2 ratios based DSSCs sensitized by crystal violet dye with water.

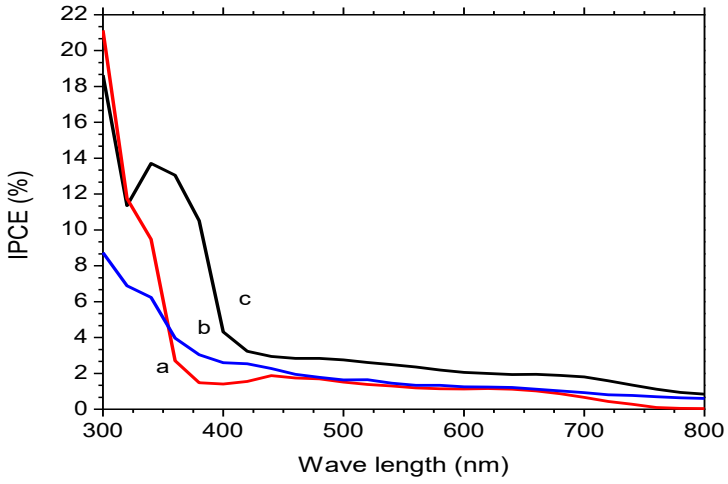

Figure 23: IPCE of CuO (a) 1:10, (b) 3:10 and (c) 1:2 ratios based DSSCs sensitized by *Kniphofia schemperi* dye with ethanol

As observed from Figure 22 and 23, IPCE of the fabricated DSSCs are very low that of course agrees with the low current density of the devices.

4. CONCLUSION

TiO_2 NPs were successfully biosynthesized using titanium tetra butoxide precursor and *kniphofia foliosa* root extract within different ratios. More crystalline nature and best performing TiO_2 NPs was obtained from the synthesis in 1:1 and 2:1 ratio. The particles were found to be thermally stable above 500^0C. XRD analysis has confirmed that the average particle size of TiO_2 NPs in the range of 8.17 - 10.15 nm. SEM-EDS reveal the surface morphology as spherical and this analysis also indicates presence of only the element Ti and O. The internal structure and crystalline nature of TiO_2 NPs were found to be spherical as confirmed using TEM and its SAED pattern. The band gap was calculated in the range of 3.95 - 4.16 eV. Among the different ratios of biosynthesized TiO_2 NPs, best solar cell with power conversion of 1.3% was achieved from the device prepared from TiO_2 TiO_2 NPs (2:1) .

The synthesized CuO NPs were extensively characterized in terms of morphology, crystalline nature, structural, and photovoltaic properties using various experimental tools. The synthesized CuO NPs possess well crystalline nature which is perfectly matched to spherical structure of bulk CuO. Moderately medium solar to electrical energy conversion efficiency of 0.165% with short circuit current density (J_{SC}) of 2.03 x 10^{-3} mA/cm^2, open circuit voltage (V_{OC}) of 139 mV and fill factor (FF) of 67% was recorded in the DSSC fabricated with synthesized CuO NPs based counter electrode. Therefore, this work showed that *Catha edulis* can be used for bio-synthesis of CuO NPs which is low cost & ecofriendly method of nanoparticle synthesis. Furthermore, this work showed that the biosynthesized CuO NPs using *Catha edulis* were applied as efficient counter electrode for the fabrication of DSSCs that may replace other expensive counter electrodes like platinum which are used for the fabrication of DSSCs.

REFERENCES

Abate G., and Etse D., (1989). "Ethiopian traditional medicien," pp. 99.

Al-Alwani. M. A. M, Mohamad. A. B, Kadhum. A.A.H and Ludin. N. A., (2015). "Natural dye extracted from Pandannus amaryllifolius leaves as sensitizer in fabrication of dye sensitized solar cells". *Mol Biomol Spectrosc. Acta Part A,* vol. 138, pp. 130.

Aparna Y., Enkateswara Rao, K.V. and Srinivasa Subbarao P., (2016). Synthesis and characterization of CuO nanoparticles by novel sol gel method. *Journal of Environmental Science and Biotechnology,* 48: pp. 30-33.

Archana Maurya, Pratima Chauhan, Amita Mishra, and Abhay. K. Pandey, (2012). "Surface functionalization of TiO2 with plant extracts and their combined antimicrobial activities against E. Faecalis and E. Coli" . *J. Res. Updates Poly. Sci.,* vol. 1, pp. 4.

Calogero. G, Dimarco. G, Cazzanti. S, Caramori. S, Argazzi. R, Dicarlo. A, Bignozzi. C.A., (2010). "Dye Sensitized Solar Cells Using Natural Pigments from Five Plants and quasi-solid State Electrolyte" . *Int J Mol Sci.,* vol. 11, pp. 254.

Chang Kook Hong, (2015). "Electrochemical Properties of Electrodeposited PEDOT Counter Electrode for DSSC". *Int J Electrochem Sci.,* vol. 10, pp. 5521.

Fan. L, Kang. S, Wu. J, Hao. S, Lan. Z, Lin. J., (2010). "Quasi-solid state Dye-sensitized solar cells based on polyvinylpyrrolidone with ionic liquid". *J Energy sourc A,* vol. 32, pp. 1559.

Figgemeier. E, Kylberg.W, Constable. E, M. Scarisoreanu, Alexandrescu. R, Morjan. I Soare. I, Birjega. R, Popovici. E, Fleaca. C, Gavrila-Florescu. L, Prodan. G., (2007). "Titanium dioxide nanoparticles prepared by laser pyrolysis: Synthesis and photocatalytic properties" . *Appl Surf Sci.,* vol. 254, pp. 1037.

Gao.Y, Masuda.Y, Peng. Z, Yonazawa. T, Kaumoto. K., (2007). "Green synthesis of TiO_2 and its Photocatalytic activity" . *J Mater Chem.,* vol. 13, pp. 608.

Gong. J, Liang .J, Sumathy. K.,(2012). "Review on dye-sensitized solar cells, Energy Reviews." *Inorg Chem.,* vol. 16, pp. 5848.

Gr¨atzel. M, Janssen. R. A. J, Mitzi. D. B, Sargent. E. H., (2012). "Material interface engineering for solution-processed photovoltaics". *Nat.,* vol. 488, pp. 304.

Jose. R, Thavasi.V, Ramakrishna. S., (2009). "Metal oxides for dye sensitized solar cells". *J Am Soc.*, vol. 92, pp. 289 - 301.

Macht. B, M, Turrion. A, Barkschat. P, Salvador. K, Ellmer, Tributsch. H., (2002). "Effects of water intrusion on the charge-carrier dynamics, performance, and stability of dye sensitized solar cells" . *Sol Energy Mater Sol Cells*, vol. 73, pp. 163.

Malarkodi. C, Chitra. K, Rajeshkumar. S, Gnanajobitha. G, Paulkumar. K, Vanaja. M, Annadurai. G., (2013). "Novel eco-friendly synthesis of titanium oxide nanoparticles by using Planomicrobium sp. and its antimicrobial evaluation" . *Der Pharmacia Sinica.*, vol. 4, no. 3, pp. 59.

Muneer M. Ba-Abbad, Abdul Amir H. Kadhum, Abu Bakar Mohamad, Mohd S. Takriff and Kamaruzzaman Sopian, (2012)."Synthesis and Catalytic Activity of TiO_2 Nanoparticles for Photochemical Oxidation of Concentrated Chlorophenols under Direct Solar Radiation". *Int J Electrochem Sci.*, vol. 7, pp. 4871.

Nazeeruddin. M. K, Kay. A, Rodicio. I, Humphrey-Baker. R, Muller. E, Liska. P, Vlachopoulos. N, Gratzel. M., (1993). "Dye Sensitized Solar Cells Using Natural Pigments from Five Plants and Quasi-Solid State Electrolyte". *J Am Chem Soci.*,vol. 115, pp. 6382.

O´Regan. B, Gr¨tzel. M., (1991). "A low-cost, high-efficiency solar cell based on dye-sensitized colloidal TiO2 films" . *Nat*, vol. 353, pp. 737.

Pusit Pookmanee, Sukon Phanichphant, (2009). "Titanium dioxide powder prepared by a sol gel method" . *J Ceram Process Res.*, vol. 10, no. 2, pp. 167.

Ramimoghadam. D. M. Z, Bin Hussein, Y. H. Taufiq-Yap., (2013). "Hydrothermal synthesi of zinc oxide nanoparticles using rice as soft biotemplate" . *Chem Cent J.*, vol. 7, no. 1, pp. 36.

Rao. G. K, Ashok. C, Rao V. K, Chakra. S.C, Rajendar. V., (2015). "Synthesis of TiO_2 nanoparticles from orange fruit waste" . *Int J Multi Adva Res Trend*, vol. 2, no. 1, pp. 82.

O´Regan.B. C, Scully. S, Mayer. A. C, Palomares. E, Durrant. J., (2005). "An efficient and low-cost TiO_2 compact layer for performance improvement of dye-sensitized solar cells". *J Phys Chem. B.*, vol. 109, pp. 14616.

Rodriguez-Sanchez. L, Blanco. M. C. and Lopez-Quintela M. A., (2000). "Electrochemical synthesis of silver nanoparticles" . *J Phys Chem.*, vol. 104, no. 41, pp. 9683.

Santhosh kumar.T, Rahuman. A, Jayaseelan. C, Rajakumar. G, Marimuthu. S, Kirthi. A., (2014). "Green synthesis of titanium dioxide nanoparticles using Psidium guajava extract and its antibacterial and antioxidant properties" . *Asian Pac J Trop Dis.*, vol. 7, pp. 96.

Suganya. P., (2014). "The effects of temperature and pH on stability of anthocyanins from red sorghum (Sorghum bicolor) bran". *Afr J Food Sci.*, vol. 6, no. 24, pp. 567.

Tamasa panigrahi, Dr. suman jha, (2013). "Synthesis and characterization of silve nanoparticles using the leaf of Azadirachta indica" . *J Radiat Res Appl Sci.*, vol. 1, pp. 12.

Vijayalakshmi. R, Rajendran.V., (2012). "Synthesis and characterization of nano-TiO_2 via different methods" . *Archi Appl Sci Res.*, vol. 4, no. 2, pp. 1183.

Wasan Maiaugree, (2015)."A dye sensitized solar cell using natural counter electrode and natural dye derived from mango steen peel waste". *Sci Rep.*, vol. 5, pp. 15230.

Xu .J, Li. L, Yan. Y, Wang. H, Wang. X, Fu. X, Li. G., (2008). "Synthesis and photoluminescence of well dispersible anatase TiO_2 nanoparticles" . *J Colloid and interface Sci.*, vol. 318, pp. 29.

Faheem I., Sammia S., Shakeel A. K., Waqar A., Sabah Z., (2017). Green synthesis of copper oxide nanoparticles using Abutilon indicum leaf extract: Antimicrobial, antioxidant and photocatalytic dye degradation activities. *Tropical Journal of Pharmaceutical Research*, 16: pp. 743-753.

Guo S. Q., Sun M.Q., Gao G. D., Liu L., (2015). Scalable low-cost CdS nanospheres@ grapheme nanocomposites counter electrode for high efficiency dye-sensitized solar cells. *Electrochimica Acta*, 176: pp. 1165- 1170.

Halme J., Vahermaa P., Miettunen K. and Lund P., (2010). Natural dye sensitized phothoelectrochemical cells based on zinc oxide nanoparticles. *Advanced Materials*, 22: pp. 210-221

Jitendra K. S., Shaheer M. A., Ameen S., Pratibha S. and Gurdip S., (2015). Green synthesis of CuO nanoparticles with leaf extract of Calotropis gigantea and its dye-sensitized solar cells applications.*Journal of Alloys and Compounds*, 632: pp. 321-325.

Mahmoud A.M. et al.,"Natural dye extracted from Pandannus amaryllifolius leaves as sensitizer in fabrication of dye sensitized solar cells," *Int. J. Electrochem. Sci.* **12** (2017) 747-761 (2016) [www.electrochemsci.org].

Mahmoud N., S. Mohammad S., Akbar R. V., (2015). Green synthesis of CuO nanoparticles by aqueous extract of *Anthemisnobilis* flowers and their catalytic activity for the A^3 coupling reaction. *Journal of Colloid and Interface Science*, 459: pp. 183-188.

Malarkodi C. et al.,"Novel eco-friendly synthesis of titanium oxide nanoparticles by using Planomicrobium sp. and its antimicrobial evaluation," *Der Pharmacia Sinica.* **4**(3), 59-66 (2013) [https://www.researchgate.net/publication/237048624].

Meidan Y., Xiaoru W., Mengye K. Wang J., (2015). Recent advances in dye-sensitized solar cells: from photoanodes, sensitizers and electrolytes to counter electrodes. *Materials Today*, 18: pp. 155-162.

Murakami T. N. and Grätzel M., (2008). Counter electrodes for DSSC application of functional materials as catalysts. *Inorganic Chemical Acta*, 361: pp. 569-572.

Naika H. R., Lingaraju K., Manjunath K., Kumar D., Nagaraju G., Suresh D. and Nagabhushana H., (2015). Green synthesis of CuO nanoparticles using *Gloriosa superba* L. extract and their antibacterial activity. *Journal* of *Taibah*an *University of Science*, 9: pp 7-15.

Rao A. N. S. and Venkatarangaiah V. T., (2014).The effect of ceyltrimethylammonium bromide on size and morphology of ZnO and CuO. *Journal of Electrochemical Science and Engineering*, 4: pp. 97-110.

Sadeghi B., Rostami A., Momeni S.S., (2015). Facile green synthesis of silver nanoparticles using seed aqueous extract of Pistacia atlantica and its antibacterial activity. *Spectrochim Acta*, 134: pp. 326-332.

Sankar R., Manikandan P., Malarvizhi V., Fathima T., Shivashangari K. S., Ravikumar V., (2014). Green synthesis of colloidal copper oxide nanoparticles using Carica papaya and its application in photocatalytic dye degradation. *Spectrochim Acta Mol Biomol Spectrosc*, 121: pp. 746-750.

Sundaramurthy N. and Parthiban C., (2015). Biosynthesis of copper oxide nanoparticles using *Pryus Pyrifolia* leaf extract and evolve the catalytic activity. *International Research Journal of Engineering and Technology*, 2: pp. 332-338.

Taleb C., Pettai M. and Pileni P., (1998).Nanoparticles and nanostructured films preparation. *Characterization applied Chemistry*, 22: pp. 1203-1203.

Zou Z., Qiu Y., Xie C., Xu J., Luo Y., Wang C. and Yan H., (2015). CdS/TiO_2 nanocomposite films and its enhanced photoelectric responses to dry air and formaldehyde induced by visible light at room temperature. *Journal of Alloys Compound*, 645: pp. 17-23.